



TESIS DOCTORAL FRANCISCO JAVIER VALVERDE MUÑOZ 2019



VNIVERSITAT [Q*] Facultat de Química
ID VALÈNCIA

INSTITUTO DE CIENCIA MOLECULAR

Programa de doctorado: Nanociencia y Nanotecnología

**Diseño, síntesis y caracterización de materiales
moleculares multifuncionales conmutables**

Tesis Doctoral presentada por:

FRANCISCO JAVIER VALVERDE MUÑOZ

Dirigida por:
Prof. Dr. José Antonio Real Cabezos

Octubre, 2019

Universitat de València

Facultat de Química
Instituto de Ciencia Molecular (ICMol)



VNIVERSITAT
DE VALÈNCIA

**Diseño, síntesis y caracterización de materiales
moleculares multifuncionales conmutables**

Programa de Doctorado:

Programa de Doctorado en Nanociencia y Nanotecnología (RD99/2011)

Doctorando:

Francisco Javier Valverde Muñoz

Director de la tesis:

Prof. Dr. José Antonio Real Cabezos

Octubre, 2019



VNIVERSITAT
DE VALÈNCIA



El Prof. Dr. **José Antonio Real Cabezos**, Catedrático del Departamento de Química Inorgánica de la Universitat de València, adscrito al Instituto de Ciencia Molecular (ICMol),

CERTIFICA:

Que la presente Tesis Doctoral, titulada: **Diseño, síntesis y caracterización de materiales moleculares multifuncionales conmutables**, se ha realizado bajo su dirección en el Instituto de Ciencia Molecular (ICMol) en la Universitat de València por el Licenciado en Química Francisco Javier Valverde Muñoz, y autoriza su presentación para optar al grado de Doctor en Nanociencia y Nanotecnología por la Universitat de València.

En Paterna, a 14 de Octubre de 2019.

Prof. Dr. José Antonio Real Cabezos
Director y tutor

“Nothing in life is to be feared, it is only to be understood.
Now is the time to understand more, so that we may fear less.”

Marie Curie

AGRADECIMIENTOS

Y llegó el día. El día en el que se cierra una de las etapas más emocionantes de mi vida. Ha sido un largo periodo de *pico y pala* pero, sinceramente, cada instante invertido ha merecido realmente la pena. Por supuesto, superar este reto hubiese sido imposible sin la presencia de gente maravillosa a mí alrededor (¡me considero un gran afortunado!), gente que ha sabido indicarme cuál era el camino correcto, gente que me ha hecho pensar y recapacitar sobre cómo enfrentarme a ciertas situaciones, personas que han sido apoyos excepcionales durante el arduo desarrollo de esta tesis... Y claro, ahora toca agradecerle a cada uno de ellos su inestimable ayuda durante estos últimos años.

Me gustaría agradecer a mi director de tesis José Antonio Real por haber depositado en mí su confianza para desarrollar esta tesis en su grupo de investigación. Han sido unos cuantos años de buenas discusiones científicas que han servido para inspirarme en el día a día y, al mismo tiempo, me han permitido crecer como investigador. Durante este periodo me he impregnado de tu sabiduría, gran capacidad de trabajo y esfuerzo constante, y gracias a ello ha sido más fácil superar los retos que me propusiste. Por supuesto, gracias por esos "breaks" en los que nos descubrías algún lugar recóndito de cualquier parte del mundo. Gracias infinitas a M^a Carmen Muñoz por toda su labor dentro de este pequeño grupo de investigación, sin lugar a duda eres el punto de apoyo que permite movilizar toda la maquinaria. Eres una persona con una ambición investigadora tremenda que ha conseguido motivarme a lo largo de estos años de una forma muy efectiva (encontraste la tecla). Gracias por compartir conmigo todos tus conocimientos sobre conceptos de cristalografía.

Agradezco a todos los miembros del tribunal y a los evaluadores por acceder a valorar esta tesis Doctoral.

Me gustaría dar las gracias a todos los miembros del grupo de investigación *Switchable Molecular Materials (SMoIMat)* de la Universitat de València con los que he convivido durante los últimos años. Gracias a Ana B. Gaspar por inocularme la semilla del espíritu crítico durante los últimos años de la carrera. Fuiste tú quien me abrió las puertas para pertenecer a este grupo de investigación y te estaré siempre agradecido por ello. Gracias a Sacramento Ferrer por compartir tu entusiasmo y sapiencia durante nuestras discusiones

científicas. Gracias a Zulema Arcís y Tanía Romero por recibirme con los brazos abiertos en el grupo de investigación, siguiendo todos vuestros consejos aprendí rápidamente a desenvolverme en el laboratorio y a manejar el SQUID. Gracias a Maksym Seredyuk por trasmitirme toda su pasión por la ciencia, eres un investigador incombustible dotado de una mente brillante, y me has facilitado ideas excelentes durante el desarrollo de mi tesis. Espero que la conexión Valencia-Kiev siga latente por muchos años. Gracias a Lucía Piñeiro por haber sido una compañera excepcional en el laboratorio, una persona bondadosa con un corazón enorme y currante como ninguna otra (creo que todavía ostentas el record de tubos de difusión por hora). Tienes un potencial tremendo y, sinceramente, he tenido mucha suerte de haberte tenido cerca durante la mayor parte de mi tesis. Gracias a Carlos Bartual, cuyo retorno a sus "orígenes" fue como una bocanada de aire fresco para el grupo de investigación. Las discusiones científicas contigo han sido excepcionales, y me has dado consejos valiosísimos que me van a ser muy útiles en el futuro. Como no, nuestras charlas futboleras (¡Amunt!) y momentos de risas han sido incontables, apareciendo siempre en el momento indicado. Has sido una figura fundamental en el último periodo de mi tesis Doctoral. Gracias a Manuel Meneses y Rubén Turo, la "nueva savia" del laboratorio. Aun siendo los últimos en llegar, habéis calado muy dentro de mí, y me habéis hecho mejorar en muchas facetas de mi vida. Sois el yin y el yang en muchos aspectos, pero tenéis en común unas ganas tremendas de aprender y mejorar, y auguro un excelente futuro para vosotros.

Agradezco también la inestimable ayuda ofrecida por los técnicos del ICMol Gloria Agustí y José María Martínez para caracterizar una buena parte de los materiales que he sintetizados durante esta tesis doctoral. Muchas gracias por vuestro buen saber hacer y, como no, toda la ayuda que me habéis proporcionado para solucionar los problemas que de forma inesperada surgían con el SQUID.

Me gustaría agradecer a Guillaume Chastanet la oportunidad de realizar una estancia de investigación en su grupo. Fue una experiencia muy enriquecedora, donde aprendí nuevas aproximaciones para enfrentarme a nuevos retos sintéticos. Gracias a toda la gente que me ayudó y acompañó durante dicha estancia, pero sobre todo a Mathieu Gonidec y a Juan H. González. Fue excepcional trabajar codo con codo junto a vosotros durante ese periodo y solo queda agradecer el haberme dado todas las herramientas necesarias para sumergirme en el intrigante mundo de la microfluídica.

Voldria agrair des de el fons de les meves entranyes el suport dels meus amics de "tota la vida". Moltíssimes gràcies a Fran Pla, Pablo Ruiz, Juanjo Lorente, Víctor Roig, Pep Fuster, Nando Marrahí, Aaron Francés, Antonio Descals, Dani Olcina i José Martí per haver estat al meu costat durant els darrers anys. Sense adonar-vos heu tingut un paper fonamental en el desenvolupament d'aquesta tesi, ja que les sortides matutines de *trail running* i esmorçarets, els *Angelus*, les infinites discussions sobre esports i les nits de "jaleo" han sigut els moments perfectes de desconexió que m'han permès carregar les piles per a afrontar els complicats reptes de la ciència. No voldria oblidar-me tampoc de tots els components de Baketà (actuals i passats) amb els que he pogut compartir grans moments en els últims anys. Gràcies per tot.

A mis padres, Maica y Paco, gracias por apoyarme en absolutamente TODO. Habéis sido un pilar fundamental desde que decidí venirme a la *capí* para estudiar, y está claro que sin vuestra ayuda nunca hubiese sido posible llegar hasta este punto. Aunque mis inicios fueron muy dubitativos, vosotros nunca dudasteis del potencial que escondía dentro. Agradeceros el haberme inculcado valores tan excepcionales como el respeto, la honestidad y la humildad que tanto me han servido para crecer rápidamente como persona en el día a día. Por supuesto, gracias por darme toques de atención cuando los merecía, sobre todo cuando me dejaba las cosas para última hora (mi gran tendencia a vivir al borde de los *deadlines*). Gracias a Carme, la pequeña de casa, por ser una persona tan preciosa por dentro y por fuera. Tus comentarios directos de carácter constructivo siempre han sido bien recibidos, fuere para lo que fuere. Os quiero muchísimo, aunque muchas veces me cueste expresarlo. También me gustaría agradecer todo el apoyo recibido de mi maravillosa familia, esa que por motivos de distancia ha estado un poco desatendida por mi parte durante el desarrollo de esta tesis (las horas perdidas se devolverán con intereses). Una pequeña parte de cada uno de vosotros se encuentra escondida en este trabajo.

I per últim agrair a l'amor de la meva vida, Mer, tota la seva estima durant aquests anys. Moltíssimes gràcies per cuidar-me com tu tant bé saps fer, has sigut la perfecta companya durant aquest viatge i ja saps que encara ens queden molts kilòmetres per recórrer junts. Has tingut una paciència infinita amb mi en aquest període, sobretot quan em tocava mesurar amb el *Nesquik* a hores intempestives o tenia que acabar qualsevol feina per a ahir. Si he superat aquest repte ha sigut gràcies a veure dibuixat un somriure en la teva cara cada matí, ja que em donava les forces necessàries per poder aconseguir-ho. T'estime molt.

Indice

| | |
|--|-----|
| Resumen | 3 |
| Summary | 9 |
| Capítulo 1.- Introducción | |
| 1.1.- Aspectos generales del fenómeno de transición de espín (SCO) | 17 |
| 1.1.1.- Fundamento teórico del fenómeno SCO: teoría del campo de ligandos y diagramas de energía potencial | 18 |
| 1.1.2.- Fotoconversión en compuestos SCO: Efecto LIESST | 24 |
| 1.1.3.- Comportamiento colectivo del conjunto de centros SCO: cooperatividad | 26 |
| 1.1.4.- Técnicas de caracterización de compuestos SCO | 30 |
| 1.2.- Objetivos de la tesis doctoral | 31 |
| 1.3.- Metodología | 33 |
| 1.4.- Bibliografía | 33 |
| Capítulo 2.- Strong Cooperative Spin Crossover in 2D and 3D Fe^{II}-M^{I,II} Hofmann-Like Coordination Polymers Based on 2-Fluoropyrazine | |
| Artículo | 39 |
| Material suplementario | 64 |
| Capítulo 3.- Switchable Spin-Crossover Hofmann-Type 3D Coordination Polymers Based on Tri- and Tetratopic Ligands | |
| Artículo | 73 |
| Material suplementario | 94 |
| Capítulo 4.- Influence of Host-Guest and Host-Host Interactions on the Spin-Crossover 3D Hofmann-type Clathrates {Fe^{II}(pina)[M^I(CN)₂]₂}. xMeOH (M^I = Ag, Au) | |
| Artículo | 107 |
| Material suplementario | 126 |

Capítulo 5.- Very Long-Lived Photogenerated High-Spin Phase of a Multistable Spin-Crossover Molecular Material

| | |
|------------------------|-----|
| Artículo | 133 |
| Material suplementario | 151 |

Capítulo 6.- Discrimination between two memory channels by molecular alloying in a doubly bistable spin crossover material

| | |
|------------------------|-----|
| Artículo | 181 |
| Material suplementario | 203 |

Capítulo 7.- Breaking the rule: access to thermodynamically prohibited “reverse” spin crossover in iron(II) complexes

| | |
|------------------------|-----|
| Artículo | 217 |
| Material suplementario | 234 |

Capítulo 8.- Conclusiones finales

| | |
|--------------|-----|
| Conclusiones | 245 |
| Conclusions | 251 |

Apéndice

| | |
|-----------|-----|
| Artículos | 259 |
|-----------|-----|

RESUMEN

Este trabajo de Tesis Doctoral recoge la síntesis y caracterización de una nueva generación de materiales moleculares conmutables que presentan el fenómeno de transición de espín (*spin crossover*, SCO). El objetivo principal de esta Tesis Doctoral se ha centrado en el diseño racional de nuevos materiales multifuncionales de Fe(II) para el desarrollo de nuevas plataformas moleculares biestables que permitan el estudio detallado del comportamiento SCO sincronizado con nuevas propiedades físico-químicas, como pueden ser la química huésped-anfitrión, transiciones de fase sólido-líquido, dopaje químico,... La estrecha interrelación entre el fenómeno SCO y la segunda propiedad ha sido monitorizada, principalmente, mediante estudios magnéticos y cristalográficos, manifestándose relaciones magneto-estructurales clave que potencian la incorporación de estos materiales prometedores en nuevas aplicaciones tecnológicas.

El capítulo uno presenta los conceptos teóricos más importantes del fenómeno SCO. Este comportamiento singular implica la conmutación electrónica reversible entre el estado paramagnético de espín alto y el estado diamagnético de espín bajo que muestran algunos complejos de metales de la primera serie de transición (mayoritariamente compuestos de Fe(II)) cuando se estimulan con una perturbación física externa, como puede ser un gradiente de temperatura y/o de presión, irradiación con luz o incluso interacción con un analito. El cambio de estado de espín en este tipo de materiales sensibles siempre va acompañado de modificaciones de sus propiedades físicas, destacándose cambios en la respuesta magnética, el color, el volumen del material, su constante dieléctrica..., los cuales dependen fuertemente de su estructura electrónica a nivel local.

Al final de este capítulo se introducen los objetivos principales que motivan al desarrollo de esta Tesis Doctoral junto con la metodología experimental establecida para la síntesis y la caracterización de los diferentes compuestos presentados en este manuscrito.

El capítulo dos introduce la síntesis y caracterización de una nueva serie de polímeros de coordinación SCO bidimensionales (2D) y tridimensionales (3D) de tipo Hofmann basados en el autoensamblaje de iones Fe(II), el ligando 2-fluoropiracina (Fpz) y las unidades de construcción $[M^{II}(\text{CN})_4]^{2-}$ ($M^{II} = \text{Ni}, \text{Pd}, \text{Pt}$) o $[\text{Au}^I(\text{CN})_2]$, los cuales muestran unas propiedades

magnéticas, calorimétricas y ópticas muy cooperativas. Los centros de Fe(II) se encuentran en centros de inversión definiendo centros octaédricos axialmente distorsionados. Las posiciones ecuatoriales están ocupadas por cuatro grupos puente centrosimétricos μ_4 - $[M^II(CN)_4]^{2-}$ equivalentes mientras que las posiciones axiales las completan dos ligandos terminales Fpz, generando las capas 2D onduladas $\{Fe(Fpz)_2[M^II(CN)_4]\}$ (**FpzM**). Los derivados **FpzPt** y **FpzPd** presentan un comportamiento SCO termo- y foto-inducido, caracterizado por temperaturas críticas $T_{1/2}$ centradas sobre 155.5 y 116 K y ciclos de histéresis térmica de alrededor de 22 K de anchura, mientras que el derivado **FpzNi** es de espín alto en todo el rango de temperaturas estudiado, incluso al someterlo a presiones hidrostáticas cercanas a 0.7 GPa. La gran estabilidad del estado de espín alto para el derivado **FpzNi** se ha asociado al empaquetamiento mucho más efectivo de las capas bidimensionales, a diferencia de lo que se observa en los estados de espín alto y espín bajo para los derivados **FpzPt** y **FpzPd**. Las redes tridimensionales con fórmula molecular $\{Fe(Fpz)[Pt(CN)_4]\cdot 1/2H_2O$ (**FpzPt3D**) y $\{Fe(Fpz)[Au(CN)_2]_2\}$ (**FpzAu**), donde el ligando Fpz actúa como puente, también se caracterizan detalladamente. La primera de ellas se encuentra en el estado de espín alto en todo el rango de temperaturas estudiado, mientras que la segunda muestra un comportamiento SCO muy cooperativo centrado a 243 K, y acompañado de un ciclo de histéresis de 42.5 K de ancho. Las estructuras cristalinas y las propiedades SCO de estos nuevos compuestos se comparan con compuestos reportados anteriormente de naturaleza similar, como son aquellos basados en los ligandos piracina, 3-fluoropiridina y piridina.

En el capítulo tres se presenta la síntesis de los ligandos 1,3,5-tris(piridin-4-iletinil)benceno (L^{N3}) y 1,2,4,5-tetrakis(piridin-4-iletinil)benceno (L^{N4}), y su uso como unidades básicas de construcción en los nuevos polímeros de coordinación SCO de tipo Hofmann formulados $\{Fe(L^{N3})[M^I(CN)_2]_2\cdot G$ [$M^I = Ag$ (**1-G**), Au (**2-G**); $G =$ nitrobenzono ($PhNO_2$), benzonitrilo ($PhCN$), o -diclorobenceno ($o-PhCl_2$)] y $\{Fe(L^{N4})[Ag_2(CN)_3][Ag(CN)_2]\cdot H_2O$ (**3-H₂O**), respectivamente. La especie L^{N3} actúa como ligando bis-monodentado definiendo redes tridimensionales doblemente interpenetradas que generan cavidades que son ocupadas por moléculas aromáticas huésped. Las redes **1-G** y **2-G** son isoestructurales y muestran un comportamiento SCO de primer orden termo- y foto-inducido, cuyas temperaturas críticas ($T_{1/2}$ y T_{LIESST}) dependen de la naturaleza de la molécula huésped ubicada en los poros del material. La formación "in situ" de las unidades aniónicas $Ag_2(CN)_3^-$ durante el proceso de cristalización permite que L^{N4} logre actuar como un ligando tetrakis-monodentado dando lugar

al compuesto **3·H₂O**, que está constituido por la interpenetración de tres redes tridimensionales idénticas que no permiten la presencia de porosidad significativa. Esta red presenta un comportamiento SCO gradual junto con una fotoconversión incompleta al estado metaestable HS* a bajas temperaturas.

En el capítulo cuatro se presenta la síntesis, caracterización estructural y propiedades magnéticas de dos nuevos compuestos tridimensionales porosos isoestructurales con fórmula molecular general $\{Fe(pina)[M'(CN)_2]_2\} \cdot xMeOH$ ($x = 0 - 5$; $M' = Ag$ y $x \sim 5$ (**1·xMeOH**); $M' = Au$ y $x \sim 5$ (**2·xMeOH**)), siendo *pina* el ligando ambidentado N-(piridin-4-il)isonicotinamida. El análisis mediante difracción de rayos X de monocristal revela que la estructura de **1·xMeOH** (y **2·xMeOH**) viene definida por dos redes tridimensionales equivalentes doblemente interpenetradas, las cuales se estabilizan a través de interacciones metalofílicas $M' \cdots M'$ ($M' = Ag$ o Au) e interacciones por puente de hidrógeno de tipo $C=O \cdots HC$ entre ligandos *pina*. A pesar de la doble interpenetración de las redes, ambos compuestos presentan canales donde es posible incorporar hasta 5 moléculas de metanol que se encuentran interaccionando con los ligandos *pina*, estableciendo una red infinita de contactos por puente de hidrógeno a lo largo de los canales. Las propiedades magnéticas muestran que **1·xMeOH** y **2·xMeOH** presentan comportamientos SCO cooperativos termo-inducidos en dos etapas y cuatro etapas, respectivamente. Sin embargo, la pérdida de las moléculas de metanol conlleva en ambos compuestos un cambio drástico del comportamiento magnético, presentando un comportamiento SCO mucho más gradual e incompleto. Este hecho evidencia la influencia decisiva de las moléculas incluidas en los poros sobre las propiedades SCO de estos materiales. En el proceso de desorción los cristales permanecen intactos, hecho que ha permitido analizar la estructura por difracción de rayos X de monocristal de los compuestos desolvatados **1** y **2** ($x = 0$) y correlacionar los cambios estructurales y la modificación de las propiedades magnéticas.

El capítulo cinco describe la generación de nuevas fases termo- y foto-inducidas del compuesto $[Fe(nBu-im)_3tren](PF_6)_2$ ($(nBu-im)_3tren = n$ -butilimidazoltris(2-etilamino)amina) que presentan una estabilidad cinética extraordinaria, desvelando el mecanismo que conduce a dicha estabilización. En un trabajo previo de nuestro grupo se demostró que este compuesto singular presenta dos comportamientos SCO bien diferenciados, caracterizados por ciclos de histéresis anchos que dependen de la velocidad de barrido de la temperatura. Para velocidades de barrido mayores de 2 K min^{-1} , el comportamiento SCO se caracteriza por una

temperatura crítica promedio $T_c^{av} = 122$ K y un ciclo de histéresis térmico de 14 K de anchura (canal A). En cambio, para barridos inferiores a 0.1 K min^{-1} el comportamiento SCO tiene lugar a la temperatura $T_c^{av} = 156$ K y presentan una anchura de histéresis térmica de 41 K (canal B). Este comportamiento está gobernado por una competición entre dos fases cristalográficamente independientes que se presentan en el estado de espín bajo: una fase cinética (LS_1), la cual es isoestructural a la fase encontrada en el estado de espín alto, y una fase termodinámica (LS_2). Las fases de espín bajo se diferencian en la disposición de las cadenas alquílicas butilo y la organización de los grupos PF_6^- . En este capítulo se constata que el desorden estructural intrínseco de las cadenas alifáticas butilo también juega un papel fundamental en las cinéticas de relajación $\text{HS}^* \rightarrow \text{LS}_1$ obtenidas a partir de las fases metaestables HS^* termo- y foto-generada a bajas temperaturas. Concretamente, la relajación $\text{HS}^* \rightarrow \text{LS}_1$ presenta un periodo de desactivación inusualmente grande de alrededor de 20 h, una vez fotogenerado el estado HS^* a 80 K. Este valor es mayor que el observado cuando el complejo se irradia en el intervalo de temperatura 10 – 70 K. Este hecho se ha estudiado de forma más precisa mediante técnicas de espectroscopia de absorción óptica y difracción de rayos X utilizando radiación sincrotrón sobre monocristal junto con medidas magnéticas. Dependiendo de la temperatura a la que se lleva a cabo la irradiación, el estado metaestable HS^* presenta una organización diferente de las cadenas butilo en los ligandos. De hecho, la reorganización estructural que tiene lugar en las cadenas butilo durante el proceso de relajación para alcanzar la estructura termodinámicamente estable LS_1 es la principal responsable de los tiempos de relajación tan grandes observados en el proceso de desactivación del estado HS^* .

El capítulo seis presenta una estrategia sintética para separar los procesos de transición de fase cristalográfica y SCO mediante el bloqueo de los canales A y B descritos previamente en el compuesto $[\text{Fe}(n\text{Bu-im})_3\text{tren}](\text{PF}_6)_2$ (**100P**). Esta estrategia consiste en la preparación de aleaciones moleculares formuladas genéricamente como $[\text{Fe}_{1-x}\text{M}_x(n\text{Bu-im})_3(\text{tren})](\text{P}_{1-y}\text{As}_y\text{F}_6)_2$ ($\text{M} = \text{Zn}^{\text{II}}, \text{Ni}^{\text{II}}$). El control cuidadoso de la composición de esta serie isomorfa de compuestos ha permitido discriminar entre los dos canales SCO. Por un lado, la sustitución $\text{AsF}_6^- \leftrightarrow \text{PF}_6^-$ estabiliza el canal B observado en **100P** para valores $[x = 0, y \approx 0.7]$, donde la conformación de los grupos butilo y de los aniones $\text{PF}_6^-/\text{AsF}_6^-$ adoptan la fase LS_2 . Por otro lado, cuando se sustituyen los centros activos $\text{Fe}(\text{II})$ por $\text{Zn}(\text{II})$ o $\text{Ni}(\text{II})$ $[x \approx 0.2, y = 0]$ se favorece la conformación de los grupos butilo y del anión PF_6^- de la fase LS_1 , característica del canal A del compuesto **100P**. De forma similar a **100P**, el derivado puro

100As ($x = 0, y = 1$) presenta un comportamiento SCO cooperativo acoplado a una transición de fase estructural reversible que tiene lugar a temperaturas mayores, sin duda debido a la presión química inducida por el volumen mayor del ion AsF_6^- , hecho que también influye sobre las cinéticas de relajación haciéndolas mucho más rápidas e impidiendo la observación de los dos canales de forma independiente. Estos mismos efectos se consiguen aplicando presiones hidrostáticas externas del orden de 0.1 GPa sobre **100P**. Es interesante resaltar que la aplicación de presión externa sobre **100P**, además, convierte su comportamiento SCO termo-inducido en un proceso en dos etapas tal cual se observa para el compuesto **100As**. Este hecho resalta que la aplicación de presión química interna y/o externa puede conducir a efectos similares sobre el comportamiento SCO del material.

El capítulo siete presenta la síntesis y caracterización de una nueva serie de complejos neutros $[\text{Fe}^{\text{II}}(\text{L}^{\text{n}})_2]$ con bajo punto de fusión basados en los ligandos de tipo base de Schiff $\text{L}^{\text{n}} = \text{pm2-n}$ o pyH-n , derivados de la condensación de benzohidracinas funcionalizadas con tres cadenas alquílicas ($\text{C}_n\text{H}_{2n+1}$) (siendo n el número de átomos de carbono que constituyen las cadenas alifáticas, que puede variar en el rango 4 – 14) con una acetona de pirimidina (pm2-n) o un aldehído de piridina (pyH-n), respectivamente. En el estado sólido los compuestos $[\text{Fe}^{\text{II}}(\text{pm2-n})_2]$ presentan dos motivos diferentes en el empaquetamiento cristalino en función de la longitud de la cadena alquílica. Los compuestos con cadenas cortas ($n = 4, 6, 8$) presentan una $T_{1/2}$ cercana a 400 K en el estado sólido, lo que conduce a un cambio abrupto en los valores de susceptibilidad cuando alcanza la fase líquida. Al enfriar, muestran un comportamiento SCO regular muy cooperativo con histéresis térmica, cuyas temperaturas críticas disminuyen al aumentar la longitud de las cadenas alquílicas. En cambio los compuestos definidos por cadenas alquílicas largas ($n = 10, 12, 14$) muestran un comportamiento SCO gradual en el estado sólido, caracterizado por una temperatura crítica $T_{1/2} \sim 275$ K. A temperaturas superiores a ~ 350 K, donde los compuestos son esencialmente HS, se produce el cambio de fase sólido \rightarrow líquido que provoca un comportamiento SCO cooperativo HS \rightarrow LS inverso, entrópicamente prohibido, el cual implica la transformación de alrededor el 50% de centros de Fe(II). Este resultado sin precedentes en complejos SCO de Fe(II) proporciona una nueva forma de modular la dirección del comportamiento SCO aprovechando la inestabilidad conformacional de las cadenas alifáticas.

En el capítulo ocho se presentan las conclusiones finales de la tesis doctoral.

Finalmente, se ha incluido un apéndice que recoge todos los artículos científicos que han dado lugar a la presente Tesis Doctoral.

SUMMARY

This thesis dissertation collects the synthesis and characterization of a new generation of switchable molecular materials that displays the well-known spin crossover (SCO) phenomena. The main goal of this Doctoral thesis has been focused on the rational design of novel multifunctional Fe(II) materials leading to excellent bi-stable molecular-based platforms that has allowed an accurate study of SCO behaviors synchronized with others newfangled physico-chemical properties, as can be host-guest chemistry, solid-liquid phase transitions, chemical doping,...The interplay between SCO and other intimately interlaced property has been monitored, mainly, by crystallographic and magnetic studies, manifesting key magneto-structural relationships that boost the use of this promising materials in new practical applications.

Chapter one of this thesis briefly reviews the most relevant theoretical concepts of the SCO phenomena. This singular behavior is related to the reversible electronic switching between a paramagnetic high spin state (HS) and diamagnetic low spin state (LS) showed by some first-row transition-metal complexes (mostly Fe(II) compounds) under an external physical perturbation, as can be a variation of temperature, pressure or irradiating with a light. The spin state change in this very sensitive class of materials is always accompanied by modifications of many physical properties, i.e. magnetic response, color, volume of the material, dielectric constant..., which strongly depends on their local electronic structure.

At the end of this chapter the motivational purpose in the development of this doctoral thesis together the general experimental procedure established for synthesise and full characterize the different herein presented compounds are introduced.

Chapter two of this thesis introduces the synthesis and characterization of new series of two- (2D) and three-dimensional (3D) Hofmann-like spin crossover (SCO) coordination polymers based on self-assembling iron(II) ions, 2-fluoropyrazine (Fpz), and $[M^{II}(\text{CN})_4]^{2-}$ ($M^{II} = \text{Ni, Pd, Pt}$) or $[\text{Au}^I(\text{CN})_2]^-$ building blocks, which display strong cooperative magnetic, calorimetric, and optical properties. The iron(II) ions, lying on inversion centers, define elongated octahedrons equatorially surrounded by four equivalent centrosymmetric μ_4 - $[M^{II}(\text{CN})_4]^{2-}$ bridging groups. The axial positions are occupied by two terminal Fpz ligands affording significantly corrugated 2D layers $\{\text{Fe}(\text{Fpz})_2[\text{M}^{II}(\text{CN})_4]\}$ (**FpzM**). The **FpzPt** and

FpzPd derivatives undergo thermal- and light-induced SCO characterized by $T_{1/2}$ temperatures centered at 155.5 and 116 K and hysteresis loops 22 K wide, while the **FpzNi** derivate is high spin at all temperatures, even at pressures of 0.7 GPa. The great stability of the high-spin state in the **FpzNi** derivate has tentatively been ascribed to the tight packing of the layers, which contrasts with that of **FpzPt** and **FpzPd** derivatives in the high- and low-spin states. The 3D frameworks formulated as $\{\text{Fe}(\text{Fpz})[\text{Pt}(\text{CN})_4]\} \cdot 1/2\text{H}_2\text{O}$ (**FpzPt3D**) and $\{\text{Fe}(\text{Fpz})[\text{Au}(\text{CN})_2]_2\}$ (**FpzAu**), where Fpz acts as bridging ligand, are also characterized in detail. The former is high spin at all temperatures, while the latter displays very strong cooperative SCO centered at 243 K accompanied by a hysteresis loop 42.5 K wide. The crystal structures and SCO properties are compared with those of related complexes derived from pyrazine, 3-fluoropyridine, and pyridine.

Chapter three of this thesis presents the synthesis of ligands 1,3,5-tris(pyridin-4-ylethynyl)benzene ($\text{L}^{\text{N}3}$) and 1,2,4,5-tetrakis(pyridin-4-ylethynyl)benzene ($\text{L}^{\text{N}4}$), and their use as basic building units in novel SCO Hofmann-like coordination polymers formulated as $\{\text{Fe}(\text{L}^{\text{N}3})[\text{M}^{\text{I}}(\text{CN})_2]_2\} \cdot \text{Guest}$ [$\text{M}^{\text{I}} = \text{Ag}$ (**1-Guest**), Au (**2-Guest**); Guest = nitrobenzene (PhNO_2), benzonitrile (PhCN), *o*-dichlorobenzene (*o*- PhCl_2)] and $\{\text{Fe}(\text{L}^{\text{N}4})[\text{Ag}_2(\text{CN})_3][\text{Ag}(\text{CN})_2] \cdot \text{H}_2\text{O}$ (**3-H₂O**), respectively. The specie $\text{L}^{\text{N}3}$ acts as a bis-monodentate ligand in the double interpenetrated tridimensional networks **1-Guest** and **2-Guest**, defining small cavities where small aromatic molecules are located. The isostructural networks **1-Guest** and **2-Guest** undergo first order thermal- and photo-induced SCO behavior, which critical temperatures ($T_{1/2}$ and T_{LIESST}) are characteristic of each guest molecule hosted in the pores. Favored by the “in situ” generated $\text{Ag}_2(\text{CN})_3^-$ anionic units, the $\text{L}^{\text{N}4}$ ligand acts as a tetrakis-monodentate in compound **3-H₂O**, leading to a poorly porous triply intricated tridimensional coordination polymer. This uncommon network displays a gradual SCO behavior with an incomplete photo-population of the HS* metastable state at low temperatures.

Chapter four of this thesis congregates the synthesis, structural characterization and magnetic properties of two new isostructural porous 3D compounds with general formula $\{\text{Fe}^{\text{II}}(\text{pina})[\text{M}^{\text{I}}(\text{CN})_2]_2\} \cdot x\text{MeOH}$ ($x = 0-5$; *pina* = N-(pyridin-4-yl)isonicotinamide; $\text{M}^{\text{I}} = \text{Ag}^{\text{I}}$ and $x \sim 5$ (**1-xMeOH**); $\text{M}^{\text{I}} = \text{Au}^{\text{I}}$ and $x \sim 5$ (**2-xMeOH**)). The single-crystal X-ray diffraction analyses have revealed that the structure of **1-xMeOH** (or **2-xMeOH**) presents two equivalent doubly interpenetrated 3D frameworks stabilized by both argentophilic (or aurophilic) interactions and interligand $\text{C}=\text{O} \cdots \text{HC}$ H-bonds. Despite the interpenetration of the networks, these

compounds display accessible void volume capable of hosting up to five molecules of methanol which interact with the host *pina* ligand and establish an infinite lattice of hydrogen bonds along the structural channels. Interestingly, the magnetic studies have shown that the solvated complexes **1**·*x*MeOH and **2**·*x*MeOH display two- and four-step hysteretic thermally driven SCO behavior, respectively. However, when these compounds lose the methanol molecules, the magnetic behavior changes drastically giving place to gradual spin conversions evidencing the relevant influence of the guest molecules on the spin-crossover properties. Importantly, since the solvent desorption takes place following a single-crystal-to-single-crystal transformation, empty structures **1** and **2** (*x* = 0) could be also determined allowing us to evaluate the correlation between the structural changes and the modification of the magnetic properties triggered by the loss of methanol molecules.

Chapter five of this thesis describes the extraordinary kinetic stability of new discovered thermo- and photo-induced phases of $[\text{Fe}(\textit{n}\text{Bu-im})_3\text{tren}](\text{PF}_6)_2$ ($(\textit{n}\text{Bu-im})_3\text{tren}$ = *n*-butylimidazoltris(2-ethylamino)amine) compound, revealing the mechanism that leads to this stabilization. In a previous work of our group was discussed the two well-differentiated SCO behaviors characterized by large hysteresis loops of this mononuclear complex, which critically depend on the sweeping rate of temperature. For scan-rates higher than 2 K min^{-1} the SCO is characterized by an average critical temperature $T_c^{\text{av}} = 122 \text{ K}$ with a hysteresis loop 14 K wide (channel A). In contrast, for rates below 0.1 K min^{-1} the SCO takes place at $T_c^{\text{av}} = 156 \text{ K}$ and the hysteresis loop widens up to a value of 41 K (channel B). This behavior is governed by competition between two crystallographically independent phases that manifest in the LS state: a kinetic phase (LS₁), which is isostructural to the HS state, and a thermodynamic phase (LS₂). The LS phases differ in the disposition of the butyl tails and the organization of the PF₆⁻ groups. Interestingly, the intrinsic structural disorder characteristic of the aliphatic tails also plays a crucial role in the kinetic HS*-to-LS₁ relaxation properties of the thermal and light generated metastable HS* phases at low temperatures. More precisely, the HS*-to-LS₁ relaxation shows an unusual long relaxation time of 20 h after light-induced excited spin state trapping (LIESST) when irradiating at 80 K. This is more longer than when irradiating in the interval 10 – 70 K. Optical absorption spectroscopy and X-ray diffraction using synchrotron radiation as well as magnetic measurements were used to characterize and compare the LIESST behavior of this compound after irradiation in the temperature interval 10 K and 100 K. Depending on the temperature at which the compound is irradiated, the generated metastable HS* LIESST state differ in the arrangement of the butyl chains of the

ligands. Hence, the structural reorganization of the butyl chains occurring during the relaxation to adopt the structure of the thermodynamically stable LS₁ phase seems to be responsible for these differences.

Chapter six of this thesis introduces an efficient synthetic strategy to separate the synchronous coupled crystallographic phase transition and SCO behavior of previously studied compound [Fe(*n*Bu-im)₃(tren)](PF₆)₂ (**100P**). This strategy is based on the preparation of molecular alloys generically formulated as [Fe_{1-x}M_x(*n*Bu-im)₃(tren)](P_{1-y}As_yF₆)₂ (M = Zn^{II}, Ni^{II}). By controlling the composition of this isomorphous series, two cooperative thermally-induced SCO events featuring distinct critical temperatures (T_c) and hysteresis width (ΔT_c , memory), can be selected at will. In fact, precise control of AsF₆⁻ ↔ PF₆⁻ substitution selectively selects the memory channel B of **100P** when [x = 0, y ≈ 0.7], stabilizing the arrangement of butyl groups and PF₆⁻/AsF₆⁻ anions of LS₂ phase. In contrast, substitution of active Fe^{II} centers with Zn^{II} or Ni^{II} [x ≈ 0.2, y = 0] favors the arrangement of butyl groups and PF₆⁻/AsF₆⁻ anions of LS₁ phase, characteristic of the low temperature memory channel A of **100P**. Analogously to **100P**, pure **100As** (x = 0, y = 1) derivative displays a hysteretic SCO behavior coupled with a structural phase transition, both located at higher temperatures due to the higher molecular volume of AsF₆⁻. The internal chemical pressure induced by AsF₆⁻ anions provokes an increase of relaxation kinetics which avoid the appearance of two independent switching channels. These effects are also reported when **100P** compound is stressed by an external hydrostatic pressure close to 0.1 GPa. Additionally, complex **100P** displays a two-step SCO behavior, as **100As** shows, when is perturbed by an external pressure, evidencing that a similar effect on the SCO properties of the material can be reached via application internal/external pressure.

Chapter seven of this thesis presents the synthesis and characterization on a series of charge neutral [Fe^{II}(Lⁿ)₂] meltable complexes based on Schiff bases Lⁿ = **pm2-n** or **pyH-n** derived from condensation of 2-pyrimidine ethyl ketone or pyridine aldehyde, respectively, with benzohydrazide functionalized with three aliphatic chains C_nH_{2n+1} (being n the number of carbon atoms that defines the substituted alkyl chains, ranging between 4 – 14). In the solid-state [Fe^{II}(pm2-n)₂] complexes show two different crystal packing motifs depending on alkyl chain length (n). However, upon heating, the compounds melt into an isotropic phase and, due to releasing the solid-state effects, reveal identical SCO behavior for all the compounds with the SCO transition midpoint temperature $T_{1/2} \approx 354$ K. For short chain compounds (n = 4,

6, 8), $T_{1/2}$ is far above 400 K in solid state, therefore they show an abrupt jump of the susceptibility on passing to the liquid phase. Cooling back shapes regular LS-to-HS (“forward”) spin transition hysteresis loop with the center shifting down on n growth. In contrast, the long chain compounds ($n = 10, 12, 14$) display a gradual SCO behavior in the solid state with characteristic critical temperatures $T_{1/2}$ centered around ~ 275 K. However, at temperatures above ~ 350 K, where are essentially HS, compounds on going to liquid phase and show entropically prohibited HS-to-LS (“reverse”) SCO behavior of up to 50% of Fe^{II} ions, while the center of the shaped hysteresis shifts up with increasing n . This finding is unprecedented in $\text{Fe}(\text{II})$ SCO complexes and provides a method of guiding the spin transition direction and its location in temperature taking in advantage the conformational instability of aliphatic chains.

Chapter eight assembled the general conclusions of this doctoral thesis.

Finally it is enlisted an appendix gathering all peer reviewed scientific articles that have led to this Doctoral Thesis.

CAPÍTULO 1

Introducción

CAPÍTULO 1

Introducción

1.1- Aspectos generales del fenómeno de transición de espín (SCO)

El fenómeno de la transición de espín (SCO) se enmarca en el campo de la magnetoquímica, y ha estado enlazado históricamente y de manera fundamental al desarrollo de la química de coordinación.^[1] Los centros SCO muestran configuraciones electrónicas lábiles intercambiables entre los estados de espín alto (HS) y espín bajo (LS), dando lugar a cambios característicos en el magnetismo, el color y la estructura de la materia, que pueden ser inducidos por variaciones de temperatura, presión, y por irradiación con luz. Cuando los cambios estructurales asociados a la transición de espín se transmiten de forma cooperativa a través del cristal se producen transiciones de espín cooperativas acompañadas de histéresis (efecto “memoria”), confiriendo carácter biestable al material.

La idea de que una molécula o conjunto de moléculas puede comportarse como un dispositivo electrónico ha estimulado la imaginación de los científicos desde hace mucho tiempo.^[2-11] Una de las estrategias más simples se basa en el concepto de biestabilidad molecular que se fundamenta en el cambio entre dos estados moleculares tal y como sucede en un interruptor binario.^[12]

La biestabilidad molecular ha sido definida como “la propiedad de un sistema molecular para cambiar entre dos estados estables de una manera reversible y detectable en respuesta a una perturbación apropiada”.^[13] En este contexto, el fenómeno de la transición de espín representa un ejemplo destacado de biestabilidad molecular. Este fenómeno tiene lugar tanto en disolución, en cristales líquidos y en estado sólido. En el primer caso, el proceso es esencialmente molecular debido al aislamiento de las moléculas. En estado sólido y en cristales líquidos la situación es muy diferente y, en general, el fenómeno viene acompañado por efectos cooperativos. La cooperatividad es una de las facetas más interesantes de las transiciones de espín, pues implica discontinuidad en las

propiedades ópticas y magnéticas y, en ocasiones, viene acompañada de histéresis térmica. Esto le confiere a dichos sistemas capacidad potencial para almacenar información a nivel molecular.

La dificultad en el estudio de la cooperatividad reside en su naturaleza intermolecular. El control de las interacciones no covalentes entre unidades individuales que constituyen un sólido es uno de los campos más activos de lo que hoy en día se conoce como química supramolecular^[14-15] y, en particular, de la ingeniería cristalina. Sin embargo, a pesar de lo mucho que se ha avanzado en la última década, no es posible todavía predecir si una disposición molecular en una red puede ser más o menos efectiva que otra desde el punto de vista de la cooperatividad, o incluso si va a favorecer o impedir la conversión de espín. A este respecto, podemos decir que actualmente el químico carece de una guía conceptual que le permita la síntesis dirigida de sólidos con unas propiedades magnéticas determinadas.

A pesar de todos estos inconvenientes, el estudio de las transiciones de espín presenta una riqueza conceptual poco imaginable a primera vista. En este apartado se presentan los conceptos más importantes de las transiciones de espín.

1.1.1- Fundamento teórico del fenómeno SCO: teoría del campo de ligandos y diagramas de energía potencial

En simetría octaédrica los complejos de metales de transición con configuraciones electrónicas $[\text{Ar}]3d^4-3d^7$ pueden presentar dos estados electrónicos fundamentales distintos, según el desdoblamiento de los orbitales d en los subconjuntos e_g y t_{2g} . Cuando la separación energética entre estos subconjuntos (fuerza del campo de ligandos), Δ , es mayor que la energía de repulsión interelectrónica, P, los electrones tienden a ocupar los orbitales de más baja energía, t_{2g} , y el complejo metálico adopta el estado de espín bajo (LS). Si Δ es menor que P los electrones d cumplen la regla de máxima multiplicidad de Hund y el complejo adopta el estado de espín alto. La mayoría de los complejos de Cr(II), Mn(II), Mn(III), Fe(II), Fe(III), Co(II) y Co(III) pueden presentar estas dos posibilidades electrónicas, si bien la familia de compuestos de Fe(II) presentando transición de espín es la más importante y la más numerosa.

En los alrededores del punto de cruce, Δ_c , donde Δ y P tienen valores similares, la diferencia de energía entre los estados HS y LS es del orden de magnitud de la energía térmica ($k_B T$). En esta región singular nace una nueva familia de compuestos denominados de transición de espín (SCO). Éstos pueden adoptar ambos estados de espín e interconvertirse de manera controlada, detectable y reversible bajo el efecto de la temperatura, presión o irradiación de luz.

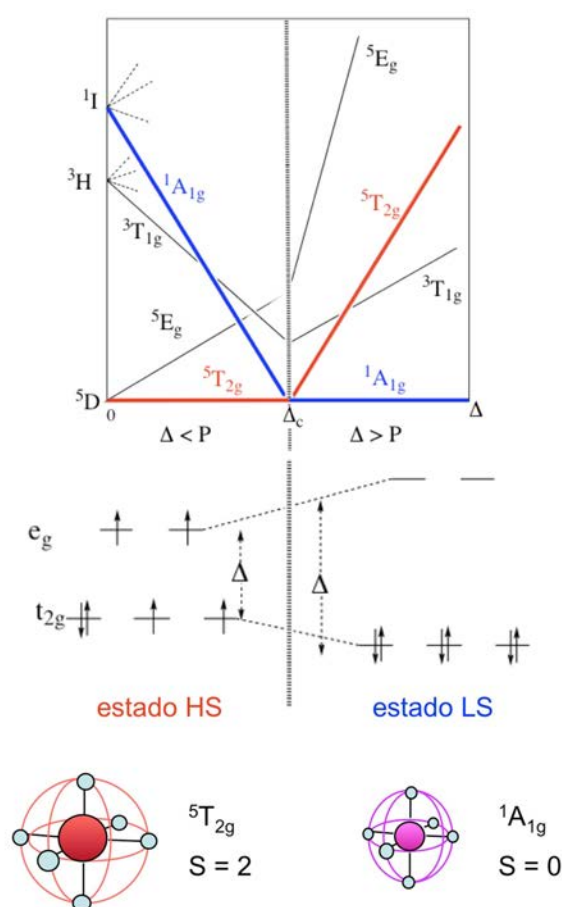


Figura 1.- Diagrama Tanabe-Sugano simplificado ilustrando la dependencia relativa de los estados HS y LS y las configuraciones electrónicas correspondientes.

En el caso de compuestos de Fe(II) los ligandos de campo débil, como el H₂O, favorecen la estabilización del estado HS (cuyo estado fundamental es el ⁵T_{2g}), mientras que al aumentar la fuerza del campo de ligandos el estado LS (cuyo estado fundamental es el ¹A_{1g}), se estabiliza automáticamente, disminuyendo su energía.

El fenómeno de las transiciones de espín puede considerarse como una transferencia electrónica intra-iónica, donde los electrones se mueven entre los orbitales e_g y t_{2g}. Dado que el subconjunto e_g tiene carácter antienlazante, su población/despoblación tiene lugar junto a un aumento/disminución de las distancias de enlace metal-ligando. Un cambio opuesto se da en la población del subconjunto t_{2g} que afecta a la retro-donación entre el ion metálico y los orbitales π* vacantes de los ligandos. Ambos factores σ y π contribuyen al cambio de las distancias de enlace metal-ligando. El cambio en las distancias de enlace metal-ligando, ΔR, es de aproximadamente 0.2, 0.15 y 0.10 Å para el Fe(II), Fe(III) y Co(III), respectivamente. Así pues, un cambio considerable de tamaño tiene lugar durante la transición de espín, no sólo en las distancias de enlace sino también en los ángulos. Consecuentemente, las moléculas experimentan un cambio drástico de Δ con el comportamiento SCO, que se estima de Δ_{LS}/Δ_{HS} ≈ (Δr_{HS}/Δr_{LS})ⁿ con n = 5 - 6. Por ejemplo Δ_{LS} ≈ 1.75Δ_{HS} para el Fe(II). Esta estimación abandona la dependencia angular de Δ y considera que Δr es el parámetro de cambio estructural más importante.^[16]

La fuerza del campo de ligandos depende no sólo del ligando coordinado al centro metálico sino también de la distancia de enlace metal-ligando. Al pasar al estado de LS las distancias Fe-N disminuyen, lo que implica un cambio en el orden de enlace y por lo tanto un aumento de la energía de vibración (fácilmente observado por las espectroscopias IR y Raman), como consecuencia del aumento de la constante de fuerza del enlace, f.

Así pues, cada estado de espín puede asociarse en primera aproximación a una parábola caracterizada por una energía potencial:

$$E_{p_i} = \frac{1}{2}(f_i R_i^2) \quad i = \text{HS, LS} \quad (1)$$

R_i = distancia media Fe-N

Esta energía potencial representa esencialmente la energía electrónica de los estados HS y LS. Ambas parábolas están separadas en sus mínimos por la distancia R características para iones Fe(II) $R_{LS} \approx 2.0 \text{ \AA}$ y $R_{HS} \approx 2.2 \text{ \AA}$ (siendo $\Delta R_{HL} \approx 0.2 \text{ \AA}$). Estas curvas contienen información acerca de la energía vibracional. Así pues, dichas parábolas representan también el modo de vibración totalmente simétrico de octaedro (A_{1g}). Una representación de las energías E_p de las parábolas asociadas a los estados HS y LS frente a R se presenta en la Figura 2. El desplazamiento horizontal de ambas parábolas corresponde a $\Delta R_{HL} \approx 0.2 \text{ \AA}$, mientras que el desplazamiento vertical indica que para una molécula aislada el estado LS está estabilizado con respecto al HS por una energía ΔE_{HL} .

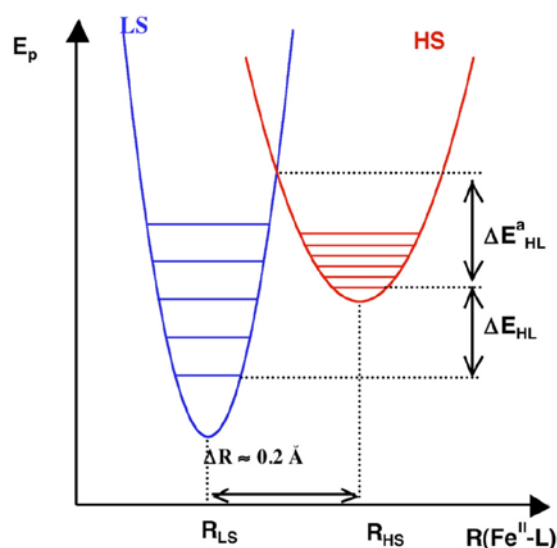


Figura 2. Curvas de energía potencial de los estados HS y LS mostrando la diferencia entálpica ΔE_{HL} , la energía de activación ΔE_{HL}^a y los estados vibracionales correspondientes.

La energía vibracional de los diferentes niveles será:

$$E^{\text{vibr}}_i(n) = (n + 1/2) h\nu_i \quad \nu_i = 1/2\pi (f_i/m)^{1/2} \quad (\text{m es la masa reducida}) \quad (2)$$

Los niveles vibracionales se representan como líneas horizontales igualmente espaciadas dentro de las correspondientes parábolas (figura 2). Dado que $f_{LS} > f_{HS}$ el

número de niveles vibracionales por unidad de energía es mayor para el estado HS que para el LS, es decir, la separación entre los niveles vibracionales es menor en el estado HS. Igualmente, la multiplicidad de espín del estado HS es mayor que la del estado LS.

A muy bajas temperaturas, la molécula se encuentra en el nivel vibracional fundamental ($n = 0$) del estado LS. A medida que aumenta la temperatura, la molécula va transformando la energía térmica aportada en energía vibracional ocupando niveles vibracionales excitados hasta alcanzar el punto de cruce de ambas parábolas donde se produce el cambio de estado de espín, en el que la geometría del estado precursor, el LS, y el sucesor, el HS, es la misma. De acuerdo con el principio de Franck-Condon es en este punto donde tiene lugar la transformación HS \leftrightarrow LS. Este punto de cruce, Δ_c , representa una región inestable donde las especies transitorias pueden cambiar su estado de espín.

El coste energético para salvar la diferencia entálpica, ΔE_{HL} , entre ambos estados está compensado por la diferencia de entropía de los mismos, que favorece la población del estado HS a altas temperaturas. Visto de otra forma, la molécula absorbe energía para compensar la diferencia entálpica ΔE_{HL} que desfavorece el estado HS. Dicha energía absorbida es de origen entrópico y tiene dos componentes diferentes. Por un lado, hay una componente electrónica relacionada con el cambio de multiplicidad de espín ($2S + 1$) [HS ($S = 2$) y LS ($S = 0$) para el ion Fe(II)]:

$$AS_{el.} = R \ln [(2S + 1)_{HS}/(2S + 1)_{LS}] = R \ln (5/1) = 13.45 \text{ J K}^{-1} \text{ mol}^{-1} \quad (3)$$

Por otro lado, hay una componente vibracional que deriva del mayor número de niveles vibracionales por unidad de energía (g_i) asociado al estado HS, dada la menor magnitud de la constante de fuerza de enlace f_{HS} :

$$AS_{vibr.intr.} = R \ln (g_{HS}/g_{LS}) \quad (4)$$

El acceso experimental a la relación g_{HS}/g_{LS} conlleva serias dificultades pero es posible estimarla a partir de la entropía total obtenida de las medidas de calorimetría y del análisis de los espectros IR y/o Raman correspondientes a los estados HS y LS.^[17] Por

consiguiente el comportamiento SCO térmicamente inducido es un proceso controlado por la entropía.

La influencia de la presión en la transición de espín también puede entenderse a partir de los pozos de potencial. Sin tener en cuenta la fuente de la presión (química o mecánica) el efecto principal de la presión es la desestabilización del estado HS, ya que el volumen de éste es mayor que el del LS. Así pues, la presión disminuye ΔR_{HL} y aumenta ΔE_{HL} , por lo que la parábola se desplaza verticalmente.^[18] Como consecuencia, la presión produce la disminución de la energía de activación, E_{HL}^a , correspondiente a la diferencia en energía entre el nivel vibracional $n = 0$ del estado HS y el punto de cruce definido por los dos pozos de potencial.

Generalmente, a temperaturas mayores de 100 K la energía térmica, $k_B T$, es mayor que la energía de activación, E_{HL}^a , hecho que determina la cinética de la conversión $HS \leftrightarrow LS$, incluso a presión atmosférica. Por ello la cinética del proceso se caracteriza por una constante de velocidad, $k_{HL} \approx 10^6 - 10^8 \text{ s}^{-1}$, que garantiza el equilibrio termodinámico de las magnitudes físicas observadas.

Cuando la energía térmica es del orden o menor que la energía de activación, $k_B T \leq E_{HL}^a$, esta afirmación ya no es válida y la constante k_{HL} disminuye hasta valores del orden de $10^{-1} - 10^{-7} \text{ s}^{-1}$, con lo que es posible “congelar” el estado HS a temperaturas donde no es estable, ya que la molécula no dispone de la energía suficiente para superar la barrera de paso E_{HL}^a desde el estado HS al LS.

A temperaturas del orden de 50 - 90 K es fácil estudiar las cinéticas de relajación, que en principio son de primer orden, pudiéndose correlacionar la variación térmica de k_{HL} en términos de la representación de Arrhenius.

Para temperaturas muy bajas, en los compuestos típicos SCO de Fe(II), se observa que el proceso de relajación ya no sigue una ley de Arrhenius pura, sino que se desvía, más cuanto menor es la temperatura, hasta observar una independencia térmica de $\ln(k_{HL})$, hecho que suele tener lugar por debajo de 40 K. De hecho por debajo de 30 K, k_{HL} es muy pequeña, $[k_{HL}(T \rightarrow 0)] \approx 10^{-7} \text{ s}^{-1}$, e independiente de la temperatura, y el proceso de

relajación tiene lugar esencialmente vía efecto túnel. La velocidad de relajación en la región túnel puede relacionarse con los desplazamientos “vertical” y “horizontal” de las curvas de energía potencial de los estados HS y LS a través del marco conceptual de los procesos de relajación no adiabáticos multifonónicos.^[19]

Sin embargo este no es el caso para compuestos de Fe(III) y Co(II), que normalmente presentan relajaciones muy rápidas incluso a temperaturas por debajo de 10 K. Para estos sistemas el cambio de energía configuracional es menor que para los compuestos de Fe(II), ya que el cambio en las distancias de enlace es mucho menor también. La relajación HS ↔ LS en compuestos SCO es un proceso modelo que participa del comportamiento clásico y el mecano-cuántico, y ha sido estudiado en profundidad por Hauser y colaboradores entre otros.^[20]

1.1.2- Fotoconversión en compuestos SCO: Efecto LIESST

La luz es un camino muy eficaz para “comunicarse” con un sistema molecular sobre todo cuando se trata de encontrar posibles aplicaciones tecnológicas. La foto-inducción en compuestos SCO fue observada por primera vez por primera vez por McGarvey y Lawthers en disolución a temperaturas relativamente altas,^[21] sin embargo, el tiempo de vida media de los estados inducidos era muy corto. Más adelante, en 1994, Decurtins y colaboradores observaron por primera vez el proceso de foto-inducción en materiales SCO en estado sólido a bajas temperaturas para el complejo $[\text{Fe}(\text{1-propiltetrazol})_6](\text{BF}_4)_2$.^[22] Al irradiar la muestra en el estado LS con luz verde ($\lambda = 514.5 \text{ nm}$) a temperaturas por debajo de 50 K el color de la muestra pasa del púrpura del estado LS al blanco, propio del HS. El fenómeno fue denominado “light induced spin state trapping” (LIESST).

A temperaturas suficientemente bajas el estado LS está totalmente poblado y el espectro visible del sistema d^6 en simetría octaédrica se caracteriza por dos bandas relativamente intensas correspondientes a las transiciones ν_1 (${}^1A_{1g} \rightarrow {}^1T_{1g}$) ($\approx 12000 - 20000 \text{ cm}^{-1}$) y ν_2 (${}^1A_{1g} \rightarrow {}^1T_{2g}$) ($\approx 20000 - 25000 \text{ cm}^{-1}$) que a menudo están enmascaradas por las bandas de transferencia de carga metal ligando TCML ($d_M \rightarrow \pi^*L$).

La irradiación con luz verde estimula la transición ${}^1A_{1g} \rightarrow {}^1T_{1g}$. El tiempo de vida media del estado excitado ${}^1T_{1g}$ es de tan sólo nanosegundos, por lo que el sistema se relaja rápidamente. Dicha relajación debería tener lugar normalmente al estado inicial ${}^1A_{1g}$. No obstante, existe una pequeña probabilidad de relajación a través de los estados de espín intermedio ${}^3T_{1g}$ y ${}^3T_{2g}$ por mecanismos de cruce entre sistemas (“intersystem crossing”, ISC) permitidos por acoplamiento espín-órbita de segundo orden. La relajación desde los estados de espín intermedio puede ocurrir de nuevo por medio de dos procesos ISC, uno implica la relajación al estado fundamental ${}^1A_{1g}$ y otro al metastable ${}^5T_{2g}$ donde las moléculas permanecerán atrapadas, siempre que $k_B T$ sea suficientemente menor que E_{HL} . A bajas temperaturas el estado metaestable ${}^5T_{2g}$ tiene un tiempo de vida media muy largo, dado que la relajación ${}^5T_{2g} \rightarrow {}^1A_{1g}$ está prohibida.

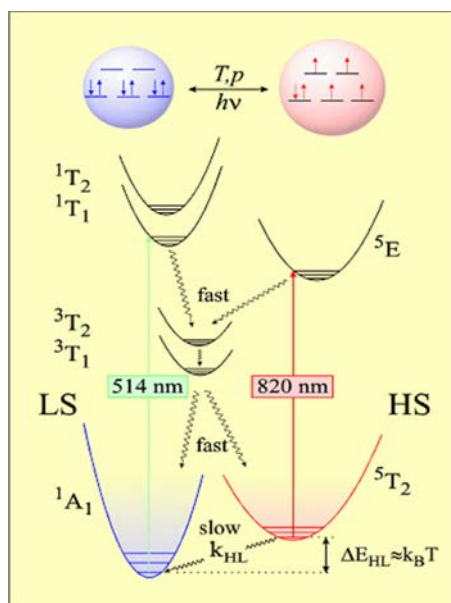


Figura 3. Esquema representativo del fenómeno de foto-inducción de una transición de espín, efecto LIESST.

La foto-excitación durante un período de tiempo suficiente, implica la población total del estado metaestable HS, ${}^5T_{2g}$, a costa del desdoblamiento del LS, con lo que se invierte la población de los estados. El estado metaestable HS puede volver al estado LS de partida

irradiando con luz roja ($\lambda = 820 \text{ nm}$), el llamado efecto LIESST inverso (${}^5T_{2g} \rightarrow {}^3T_{1g} \rightarrow {}^1A_{1g}$), o simplemente aumentando la temperatura.

El descubrimiento del efecto LIESST representó un avance importante en el estudio de la dinámica del comportamiento SCO en estado sólido, dado que el rango de temperaturas en las cuales el equilibrio termodinámico podía ser foto-perturbado se extendió considerablemente. Desde entonces, el número de compuestos en los que se ha observado el efecto LIESST ha aumentado considerablemente.

1.1.3- Comportamiento colectivo del conjunto de centros SCO: cooperatividad

Aunque el origen del fenómeno de transición de espín es puramente molecular la manifestación macroscópica del sólido es el resultado de la interacción cooperativa entre las moléculas que constituyen el material. La naturaleza cooperativa de la conversión de espín ha estimulado mucho interés dado que las transiciones de fase de primer orden que se producen acompañadas de histéresis térmica confieren a estos materiales un cierto grado de memoria, que podría ser potencialmente aprovechada en futuras aplicaciones. La cooperatividad radica esencialmente en la diferencia de tamaño que presenta la molécula en cada uno de los estados de espín. Así pues, tiene un origen elástico que da lugar a interacciones de largo alcance. Estas interacciones podrían ilustrarse como una presión interna, que crece con el aumento de las especies LS e interactúa con todas las moléculas del cristal con la misma intensidad, independientemente de las distancias.^[23]

Es posible explicar el carácter continuo, discontinuo, histéresis o incluso la temperatura crítica $T_{1/2}$ (temperatura para la cual la fracción molar de especies HS y LS es 0.5) en términos de la termodinámica de transiciones de fase debida a Slichter y Drickamer.^[24]

Si se considera un número N de moléculas que pueden dar lugar al fenómeno SCO, cada molécula podrá existir en el estado HS o en el estado LS, de manera que podemos definir la fracción molar de las moléculas HS como γ_{HS} , siéndola fracción molar de

moléculas LS ($1 - \gamma_{HS}$). En ausencia de interacciones intermoleculares podemos introducir en la expresión de la energía libre de Gibbs, G , un término para la entropía de mezcla, S_{mix} . Este término representa las diferentes posibilidades de distribución de las poblaciones HS (γ_{HS}) y LS ($1 - \gamma_{HS}$), para el total de moléculas N . La entropía de mezcla S_{mix} se expresa como:

$$S_{mix} = k [N \ln N - \gamma_{HS} N \ln \gamma_{HS} N - (1 - \gamma_{HS}) N \ln (1 - \gamma_{HS}) N] \quad (5)$$

que puede describirse como:

$$S_{mix} = -R[\gamma_{HS} \ln \gamma_{HS} - (1 - \gamma_{HS}) \ln(1 - \gamma_{HS})] \quad (6)$$

donde R es la constante de gases. S_{mix} es máxima para $\gamma_{HS} = 0.5$ y desaparece para $\gamma_{HS} = 0$ o 1 . Al tener en cuenta el término S_{mix} , la expresión de la energía libre de Gibbs queda:

$$G = \gamma_{HS} G_{HS} + (1 - \gamma_{HS}) G_{LS} - T S_{mix} \quad (7)$$

donde G_{HS} y G_{LS} corresponden a las energías libres de Gibbs para los estados electrónicos HS y LS, respectivamente. La derivada parcial de G con respecto a γ_{HS} es

$$\left(\frac{\partial G}{\partial \gamma_{HS}} \right) = \Delta G + RT \ln \left(\frac{\gamma_{HS}}{1 - \gamma_{HS}} \right) \quad (8)$$

La condición de equilibrio termodinámico para el fenómeno SCO a cualquier temperatura y presión es:

$$\left(\frac{\partial G}{\partial \gamma_{HS}} \right)_{T, P} = 0 \quad (9)$$

por lo que

$$\ln \left(\frac{1 - \gamma_{HS}}{\gamma_{HS}} \right) = \frac{\Delta G}{RT} = \frac{\Delta H}{RT} - \frac{\Delta S}{R} \quad (10)$$

Teniendo en cuenta que $\Delta G = 0$ cuando $\gamma_{HS} = \gamma_{LS} = 0.5$ y que por tanto $T_{1/2} = \Delta H/\Delta S$, se obtiene

$$\gamma_{HS} = \frac{1}{1 + \exp\left[\frac{\Delta H}{R} \left(\frac{1}{T} - \frac{1}{T_{1/2}}\right)\right]} \quad (11)$$

Las interacciones moleculares vienen reflejadas en el modelo de Slichter y Drickamer por un parámetro de interacción, G_{int} .

$$G_{int} = \Gamma \gamma_{HS} (1 - \gamma_{HS}) \quad (12)$$

donde Γ es el parámetro de la cooperatividad.

Tomando G_{LS} como el origen de energías, podemos escribir,

$$G = \gamma_{HS}\Delta H + \Gamma\gamma_{HS}(1 - \gamma_{HS}) + T[R\gamma_{HS}\ln\gamma_{HS} + R(1 - \gamma_{HS})\ln(1 - \gamma_{HS}) - \gamma_{HS}\Delta S] \quad (13)$$

Esta ecuación permite representar curvas de energía libre, G , frente a la fracción molar de HS, γ_{HS} , para diferentes valores de ΔH , ΔS , Γ y T . Teniendo en cuenta de nuevo la condición de equilibrio se llega a

$$\ln\left(\frac{1-\gamma_{HS}}{\gamma_{HS}}\right) = \frac{\Delta H + \Gamma(1-2\gamma_{HS})}{RT} - \frac{\Delta S}{R} \quad (14)$$

Si $\Delta G < 0$ el estado electrónico de las moléculas es HS y cuando $\Delta G > 0$ el estado de las moléculas es el LS. En condiciones de equilibrio termodinámico, $\Delta G = 0$ y $\gamma_{HS} = \gamma_{LS}$. Si además se tiene en cuenta la influencia de la presión en la TS, se introduce un nuevo término en la ecuación, quedando:

$$\ln\left(\frac{1-\gamma_{HS}}{\gamma_{HS}}\right) = \frac{\Delta H + P\Delta V + \Gamma(1-2\gamma_{HS})}{RT} - \frac{\Delta S}{R} \quad (15)$$

Resumiendo, la ecuación de estado puede describirse de la forma siguiente:

$$\ln[(1-\gamma_{HS})/\gamma_{HS}] = [\Delta H + P\Delta V + \Gamma (1 - 2\gamma_{HS}) - T \Delta S] / RT \quad (16)$$

siendo γ_{HS} la fracción molar de HS. ΔH y ΔS son las variaciones de entalpía y entropía por mol involucradas en el cambio de estado de espín y se pueden obtener directamente a partir de las medidas de calorimetría (C_p vs. T), y ΔV es el cambio de volumen molar asociado a SCO que se suele obtener directamente de las medidas de difracción de rayos X a bajas temperaturas (este término es despreciable a presión atmosférica). Es importante resaltar que la relación $\Delta H/\Delta S$ corresponde a la temperatura característica de la transición, T_c o $T_{1/2}$, a la cual $\gamma_{HS} = \gamma_{LS} = 0.5$, y se obtiene directamente de la curva SCO. Por otro lado, se considera que el término $P\Delta V$ es puramente entálpico y aumenta principalmente la diferencia de energía libre entre las fases HS y LS.

El parámetro de la cooperatividad, Γ , representa la tendencia que tiene una molécula o centro activo, en un estado de espín determinado, a rodearse de moléculas o centros activos con el mismo espín. Por tanto, Γ es un reflejo de la eficacia con que se transmiten a lo largo del cristal los cambios estructurales asociados a la transición de espín vía interacciones intermoleculares y es responsable de la manifestación cooperativa de las propiedades físicas del sistema.

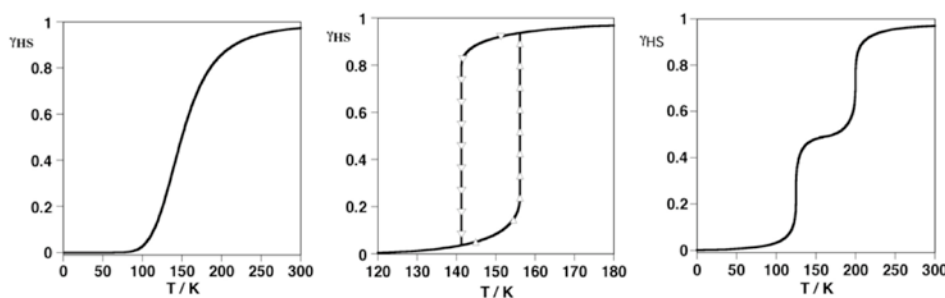


Figura 4.- Tipos principales de curvas SCO representadas en la forma de γ_{HS} frente a T : gradual (izquierda), abrupta y con histéresis (centro) y en dos etapas (derecha).

La ecuación de estado hace posible simular los comportamientos más representativos de las curvas SCO, que van desde la transición gradual ($\Gamma = 0$) a una transición de primer orden y con histéresis ($\Gamma > 2RT_c$) (Figura 4 izquierda y centro,

respectivamente). Si se modifica esta ecuación de la manera conveniente pueden simularse también transiciones incompletas con fracciones residuales de HS y/o LS a temperaturas bajas y altas respectivamente, o incluso transiciones en dos etapas (4 derecha).

El parámetro γ_{HS} se obtiene normalmente a partir de medidas magnéticas, espectroscopía Mössbauer (en el caso de compuestos con hierro), espectroscopia electrónica (en el visible) y vibracional o incluso a partir de medidas de difracción de rayos X.

Este modelo, al igual que otros equivalentes explica los aspectos principales de la transición de fase. Por lo tanto, es insensible con respecto a pequeñas modificaciones estructurales y electrónicas, que afectan drásticamente a la cooperatividad y al campo de ligandos del centro metálico. Estas modificaciones vienen inducidas normalmente por grupos voluminosos, o ligandos capaces de dar lugar a apilamiento π o a interacción por puentes de H, pero también por la presencia de moléculas de disolvente y aniones en la red cristalina.

Otro punto importante es la aparición de polimorfismo, que puede surgir a raíz de pequeñas diferencias en el proceso de cristalización, tales como temperaturas distintas, métodos distintos, mezclas de disolventes, etc. Por desgracia, la racionalización de estos factores es relativamente difícil, dado que no son siempre coherentes de un sistema a otro y por lo general son impredecibles.

1.1.4- Técnicas de caracterización de compuestos SCO

Las técnicas experimentales que se emplean en la caracterización de los materiales con transición de espín pueden agruparse según el tipo de información que proporcionen.

Por un lado se emplean técnicas para investigar las configuraciones electrónicas de los centros SCO, entre las que se encuentran la espectroscopia UV-Visible, la espectroscopia IR, la espectroscopia Mössbauer y las medidas de susceptibilidad magnética. Por otro lado, encontramos técnicas que permiten obtener los parámetros termodinámicos asociados al fenómeno SCO, entre las que se encuentran las medidas de

calorimetría (DSC). Por último, los métodos de resolución estructural permiten estudiar los cambios estructurales que tienen lugar en la esfera de coordinación de los centros SCO, así como cambios en la red cristalina. Entre los distintos métodos encontramos la difracción de rayos X (para polvo y monocristal), estudios de radiación sincrotrón (XAS o “X-ray Absorption Spectroscopy”, EXAFS o “Extended X-ray Absorption Fine Structure”, XANES o “X-ray absorption near edge structure”, NFS o “Nuclear Forward Scattering”).^[25]

Además de las técnicas arriba mencionadas, el desarrollo y el avance en el estudio de las transiciones de espín ha comenzado a hacer uso de técnicas no tan convencionales que permiten obtener información y realizar un seguimiento de la conversión, como por ejemplo la resonancia magnética nuclear (RMN), la resonancia paramagnética electrónica (EPR, sólo para compuestos de Fe^{III} y Co^{II}), la elipsometría, la espectroscopía de aniquilación de positrones (PAS) o la rotación del espín muónico (MuSR).^[25]

1.2- Objetivos de la tesis doctoral

Aprovechando la dilatada experiencia de nuestro grupo de investigación en el estudio de materiales multifuncionales conmutables que presentan el fenómeno SCO, la presente tesis doctoral se ha centrado en el diseño racional de una nueva generación de complejos de Fe(II) biestables que permitan estudiar nuevas sinergias entre el comportamiento SCO y otras propiedades físico-químicas de interés (química huésped-anfitrión, transformaciones sólido-líquido,...).

A grandes rasgos, los trabajos presentados en la correspondiente tesis doctoral pueden dividirse en dos grupos:

El primer grupo (incluye a los capítulos dos, tres, y cuatro) está focalizado en el desarrollo de una nueva familia de polímeros de coordinación porosos de Fe(II) con estructuras de tipo Hofmann, con el objetivo de explotar la gran estabilidad química y riqueza estructural de este tipo de derivados para investigar nuevas propiedades físico-químicas interesantes. En el capítulo dos se propone la utilización de una piracina funcionalizada, concretamente la 2-fluoropiracina, para construir nuevos clatratos de Hofmann de diferente dimensionalidad. La motivación en el uso de este ligando se basa en

la consecución de un compuesto isoestructural al complejo modelo 3D $\{\text{Fe}(\text{pz})[\text{Pt}(\text{CN})_4]\}$, para estudiar más tarde el efecto del átomo de fluor sobre las propiedades SCO. En el capítulo tres se buscan nuevas topologías estructurales dentro de la familia de los clatratos de Hofmann de Fe(II) en base a la utilización de ligandos de topología no lineal, como son los ligandos tritopico y tetratopico L^{N^3} y L^{N^4} , respectivamente. Al mismo tiempo, dado el gran tamaño de estos ligandos, se busca conseguir redes de gran porosidad que permitan investigar la capacidad de inclusión de moléculas huésped en los canales del material para investigar cómo influye su naturaleza en el comportamiento SCO. En el capítulo cuatro se desea utilizar el ligando lineal bis-monodentado *pina* para construir polímeros de coordinación de tipo Hofmann de gran porosidad. El grupo amida que define el ligando *pina* favorece, muy probablemente, la inclusión de moléculas de naturaleza polar en los canales del material, permitiendo así estudiar como la adsorción-desorción de moléculas huésped afectan a las propiedades SCO del material.

El segundo grupo (el cual incluye los capítulos cinco, seis y siete) tiene como reto sintético la obtención de entidades moleculares de Fe(II) funcionalizadas con cadenas alquílicas hidrocarbonadas de diferente longitud, con el objetivo de encontrar organizaciones supramoleculares singulares en las que la disposición de las cadenas alquílicas tengan una influencia notable sobre las propiedades SCO del material. En los capítulos cinco y seis se propone utilizar el complejo multiestable $[\text{Fe}(n\text{Bu-im})_3\text{tren}](\text{PF}_6)_2$ como plataforma idónea para investigar nuevas propiedades ligadas a su intrínseca transición de fase cristalográfica, la cual implica la reorganización de las cadenas butilo y los aniones PF_6^- en la red cristalina. Así, en el capítulo cinco se desea estudiar nuevas fases generadas del complejo $[\text{Fe}(n\text{Bu-im})_3\text{tren}](\text{PF}_6)_2$ al irradiar dicho complejo en el rango de temperaturas 10 – 100 K. En cambio, en el capítulo seis, se busca desacoplar la transición de fase y el comportamiento SCO de $[\text{Fe}(n\text{Bu-im})_3\text{tren}](\text{PF}_6)_2$ utilizando el dopaje químico como herramienta sintética. En el capítulo siete se propone sintetizar una nueva familia de complejos de Fe(II) constituidos por ligandos de tipo base de Schiff funcionalizados, cuya reorganización molecular durante el cambio de fase sólido \rightarrow líquido influya notablemente sobre las propiedades SCO del material.

1.3- Metodología

Preparación de ligandos. Los ligandos no comerciales L^{N3} , L^{N4} , *pina*, $[nBu-im]_3tren$ y *pm2-n* se sintetizaron según procedimientos experimentales estandarizados y previamente publicados. Posteriormente, fueron caracterizados mediante estudios de resonancia magnética nuclear (RMN)

Síntesis de los compuestos SCO. La síntesis de los polímeros de coordinación SCO de tipo Hofmann se llevaron a cabo mediante técnicas de cristalización basadas en la difusión lenta de los reactivos. Principalmente, los recipientes utilizados para realizar las cristalizaciones fueron tubos en forma de H (o alguna de sus variantes, como son los tubos de 3 brazos) y tubos de ensayo. Para los complejos mononucleares SCO se propusieron técnicas de precipitación en disolución bajo atmósfera inerte. La evaporación lenta de estas disoluciones facilitó la obtención de monocristales que se utilizaron para analizar mediante difracción de rayos X.

Caracterización físico-química. En una primera etapa, los compuestos SCO sintetizados se caracterizaron a través de análisis elemental, análisis EDX, análisis termogravimétrico (TGA) y espectroscopía infrarroja. Posteriormente, las propiedades magnéticas de cada material se evaluaron mediante el susceptómetro SQUID en el rango de temperaturas 2 – 400 K. A continuación se realizaron medidas de calorimetría diferencial de barrido (DSC) en el intervalo de temperatura 120 – 410 K, lo cual permitió conocer los parámetros termodinámicos ΔH y ΔS asociados al fenómeno SCO. Finalmente, la estructura cristalina de los diferentes compuestos SCO se determinó a diferentes temperaturas mediante técnicas de difracción de rayos X sobre monocristal y/o polvo microcristalino, utilizando en alguno de los casos radiación sincrotrón. Además, en algún ejemplo en concreto, se monitorizó el comportamiento SCO en función de la temperatura mediante espectroscopia de absorción UV-vis.

1.4- Bibliografía

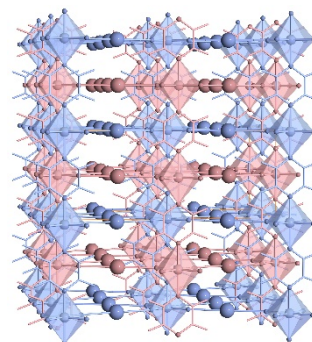
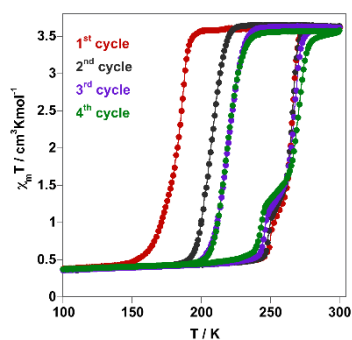
- [1] O. Kahn, *Molecular Magnetism*; VCH, New York, 1993.

- [2] R. Feynman, *Miniturization, Ed. A. Gilbert* (Reinhold, New York), **1961**, 282.
- [3] W. A. Little, *Phys. Rev.*, **1964**, A 134, 1416.
- [4] W. A. Little, *J. Polym. Sci., Polym. Lett. Ed.*, **1970**, 29.
- [5] K. E. Drexler, *Proc. Natl. Acad. Sci. USA*, **1981**, 78, 5275.
- [6] F. L. Cater, *Ed., Molecular Electronic Devices* (M. Dekker, New York), **1982**.
- [7] F. L. Cater, *Ed., Molecular Electronic Devices II* (M. Dekker, New York), **1987**.
- [8] J. S. Miller, *Adv. Mater.*, **1990**, 2, 378.
- [9] J. S. Miller, *Adv. Mater.*, **1990**, 2, 495.
- [10] J. S. Miller, *Adv. Mater.*, **1990**, 2, 601.
- [11] D. Goldhaber-Gordon, M. S. Montemerlo, J. C. Love, G. J. Opiteck, J. C. Ellenbogen, *Proceeding of the IEEE*, **1997**, 85, 521.
- [12] R. C. Haddon, A. A. Lamola, *Proc. Natl. Acad. Sci. USA*, **1985**, 82, 1874.
- [13] O. Kahn, J. P. Launay, *Chemtronics* 3, **1988**, 151.
- [14] J. M. Lehn, *Supramolecular Chemistry. Concepts and perspectives*, VCH, Weinheim, **1995**.
- [15] J. P. Sauvage, *Acc. Chem. Res.*, **1990**, 23, 151.
- [16] A. Hauser, *J. Chem. Phys.*, **1991**, 94, 2741.
- [17] a) A. Bousseksou, J. J. McGarvey, F. Varret, J. A. Real, J. P. Tuchagues, A. C. Dennis, M. L. Boillot, *Chem. Phys. Lett.*, **2000**, 318, 419; b) N. Moliner, L. Salmon, L. Capes, M. C. Muñoz, J. F. Létard, A. Bousseksou, J. P. Tuchagues, J. J. McGarvey, A. C. Dennis, M. Castro, R. Burriel, J. A. Real, *J. Phys. Chem. B.*, **2002**, 106, 4276; c) G. Molnár, V. Niel, A. B. Gaspar, J. A. Real, A. Zwick, A. Bousseksou, J. J. McGarvey, *J. Phys. Chem. B.*, **2002**, 106, 9701; d) M. Sorai, S. Seki, *J. Phys. Chem. Solids*, **1974**, 35, 555.

-
- [18] a) T. Granier, B. Gallois, J. Gaultier, J. A. Real, J. Zarembowitch, *Inorg. Chem.*, **1993**, 32, 5305; b) P. Güttlich, V. Ksenofontov, A. B. Gaspar, *Coord. Chem. Rev.*, **2005**, 249, 1811-1829.
- [19] a) E. Buhks, M. Bixon, J. Jortner, *J. Am. Chem. Soc.*, **1980**, 102, 2918; b) C. L. Xie, D. N. Hendrickson, *J. Am. Chem. Soc.*, **1987**, 109, 6981.
- [20] A. Hauser, *Comments Inorg. Chem.*, **1995**, 17, 17.
- [21] J. J. McGarvey y I. Lawthers, *J. Chem. Soc., Chem. Commun.*, **1982**, 906.
- [22] a) S. Decurtins, P. Güttlich, C. P. Köhler, H. Spiering, A. Hauser, *Chem. Phys. Lett.*, **1984**, 139, 1; b) S. Decurtins, P. Güttlich, K. M. Hasselbach, H. Spiering, A. Hauser, *Inorg. Chem.*, **1985**, 24, 2174.
- [23] H. Spiering, T. Kohlhaas, H. Romstedt, A. Hauser, C. Bruns-Yilmaz, J. Kusz, P. Güttlich, *Coord. Chem. Rev.*, **1999**, 190-192, 471.
- [24] a) C. P. Slichter, H G. Drickamer, *J. Chem. Phys.*, **1972**, 56, 2142; b) J. M. Honig, *J. Chem. Ed.*, **1999**, 76, 848.
- [25] a) Eds. Güttlich, Goodwin, *Top. Curr. Chem.*, **2004**, vol. 233-235; b) Ed. M. A. Halcrow, John Wiley & Sons, Ltd., **2013**.

CAPÍTULO 2

Strong Cooperative Spin Crossover in 2D and 3D Fe^{II}-M^{I,II} Hofmann-Like Coordination Polymers Based on 2-Fluoropyrazine



REVISTA: Inorganic Chemistry

ÍNDICE DE IMPACTO: 4.857

CAPÍTULO 2

Strong Cooperative Spin Crossover in 2D and 3D Fe^{II}-M^{I,II} Hofmann-Like Coordination Polymers Based on 2-Fluoropyrazine

2.1.- Abstract

Self-assembling iron(II), 2-fluoropyrazine (Fpz), and $[M^{II}(\text{CN})_4]^{2-}$ ($M^{II} = \text{Ni, Pd, Pt}$) or $[\text{Au}^I(\text{CN})_2]^-$ building blocks have afforded a new series of two- (2D) and three-dimensional (3D) Hofmann-like spin crossover (SCO) coordination polymers with strong cooperative magnetic, calorimetric, and optical properties. The iron(II) ions, lying on inversion centers, define elongated octahedrons equatorially surrounded by four equivalent centrosymmetric μ_4 - $[M^{II}(\text{CN})_4]^{2-}$ groups. The axial positions are occupied by two terminal Fpz ligands affording significantly corrugated 2D layers $\{\text{Fe}(\text{Fpz})_2[M^{II}(\text{CN})_4]\}$. The Pt and Pd derivatives undergo thermal- and light-induced SCO characterized by $T_{1/2}$ temperatures centered at 155.5 and 116 K and hysteresis loops 22 K wide, while the Ni derivative is high spin at all temperatures, even at pressures of 0.7 GPa. The great stability of the high-spin state in the Ni derivative has tentatively been ascribed to the tight packing of the layers, which contrasts with that of Pt and Pd derivatives in the high- and low-spin states. The synthesis and structure of the 3D frameworks formulated $\{\text{Fe}(\text{Fpz})[\text{Pt}(\text{CN})_4]\cdot 1/2\text{H}_2\text{O}$ and $\{\text{Fe}(\text{Fpz})[\text{Au}(\text{CN})_2]_2\}$, where Fpz acts as bridging ligand, which is also discussed. The former is high spin at all temperatures, while the latter displays very strong cooperative SCO centered at 243 K accompanied by a hysteresis loop 42.5 K wide. The crystal structures and SCO properties are compared with those of related complexes derived from pyrazine, 3-fluoropyridine, and pyridine.

2.2.- Introduction

Iron (II) spin crossover (SCO) complexes are a well-known class of switchable molecular materials.^[1] They switch between the electronic low-spin (LS) and high-spin (HS) states in a reversible, controllable, and detectable manner through the action of external stimuli, i.e., temperature, light, pressure, analytes, and electric and magnetic fields. The switch occurs with concomitant changes in the magnetic, optical, electric, and structural properties. In some cases the changes are strongly cooperative and confer to the material a bistable character, i.e., hysteresis. These features have fueled much activity in the field and

created important expectancies in view of potential applications in molecular spintronics, sensors, and memories.^[2]

Hofmann-like SCO compounds are one of the most important sources of bistable SCO materials and have stimulated much research in the last 15 years. The prototypal Hofmann-like compound, {Ni(NH₃)₂[Ni(CN)₄]}, was reported by Hofmann and Küspert in 1897.^[3] Its structure was described in 1950s by Powell and Rainer as a pile of two-dimensional (2D) layers constituted of square-planar [Ni(CN)₄]²⁻ centers equatorially linked to octahedral Ni(II) sites, which saturate its coordination sphere with two axial NH₃ molecules.^[4] Schwarzenbach^[5] and later Iwamoto^[6] and coworkers synthesized the first heterobimetallic 2D {M(NH₃)₂[M'(CN)₄]} derivatives and three-dimensional (3D) {M(L)[M'(CN)₄]} homologues, generically referred as Hofmann clathrates due to their ability to adsorb small aromatic molecules. In 1996 Kitazawa and co-workers reported the first Hofmann-like 2D SCO coordination polymer {Fe(pyridine)₂[Ni(CN)₄]}.^[7] This compound displays a cooperative thermal-induced SCO accompanied by drastic changes of the magnetic and optical (color) properties. Later, our group extended this idea to the homologous [Pd(CN)₄]²⁻ and [Pt(CN)₄]²⁻ SCO derivatives, the new 3D porous {Fe(pyrazine)[M^{II}(CN)₄]} (M^{II} = Ni, Pd, Pt),^[8] and the 2D and 3D {FeL_x[M^I(CN)₂]₂} related families of SCO coordination polymers (L = monodentate or bis-monodentate ligand; M^I = Cu, Ag, Au).^[9] Systematic replacement of pyridine and pyrazine with related monodentate and bismonodentate L ligands afforded an important number of coordination polymers with interesting thermo-, piezo-, photo-, and chemoswitchable cooperative SCO behaviors, which combine with a rich variety of additional relevant properties such as reversible ligand exchange in the solid state, polymorphism, metallophilic interactions, or porosity and inclusion chemistry. Furthermore, the amenability to being processed as thin films and nanocrystals has converted the porous {Fe(L)[Pt^{II}(CN)₄]} derivatives in excellent platforms to systematically investigate the SCO behavior at nanoscale. The structure and properties of these thermo-, piezo-, photo-, and chemoswitchable SCO iron(II)-metallocyanate-based coordination polymers have been recently reviewed.^[10]

Despite the short time elapsed since this review, interest in these materials has been continuously growing. For example, in the series of {Fe(pyrazine)[M^{II}(CN)₄]} the quality of continuous and nanopatterned thin films of {Fe(pyrazine)[Pt^{II}(CN)₄]} has been assessed by means of atomic force microscopy and surface plasmon resonance^[11] as well as by synchrotron X-Ray diffraction.^[12] The cooperative SCO properties of {Fe(pyrazine)[M^{II}(CN)₄]}
40

nanocrystals were modulated through chemical pressure, induced by different polymeric coatings ($M^{II} = Pt$),^[13] and through correlative effects between size decrease and increase of stiffness in ultrasmall (ca. 2 nm) nanoparticles ($M^{II} = Ni$).^[14] Interest has also been focused on the modulation of the critical temperatures and cooperativity of the SCO induced by guests. In this respect, precise control of the critical SCO temperature has been achieved through the combined effects of oxidative I_2 adsorption, on the Pt^{II} sites, and chemical migration of the iodine centers.^[15] Modulation of cooperativeness has been described for clathrate systems constituted of thiourea ($M^{II} = Pd, Pt$),^[16] maleic anhydride ($M^{II} = Pt$),^[17] and five-membered aromatic rings (furan, thiophene, pyrrole; $M^{II} = Pt$)^[18] as guest molecules. In addition, the effect of the spin state on the adsorption of CO_2 ,^[19] the stabilization of the LS state upon SO_2 adsorption,^[20] and the adsorption of H_2 and its catalytic ortho-para conversion in the pores^[21] have been recently investigated. The effect of host-guest interactions and its influence on the SCO behavior has also been a subject of interest from a theoretical point of view.^[16,18,20,22] Application of specific physical techniques have uncovered new important properties of $\{Fe(pyrazine)[M^{II}(CN)_4]\}$. For example, combination of neutron spectroscopy and NMR solid-state studies has demonstrated, for $M^{II} = Pt$, that the pyrazine pillars act as switchable molecular rotators whose frequency depends on the spin state of the iron(II) center and on the presence of guests.^[23] Synchrotron powder diffraction on microcrystalline samples of $M^{II} = Pt$ showed complete photoconversion of the LS state to the metastable HS state and subsequent relaxation at 10 K.^[24] Photoconversion between the LS and the HS states at ca. 290K irradiating inside the hysteresis loop has been analyzed through differential scanning calorimetry (DSC)^[25] and single-crystal X-ray diffraction.^[26]

The synthesis of new 2D and 3D Hofmann-like coordination polymers has also attracted much interest in the last years. On one hand, replacement of pyrazine with longer rod-like ditopic ligands, L, has allowed us to investigate new series of 3D $\{Fe(L)[M^{II}(CN)_4]\}$ SCO homologues with enhanced porous capacity.^[27] Similarly, the use of monodentate ligands conveniently functionalized has afforded 2D $\{Fe(L)_2[Pt^{II}(CN)_4]\}$ SCO compounds featuring interdigitated interlayer structures with tailored host-host and host-guest interactions.^[28] On the other hand, interesting inclusion chemistry and cooperative SCO behaviors have been described for the series related 2D and 3D Hofmann-like compounds based on the $[M^I(CN)_2]^-$ ($M^I = Ag$ and Au) bridging ligands.^[29]

In this context Gural'skiy and co-workers recently reported a new family of 2D Hofmann-like coordination polymers {Fe(L)₂[M^{II}(CN)₄]} (M^{II} = Ni, Pd, Pt) based on 2-substituted pyrazine ligands.^[28e] Cooperative SCO was observed for the 6 complexes derived from 2-chloropyrazine and 2-methylpyrazine complexes. Coincidentally, with the aforementioned work, we focused our attention on the synthesis of Fe^{II} SCO Hofmann-like coordination polymers based on 2-fluoropyrazine (Fpz). Here, we report on the synthesis, crystal structure, magnetic, photomagnetic, and calorimetric properties of {Fe(Fpz)₂[M^{II}(CN)₄]} (M^{II} = Ni (**FpzNi**), Pd (**FpzPd**), Pt (**FpzPt**)), {Fe(Fpz)[Pt^{II}(CN)₄]}·1/2H₂O (**FpzPt3D**), and {Fe(Fpz)[Au^I(CN)₂]₂} (**FpzAu**).

2.3.- Results

2.3.1.- Magnetic properties

The thermal dependence of the $\chi_M T$ product measured at 2 K/min (χ_M is the molar magnetic susceptibility and T temperature) for **FpzNi**, **FpzPd**, and **FpzPt** is shown in Figure 1a. The $\chi_M T$ value about 3.84 cm³ K mol⁻¹ indicates that the three derivatives are HS at 300 K. It remains practically constant down to 151 and 118 K for **FpzPt** and **FpzPd**. Upon further cooling, $\chi_M T$ drops abruptly to a value of 0.16 cm³ K mol⁻¹ at 137 K (**FpzPt**) and 0.22 cm³ K mol⁻¹ at 110 K (**FpzPd**), indicating that these derivatives undergo a complete spin transition characterized by equilibrium temperatures $T_{1/2}^{\downarrow} \approx 144.5$ (**FpzPt**) and 105 K (**FpzPd**). The $\chi_M T$ vs T plot in the heating mode shows the occurrence of a 22 K wide hysteresis loop with $T_{1/2}^{\uparrow} \approx 166.5$ (**FpzPt**) and 127 K (**FpzPd**). Consequently, these spin transitions are strongly cooperative. The magnetic behavior of **FpzNi** is characteristic of an Fe^{II} ion in the HS state; the slight decrease of $\chi_M T$ below 100 K can be ascribed to the effect of zero-field splitting and/or very weak magnetic coupling. This HS behavior persists even at pressures as high as 0.7 GPa (see Figure S1 in SI). A similar thermal dependence of $\chi_M T$ at ambient pressure has been observed for **FpzPt3D** (see Figure S2 in SI).

Photogeneration of the metastable HS* state at low temperature, the so-called light-induced excited spin state trapping experiment (LIESST),^[30] was carried out on microcrystalline samples of **FpzPt** (1.7 mg) and **FpzPd** (2.1 mg) spread over a 16 mm² surface, fastened with permanent adhesive (Figure 1b and 1c). The samples were cooled down to 10 K where $\chi_M T \approx 0.10$ cm³ K mol⁻¹, and then irradiated with green (**FpzPt**, $\lambda = 532$

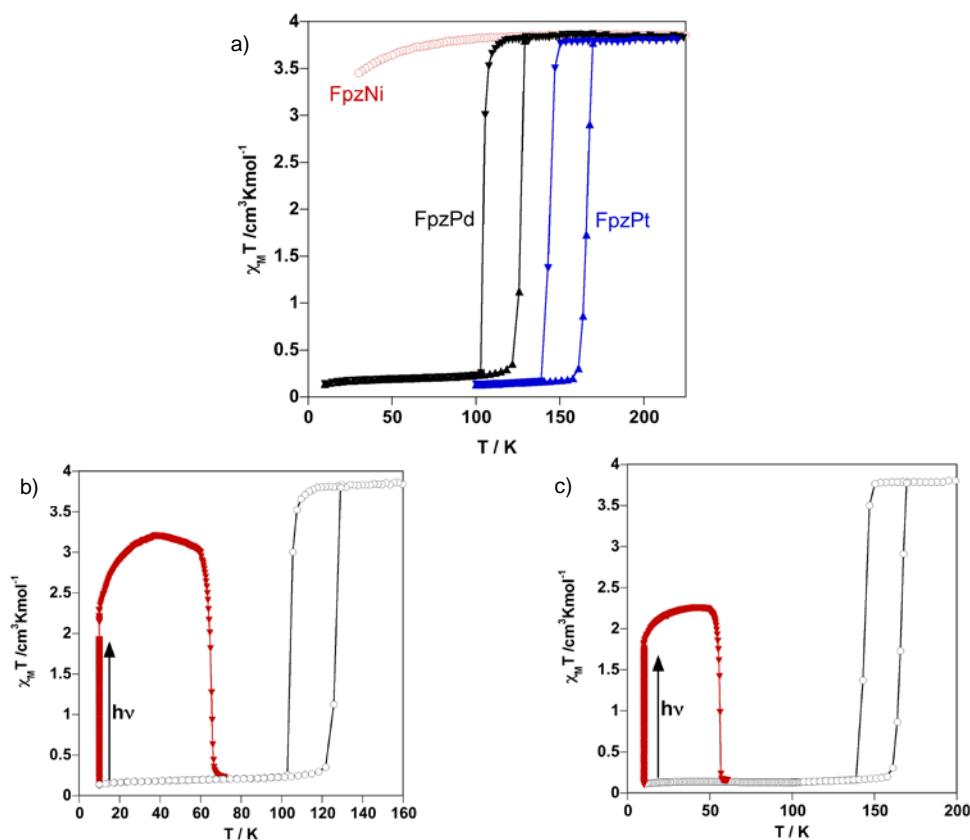


Figure 1.- (a) $\chi_M T$ vs T plots for **FpzNi**, **FpzPd**, and **FpzPt** (temperature scan rate 2 K min^{-1}). LIESST effect for compounds **FpzPd** (b) and **FpzPt** (c) (see text for experimental details).

nm) or red (**FpzPd**, $\lambda = 633 \text{ nm}$) light, attaining a $\chi_M T$ saturation value of ca. 1.80 (**FpzPt**) and $2.15 \text{ cm}^3 \text{ K mol}^{-1}$ (**FpzPd**) in ca. 3 h. The light was then switched off and temperature increased at a rate of 0.3 K min^{-1} . In the 10-39 K temperature range $\chi_M T$ increased up to a maximum value of ca. 2.26 (**FpzPt**) and $3.21 \text{ cm}^3 \text{ K mol}^{-1}$ (**FpzPd**) at 39 K, which reflects the thermal population of the different microstates arising from the zero-field splitting of the HS* ($S = 2$) state and/or antiferromagnetic coupling. This suggests that the light-induced population of the HS* state is ca. 57% and 85% at 10 K for **FpzPt** and **FpzPd**, respectively. For **FpzPd**, $\chi_M T$ drops slowly to attain a value of $3.04 \text{ cm}^3 \text{ K mol}^{-1}$ at 60 K and then rapidly decreases and reaches a value of about $0.24 \text{ cm}^3 \text{ K mol}^{-1}$ at ca. 72 K, indicating complete HS* \rightarrow LS relaxation. By contrast, $\chi_M T$ drops rapidly to $0.16 \text{ cm}^3 \text{ K mol}^{-1}$ at 58 K. The T_{LIESST} temperature^[31] determined from the maximum variation of $\chi_M T$ in the HS \rightarrow LS relaxation is

56.3 and 65.5 K for **FpzPt** and **FpzPd**, respectively. These values reflect the relative stabilization of the LS state with respect to the HS state in each compound, and it is a consequence of the so-called inverse energy-gap law, i.e., the metastability of the photogenerated HS* species decreases as the stability of the LS increases.^[32]

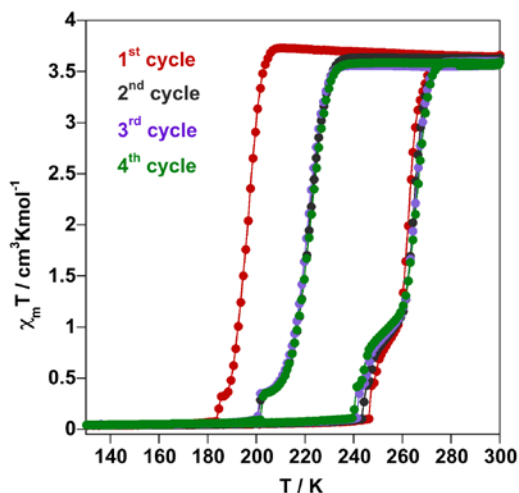


Figure 2. - $\chi_M T$ vs T plots for compound **FpAu** (see text; temperature scan rate 1 K min⁻¹).

The magnetic properties of compound **FpzAu** measured at 1 K/min are displayed in Figure 2. At 300 K $\chi_M T$ is ca. 3.6 cm³ K mol⁻¹ and remains practically constant down to 208 K. Below this temperature $\chi_M T$ displays a steep and complete spin transition ($\chi_M T \approx 0$ at 180 K) characterized by a small plateau at ca. 91% of the HS \rightarrow LS transformation (centered at 187 K) and $T_{1/2}^\downarrow = 196$ K. Upon heating $\chi_M T$ does not match the cooling mode. Indeed, a more marked plateau occurs at 23% of LS \rightarrow HS transformation, and $T_{1/2}^\uparrow = 262$ K shows the occurrence of a hysteresis 66 K wide. In order to check the hysteresis stability, the same cooling-heating cycle was repeated three times more at the same scan temperature rate. In the second cycle, the cooling mode shows that the spin transition takes place at $T_{1/2}^\downarrow = 221$ K, 25 K higher than observed for the first cycle, while small differences are observed in the heating mode ($T_{1/2}^\uparrow = 263$ K). The third and fourth cycles give essentially the same transition as the second one. Consequently, the stable hysteresis loop is 42 K wide, which indeed reflects a strong cooperative behavior. It deserves to be noted that these measurements were performed on single crystals and that after the cycles the crystals are self-destroyed

becoming powder. Precipitated microcrystalline samples of **FpzAu** behave in a similar way (see Figure S3 and Table S1 in SI). However, they show the following relevant differences with respect to the single-crystal ones: (i) they display approximately 10% of residual paramagnetism; (ii) the first and second cycles show $T_{1/2}^{\downarrow}$ = values ca. 14 K smaller (larger hysteresis) while essentially coincide for the third and fourth cycles, (iii) the small step observed in the $\chi_M T$ vs T plot for the single-crystals samples is not observed for the precipitated ones. The different texture of these samples and/or the presence of residual paramagnetism are two reasonable speculative explanations for this observation.

2.3.2.- Calorimetric properties

Quantitative differential scanning calorimetry (DSC) measurements were carried out at a temperature scan rate of 10 K/min for **FpzPt** and **FpzAu** ($T_{1/2}$ values for **FpzPd** are out of the temperature range of our DSC). The anomalous variation of the molar specific heat ΔC_p versus T for the cooling and heating modes is displayed in Figure 3. The average enthalpy ΔH and entropy ΔS variations are gathered in Table 1 together with the critical temperatures obtained from the maximum/minimum values of ΔC_p . The critical temperatures obtained from these DSC data agree reasonably well with those deduced from the magnetism measurements for **FpzPt** and **FpzAu**. The large ΔS and ΔH values are consistent with those reported for related Hofmann-like coordination polymers undergoing strong cooperative spin transitions.^[10]

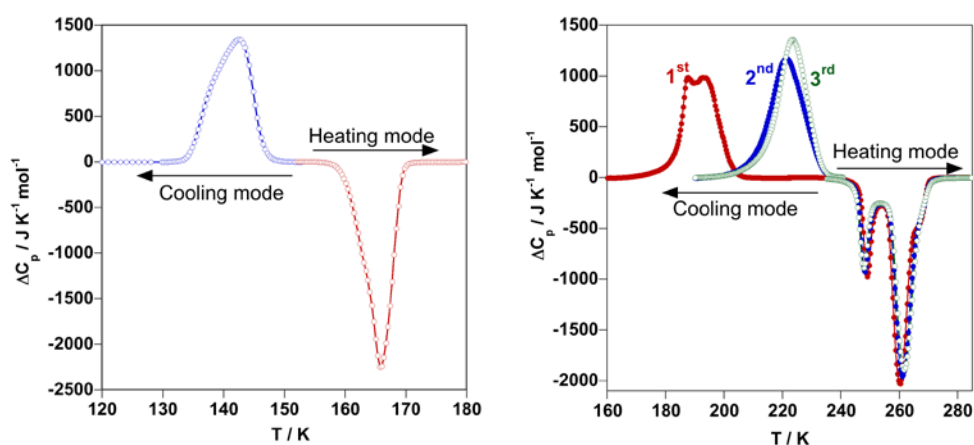


Figure 3.- Anomalous heat capacity (DSC) for **FpzPt** (left) and **FpzAu** (right). Red, blue, and green curves in **FpzAu** refer to the first, second, and third cooling-heating cycles (temperature scan rate 10 K min^{-1}).

Table 1. Thermodynamic data obtained from calorimetric DSC measurements for the SCO of **FpzPt** and **FpzAu**.

| | FpzPt | FpzAu | | |
|---|--------------|-----------------|--------------------------|-----------------|
| | | 1 st | cycle 2 nd | 3 rd |
| $T_{1/2}^{\downarrow}$ (K) | 142.5 | 193.1 | 221.5 | 223.4 |
| $T_{1/2}^{\uparrow}$ (K) | 165.7 | 260.4 | 261.0 | 261.0 |
| ΔT (K) | 22 | 66 | 39.5 | 37.6 |
| ΔS^{av} (J K ⁻¹ mol ⁻¹) | 71.2 | 73.4 | 73.7 | 75.1 |
| ΔH^{av} (kJ mol ⁻¹) | 10.95 | 16.57 | 17.34 | 18.14 |

2.3.3.- Crystal structures

2.3.3.1.- Structures of the 2D complexes **FpzM**

The crystal structure was measured at 200 K for **FpzNi**, **FpzPd**, and **FpzPt** and at 98.5 and 120 K for **FpzPd** and **FpzPt**, respectively. These compounds are isostructural (see Figure S4 in SI) and, in the temperature interval investigated, show the orthorhombic *Pmna* space group. Crystallographic data, bond distances, and angles are given in Tables 2 and 3. Figure 4a displays an ORTEP view of a fragment of the structure showing the asymmetric unit with the numbering atom scheme representative for the three compounds. The Fe^{II} atom lies at an inversion center which defines an elongated octahedral coordination site [Fe^{II}N₆]. The equatorial positions are occupied by the nitrogen atoms of four equivalent centrosymmetric square-planar [M(CN)₄]²⁻ groups. The Fe-N_{eq} bond distances [Fe-N(2)_{eq} = 2.145(3) Å (**FpzNi**), 2.138(2) Å (**FpzPd**), and 2.135(3) Å (**FpzPt**) at 200 K] are shorter than the axial positions, which are occupied by the nitrogen atoms of the Fpz ligands [Fe-N(1)_{ax} = 2.240(4) Å (**FpzNi**), 2.229(3) Å (**FpzPd**), and 2.225(4) Å (**FpzPt**)]. The M^{II}-C and C-N bond distances are in the range 1.855 - 1.998 and 1.137 - 1.157 Å, respectively. The Fe-N average bond length of about 2.170 Å is consistent with the Fe^{II} in the HS state, in agreement with the magnetic data at this temperature.

At 98.5 (**FpzPd**) or 120 K (**FpzPt**) the Fe-N(1)_{ax} are shortened by 0.242 (**FpzPd**) and 0.235 (**FpzPt**) Å while the decrease of the Fe-N(2)_{eq} bond lengths is slightly smaller, 0.195 (**FpzPd**) and 0.194 (**FpzPt**) Å. The total average variation of about 0.21 Å is consistent with

Table 2. Crystal data of **FpzM** (M = Ni, Pd, Pt), **FpzPt3D** and **FpzAu**.

| | FpzNi | FpzPd | | FpzPt | |
|---|---|---|-------------|---|-------------|
| Empirical formula | C ₁₂ H ₆ N ₈ F ₂ NiFe | C ₁₂ H ₆ N ₈ F ₂ PdFe | | C ₁₂ H ₆ N ₈ F ₂ PtFe | |
| Mr | 414.81 | 462.50 | | 551.19 | |
| Crystal system | orthorhombic | orthorhombic | | orthorhombic | |
| Space group | <i>Pmna</i> | <i>Pmna</i> | | <i>Pmna</i> | |
| T/ K | 200 | 98.5 | 200 | 120 | 200 |
| <i>a</i> (Å) | 7.2842(2) | 7.2646(2) | 7.4526(5) | 7.2572(3) | 7.4534(4) |
| <i>b</i> (Å) | 6.9449(2) | 6.9726(3) | 7.1125(4) | 6.9861(3) | 7.1275(4) |
| <i>c</i> (Å) | 14.4255(5) | 14.7703(5) | 14.7770(11) | 14.9922(6) | 15.0455(10) |
| β (°) | | | | | |
| <i>V</i> (Å ³) | 729.75(5) | 748.17(5) | 783.28(9) | 760.10(5) | 799.28(8) |
| <i>Z</i> | 2 | 2 | 2 | 2 | 2 |
| <i>D_c</i> (mg cm ⁻³) | 1.888 | 2.053 | 1.961 | 2.408 | 2.290 |
| <i>F</i> (000) | 412 | 448 | | 512 | |
| μ (Mo-K α)(mm ⁻¹) | 2.319 | 2.206 | 2.107 | 10.181 | 9.682 |
| Crystal size (mm) | 0.12x0.15x0.15 | 0.08x0.08x0.15 | | 0.06x0.10x0.10 | |
| No of total reflections | 1006 | 1018 | 1144 | 1091 | 1167 |
| No. of reflections [<i>I</i> >2 σ (<i>I</i>)] | 869 | 761 | 933 | 816 | 968 |
| <i>R</i> [<i>I</i> >2 σ (<i>I</i>)] | 0.0482 | 0.0346 | 0.0349 | 0.0200 | 0.0242 |
| <i>R</i> [all data] | 0.0482 | 0.0564 | 0.0496 | 0.0318 | 0.0319 |
| <i>S</i> | 0.970 | 0.975 | 1.178 | 0.951 | 1.088 |

| | FpzPt3D | FpzAu | |
|---|---|--|-------------|
| Empirical formula | C ₈ H ₃ FN ₆ O _{0.5} PtFe | C ₈ H ₃ N ₆ FAu ₂ Fe | |
| Mr | 461.10 | 651.93 | |
| Crystal system | monoclinic | orthorhombic | |
| Space group | <i>P2/m</i> | <i>Cmca</i> | |
| T/ K | 120 | 120 | 250 |
| <i>a</i> (Å) | 7.2782(3) | 7.1107(10) | 7.2563(3) |
| <i>b</i> (Å) | 7.5613(2) | 10.1715(13) | 10.1992(5) |
| <i>c</i> (Å) | 7.4820(4) | 17.657(2) | 17.8959(7) |
| β (°) | 101.494(5) | | |
| <i>V</i> (Å ³) | 403.50(3) | 1277.1(3) | 1324.46(10) |
| <i>Z</i> | 1 | 4 | 4 |
| <i>D_c</i> (mg cm ⁻³) | 1.898 | 3.391 | 3.270 |
| <i>F</i> (000) | 210 | 1143 | |
| μ (Mo-K α)(mm ⁻¹) | 9.559 | 24.040 | 23.180 |
| Crystal size (mm) | 0.06x0.02x0.02 | 0.06x0.06x0.08 | |
| No of total reflections | 1413 | 812 | 906 |
| No. of reflections [<i>I</i> >2 σ (<i>I</i>)] | 1384 | 524 | 659 |
| <i>R</i> [<i>I</i> >2 σ (<i>I</i>)] | 0.0406 | 0.0516 | 0.0301 |
| <i>R</i> [all data] | 0.0421 | 0.0825 | 0.0439 |
| <i>S</i> | 0.985 | 0.885 | 1.005 |

^a $R_1 = \sum ||F_o| - |F_c|| / \sum |F_o|$; $wR = [\sum [w(F_o^2 - F_c^2)^2] / \sum [w(F_o^2)^2]]^{1/2}$; $w = 1 / [\sigma^2(F_o^2) + (m P)^2 + n P]$ where $P = (F_o^2 + 2F_c^2) / 3$;
 $m = 0.0231$ (**200 K**), 0.0177 (**98.5 K**), 0.0121 (**200 K**), 0.0254 (**120 K**), 0.0172 (**200 K**), 0.0702 (**120 K**), 0.0155 (**120 K**), 0.0324 (**250 K**); $n = 6.0177$ (**200 K**), 1.5654 (**98.5 K**), 0.7115 (**200 K**), 0.9728 (**120 K**), 1.7518 (**200 K**), 0.000 (**120 K**), 160.1028 (**120 K**), 0.000 (**250 K**).

Table 3. Selected bond lengths [Å] and angles [°] of **FpzM** (M = Ni, Pd, Pt), **FpzPt3D** and **FpzAu**.

| T / K | FpzNi | FpzPd | | FpzPt | | FpzPt3D | FpzAu | |
|-------------------|-----------|-----------|----------|-----------|-----------|----------|-----------|----------|
| | 200 | 98.5 | 200 | 120 | 200 | 120 | 120 | 250 |
| Fe-N(1) | 2.240(4) | 1.987(4) | 2.229(3) | 1.990(4) | 2.225(4) | 2.175(9) | 2.046(9) | 2.235(7) |
| Fe-N(2) | 2.145(3) | 1.943(3) | 2.138(2) | 1.941(3) | 2.135(3) | 2.133(5) | 2.04(2) | 2.131(6) |
| Fe-N(3) | | | | | | | 2.07(2) | 2.142(6) |
| Ni-C(5) | 1.855(3) | | | | | | | |
| Pd-C(5) | | 1.998(3) | 1.992(3) | | | | | |
| Pt-C(5) | | | | 1.989(4) | 1.986(3) | | | |
| Pt-C(3) | | | | | | 1.978(5) | | |
| Au-C(2) | | | | | | | 1.78(5) | 1.990(7) |
| Au-C(3) | | | | | | | 2.05(2) | 1.981(8) |
| N(1)-Fe-N(2) | 87.71(11) | 88.39(11) | 88.27(8) | 88.54(12) | 88.37(11) | 88.1(2) | 90.00 | 90.00 |
| N(1)-Fe-N(3) | | | | | | | 90.00 | 90.00 |
| N(2)-Fe-N(3) | | | | | | | 87.0(6) | 86.9(3) |
| C(2)-Au-C(3) | | | | | | | 176.1(11) | 179.8(3) |
| Fe-N _i | 2.177 | 1.958 | 2.168 | 1.957 | 2.165 | 2.147 | 2.052 | 2.169 |
| Σ | 19.12 | 15.28 | 16.04 | 15.28 | 14.76 | 18 | 12 | 12.4 |

Table 4. Interlayer short contacts of **FpzM** (M = Ni, Pd, Pt).

| Short Contact | FpzNi | FpzPd | | FpzPt | |
|----------------------|----------|----------|----------|----------|----------|
| | 200 K | 200 K | 98.5 K | 200 K | 120 K |
| M...N3 ⁱ | 2.981(5) | 3.206(4) | 3.514(5) | 3.358(6) | 3.670(5) |
| C5...N3 ⁱ | 3.292(6) | 3.485(4) | 3.482(5) | 3.545(7) | 3.532(5) |
| F...C4 ⁱ | 3.130(7) | 3.281(5) | 3.270(6) | 3.327(7) | 3.352(7) |

complete transformation of the [Fe^{II}N₆] core from the HS state to the LS state, a fact confirmed by the magnetic data. The sum of deviations from the ideal octahedron of the 12 “cis” N-Fe-N angles ($\Sigma = \sum_{i=1}^{12} |\theta_i - 90|$) shows that the coordination center is weakly distorted in the HS state with Σ values in the range 15-19° and do not change significantly in the LS state.

The [M(CN)₄]²⁻ groups link four equivalent Fe^{II}, thereby generating 2D [Fe₂M^{II}₂(CN)₄]_n grids which are markedly corrugated (Figure 4b). The equatorial [FeN₄^{eq}] plane defines an angle 36.9° (**FpzNi**), 35.7° (**FpzPd**), and 33.1° (**FpzPt**) with respect to the [M(CN)₄]²⁻ plane at 200 K and decreases down to 26.1° and 20.3° for the Pd and Pt derivatives at 98.5 and 120 K, respectively (Figure 4c). The layers stack in such a way that the metallic atoms of a layer, which lie in the (100) plane, project on the center of the [Fe-CN-M]₄ square windows defined

by adjacent layers. The separation between consecutive planes is 7.213(6) (**FpzNi**), 7.388(5) (**FpzPd**), and 7.523(7) Å (**FpzPt**) at 200 K and 7.385(6) (**FpzPd**) and 7.496(6) Å (**FpzPt**) at 98.5 and 120 K respectively. The protruding Fpz ligands of consecutive layers interdigitate, defining almost face-to-face superposition along the [100] direction with centroid-to-centroid distances indicating the occurrence of weak π stacking: 3.642 (**FpzNi**), 3.726 (**FpzPd**), and 3.727 Å (**FpzPt**) at 200 K and 3.632 (**FpzPd**) and 3.629 Å (**FpzPt**) at 98.5 and 120 K, respectively (Figure 4c). Interestingly, due to the singular disposition of consecutive layers, the uncoordinated N atom of the Fpz of one layer points directly toward the unsaturated axial coordination positions of the $[M(CN)_4]^{2-}$ groups of the adjacent layers, with the distance being particularly short for **FpzNi** ($d(\text{Ni}\cdots\text{N}(3))$ is 2.981(5) Å). Other very short contacts between layers are defined by the atoms N(3) and F with the C(5) atom of the CN group ($d(\text{N}(3)\cdots\text{C}(5)) = 3.292(6)$ Å) and the C(4) atom ($d(\text{F}\cdots\text{C}(4)) = 3.130(7)$ Å), respectively. These short contacts are remarkably larger for Pd and Pt, and interestingly, the $\text{M}\cdots\text{N}(3)$ contact increases by ca. 0.3 Å when moving from the HS to the LS state (see Table 4). Most likely, this is a consequence of the aforementioned change of dihedral angle between the equatorial FeN_4 and the $[M(CN)_4]^{2-}$ planes.

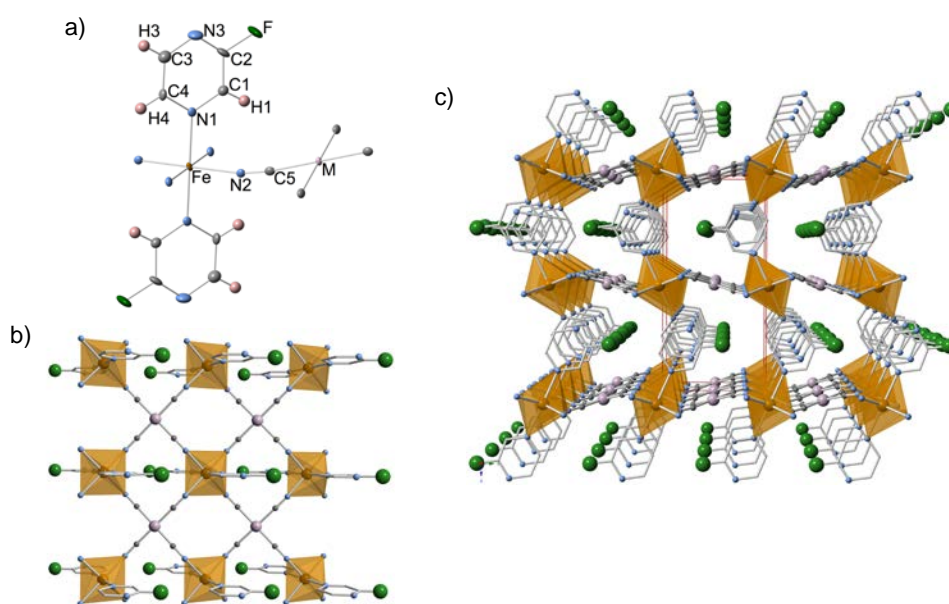


Figure 4. (a) ORTEP representation of a molecular fragment of **FpzM** ($M = \text{Ni}, \text{Pd}, \text{Pt}$) (thermal ellipsoids are given at 50% probability for $M = \text{Ni}$ at 200 K). (b) View of a layer along the [001] direction. (c) Crystal packing view along the [100] direction. Hydrogen atoms have omitted for simplicity in b and c.

2.3.3.2.- Structure of the 3D complex **FpzPt3D**

Compound **FpzPt3D** shows the monoclinic $P2/m$ unit cell in the temperature range 120-200 K (Tables 2 and 3). Figure 5a displays an ORTEP view of a fragment of the structure showing the asymmetric unit together with atom numbering. The Fe^{II} and Pt^{II} atoms lie at an inversion center. The former defines a slightly elongated octahedral coordination [Fe^{II}N₆] site with axial and equatorial Fe-N bond distances Fe-N(1) = 2.175(9) Å and Fe-N(2) = 2.133(5) Å, respectively. The latter defines square-planar [Pt(CN)₄]²⁻ units with usual Pt-C and C-N bond distances [Pt-C(3) = 1.978(5) Å and C-N = 1.154(8) Å]. The average Fe-N bond length, 2.147 Å, clearly indicates that this compound is HS at 120 K, in agreement with the magnetic properties.

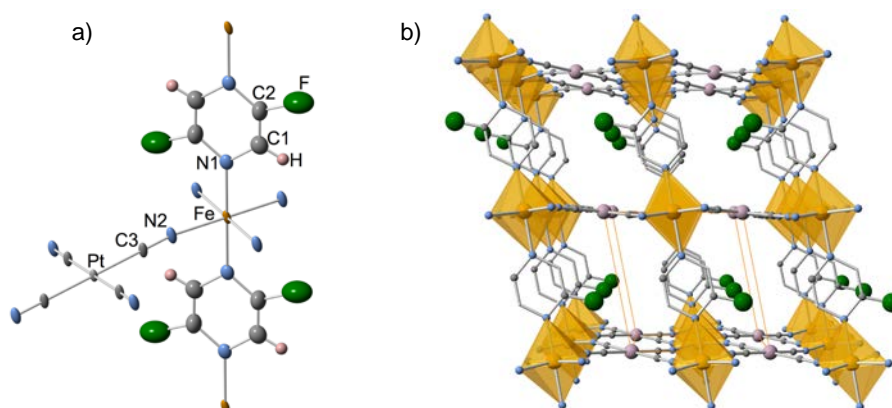


Figure 5. (a) ORTEP representation of a molecular fragment of **FpzPt3D** (thermal ellipsoids are given at 30% probability). (b) Crystal packing view along the [010] direction showing only one of the two equivalent positions for the F atom (hydrogen atoms have been omitted for simplicity).

As described for the **FpzM** series, 2D [Fe₂M^{II}₂(CN)₄]_n grids are generated by coordination of the equatorial Fe^{II} sites by four equivalent [Pt(CN)₄]²⁻ units, thus generating an infinite stack. However, at variance with **FpzM**, the [Fe₂M^{II}₂(CN)₄]_n 2D layers are almost planar and the Fpz ligands act as pillars linking adjacent layers through the Fe^{II} centers in a similar way as described for the 3D Hofmann clathrate system {Fe(pz)[M(CN)₄]} (Figure 5b). Indeed, the structure of **FpzPt3D** is a slightly distorted version of {Fe(pz)[Pt(CN)₄]} since the equatorial plane of the [Fe^{II}N₆] sites is not strictly in the same plane of the [Pt(CN)₄]²⁻ sites. In spite of this, the angle defined between these sites, 13.7°, is ca. 59% smaller than that observed for compound **FpzPt**. The F atom displays static disorder with an occupation factor

of 0.5. The water molecules are located at the middle of the channels, showing positional disorder (see Figure S5 in SI).

2.3.3.3.- Structure of the 3D FpAu Complex

The compound **FpzAu** was investigated at 250 and 120 K. At both temperatures the unit cell corresponds to the orthorhombic *Cmca* space group (Tables 2 and 3). The Fe^{II} lies in an inversion center and defines an elongated [FeN₆] octahedron whose axial positions are occupied by two equivalent Fpz ligands, while the equatorial positions are occupied by four

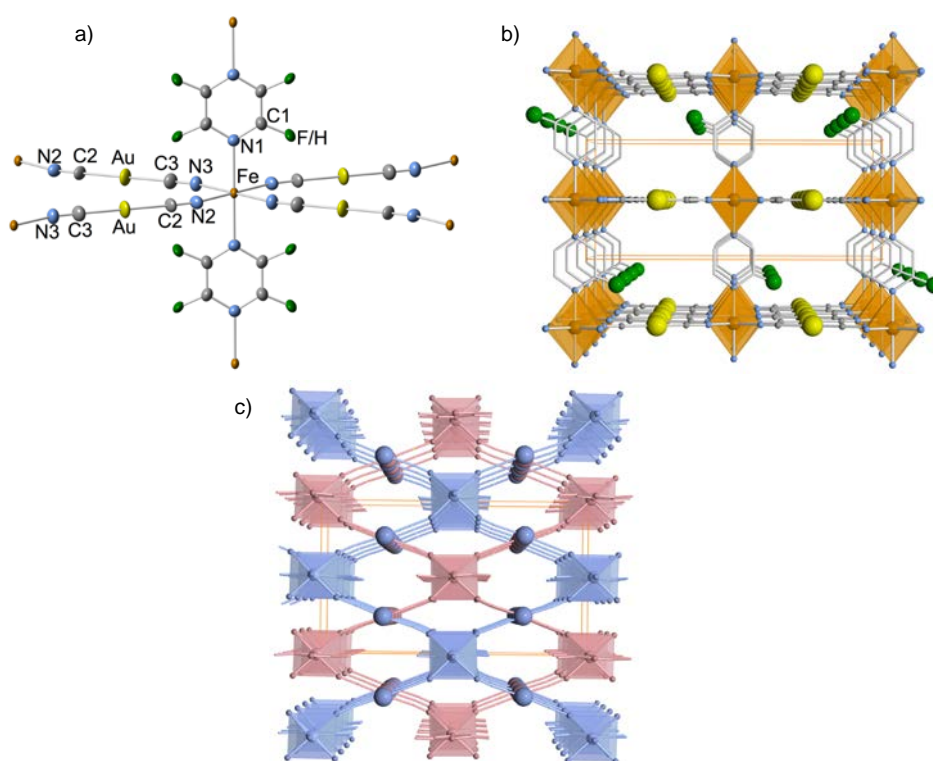


Figure 6. (a) ORTEP representation of a molecular fragment of **FpzAu** (thermal ellipsoids are given at 50% probability). (b) Crystal packing view along the [010] direction showing only one of the four equivalent positions for the F atom (hydrogen atoms have been omitted for simplicity). (c) View illustrating the two interpenetrated 3D frameworks.

equivalent [Au(CN)₂]⁻ groups (Figure 6a). It is worth noting that due to symmetry reasons the fluorine atom is occupationally disordered (occupation factor of 0.25). At 250 K, the axial bond lengths, Fe-N(1) = 2.235(7) Å, are remarkably longer than the equatorial ones (Fe-N(2) = 2.131(6) Å and Fe-N(3) = 2.142(6) Å). As in the precedent examples the angular distortion

of the coordination center is small ($\Sigma = 12.4^\circ$) and the Fe-NC-Au linkage is not linear since it forms an average angle of 156.8° and changes very little with the spin state change. The average Fe-N bond length of 2.169 Å is consistent with HS state of the Fe^{II} fully populated, in agreement with the magnetic properties at the same temperature. However, at 120 K the axial (Fe-N(1)) and equatorial (Fe-N(2), Fe-N(3)) bond lengths decrease down to 2.046(9) and 2.04(2) Å and 2.07(2) Å, respectively. The average decrease of the axial bond length, 0.19 Å, is ca. 20% smaller than observed for the **FpzM**, while the average decrease of the equatorial bond lengths, 0.08 Å, is ca. 58% smaller than expected. Despite the satisfactory *R* value obtained for this structure at 120 K, and as aforementioned, the single crystals deteriorate markedly during the SCO. This is particularly reflected in the strong distortion of the thermal ellipsoids of the C2 atoms in the LS.

The four [Au(CN)₂]⁻ groups equatorially coordinated to the Fe^{II} site act as bimonodentate bridging ligands linking four equivalent Fe^{II} sites, thus generating 2D {Fe₄[Au(CN)₂]₄}_n grids which lie in the plane (011). In a similar way as described for **FpzPt3D**, the grids stack along the [100] direction and are pillared through the Fpz ligands, which act as bridges linking the Fe^{II} sites (Figure 6b). However, at variance with **FpzPt3D**, the [Au(CN)₂]⁻ group defines a much more expanded 3D framework which allows the mutual interpenetration of two identical 3D coordination polymers (Figure 6c).

2.4.- Discussion

This work was undertaken to investigate the coordination abilities of the Fpz ligand to form new 3D Hofmann-like SCO materials based on [M^{II}(CN)₄]²⁻ and [M^I(CN)₂]⁻ (M^{II} = Ni, Pd, Pt; M^I = Ag, Au) building blocks. A priori, the steric hindrance and electron withdrawing induced by F atom should debilitate the capability of Fpz to act as a bridging ligand and, consequently, favor the formation of 2D frameworks. The results obtained with [M^{II}(CN)₄]²⁻ confirm in part this conjecture. Three light-yellow 2D coordination polymers, **FpzM** (M^{II} = Ni, Pd, Pt), are obtained by direct precipitation and slow diffusion in H-shaped containers. However, the presence of the F atom in the pyrazine ring does not fully deactivate the capability of Fpz to act as a bimonodentate ligand. Indeed, slow diffusion of the components using the layering method forms exclusively the red porous 3D Hofmann-like coordination polymer **FpzPt3D** (the homologous Pd compound is also formed in the same

conditions but with much lower yield). By contrast, whatever the synthetic method used the yellow 2D system is obtained when $M = \text{Ni}$.

The three **FpzM** ($M^{\text{II}} = \text{Ni, Pd, Pt}$) derivatives display significantly corrugated 2D layers, a fact that contrasts with the much less corrugated layers defined by the homologous **ClpzNi** structure reported by Gural'skiy and co-workers^[28e] or related 3X-pyridine ($X = \text{F, Cl}$) 2D derivatives formulated **XpyM** (Pd, Pt) previously reported by our group.^[33] Similarly, the HS compound **FpzPt3D** displays almost flat $\{\text{Fe}[\text{Pt}(\text{CN})_4]\}_n$ layers, which in this case are pillared by the axial linkers Fpz. In the latter, the F atom shows positional disorder due to symmetry reasons, and consequently, the Fe-N(1) (Fpz) axial bond length is averaged. Paradoxically, this bond length is ca. 0.05-0.04 Å shorter than that observed for **FpzPt** and the homologous 3D compound $\{\text{Fe}(\text{pz})[\text{Pt}(\text{CN})_4]\}$ in the HS state. In spite of this **FpzPt3D** remains HS at all temperatures. A reasonable conjecture to explain this fact could be related to the low thermal stability shown by **FpzPt3D**. This compound includes ca. 0.5 disordered water molecules in the channels that desorb at 350 K, a temperature at which the Fpz ligand starts to be lost (see figure S6 in SI). By contrast, the 2D **FpzPt** and 3D $\{\text{Fe}(\text{pz})[\text{Pt}(\text{CN})_4]\}$ homologues are clearly more stable since no loss of Fpz/pz occurs up to 395/480 K (see Figure S6 in SI). Although it is always speculative to give an explanation in these circumstances, the lack of SCO and low thermal stability of **FpzPt3D** might reflect a much more strained structure. By contrast, the lack of thermal SCO in **FpzNi** could be related to the tight crystal packing and very short interlayer contacts observed in the HS state, which presumably prevents the change to a more packed LS structure even at pressures of 0.7 GPa. Furthermore, an important feature of the two SCO complexes **FpzPd** and **FpzPt** is the drastic change of color from light-yellow (HS) to dark-red (LS) upon SCO.

FpzAu invariably affords a 3D coordination polymer whatever the synthetic method employed. This structure resembles that of **FpzPt3D**, but obviously the latter is more reticulated due to the different connectivity of $[\text{M}^{\text{II}}(\text{CN})_4]^{2-}$ and $[\text{M}^{\text{I}}(\text{CN})_2]^-$ building blocks. Consequently, **FpzAu** affords a more open and presumably less strained framework. In this respect, the thermal stability of this framework is notably higher (ca. 480 K, see Figure S6 in SI) than that of **FpzPt3D**. In **FpzPt3D** the two metallic building blocks act as 4-connected nodes and must match their coordination angles as close to 90° as possible. By contrast, the **FpzAu** structure is more relaxed since there is only one type of 4-connected node, namely, the Fe^{II} linked to other equivalent sites through four $[\text{Au}(\text{CN})_2]^-$ linkers defining infinite $\{\text{Fe}_4[\text{Au}(\text{CN})_2]_4\}_n$ grids. Although the equatorial angles in the $[\text{FeN}_6]$ coordination center

deviate only 3.1° from 90°, the Fe-N-C-Au-C-N linkages deviate 23.2° from linearity, and consequently, the Fe₄ units define rhombuses. As in **FpzPt3D**, the {Fe₄[Au(CN)₂]₄}_n grids are similarly connected through Fpz bridges. The F atom is averaged in four positions defining Fe-N(Fpz) bonds similar to that found for **FpzPt**, which is ca. 0.06 Å longer than those found for **FpzPt3D**. The void space generated by the resulting less dense 3D framework enables interpenetration of an identical framework. This situation has been previously reported by our group for the homologous compound {Fe(pz)₂[Ag(CN)₂]₂} and more recently by Ni and Tong et al. for [Fe(2,5-bpp){Au(CN)₂]₂·xSolvent (2,5-bpp = 2,5-bis(pyrid-4-yl)pyridine),^[29k] Kepert et al. for [Fe(bipytz)(Au(CN)₂]₂] (bipytz = 3,6-bis(4-pyridyl)-1,2,4,5-tetrazine),^[29j] and more recently by Gural'skiy et al. for {Fe(pz)[Au(CN)₂]₂} (hereafter **HpzAu**).^[34]

Table 5. Characteristic temperatures of the SCO for the related compounds **HpyM**, **FpyM** and **FpzM** (see text).

| compound | $T_{1/2}^{\downarrow} / K$ | $T_{1/2}^{\uparrow} / K$ | $\Delta T / K$ | <i>nD</i> | ref. |
|--------------|----------------------------|--------------------------|-------------------|-----------|------------------|
| HpyNi | 186 | 195 | 9 | 2D | 7 |
| HpyPd | 208 | 213 | 5 | 2D | 8 |
| HpyPt | 208 | 216 | 8 | 2D | 8 |
| HpyAu | - | - | - | 2D | 35a ^a |
| FpyNi | 205.8 | 234.4 | 28.6 | 2D | 33 |
| FpyPd | 213.6 | 248.4 | 34.8 | 2D | 33 |
| FpyPt | 214 | 239.5 | 25.5 | 2D | 33 |
| FpyAu | 123.9 ^b | 108.8 ^b | 15.1 ^b | 2D | 35b |
| HpzNi | 287 | 307 | 20 | 3D | 36 |
| HpzPd | 286 | 310 | 24 | 3D | 36 |
| HpzPt | 285 | 309 | 24 | 3D | 36 |
| HpzAu | 349 | 367 | 18 | 3D | 34 |
| FpzNi | HS | HS | HS | 2D | this work |
| FpzPd | 105 | 127 | 22 | 2D | this work |
| FpzPt | 144.5 | 166.5 | 22 | 2D | this work |
| FpzAu | 221.5 | 264.5 | 43 | 3D | this work |

^aThis compound is HS at all temperatures. ^bThis compound displays two steps with $T_{1/2}^{11} = 147$ K, $T_{1/2}^{12} = 98.2$ K, $T_{1/2}^{12} = 118.6$ K, and $T_{1/2}^{11} = 147$ K.

Following the same synthetic method described for **FpzAu**, mixtures of Fe^{II}/Fpz solutions with solutions of [Ag^I(CN)₂]⁻ gave in all cases dark-gray precipitates. After many attempts we concluded that the homologous compound **FpzAg** is not a stable species.

Table 5 gathered the spin transition temperatures for the series of complexes here investigated and related pyridine (**HpyM**),^[7,8,35a] 3-fluoropyridine (**FpyM**).^[33, 35b] and pyrazine {Fe(pz)[M(CN)_x]_z} (M^{II} = Ni, Pd, Pt, x = 4, z = 1;^[36] and M^I = Au,^[34] x = 2, z = 2) (**HpzM**) derivatives. From the critical temperatures observed for the title **FpzM** 2D compounds, it is safe to state that the LS state is destabilized when moving from Pt to Ni derivate. However, rationalizing of this trend is not obvious, as it seems to depend on the particular studied system. For example, the opposite trend has been observed for the related series of 2D compounds **ClpzM** (M = Ni, Pd, Pt).^[28e] Another relevant observation is the increase of cooperativeness regarding **HpyM** (M = Ni, Pd, Pt). This is, presumably, due to the presence of short interlayer contacts facilitated by the presence of the fluorine atom in the pyridine and pyrazine rings in the series **FpyM** and **FpzM** (M = Ni, Pd, Pt). It is worth noting that when comparing **HpyM** and **FpyM** series the increase in cooperativeness is essentially reflected in the increase of the characteristic $T_{1/2}^{\downarrow}$ transition temperatures. The clear destabilization of the LS state in the 2D **FpzM** (M = Ni, Pd, Pt) series can be ascribed to the weaker ligand field induced by the ligand pz with respect to the ligands py and Fpy. As far as the gold derivatives are concerned, the strong cooperative behavior and much higher $T_{1/2}$ temperatures reflect the change of dimensionality from 2D to 3D.

The light-induced excited spin state trapping (LIESST) effect has been investigated for the three derivatives undergoing thermal-induced SCO. As a consequence of the characteristic high-spin transition temperature, relaxation of the photogenerated HS* state in **FpzAu** is very rapid, even at 10 K, and no LIESST effect could be recorded in our magnetometer set up. This is consistent with the rapid HS* → LS relaxation (ca. 15 min) observed at 10 K for the 3D compound {Fe(pz)[Pt(CN)₄]₂·nH₂O} which undergoes a cooperative SCO characterized by a hysteresis ca. 25 K wide centered at about 290 K.^[24] Despite the average $T_{1/2}$ not being too high for **FpzPt**, only 57% of HS* population was produced at 10 K. In contrast, practically complete transformation to the HS* was achieved for **FpzPd** compound. The T_{LIESST} values, 56.3 and 65.5 K, respectively, compare well with that obtained for the related 2D Hofmann-like compound **ClpyPd**, which undergoes a two-step cooperative spin transition with characteristic temperatures centered at 162 and 145 K.^[37]

2.5.- Conclusion

The SCO behavior of a new series of 2D and 3D Hofmann-like Fe^{II} compounds obtained from self-assembling of Fe^{II}, fluoropyrazine (Fpz), and [M^{II}(CN)₄]²⁻ (M^{II} = Ni, Pd, Pt) and [Au^I(CN)₂]⁻ building blocks has been investigated. The compounds based on [M^{II}(CN)₄]²⁻ building blocks are stable 2D coordination polymers, **FpzM**. The Pd and Pt derivatives undergo strong cooperative thermal- and light-induced SCO behavior accompanied by drastic color changes from light-yellow (HS) to deep-red (LS), in contrast to the Ni derivate that is HS at all temperatures even at a pressure of 0.7 GPa. From $T_{1/2}$ values destabilization of the LS state follows the trend Pt > Pd > Ni. The lack of SCO in the Ni derivate has tentatively been associated with dense packing of the corrugated layers. The 3D metal organic framework **FpzPt3D**, obtained from different synthetic conditions, is a distorted version of the well-known Hofmann-like compound {Fe(pz)[Pt(CN)₄]. It displays unusual low thermal stability tentatively ascribed to structural strain and is HS at all temperatures. By contrast, the 3D compound **FpzAu** constituted of two identical interpenetrated 3D frameworks displays very cooperative SCO with a stable hysteresis larger than 40 K.

2.6.- Experimental section

All chemicals were purchased from commercial suppliers and used without further purification. Elemental and thermogravimetric analyses were performed, respectively, on LECO CHNS-932 and Mettler Toledo TGA/SDTA 851e (working in the 290-800 K temperature range under a nitrogen atmosphere with a rate of 10 K min⁻¹) analyzers. IR spectra were recorded at 293 K by using a Nicolet 5700 FTIR spectrometer with the samples prepared as KBr discs. Powder X-ray measurements were performed on a PANalytical Empyrean X-Ray powder diffractometer (monochromatic Cu K α radiation).

2.6.1.- Synthesis of {Fe(Fpz)₂[M(CN)₄]}

Microcrystalline samples of **FpzM** (M = Ni, Pd, Pt) were obtained in Ar atmosphere by adding dropwise, under vigorous stirring, an aqueous solution of K₂[M(CN)₄] \cdot 3H₂O (0.4 mmol, 5 mL) to an aqueous solution containing Fe(BF)₄ \cdot 6H₂O (0.4 mmol, 3 mL) and

fluoropyrazine (0.8 mmol, 3 mL). The resulting yellowish solid was stirred for 15 min, filtered, washed with water, and dried in air (yield ca. 80%). Suitable single crystals for X-ray studies were prepared by slow diffusion methods using a H-shaped tube. In one side of the H tube were dissolved 0.15 mmol (41.7 mg) of $\text{FeSO}_4 \cdot 7\text{H}_2\text{O}$ and 0.3 mmol (29.4 mg) of fluoropyrazine in 1 mL of water, while the opposite side contained 1 mL of a solution (0.15 mmol) of $\text{K}_2[\text{M}(\text{CN})_4] \cdot 3\text{H}_2\text{O}$ [36.2 mg (Ni); 51.5 mg (Pd) and 64.7 mg (Pt)]. The H vessel was carefully filled with water and sealed. Yellow single crystals of the title compounds appear in 2 weeks (yield ca. 20%). EDX analysis (energy-dispersive X-ray analysis) confirmed the stoichiometric relationship between metallic coordination centers: $[\text{Fe}:\text{Ni}] = [1:1]$, $[\text{Fe}:\text{Pd}] = [1:1]$, and $[\text{Fe}:\text{Pt}] = [1:1]$. The CN bond stretching mode features intense IR bands at $\nu(\text{CN}) = 2157 \text{ cm}^{-1}$ (shoulder) and 2145 cm^{-1} (sharp) for **FpzNi**, 2161 cm^{-1} (sharp) for **FpzPd**, and 2168 cm^{-1} (shoulder) and 2158 cm^{-1} (sharp) for **FpzPt**. Anal. Calcd for $\text{C}_{12}\text{H}_6\text{F}_2\text{FeN}_8\text{Ni}$: C, 34.75; H, 1.46; N, 27.02. Found: C, 33.98; H, 1.52; N, 27.45. Anal. Calcd for $\text{C}_{12}\text{H}_6\text{F}_2\text{FeN}_8\text{Pd}$: C, 31.16; H, 1.31; N, 24.23. Found: C, 31.01; H, 1.35; N, 23.98. Anal. Calcd for $\text{C}_{12}\text{H}_6\text{F}_2\text{FeN}_8\text{Pt}$: C, 26.15; H, 1.10; N, 20.33. Found: C, 26.38; H, 1.15; N, 20.98.

2.6.2.- Synthesis of $\{\text{Fe}(\text{Fpz})[\text{Pt}(\text{CN})_4]\} \cdot 1/2\text{H}_2\text{O}$

Compound **FpzPt3D** was produced by slow diffusion method, more precisely by layering in standard test tubes. The layering sequence was as follows: the bottom layer contains a mixture of Mohr's salt (0.2 mmol, 76 mg), fluoropyrazine (0.4 mmol, 40 mg), and a few crystals of ascorbic acid in 3 mL of water. Then an interphase containing a mixture of water:isopropanol (5 mL, 1:1) was added. Finally, a solution of $\text{K}_2[\text{Pt}(\text{CN})_4] \cdot 3\text{H}_2\text{O}$ (0.2 mmol, 86.3 mg) in water:isopropanol (5 mL, 1:4) was gently poured on top of the interphase. The tube was sealed, and red single crystals appeared in 3-4 weeks (yield ca. 30-40%). EDX confirms the stoichiometric relationship between metallic coordination centers: $[\text{Fe}:\text{Pt}] = [1:1]$. The CN bond stretching mode features an intense IR band at $\nu(\text{CN}) = 2168 \text{ cm}^{-1}$. Anal. Calcd for $\text{C}_8\text{H}_3\text{FFeN}_6\text{O}_{0.5}\text{Pt}$: C, 20.84; H, 0.66; N, 18.23. Found: C, 20.68; H, 0.70; N, 18.60.

2.6.3.- Synthesis of $\{\text{Fe}(\text{Fpz})[\text{Au}(\text{CN})_2]_2\}$

Microcrystalline samples of **FpzAu** were prepared in Ar atmosphere by adding dropwise, under vigorous stirring, an aqueous solution of $\text{K}[\text{Au}(\text{CN})_2]$ (0.4 mmol, 5 mL) to an

aqueous solution containing Fe(BF₄)₂·6H₂O (0.2 mmol, 3 mL) and fluoropyrazine (0.2 mmol, 3 mL). The resulting yellowish solid was stirred for 15 min, filtered, washed with water, and dried in air (yield ca. 85%). Suitable single crystals for X-ray studies were prepared by layering of the components as follows: the bottom layer contained a mixture of FeCl₂·4H₂O (0.2 mmol, 39.8 mg), fluoropyrazine (0.2 mmol, 19.6 mg), and a few crystals of ascorbic acid in 3 mL of water. Then an interphase was generated adding 10 mL of a H₂O:MeOH (3:1) mixture. Finally, a solution of K[Au(CN)₂] (0.4 mmol, 2 mL) in a H₂O:MeOH (1:2) mixture was gently poured on top of the interphase. EDX analysis confirms the stoichiometric relationship between metallic coordination centers: [Fe: Au] = [1:2]. The CN bond stretching mode features an intense IR band at $\nu(\text{CN}) = 2175 \text{ cm}^{-1}$ and a shoulder at 2159 cm^{-1} . Anal. Calcd for C₈H₃Au₂FFeN₆: C, 14.74; H, 0.46; N, 12.89. Found: C, 14.92; H, 0.50; N, 13.05.

2.6.4.- Single-crystal X-ray diffraction

Single-crystal X-ray data were collected on an Oxford Diffraction Supernova. In all cases Mo K α radiation ($\lambda = 0.71073 \text{ \AA}$) was used. A data scaling and empirical or multiscan adsorption correction was performed. The structures were solved by direct methods using SHELXS-2014 and refined by full-matrix least-squares of F^2 using SHELXL-2014.^[38] Non-hydrogen atoms were refined anisotropically, and hydrogen atoms were placed in calculated positions refined using idealized geometries (riding model) and assigned fixed isotropic displacement parameters.

2.6.5.- Magnetic and calorimetric measurements

Variable-temperature magnetic susceptibility data (15-20 mg) were recorded with a Quantum Design MPMS2 SQUID susceptometer equipped with a 7 T magnet, operating at 1T and at temperatures 2-400 K. Variable-temperature magnetic measurements under pressure were performed on **FpzNi** using a hydrostatic pressure cell made of hardened beryllium bronze with silicon oil as pressure transmitting medium and operating over the pressure range $10^5 \text{ Pa} < P < 1.2 \text{ GPa}$ (accuracy ca. $\pm 0.025 \text{ GPa}$). The compound was packed in a cylindrically shaped sample holder (1 mm in diameter and 5-7 mm in length) (8-10 mg) made up of very thin aluminium foil. The pressure was calibrated using the transition temperature of superconducting lead of high purity, 99.999%.^[39] Experimental

susceptibilities were corrected for diamagnetism of the constituent atoms by use of Pascal's constants.

Differential scanning calorimetry (DSC) measurements were performed on dry samples of the title compounds using a Mettler Toledo DSC 821e DSC calorimeter. Low temperatures were obtained with an aluminium block which was attached to the sample holder, refrigerated with a flow of liquid nitrogen, and stabilized at a temperature of 110 K. The sample holder was kept in a drybox under a flow of dry nitrogen gas to avoid water condensation. The measurements were carried out using about 10 mg of crystalline samples sealed in aluminium pans with a mechanical crimp. An overall accuracy of 0.2 K in the temperature and 2% in the heat capacity is estimated. The uncertainty increases for determination of the anomalous enthalpy and entropy due to subtraction of an unknown baseline.

2.7.- References

- [1] See for example: (a) Goodwin, H. A. *Coord. Chem. Rev.* **1976**, *18*, 293. (b) Gütlich, P. *Struct. Bonding (Berlin)* **1981**, *44*, 83. (c) König, E.; Ritter, G.; Kulshreshtha, S. K. *Chem. Rev.* **1985**, *85*, 219. (d) Hauser, A. *Comments Inorg. Chem.* **1995**, *17*, 17. (e) König, E. *Struct. Bonding (Berlin, Ger.)* **1991**, *76*, 51. (f) Gütlich, P.; Hauser, A.; Spiering, H. *Angew. Chem., Int. Ed. Engl.* **1994**, *33*, 2024. (g) Sato, O. *Acc. Chem. Res.* **2003**, *36*, 692. (h) Real, J. A.; Gaspar, A. B.; Niel, V.; Muñoz, M. C. *Coord. Chem. Rev.* **2003**, *236*, 121. (i) Gütlich, P.; Goodwin, H. A. *Topics in Current Chemistry* **2004**, Vols. 233-235. (j) Real, J. A.; Gaspar, A. B.; Muñoz, M. C. *Dalton Trans.* **2005**, 2062. (k) Halcrow, M. A. *Polyhedron* **2007**, *26*, 3523. (l) Halcrow, M. A. *Coord. Chem. Rev.* **2009**, *253*, 2493. (m) Olguin, J.; Brooker, S. *Coord. Chem. Rev.* **2011**, *255*, 203. (n) Bousseksou, A.; Molnár, G.; Salmon, L.; Nicolazzi, W. *Chem. Soc. Rev.* **2011**, *40*, 3313.
- [2] (a) Meded, V.; Bagrets, A.; Fink, K.; Chandrasekar, R.; Ruben, M.; Evers, F.; Bernard-Mantel, A.; Seldenthuis, J. S.; Beukman, A.; van der Zant, H. S. J. *Phys. Rev. B: Condens. Matter Mater. Phys.* **2011**, *83*, 245415. (b) Prins, F.; Monrabal-Capilla, M.; Osorio, E. A.; Coronado, E.; van der Zant, H. S. J. *Adv. Mater.* **2011**, *23*, 1545. (c) Cavallini, M.; Bergenti, I.; Milita, S.; Kengne, J. C.; Gentili, D.; Ruani, G.; Salitros, I.; Meded, V.; Ruben, M. *Langmuir* **2011**, *27*, 4076. (d) Miyamachi, T.; Gruber, M.;

- Davesne, V.; Bowen, M.; Boukari, S.; Joly, L.; Scheurer, F.; Rogez, G.; Yamada, T. K.; Ohresser, P.; Beaurepaire, E.; Wulfhekel, W. *Nat. Commun.* **2012**, *3*, 938. (e) Martinho, P. N.; Rajnak, C.; Ruben, M. In *Spin-Crossover Materials: Properties and Applications*; Halcrow, M. A. Ed.; Wiley: **2013**, pp 376-404 and references therein. (f) Sheperd, H. J.; Molnár, G.; Nicolazzi, W.; Salmon, L.; Bousseksou, A. *Eur. J. Inorg. Chem.* **2013**, 653. (g) Rotaru, A.; Dugay, J.; Tan, R. P.; Gural'skiy, I. A.; Salmon, L.; Demont, P.; Carrey, J.; Molnár, G.; Respaud, M.; Bousseksou, A. *Adv. Mater.* **2013**, *25*, 1745. (h) Gural'skiy, I. A.; Quintero, C. M.; Costa, J. S.; Demont, P.; Molnár, G.; Salmon, L.; Shepherd, H. J.; Bousseksou, A. *J. Mater. Chem. C* **2014**, *2*, 2949. (i) Bartual-Murgui, C.; Akou, A.; Thibault, C.; Molnár, G.; Vieu, C.; Salmon, L.; Bousseksou, A. *J. Mater. Chem. C* **2015**, *3*, 1277. (j) Aragonés, A. C.; Aravena, D.; Cerdá, J. I.; Acís-Castillo, Z.; Li, H.; Real, J. A.; Sanz, F.; Hihath, J.; Ruiz, E.; Díez-Pérez, I. *Nano Lett.* **2016**, *16*, 218.
- [3] Hofmann, K. A.; Küspert, F. A. Z. *Anorg. Allg. Chem.* **1897**, *15*, 204.
- [4] Powell, H. M.; Rayner, J. H. *Nature (London, U. K.)* **1949**, *163*, 566.
- [5] Baur, R.; Schwarzenbach, G. *Helv. Chim. Acta* **1960**, *43*, 842.
- [6] (a) Iwamoto, T. In *Inclusion Compounds*; Atwood, J. L.; Davies, J. E. D.; MacNicol, D. D., Eds. Oxford University Press: Oxford, **1991**, *5*, 177. (b) Iwamoto, T. In *Chemistry of Microporous Crystals*; Inui, T.; Namba, S.; Tatsumi, T., Eds. Kodansha/Elsevier: Tokyo, **1991**, *1*. (c) Soma, T.; Yuge, H.; Iwamoto, T. *Angew. Chem., Int. Ed. Engl.* **1994**, *33*, 1665.
- [7] Kitazawa, T.; Gomi, Y.; Takahashi, M.; Takeda, M.; Enomoto, M.; Miyazaki, A.; Enoki, T. *J. Mater. Chem.* **1996**, *6*, 119.
- [8] Niel, V.; Martínez-Agudo, J. M.; Muñoz, M. C.; Gaspar, A. B.; Real, J. A. *Inorg. Chem.* **2001**, *40*, 3838.
- [9] (a) Niel, V.; Muñoz, M. C.; Gaspar, A. B.; Galet, A.; Levchenko, G.; Real, J. A. *Chem. – Eur. J.* **2002**, *8*, 2446. (b) Niel, V.; Galet, A.; Gaspar, A. B.; Muñoz, M. C.; Real, J. A. *Chem. Commun.* **2003**, 1248.
- [10] Muñoz, M. C.; Real, J. A. *Coord. Chem. Rev.* **2011**, *255*, 2068.

- [11] Bartual-Murgui, C.; Salmon, L.; Akou, A.; Thibault, C.; Molnár, G.; Mahfoud, T.; Sekkat, Z.; Real, J. A. *New J. Chem.* **2011**, *35*, 2089.
- [12] Otsubo, K.; Haraguchi, T.; Sakata, O.; Fujiwara, A.; Kitagawa, H. *J. Am. Chem. Soc.* **2012**, *134*, 9605.
- [13] Raza, Y.; Volatron, F.; Moldovan, S.; Ersen, O.; Huc, V.; Martini, C.; Brisset, F.; Gloter, A.; Stéphan, O.; Bousseksou, A.; Catala, L.; Mallah, T. *Chem. Commun.* **2011**, *47*, 11501.
- [14] Peng, H.; Tricard, S.; Félix, G.; Molnár, G.; Nicolazzi, W.; Salmon, L.; Bousseksou, A. *Angew Chem., Int. Ed.* **2014**, *53*, 10894.
- [15] Ohtani, R.; Yoneda, K.; Furukawa, S.; Honrike, N.; Kitagawa, S.; Gaspar, A. B.; Muñoz, M. C.; Real, J. A.; Ohba, M. *J. Am. Chem. Soc.* **2011**, *133*, 8600.
- [16] Muñoz-Lara, F. J.; Gaspar, A. B.; Aravena, D.; Ruiz, E.; Muñoz, M. C.; Ohba, M.; Ohtani, R.; Kitagawa, S.; Real, J. A. *Chem. Commun.* **2012**, *48*, 4686.
- [17] Bao, X.; Shepherd, H. J.; Salmon, L.; Molnár, G.; Tong, M. L.; Bousseksou, A. *Angew. Chem., Int. Ed.* **2013**, *52*, 1198.
- [18] Aravena, D.; Arcís-Castillo, Z.; Muñoz, M. C.; Gaspar, A. B.; Yoneda, K.; Ohtani, R.; Mishima, A.; Kitagawa, S.; Ohba, M.; Real, J. A.; Ruiz, E. *Chem. - Eur. J.* **2014**, *20*, 12864.
- [19] Culp, J. T.; Chen, D. L.; Liu, J.; Chirdon, D.; Kauffman, K.; Goodman, A.; Johnson, J. K. *Eur. J. Inorg. Chem.* **2013**, 511.
- [20] Arcís-Castillo, Z.; Muñoz-Lara, F. J.; Muñoz, M. C.; Aravena, D.; Gaspar, A. B.; Sánchez-Royo, J. F.; Ruiz, E.; Ohba, M.; Matsuda, R.; Kitagawa, S.; Real, J. A. *Inorg. Chem.* **2013**, *52*, 12777.
- [21] Kosone, T.; Hori, A.; Nishibori, E.; Kubota, Y.; Mishima, A.; Ohba, M.; Tanaka, H.; Kato, K.; Kim, J.; Real, J. A.; Kitagawa, S.; Takata, M. *R. Soc. Open. Sci.* **2015**, *2*, 150006.
- [22] Cirera, J.; Babin, V.; Paesani, F. *Inorg. Chem.* **2014**, *53*, 11020.

- [23] Rodríguez-Velamazán, J. A.; González, M. A.; Real, J. A.; Castro, M.; Muñoz, M. C.; Gaspar, A. B.; Ohtani, R.; Ohba, M.; Yoneda, K.; Hijikata, Y.; Yanai, N.; Mizuno, M.; Ando, H.; Kitagawa, S. *J. Am. Chem. Soc.* **2012**, *134*, 5083.
- [24] Delgado, T.; Tissot, A.; Besnard, C.; Guénee, L.; Pattison, P.; Hauser, A. *Chem. - Eur. J.* **2015**, *21*, 3664.
- [25] Castro, M.; Roubeau, O.; Piñeiro-López, L.; Real, J. A.; Rodríguez-Velamazán, J. A. *J. Phys. Chem. C* **2015**, *119*, 17334.
- [26] Collet, E.; Henry, L.; Piñeiro-López, L.; Toupet, L.; Real, J. A. *Curr. Inorg. Chem.* **2016**, *6*, 61.
- [27] (a) Bartual-Murgui, C.; Ortega-Villar, N. A.; Shepherd, H. J.; Muñoz, M. C.; Salmon, L.; Molnár, G.; Bousseksou, A.; Real, J. A. *J. Mater. Chem.* **2011**, *21*, 7217. (b) Bartual-Murgui, C.; Akou, A.; Salmon, L.; Molnár, G.; Thibault, C.; Real, J. A.; Bousseksou, A. *Small*, **2011**, *7*, 3385. (c) Bartual-Murgui, C.; Salmon, L.; Akou, A.; Ortega-Villar, N. A.; Shepherd, H. J.; Muñoz, M. C.; Molnár, G.; Real, J. A.; Bousseksou, A. *Chem. - Eur. J.* **2012**, *18*, 507. (d) Muñoz-Lara, F. J.; Gaspar, A. B.; Muñoz, M. C.; Arai, M.; Kitagawa, S.; Ohba, M.; Real, J. A. *Chem. - Eur. J.* **2012**, *18*, 8013. (e) Muñoz-Lara, F. J.; Gaspar, A. B.; Muñoz, M. C.; Ksenofontov, V.; Real, J. A. *Inorg. Chem.* **2013**, *52*, 3. (f) Sciortino, N. F.; Scherl-Gruenwald, K. R.; Chastanet, G.; Halder, G. J.; Chapman, K. W.; Létard, J. F.; Kepert, C. J. *Angew. Chem., Int. Ed.* **2012**, *51*, 10154. (g) Piñeiro-López, L.; Seredyuk, M.; Muñoz, M. C.; Real, J. A. *Chem. Commun.* **2014**, *50*, 1833.
- [28] (a) Ohtani, R.; Arai, M.; Ohba, H.; Hori, A.; Takata, M.; Kitagawa, S.; Ohba, M. *Eur. J. Inorg. Chem.* **2013**, 738. (b) Ragon, F.; Yaksi, K.; Sciortino, N. F.; Chastanet, G.; Létard, J. F.; D'Alessandro, D. M.; Kepert, C. J.; Neville, S. M. *Aust. J. Chem.* **2014**, *67*, 1563. (c) Klein, Y. M.; Sciortino, N. F.; Ragon, F.; Housecroft, C. E.; Kepert, C. J.; Neville, S. M. *Chem. Commun.* **2014**, *50*, 3838. (d) Gaspar, A. B.; Levchenko, G.; Terekhov, S.; Bukin, G.; Valverde-Muñoz, J.; Muñoz-Lara, F. J.; Seredyuk, M.; Real, J. A. *Eur. J. Inorg. Chem.* **2014**, 429. (e) Kucheriv, O. I.; Shylin, S. I.; Ksenofontov, V.; Dechert, S.; Haukka, M.; Fritsky, I. O.; Gural'skiy, I. A. *Inorg. Chem.* **2016**, *55*, 4906.
- [29] (a) Shepherd, H. J.; Bartual-Murgui, C.; Molnár, G.; Real, J. A.; Muñoz, M. C.; Salmon, L.; Bousseksou, A. *New J. Chem.* **2011**, *35*, 1205. (b) Yoshida, K.; Kosone, T.; Kanadani, C.; Saito, T.; Kitazawa, T. *Polyhedron* **2011**, *30*, 3062. (c) Muñoz-Lara, F. J.;

- Gaspar, A. B.; Muñoz, M. C.; Lysenko, A. B.; Domasevitch, K. V.; Real, J. A. *Inorg. Chem.* **2012**, *51*, 13078. (d) Arcís-Castillo, Z.; Muñoz, M. C.; Molnár, G.; Bousseksou, A.; Real, J. A. *Chem. - Eur. J.* **2013**, *19*, 6851. (e) Li, J. Y.; Yan, Z.; Ni, Z. P.; Zhang, Z. M.; Chen, Y. C.; Liu, W.; Tong, M. L. *Inorg. Chem.* **2014**, *53*, 4039. (f) Xu, H.; Xu, Z. L.; Sato, O. *Microporous Mesoporous Mater.* **2014**, *197*, 72. (g) Piñeiro-López, L.; Arcís-Castillo, Z.; Muñoz, M. C.; Real, J. A. *Cryst. Growth Des.* **2014**, *14*, 6311. (h) Yan, Z.; Li, J. Y.; Liu, T.; Ni, Z. P.; Chen, Y. C.; Guo, F. S.; Tong, M. L. *Inorg. Chem.* **2014**, *53*, 8129. (i) Sugaya, A.; Ueno, S.; Okabayashi, J.; Kitazawa, T. *New J. Chem.* **2014**, *38*, 1955. (j) Clements, J. E.; Price, J. R.; Neville, S. M.; Kepert, C. J. *Angew. Chem., Int. Ed.* **2014**, *53*, 10164. (k) Li, J. Y.; Chen, Y. C.; Zhang, Z. M.; Liu, W.; Ni, Z. P.; Tong, M. L. *Chem. - Eur. J.* **2015**, *21*, 1645.
- [30] (a) Decurtins, S.; Gütllich, P.; Köhler, P. C.; Spiering, H.; Hauser, A. *Chem. Phys. Lett.* **1984**, *105*, 1. (b) Hauser, A. *Chem. Phys. Lett.* **1986**, *124*, 543. (c) Hauser, A. *Top. Curr. Chem.* **2004**, *234*, 155.
- [31] Létard, J. F. *J. Mater. Chem.* **2006**, *16*, 2550.
- [32] (a) Hauser, A. *Coord. Chem. Rev.* **1991**, *111*, 275. (b) Hauser, A.; Enachescu, C.; Daku, M. L.; Vargas, A.; Amstutz, N. *Coord. Chem. Rev.* **2006**, *250*, 1642.
- [33] Martínez, V.; Gaspar, A. B.; Muñoz, M. C.; Bukin, G. V.; Levchenko, G.; Real, J. A. *Chem. - Eur. J.* **2009**, *15*, 10960.
- [34] Gural'skiy, I. A.; Golub, B. O.; Shylin, S. I.; Ksenofontov, V.; Shepherd, H. J.; Raithby, P. R.; Tremel, W.; Fritsky, I. O. *Eur. J. Inorg. Chem.* **2016**, 3191.
- [35] (a) Kosone, T.; Kachi-Terajima, C.; Kanadani, C.; Saito, T.; Kitazawa, T. *Chem. Lett.* **2008**, *37*, 754. (b) Kosone, T.; Kachi-Terajima, C.; Kanadani, C.; Saito, T.; Kitazawa, T. *Chem. Lett.* **2008**, *37*, 422.
- [36] (a) Bonhommeau, S.; Molnár, G.; Galet, A.; Zwick, A.; Real, J. A.; McGarvey, J. J.; Bousseksou, A. *Angew. Chem., Int. Ed.* **2005**, *44*, 4069. (b) Ohba, M.; Yoneda, K.; Agustí, G.; Muñoz, M. C.; Gaspar, A. B.; Real, J. A.; Yamasaki, M.; Ando, H.; Nakao, Y.; Sakaki, S.; Kitagawa, S. *Angew. Chem., Int. Ed.* **2009**, *48*, 4767. (c) Southon, P. D.; Liu, L.; Fellows, E. A.; Price, D. J.; Halder, G. J.; Chapman, K. W.; Moubaraki, B.; Murray, K. S.; Létard, J. F.; Kepert, C. J. *J. Am. Chem. Soc.* **2009**, *131*, 10998.

[37] Martínez, V.; Arcís-Castillo, Z.; Muñoz, M. C.; Gaspar, A. B.; Etrillard, C.; Létard, J. F.; Terekhov, S. A.; Bukin, G. V.; Levchenko, G.; Real, J. A. *Eur. J. Inorg. Chem.* **2013**, 813.

[38] Sheldrick, G. M. *Acta Crystallogr., Sect. A: Found. Crystallogr.* **2008**, 64, 112.

[39] Eiling, A; Schilling, J. S. *J. Phys. F: Met. Phys.* **1981**, 11, 623.

2.8.- Supporting Information

Figure S1.- Magnetic behavior of **FpzNi** at 1 bar (10⁻⁴ GPa) (blue) and at 7 kbar (0.7 GPa) (red).

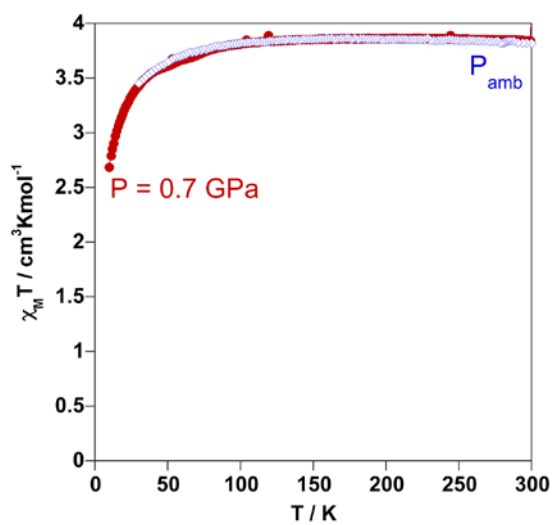


Figure S2.- a) Magnetic behavior of **FpzPt3D** at 1 bar (10^{-4} Gpa). b) Powder X-ray diffraction pattern of **FpzPt3D**: i) calculated from single crystal; ii) measured from microcrystalline powder. c) IR spectrum of **FpzPt3D**.

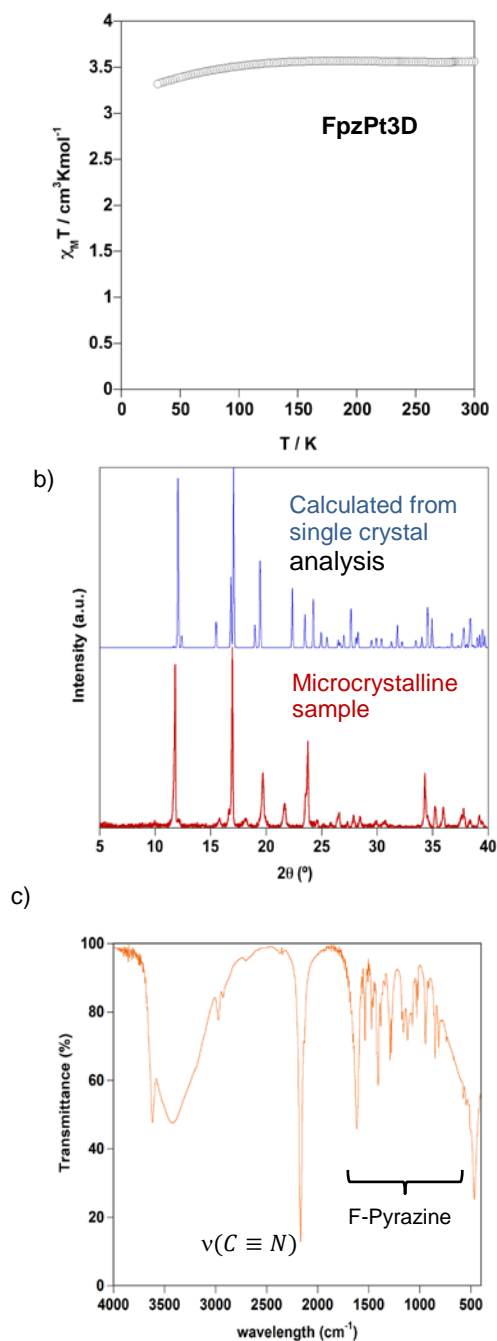


Figure S3.- Precipitated microcrystalline **FpzAu** sample: a) Magnetic behavior (several cycles); b) Powder X-ray patterns: i) calculated from single crystal data (blue); ii) experimental obtained from precipitated samples (red). C) IR spectrum.

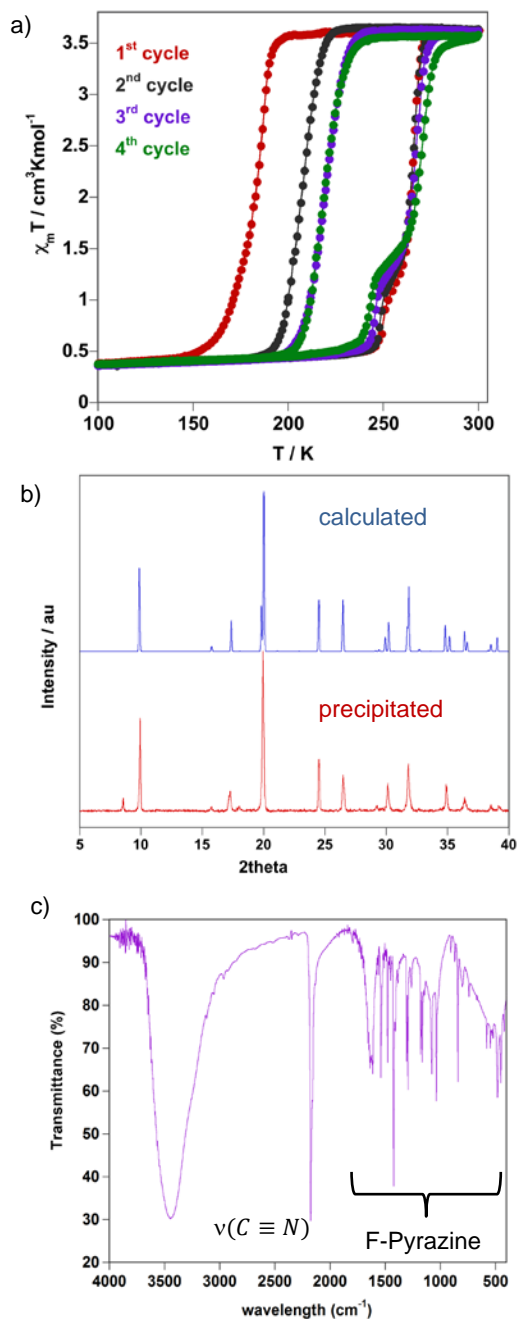


Figure S4.- IR spectra (a) and powder X-ray diffraction patterns (b) for precipitated samples of **FpzNi**, **FpzPd**, and **FpzPt**.

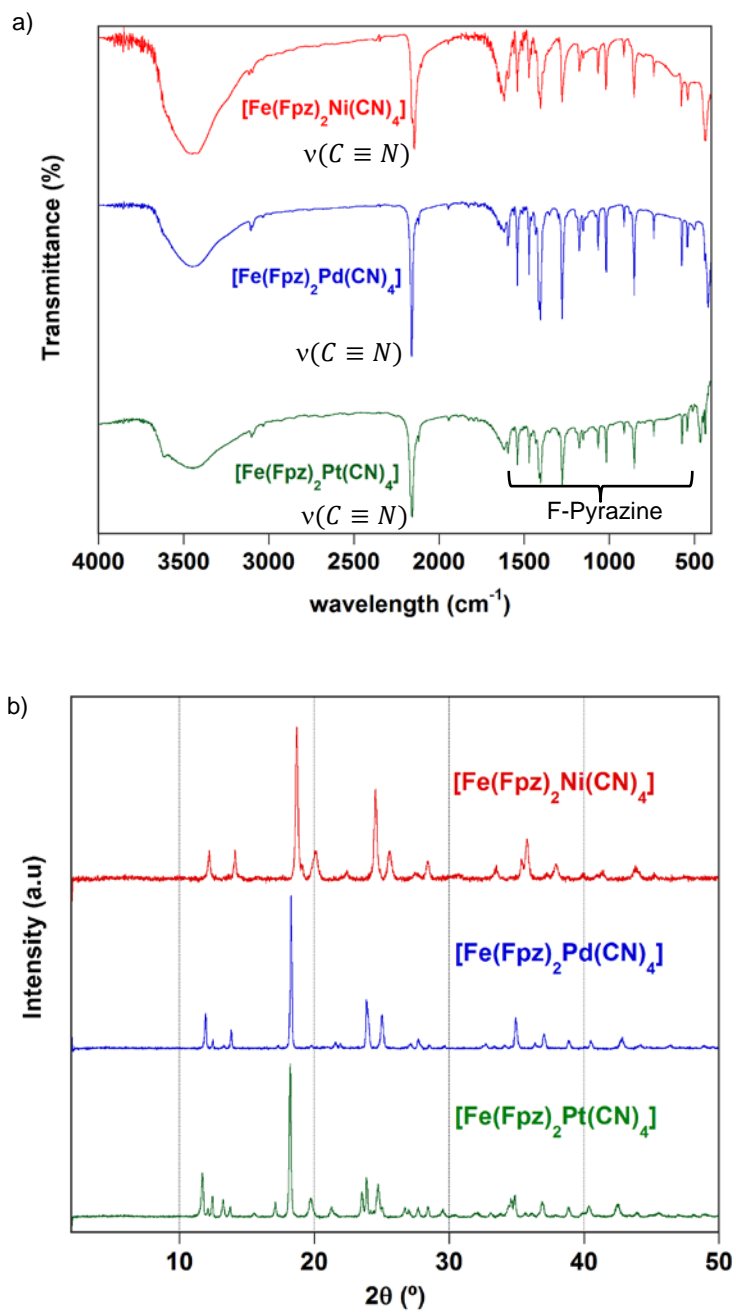


Figure S5.- Perspective view, along [100] direction, of the porous compound **FpzPt3D** showing the location of the H₂O molecules.

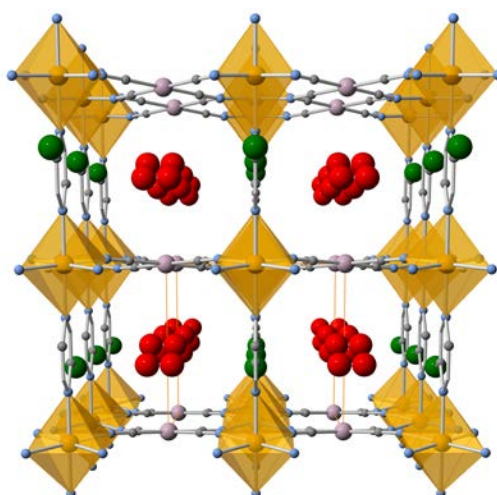


Figure S6.- Thermogravimetric analysis of **FpzAu**, **Fpz3D** and **FpzPt**.

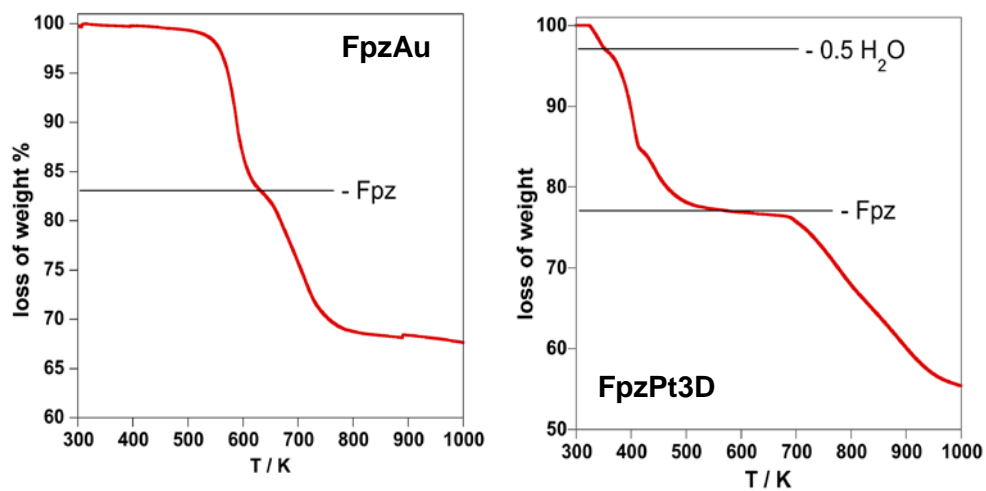


Figure S6 (cont).- Thermogravimetric analysis of FpzAu, Fpz3D and FpzPt.

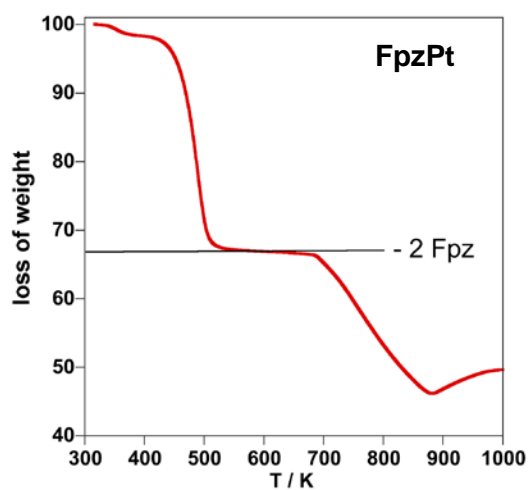
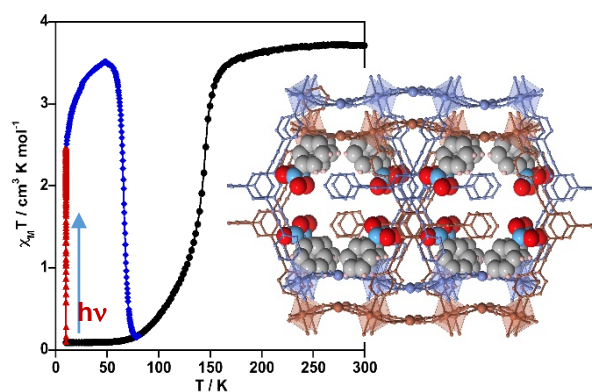


Table S1.- Equilibrium temperatures, $T_{1/2}^{\downarrow}$ and $T_{1/2}^{\uparrow}$ for single crystal and precipitated crystalline samples of **FpzAu**. These temperatures correspond to the 50% of spin conversion where the molar fractions of the HS and LS molar fractions are equal to 0.5. T^{\uparrow} (plateau) corresponds to the temperature at which the small plateau (ca. 23%) occurs in the heating branch.

| Cycle | Single crystals | | | Precipitated microcrystalline | | |
|-----------------|--------------------------|------------------------|----------------------------|-------------------------------|------------------------|----------------------------|
| | $T_{1/2}^{\downarrow}/K$ | $T_{1/2}^{\uparrow}/K$ | T^{\uparrow} (plateau)/K | $T_{1/2}^{\downarrow}/K$ | $T_{1/2}^{\uparrow}/K$ | T^{\uparrow} (plateau)/K |
| 1 st | 196 | 262 | 247 | 183 | 265 | 250 |
| 2 nd | 221 | 263 | 246 | 207 | 264 | 248 |
| 3 rd | 220 | 263 | 245 | 219 | 265 | 245 |
| 4 th | 222 | 263 | 245 | 218 | 267 | 243 |

CAPÍTULO 3

Switchable Spin-Crossover Hofmann-Type 3D Coordination Polymers Based on Tri- and Tetratopic Ligands



REVISTA: Inorganic Chemistry

ÍNDICE DE IMPACTO: 4.850

CAPÍTULO 3

Switchable Spin-Crossover Hofmann-Type 3D Coordination Polymers Based on Tri- and Tetratopic Ligands

3.1.- Abstract

Fe^{II} spin-crossover (SCO) coordination polymers of the Hofmann type have become an archetypal class of responsive materials. Almost invariably, the construction of their architectures has been based on the use of monotopic and linear ditopic pyridine-like ligands. In the search for new Hofmann-type architectures with SCO properties, here we analyze the possibilities of bridging ligands with higher connectivity degree. More precisely, the synthesis and structure of {Fe^{II}(L^{N3})[M^I(CN)₂]₂·(Guest) (Guest = nitrobenzene, benzonitrile, o-dichlorobenzene; M^I = Ag, Au) and {Fe^{II}(L^{N4})[Ag₂(CN)₃][Ag(CN)₂]}·H₂O are described, where L^{N3} and L^{N4} are the tritopic and tetratopic ligands 1,3,5-tris(pyridin-4-ylethynyl)benzene and 1,2,4,5-tetrakis(pyridin-4-ylethynyl)benzene. This new series of Hofmann clathrates displays thermo- and photoinduced SCO behaviors.

3.2.- Introduction

Iron (II) spin crossover (SCO) complexes are remarkable types of responsive molecular materials that can be reversibly switched between the electronic high-spin (HS) and low-spin (LS) states in response to environmental stimuli, such as temperature, pressure, light irradiation, and analytes.^[1] The LS ↔ HS switch is manifested by reversible, controllable, and detectable changes in the physicochemical properties (optical, magnetic, electrical, and structural), making these functional molecular materials excellent prototypes of sensors, switches, and memories.^[2]

Within the so-called polymeric approach to the synthesis of Fe^{II} SCO compounds, Hofmann-type coordination polymers have been gaining considerable attention in the past decade and now they constitute an archetypal family in the SCO area.^[3] They are a class of two- and three-dimensional cyanide-bridged bimetallic compounds formulated as {Fe^{II}(L)_x[M^I(CN)₄]_n, where M^I is Ni, Pd, or Pt and L can be an N-donor monodentate ($x = 2$) or bis-monodentate rodlike ($x = 1$) ligand. The structure is invariably constituted of parallel

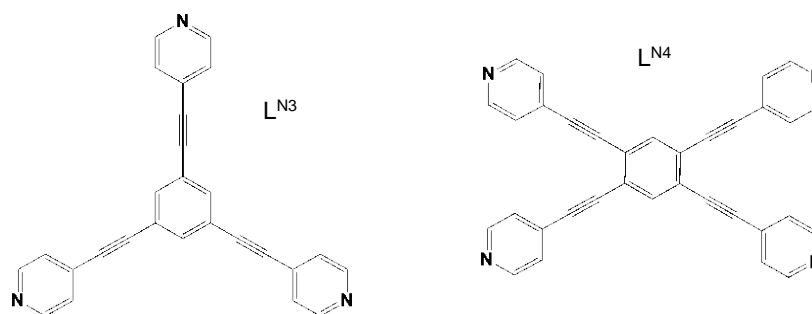
stacks of two-dimensional $\{\text{Fe}^{\text{II}}[\text{M}^{\text{II}}(\text{CN})_4]\}_n$ square grids in which Fe^{II} is equatorially coordinated to four $[\text{M}^{\text{II}}(\text{CN})_4]^{2-}$ planar units through the N atom while the axial positions are occupied by two L ligands, defining two-dimensional (2D)^[4] or three-dimensional (3D)^[5] coordination polymers when L is a terminal monodentate or a bis-monodentate bridging ligand, respectively. The latter connects the Fe^{II} centers of consecutive layers, thus generating bifunctional porous **fsc** (RCSE database) frameworks in which SCO properties and host-guest chemistry interplay in a synergetic way.^[5f-h,6]

Coordination polymers with the formula $\{\text{Fe}^{\text{II}}(\text{L})_x[\text{M}^{\text{II}}(\text{CN})_2]_2\}_n$, where $\text{M}^{\text{I}} = \text{Cu}, \text{Ag}, \text{Au}$, are usually included in the family of Hofmann-type compounds. The Fe^{II} sites can be structurally described in the same terms as for $\{\text{Fe}^{\text{II}}(\text{L})_x[\text{M}^{\text{II}}(\text{CN})_4]\}_n$. However, the linear bis-monodentate rodlike $[\text{M}^{\text{I}}(\text{CN})_2]^-$ bridges produce more open frameworks with **pcu** topology, which usually favor double, triple, and even quadruple interpenetration of the frameworks.^[3a,c] At variance with $\{\text{Fe}^{\text{II}}(\text{L})_2[\text{M}^{\text{II}}(\text{CN})_4]\}_n$, which only form 2D frameworks, monodentate L ligands can also form 3D frameworks with more varied topologies (e.g., **nbo** and **cds** among others).^[7] Usually, the $\{\text{Fe}^{\text{II}}(\text{L})_x[\text{M}^{\text{I}}(\text{CN})_2]_2\}_n$ frameworks interact with each other through short $\text{M}^{\text{I}}-\text{M}^{\text{I}}$ metallophilic contacts. Furthermore, the susceptibility of M^{I} -(Cu, Ag) to expand the coordination sphere or generate oligomers (e.g., $[\text{Ag}_2(\text{CN})_3]^-$) also adds interesting features to this subfamily of compounds.

Hofmann-type Fe^{II} SCO coordination polymers have afforded excellent examples of thermo- and piezohysteretic behaviors, multistep cooperative transitions, relevant examples of porous systems where the SCO behavior can be tuned by guest molecules favoring selective host-guest interactions, catalytic activity, and/or solid-state transformations.^[8] In addition, these compounds are excellent platforms to investigate the SCO properties at the nanoscale (nanocrystals, thin films)^[5b,9] and their potential application as prototypes of spintronic and micromechanical devices.^[10] Thus, the design and synthesis of new Hofmann-type Fe^{II} SCO compounds are essential steps for discovering new, interesting properties and applications. In this respect, almost all Hofmann-type Fe^{II} SCO compounds so far investigated have been prepared from mono- and ditopic ligands. Indeed, as far as we know, the only exception corresponds to the porous coordination polymers $\{\text{Fe}(\text{TPT})_{2/3}[\text{M}^{\text{I}}(\text{CN})_2]_2\} \cdot n(\text{Guest})$, where TPT is 2,4,6-tris(4-pyridyl)-1,3,5-triazine, a tritopic ligand with D_{3h} symmetry.^[11]

As a further step in this study, herein we report on the synthesis and characterization of two unprecedented series of Fe^{II} SCO coordination polymers based on the tritopic and tetratopic ligands L^{N3} = 1,3,5-tris(pyridin-4-ylethynyl)benzene and L^{N4} = 1,2,4,5-tetrakis(pyridin-4-ylethynyl)benzene (Scheme 1) and ditopic [M^I(CN)₂]⁻ inorganic bridges. The L^{N3} ligand is an expanded version of the previously investigated TPT ligand, while the topology of the L^{N4} ligand is investigated for the first time in the family of Hofmann clathrates. More precisely, we will present the crystal structures and magnetic and photomagnetic properties of {Fe^{II}(L^{N3})[M^I(CN)₂]₂}·(Guest) (M^I = Ag (**1·Guest**), M^I = Au (**2·Guest**); Guest = C₆H₅X (X = NO₂, CN), *o*-C₆H₄Cl₂) and {Fe^{II}(L^{N4})[Ag₂(CN)₃][Ag(CN)₂]}·H₂O (**3·H₂O**).

Scheme 1. Organic bridging ligands used in this work.



3.3.- Results

3.3.1.- Synthesis

The synthesis of the title compounds was conditioned by the high insolubility of the ligands L^{N3} and L^{N4} and the resulting coordination polymers. Thus, in order to get reasonably good microcrystalline samples and single crystals of **1·Guest**, **2·Guest**, and **3·H₂O**, the synthesis was carried out by slow diffusion of the components (see also the Experimental Section). The presence of guest molecules was an additional key condition for the synthesis of complexes with L^{N3}. Thus, we found that the use of an H-type diffusion system made up of four connected vessels resulted in the most appropriate strategy. In such configuration, methanolic solutions of Fe^{II} and [M^I(CN)₂]⁻ were poured separately into the peripheral vessels, while L^{N3} was placed as a solid (due to its insolubility) at the bottom of the vessel next to the Fe^{II} solution, and a large excess of Guest was placed in the remainder vessel.

Alternatively, to slow the diffusion, it is also possible to add the Fe^{II} and [M(CN)₂]⁻ salts as solids at the bottom of the corresponding tubes. Finally, the four vessels were filled with methanol and sealed (Figure S1). The most appropriate guest molecules turned out to be the following benzene derivatives: PhNO₂, *o*-PhCl₂, and PhCN. In contrast, the use of five-membered rings as guests, i.e. pyrrole, furan, and thiophene, was unsuccessful and no product was formed. PXRD patterns for the **1-Guest** and **2-Guest** series are practically identical, demonstrating their isostructural nature (Figure S2). Despite the high crystallinity of these compounds, adequate single crystals to get reasonably good structural X-ray diffraction analyses were achieved only for **1-PhNO₂** and **2-PhNO₂**.

Given that L^{N4} is soluble in CHCl₃ and that the structure of **3-H₂O** cannot accept guest molecules (vide infra), a three-vessel modification was employed (see Figure S1). At variance with **3-H₂O**, self-assembly of Fe^{II}, L^{N4}, and [Au(CN)₂]⁻ does not give any type of complex even in the presence of guest molecules. This may be due to metric and/or geometric incompatibilities between connectors and nodes and the fact that the Au atom cannot expand the coordination sphere as Ag does in the case of **3-H₂O** (vide infra).

The thermogravimetric analysis (TGA) for **1-Guest**, **2-Guest**, and **3-H₂O** confirmed the amount of guest molecules (Figure S3). The TGA for fresh samples of **1-PhNO₂** and **2-PhNO₂** shows, prior to the loss of the PhNO₂ molecule, a quite small weight loss (ca. 0.5 and 0.3%, respectively) on starting from room temperature, which could be tentatively associated with the presence of a quite small amount of methanol. Because the amount of these molecules is less than ca. 1/8 CH₃OH and these species are very labile, we have considered that, under vacuum conditions of the SQUID magnetometer or even under ambient storage conditions, these molecules spontaneously desolvate, as suggested by the structure analysis and the magnetic properties (vide infra). The average yields for **1-Guest** and **2-Guest** were ca. 15-20%, and that of **3-H₂O** was 10-15%.

3.3.2.- Crystal structures

The crystal structure was determined by single-crystal X-ray analysis at 120 and 250 K for **1-PhNO₂** and **3-H₂O** and at 100 and 250 K for **2-PhNO₂**. Compounds **1-PhNO₂** and **2-PhNO₂** crystallize in the orthorhombic *Pbcn* space group, while compound **3-H₂O** crystallizes in the triclinic *P* $\bar{1}$ space group. Relevant crystallographic parameters are shown in Table 1. Selected significant bond lengths and angles are given in Table 2 and Table S1, respectively.

Table 1. Crystallographic parameters for **1-PhNO₂**, **2-PhNO₂**, and **3-H₂O**.

| | 1-PhNO₂ | | 2-PhNO₂ | | 3-H₂O | |
|--|---|--------------|---|--------------|--|--------------|
| Empirical formula | C ₃₇ H ₂₀ Ag ₂ FeN ₈ O ₂ | | C ₃₇ H ₂₀ Au ₂ FeN ₈ O ₂ | | C ₃₉ H ₁₈ Ag ₃ FeN ₉ O | |
| Mr | 880.20 | | 1058.39 | | 1008.08 | |
| Crystal system | Orthorhombic | | Orthorhombic | | Triclinic | |
| Space group | Pbcn | | Pbcn | | P-1 | |
| <i>T</i> / K | 120 K | 250 K | 100 K | 250 K | 120 K | 250 K |
| <i>a</i> (Å) | 36.5834(10) | 36.806(2) | 36.7927(12) | 36.931(2) | 7.9977(5) | 7.9807(5) |
| <i>b</i> (Å) | 15.2354(4) | 15.8826(5) | 15.1716(5) | 15.6980(4) | 9.5996(9) | 9.8952(6) |
| <i>c</i> (Å) | 13.2204(3) | 13.4475(5) | 13.1200(4) | 13.3384(4) | 13.5845(5) | 13.8305(8) |
| α | | | | | 89.642(5) | 89.434(4) |
| β | | | | | 80.717(5) | 80.842(5) |
| γ | | | | | 71.166(7) | 71.898(5) |
| <i>V</i> (Å ³) | 7368.6(3) | 7861.0(5) | 7323.6(4) | 7732.8(4) | 973.00(12) | 1024.00(11) |
| <i>Z</i> | 8 | 8 | 8 | 8 | 1 | 1 |
| <i>F</i> (000) | 3472 | | 3984 | | 490 | |
| <i>D_c</i> (mg cm ⁻³) | 1.587 | 1.487 | 1.920 | 1.818 | 1.720 | 1.661 |
| μ (Mo-K α)(mm ⁻¹) | 1.484 | 1.391 | 8.427 | 7.982 | 1.895 | 1.804 |
| No. of total reflections [<i>I</i> > 2 σ (<i>I</i>)] | 7681 | 5381 | 7739 | 6638 | 3694 | 3496 |
| <i>R</i> [<i>I</i> > 2 σ (<i>I</i>)] | 0.0681 | 0.0672 | 0.0383 | 0.0463 | 0.0609 | 0.0670 |
| <i>wR</i> [<i>I</i> > 2 σ (<i>I</i>)] | 0.1453 | 0.1674 | 0.0905 | 0.0859 | 0.1569 | 0.1776 |
| <i>S</i> | 1.068 | 1.014 | 1.033 | 1.066 | 1.046 | 1.050 |

Table 2. Selected bond lengths (Å) for **1-PhNO₂**, **2-PhNO₂**, and **3-H₂O**.

| | 1-PhNO₂ | | 2-PhNO₂ | | 3-H₂O | |
|---------|---------------------------|--------------|---------------------------|--------------|-------------------------|--------------|
| | 120 K | 250 K | 100 K | 250 K | 120 K | 250 K |
| Fe-N1 | 2.033(4) | 2.217(6) | 2.048(5) | 2.220(5) | 2.045(4) | 2.241(4) |
| Fe-N2 | 2.046(4) | 2.228(5) | 2.061(5) | 2.217(5) | 1.955(4) | 2.117(5) |
| Fe-N3 | 1.968(4) | 2.166(5) | 1.975(5) | 2.157(6) | 1.957(4) | 2.141(5) |
| Fe-N4 | 1.969(4) | 2.145(5) | 1.994(5) | 2.148(5) | | |
| Fe-N5 | 1.971(5) | 2.151(5) | 1.982(5) | 2.149(6) | | |
| Fe-N6 | 1.973(5) | 2.151(5) | 1.986(5) | 2.154(6) | | |
| Ag1-C28 | 2.043(5) | 2.031(6) | | | | |
| Ag1-C29 | 2.044(5) | 2.049(6) | | | | |
| Ag2-C30 | 2.053(6) | 2.052(6) | | | | |
| Ag2-C31 | 2.059(6) | 2.060(6) | | | | |
| Au1-C28 | | | 1.986(6) | 1.987(7) | | |
| Au1-C29 | | | 1.970(6) | 1.982(7) | | |
| Au2-C30 | | | 1.989(7) | 1.989(7) | | |
| Au2-C31 | | | 1.983(6) | 1.977(6) | | |
| Au1-Au2 | | | 3.268(1) | 3.270(1) | | |
| Ag1-N4 | | | | | 2.435(4) | 2.470(6) |
| Ag1-N5 | | | | | 2.119(5) | 2.095(7) |
| Ag1-C18 | | | | | 2.068(5) | 2.054(6) |
| Ag1-C19 | | | | | 2.119(5) | 2.095(7) |
| Ag2-C20 | | | | | 2.058(5) | 2.060(6) |
| Ag1-Ag2 | 3.275(1) | 3.247(1) | | | | |

3.3.2.1.- Structures of **1-PhNO₂** and **2-PhNO₂**

Given that **1-PhNO₂** and **2-PhNO₂** are isostructural, we will describe their structures simultaneously. There is a crystallographically unique Fe^{II} site that is situated in the center of a slightly elongated [FeN₆] octahedron. Figure 1 displays the coordination sphere of the Fe^{II} with the atom labeling of the asymmetric unit, which is the same for **1-PhNO₂** and **2-PhNO₂**. The axial positions (Fe-N1 and Fe-N2), occupied by the pyridine moieties of the ligand L^{N3}, are about 3% longer than the equatorial positions. The four equatorial positions are occupied by two crystallographically distinct [M^I(CN)₂]⁻ groups (Ag1/2 and Au1/2). The average [FeN₆] bond lengths are 1.993(5) [2.176(5)] Å for **1-PhNO₂** at 120 K [250 K] and 2.008(5) [2.174(6)] Å for **2-PhNO₂** at 100 K [250 K]. The difference values Δ*R* between high- and low-temperature forms equal to 0.183 Å (**1-PhNO₂**) and 0.166 Å (**2-PhNO₂**) are in agreement with the magnetic data and are consistent with the occurrence of a practically complete SCO transition for **1-PhNO₂** and 90% conversion at 100 K for **2-PhNO₂**. It is worth stressing at this point that, when single crystals of the latter compound are selected directly from the mother liquor and cooled to 120 K, the crystal parameters and Fe-N bond lengths

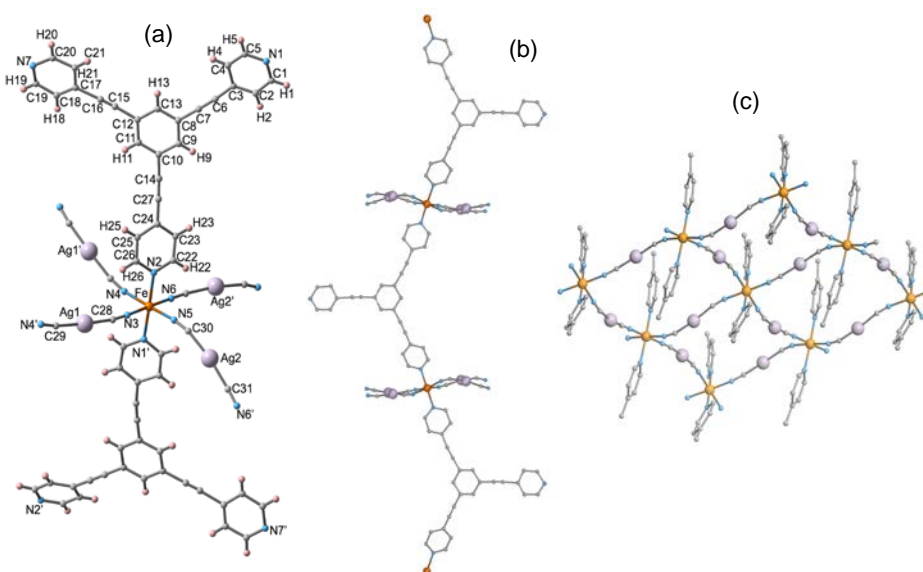


Figure 1. (a) Coordination center of **1-PhNO₂** at 120 K showing the atom labeling of the asymmetric unit (the atom labeling for the Au derivative (**2-PhNO₂**) is the same). (b) Fragment of the zigzag chain running along [100]. (c) {Fe₄[M^I(CN)₂]₄} corrugated 2D grids.

are similar to those obtained at 250 K and are consistent with the results obtained from the magnetic data measured in solution: namely, that **2-PhNO₂** remains in the HS state (vide infra) (see Table S2). Consistent with TGA, this notable difference suggests the presence of very small amounts of strongly disordered labile methanol molecules included in the structure (ca. less than 0.2 molecule) at 120 K. Indeed, there is some nonassigned electron density within the cavities of the structure. An analysis using PLATON shows the occurrence of a void volume of $2 \times 67 \text{ \AA}^3$ centered at (0.0, 0.72, 0.25) close (ca. 2.7 Å) to the uncoordinated N7 atom. No such behavior was observed for the single-crystal study of **1-PhNO₂**.

The sums of deviations from the ideal octahedron of the 12 “cis” N-Fe-N angles ($\Sigma = \sum_{i=1}^{12} |\theta_i - 90|$) are respectively 17.3° [26.8°] and 24.1° [25.3°] for **1-PhNO₂** and **2-PhNO₂** at 120 K [250 K], confirming that the [FeN₆] site is weakly distorted, whatever the spin state of the Fe^{II} centers. The average Fe-N-C(M^I) angles separate from 180° by 15.4° (250 K) and 10.2° (120 K) for Fe-N-C(Ag) and 16.8° (250 K) and 11.7° (100 K) for Fe-N-C(Au). Similarly, the average M^I-C-N angles deviate from linearity by 6.5° (250 K) and 10.6° (120 K) for [Ag(CN)₂]⁻ and 4.6° (250 K) and 7.4° (100 K) for [Au(CN)₂]⁻.

The L^{N3} ligand is not completely flat. Indeed, the mean planes defined by the pyridine moieties containing N1, N7, and N2 define angles with respect to the mean plane containing the benzene ring equal to 4.7° (4.2°), 18.9° (26.9°), and 5.4° (13.6°) for **1-PhNO₂** at 120 (250) K and 4.6° (4.2°), 18.9° (29.1°), and 5.1° (6.8°) for **2-PhNO₂** at 100 (250) K, respectively. It is noteworthy to stress the strong dependence of the angles defined by N2 and N7 on the spin state of the Fe^{II}. Furthermore, the pyridine-benzene connectors deviate slightly from linearity (by 5-6°). The pyridyl group containing the N7 atom does not coordinate either the Fe^{II} or M^I ion and is strongly disordered. Consequently, L^{N3} acts as a ditopic ligand, thereby defining zigzag chains running along [100]. In addition, the [M^I(CN)₂]⁻ linkers radiate almost perpendicularly to the [100] direction connecting the Fe^{II} centers of four adjacent zigzag chains. Alternatively, the structure can be seen as a parallel stack of slightly corrugated 2D grids {Fe₄[M^I(CN)₂]₄} connected by L^{N3}. The distances between two Fe^{II} centers of consecutive layers connected by L^{N3} are 18.466 (1) Å at 120 K for **1-PhNO₂** and 18.396(2) Å at 100 K for **2-PhNO₂**. The resulting 3D network generates enough empty room so as to favor interpenetration of two identical networks (Figure 2). The frameworks interact with each other through weak metallophilic M^I...M^I interactions (see Table 2) but,

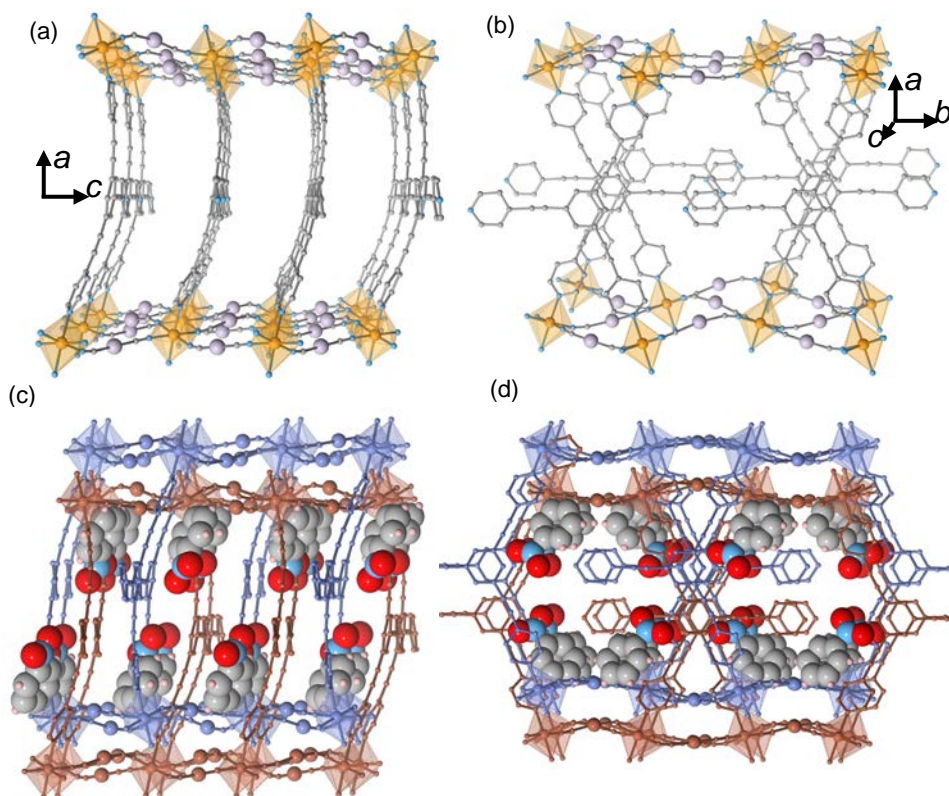


Figure 2. Perspective views of a fragment of the 3D framework of **1-PhNO₂** at 120 K: a single framework running along the [001] (a) and [010] (b) directions and the same perspectives showing the double-interpenetrated frameworks loaded with PhNO₂ (c, d).

more importantly, through the L^{N3} ligands, which stack along the *c* direction, generating a large number of intermolecular C...C π short contacts smaller than the sum of the van der Waals radii (ca. 3.7 Å). These contacts increase in number and intensity when the compound moves from the HS state to the LS state (see Figures S4 and S5 and Table S3). Despite this fact, the interpenetrating frameworks generate room for inclusion of one PhNO₂ molecule, which are located between the L^{N3} ligands (Figure 2) and define strong π interactions with one of the pyridine rings coordinated to the Fe^{II} centers, while the other coordinated pyridine group also interacts via π with the central benzene ring of a L^{N3} ligand belonging to the adjacent framework (see Figures S4 and S5).

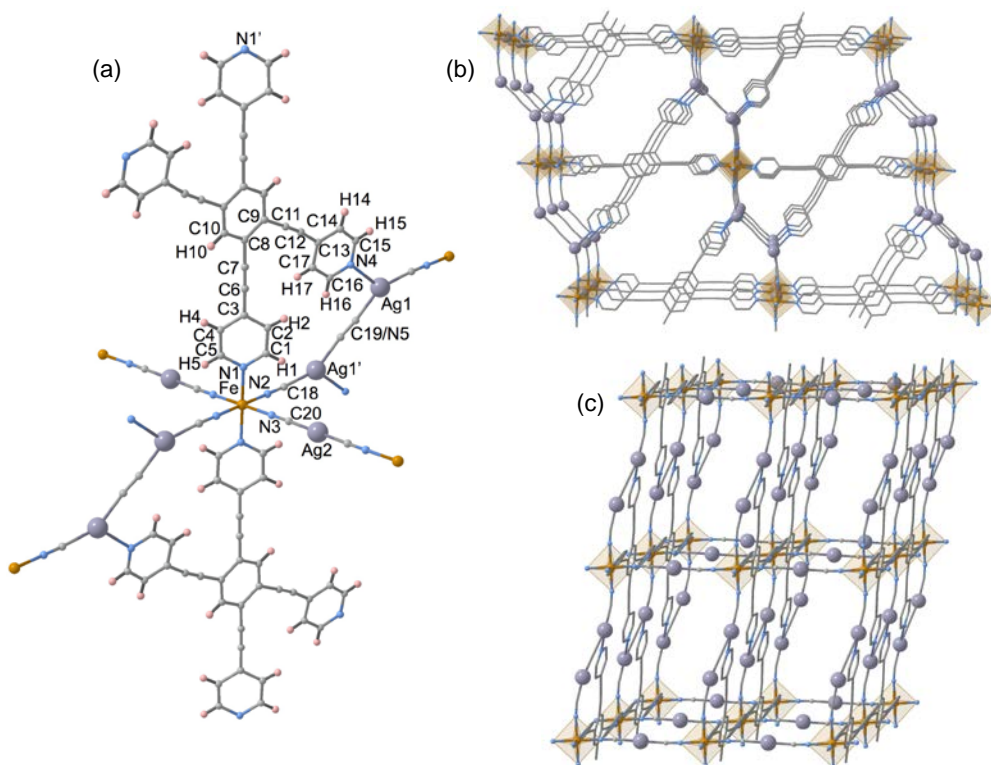
3.3.2.2.- Structure of $3 \cdot H_2O$ 

Figure 3. Coordination center of $3 \cdot H_2O$ at 120 K showing the atom labeling of the asymmetric unit (a). Perspective views of a fragment of the 3D framework of $3 \cdot H_2O$ at 120 K: two perspectives of the same fragment of a single framework emphasizing the coordination mode of L^{N4} and $[Ag_2(CN)_3]^-$ bridges (b) and the connection of the formed layers via $[Ag(CN)_2]^-$ ligands (c).

Figure 3 displays a fragment of the structure of $3 \cdot H_2O$ at 120 K together with the atom labeling of the asymmetric unit. There is one crystallographically unique $[FeN_6]$ site which lies in an inversion center defining a slightly elongated octahedron. The axial bond lengths are occupied by the pyridine moieties of the L^{N4} ligand (Fe-N1), while the four equatorial positions are occupied by $[Ag(CN)_2]^-$ and $[Ag_2(CN)_3]^-$ units through the Fe-N2 and Fe-N3 bonds. The $[FeN_6]$ values equal to 1.986(4) and 2.166(4) Å at 120 and 250 K, respectively, indicate that the Fe^{II} centers are essentially in the LS and HS spin states according to the magnetic data. In this case the angular distortions of the $[FeN_6]$ octahedron,

$\Sigma^{120\text{K}} = 6.9(2)^0$ and $\Sigma^{250\text{K}} = 5.0(2)^0$, are remarkably smaller than those in the case of **1-PhNO₂** and **2-PhNO₂**.

The L^{N4} ligand is essentially flat, but the pyridine moiety bearing the N1 atom is rotated 27.1° with respect to the plane defined by the central benzene ring, which also lies in an inversion center. The Ag site in the [Ag(CN)₂]⁻ unit is strictly linear. In contrast, the Ag site in the in situ generated [Ag₂(CN)₃]⁻ species expands the coordination sphere to 3, affording a distorted-trigonal geometry. The trigonal geometry is generated through coordination of the N4 atom belonging to L^{N4}. Consequently, L^{N4} acts as a tetratopic ligand connecting the Fe^{II} and the Ag^I of the [Ag₂(CN)₃]⁻ units, defining an irregular 2D grid with triangular and hexagonal windows. These layers are connected through the linear [Ag(CN)₂]⁻ bridges, thus defining a quite open 3D framework. Alternatively, the structure can be described as constituted by an infinite stack of undulated {Fe₄[Ag(CN)₂]₂[Ag₂(CN)₃]₂}_n layers pillared by L^{N4}. The space generated by the undulated rectangular windows allows interpenetration of two additional identical frameworks, thus filling the void space and affording a triple-interpenetrated system where there is only free room for one H₂O per formula unit (see Figure S6a). A simplified version of the structure showing the topology of the resulting (2-c)(3-c)2(4-c)(6-c) 4-nodal net analyzed with ToposPro^[12] is given in Figure S6b.

3.3.3.- Magnetic and photomagnetic properties

The thermal dependence of the $\chi_M T$ product (χ_M is the molar magnetic susceptibility and T is the temperature) was measured at 1 K min⁻¹ using a magnetic field of 1 T in the temperature region 10-300 K for compounds **1-Guest**, **2-Guest**, and **3-H₂O**. The corresponding $\chi_M T$ versus T curves are shown in Figure 4. At 300 K, the $\chi_M T$ value was found in the interval 3.70-3.76 cm³ K mol⁻¹ for **1-Guest** and **2-Guest** and 3.34 cm³ K mol⁻¹ for **3-H₂O**. These values are typical for an $S = 2$ ground state with noticeable orbital contribution, as usually observed for the Fe^{II} ion in the HS state. For **1-Guest** and **2-Guest**, $\chi_M T$ is nearly constant in the temperature interval 300-210 K. Upon further cooling, $\chi_M T$ decreases abruptly, attaining values in the interval 0.10-0.25 cm³ K mol⁻¹ at 50 K, indicating that the LS state ($S = 0$) is practically fully populated. The equilibrium temperatures of the SCO, at which the molar fractions of the HS and the LS species are equal to $\gamma_{\text{LS}} = \gamma_{\text{HS}} = 0.5$ ($\Delta G_{\text{HL}} = 0$), have $T_{1/2}$ values equal to 156 K (**1-PhCN**), 145 K (**2-PhCN**), 166 K (**1-PhNO₂**), 143 K (**2-PhNO₂**), 180 K (**1-oPhCl₂**), and 187 K (**2-oPhCl₂**).

As mentioned in the structural analysis, an apparent inconsistency in the degree of spin-state conversion was found when the $\chi_M T$ product and the averaged Fe-N bond distance of **2-PhNO₂** at 120 K were correlated. This was associated with the clathration of a variable small amount of loosely attached methanol molecules, which spontaneously desorb at higher temperatures. To clarify this, the thermal variation of $\chi_M T$ was recorded for a crystalline sample of **2-PhNO₂** soaked in mother liquor. The results included in Figure 4 (open circles) demonstrates that under these conditions **2-PhNO₂** remains in the HS state at all temperatures.

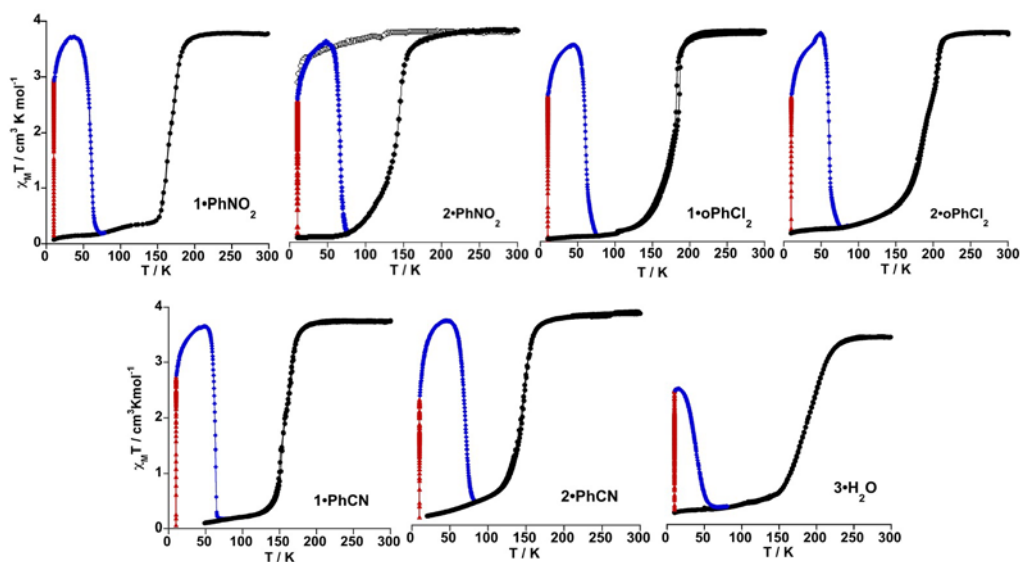


Figure 4. Magnetic and photomagnetic properties of **1-Guest**, **2-Guest**, and **3-H₂O**: irradiation at 10 K (red triangles); thermal dependence of $\chi_M T$ upon heating at 0.3 K/min (blue circles) and heating/cooling at 1 K/min (black circles); thermal variation of $\chi_M T$ for crystals of **2-PhNO₂** soaked in mother liquor (open circles).

Compounds **3-H₂O** experiments a similar SCO behavior starting at higher temperature (ca. 250 K), but the $\chi_M T$ product decreases more gradually. Indeed, the $\chi_M T$ value changes from 3.34 to 0.56 cm³ K mol⁻¹ ($\gamma_{HS} \approx 0.17$) in the temperature interval 250-150 K. Furthermore, a subsequent smoother decrease of $\chi_M T$ is observed in the temperature range 150-50 K, attaining a value of 0.26 cm³ K mol⁻¹ at 50 K ($\gamma_{HS} \approx 0.08$). The SCO can also be considered complete and characterized by a $T_{1/2}$ value of ca. 187 K.

Photogeneration of the metastable HS* state at low temperature, the so-called light-induced excited spin state trapping (LIESST) experiment,^[13] was carried out at 10 K on irradiation of microcrystalline samples (0.8 mg) of **1-Guest** and **2-Guest** with red light ($\lambda = 633$ nm), in the time required to attain saturation (Figure 4 and Figure S7). Under these conditions, the samples saturate in 3 h, with values of $\chi_M T$ in the interval 2.97-2.21 cm³ K mol⁻¹. Subsequently, the light irradiation was switched off and the temperature increased at a rate of 0.3 K min⁻¹. Then, $\chi_M T$ keeps on increasing to reach a maximum of 3.72-3.54 cm³ K mol⁻¹ in the temperature interval 37-50 K. This increase in $\chi_M T$ corresponds to the thermal population of different microstates originating from the zero-field splitting of the $S = 2$ HS* spin state. At higher temperatures, $\chi_M T$ decreases rapidly until it joins the thermal SCO curve in the 65-84 K temperature range, indicating that the metastable HS* state has completely relaxed to the stable LS state. In contrast, after saturation $\chi_M T$ values experience just a slight increase to attain a maximum of ca. 2.47 cm³ K mol⁻¹ at 14 K for **3-H₂O**. This less stable HS* state relaxes back to the LS state at significantly lower temperatures. The characteristic T_{LIESST} temperatures,^[14] obtained from $\partial\chi_M T / \partial T$ in the 10-77 K interval, are 63.6 K (**1-PhCN**), 70.5 K (**2-PhCN**), 61.0 K (**1-PhNO₂**), 66.0 K (**2-PhNO₂**), 60.5 K (**1-oPhCl₂**), and 60.0 K (**2-oPhCl₂**), and 37 K (**3-H₂O**).

3.4.- Discussion

The objective of the present work was to investigate new cyanido-bridged bimetallic Fe^{II}-M^I SCO coordination polymers. We focused our attention on L^{N3} and L^{N4} tri- and tetratopic ligands, respectively. As mentioned above, it is relevant to stress that the isostructural doubly interpenetrated frameworks **1-Guest** and **2-Guest** could only be obtained in the presence of appropriate guest molecules such as PhNO₂, *o*-PhCl₂, and PhCN, which apparently act as templates during the self-assembly process. In addition, this template function was critically dependent on the size of the guest molecule.

Despite being L^{N3} topologically identical with the ligand TPT, they form in combination with Fe^{II} and [M^I(CN)₂]⁻ (M^I = Ag, Au) complexes with different stoichiometries and radically distinct {Fe[M^I(CN)₂]₂}_n frameworks.^[11] The complexes {Fe(TPT)_{2/3}[M^I(CN)₂]₂·*n*(Guest) (M^I = Ag, Au) generate two interlocking 3D networks with an NbO-type topology defined by the [N≡C-M^I-C≡N]⁻ linkers. The *c* axis of the network

coincides with one of the diagonals of the NbO units, which in turn runs along the C_3 axis passing through the TPT ligands (see Figure 5). Indeed, the TPT ligand is perfectly complementary with the voids generated by the pseudo-hexagonal circuits $\{\text{Fe}[\text{M}'(\text{CN})_2]_6\}$ (chair conformation) and acts as an additional tritopic bridge between the Fe^{II} centers. Obviously, extension of the linker between the pyridine and triazine moieties of the TPT ligand with alkaline spacers to afford a ligand having the same metrics as $\text{L}^{\text{N}3}$ would provoke a severe misfit of the resulting ligand with respect to the size of the $\{\text{Fe}[\text{M}'(\text{CN})_2]_6\}$ circuits. As a consequence, the framework $\{\text{Fe}[\text{M}'(\text{CN})_2]_2\}_n$ cannot generate the intricate 3D NbO-type structure observed for the TPT system; in contrast, it readapts to form an infinite stack of 2D corrugated layered structures pillared by $\text{L}^{\text{N}3}$ to afford **1-Guest** and **2-Guest** frameworks. Apparently, there is no stable structural arrangement compatible with $\text{L}^{\text{N}3}$ acting as a tritopic ligand.

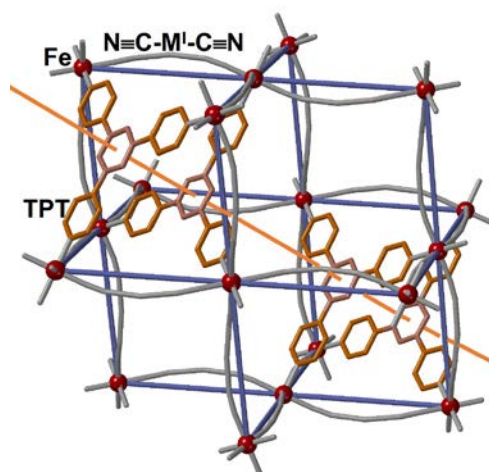


Figure 5. Fragment of the $\{\text{Fe}(\text{TPT})_{2/3}[\text{M}'(\text{CN})_2]_2\}$ framework displaying the NbO-type topology defined by blue bars connecting the Fe^{II} centers (red spheres). The $[\text{M}'(\text{CN})_2]^-$ units are the undulating gray segments linking the Fe^{II} centers. The orange line denotes the diagonal and C_3 axis of the structure passing through the TPT ligands.

In contrast to $\text{L}^{\text{N}3}$, self-assembly of Fe^{II} , $\text{L}^{\text{N}4}$, and $[\text{M}'(\text{CN})_2]^-$ only gave positive results for $\text{M}' = \text{Ag}$, affording **3-H₂O** in low yield. During the slow diffusion process, part of the $[\text{Ag}'(\text{CN})_2]^-$ groups dissociate to generate in situ the relatively uncommon oligomeric species $[\text{Ag}'_2(\text{CN})_3]^-$, which has been described for a few related SCO compounds.^[15] This fact together with the particular configuration of the pyridine rings in $\text{L}^{\text{N}4}$ favors the expansion of the coordination number of the two equivalent Ag' centers of $[\text{Ag}'_2(\text{CN})_3]^-$ to 3

(pseudotrigonal), thereby provoking strong distortion from linearity in this species and marked corrugation in the resulting 2D $\{\text{Fe}[\text{Ag}(\text{CN})_2][\text{Ag}_2(\text{CN})_3]\}_n$ layers. These layers stack along the [100] direction and are firmly attached to each other through $\text{L}^{\text{N}4}$, which act as double pillars linking two Fe^{II} and Ag^{I} (pseudotrigonal) pairs of adjacent layers, forming an open 3D framework. Furthermore, the wide rectangular $\{\text{Fe}_4[\text{Ag}(\text{CN})_2]_2[\text{Ag}_2(\text{CN})_3]_2\}$ windows facilitate interpenetration of two other identical frameworks in such a way that there is no room for inclusion of guest molecules. Indeed, only a loosely attached molecule of water is retained. The much more inert nature of the Au^{I} coordination sphere does not enable generating similar species, and consequently, the homologous gold compound of **3-H₂O** cannot form.

As far as the SCO equilibrium temperatures ($T_{1/2}$) are concerned, a moderate increase in $T_{1/2}$ is observed for **1-Guest** in the sequence PhCN (156 K) < PhNO_2 (166 K) < $o\text{-PhCl}_2$ (180 K). A possible explanation for this trend could be related to the slightly different sizes and shapes of these molecules. Their different accommodation requirements in the available space most likely favors distinct distributions of the intermolecular interactions which enhance the stabilization of the LS. This is also valid, to a first approximation, for **2-Guest** (PhCN (145 K) \approx PhNO_2 (143 K) < $o\text{-PhCl}_2$ (187 K)), although it is not obvious to explain why $T_{1/2}$ for the PhNO_2 derivative is virtually the same as that for the PhCN derivative. In this respect, it is well known the high sensitivity of $T_{1/2}$ to very small changes in free energy between the HS and LS states, ΔG_{HL} ,^[6e] is well-known, which in turn reflects the high sensitivity of the SCO centers to chemical pressure. Consequently, stabilization/destabilization of the LS (HS) state, and hence the value $T_{1/2}$, depends on a delicate balance between electronic and structural factors that often are difficult (if not impossible) to evaluate/discuss without a notable dose of speculation.

The general trend of the T_{LIESST} values is consistent with the empirical inverse-energy-gap-law.^[16] i.e., the metastability of the photogenerated HS^* species decreases as the stability of the LS increases. This is particularly true for the $T_{1/2} - T_{\text{LIESST}}$ ^[14] values of homologous pairs **1-Guest-2-Guest** (Guest = PhCN , PhNO_2), although in the case of Guest = $o\text{-PhCl}_2$ the smaller difference in $T_{1/2}$ is reflected in virtually similar T_{LIESST} values (the same can be observed when 2- PhCN and 2- PhNO_2 are compared). It is important to remark that all the $T_{1/2} - T_{\text{LIESST}}$ pairs in the **1-Guest-2-Guest** series are located close to the correlation line $T_{\text{LIESST}} = T_0 - 0.3T_{1/2}$, with $T_0 = 100$ K being typical for less rigid coordination centers $[\text{Fe}^{\text{II}}\text{N}_6]$ constituted of monodentate ligands and being consistent with their

isostructural nature.^[14] In contrast, despite the fact that $[\text{Fe}^{\text{II}}\text{N}_6]$ centers are similar for **3-H₂O**, its corresponding $T_{1/2} - T_{\text{LIESST}}$ pair is well below this line. This may reflect the distinct structural nature of the latter, which displays a densely packed triply interpenetrated 3D rigid structure versus a less densely packed and probably less rigid doubly interpenetrated 3D structure in **1-Guest** and **2-Guest**.

It is a general fact when series of isostructural Ag^{I} and Au^{I} SCO complexes are compared that $(T_{1/2})^{\text{Ag}} > (T_{1/2})^{\text{Au}}$. This is usually rationalized in terms of lower donor ability associated with the greater electron-withdrawing ability of the cyanide group due to a more covalent NC-Au interaction. This general trend applies for the isostructural **1-Guest** and **2-Guest** compounds when Guest is PhNO_2 and PhCN , but it does not apply for $o\text{-PhCl}_2$. In line with what is mentioned above, the presume extra space required by $o\text{-PhCl}_2$ together with the more rigid nature of the Au^{I} framework, in comparison with the Ag^{I} framework, may favor an extra chemical pressure which results in a higher than expected $T_{1/2}$ value. This conjecture is supported by the greater number of short intermolecular contacts observed for **2-PhNO₂** in comparison with **1-PhNO₂**.

3.5.- Conclusions

Two new ligands with unusual coordination denticities, trigonal ($\text{L}^{\text{N}3}$) and square ($\text{L}^{\text{N}4}$), have been included in the library of SCO Hofmann-type metal-organic frameworks derived from $[\text{M}^{\text{I}}(\text{CN})_2]^-$ ($\text{M}^{\text{I}} = \text{Ag}, \text{Au}$). Using slow diffusion methods in presence of appropriate guest molecules, $\text{L}^{\text{N}3}$ affords six new isostructural clathrate compounds generically formulated as **1-Guest** and **2-Guest** with Guest = PhCN , PhNO_2 , $o\text{-PhCl}_2$. The structure of the PhNO_2 derivative shows that $\text{L}^{\text{N}3}$ works as a bis-monodentate ligand to satisfy, most likely, the metrics imposed by the $\{\text{Fe}[\text{M}^{\text{I}}(\text{CN})_2]_2\}_n$ layers, thereby acting as a pillar between the layers, thus affording an open 3D framework. Two identical frameworks interpenetrate in the same space and hold together through short intermolecular interactions including weak $\text{M}^{\text{I}} \cdots \text{M}^{\text{I}}$ metallophilic interactions. The six clathrates exhibit thermal- and light-induced SCO properties. Concerning the ligand $\text{L}^{\text{N}4}$, one should expect coordination of four Fe^{II} and generation of a complicated framework via $[\text{M}^{\text{I}}(\text{CN})_2]^-$; however, the occurrence of geometric incompatibilities is apparent, which are solved for the Ag^{I} derivative by virtue of its much more labile coordination sphere. Consequently, the structure of **3-H₂O** is made up of extended $\{\text{Fe}[\text{Ag}^{\text{I}}(\text{CN})_2][\text{Ag}_2^{\text{I}}(\text{CN})_3]\}_n$ layers pillared by two opposite pyridine rings of $\text{L}^{\text{N}4}$,

which act as axial ligands of Fe^{II}, while the remaining two pyridine rings coordinate the Ag^I centers of the in situ generated [Ag^I(CN)₃]⁻ units. The much more inert of Au^I prevents the formation of this uncommon triple-interpenetrated network. The higher characteristic $T_{1/2}$ value of the SCO is consistent with the incomplete photogeneration of the LS state at low temperatures.

3.6.- Experimental section

Fe(BF₄)₂·6H₂O, K[Ag(CN)₂], K[Au(CN)₂], and organic precursors were purchased from commercial sources and used as received. 4-Ethynylpyridine and the ligands L^{N3} and L^{N4} were prepared by the published methods.^[17]

3.6.1.- Synthesis of {Fe^{II}(L^{N3})[M^I(CN)₂]₂·Guest (M^I = Ag (1-Guest), Au (2-Guest))

Crystals of **1-Guest** and **2-Guest** were obtained in the same manner by slow diffusion of methanolic solutions of four reagents placed in a modified H-shaped vessels with four arms. Each reagent was deposited in one of the arms, in the following order: Fe(BF₄)₂·6H₂O (0.0787 mmol, 26.6 mg), L^{N3} (0.0787 mmol, 30 mg), Guest (= PhNO₂, PhCN, *o*-PhCl₂; 2 mL, large excess), and K[Ag(CN)₂] (0.1574 mmol, 31.5 mg) (**1**) / K[Au(CN)₂] (0.1574 mmol, 47.3 mg) (**2**). Finally, the vessel was filled completely with methanol and sealed. In all cases, yellow crystals appeared within 2 weeks, in low yield (ca. 20%). EDX analysis (energy dispersive X-ray analysis) confirmed the stoichiometric relationship between metallic coordination centers: for **1-Guest**, Fe:Ag = 1:2; for **2-Guest**, Fe:Au = 1:2.

Complex 1-Guest. Anal. Calcd for C₃₇H₂₀Ag₂FeN₈O₂ (880.20): C, 50.49; H, 2.29; N, 12.73. Found: C, 50.38; H, 2.32; N, 12.58. Calcd for C₃₇H₁₉Ag₂FeN₇Cl₂ (904.09): C, 49.16; H, 2.12; N, 10.85. Found: C, 50.18; H, 2.22; N, 10.98. Calcd for C₃₈H₂₀Ag₂FeN₈ (860.22): C, 53.06; H, 2.34; N, 13.03. Found: C, 52.58; H, 2.32; N, 12.68. IR (cm⁻¹): $\nu(\text{C}\equiv\text{C})$ 2219 cm⁻¹ (m), $\nu(\text{C}\equiv\text{N})$ 2163 cm⁻¹ (s), $\nu(\text{C}=\text{N})$ 1613 (vs), $\nu(\text{pyridine ring})$ 1418 (s), 825 (s). The symmetric and asymmetric stretching modes of the NO₂ group in PhNO₂ were unambiguously assigned to $\nu_a(\text{NO}_2)$ 1525 (vs) and $\nu_s(\text{NO}_2)$ 1344 (vs). No singular signals could be associated with PhCN and *o*-PhCl₂.

Complex 2-Guest. Anal. Calcd for $C_{37}H_{20}Au_2FeN_8O_2$ (1058.39.20): C, 41.99; H, 1.90; N, 10.59. Found: C, 41.78; H, 1.98; N, 10.43. Calcd for $C_{37}H_{19}Au_2FeN_7Cl_2$ (1082.29): C, 41.06; H, 1.77; N, 9.06. Found: C, 42.03; H, 1.85; N, 10.43. Calcd for $C_{38}H_{20}Au_2FeN_8$ (1038.41): C, 43.95; H, 1.94; N, 10.79. Found: C, 43.58; H, 2.01; N, 10.68. IR (cm^{-1}): $\nu(C\equiv C)$ 2220 cm^{-1} (m), $\nu(C\equiv N)$ 2170 cm^{-1} (s), $\nu(C=N)$ 1610 (vs), ν (pyridine ring) 1420 (s), 820 (s). The symmetric and asymmetric stretching modes of the NO_2 group in $PhNO_2$ were unambiguously assigned to $\nu_a(NO_2)$ 1520 (vs) and $\nu_s(NO_2)$ 1340 (vs). No singular signals could be associated with $PhCN$ and $o-PhCl_2$.

3.6.2.- Synthesis of $\{Fe^II(L^{N4}) [Ag_2(CN)_3][Ag(CN)_2]\cdot H_2O (3\cdot H_2O)$

Crystals of **3-H₂O** were obtained by slow diffusion of solutions of three reagents placed in a modified H-shaped vessel with three arms, the arm in the middle being broader than the peripheral arms. This feature was introduced due to the high insolubility of L^{N4} (a high volume of solvent was needed to dissolve the appropriated amount of ligand). The peripheral vessel arms contained $Fe(BF_4)_2\cdot 6H_2O$ (0.05925 mmol, 20 mg) and $K[Ag(CN)_2]$ (0.1185 mmol, 23.7 mg), respectively; the central vessel arm contained a solution of L^{N4} (0.05925 mmol, 28.6 mg, dissolved in 7 mL of $CHCl_3$). Finally, the tube was filled completely with methanol and sealed. Orange single crystals of **3-H₂O** appeared within 4 weeks, in low yield (ca. 20%). EDX analysis (energy dispersive X-ray analysis) confirmed the stoichiometric relationship between metallic coordination centers for **3-H₂O**, Fe:Ag = 1:3.

Complex 3-H₂O. Anal. Calcd for $C_{39}H_{20}Ag_3FeN_9O$ (1010.10): C, 46.37; H, 2.00; N, 12.48. Found: C, 46.59; H, 2.10; N, 12.73. IR (cm^{-1}): $\nu(C\equiv C)$ 2212 cm^{-1} (w), $\nu(C\equiv N)$ 2150 cm^{-1} (m), $\nu(C=N)$ 1604(vs), ν (pyridine ring) 1419 (s), 813 (s).

3.6.3.- Physical characterization

Variable-temperature magnetic susceptibility measurements were performed on samples (20-30 mg) consisting of crystals, using a Quantum Design MPMS2 SQUID susceptometer equipped with 5.5 T magnet, operating at 1 T and at temperatures in the range 300-1.8 K. Experimental susceptibilities were corrected for diamagnetism of the constituent atoms by the use of Pascal's constants. Thermogravimetric analysis was

performed on a Mettler Toledo TGA/SDTA 851e instrument in the 290-800 K temperature range under a nitrogen atmosphere with a rate of 10 K min⁻¹.

3.6.4.- Single-crystal X-ray diffraction

Single-crystal X-ray data were collected with an Oxford Diffraction Supernova diffractometer. In all cases, Mo K α radiation ($\lambda = 0.71073 \text{ \AA}$) was used. Data scaling and empirical or multiscan absorption corrections was performed. The structures were solved by direct methods using SHELXT or SIR2004 and refined by full-matrix least-squares techniques on F^2 with SHELXL.^[18] Non-hydrogen atoms were refined anisotropically, and hydrogen atoms were placed in calculated positions and refined in idealized geometries (riding model) with fixed isotropic displacements parameters.

3.7.- References

- [1] See for example: (a) Hauser, A. *Comments Inorg. Chem.* **1995**, *17*, 17. (b) König, E. *Struct. Bonding (Berlin, Ger.)* **1991**, *76*, 51. (c) Gütlich, P.; Hauser, A.; Spiering, H. *Angew. Chem., Int. Ed. Engl.* **1994**, *33*, 2024. (d) Sato, O. *Acc. Chem. Res.* **2003**, *36*, 692. (e) Real, J. A.; Gaspar, A. B.; Niel, V.; Muñoz, M. C. *Coord. Chem. Rev.* **2003**, *236*, 121. (f) Gütlich, P.; Goodwin, H. A. *Topics in Current Chemistry* **2004**, *Vols. 233-235*. (g) Real, J. A.; Gaspar, A. B.; Muñoz, M. C. *Dalton Trans.* **2005**, 2062. (h) Halcrow, M. A. *Polyhedron* **2007**, *26*, 3523. (i) Halcrow, M. A. *Coord. Chem. Rev.* **2009**, *253*, 2493. (j) Olguin, J.; Brooker, S. *Coord. Chem. Rev.* **2011**, *255*, 203. (k) Bousseksou, A.; Molnár, G.; Salmon, L.; Nicolazzi, W. *Chem. Soc. Rev.* **2011**, *40*, 3313.
- [2] (a) Meded, V.; Bagrets, A.; Fink, K.; Chandrasekar, R.; Ruben, M.; Evers, F.; Bernard-Mantel, A.; Seldenthuis, J. S.; Beukeman, A.; van der Zant, H. S. J. *Phys. Rev. B: Condens. Matter Mater. Phys.* **2011**, *83*, 245415. (b) Prins, F.; Monrabal-Capilla, M.; Osorio, E. A.; Coronado, E.; van der Zant, H. S. J. *Adv. Mater.* **2011**, *23*, 1545. (c) Cavallini, M.; Bergenti, I.; Milita, S.; Kengne, J. C.; Gentili, D.; Ruani, G.; Salitros, I.; Meded, V.; Ruben, M. *Langmuir* **2011**, *27*, 4076. (d) Miyamachi, T.; Gruber, M.; Davesne, V.; Bowen, M.; Boukari, S.; Joly, L.; Scheurer, F.; Rogez, G.; Yamada, T. K.; Ohresser, P.; Beaurepaire, E.; Wulfhekel, W. *Nat. Commun.* **2012**, *3*, 938. (e) Martinho,

- P. N.; Rajnak, C.; Ruben, M. In *Spin-Crossover Materials: Properties and Applications*; Halcrow, M. A. Ed.; Wiley: **2013**, pp 376-404 and references therein. (f) Sheperd, H. J.; Molnár, G.; Nicolazzi, W.; Salmon, L.; Bousseksou, A. *Eur. J. Inorg. Chem.* **2013**, *2013*, 653. (g) Rotaru, A.; Dugay, J.; Tan, R. P.; Gural'skiy, I. A.; Salmon, L.; Demont, P.; Carrey, J.; Molnár, G.; Respaud, M.; Bousseksou, A. *Adv. Mater.* **2013**, *25*, 1745. (h) Gural'skiy, I. A.; Quintero, C. M.; Costa, J. S.; Demont, P.; Molnár, G.; Salmon, L.; Shepherd, H. J.; Bousseksou, A. *J. Mater. Chem. C* **2014**, *2*, 2949. (i) Bartual-Murgui, C.; Akou, A.; Thibault, C.; Molnár, G.; Vieu, C.; Salmon, L.; Bousseksou, A. *J. Mater. Chem. C* **2015**, *3*, 1277. (j) Aragonés, A. C.; Aravena, D.; Cerdá, J. I.; Acís-Castillo, Z.; Li, H.; Real, J. A.; Sanz, F.; Hihath, J.; Ruiz, E.; Díez-Pérez, I. *Nano Lett.* **2016**, *16*, 218.
- [3] (a) Muñoz, M. C.; Real, J. A. *Coord. Chem. Rev.* **2011**, *255*, 2068. (b) Muñoz, M. C.; Real, J. A. In *Spin-Crossover Materials: Properties and Applications*; Halcrow, M. A. Ed.; Wiley: **2013**, pp 121-146. (c) Ni, Z.-P.; Liu, J.-L.; Hoque, M. N.; Liu, W.; Li, J.-Y.; Chen, Y.-C.; Tong, M.-L. *Coord. Chem. Rev.* **2017**, *335*, 28.
- [4] (a) Martínez, V.; Gaspar, A. B.; Muñoz, M. C.; Bukin, G.; Levchenko, G.; Real, J. A. *Chem. – Eur. J.* **2009**, *15*, 10960. (b) Ohtani, R.; Arai, M.; Ohba, H.; Hori, A.; Takata, M.; Kitagawa, S.; Ohba, M. *Eur. J. Inorg. Chem.* **2013**, 738. (c) Klein, Y. M.; Sciortino, N. F.; Ragon, F.; Housecroft, C. E.; Kepert, C. J.; Neville, S. M. *Chem. Commun.* **2014**, *50*, 3838. (d) Liu, W.; Wang, L.; Su, Y.-J.; Chen, Y.-C.; Tucek, J.; Zboril, R.; Ni, Z.-P.; Tong, M.-L. *Inorg. Chem.* **2015**, *54*, 8711. (e) Milin, E.; Patinec, V.; Triki, S.; Bendeif, E.-E.; Pillet, S.; Marchivie, M.; Chastanet, G.; Boukheddaden, K. *Inorg. Chem.* **2016**, *55*, 11652. (f) Valverde-Muñoz, F. J.; Seredyuk, M.; Muñoz, M. C.; Znovjyak, K.; Fritsky, I. O.; Real, J. A. *Inorg. Chem.* **2016**, *55*, 10654. (g) Kucheriv, O. I.; Shylin, S. I.; Ksenofontov, V.; Dechert, S.; Haukka, M.; Fritsky, I. O.; Gural'skiy, I. A. *Inorg. Chem.* **2016**, *55*, 4906. (h) Sciortino, N.; Zenere, K. A.; Corrigan, M. E.; Halder, G. J.; Chastanet, G.; Létard, J.-F.; Kepert, C. J.; Neville, S. M. *Chem. Sci.* **2017**, *8*, 701. (i) Liu, F.-L.; Tao, J. *Chem. – Eur. J.* **2017**, *23*, 18252.
- [5] (a) Niel, V.; Martínez-Agudo, J. M.; Muñoz, M. C.; Gaspar, A. B.; Real, J. A. *Inorg. Chem.* **2001**, *40*, 3838. (b) Agustí, G.; Cobo, S.; Gaspar, A. B.; Molnár, G.; Moussa, N. O.; Szilágyi, P. A.; Pálfi, V.; Vieu, C.; Muñoz, M. C.; Real, J. A.; Bousseksou, A. *Chem. Mater.* **2008**, *20*, 6721. (c) Bartual-Murgui, C.; Ortega-Villar, N. A.; Sepherd, H. J.; Muñoz, M. C.; Salmon, L.; Molnár, G.; Bousseksou, A.; Real, J. A. *J. Mater. Chem.*

- 2011**, *21*, 7217. (d) Sciortino, N. F.; Scherl-Gruenwald, K. R.; Chastanet, G.; Hader, G. J.; Chapman, K. W.; Létard, J.-F.; Kepert, C. *J. Angew Chem.* **2012**, *124*, 10301. (e) Muñoz-Lara, F. J.; Gaspar, A. B.; Muñoz, M. C.; Ksenofontov, V.; Real, J. A. *Inorg. Chem.* **2013**, *52*, 3. (f) Muñoz-Lara, F. J.; Gaspar, A. B.; Muñoz, M. C.; Arai, M.; Kitagawa, S.; Ohba, M.; Real, J. A. *Chem. - Eur. J.* **2012**, *18*, 8013. (g) Piñeiro-López, L.; Seredyuk, M.; Muñoz, M. C.; Real, J. A. *Chem. Commun.* **2014**, *50*, 1833. (h) Piñeiro-López, L.; Valverde-Muñoz, F. J.; Seredyuk, M.; Muñoz, M. C.; Haukka, M.; Real, J. A. *Inorg. Chem.* **2017**, *56*, 7038. (i) Bao, X.; Shepherd, H. J.; Salmon, L.; Molnár, G.; Tong, M.-L.; Bousseksou, A. *Angew. Chem., Int. Ed.* **2013**, *52*, 1198. (j) Liu, W.; Peng, Y. Y.; Wu, S. G.; Chen, Y. C.; Hoque, M. N.; Ni, Z. P.; Chen, X. M.; Tong, M.-L. *Angew. Chem., Int. Ed.* **2017**, *56*, 14982.
- [6] (a) Bartual-Murgui, C.; Salmon, L.; Akou, A.; Ortega-Villar, N. A.; Shepherd, H. J.; Muñoz, M. C.; Molnár, G.; Real, J. A.; Bousseksou, A. *Chem. – Eur. J.* **2012**, *18*, 507. (b) Muñoz-Lara, F. J.; Gaspar, A. B.; Aravena, D.; Ruiz, E.; Muñoz, M. C.; Ohba, M.; Ohtani, R.; Kitagawa, S.; Real, J. A. *Chem. Commun.* **2012**, *48*, 4686. (c) Bartual-Murgui, C.; Amal, A.; Shepherd, H. J.; Molnár, G.; Real, J. A.; Salmon, L.; Bousseksou, A. *Chem. - Eur. J.* **2013**, *19*, 15036. (d) Arcís-Castillo, Z.; Muñoz-Lara, F.J.; Muñoz, M. C.; Aravena, D.; Gaspar, A. B.; Sánchez-Roty, J. F.; Ruiz, E.; Ohba, M.; Matsuda, R.; Kitagawa, S.; Real, J. A. *Inorg. Chem.* **2013**, *52*, 12777. (e) Aravena, D.; Arcís-Castillo, Z.; Muñoz, M. C.; Gaspar, A. B.; Yoneda, K.; Ohtani, R.; Mishima, A.; Kitagawa, S.; Ohba, M.; Real, J. A.; Ruiz, E. *Chem. – Eur. J.* **2014**, *20*, 12864.
- [7] (a) Niel, V.; Thompson, A. L.; Muñoz, M. C.; Galet, A.; Goeta, A. E.; Real, J. A. *Angew. Chem., Int. Ed.* **2003**, *42*, 3760. (b) Galet, A.; Niel, V.; Muñoz, M. C.; Real, J. A. *J. Am. Chem. Soc.* **2003**, *125*, 14224. (c) Galet, A.; Muñoz, M. C.; Martínez, V.; Real, J. A. *Chem. Commun.* **2004**, 2268.
- [8] (a) Galet, A.; Gaspar, A. B.; Muñoz, M. C.; Bukin, G. V.; Levchenko, G.; Real, J. A. *Adv. Mater.* **2005**, *17*, 2949. (b) Ohba, M.; Yoneda, K.; Agustí, G.; Muñoz, M. C.; Gaspar, A. B.; Real, J. A.; Yamasaki, M.; Ando, H.; Nakao, Y.; Sakaki, S.; Kitagawa, S. *Angew. Chem., Int. Ed.* **2009**, *48*, 4767. (c) Murphy, M. J.; Zenere, K. A.; Ragon, F.; Southon, P. D.; Kepert, C. J.; Neville, S. M. *J. Am. Chem. Soc.* **2017**, *139*, 1330. (d) Clements, J. E.; Price, J. R.; Neville, S. M.; Kepert, C. J. *Angew. Chem., Int. Ed.* **2014**, *53*, 10164. (e) Li,

- J.-Y.; Chen, Y.-C.; Zhang, Z.-M.; Liu, W.; Ni, Z.-P.; Tong, M.-L. *Chem. – Eur. J.* **2015**, *21*, 1645.
- [9] (a) Cobo, S.; Molnár, G.; Real, J. A.; Bousseksou, A. *Angew. Chem., Int. Ed.* **2006**, *45*, 5786. (b) Molnár, G.; Cobo, S.; Real, J. A.; Carcenac, F.; Dara, E.; Vieu, C.; Bousseksou, A. *Adv. Mater.* **2007**, *19*, 2163. (c) Volatron, F.; Catala, L.; Rivière, E.; Gloter, A.; Stéphan, O.; Mallah, T. *Inorg. Chem.* **2008**, *47*, 6584. (d) Boldog, I.; Gaspar, A. B.; Martínez, V.; Pardo-Ibañez, P.; Ksenofontov, V.; Bhattacharjee, A.; Gütllich, P.; Real, J. A. *Angew. Chem., Int. Ed.* **2008**, *47*, 6433. (e) Martínez, V.; Boldog, I.; Gaspar, A. B.; Ksenofontov, V.; Bhattacharjee, A.; Gütllich, P.; Real, J. A. *Chem. Mater.* **2010**, *22*, 4271. (f) Bartual-Murgui, C.; Akou, A.; Salmon, L.; Molnár, G.; Thibault, C.; Real, J. A.; Bousseksou, A. *Small* **2011**, *7*, 3385. (g) Bartual-Murgui, C.; Akou, A.; Thibault, C.; Molnár, G.; Vieu, C.; Salmon, L.; Bousseksou, A. *J. Mater. Chem. C* **2015**, *3*, 1277.
- [10] Shepherd, H. J.; Gural'skiy, I. A.; Quintero, C. M.; Tricard, S.; Salmon, L.; Molnar, G.; Bousseksou, A. *Nat. Commun.* **2013**, *4*, 2607..
- [11] (a) Arcís-Castillo, Z.; Muñoz, M. C.; Molnár, G.; Bousseksou, A.; Real, J. A. *Chem. – Eur. J.* **2013**, *19*, 6851. (b) Piñeiro-López, L.; Arcís-Castillo, Z.; Muñoz, M. C.; Real, J. A. *Cryst. Growth Des.* **2014**, *14*, 6311.
- [12] Blatov, V. A.; Shechenko, A. P.; Proserpio, D. M. *Cryst. Growth Des.* **2014**, *14*, 3576.
- [13] (a) Decurtins, S.; Gütllich, P.; Köhler, P. C.; Spiering, H.; Hauser, A. *Chem Phys. Lett.* **1984**, *105*, 1. (b) Hauser, A. *Chem Phys. Lett.* **1986**, *124*, 543.
- [14] (a) Létard, J. F.; Guionneau, P.; Rabardel, L.; Howard, J. A. K.; Goeta, A. E.; Chasseau, D.; Kahn, O. *Inorg. Chem.* **1998**, *37*, 4432. (b) Létard, J. F.; Chastanet, G.; Guionneau, P. In *Spin-Crossover Materials: Properties and Applications*, Halcrow, M. A. Ed, Wiley: **2013**, pp 475..
- [15] (a) Niel, V.; Thompson, A. L.; Goeta, A. E.; Enachescu, C.; Hauser, A.; Galet, A.; Muñoz, M. C.; Real, J. A. *Chem. – Eur. J.* **2005**, *11*, 2047. (b) Kosone, T.; Suzuki, Y.; Ono, S.; Kanadani, C.; Saito, T.; Kitazawa, T. *Dalton Trans.* **2010**, *39*, 1786. (c) Li, J.-Y.; Yan, Z.; Ni, Z.-P.; Zhang, Z.-M.; Chen, Y.-C.; Liu, W.; Tong, M.-L. *Inorg. Chem.* **2014**, *53*, 4039. (d) Piñeiro-López, L.; Valverde-Muñoz, F. J.; Seredyuk, M.; Bartual-Murgui, C.; Muñoz, M. C.; Real, J. A. *Eur. J. Inorg. Chem.* **2018**, 289.

[16] (a) Hauser, A. *Coord. Chem. Rev.* **1991**, *111*, 275. (b) Hauser, A.; Vef, A.; Adler, P. J. *Chem. Phys.* **1991**, *95*, 8710. (c) Hauser, A.; Enachescu, C.; Daku, M. L.; Vargas, A.; Amstutz, N. *Coord. Chem. Rev.* **2006**, *250*, 1642.

[17] (a) Ciana, L. D.; Haim, A. J. *J. Heterocycl. Chem.* **1984**, *21*, 607 (b) Amoroso, A. J.; Cargill-Thompson, A. M W.; Maher, J. P.; McCleverty, J. A.; Ward, M. D. *Inorg. Chem.* **1995**, *34*, 4828.

[18] Sheldrick, G. M. *Acta Crystallogr., Sect. C: Struct. Chem.* **2015**, *71*, 3.

3.8.- Supporting Information

Figure S1.- Experimental set up for the synthesis of **1-Guest** and **2-Guest** (a) and for the synthesis of **3-H₂O** (b).

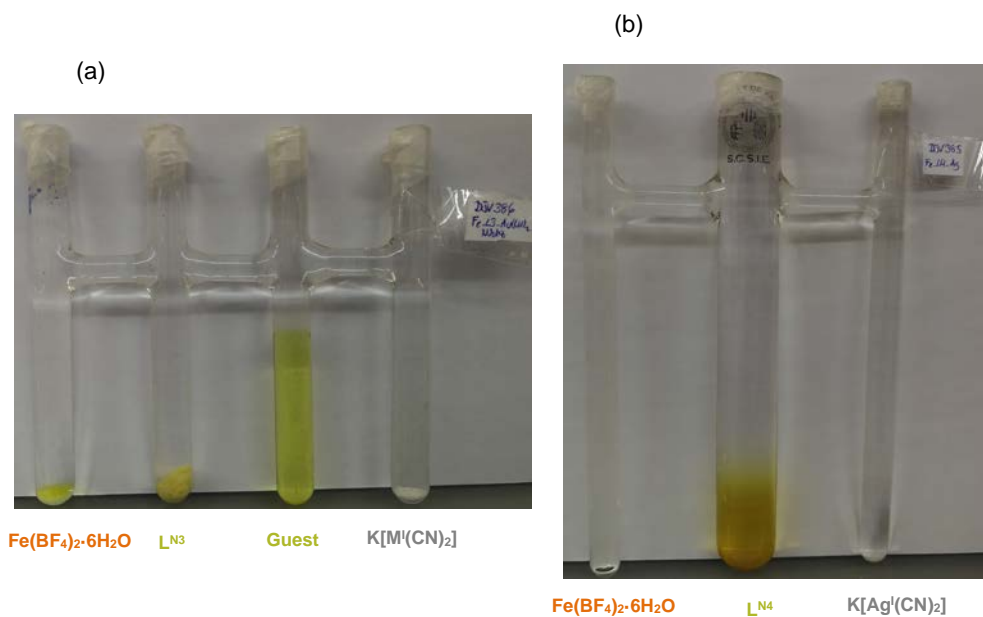


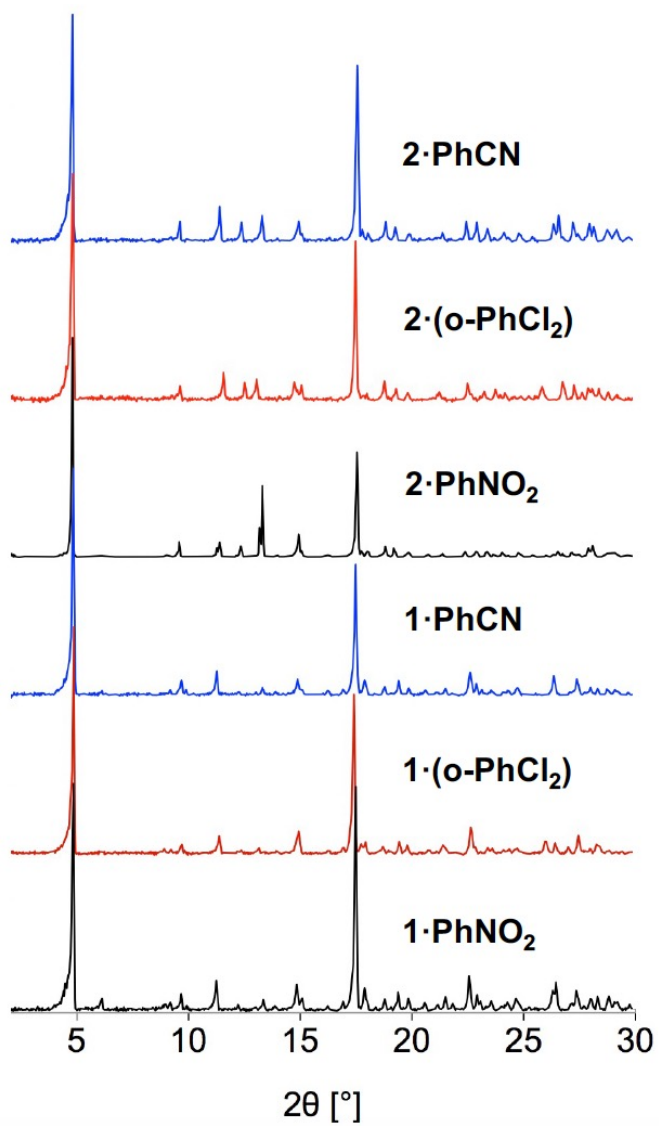
Figure S2.- Experimental PXRD patterns for **1-Guest** and **2-Guest**.

Figure S3.- Thermal analysis of **1·Guest**, **2·Guest** and **3·H₂O**.

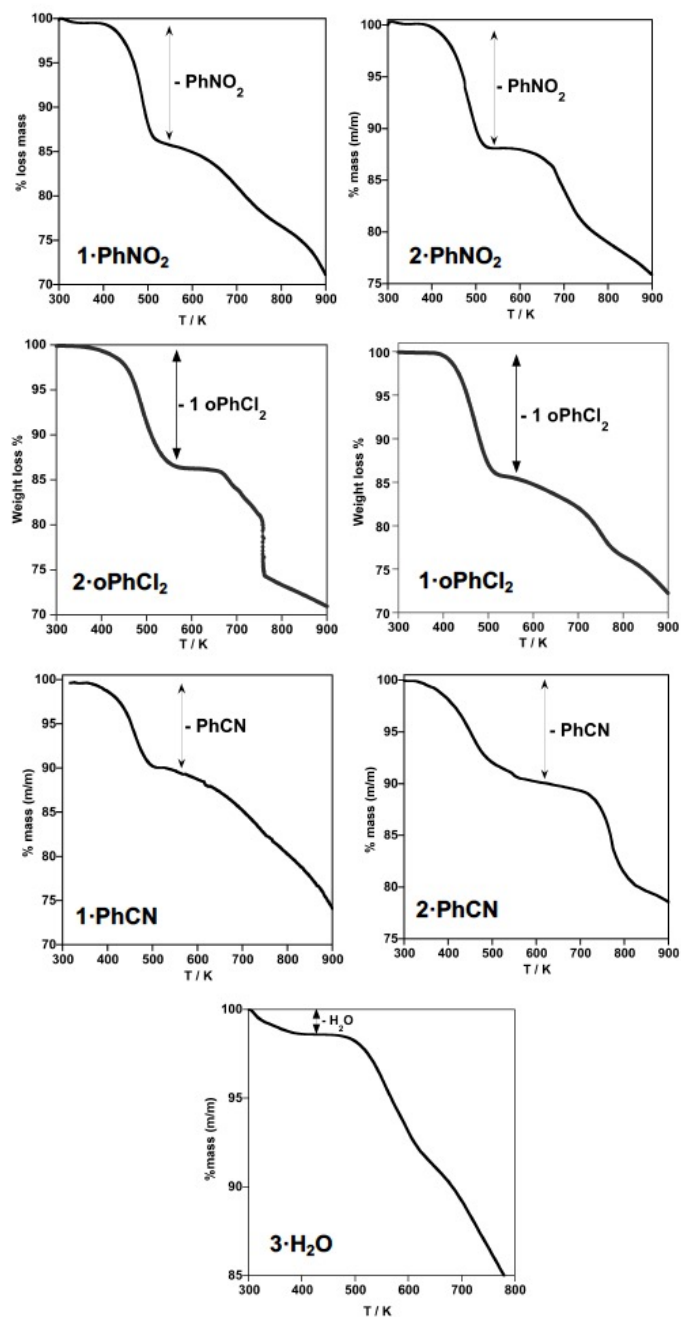


Table S1.- Selected angles ($^{\circ}$) for **1-PhNO₂**, **2-PhNO₂** and **3-H₂O**.

| | 1-PhNO ₂ | | 2-PhNO ₂ | | 3-H ₂ O | |
|-------------|---------------------|----------|---------------------|----------|--------------------|----------|
| | 120 K | 250 K | 100 K | 250 K | 120 K | 250 K |
| N1-Fe-N2 | 177.2(2) | 176.0(2) | 177.3(2) | 176.6(2) | 90.9(2) | 90.0(2) |
| N1-Fe-N3 | 89.0(2) | 92.2(2) | 89.0(2) | 92.2(2) | 90.3(2) | 90.2(2) |
| N1-Fe-N4 | 92.1(2) | 89.0(2) | 92.4(2) | 88.4(2) | | |
| N1-Fe-N5 | 90.6(2) | 88.4(2) | 90.8(2) | 88.4(2) | | |
| N1-Fe-N6 | 89.4(2) | 90.8(2) | 89.1(2) | 91.5(2) | | |
| N2-Fe-N3 | 92.1(2) | 84.5(2) | 92.3(2) | 85.0(2) | 90.5(2) | 91.3(2) |
| N2-Fe-N4 | 85.4(2) | 93.2(2) | 85.2(2) | 93.4(2) | | |
| N2-Fe-N5 | 92.0(2) | 89.4(2) | 91.6(2) | 89.8(2) | | |
| N2-Fe-N6 | 89.5(2) | 92.6(2) | 89.6(2) | 91.3(2) | | |
| N3-Fe-N4 | 88.7(2) | 87.3(2) | 88.3(2) | 87.4(2) | | |
| N3-Fe-N5 | 90.8(2) | 92.7(2) | 90.8(2) | 92.6(2) | | |
| N3-Fe-N6 | 178.4(2) | 176.8(2) | 178.1(2) | 176.1(2) | | |
| N4-Fe-N5 | 177.3(2) | 177.4(2) | 176.7(2) | 176.8(2) | | |
| N4-Fe-N6 | 91.1(2) | 91.7(2) | 91.7(2) | 91.7(2) | | |
| N5-Fe-N6 | 89.6(2) | 88.4(2) | 89.3(2) | 88.6(2) | | |
| C28-Ag1-C29 | 176.7(2) | 177.8(3) | | | | |
| C30-Ag2-C31 | 171.6(2) | 172.9(3) | | | | |
| C28-Au1-C29 | | | 177.2(2) | 178.0(3) | | |
| C30-Au2-C31 | | | 173.6(2) | 174.5(3) | | |
| N5-Ag1-N4 | | | | | 89.6(2) | 90.7(2) |
| C18-Ag1-N4 | | | | | 126.2(2) | 121.9(2) |
| C19-Ag1-N4 | | | | | 89.6(2) | 90.7(2) |
| C18-Ag1-N5 | | | | | 143.7(2) | 146.8(3) |
| C18-Ag1-C19 | | | | | 143.7(2) | 146.8(3) |

Figure S4.- (a) Stacking of the ligands L^{N3} down to [001] direction. (b) Same view projected in the [010] direction. Short C...C contacts (smaller than the sum of the van der Waals radii) between PhNO_2 (c) or central benzene ring of L^{N3} (d) and the pyridyl groups coordinated to Fe^{II} for **2-PhNO₂** at 100 K, respectively.

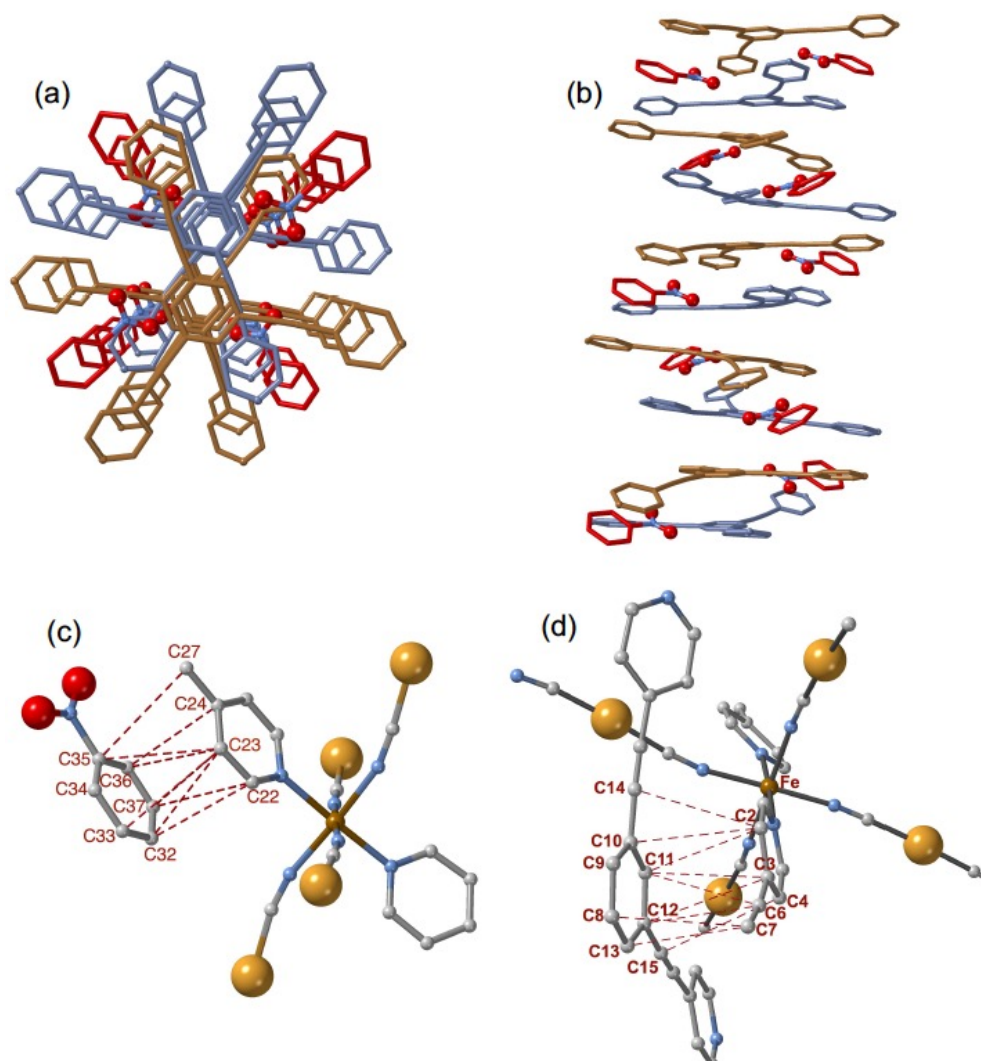


Figure S5.- Short C...C contacts (smaller than the sum of the van der Waals radii) between consecutive L^{NS} ligands (two different arrangements, see stacking Figure S4b) in **2-PhNO₂** at 100 K.

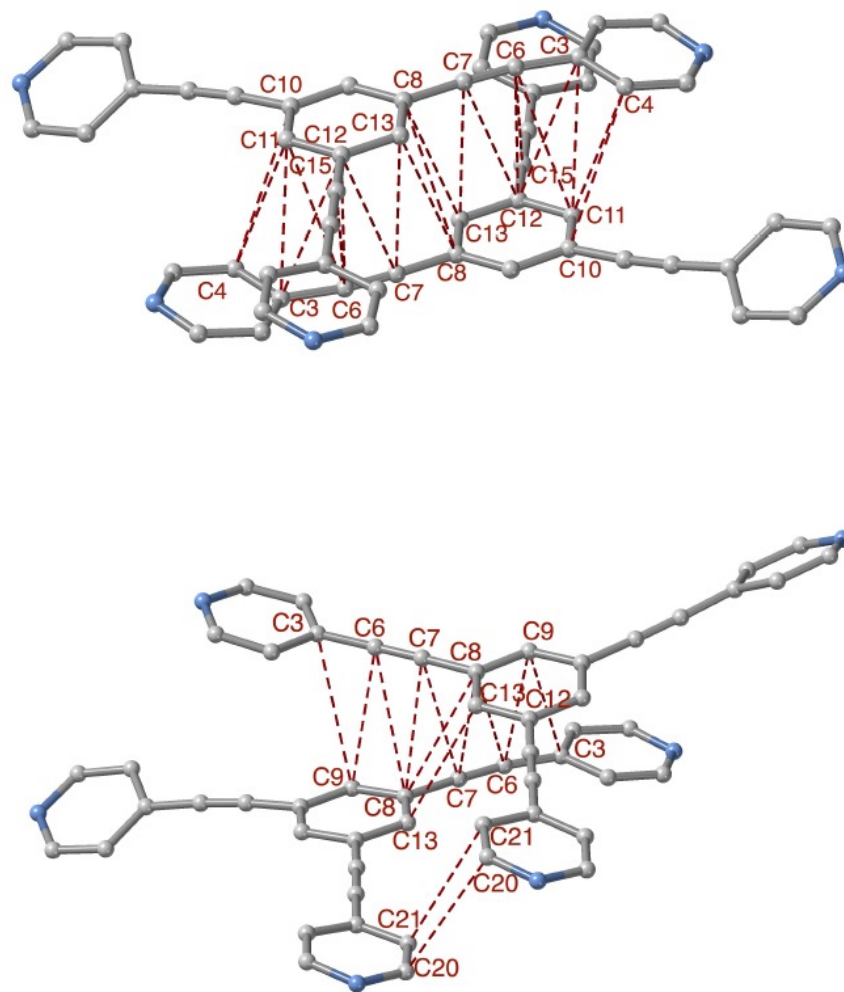


Table S2.- (a) Crystallographic data for **2-PhNO₂** single crystals selected from the mother liquor and measured directly at 120 K. (b) Fe^{II}-N and Au-C bond lengths (Å) and angles (°) of the [FeN₆] [AuC₂] coordination spheres. The average Fe^{II}-N bond length equal to 2.174 Å is consistent with the HS state of the Fe^{II} centers and the magnetic properties of this compound measured soaked with the mother liquor.

(a)

| | |
|---------------------------------------|---|
| Empirical formula | C ₃₇ H ₂₀ Au ₂ FeN ₆ O ₂ |
| Mr | 1058.39 |
| Space group | <i>Pbcn</i> |
| T / K | 120 K |
| a (Å) | 36.9053(11) |
| b (Å) | 15.9660(5) |
| c (Å) | 13.0127(4) |
| V (Å ³) | 7667.5(4) |
| Z | 8 |
| F(000) | 3984 |
| D _c (mg cm ⁻³) | 1.834 |
| μ (Mo-Kα)(mm ⁻¹) | 8.050 |
| No. of total reflections | 7740 |
| [I > 2σ(I)] | |
| R [I > 2σ(I)] | 0.0750 |
| wR [I > 2σ(I)] | 0.1757 |

(b)

| | Bond Lengths | Bond Angles | |
|------------------|--------------|-------------|----------|
| T = 120 K | | | |
| Fe-N1 | 2.212(11) | N1-Fe-N2 | 176.3(4) |
| Fe-N2 | 2.196(12) | N1-Fe-N3 | 91.6(4) |
| Fe-N3 | 2.154(12) | N1-Fe-N4 | 90.0(4) |
| Fe-N4 | 2.155(12) | N1-Fe-N5 | 93.1(4) |
| Fe-N5 | 2.156(12) | N1-Fe-N6 | 84.7(5) |
| Fe-N6 | 2.171(12) | N2-Fe-N3 | 91.4(5) |
| Au1-C28 | 1.962(14) | N2-Fe-N4 | 87.9(4) |
| Au1-C29 | 1.969(15) | N2-Fe-N5 | 89.0(4) |
| Au2-C30 | 1.988(13) | N2-Fe-N6 | 92.4(5) |
| Au2-C31 | 2.002(14) | N3-Fe-N4 | 88.1(5) |
| | | N3-Fe-N5 | 91.5(5) |
| | | N3-Fe-N6 | 175.8(5) |
| | | N4-Fe-N5 | 176.8(5) |
| | | N4-Fe-N6 | 93.9(5) |
| | | N5-Fe-N6 | 86.7(5) |
| | | C28-Au1-C29 | 174.1(6) |
| | | C30-Au2-C31 | 177.0(6) |

Table S3.- Short intermolecular contacts for 1-PhNO₂ and 2-PhNO₂.

| C...C Interactions between PhNO ₂ and L ^{N3} (pyridyl ring) | | | | | | | |
|---|-----------|---------------------------|-----------|---------------------------|-----------|---------------------------|-----------|
| 1-PhNO ₂ 250 K | | 2-PhNO ₂ 250 K | | 1-PhNO ₂ 120 K | | 2-PhNO ₂ 100 K | |
| C22-C32 ⁱ | 3.54(3) | C22-C34 ⁱ | 3.59(3) | C22-C32 ⁱ | 3.412(9) | C22-C32 | 3.36(2) |
| C23-C32 ⁱ | 3.82(3) | C22-C35 ⁱ | 3.56(3) | C22-C37 ⁱ | 3.407(9) | C23-C32 | 3.45(2) |
| C23-C35 ⁱ | 3.66(2) | C23-C35 ⁱ | 3.66(3) | C23-C32 ⁱ | 3.599(10) | C23-C33 | 3.63(2) |
| | | C23-C36 ⁱ | 3.67(2) | C23-C35 ⁱ | 3.633(9) | C27-C35 | 3.690(11) |
| | | C24-C36 ⁱ | 3.56(2) | C23-C36 ⁱ | 3.523(9) | C24-C36 | 3.468(12) |
| | | | | C23-C37 ⁱ | 3.506(9) | C23-C36 | 3.512(12) |
| | | | | C24-C36 ⁱ | 3.551(8) | C23-C37 | 3.435(13) |
| | | | | | | C22-C37 | 3.453(13) |
| | | | | | | C23-C35 | 3.660(10) |
| | | | | | | C16-C35 ^j | 3.641(12) |
| C...C Interactions between adjacent L ^{N3} ligands | | | | | | | |
| 1-PhNO ₂ 250 K | | 2-PhNO ₂ 250 K | | 1-PhNO ₂ 120 K | | 2-PhNO ₂ 100 K | |
| C3-C9 ⁱⁱ | 3.801(11) | C2-C16 ⁱⁱ | 3.658(13) | C3-C11 ⁱⁱ | 3.431(8) | C3-C11 ⁱⁱ | 3.468(10) |
| C4-C10 ⁱⁱ | 3.740(11) | C3-C11 ⁱⁱ | 3.410(10) | C3-C12 ⁱⁱ | 3.623(8) | C6-C8 ⁱⁱⁱ | 3.516(10) |
| C7-C7 ⁱⁱ | 3.389(12) | C4-C11 ⁱⁱ | 3.497(11) | C4-C10 ⁱⁱ | 3.632(9) | C6-C9 ⁱⁱⁱ | 3.461(9) |
| C7-C8 ⁱⁱ | 3.441(11) | C4-C14 ⁱⁱⁱ | 3.673(11) | C4-C11 ⁱⁱ | 3.356(9) | C7-C7 ⁱⁱⁱ | 3.298(9) |
| C7-C12 ⁱⁱ | 3.718(13) | C6-C12 ⁱⁱ | 3.489(10) | C6-C11 ⁱⁱ | 3.601(9) | C7-C8 ⁱⁱⁱ | 3.326(9) |
| C7-C13 ⁱⁱ | 3.860(12) | C6-C8 ^{iv} | 3.554(11) | C6-C12 ⁱⁱ | 3.447(9) | C8-C8 ⁱⁱⁱ | 3.633(10) |
| C8-C8 ⁱⁱ | 3.763(11) | C7-C7 ^{iv} | 3.326(11) | C7-C7 ⁱⁱⁱ | 3.300(9) | C8-C8 ⁱⁱⁱ | 3.637(9) |
| C8-C13 ⁱⁱ | 3.894(12) | C7-C8 ^{iv} | 3.393(11) | C7-C8 ⁱⁱⁱ | 3.342(9) | C12-C3 ⁱⁱⁱ | 3.635(9) |
| C8-C15 ⁱⁱ | 3.758(14) | C7-C9 ^{iv} | 3.501(10) | C7-C8 ⁱⁱⁱ | 3.698(9) | C12-C7 ⁱⁱⁱ | 3.578(9) |
| | | C8-C8 ^{iv} | 3.562(10) | C7-C12 ⁱⁱ | 3.654(9) | C13-C7 ⁱⁱⁱ | 3.432(9) |
| | | C9-C9 ^{iv} | 3.505(10) | C7-C13 ⁱⁱ | 3.465(8) | C13-C13 ⁱⁱⁱ | 3.454(9) |
| | | C11-C6 ⁱⁱ | 3.578(10) | C7-C13 ⁱⁱⁱ | 3.793(10) | C12-C6 ⁱⁱⁱ | 3.402(9) |
| | | C12-C3 ⁱⁱ | 3.648(10) | C8-C6 ⁱⁱⁱ | 3.520(9) | C20-C20 ⁱⁱⁱ | 3.50(4) |
| | | C13-C6 ^{iv} | 3.525(10) | C8-C8 ⁱⁱⁱ | 3.632(8) | C21-C21 ⁱⁱⁱ | 3.53(3) |
| | | | | C8-C13 ⁱⁱ | 3.670(8) | C3-C9 ⁱⁱⁱ | 3.695(10) |
| | | | | C13-C13 ⁱⁱⁱ | 3.463(8) | C4-C11 ⁱⁱ | 3.348(9) |
| | | | | C20-C20 ⁱⁱⁱ | 3.43(7) | C4-C10 ⁱⁱ | 3.674(10) |
| | | | | C21-C21 ⁱⁱⁱ | 3.43(6) | C11-C6 ⁱⁱ | 3.584(9) |
| | | | | C6-C9 ⁱⁱⁱ | 3.486(9) | C6-C15 ⁱⁱ | 3.693(11) |
| | | | | C8-C8 ⁱⁱⁱ | 3.658(9) | C13-C8 ⁱⁱⁱ | 3.595(9) |
| | | | | C14-C4 ⁱⁱ | 3.654(9) | | |

1-PhNO₂ 250 K:

i= x-1/2, -y+3/2, -z+2; ii= -x+1, y, -z+5/2

2-PhNO₂ 250 K:

i= -x+3/2, -y+1/2, z+1/2; ii= -x+1, -y, -z+1; iii= -x+3/2, y-1/2, z; iv= -x+1, y, -z+3/2

1-PhNO₂ 120 K:

i= -x+1/2, -y+1/2, z+1/2; ii= -x, -y+1, -z+1; iii= -x, y, -z+3/2

2-PhNO₂ 100 K:

i= x, -y+1, z+1/2; ii= -x+1, -y+1, -z+1; iii= -x+1, y, -z+1/2

Figure S6.- (a) Fragment of the structure of **3·H₂O** showing the triple interpenetration of the network marked in different colors (red, violet and green). Orange spheres correspond to the oxygen atom of the included water molecule. (b) Fragment of a simplified view of the tetranodal framework of **3·H₂O** with 2,3,4,6-c net and stoichiometry (2-c)(3-c)₂(4-c)(6-c) characterized by the point symbol for net with loops: {4².6².8.6}{4².6⁶.8⁷}{4².6₂}{6}. For this definition of network the site Ag(2) has been considered as a 2-connected node. Code color: Ag(1) (3-connected, grey), Ag(2) (2-connected, green), L^{N4} (4-connected, blue) and Fe^{II} (6-connected, red).

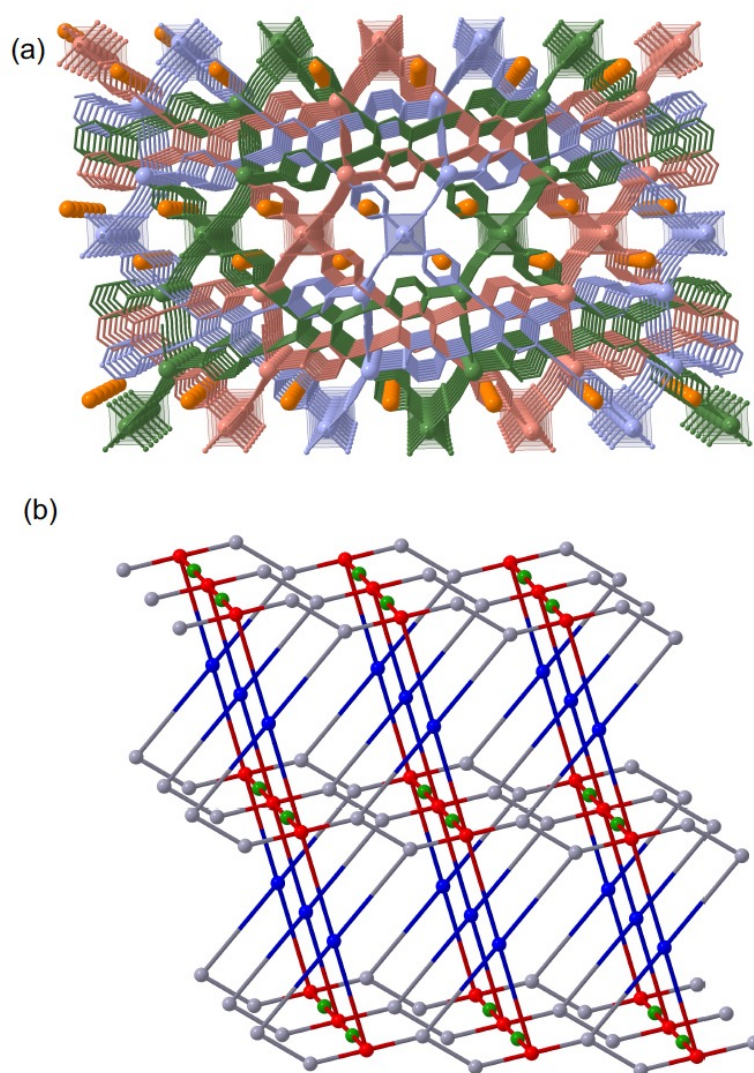
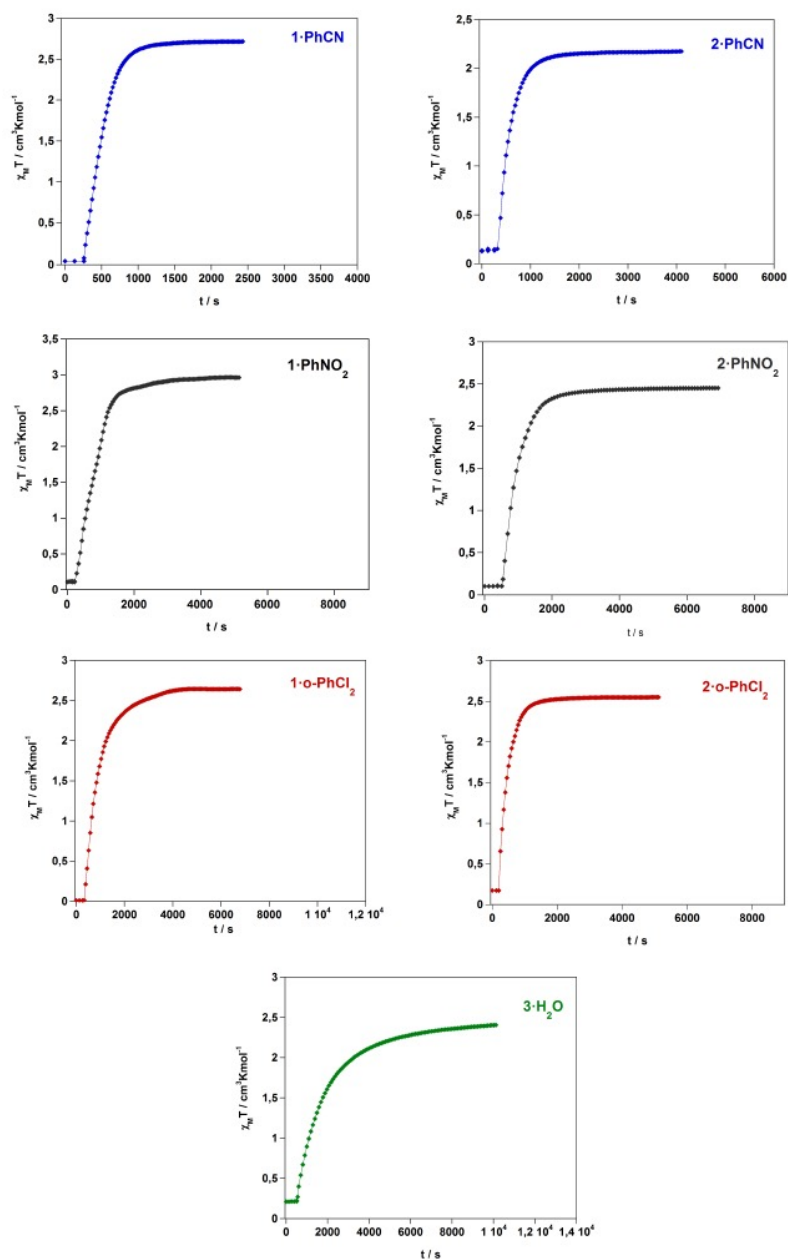
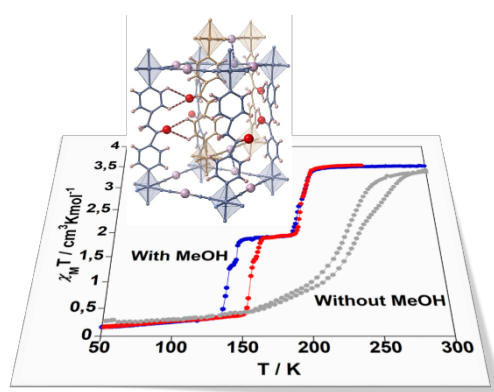


Figure S7. Time dependence of the $\chi_{M,T}$ product upon irradiation with red light ($\lambda = 633 \text{ nm}$) during the LIESST effect at 10 K.



CAPÍTULO 4

Influence of Host-Guest and Host-Host Interactions on the Spin-Crossover 3D Hofmann-type Clathrates $\{\text{Fe}^{\text{II}}(\textit{pina})[\text{M}^{\text{I}}(\text{CN})_2]_2\} \cdot x\text{MeOH}$ ($\text{M}^{\text{I}} = \text{Ag}, \text{Au}$)



REVISTA: Inorganic Chemistry

ÍNDICE DE IMPACTO: 4.850

CAPÍTULO 4

Influence of Host-Guest and Host-Host Interactions on the Spin-Crossover 3D Hofmann-type Clathrates $\{\text{Fe}^{\text{II}}(\text{pina})[\text{M}^{\text{I}}(\text{CN})_2]_2\} \cdot x\text{MeOH}$ ($\text{M}^{\text{I}} = \text{Ag}, \text{Au}$)

4.1.- Abstract

The synthesis, structural characterization and magnetic properties of two new isostructural porous 3D compounds with general formula $\{\text{Fe}^{\text{II}}(\text{pina})[\text{M}^{\text{I}}(\text{CN})_2]_2\} \cdot x\text{MeOH}$ ($x = 0-5$; *pina* = N-(pyridin-4-yl)isonicotinamide; $\text{M}^{\text{I}} = \text{Ag}^{\text{I}}$ and $x \sim 5$ (**1**·**xMeOH**); $\text{M}^{\text{I}} = \text{Au}^{\text{I}}$ and $x \sim 5$ (**2**·**xMeOH**)) are presented. The single-crystal X-ray diffraction analyses have revealed that the structure of **1**·**xMeOH** (or **2**·**xMeOH**) presents two equivalent doubly interpenetrated 3D frameworks stabilized by both argentophilic (or aurophilic) interactions and interligand C=O...HC H-bonds. Despite the interpenetration of the networks, these compounds display accessible void volume capable of hosting up to five molecules of methanol which interact with the host *pina* ligand and establish an infinite lattice of hydrogen bonds along the structural channels. Interestingly, the magnetic studies have shown that the solvated complexes **1**·**xMeOH** and **2**·**xMeOH** display two- and four-step hysteretic thermally driven spin transitions, respectively. However, when these compounds lose the methanol molecules, the magnetic behavior changes drastically giving place to gradual spin conversions evidencing the relevant influence of the guest molecules on the spin-crossover properties. Importantly, since the solvent desorption takes place following a single-crystal-to-single-crystal transformation, empty structures **1** and **2** ($x = 0$) could be also determined allowing us to evaluate the correlation between the structural changes and the modification of the magnetic properties triggered by the loss of methanol molecules.

4.2.- Introduction

The spin crossover (SCO) is a molecular phenomenon observed for first row d^4-d^7 transition metal complexes that involves the reversible conversion between the low spin (LS) and the high spin (HS) electronic states. This spin-state switching, that has been mostly studied for Fe^{II} complexes, can be induced by the application of external perturbations (temperature or pressure changes, light, or guest molecules adsorption)^[1-4] and, importantly,

leads to the modification of many physical parameters, i.e., the magnetic response, dielectric constant, color, or volume of the material. Indeed, this fascinating external perturbation-physical change coupling makes of this kind of complexes promising materials for their further practical applications.

The versatility offered by the coordination chemistry when designing and synthesizing new SCO materials provides the possibility of accessing to multitude of different structural topologies and dimensionalities.^[5,6] This rational way of synthesis is crucial because the control of the degree of connectivity between SCO centers is directly related to the cooperativity of the system and therefore is the key to modulate and predict the spin transition properties. In the last 2 decades, many scientific groups have focused a special attention on two-dimensional (2D) and three-dimensional (3D) systems and, especially, on complexes presenting the Hofmann-like clathrate topology $\{Fe^II(L)_x[M^II(CN)_4]\}$ ($x = 1$ or 2 ; $M = Pt^{II}, Pd^{II},$ or Ni^{II}), probably due to their attracting SCO properties,^[7] host-guest chemistry^[4,8] and the possibility of obtaining them as nanoparticles^[9-11] or thin films.^[12,13] Hence, when L is a monotopic ligand, these compounds display 2D structures formed by planes that are pillared presenting poor, if any, porosity.^[14] Conversely, if L is a ditopic bridging ligand, then the resulting complexes exhibit 3D topologies and use to be porous structures.

Another well-known synthetic approach deals with introducing dicyanometalates anions ($[Ag^I(CN)_2]^-$ or $[Au^I(CN)_2]^-$) instead of the $[M^II(CN)_4]^{2-}$ ones giving place to compounds of the type $\{Fe^II(L)[M^I(CN)_2]_2\}$.^[7] In this case, the high void space volume of the 3D generated structures is occupied by interpenetrating two (or more) networks. The first examples of this kind of compounds were published in 2002 by our group, being $M^I = Ag^I$ and $L =$ pyrazine (pz), 4,4'-bipyridine (4,4'-bipy) or bis-pyridil-ethylene (bpe) which acted as ditopic bridging ligands.^[15] The magnetic measurements showed that the pyrazine derivative is in the LS state in the studied temperature range, whereas the 4,4'-bipy based complex is HS in all range of temperatures although an incomplete SCO can be induced by applying an external pressure of at least 4.6 kbar. Besides, the bpe derivative displays an incomplete SCO curve with a wide hysteresis (95 K) at room pressure.

This family of compounds has been enlarged in the past decade by the use of a number of bridging ligands such as bpac,^[16,17] bpmp,^[18] bpben,^[19,20] pz,^[21,22] 4,4'-bipy,^[8] bipytz/bipydz,^[23,24] 2,5-bpp,^[25] 4-abpt,^[26] Fpz,^[27] and naphty.^[28] Interestingly, despite their

interpenetrated nature, most of these frameworks are able to host guest molecules showing an interplay between the host-guest chemistry and the SCO behavior. Moreover, in some of them,^[24,26] the adsorption of guest molecules induces the apparition of hysteretic multi-stepped spin transitions which are relatively rare but very interesting since they allow for the possibility to act as a multiswitching system. According to these studies, the multistep phenomenon stems from strong and directional H-bonds generated between the trapped solvents and the pillar ligand that may provoke symmetry breaking during the SCO.

Here, we report on the synthesis, crystal structures and magnetic behavior of two new doubly interpenetrated 3D Hofmann-type clathrates formulated as $\{Fe^{II}(pina)[M'(CN)_2]_2\} \cdot xMeOH$ [being x a value between 0 and 5; $pina$ = N-(pyridin-4-yl)isonicotinamide (Figure 1a); $M' = Ag^I$ and $x \approx 5$ (**1**· $xMeOH$) or $M' = Au^I$ and $x \approx 5$ (**2**· $xMeOH$)] and its desolvated forms **1** and **2** ($x = 0$). The novelty of the $pina$ bridging ligand, which was previously used to design other SCO-active^[29] (and -inactive)^[30] Fe^{II} complexes, is that both carbonyl and -NH moieties of the amide group are susceptible of interacting via H-bonding with the adsorbed guest molecules. Indeed, our magnetic characterizations show a strong impact of the presence of intrapore methanol guest molecules on the SCO properties and, in particular, reveal the generation of hysteretic multistep spin transitions presumably related to the presence of host-guest H-bonding interactions.

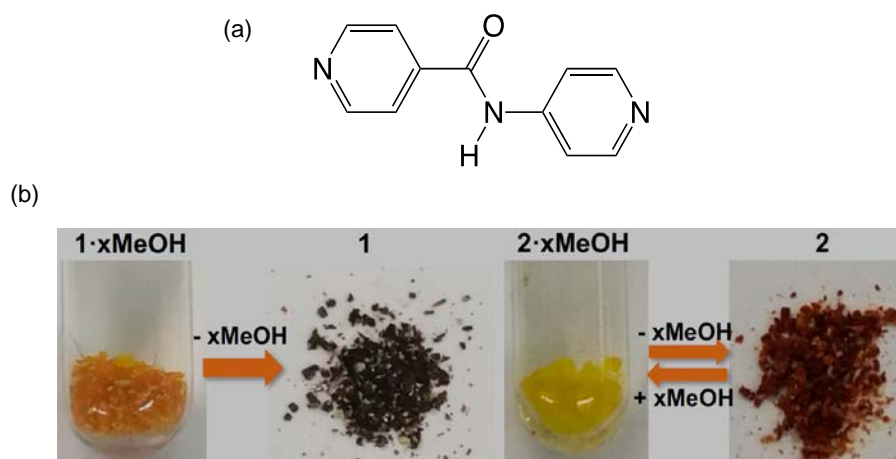


Figure 1. (a) Structure of the ligand $pina$. (b) Single crystals of compound $\{Fe^{II}(pina)[Ag^I(CN)_2]_2\} \cdot xMeOH$ (left) and $\{Fe^{II}(pina)[Au^I(CN)_2]_2\} \cdot xMeOH$ (right) in mother liquor (**1**· $xMeOH$ and **2**· $xMeOH$, $x \approx 5$) and desolvated dry product (**1** and **2**, $x = 0$).

4.3.- Results

4.3.1.- Synthesis

The slow diffusion of Fe(BF₄)₂·6H₂O, *pina* ligand and the corresponding K[M^I(CN)₂] salt (M^I = Ag^I or Au^I) in methanol solutions yielded, after 2 weeks, single crystals corresponding to compounds {Fe^{II}(*pina*)[Ag^I(CN)₂]₂·xMeOH (**1**·xMeOH) or {Fe^{II}(*pina*)[Au^I(CN)₂]₂·xMeOH (**2**·xMeOH) with x ≈ 5. Out of the mother liquor, the included ca. 5 molecules of methanol undergo rapid desorption provoking loss of crystallinity and apparent change of color from orange to almost black and from yellow to dark orange for samples **1**·xMeOH and **2**·xMeOH, respectively (Figure 1b), giving rise to the desolvated counterparts **1** and **2**. Figure 2 displays the X-ray powder diffraction patterns of **1** and **2** recorded at 298 K (blue and red spectra, respectively) together with the simulated ones from single-crystal X-ray diffraction data for **1**·xMeOH, **2**·xMeOH, **1**, and **2** (*vide infra*) also depicted for comparison. Although the powder samples of **1** and **2** present low crystallinity, the similarity of the spectra confirms that both compounds are essentially isostructural since the most intense peaks are clearly reproduced for both derivatives, in particular those in the intervals 6-7° and 15-20°. Moreover, they are also comparable to the simulated patterns of

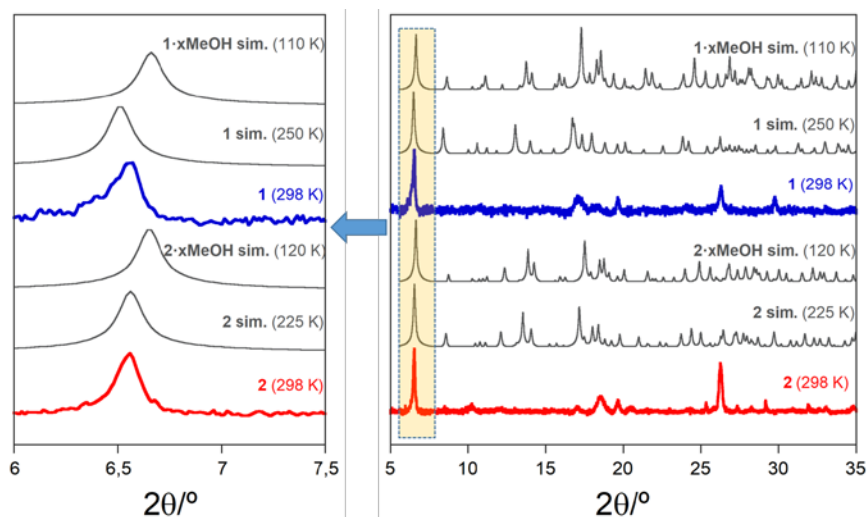


Figure 2. Ranges of $2\theta = 5\text{-}35^\circ$ (right) and $2\theta = 6\text{-}7.5^\circ$ (left) of the X-ray powder diffraction patterns for **1** (blue line) and **2** (red line), collected at room temperature. Simulated spectra of solvated (**1**·xMeOH sim. (110 K) and **2**·xMeOH sim. (120 K)) and empty (**1** sim. (250 K) and **2** sim. (225 K)) are also shown for comparison.

the compounds before (**1·xMeOH sim.** [110 K] and **2·xMeOH sim.** [120 K]) and after (**1 sim.** [250 K] and **2 sim.** [225 K]) desorption of the methanol molecules. Indeed, in spite of the slight differences observed between the simulated patterns of the solvated and desolvated samples, it is not straightforward to assess which is more similar to the experimental spectra. Nevertheless, the slight downshift of about 0.15° observed for most of the simulated peaks in the desolvated samples (**1 sim.** [250 K] and **2 sim.** [225 K]), and especially for the peak centered around $2\theta = 6.5^\circ$ (Figure 2 left), seems to match better with the desolvated experimental ones. This shift is clearly related to an increase of the unit cell volume due to a LS \rightarrow HS transition (*vide infra*) whose structural changes facilitate the labilization and concomitant desorption of the included methanol molecules. The complete desorption of the methanol molecules in **1** and **2** was confirmed by thermogravimetric analysis of samples freshly taken (ca. 15 minutes) from the mother solution since no loss of mass was observed between 298 K and 500-550 K where the decomposition of the samples starts (Figure S1).

4.3.2.- Magnetic properties

The solvated compounds **1·xMeOH** and **2·xMeOH** were measured soaked with their mother liquor to prevent the desorption of the methanol molecules. Afterwards, the same samples were removed from the solution to allow the desorption of MeOH to give **1** and **2**. The thermal dependence of the $\chi_M T$ product (where χ_M is the molar magnetic susceptibility and T is temperature) for **1·xMeOH** and **2·xMeOH** and their desolvated forms (**1** and **2**), measured at 1 K min^{-1} in the cooling and heating mode, is depicted in Figure 3.

At 290 K, **1·xMeOH** shows a $\chi_M T$ value of $3.0 \text{ cm}^3 \text{ K mol}^{-1}$, although it is consistent with an octahedral Fe^{II} ion in the HS state, this value can be considered lower than that typically observed ($3.3\text{-}3.8 \text{ cm}^3 \text{ K mol}^{-1}$). This slightly low $\chi_M T$ may be attributed to an overestimation of the considered mass which should also vary with the solvent content. This value remains practically constant down to 245 K when a relatively sharp drop of $\chi_M T$ in two steps takes place reaching a value of $0.1 \text{ cm}^3 \text{ K mol}^{-1}$ at 150 K. This behavior is consistent with a complete HS \leftrightarrow LS thermal spin transition. The $\chi_M T$ vs T curve in the heating mode does not match that of the cooling mode defining a narrow hysteresis loop $\sim 5 \text{ K}$ wide. The critical temperatures (T_c) of **1·xMeOH** are $T_{c1(\downarrow)} = 215 \text{ K}$, $T_{c2(\downarrow)} = 179 \text{ K}$ for the cooling mode, and $T_{c1(\uparrow)} = 220 \text{ K}$, $T_{c2(\uparrow)} = 185 \text{ K}$ for the heating mode (Figure 3a).

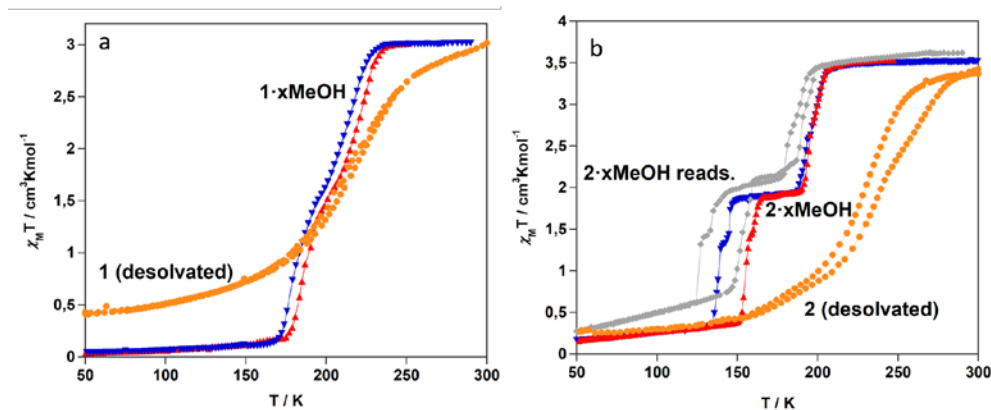


Figure 3. $\chi_M T$ versus T plots for (a) $1 \cdot x\text{MeOH}$ and **1** and (b) $2 \cdot x\text{MeOH}$, **2**, and $2 \cdot x\text{MeOH}$ reads. Red and blue triangles correspond to the cooling and heating modes for the solvated compounds, orange circles correspond to the solvent free derivatives, and gray circles correspond to the readsorbed sample.

Compound $2 \cdot x\text{MeOH}$ displays a $\chi_M T$ value ca. $3.50 \text{ cm}^3 \text{ K mol}^{-1}$ at room temperature indicating that 100% of Fe^{II} ions are in the HS state ($S = 2$) but with slightly higher orbital contributions than $1 \cdot x\text{MeOH}$ (Figure 3b). This value remains constant until 210 K when the $\chi_M T$ product decreases abruptly, first reaching a tiny plateau at 194 K which corresponds to 25%LS:75%HS state and, later, a second wider plateau between 185 and 150 K consolidating a 50%LS:50%HS mixed spin state. Further cooling of the sample unveils two additional steps giving an almost complete SCO curve. The steps are separated by a narrow plateau centered at a $\chi_M T$ value ca. $1.40 \text{ cm}^3 \text{ K mol}^{-1}$ at 142 K which involves an additional $\chi_M T$ drop ca. 15% reaching a $\approx 65\text{LS}:35\text{HS}$ state. In the heating mode, the steeped spin transitions for the last three steps are shifted to higher temperatures generating thermal hysteresis of 2, 16 and 17 K, for the second, third and fourth step, respectively. The critical temperatures, extracted from the $\partial(\chi_M T)/\partial T$ vs T plot (Figure S2), are $T_{c1}(\downarrow) = 199 \text{ K}$, $T_{c2}(\downarrow) = 191 \text{ K}$, $T_{c3}(\downarrow) = 144 \text{ K}$, $T_{c4}(\downarrow) = 137 \text{ K}$ for the cooling mode, and $T_{c1}(\uparrow) = 199 \text{ K}$, $T_{c2}(\uparrow) = 193 \text{ K}$, $T_{c3}(\uparrow) = 160 \text{ K}$, $T_{c4}(\uparrow) = 154 \text{ K}$ for the heating mode.

As observed in Figure 3, freshly prepared **1** and **2** samples display substantial changes in the magnetic properties. At 300 K, $\chi_M T$ value for **1** and **2**, 3.00 and $3.3 \text{ cm}^3 \text{ K mol}^{-1}$, respectively, is similar to that of the corresponding solvated forms. However, upon cooling down, an almost complete but much more gradual HS \rightarrow LS spin state conversion without

marked steps takes place. The $\chi_M T$ attains values of $0.4 \text{ cm}^3 \text{ K mol}^{-1}$ (**1**, $T_{1/2(\downarrow)} = 204 \text{ K}$) and 0.2 (**2**, $T_{1/2(\downarrow)} = 225 \text{ K}$) $\text{cm}^3 \text{ K mol}^{-1}$ at 50 K . The $\chi_M T$ vs T plots in the heating mode do not match those observed in the cooling mode, thereby generating a hysteresis of 3 K ($T_{1/2(\uparrow)}=204$) and 9 K ($T_{1/2(\uparrow)}=234$) for **1** and **2**, respectively. Interestingly, evolution of these $\chi_M T$ vs T plots was observed during a period of 2 weeks. As shown in Figure 4, the SCO behavior becomes extremely gradual and incomplete with high percentages of HS and LS centers at low and high temperatures, respectively. Comparison of the PXRD patterns of **2** freshly prepared and two weeks later shows that the most characteristic reflections of the structure can be identified in both patterns, namely $[0,0,1]$ at $2\theta = 6.5^\circ$ ($d = 13.56 \text{ \AA}$) associated with the first-order reflection of planes containing the $\{\text{Fe}_4[\text{Au}(\text{CN})_2]_4\}$ layers (vide infra) and the subsequent second- ($2\theta = 13.04^\circ$; $d = 6.78 \text{ \AA}$), third- ($2\theta = 19.61^\circ$; $d = 4.52 \text{ \AA}$) and fourth-order ($2\theta = 26.25^\circ$; $d = 3.39 \text{ \AA}$) planes. This indicates that the main features of the structure remain in the aged sample **2** (see Figure S3).

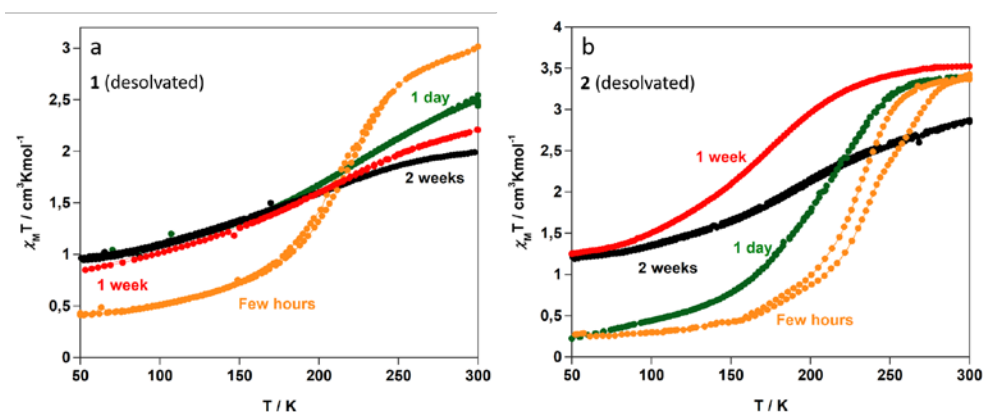


Figure 4. Aging of the desolvated compounds (a) **1** and (b) **2** monitored through time evolution of the $\chi_M T$ versus T plots.

After immersing **1** in pure methanol for 1 month, the almost black crystals (Figure 1) recover neither the orange color nor the original spin transition properties of **1·xMeOH** indicating the irreversibility of the desolvation process. In contrast, and despite being isostructural, in the same conditions, the dark orange crystals **2** become bright yellow (Figure S4) and essentially recover the HS \leftrightarrow LS thermal spin transition likely due to the readsorption of MeOH molecules yielding **2·xMeOH reads**. Effectively, **2·xMeOH reads** shows the four-step spin transition of the genuine solvated **2·xMeOH** although presenting a

~ 10 K down shift of the critical temperatures as well as an increase by 5 K of the hysteresis width ($T_{c1}(\downarrow) = 189$ K, $T_{c2}(\downarrow) = 181$ K, $T_{c3}(\downarrow) = 134$ K, $T_{c4}(\downarrow) = 126$ K for the cooling mode, and $T_{c1}(\uparrow) = 194$ K, $T_{c2}(\uparrow) = 189$ K, $T_{c1}(\uparrow) = 156$ K, $T_{c4}(\uparrow) = 150$ K for the heating mode (see gray line in Figure 3b).

4.3.3.- Single crystal X-Ray diffraction (SCXRD)

Given the lability of the MeOH molecules in compounds **1·xMeOH** and **2·xMeOH**, the crystals were picked directly from the mother liquor, immersed in oil and immediately placed on the goniometer at 110 and 120 K, respectively, and subsequently their LS crystal structures measured. Then, based on their magnetic behavior and trying to avoid any desorption of MeOH preserving the quality of the single crystals, the structures of the corresponding HS states were measured at the lowest possible temperatures, namely 250 and 225 K, respectively. As we will see, the resulting structures corresponded to those of desolvated **1** and **2** forms. The relevant structural parameters are shown in Table 1.

Compounds **1·xMeOH** and **2·xMeOH** crystallize in the monoclinic $P2_1/n$ space group. Tables S1 and S2 contain a list of significant bond lengths and angles, respectively. Both solvated complexes are isostructural, and will be described simultaneously. The Fe^{II} defines slightly elongated $[\text{Fe}^{\text{II}}\text{N}_6]$ octahedral sites with the axial positions occupied by the *pina*

Table 1. Crystallographic parameters for the studied compounds at different temperatures.

| Compound | 1·xMeOH | 1 | 2·xMeOH | 2 |
|---|---|--|---|--|
| T (K) | 110 | 250 | 120 | 225 |
| Empirical formula | $\text{C}_{20}\text{H}_{29}\text{FeAg}_2\text{N}_7\text{O}_6$ | $\text{C}_{15}\text{H}_9\text{FeAg}_2\text{N}_7\text{O}$ | $\text{C}_{15.5}\text{H}_{10.5}\text{FeAu}_2\text{N}_7\text{O}_{1.5}$ | $\text{C}_{15}\text{H}_9\text{FeAu}_2\text{N}_7\text{O}$ |
| Mr | 735.09 | 574.88 | 768.59 | 753.07 |
| Crystal system | monoclinic | | | |
| Space group | $P2_1/n$ | $P2_1/m$ | $P2_1/n$ | $P2_1/m$ |
| <i>a</i> (Å) | 16.4143(9) | 10.585(2) | 16.3264(4) | 10.327(2) |
| <i>b</i> (Å) | 10.2435(5) | 10.588(2) | 10.1192(2) | 10.3245(14) |
| <i>c</i> (Å) | 17.1163(8) | 13.659(2) | 17.0738(4) | 13.491(2) |
| β | 104.701(5) | 96.70(2) | 105.493(2) | 93.689(11) |
| <i>V</i> (Å ³) | 2783.7(2) | 1520.4(4) | 2718.27(11) | 1435.4(3) |
| <i>Z</i> | 4 | 2 | 4 | 2 |
| <i>D_c</i> (mg cm ⁻³) | 1.754 | 1.256 | 1.878 | 1.742 |
| <i>F</i> (000) | 1464 | 552 | 1394 | 680 |
| μ (Mo-K α) (mm ⁻¹) | 1.953 | 1.757 | 11.310 | 10.706 |

ligand and the equatorial positions by the CN moiety of two crystallographically distinct $[M^I(CN)_2]^-$ anions (Figure 5a). The average axial Fe-N_{ax} bond length, 1.996 Å (**1·xMeOH**) and 1.998 Å (**2·xMeOH**), are slightly larger than the equatorial Fe-N_{eq} one, 1.929 Å (**1·xMeOH**) and 1.928 Å (**2·xMeOH**). These values are typical for the Fe^{II} ion in the LS state in agreement with the magnetic properties.

The two crystallographically distinct $[M^I(CN)_2]^-$ groups are essentially linear and connect two adjacent Fe^{II} centers defining a stack of almost planar 2D $\{Fe^II[M^I(CN)_2]\}_n$ grids. The layers are pillared by the axial *pina* ligands, thus defining a 3D framework with typical **pcu** topology. Although the two pyridine rings of the *pina* ligand are ordered, the asymmetric amide moiety that connects both rings is disordered and has been modeled in two positions with 50% occupational distribution (Figure S5). The open nature of the framework allows the interpenetration of a second equivalent network (Figure 5b) in such a way that the *pina* ligands of one framework threads the $\{Fe^II_4[M^I(CN)_2]_4\}$ windows of the other framework. In addition to argentophyllic [Ag...Ag = 3.080 Å, **1·xMeOH**] or aurophyllic [Au...Au = 3.131 Å, **2·xMeOH**] short contacts, there have been observed reciprocal C=O...HC interactions [C=O(1)...C(11) = 3.260(14) Å and C=O(1)...C(12) = 3.37(2) Å] for **1·xMeOH** and [C=O(1a)...C(11) = 3.33(2) and C=O(1b)...C(12) = 3.28(2) Å] for **2·xMeOH** established between the C=O moiety and the pyridinic hydrogen atoms of adjacent *pina* ligands belonging to different frameworks (see Figure 5c).

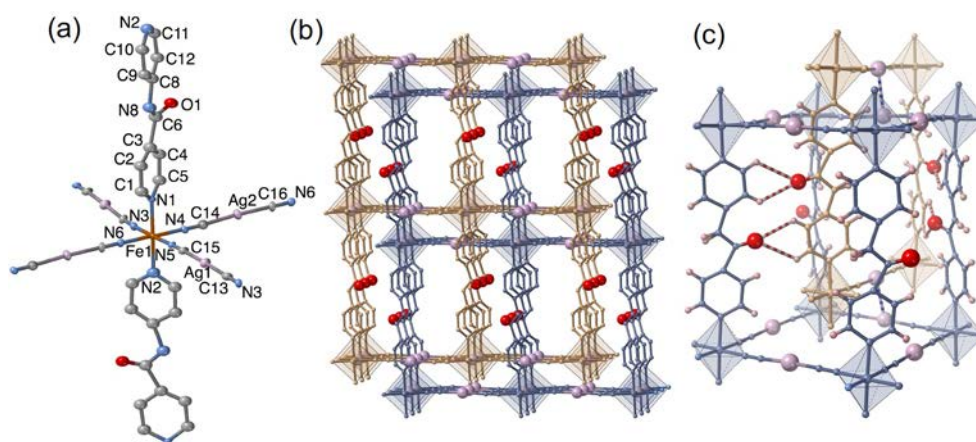


Figure 5. a) ORTEP representation of the Fe^{II} environment displaying the numbering of the asymmetric unit for **1·xMeOH**. b) Fragment of the two 3D interpenetrated networks denoted in beige and blue. c) View of the C=O...HC hydrogen-bonding (red and white dashed line) and metallophyllic interactions (blue and white dashed line).

Table 2. Selected H-bond lengths (Å) found in compounds **1·xMeOH**, **2·xMeOH**, **1** and **2**.

| <i>H-bond</i> | 1·xMeOH (110 K) | 2·xMeOH (120 K) | 1 (250 K) | 2 (225 K) |
|-----------------------|---------------------------|---------------------------|---------------------|---------------------|
| O1-O4 | 3.14(2) | | | |
| O2-O3 ⁱ | 3.35(2) | | | |
| O2-O6 ⁱ | 2.73(3) | | | |
| O3-O4 | 3.73(3) | | | |
| O3-O5 ⁱⁱ | 2.82(3) | | | |
| O4-O5 | 3.50(3) | | | |
| O5-O6 | 2.69(3) | | | |
| O2-N7 | 2.92(3) | 2.84(4) | | |
| O3-N7 ⁱⁱ | 3.22(3) | | | |
| O1-C11 ⁱⁱⁱ | 3.260(14) | | | |
| O1-C12 ⁱⁱⁱ | 3.37(2) | | | |
| O1a-C11 ^{iv} | | 3.33(2) | | |
| O1b-C12 ^{iv} | | 3.28(2) | | |
| O1-C4 ^v | | | 3.51(6) | |
| O1-C5 ^v | | | 3.60(6) | |
| O1-C4 ^{vi} | | | | 3.47(5) |
| O1-C5 ^{vi} | | | | 3.48(5) |

i = $-x+3/2, y-1/2, -z+3/2$; ii = $-x+3/2, y+1/2, -z+3/2$; iii = $-x+1, -y+2, -z+1$; iv = $-x+2, -y, -z$; v = $-x+2, -y+1, -z$; vi = $-x+1, -y+1, -z$.

The free space of the structure is filled with solvent molecules but the results denote the mentioned marked lability of the MeOH molecules even at low temperatures (Figure 6 and S6). Regarding compound **1·xMeOH**, five methanol molecules per Fe^{II} are located in defined positions with occupancies ranging from 0.5 to 1 (although for practical reasons the structure has been modelled with an occupancy equal to 1 for all methanol molecules) whereas for **2·xMeOH**, due to their even larger lability, only one discrete methanol molecule with an occupancy of 0.5 could be observed. This latter methanol molecule interacts with the $-\text{NH}$ moiety of the *pina* ligand *via* H-bonding (2.84(4) Å). However, in the case of complex **1·xMeOH**, an infinite virtual intricate H-bonding lattice is generated throughout the channels of the structure: three of the five guest methanol molecules interact directly with the amide group of the *pina* ligand [two of them are connected to the $-\text{NH}$ moiety ($\text{N}(7)\cdots\text{O}(2) = 2.92(3)$ and $\text{N}(7)\cdots\text{O}(3) = 3.22(3)$ Å) and the other one with the carbonyl group ($\text{O}(4)\cdots\text{O}(1)=\text{C} = 3.14(2)$ Å)]. Besides, all methanol molecules are interconnected in such a way that they establish intra- and inter-network communications between *pina* ligands through H-bond interactions (Figure S6). The distances of the strongest H-bonds found are summarized in

Table 2 and the most relevant interatomic distances and angles are showed in Tables S1 and S2.

In order to characterize the HS state and taking into account the lability of the MeOH molecules we measured the crystals at temperatures as low as possible according to their magnetic curves (Figure 3), namely at 250 K for **1**·*x*MeOH and 225 K for **2**·*x*MeOH. Upon increasing the temperature both compounds display a crystallographic transformation from the $P2_1/n$ (monoclinic) to the $P2_1/m$ (monoclinic) space group. As we will see below, this change of symmetry seems to be most likely driven by a complete loss of solvent molecules.

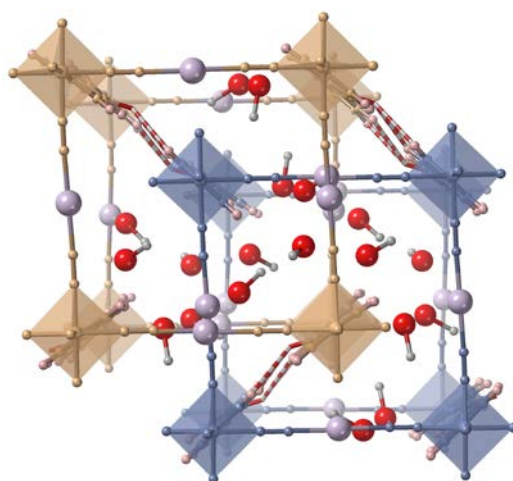


Figure 6. Top view of the two interpenetrated networks displaying the MeOH guest molecules. The red dashed lines represent the C=O...HC connections between the interpenetrated frameworks.

Although essentially the crystal structure is very similar to that described above for the LS state, it presents several important differences: i) the Fe-N average distance increases by 0.198 Å for **1** and 0.111 Å for **2**, indicating that whereas the former presents a practically complete LS → HS spin transition, only 50-60% of the Fe^{II} ions switch to the HS state for the latter; ii) Unlike the LS structures, the pyridine rings and the amide moiety of the *pina* ligand are disordered in two different orientations with respect to the *b* axis (Figure S7); iii) Although the C=O...HC contacts are kept in the framework, they are significantly weaker (C=O(1)...C(4) = 3.51(6) and C=O(1)...C(5) = 3.60(6) Å for **1**; C=O(1)...C(4) = 3.47(5) and C=O(1)...C(5) = 3.48(5) Å for **2**); iv) Due to the positional disorder of the *pina* ligand, the C=O...HC interactions are not only reciprocally established between adjacent *pina* pairs as

previously shown for **1·xMeOH** and **2·xMeOH** in Figure 5c and schematized in Figure 7a, but also between a given *pina* ligand and two different neighboring *pina* ligands (red dashed lines in Figure 7b); v) The argentophilic and aurophilic interactions are weakened (3.110 and 3.155 Å). vi) The lack of meaningful residual electronic density within the cavities of the structure suggests that no solvent molecules, $x \approx 0$, remain within the structural cavities.

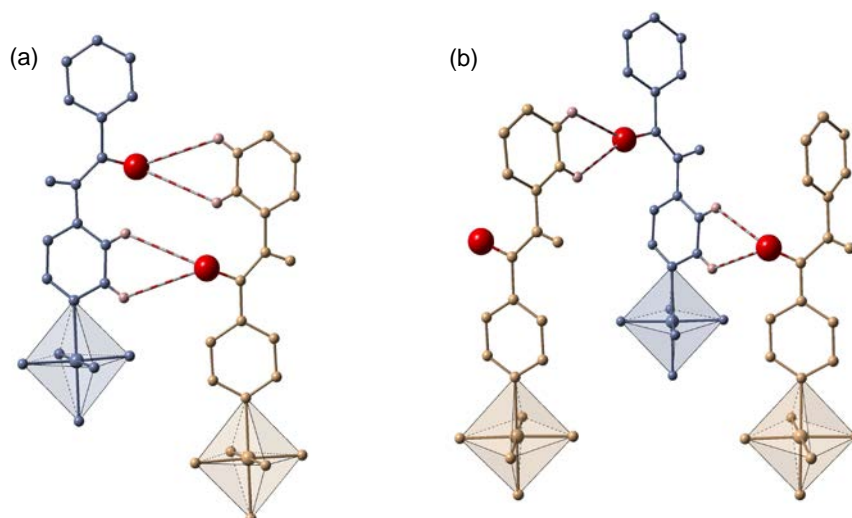


Figure 7. The two operative hydrogen bonding C=O...HC interactions established between consecutive *pina* ligands of different interpenetrated frameworks in **1** and **2**: (a) Reciprocal interactions generated between *pina* ligands with parallel pyridine groups; (b) Non reciprocal interactions arisen from the two orthogonal possible orientations of the pyridine rings.

4.4.- Discussion

The reaction between Fe^{II} , $[Ag^I(CN)_2]^-$ or $[Au^I(CN)_2]^-$ and the ditopic *pina* ligand has originated two new porous 3D Hofmann clathrates with general formula $\{Fe^{II}(pina)[M^I(CN)_2]_2\} \cdot xMeOH$ ($M^I = Ag^I$ or Au^I). On the basis of the magnetic and structural data, the samples soaked in the mother liquor are consistent with a value of $x \approx 5$ (**1·xMeOH** and **2·xMeOH**). The $\chi_M T$ vs T plots reveal that both solvated complexes undergo cooperative spin transitions featuring two and four steps for **1·xMeOH** and **2·xMeOH** derivatives, respectively. However, the labile MeOH molecules spontaneously desorb affording **1** and **2** when they are out of the mother liquor. This fact provokes subtle structural modifications accompanied by dramatic changes in the magnetic properties. Interestingly,

the methanol desorption process occurs following a single-crystal-to-single-crystal transformation allowing us to determine the structures for both the solvated and desolvated counterparts and giving the possibility to relate them with their corresponding SCO properties. The higher cooperativity observed for the stepped SCO in the methanol containing derivatives is likely associated to the efficient transmission of the structural changes occurred during the SCO in the Fe^{II} environments. This cooperativity may be promoted by both the intricate H-bonding lattice generated by the MeOH molecules along the structural channels and by the reciprocal inter-framework C=O...HC interactions established between *pina* ligands. Contrarily, when the methanol molecules are desorbed the communication between the Fe^{II} ions is disrupted thereby affording gradual SCO curves. This decrease in cooperativity demonstrates the efficiency of the host-guest and host-host H-bonding interactions in these systems. Related results were recently reported on analogue compounds. For example, complex {Fe^{II}(bipydz)[Au^I(CN)₂]₂·4EtOH (bipydz = 3,6-bis(4-pyridyl)-1,2-diazine), which presents a four-step hysteretic SCO similar to that of **2·xMeOH**, switches to a gradual one-step spin transition behavior when it desorbs the ethanol guest molecules.^[24] In the same line, whereas compound {Fe^{II}(4-abpt)[Ag^I(CN)₂]₂·2DMF·EtOH (4-abpt = 4-amino-3,5-bis(4-pyridyl)-1,2,4-triazole) displays also a SCO in four steps, its solvent-free counterpart loses completely this property showing a constant $\chi_M T$ corresponding to a 50% HS/LS Fe^{II} ions mixture.^[26] In addition, compound {Fe^{II}(dpni)[Ag^I(CN)₂]₂·4CH₃CN (dpni = N,N'-di-(4-pyridyl)-1,4,5,8-naphthalene tetracarboxydiimide) shows an evident decrease of cooperativity and change of SCO nature (from a complete two steps to an incomplete single step spin transition) when reversibly desorbs acetonitrile molecules.^[31] All these examples highlight the close relationship between the host-guest interactions (and particularly, the H-bonding contacts) and the occurrence of a multistep SCO behavior.

The high lability of the methanol molecules observed for the as-synthesized **1·xMeOH** and **2·xMeOH** compounds, even at temperatures as low as 250 K, did not allow us to characterize the intermediate structures associated to the plateaus observed in the magnetic curves of the solvated complexes. However, despite the nominal differences in MeOH content between the single crystals used for the crystal analysis and the methanol soaked microcrystalline samples used in magnetism, the average Fe-N bond length inferred from the crystal structures at 110/120 K correlates reasonably well with the fully populated LS state expected from the magnetic curves. When heating up the crystals to 250/225 K, the

absence of meaningful electronic density within the pores in both structures confirms the desorption of the MeOH molecules yielding the desolvated frameworks **1** and **2**. The variations of the average Fe-N bond length (ΔR) observed for **1** and **2** with respect to the LS structures is $\Delta R = 0.198 \text{ \AA}$ and 0.111 \AA , respectively. On the basis of the fact that the typical ΔR value for a complete LS \leftrightarrow HS transformation is c.a. 0.2 \AA , these values are consistent with ca. 99% and 55% transformation from the LS to the HS state and correlate reasonably well with the values of $\chi_{\text{M}}T$ at the same temperature, which corresponds to ca. 86% and 53% for **1** and **2**, respectively. The slight discrepancies can be ascribed to the time dependence of the magneto-structural properties observed for both compounds (although more marked for **2**) activated upon the loss of the solvent molecules. Consequently, the HS fraction at 225/250 K markedly depends on the elapsed time (especially within the first hours after the desorption) and provokes misfits between the magnetic and the crystallographic results due to aging. Unfortunately, the rapid deterioration of the desolvated crystals quality prevented us from analyzing the aged structures. A similar time-dependent process of the SCO behavior was previously reported for the double interpenetrated coordination polymer $\{\text{Fe}^{\text{II}}(\text{TPT})_{2/3}[\text{Ag}^{\text{I}}(\text{CN})_2]_2\} \cdot n\text{Solv}$ (TPT = [(2,4,6,-tris(4-pyridyl)-1,3,5-triazine)) with **NbO** structure type.^[32] In the latter case, aging was associated with subtle structural reorganization/relaxation of the structure denoted by a noticeable decrease, 25%, of the unit cell volume, which was tentatively related to the flexible nature of the $[\text{Ag}(\text{CN})_2]^-$ moiety, together with mutual displacement and/or compression of the interpenetrated frameworks. The compression mechanism was demonstrated for the double interpenetrated 3D coordination polymer $\{(\text{ZnI}_2)_3(\text{TPT})_2\} \cdot 6\text{C}_6\text{H}_5\text{NO}_2$ where desorption/sorption of the nitrobenzene molecules involves reversible distortion of the interpenetrated frameworks.^[33] A similar hypothesis can be drawn for both desolvated derivatives **1** and **2**. However, it is clear that the aging process does not occur exactly in the same way in both compounds since **2** readsorbs reversibly the methanol molecules with subsequent recovering of the magnetic properties. The small difference in SCO critical temperature, $T_{1/2}$, of about 10 K between the as-synthesized (**2**·**xMeOH**) and readsorbed (**2**·**xMeOH reads.**) samples may arise from small differences in methanol content. Taking into account the isostructural character of both compounds, it is in principle surprising that, in the same conditions, **1** cannot recover the original SCO properties indicating that no methanol is readsorbed. A pure speculative explanation could be based on the higher flexibility of the $[\text{Ag}(\text{CN})_2]^-$ moiety, namely, its easy tendency to depart from linearity. This flexibility can conduct to

structural differences characterized by much slower recovering kinetics, which cannot be expected for **2** due to the much more rigid nature of the $[\text{Au}(\text{CN})_2]^-$ moiety.

4.5.- Conclusion

Herein, we have shown that functionalization of a 3D double interpenetrated porous Hofmann-type coordination polymer with a pillar ligand such *pina*, bearing an amide group, favors the interplay between host-guest and host-host interactions which have dramatic consequences on the SCO properties of the material. Similar host-guest effects were already observed for a series of iron(II) 1D coordination polymers with the general formula $[\text{Fe}^{\text{II}}\text{L1}(\textit{pina})] \cdot x\text{solvent}$ with L1 being a tetradentate $\text{N}_2\text{O}_2^{2-}$ coordinating Schiff-base-like ligand.^[29] The spin crossover properties of these compounds turned out to be highly dependent on the solvent content which in turn was intimately interacting with the *pina* ligand *via* H-bonding. Similarly, the not-SCO-active 2D compound $[\text{Fe}^{\text{II}}(\text{NCS})_2(\textit{pina})_2] \cdot 2(\text{CH}_3\text{CN})$ not only presents H-bonds between the amide moieties and the acetonitrile molecules but also between the *pina* ligands through $\text{C}=\text{O} \cdots \text{HN}$ contacts.^[30] Here, we have implemented, for the first time, the bridging *pina* ligand to build a 3D structure that exhibits accessible void volume, ca. 40%, where methanol molecules can be trapped affording an infinite lattice of H-bonds. Besides, we have proved the readsorption of the MeOH molecules, thus recovering the original SCO properties of the Au derivative. This result opens the door to investigate the adsorption of other protic and aprotic guest molecules in order to modulate the steeped SCO characteristics. Furthermore, the double interpenetrated structure is also stabilized by strong interligand $\text{C}=\text{O} \cdots \text{HC}$ interactions which are very common in biologic systems^[34] but as far as we know are uncommon for 3D SCO porous compounds.

4.6.- Experimental section

All precursors reagents were obtained from commercial sources.

4.6.1.- Synthesis of ligand N-(pyridin-4-yl)isonicotiamide (*pina*)

First, 2 g of isonicotinic acid (16.24 mmol) and 160 mL of THF were gently stirred obtaining a white suspension. Hereafter, 1.64 g of trimethylamine (16.24 mmol, 2.26 mL) was added in one portion, and the resulting mixture was stirred over 10 minutes. After cooling down to 0 °C using an ice-bath, 1.95 g of ethyl chloroformate (18 mmol, 1.71 mL) was added dropwise, keeping the mixture under vigorously stirring for 30 minutes. Then, to the ice-cooled white suspension, was gradually added of 1.27 g of 4-aminopyridine (13.52 mmol) previously dissolved in 40 mL of THF, and the mixture was stirred at 0 °C for 1 h. Finally, the solution was allowed to warm up to room temperature under continuously stirring overnight, registering an apparently change of color from white to yellowish. THF solvent was removed under reduce pressure, collecting a white-yellowish powder, which was washed with K₂CO₃ aqueous solution (10% w/w) [3 x 10 mL], cold water [2 x 10 mL] and Et₂O [2 x 20 mL]. The resulting white powder was dried completely in a desiccator for 5 days (yield = 75%). ¹H-NMR (DMSO-*d*₆) = 7.74 (2H, dd), 7.88 (2H, dd), 8.47 (2H, dd), 8.78 (2H, dd).

4.6.2.- Synthesis of complexes 1·xMeOH and 2·xMeOH

A slow diffusion method using a modified H-shape container with 3 tubes was used for growing single-crystals of the double interpenetrated networks [Fe^{II}(*pina*)(Ag^I(CN)₂)₂·xMeOH (**1·xMeOH**) and [Fe^{II}(*pina*)(Au^I(CN)₂)₂·xMeOH (**2·xMeOH**). The peripheral tubes were filled with 0.1 mmol (33.7 mg) of Fe(BF₄)₂·6H₂O and 0.2 mmol of K[M^I(CN)₂] (39.8 mg [M^I = Ag^I], 58.0 mg [M^I = Au^I]), respectively, and finally the center arm was filled with 0.1 mmol (20 mg) of the *pina* ligand. Afterwards, each individual tube was carefully filled with MeOH and sealed with parafilm. After 2 weeks, orange (**1·xMeOH**) and yellow (**2·xMeOH**) platelet crystals suitable for single crystal X-ray analysis appeared within the H tube. Elemental Analysis: Calculated for **1** [C₁₅H₉Ag₂FeN₇O (574.9) (%): C 31.34; H 1.58; N 17.06. Found (%): C 31.18; H 1.65; N 16.58. Calculated for **2** [C₁₅H₉Au₂FeN₇O (753.1) (%): C 23.92; H 1.20; N 13.02. Found (%): C 24.12; H 1.22; N 12.93.

4.6.3.- Physical measurements

Variable-temperature magnetic susceptibility data were recorded with a Quantum Design MPMS2 SQUID magnetometer equipped with a 7 T magnet, operating at 1 T and at temperatures 1.8-400 K. Experimental susceptibilities were corrected for diamagnetism of the constituent atoms by the use of Pascal's constants. Powder X-ray measurements were performed on a PANalytical Empyrean X-ray powder diffractometer (monochromatic CuK α radiation). Thermogravimetric analysis was performed on a Mettler Toledo TGA/SDTA 851e, in the 290-900 K temperature range under nitrogen atmosphere with a rate of 10 K min⁻¹.

4.6.4.- Single-crystal X-ray diffraction

Single-crystal X-ray data were collected on an Oxford Diffraction Supernova diffractometer using graphite mono-chromated Mo K α radiation ($\lambda = 0.71073 \text{ \AA}$). A multi-scan absorption correction was performed. The structures were solved by direct methods using SHELXS-2014 and refined by full-matrix least squares on F^2 using SHELXL-2014.^[35] Non-hydrogen atoms were refined anisotropically and hydrogen atoms were placed in calculated positions refined using idealized geometries (riding model) and assigned fixed isotropic displacement parameters.

4.7.- References

- [1] Gütlich, P.; Hauser, A.; Spiering, H. *Angew. Chem., Int. Ed. Engl.* **1994**, *33*, 2024.
- [2] Ni, Z.-P.; Liu, J.-L.; Hoque, M. N.; Liu, W.; Li, J.-Y.; Chen, Y.-C.; Tong, M.-L. *Coord. Chem. Rev.* **2017**, *335*, 28.
- [3] Real, J. A.; Gaspar, A. B.; Muñoz, M. C. *Dalton Trans.* **2005**, 2062.
- [4] Ohtani, R.; Hayami, S. *Chem. – Eur. J.* **2017**, *23*, 2236.
- [5] Real, J. A.; Gaspar, A. B.; Niel, V.; Muñoz, M. C. *Coord. Chem. Rev.* **2003**, *236*, 121.
- [6] Garcia, Y.; Niel, V.; Muñoz, M. C.; Real, J. A. *Top. Curr. Chem.* **2004**, *233*, 229.
- [7] Muñoz, M. C.; Real, J. A. *Coord. Chem. Rev.* **2011**, *255*, 2068.

- [8] Yoshida, K.; Akahoshi, D.; Kawasaki, T.; Saito, T.; Kitazawa, T. *Polyhedron* **2013**, *66*, 252.
- [9] Martínez, V.; Boldog, I.; Gaspar, A. B.; Ksenofontov, V.; Bhattacharjee, A.; Gütllich, P.; Real, J. A. *Chem. Mater.* **2010**, *22*, 4271.
- [10] Boldog, I.; Gaspar, A. B.; martínez, V., pardo-Ibañez, P.; Ksenofontov, V.; Bhattacharjee, A.; Gütllich, P.; Real, J. A. *Angew. Chem., Int. Ed.* **2008**, *47*, 6433.
- [11] Volatron, F.; Catala, L.; Rivière, E.; Gloter, A.; Stéphan, O.; Mallah, T. *Inorg. Chem.* **2008**, *47*, 6584.
- [12] Haraguchi, T.; Otsubo, K.; Kitagawa, H. *Eur. J. Inorg. Chem.* **2018**, 1697.
- [13] Otsubo, K.; Haraguchi, T.; Kitagawa, H. *Coord. Chem. Rev.* **2017**, *346*, 123.
- [14] Ueno, S.; Kawasaki, T.; Okabayashi, J.; Kitazawa, T. *Bull. Chem. Soc. Jpn.* **2016**, *89*, 581.
- [15] Niel, V.; Muñoz, M. C.; Gaspar, A. B.; Galet, A.; Levchenko, G.; Real, J. A. *Chem. – Eur. J.* **2002**, *8*, 2446.
- [16] Shepherd, H. J.; Bartual-Murgui, C.; Molnár, G.; Real, J. A.; Muñoz, M. C.; Salmon, L.; Bousseksou, A. *New. J. Chem.* **2011**, *25*, 1205.
- [17] Mullaney, B. R.; Goux-Capes, L.; Price, D. J.; Chastanet, G.; Létard, J. F.; Kepert, C. J. *Nat. Commun.* **2017**, *8*, 1053.
- [18] Li, J.-Y.; Ni, Z.-P.; Yan, Z.; Zhang, Z.-M.; Chen, Y.-C.; Liu, W.; Tong, M.-L. *CrystEngComm* **2014**, *16*, 6444.
- [19] Li, J.-Y.; Yan, Z.; Ni, Z.-P.; Zhang, Z.-M.; Chen, Y.-C.; Liu, W.; Tong, M.-L. *Inorg. Chem.* **2014**, *53*, 4039.
- [20] Li, J.-Y.; He, C.-T.; Chen, Y.-C.; Zhang, Z.-M.; Liu, W.; Ni, Z.-P.; Tong, M.-L. *J. Mater. Chem. C* **2015**, *3*, 7830.
- [21] Gural'skiy, I. A.; Golub, B. O.; Shylin, S. I.; Ksenofontov, V.; Shepherd, H. J.; Raithby, P. R.; Tremel, W.; Fritsky, I. O. *Eur. J. Inorg. Chem.* **2016**, 3191.

- [22] Gural'skiy, I. A.; Shylin, S. I.; Golub, B. O.; Ksenofontov, V.; Fritsky, I. O.; Tremel, W. *New J. Chem.* **2016**, *40*, 9012.
- [23] Clements, J. E.; Price, J. R.; Neville, S. M.; Kepert, C. J. *Angew. Chem., Int. Ed.* **2014**, *53*, 10164.
- [24] Clements, J. E.; Price, J. R.; Neville, S. M.; Kepert, C. J. *Angew. Chem.* **2016**, *128*, 15329.
- [25] Li, J. Y.; Chen, Y. C.; Zhang, Z. M.; Liu, W.; Ni, Z. P.; Tong, M. L. *Chem. – Eur. J.* **2015**, *21*, 1645.
- [26] Liu, W.; Peng, Y.-Y.; Wu, S.-G.; Chen, Y.-C.; Hoque, M. N.; Ni, Z.-P.; Chen, X.-M.; Tong, M.-L. *Angew. Chem., Int. Ed.* **2017**, *56*, 14982.
- [27] Valverde-Muñoz, F. J.; Seredyuk, M.; Muñoz, M. C.; Znovjyak, K.; Fritsky, I. O.; Real, J. A. *Inorg. Chem.* **2016**, *55*, 10654.
- [28] Piñeiro-López, L.; Valverde-Muñoz, F. J.; Seredyuk, M.; Bartual-Murgui, C.; Muñoz, M. C.; Real, J. A. *Eur. J. Inorg. Chem.* **2018**, 289.
- [29] Lochenie, C.; Bauer, W.; Railliet, A. P.; Schlamp, S.; Garcia, Y.; Weber, B. *Inorg. Chem.* **2014**, *53*, 11563.
- [30] Roxburgh, M. A. D.; Zaiter, S.; Hudson, X. I. B.; Mullaney, B. R.; Clements, J. E.; Moubaraki, B.; Murray, K. S.; Neville, S. M.; Kepert, C. J. *Aust. J. Chem.* **2017**, *70*, 623.
- [31] Meng, Y.; Dong, Y. J.; Yan, Z.; Chen, Y. C.; Song, X. W.; Li, Q. W.; Zhang, C. L.; Ni, Z. P.; Tong, M. L. *Cryst. Growth Des.* **2018**, *18*, 5214.
- [32] Arcís-Castillo, Z.; Muñoz, M. C.; Molnár, G.; Bousseksou, A.; Real, J. A. *Chem. Eur. J.* **2013**, *19*, 6851.
- [33] Biradha, K.; Fujita, M. A. *Angew. Chem., Int. Ed.* **2002**, *41*, 3392.
- [34] Wahl, M. C.; Sundaralingam, M. *Trends Biochem. Sci.* **1997**, *22*, 97.
- [35] Sheldrick, G. M. *Acta Crystallogr., Sect. C: Struct. Chem.* **2015**, *71*, 3.

4.8.- Supporting Information

Table S1.- Selected bond lengths (Å) for compounds **1·xMeOH**, **1**, **2·xMeOH**, and **2**.

| Compound | 1·xMeOH | 1 | 2·xMeOH | 2 |
|-----------------|-----------------------------------|-----------------------------------|-----------------------------------|-----------------------------------|
| T | X = Ag^I (110 K) | X = Ag^I (250 K) | X = Au^I (120 K) | X = Au^I (225 K) |
| Fe-N1 | 1.993(8) | 2.190(12) | 1.994(6) | 2.111(10) |
| Fe-N2 | 1.999(11) | 2.186(13) | 2.002(5) | 2.122(10) |
| Fe-N3 | 1.931(8) | 2.13(2) | 1.923(9) | 2.05(2) |
| Fe-N4 | 1.923(8) | 2.106(13) | 1.933(8) | 2.013(14) |
| Fe-N5 | 1.931(8) | 2.09(2) | 1.927(8) | 2.07(2) |
| Fe-N6 | 1.930(8) | | 1.931(8) | |
| X1-C13 | 2.066(10) | | 1.994(11) | |
| X1-C15 | 2.046(9) | | 2.014(12) | |
| X2-C14 | 2.076(11) | | 1.978(10) | |
| X2-C16 | 2.045(10) | | 2.004(10) | |
| X1-C12 | | 1.96(2) | | 2.01(2) |
| X1-C14 | | 2.12(2) | | 1.98(2) |
| X2-C13 | | 2.04(2) | | 2.01(2) |
| X1-X2 | 3.0805(13) | 3.110(3) | 3.1296(6) | 3.1552(12) |

Table S2.- Selected angles (°) for compounds **1·xMeOH**, **1**, **2·xMeOH**, and **2**.

| Compound (T) | 1·xMeOH (110 K) X = Ag^I | 1 (250 K) X = Ag^I | 2·xMeOH (120 K) X = Au^I | 2 (225 K) X = Au^I |
|---------------------|---|---|---|---|
| N1-Fe-N2 | 178.1(4) | 179.6(10) | 178(2) | 176.0(6) |
| N1-Fe-N3 | 87.7(3) | 92.2(8) | 91(2) | 91.5(5) |
| N1-Fe-N4 | 89.5(3) | 88.9(11) | 92(2) | 89.5(3) |
| N1-Fe-N5 | 90.7(3) | 87.4(8) | 90(2) | 90.4(6) |
| N1-Fe-N6 | 91.1(3) | | 87(2) | |
| N2-Fe-N3 | 90.5(4) | 87.7(8) | 89.3(3) | 84.5(6) |
| N2-Fe-N4 | 90.0(4) | 90.7(4) | 90.5(3) | 90.5(3) |
| N2-Fe-N5 | 91.1(4) | 92.7(8) | 89.9(4) | 93.6(6) |
| N2-Fe-N6 | 89.4(4) | | 90.8(3) | |
| N3-Fe-N4 | 89.5(3) | 91.0(4) | 89.6(3) | 90.7(4) |
| N3-Fe-N5 | 178.3(3) | 179.6(7) | 179.1(4) | 178.0(6) |
| N3-Fe-N6 | 90.2(3) | | 90.4(3) | |
| N4-Fe-N4' | | 177.5(8) | | 178.4(7) |
| N4-Fe-N5 | 90.0(3) | 89.0(4) | 90.0(4) | 89.3(4) |
| N5-Fe-N6 | 90.3(3) | | 90.0(4) | |
| C13-X1-C15 | 178.1(4) | | 178.2(4) | |
| C14-X2-C16 | 176.4(4) | | 177.2(4) | |
| C12-X1-C14 | | 179.5(8) | | 176.6(7) |
| C13-X2-C13' | | 175.2(10) | | 178.2(7) |

Figure S1.- Thermogravimetric analysis of desolvated networks 1 and 2.

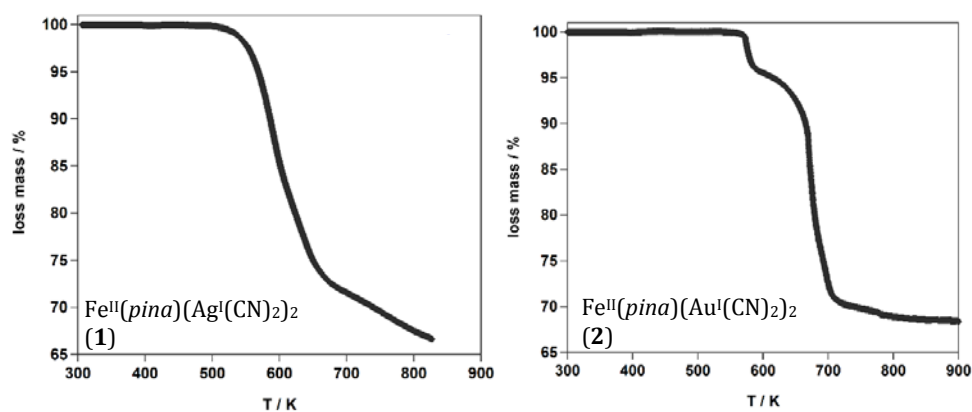


Figure S2.- Representation of $\chi_{\text{M}}T$ and $\partial(\chi_{\text{M}}T)/\partial T$ vs T of 1·xMeOH and 2·xMeOH. The cooling and the warming modes are shown in red and blue, respectively.

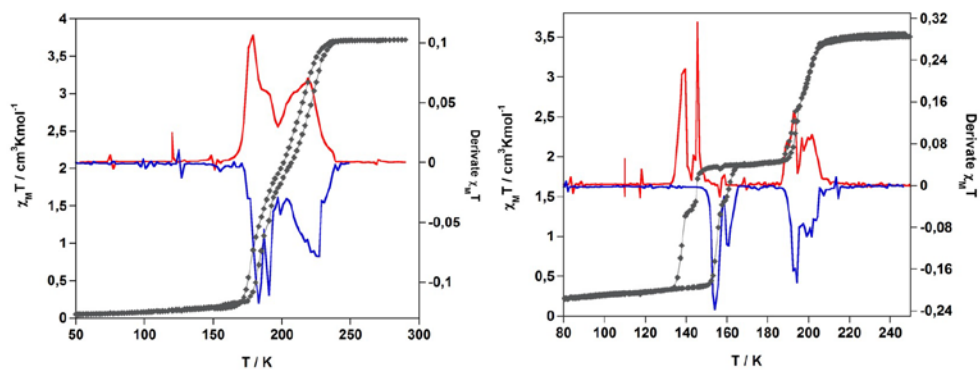


Figure S3.- PXRD patterns of compound **2** a few hours (up) and two weeks (bottom) after desorption of the methanol molecules.

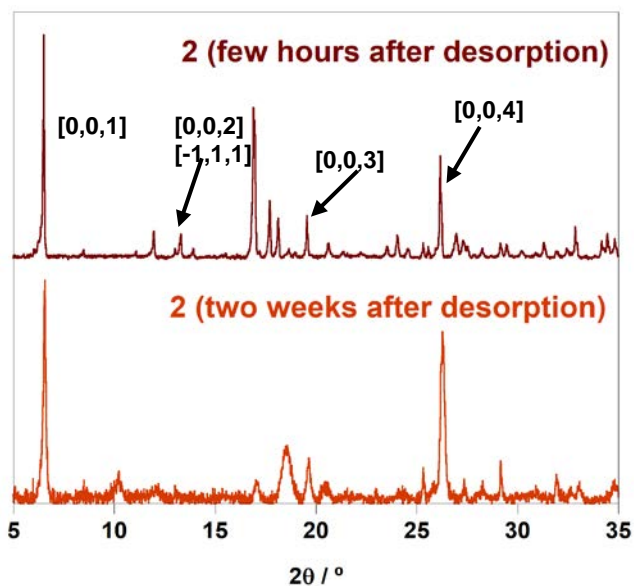


Figure S4.- Picture showing the aspect of crystals of compounds **1** (left) and **2** (right) after 1 month in methanol solution.



Figure S5.- View of the bridging *pina* ligand showing the positional disorder of the amide group in compounds **1·xMeOH** and **2·xMeOH**. Color codes: Fe (orange), N (blue), C (dark grey) and O (red).

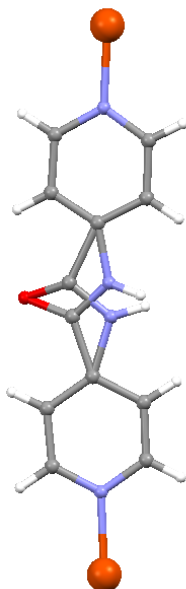


Figure S6.- View of a fragment of the two interpenetrated frameworks of **1·xMeOH** illustrating the H-bonds between methanol molecules (black dashed lines) and between the *pina* ligands and the methanol molecules (green dashed lines).

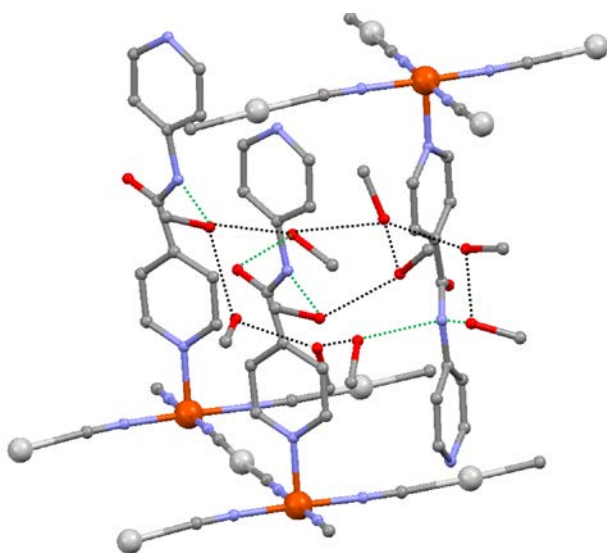
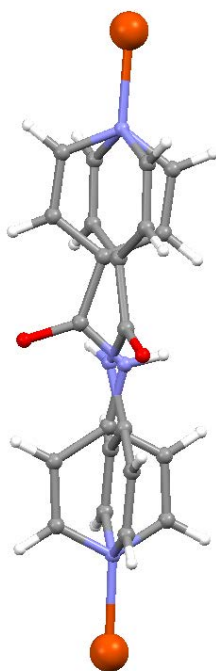
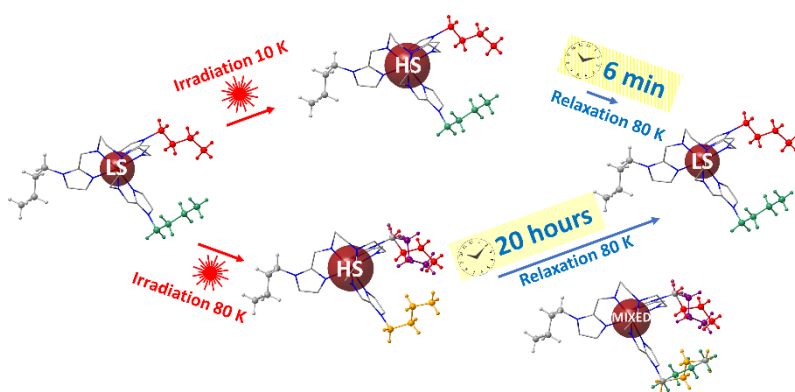


Figure S7. Positional disorder of the pyridine and amide groups on the bridging *pina* ligand in compounds **1** and **2**. Color codes: (Fe (orange), N (blue), C (dark grey) and O (red).



CAPÍTULO 5

Very Long-Lived Photogenerated High-Spin Phase of a Multistable Spin-Crossover Molecular Material



REVISTA: Journal of the American Chemical Society

ÍNDICE DE IMPACTO: 14.695

CAPÍTULO 5

Very Long-Lived Photogenerated High-Spin Phase of a Multistable Spin-Crossover Molecular Material

5.1.- Abstract

The spin-crossover compound $[\text{Fe}(n\text{Bu-im})_3(\text{tren})](\text{PF}_6)_2$ shows an unusual long relaxation time of 20 h after light-induced excited spin state trapping when irradiating at 80 K. This is more than 40 times longer than when irradiating at 10 K. Optical absorption spectroscopy, magnetometry, and X-ray diffraction using synchrotron radiation were used to characterize and explain the different relaxation behaviors of this compound after irradiation below and above 70 K. Rearrangement of the butyl chains of the ligands occurring during the relaxation after irradiation above 70 K is thought to be responsible for the unusually long relaxation time at this temperature.

5.2.- Introduction

Responsive switchable materials have always attracted widespread attention because they afford excellent study examples for the understanding of mechanisms involved in phase transitions and provide opportunities for future and emerging technologies.^[1-3]

Some of the most investigated switchable molecular materials are pseudo-octahedral iron(II) spin-crossover (SCO) complexes. They reversibly switch between the high-spin (HS, $t_{2g}^4e_g^2$) and low-spin (LS, $t_{2g}^6e_g^0$) electronic states by the action of external stimuli (temperature, pressure, light and analytes). Given the antibonding nature of the e_g orbitals, the HS \leftrightarrow LS conversion is accompanied by changes in Fe-ligand bond lengths and angles, which confer bistability (memory) to the magnetic, optical, dielectric, structural, and mechanical properties, when elastic interactions between the SCO centers favor strong cooperativity in the crystal.^[4-6] This appealing feature can be combined with other relevant properties such as luminescence, electronic transport, chirality, or host-guest chemistry in a synergetic fashion, thereby transferring their intrinsic bistable nature to the second property,

thus resulting in multifunctional materials that can be processed at different levels, from bulk to single molecules.^[7,8]

These important attributes have created solid expectancies for the generation of sensors, actuators and spintronic devices based on the on-off switching properties of the SCO materials.^[9-14] In this context, light is a desirable channel for triggering the HS ↔ LS switch since it may improve flexibility and storage density in such devices.^[1-3] In fact, it is possible to achieve a quantitative LS → HS conversion in Fe^{II} SCO complexes by irradiating the sample in the UV-Vis or near-IR regions at low temperature, typically at 10 K. This phenomenon is known as light-induced excited spin state trapping (LIESST).^[15] The lifetime of the photogenerated metastable HS state is inversely proportional to the thermal SCO temperature, $T_{1/2}$, at which the molar HS and LS fractions are equal to 0.5 and the Gibbs free energy difference ΔG_{HL} is equal to 0.^[16,17] The kinetic stability of the photogenerated HS state can be roughly estimated following a precise protocol that determines the characteristic temperature T_{LIESST} at which the photogenerated HS state relaxes to the LS state within a few minutes.^[18] The goal is to correlate T_{LIESST} - $T_{1/2}$ data with relevant structural parameters that may help chemical design aiming at increasing T_{LIESST} toward room temperature. The FeN₆ core, determined by the nature of the ligands, plays a crucial role in the magnitude of T_{LIESST} .^[18] In pure SCO compounds T_{LIESST} values are usually in the interval 20 - 100 K.

On the other hand crystallographic studies are crucial to provide the knowledge of the structural rearrangements occurring during the spin transition.^[19] Different kinds of phase transitions can accompany the spin crossover, for example, order-disorder transitions originating from the counteranions,^[20-23] the solvent,^[24-27] or some part of the ligand.^[22,28-30]

[Fe(*n*Bu-im)₃tren](PF₆)₂ [(*n*Bu-im)₃tren] = *n*-butylimidazoltris(2-ethylamino)amine] has a complex behavior previously studied by magnetic measurements. Two different thermal spin transitions have been observed depending on the sweeping rate of the temperature.^[31] For a scan rate of 4 K/min, the SCO between the HS and the LS phase (called LS₁) is characterized by an average critical temperature of 122 K with a hysteresis loop of 14 K, while for a slower scan rate of 0.1 K/min the SCO between the HS phase and a different LS phase (called LS₂) is characterized by an average critical temperature of 156 K and a hysteresis loop of 41 K. For intermediate scan rates, coalescence of the two

hysteric behaviors is observed. The phase transition occurring between the HS and LS states involves several conformational changes of the butyl chains of the substituent of the ligand. Besides the usual HS to LS FeN₆ coordination sphere rearrangements, the HS and LS₁ structures only differ by moderate structural modifications. The HS and LS₂ structures, on the other hand, strongly differ from each other in the orientation of several butyl groups and of the counteranions. In other words, the two different LS phases, LS₁ and LS₂, present remarkable structural differences. Consequently, the crystal packing is different due to different C...F contacts between the complex and the PF₆⁻ groups. In the HS phase, only one discrete C...F interaction is produced, whereas in the case of the LS₁ and LS₂ phases, many interactions are present.

Herein, the scan rate dependence of the thermal spin transition of [Fe(*n*Bu-im)₃tren](PF₆)₂ is confirmed, and the LIESST behavior of the LS₁ and LS₂ phases investigated by single-crystal optical absorption spectroscopy measurements and X-ray diffraction. Irradiating LS₁ below 70 K quantitatively photogenerates an HS state which relaxes within half an hour at 80 K. Unexpectedly, irradiating LS₁ at the relatively high temperature of 80 K quantitatively photogenerates another HS state, which relaxes unusually slowly, in around 20 h. The structures of both HS states were characterized by single-crystal diffraction, and the structural rearrangements explaining the long relaxation after irradiation above 70 K were monitored by synchrotron single-crystal X-Ray diffraction.

5.3.- Results and discussion

5.3.1.- Thermal Spin Transition

Crystals of around $20 \pm 1 \mu\text{m}$ thickness were used for all the measurements. The dependence of the thermal spin transition behavior with the scan rate of the temperature observed by Real et al.^[31] was confirmed by absorption spectroscopy measurements (see Figure S1 in Supporting Information for more details) and powder diffraction measurements (Figure S2). By looking more carefully at the 3D plots of the powder diffraction measurements, it is possible to observe that the transition is mainly associated with an intensity change of the HS and LS peaks without large shifts of the peaks in both heating and cooling. This can be associated with a nucleation and growth phenomenon.^[38] Furthermore, the HS → LS₂ thermal relaxation was followed by optical spectroscopy at

different temperatures around the HS-LS₂ thermal transition. This confirmed that the relaxation rate decreases with the temperature, which is in line with a first order phase transition.^[39] The relaxation is strongly sigmoidal due to the kinetics of the crystallographic phase transition reflecting the nucleation and growth mechanism (Figure S3).

5.3.2.- Kinetics of the HS → LS₁ relaxation

5.3.2.1.- HS → LS₁ relaxation after irradiation of the LS₁ phase at 10 K followed by absorption spectroscopy

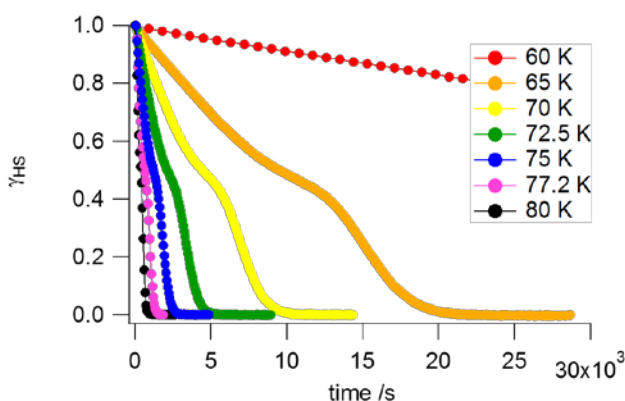


Figure 1. Evolution of the normalized photoinduced HS fraction as function of time at various temperatures for the HS → LS₁ relaxation after irradiation of the LS₁ phase. All the experiments start from a quantitative population of the HS state at 10 K followed by a relaxation at the indicated temperature.

The LS₁ phase was obtained using a cooling rate of 4 K/min. The absorption spectrum collected after irradiation at 10 K corresponds to a pure HS state (Figure S4a). Considering the $T_{LIESST}(HS)$ value of 79.8 K (Figure S14a), we selected six temperatures for the relaxation: 80, 77.5, 75, 72.5, 70, 65, and 60 K. For all the temperatures, a plateau is present in the relaxation curves when the HS fraction is around 0.5 (Figure 1 and Figure S7). This can be due to a specific structural reorganization, which could be, for example, an ordering of the HS and/or LS states.^[40] Evidently, the mean-field approach is not appropriate in this case. Instead, average relaxation rate constants were taken from the time necessary to relax to $\gamma_{HS} = 0.5$. The linear evolution of $\ln k_{HL}$ vs $1/T$ indicates that the relaxation from

the photoinduced HS state to the ground state LS_1 is quasi thermally activated (Figure S5a). An activation energy of 10.2 kJ/mol (850 cm^{-1}) was extracted from the slope of the Arrhenius plot. This indicates that we are in a transition regime between low-temperature tunnelling and classical behaviour.^[41]

5.3.2.2.- HS \rightarrow LS_1 relaxation after irradiation of the LS_1 phase around T_{LIESST} followed by magnetometry and absorption spectroscopy

As shown in Figure 2a, the obtained relaxation curves at 80 K by optical spectroscopy after irradiation at 10 K and 80 K of the LS_1 phase differs tremendously: irradiating at 80 K leads to a relaxation time close to 20 h - more than 40 times that of the relaxation time observed when irradiating at 10 K (Figure 2a) - with a very long nucleation process of around 14 h. The relaxation curve is very sigmoidal, with a kink observed at an HS fraction of around 0.4.

Using magnetometry, we recorded the HS \rightarrow LS_1 relaxation at 80 K after irradiation at different temperatures. We observed that the relaxation gets longer after irradiation above 70 K (Figure 2b).

Experiments were also performed by absorption spectroscopy with irradiation and relaxation at 80 K, 87 K, 90 K, and 100 K (Figure S8b). At 87 K, the process is considerably faster (total relaxation time 11 h, nucleation time 4 h) and a second step is observed after approximately 5 h when the HS fraction is around 0.6. At 90 K and 100 K the plateau can be still observed, and the relaxation becomes faster when the temperature increases.

In summary, irradiation at temperatures above 70 K of the LS_1 phase leads to unexpectedly long HS \rightarrow LS_1 relaxation times. The relaxation curves show a plateau for the HS fraction of around 0.4, and a small change in the irradiation and relaxation temperature can drastically change the relaxation time.

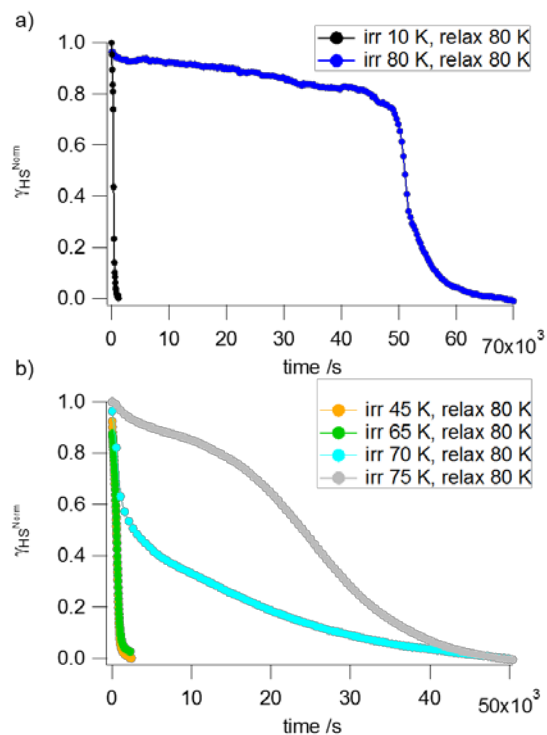


Figure 2. Evolution of the normalized photoinduced HS fraction as a function of time at 80 K for the HS \rightarrow LS₁ relaxation after irradiation of the LS₁ phase at various temperatures. (a) Optical spectroscopy data. (b) Magnetic data. All the experiments start from a quantitative population of the HS state by irradiation at the indicated temperature followed by a relaxation at 80 K.

5.3.2.3.- Structural studies

In order to understand the different relaxation behaviors for the LIESST HS state generated below and above 70 K from the LS₁ phase, structural investigations were carried out using single crystal X-ray diffraction. In particular the butyl chains of the ligands, which adopt different conformations in the already characterized LS₁, LS₂ and HS states, were closely examined.

An LS₁ structure was obtained at 25 K^[42], which is similar to the one reported at 110 K.^[31] The sample was then irradiated with a 532 nm laser for 1 h while continuously rotating the crystal, and a HS structure was obtained (Table S1). The HS structure of the irradiated

sample at 25 K, which we will call $\text{HS}_1^{1\text{irr}}$, presents a complete ordering of all the alkyl substituents, in the same conformation as in the LS_1 state. There is no noticeable change in the geometry of the ligands between the LS_1 and $\text{HS}_1^{1\text{irr}}$ structures, except some structural rearrangements induced by the different Fe-N bond lengths between the two spin states (Figure S9, superposition).

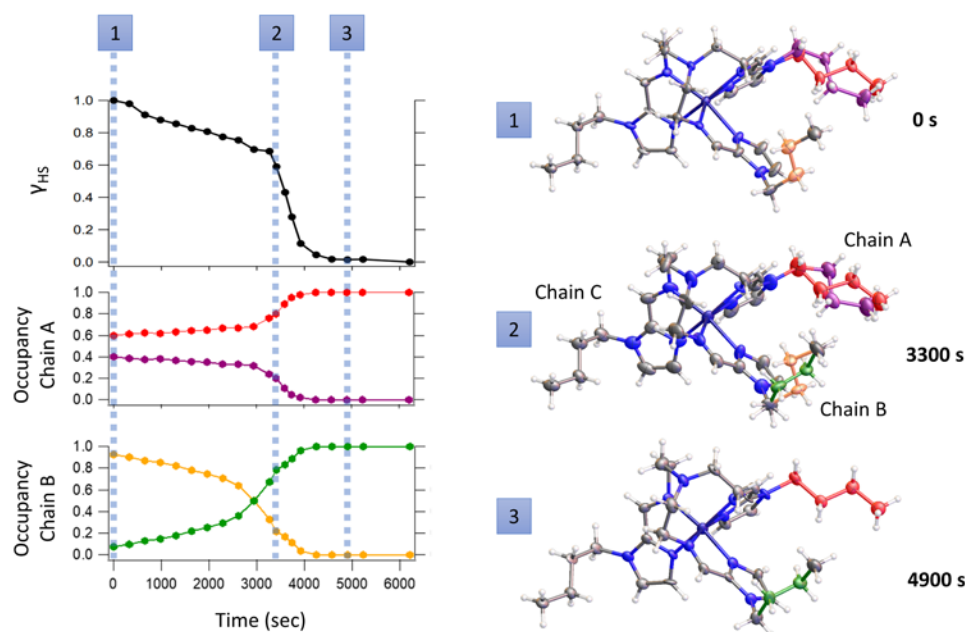


Figure 3. Relaxation curve obtained by single crystal X-ray diffraction using synchrotron radiation at 90 K after irradiation at the same temperature of the LS_1 phase. The HS fraction curve (black) is derived from the crystallographic Fe-N distances. The structure of the complex is shown at three different relaxation times on this curve, with displacement ellipsoids depicted at 40% probability level. An order/disorder phase transition takes place in two different butyl groups of the ligand, chains A and B during the relaxation from $\text{HS}_1^{1\text{irr}}$ to LS_1 . For each chain, two different positions of the butyl group are observed, represented with different colors. The occupancy factor defines the proportion of the chain being in the given position. The evolutions with time of the occupancy factors for chain A and chain B are shown below the relaxation curve.

Using a liquid-nitrogen cooler, an LS_1 structure was recorded around 90 K, which is very similar to the LS_1 structure determined at 25 K (Figure S10, superposition).^[43] The sample was then irradiated at 690 nm with 10 mW/mm^2 during 10 min and the structure of the metastable HS excited state that we will call $\text{HS}_1^{2\text{irr}}$ was subsequently determined. The structures of $\text{HS}_1^{1\text{irr}}$ and $\text{HS}_1^{2\text{irr}}$ differ: in $\text{HS}_1^{2\text{irr}}$, one of the butyl chains is disordered and

another butyl chain is in a different conformation compared to the structure of LS₁ or HS₁^{1irr}. (Figure S11, superposition).

The HS₁^{2irr} → LS₁ relaxation was also monitored by single-crystal X-ray diffraction at 90 K after photoexcitation. The time evolution of the HS fraction was calculated through Vegard's law on the Fe-N bond length (Equation 1).

$$V_{\text{HS}}(t) = \frac{r_{(\text{Fe-N})}^{(t)} - r_{(\text{Fe-N})_{\text{LS}}}}{r_{(\text{Fe-N})_{\text{HS}}} - r_{(\text{Fe-N})_{\text{LS}}}} \quad \{1\}$$

where $r_{(\text{Fe-N})}(t)$ is the average Fe-N distance at the time t , $r_{(\text{Fe-N})_{\text{HS}}}$ is the average Fe-N distance of the HS state at 90 K (obtained under continuous irradiation) and $r_{(\text{Fe-N})_{\text{LS}}}$ is the average Fe-N distance of the LS₁ state at 90 K. The corresponding used Fe-N bond length and unit-cell parameters obtained for all the structures taken during the relaxation are summarized in Table S3. The relaxation curve obtained by single-crystal diffraction is compared to the relaxation curves obtained by absorption spectroscopy in Figure S8c. The relaxation time indicates a temperature of around 90 K.

The structures during the relaxation are shown in Figure 3 alongside the obtained relaxation curve. In the photoinduced HS₁^{2irr} state, the butyl chain of one ligand is disordered (chain A) with two randomly distributed orientations (red and violet chains). The other butyl chains (B and C) are ordered. After cutting off the laser irradiation, the relaxation proceeds very slowly for approximately 1 h. During this nucleation time, disorder grows on chain B (green and orange chains). As the relaxation becomes faster, chain A orders in one of its initial orientations (red). Chain B also starts to order, flipping its initial orientation (from the initial orange chain to the final green one). Clearly, this order/disorder phase transition that takes place in two different butyl groups of the ligands is directly related with the kink observed in the middle of the relaxation and with the long relaxation time. The rearrangements of the structure create different interactions patterns between the butyl groups and the counteranions, especially through the H (butyl) – F(PF₆⁻) bonds (Tables S4 and S5).

Alternatively, the unexpected long-time scale of the HS₁^{2irr} → LS₁ relaxation was also monitored by magnetic measurements (Figure S15) and synchrotron-based X-ray powder

diffraction (Figure S16). The timescale of the relaxation obtained by both techniques are on the same order of magnitude than the one observed on single crystals. However, the nucleation time decreases and the relaxation speeds up compared to single-crystal XRD (Table S6 summarizes the different relaxation time obtained by the different measurements).

The differences observed between the different measurement techniques can be attributed to the sample preparation. Indeed, the crushing of the crystals to produce powdered samples affects the crystal quality. We have also observed that the exact shape of the relaxation curve differs slightly from crystal to crystal. Two relaxation cycles on the same crystal gave reproducible results (Figure S17 and Figure S8d). However, as shown in Figure S8d, we observed different relaxation curves on the same crystal after irradiation at 90 K when going back to room temperature and cooling again to 90 K between the irradiations. Cycling to room temperature induces cracks and defects in the crystals, which reduces the size of the domains and cancels the long nucleation time during which chain B is slowly disordering. As a consequence, the relaxation time is shortened and the relaxation curve depends on the size/quality of the crystals.

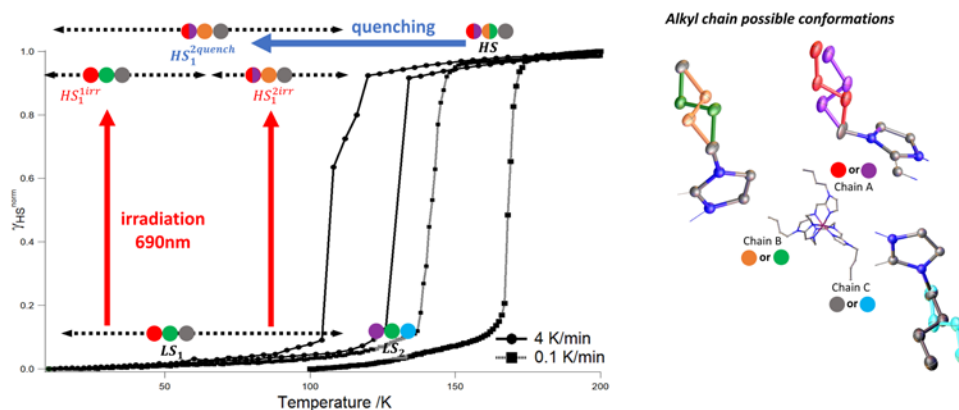


Figure 4. Simplified structural diagram of $[\text{Fe}(\text{nBu-im})_3\text{tren}](\text{PF}_6)_2$; $(\text{nBu-im})_3(\text{tren}) = \text{n-butyl imidazoltris}(2\text{-ethylamino})\text{amine}$. The different conformations that the alkyl chains can adopt are shown on the right. For each phase of the phase diagram, three colored disks indicate the positions adopted by chain A, B and C. Two-colored disks indicate that the chain is disordered over both positions. For the quenched phases, a small disorder on chain B is sometimes observed, depending on the temperature, but only the main conformation of the chain has been indicated (see table S7a).

Finally, quenching of the HS phase by quickly lowering the temperature gave a HS^{quench} phase whose structure is similar to HS₁^{2irr}. The relaxation of this quenched phase was studied by magnetic measurements and the relaxation time is of the same order of magnitude than the photo-excited HS₁^{2irr} phase (Figure S18). This is expected, as the same rearrangement of the butyl chains has to occur during the relaxation.

In Figure 4, the structural diagram of the different HS and LS states, whose structures are elucidated, is presented. This system is a very nice example of how multistability can influence the spin crossover properties. Two low spin states are observed for different cooling rates. Two HS states are also observed at low temperature, one that can be reached by irradiation below 70 K and one that can be reached either by irradiation above 70 K or quenching of the room-temperature HS state. The reorganization of the butyl side chains between these states governs the LIESST relaxation kinetics.

5.3.3.- Kinetics of the HS → LS₂ relaxation

5.3.3.1.- HS → LS₂ relaxation after irradiation of the LS₂ phase at 10 K followed by absorption spectroscopy

The LS₂ phase was obtained using a cooling rate 0.1 K/min. The spectrum collected after irradiation at 10 K corresponds to a pure HS state (Figure S4b). Considering the T_{LIESST}(HS₂) value of 50 K (Figure S14b), six temperatures for the relaxation were selected: 55, 50, 45, 40, 35 and 30 K. The relaxation curves show a slightly sigmoidal behavior (Figure 5). Therefore, they were fitted within the framework of the mean-field model,^[44] with the relaxation rate constant k_{HL} depending not only on the temperature but also on the LS fraction (Equation 2) in such a way that in the differential equation of $d\gamma_{HS}/dt$, a new term that accounts for the cooperative effects is introduced (Equation 3).

$$k_{HL}(T, \gamma_{HS}) = k_{HL}(T, \gamma_{HS} = 0) e^{\alpha \gamma_{LS}} \quad \{2\}$$

$$\frac{d\gamma_{HS}}{dt} = -k_{HL}^0 \cdot e^{\frac{-E_a}{k_B T}} \cdot e^{\alpha (1-\gamma_{HS})} \cdot \gamma_{HS} \quad \{3\}$$

In equation (2) k_{HL}^0 is the relaxation rate constant and E_a the activation energy at the beginning of the relaxation, and α is the acceleration factor. k_{HL}^0 was obtained from the slope of the relaxation curve considering only the first relaxation points, that is, between $t = 0$ and $t \approx 1000$ s. The apparent E_a value was then calculated from the slope of an Arrhenius plot (Figure S5b). The resulting value for E_a of 3.3 kJ/mol (276 cm^{-1}) is rather small and indicates that in the temperature interval from 30 to 55 K the system is only just above the low-temperature tunneling regime. This is also born out by the slight curvature of the Arrhenius plot. The above value of E_a has subsequently been introduced into equation 2 in order to obtain the value of α via least squares numerical fitting. The calculated value of α is 1.5 at 35 K (Figure S6) and corresponds to a moderately cooperative relaxation curve. It should be noted that toward the end of the relaxation curve, the experimental data deviate quite strongly from the calculated mean-field curve. Such a behavior, with a long tail, is indicative of a comparatively large inhomogeneous distribution of activation energies.^[44]

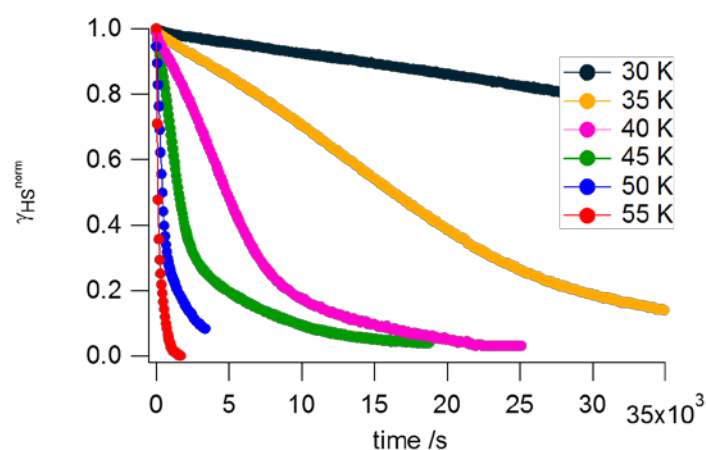


Figure 5. Evolution of the normalized photoinduced HS fraction as a function of time at various temperatures for the HS \rightarrow LS₂ relaxation after irradiation of the LS₂ phase. All the experiments start from a quantitative population of the HS state at 10 K followed by a relaxation at the indicated temperature.

Overall, the HS \rightarrow LS relaxation after irradiation of the LS₂ phase (irradiation at 10 K) is faster than the HS \rightarrow LS relaxation after irradiation of the LS₁ phase (irradiation at 10 K). This can be directly correlated with the thermal transition temperature, which is higher for LS₂ (see Figure S1).

5.3.3.2.- HS → LS₂ relaxation after irradiation of the LS₂ phase around T_{LIESST}, studied by magnetometry

Contrary to what we observed with the LS₁ phase, irradiating at higher temperature does not significantly change the relaxation time for a given relaxation temperature. The relaxation curves measured at 45 K overlap wherever the irradiation is performed at 10 K or 45 K (Figure S19a). As expected, the lifetime of the irradiated HS₂ is short at 55 K, and no complete conversion could be reached (Figure S19b). This suggests that for LS₂ the photogenerated state is the same, whatever the irradiation temperature.

5.4.- Conclusion

The two different thermal transitions previously observed by Real et al. with the [Fe(nBu-im)₃(tren)](PF₆)₂ compound have been confirmed by single-crystal optical absorption spectroscopy. The HS → LS relaxation after irradiation has been studied for both LS phases after excitation at 10 K. In each case, we observed a sigmoidal behavior characteristic of cooperative effects, with a plateau observed only in the HS → LS₁ relaxation. The larger E_a values obtained for the HS → LS₁ relaxation compared to the HS → LS₂ relaxation (10.2 kJ/mol compared to 3.3 kJ/mol) agrees with the slower dynamics found for the HS → LS₁ relaxation and the thermal stabilization of the LS₂ observed during the thermal spin transition.

For the LS₁ phase, we observed two relaxation behaviors depending on the irradiation temperature. Irradiation above 70 K led to unexpected long relaxation time compared to irradiating below 70 K. This was explained by the existence of two different photogenerated HS states: HS₁^{1irr} state, whose structure was determined under irradiation at 25 K, and the HS₁^{2irr} state, whose structure was determined under irradiation of LS₁ at 90 K. The conformations of the butyl chains of the ligand are identical in HS₁^{1irr} and in LS₁ state, whereas two of the HS₁^{2irr} butyl chains adopt a different conformation. Alongside the relaxation, followed by single crystal X-ray diffraction, reorientations of the butyl chains occur through order/disorder transitions. We believe that these reorientations of the butyl chains are responsible for the long relaxation time after excitation above 70 K.

Interestingly, an HS^{quench} state can also be reached via thermal quenching, with a structure identical to the HS₁^{2irr}. The relaxation time of those structurally identical states are of the same order of magnitude.

With the exception of a few Fe-Co charge transfer systems with a cyanide bridge, (Prussian blue analogues) there are only two SCO pure systems that have a $T_{1/2}$ above 100 K,^[45,46] while other SCO complexes of Fe (II) present a T_{LIESST} around 90 - 100 K. However, in the present study, a new type of spin-crossover compound is presented: a spin-crossover compound with $T_{LIESST} = 80$ K that can be completely populated back to the HS by irradiating at 80 K with a surprisingly high kinetic stability of the photogenerated state.

5.5.- Experimental section

5.5.1.- Single-crystal optical absorption spectroscopy

Single crystals of $[\text{Fe}(n\text{Bu-im})_3(\text{tren})](\text{PF}_6)_2$ were mounted on a copper plate with a previously drilled hole of approximately 150 μm in diameter. One crystal was deposited in the middle of the hole and fixed with silver paste to ensure a good thermal conductivity. The sample was then introduced into a closed cycle cryostat (Janis-Sumimoto SHI-4.5), which operates between 4 and 300 K and is equipped with a programmable temperature controller (Lakeshore Model 331). The cryostat was introduced into a double beam spectrometer (Varian Cary 5000).

In all experiments, an LS reference spectrum was first collected at 10 K. Then the sample was irradiated with a 690 nm laser, which corresponds to the tail of the LS band centered at 669 nm, during 10 min at 10 mW/mm², and a reference HS spectrum was recorded likewise at 10 K. The HS fraction (γ_{HS}) was obtained using equation 4.

$$\gamma_{\text{HS}} = (\text{OD}_{\text{LS}} - \text{OD}_T) / (\text{OD}_{\text{LS}} - \text{OD}_{\text{HS}}) \quad \{4\}$$

where OD_{LS} is the optical density of the LS state, OD_{HS} is the optical density of the HS state at 10 K and OD_T is the optical density at a given temperature. The optical density is corrected from an eventual baseline jump or shift by taking the difference between the OD at 600 nm and the OD at 750 nm, where there is no noticeable absorption in the two states.

In the case of the LIESST experiment, after irradiation at 10 K, the temperature was quickly raised to the desired temperature for the relaxation measurement (at about 20 K/min), and spectra were then recorded in appropriate time intervals during the relaxation. In the case of the LIESST experiment at 80 – 100 K, the irradiation and the relaxation was performed at the same temperature. In these cases γ_{HS} is calculated using equation 4 but replacing OD_T by OD_t , which is the optical density at a given time during the relaxation.

5.5.2.- Synchrotron-based X-ray diffraction

The thermal and photoinduced spin transitions were studied using X-ray diffraction at the Swiss Norwegian Beamline at the European Synchrotron Radiation Facility in Grenoble (France). The same diffractometer equipped with a 2D PILATUS2M detector was used for single-crystal and powder diffraction experiments. The temperature was controlled using an Oxford Cryostream 700. All the samples (single crystals and powders) were placed in Mitegen Kapton loops.

For single crystals: 360° phi-rotations of 6 min each were collected. Data were integrated with CryAlis Pro.^[32] Further X-ray data analyses were carried out using the Olex² Crystallography Software^[33] and Shelxl.^[34] For the relaxation experiment, the samples were irradiated at 90 K with a DPSS 690 nm laser during around 10 minutes at 10 mW/mm².

For powders, the powder was obtained by carefully crushing a few single crystals of $[\text{Fe}(n\text{Bu-im})_3(\text{tren})](\text{PF}_6)_2$. For the thermal transition, the scan rate was 4 K/min. The relaxation was followed by recording diffraction patterns every 22 s. The 2D data were integrated using the SNBL-home-made software BUBBLE.^[35] Further X-ray data analyses were carried out using the Topas academic software.^[36]

5.5.3.- Home-lab X-ray diffraction

The single-crystal diffraction data for the 10 K thermally quenched and 125 K thermally quenched states were collected with an Oxford Diffraction SuperNova diffractometer equipped with an Atlas CCD detector, an helium open flow cryosystem (Oxford Diffraction Helijet), or a nitrogen cryostream cooling device, depending on the temperature. The unit-cell determination and data reduction were performed using the

CryAlis Pro^[32] program suite on the full data set. An analytical absorption correction was carried out. The crystal structures were refined on F^2 by weighted full-matrix least-squares methods using the SHELXL97 program.^[34]

The 25 K diffraction data was collected using a Nonius Kappa CCD diffractometer equipped with a Helix He cryosystem. In a first step, the small size (100 μm) single-crystal sample was quickly cooled to 120 K, then slowly down to 25 K in the LS₁ state. A complete data set on the LS state was recorded at 25 K. The sample was then irradiated with a laser at 532 nm (laser power of 10 mW, enlarging the beam to ensure a homogeneous irradiation) for 1 hour while continuously rotating the crystal, and a complete data set on the HS state was then recorded. The diffraction data were integrated and reduced using the HKL package.^[37] An empirical absorption correction was applied. The crystal structures were refined on F^2 by weighted full-matrix least-squares methods using the SHELXL97 program.^[34]

5.5.4.- Magnetic measurements

Magnetic susceptibility measurements were carried out using a Quantum Design MPMS2 SQUID susceptometer equipped with a 5.5 T magnet, operating at 1 T and at temperatures from 300-1.8 K. Irradiations were performed at 690 nm.

5.6.- References

- [1] Sato, O. *Nat. Chem.* **2016**, 8, 644.
- [2] Bennemann, K. H. *J. Phys.: Condens. Matter* **2011**, 23, 073202.
- [3] Koshihara, S.-Y. *J. Phys.: Conf. Ser.* **2005**, 21, 7.
- [4] König, E. *Struct. Bonding (Berlin, Ger.)* **1991**, 76, 51.
- [5] Gütlich, P; Goodwin, H. A., Eds. Spin Crossover in Transition Metal Compounds I. In *Topics in Current Chemistry*, vol. 233, Springer-Verlag, **2004**.

- [6] Halcrow, M. A., Ed. *Spin-Crossover Materials: Properties and Applications*; John Wiley & Sons Ltd., **2013**.
- [7] Molnár, G.; Rat, S.; Salmon, L.; Nicolazzi, W.; Bousseksou, A. *Adv. Mater.* **2018**, *30*, 17003862.
- [8] Senthil Kumar, K.; Ruben, M. *Coord. Chem. Rev.* **2017**, *346*, 176.
- [9] Kahn, O.; Martinez, C. J. *Science (Washington, DC, U.S.)* **1998**, *279*, 44.
- [10] Prins, F.; Monrabal-Capilla, M.; Osorio, E. A.; Coronado, E.; van der Zant, H. S. J. *Adv. Mater.* **2011**, *23*, 1545.
- [11] Ohba, M.; Yoneda, K.; Agusti, G.; Muñoz, M. C.; Gaspar, A. B.; Real, J. A.; Yamasaki, M.; Ando, H.; Nakao, Y.; Sakaki, S.; Kitagawa, S. *Angew. Chem., Int. Ed.* **2009**, *48*, 4767.
- [12] Salmon, L.; Molnár, G.; Zitouni, D.; Quintero, C.; Bergaud, C.; Micheau, J.-C.; Bousseksou, A. *J. Mater. Chem.* **2010**, *20*, 5499.
- [13] Matsuda, M.; Kiyoshima, K.; Uchida, R.; Kinoshita, N.; Tajima, H. *Thin Solid Films* **2013**, *531*, 451.
- [14] Shepherd, H. J.; Gural'skiy, I. A.; Quintero, C. M.; Tricard, S.; Salmon, L.; Molnár, G.; Bousseksou, A. *Nat. Commun.* **2013**, *4*, 1.
- [15] Decurtins, S.; Gütlich, P.; Köhler, C. P.; Spiering, H.; hauser, A. *Chem. Phys. Lett.* **1984**, *105*, 1.
- [16] Hauser, A.; Vef, A.; Adler, P. *J. Chem. Phys.* **1991**, *95*, 8710.
- [17] Hauser, A. *Comments Inorg. Chem.* **1995**, *17*, 17.
- [18] Létard, J.-F. *J. Mater. Chem.* **2006**, *16*, 2550.
- [19] Collet, E.; Guionneau, P. *C. R. Chim.* **2018**, *21*, 1133.
- [20] Matouzenko, G. S.; Luneau, D.; Molnár, G.; Ould-Moussa, N.; Zein, S.; Borshch, S. A.; Bousseksou, A.; Averseng, F. *Eur. J. Inorg. Chem.* **2006**, 2671.
- [21] König, E.; Ritter, G.; Kulshreshtha, S. K.; Nelson, S. M. *Inorg. Chem.* **1982**, *21*, 3022.

- [22] Matouzenko, G. S.; Bousseksou, A.; Borshch, S. A.; Perrin, M.; Zein, S.; Salmon, L.; Mólnar, G.; Lecocq, S. *Inorg. Chem.* **2004**, *43*, 227.
- [23] Money, V. A.; Elhaïk, J.; Radosavljevic Evans, I.; Halcrow, M. A.; Howard, J. A. K. *Dalton Trans.* **2004**, *1*, 65.
- [24] Chernyshov, D.; Hostettler, M.; Törnroos, K. W.; Bürgi, H.-B. *Angew. Chem., Int. Ed.* **2003**, *42*, 3825.
- [25] König, E.; Ritter, G.; Kulshreshtha, S. K.; Waigel, J.; Sacconi, L. *Inorg. Chem.* **1984**, *23*, 1241.
- [26] Wu, C.-C.; Jung, J.; Gantzel, P. K.; Gütllich, P.; Hendrickson, D. N. *Inorg. Chem.* **1997**, *36*, 5339.
- [27] Hostettler, M.; Törnroos, K. W.; Chernyshov, D.; Vangdal, B.; Bürgi, H.-B. *Angew. Chem.* **2004**, *116*, 4689.
- [28] Miyazaki, Y.; Nakamoto, T.; Ikeuchi, S.; Saito, K.; Inaba, A.; Sorai, M.; Tojo, T.; Atake, T.; Matouzenko, G. S.; Zein, S.; Borshch, S. A. *J. Phys. Chem. B* **2007**, *111*, 12508.
- [29] Kusz, J.; Zubko, M.; Neder, R. B.; Gütllich, P. *Acta Crystallogr. Sect. B: Struct. Sci.* **2012**, *68*, 40.
- [30] Sheu, C.-F.; Pillet, S.; Lin, Y.-C.; Chen, S.-M.; Hsu, I. J.; Lecomte, C.; Wang, Y. *Inorg. Chem.* **2008**, *47*, 10866.
- [31] Seredyuk, M.; Muñoz, M. C.; Castro, M.; Romero-Morcillo, T.; Gaspar, A. B.; Real, J. A. *Chem. – Eur. J.* **2013**, *19*, 6591.
- [32] <https://www.rigaku.com/en/products/smc/crysalis>.
- [33] Dolomanov, O. V.; Blake, A. J.; Champness, N. R.; Schröder, M. *J. Appl. Crystallogr.* **2003**, *36*, 1283.
- [34] Sheldrick, G. *Acta Crystallogr., Sect. C: Struct. Chem.* **2015**, *71*, 3.
- [35] <http://www.esrf.eu/home/UsersAndScience/Experiments/CRG/BM01/bm01/image.htm/snbl-tool-box.html>.
- [36] Coelho, A. A. *J. Appl. Crystallogr.* **2018**, *51*, 210.

- [37] Otwinowski, Z.; Minor, W. Processing of X-ray diffraction data collected in oscillation mode. In *Methods in Enzymology*; Academic Press, **1997**; Vol. 276, 307.
- [38] Pillet, S.; Legrand, V.; Souhassou, M.; Lecomte, C. *Phys. Rev. B: Condens. Matter Mater. Phys.* **2006**, *74*, 140101.
- [39] Landau, L. D.; Lifshitz, E. M.; Eds. *Statistical Physics Part 1*; Pergamon, **1994**.
- [40] Mariette, C.; Trzop, E.; Zerdane, S.; Fertey, P.; Zhang, D.; Valverde-Muñoz, F. J.; Real, J. A.; Collet, E. *Acta Crystallogr., Sect. B: Struct. Sci., Cryst. Eng. Mater.* **2017**, *73*, 660.
- [41] Hauser, A.; Enachescu, C.; Daku, M. L.; Vargas, A.; Amstutz, N. *Coord. Chem. Rev.* **2006**, *250*, 1642.
- [42] A rapid cooling of the sample freezes the HS state at low temperature, and the lack of control of the temperature of a helijet-type cooling device above 60 K hampered obtaining the LS₁ phase at 10 K. We therefore used another cooling device with the lowest possible temperature of 25 K.
- [43] The nominal temperature indicated by the cryostream was 80 K. However, the sample temperature was lower and was determined to be around 90 K by comparison with the spectroscopic measurements.
- [44] Hauser, A.; Jeftić, J.; Romstedt, H.; Hinek, R.; Spiering, H. *Coord. Chem. Rev.* **1999**, *190-192*, 471.
- [45] Marcén, S.; Lecren, L.; Capes, L.; Goodwin, H. A.; Létard, J.-F. *Chem. Phys. Lett.* **2002**, *358*, 87.
- [46] Costa, J. S.; Balde, C.; Carbonera, C.; Denux, D.; Wattiaux, A.; Desplances, C.; Ader, J.-P.; Güttlich, P.; Létard, J.-F. *Inorg. Chem.* **2007**, *46*, 4114.

5.7.- Supporting Information

Figure S1.- a) Evolution of single crystal absorption spectra of $[\text{Fe}(\text{nBu-im})_3(\text{tren})](\text{PF}_6)_2$ during heating at 4 K/min; b) evolution of the normalized HS fraction as a function of the temperature for temperature scan rates of 4 K/min and 0.1 K/min and of c) 2 K/min, d) 1 K/min and e) 0.25 K/min. All the absorption spectra were recorded from 400 to 750 nm to follow the evolution of the absorption bands characteristic of the LS state centered at 600 and 670 nm (Figure S1a). In all probability these bands can be assigned to spin-allowed d-d transitions of the LS state, that is, the low-symmetry split components of the ${}^1A_1 \rightarrow {}^1T_1$ transition. The evolution of the HS fraction (y_{HS}) can be obtained by following the evolution of the LS absorption band intensity at 600 nm (see full article).

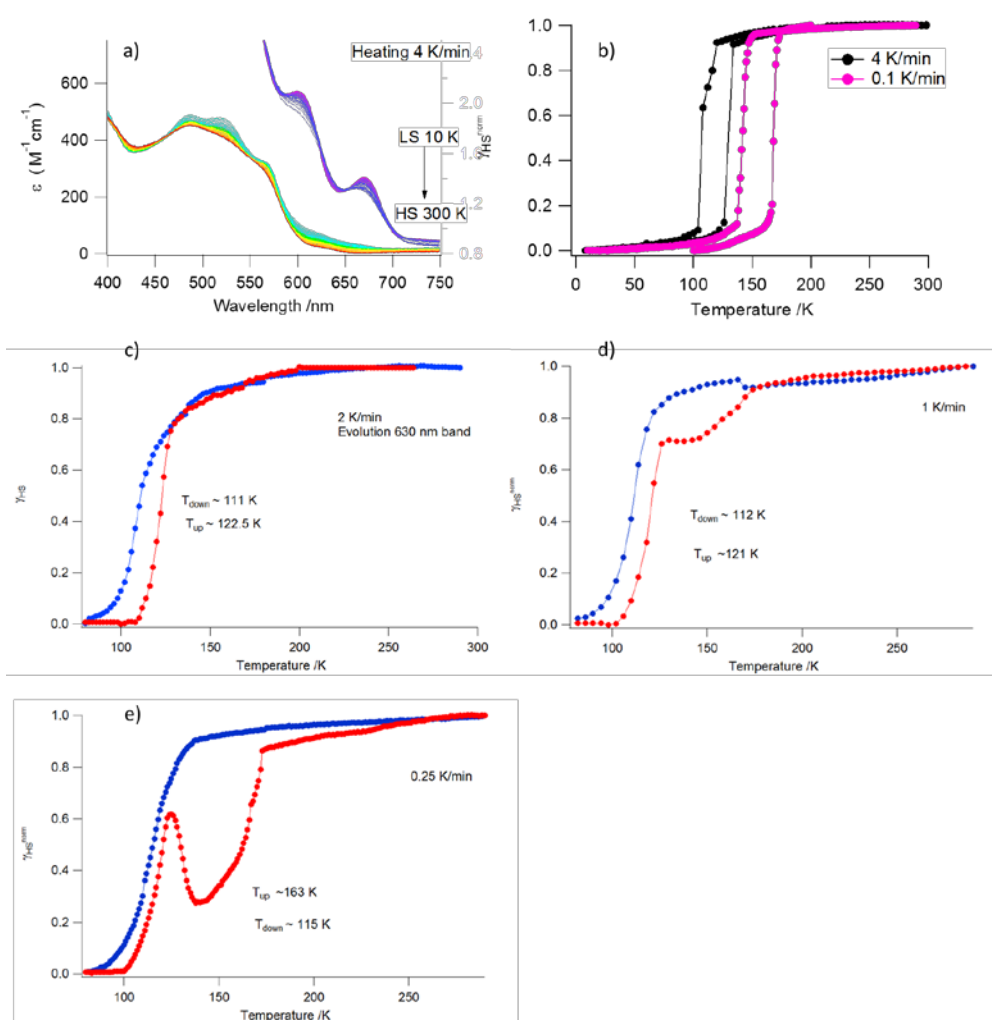


Figure S2.- Evolution of the X-ray pattern during the heating (top) and cooling (bottom) at 4 K/min of $[\text{Fe}(n\text{Bu-im})_3(\text{tren})](\text{PF}_6)_2$ powder obtained by carefully crushing small crystals.

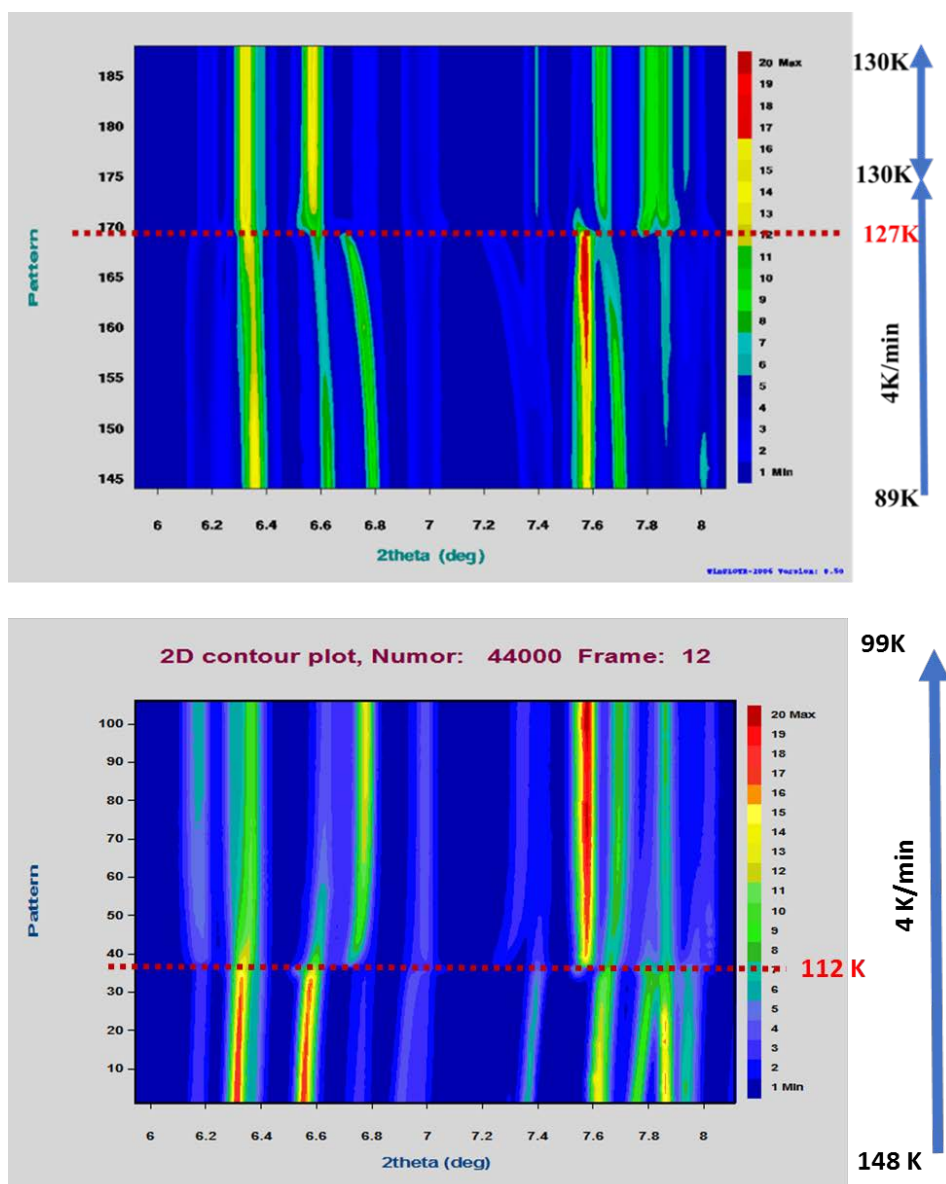


Figure S3. - Absorption spectra of the thermal HS \rightarrow LS₂ relaxation of [Fe(*n*Bu-im)₃(tren)](PF₆)₂ at 130 K after cooling from 290 K at 5 K/min (top) and evolution of the normalized HS fraction as a function of time at 130, 140 and 150 K after cooling from 290 K at 5 K/min (bottom).

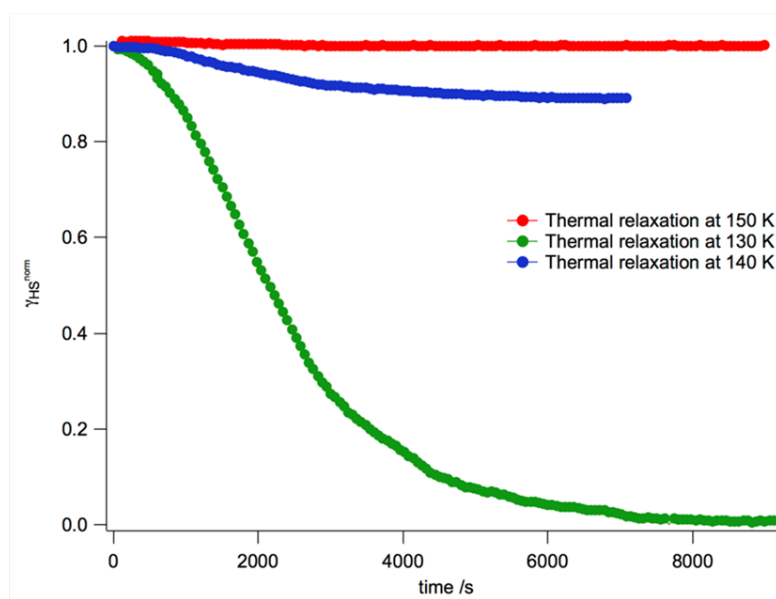
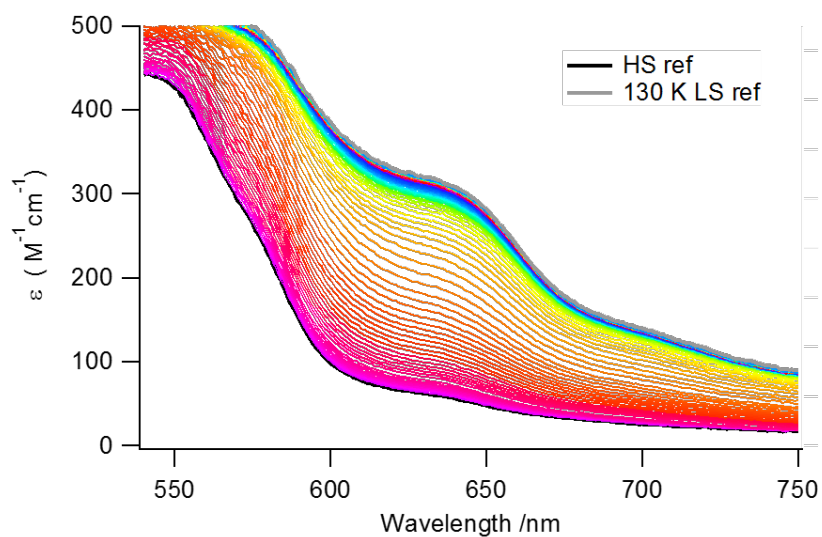


Figure S4. - Absorption spectra of $[\text{Fe}(\text{nBu-im})_3(\text{tren})](\text{PF}_6)_2$ during a) the thermal HS \rightarrow LS₁ relaxation at 70 K after irradiation of the LS₁ phase at 10 K and during b) the thermal HS \rightarrow LS₂ relaxation at 50 K after irradiation into the LS₂ phase at 10 K. Irradiation was made with a 690 nm laser during 10 min at 10 mW/mm².

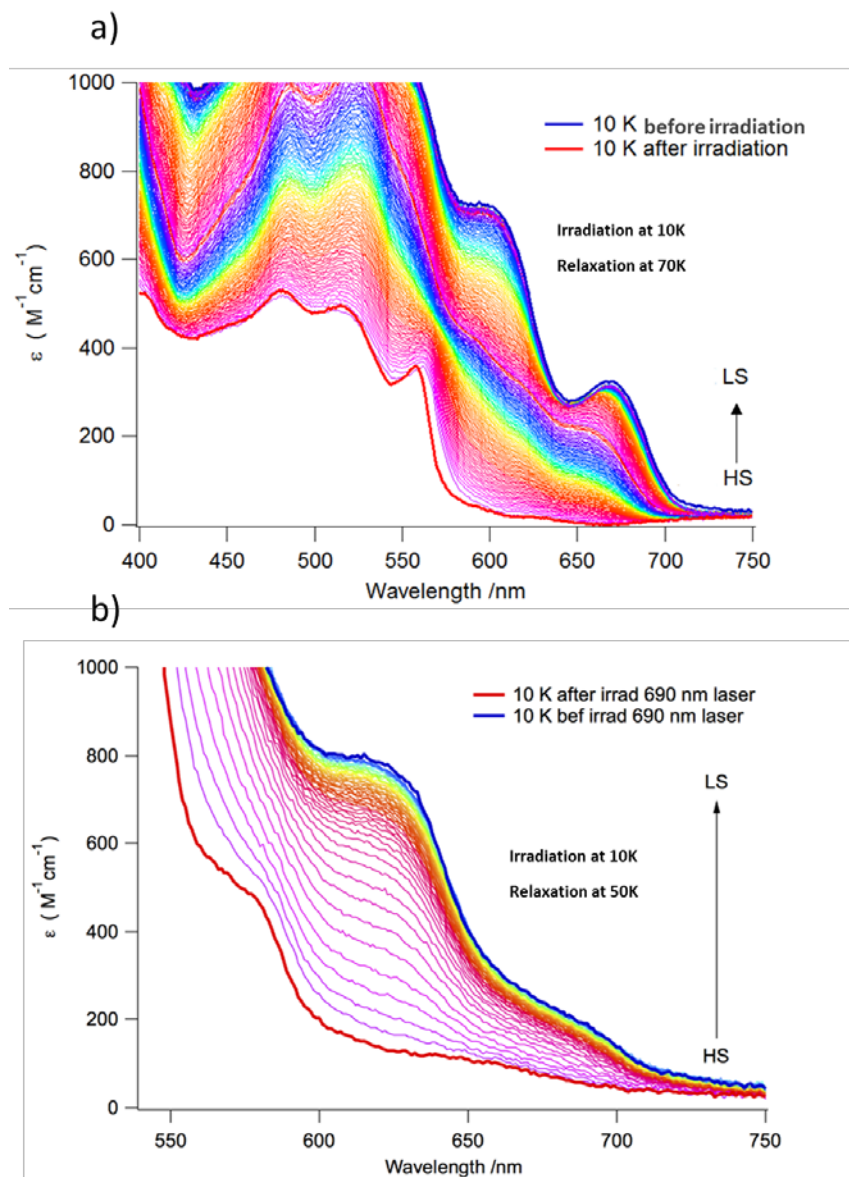


Figure S5.- Average rate constant values estimated from the experimental relaxation curves at different temperatures as a function of $1/T$ for a) the HS \rightarrow LS₁ relaxation after irradiation of the LS₁ phase and for b) the HS \rightarrow LS₂ relaxation after irradiation of the LS₂ phase.

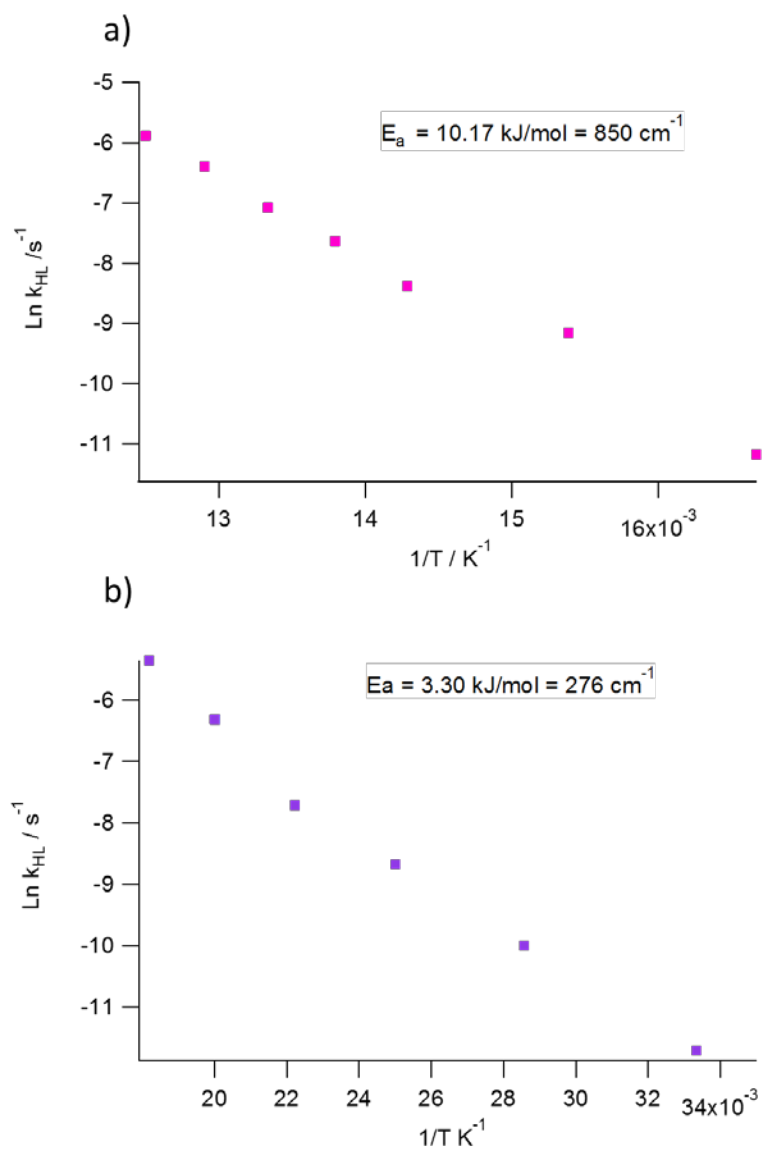


Figure S6.- Evolution of the normalized photo-induced HS fraction as a function the time for the HS → LS₂ relaxation after irradiation of the LS₂ phase at 35 K and the corresponding mean-field fit.

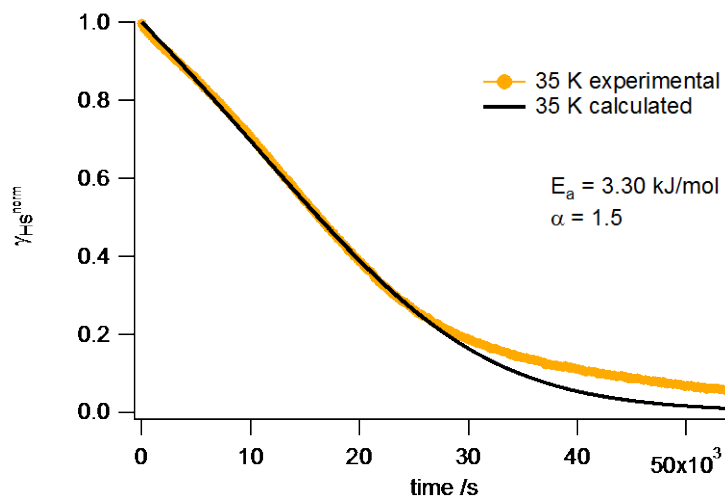


Figure S7.- Evolution of the normalized photo-induced HS fraction as a function of time at various temperatures for the HS → LS₁ relaxation after irradiation of the LS₁ phase at 10 K. All the experiments start from a quantitative population of the HS state by irradiation at 690 nm.

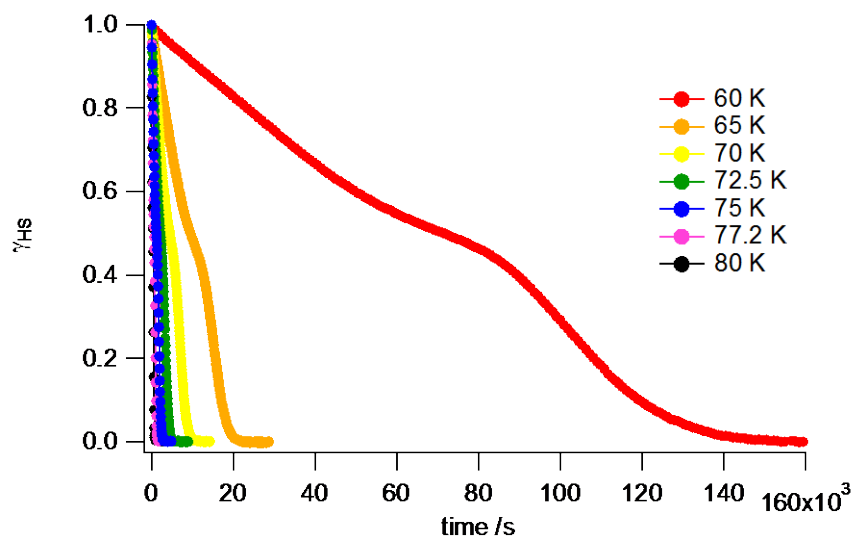


Figure S8. - a) Absorption spectra during the thermal HS \rightarrow LS₁ relaxation at 90 K after irradiation with a 690 nm laser at 90 K during 10 min at 10 mW/mm². The red arrow indicates the irradiation in the LS₁ phase spectrum at 690 nm with a quantitative conversion into the HS phase. The blue arrow indicates the evolution of the spectrum from the HS to the LS₁ at the LS₁ maximum during the HS₁^{2irr} \rightarrow LS₁ relaxation after photo-excitation at 90 K; b) evolution of the normalized photo-induced HS fraction as a function of time at various temperatures for the HS \rightarrow LS₁ relaxation after irradiation of the LS₁ phase at temperatures 80 K-100 K at 690 nm at 10 mW/mm² during 10 min; c) comparison of the HS₁^{2irr} \rightarrow LS₁ relaxation curves obtained by absorption spectroscopy and XRD, and d) HS₁^{2irr} \rightarrow LS₁ relaxation curves obtained at 90 K on the same crystal after a first irradiation at 90 K (grey), after a second irradiation at 90 K (pink), and after going to room temperature and back to 90 K at 4 K/min and performing a third irradiation at 90 K (black).

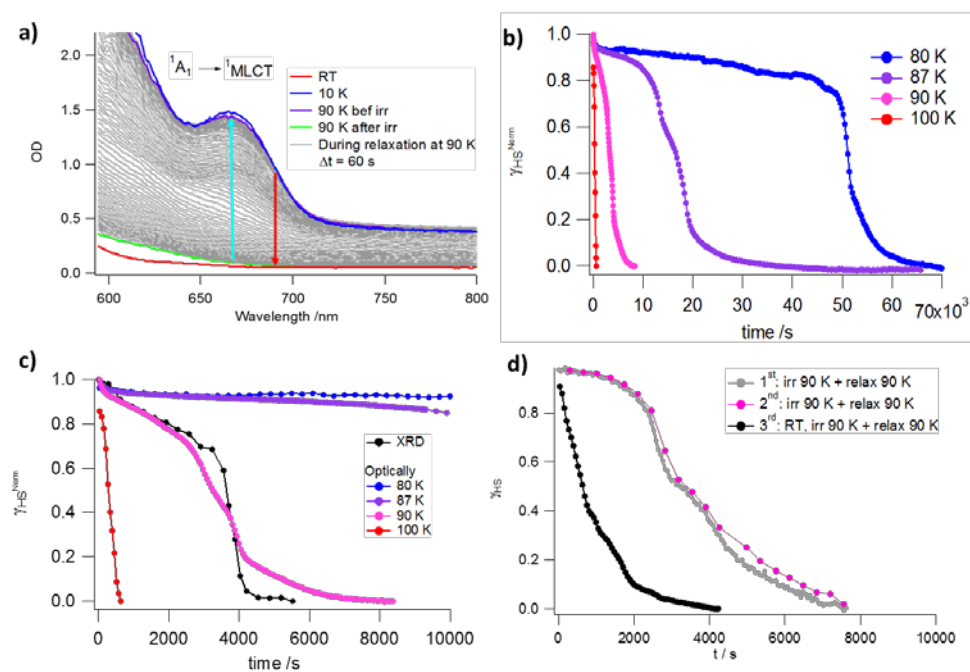


Table S1a. - Crystal data and structure refinement for the **LIESST HS state at 25K**.

| | | | |
|-----------------------------------|---|---------------------------|----------------------------|
| Empirical formula | C30 H48 F12 Fe N10 P2 | | |
| Formula weight | 894.57 | | |
| Temperature | 25(2) K | | |
| Wavelength | 0.71073 Å | | |
| Crystal system | Triclinic | | |
| Space group | P-1 | | |
| Unit cell dimensions | a = 9.1236(13) Å | b = 10.3986(17) Å | c = 21.917(3) Å |
| | $\alpha = 82.664(6)^\circ$ | $\beta = 79.143(8)^\circ$ | $\gamma = 81.735(7)^\circ$ |
| Volume | 2010.0(5) Å ³ | | |
| Z | 2 | | |
| Density (calculated) | 1.478 Mg/m ³ | | |
| Absorption coefficient | 0.547 mm ⁻¹ | | |
| F(000) | 924 | | |
| Crystal size | 0.15 x 0.07 x 0.07 mm ³ | | |
| Theta range for data collection | 1.90 to 25.00° | | |
| Index ranges | -10 ≤ h ≤ 10, -12 ≤ k ≤ 12, -26 ≤ l ≤ 26 | | |
| Reflections collected | 20736 | | |
| Independent reflections | 6907 [R(int) = 0.1560] | | |
| Completeness to theta = 25.00° | 97.5% | | |
| Absorption correction | Semi-empirical from equivalents | | |
| Max. and min. transmission | 0.963 and 0.922 | | |
| Refinement method | Full-matrix least-squares on F ² | | |
| Data / restraints / parameters | 6907 / 0 / 496 | | |
| Goodness-of-fit on F ² | 1.084 | | |
| Final R indices [I > 2σ(I)] | R1 = 0.0851, wR2 = 0.1570 | | |
| R indices (all data) | R1 = 0.1816, wR2 = 0.1965 | | |
| Largest diff. peak and hole | 0.659 and -0.433 e.Å ⁻³ | | |

Table S1b. - Crystal data and structure refinement for the **LIESST LS state at 25K.**

| | | | |
|-----------------------------------|---|---------------------------|----------------------------|
| Empirical formula | C30 H48 F12 Fe N10 P2 | | |
| Formula weight | 894.57 | | |
| Temperature | 25(2) K | | |
| Wavelength | 0.71073 Å | | |
| Crystal system | Triclinic | | |
| Space group | P-1 | | |
| Unit cell dimensions | a = 9.0037(6) Å | b = 10.6349(8) Å | c = 20.9238(16) Å |
| | $\alpha = 87.427(3)^\circ$ | $\beta = 80.838(4)^\circ$ | $\gamma = 83.926(3)^\circ$ |
| Volume | 1966.1(2) Å ³ | | |
| Z | 2 | | |
| Density (calculated) | 1.511 Mg/m ³ | | |
| Absorption coefficient | 0.559 mm ⁻¹ | | |
| F(000) | 924 | | |
| Crystal size | 0.22 x 0.14 x 0.13 mm ³ | | |
| Theta range for data collection | 1.93 to 25.00° | | |
| Index ranges | -10 ≤ h ≤ 10, -12 ≤ k ≤ 12, -24 ≤ l ≤ 24 | | |
| Reflections collected | 19314 | | |
| Independent reflections | 6874 [R(int) = 0.0849] | | |
| Completeness to theta = 25.00° | 98.9% | | |
| Absorption correction | Semi-empirical from equivalents | | |
| Max. and min. transmission | 0.931 and 0.887 | | |
| Refinement method | Full-matrix least-squares on F ² | | |
| Data / restraints / parameters | 6874 / 0 / 496 | | |
| Goodness-of-fit on F ² | 1.109 | | |
| Final R indices [I > 2σ(I)] | R1 = 0.0623, wR2 = 0.1129 | | |
| R indices (all data) | R1 = 0.1025, wR2 = 0.1234 | | |
| Largest diff. peak and hole | 0.547 and -0.407 e.Å ⁻³ | | |

Figure S9.- $LS_1 \rightarrow HS$ LIESST transition at 25 K. No order-disorder phase transition associated to the spin state change is observed.

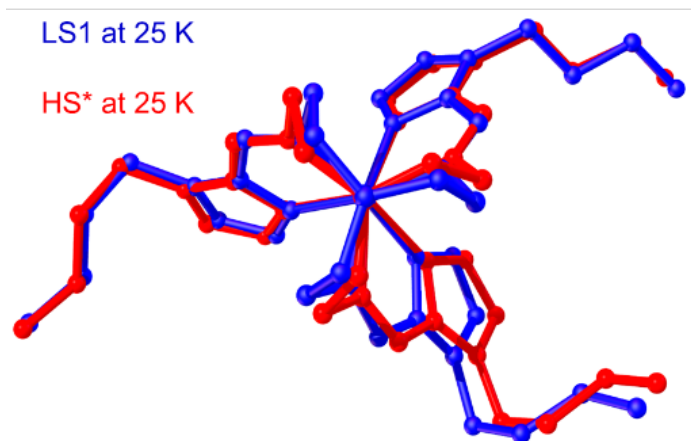


Figure S10.- Superposition of the LS_1 (25 K) in red and LS_1 (90 K) in blue molecular structures. The two structures are almost superimposable.

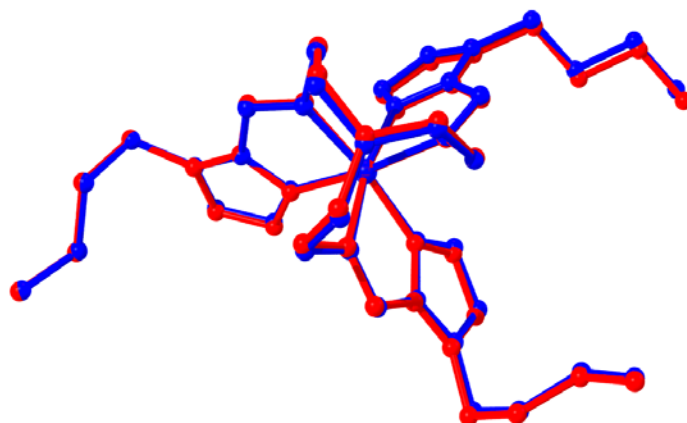


Figure S11.- Superposition of the HS₁^{1irr} (25 K) in green and HS₁^{2irr} (90 K) molecular structures. For this latter, the different butyl groups of the chains A and B are coloured according to figure 3 of the manuscript.

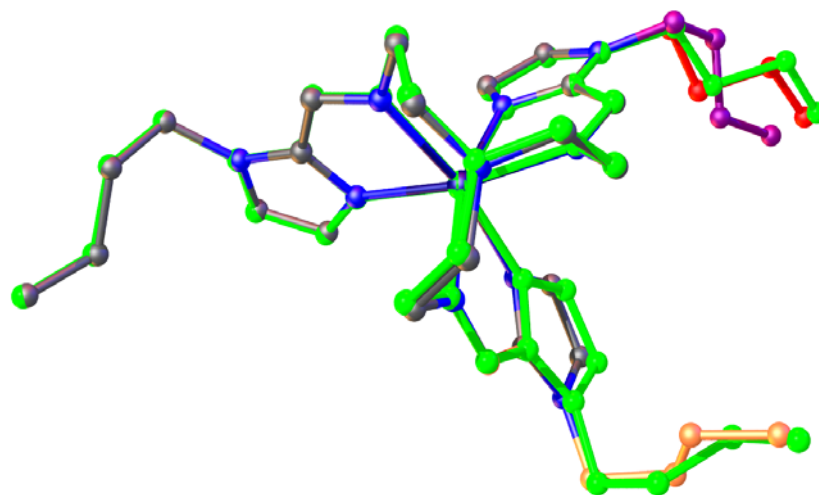


Table S2a.- Crystal data and structure refinement for the **LS state at 80 K before irradiation**. (The unit-cell was chosen to match the setting of the HS state, see fig S10).

| | | | |
|--------------------------------------|---|----------------------------|----------------------------|
| Empirical formula | C ₃₀ H ₄₈ F ₁₂ Fe N ₁₀ P ₂ | | |
| Formula weight | 894.57 | | |
| Temperature | 80 K | | |
| Wavelength | 0.7121 Å | | |
| Crystal system | Triclinic | | |
| Space group | $P\bar{1}$ | | |
| Unit cell dimensions | a = 8.9994(7) Å | b = 10.5624(9) Å | c = 21.358(2) Å |
| | $\alpha = 90.096(8)^\circ$ | $\beta = 104.654(8)^\circ$ | $\gamma = 96.526(7)^\circ$ |
| Volume | 1950.4(3) Å ³ | | |
| Z | 2 | | |
| Density (calculated) | 1.523 Mg/m ³ | | |
| Absorption coefficient | 0.564 mm ⁻¹ | | |
| F(000) | 924 | | |
| Theta range for data collection | 1.976 to 25.468° | | |
| Index ranges | -10 ≤ h ≤ 10, -10 ≤ k ≤ 10, -24 ≤ l ≤ 24 | | |
| Reflections collected | 6788 | | |
| Independent reflections | 3532 [R(int) = 0.0269] | | |
| Completeness to theta = 25.294° | 49.8% | | |
| Absorption correction | Semi-empirical from equivalents | | |
| Max. and min. transmission | 1.00000 and 0.97080 | | |
| Refinement method | Full-matrix least-squares on F^2 | | |
| Data / restraints / parameters | 3532 / 0 / 499 | | |
| Goodness-of-fit on F^2 | 1.296 | | |
| Final R indices [$I > 2\sigma(I)$] | R1 = 0.0771, wR2 = 0.1755 | | |
| R indices (all data) | R1 = 0.0879, wR2 = 0.1821 | | |
| Extinction coefficient | n/a | | |
| Largest diff. peak and hole | 0.742 and -0.296 e.Å ⁻³ | | |

Table S2b. - Crystal data and structure refinement for the HS state at 80 K under irradiation.

| | | | |
|--------------------------------------|--|----------------------------|----------------------------|
| Empirical formula | C30 H48 F12 Fe N10 P2 | | |
| Formula weight | 894.57 | | |
| Temperature | 80 K | | |
| Wavelength | 0.7121 Å | | |
| Crystal system | Triclinic | | |
| Space group | $P\bar{1}$ | | |
| Unit cell dimensions | a = 9.2022(7) Å | b = 10.1887(7) Å | c = 21.8917(18) Å |
| | $\alpha = 91.390(6)^\circ$ | $\beta = 101.321(7)^\circ$ | $\gamma = 98.577(6)^\circ$ |
| Volume | 1987.1(3) Å ³ | | |
| Z | 2 | | |
| Density (calculated) | 1.495 Mg/m ³ | | |
| Absorption coefficient | 0.553 mm ⁻¹ | | |
| F(000) | 924 | | |
| Theta range for data collection | 1.904 to 25.586° | | |
| Index ranges | -11 ≤ h ≤ 11, -10 ≤ k ≤ 10, -25 ≤ l ≤ 25 | | |
| Reflections collected | 6962 | | |
| Independent reflections | 3599 [R(int) = 0.0284] | | |
| Completeness to theta = 25.294° | 49.9% | | |
| Absorption correction | Semi-empirical from equivalents | | |
| Max. and min. transmission | 1.00000 and 0.93650 | | |
| Refinement method | Full-matrix least-squares on F^2 | | |
| Data / restraints / parameters | 3598 / 38 / 513 | | |
| Goodness-of-fit on F^2 | 1.002 | | |
| Final R indices [$I > 2\sigma(I)$] | R1 = 0.0368, wR2 = 0.0862 | | |
| R indices (all data) | R1 = 0.0651, wR2 = 0.0991 | | |
| Extinction coefficient | n/a | | |
| Largest diff. peak and hole | 0.303 and -0.283 e.Å ⁻³ | | |

Table S3a. Selected bond lengths, angles and unit-cell parameters during the HS₁^{2irr} → LS₁ relaxation. The unit-cell settings of the HS phase were used for all the integrations, since the LS₁ phase can be transformed to the HS phase via the transformation shown in Figure S11. The indicated times correspond to the middle of the data collection, which lasted 326 s. For times between 3330 and 4411 the data collection was divided in two sets of images so that the integration time is only 163 sec.

| Time(s) | 0 | 490 | 817 | 1144 | 1471 | 1797 | 2124 |
|--------------------------------------|---------------|---------------|---------------|---------------|---------------|---------------|---------------|
| Fe(1)-N(2) | 2.193 | 2.18 | 2.17 | 2.161 | 2.16 | 2.15 | 2.146 |
| Fe(1)-N(3) | 2.192 | 2.185 | 2.174 | 2.164 | 2.161 | 2.16 | 2.159 |
| Fe(1)-N(5) | 2.189 | 2.183 | 2.177 | 2.174 | 2.172 | 2.167 | 2.16 |
| Fe(1)-N(6) | 2.158 | 2.149 | 2.139 | 2.131 | 2.122 | 2.117 | 2.111 |
| Fe(1)-N(8) | 2.158 | 2.155 | 2.148 | 2.144 | 2.139 | 2.132 | 2.13 |
| Fe(1)-N(9) | 2.2 | 2.188 | 2.177 | 2.174 | 2.165 | 2.16 | 2.156 |
| Fe – N | 2.182 | 2.178 | 2.164 | 2.158 | 2.153 | 2.148 | 2.144 |
| a (Å) | 9.2022(7) | 9.1980(7) | 9.1923(7) | 9.1878(7) | 9.1826(7) | 9.1794(7) | 9.1759(7) |
| b (Å) | 10.1887(7) | 10.1937(7) | 10.2050(7) | 10.2125(7) | 10.2202(7) | 10.2270(7) | 10.2325(7) |
| c (Å) | 21.892(2) | 21.863(2) | 21.841(2) | 21.830(2) | 21.819(2) | 21.810(2) | 21.799(2) |
| α (°) | 91.390(6) | 91.353(6) | 91.361(6) | 91.349(6) | 91.355(7) | 91.359(7) | 91.366(7) |
| β (°) | 101.321(7) | 101.360(7) | 101.400(7) | 101.450(7) | 101.484(7) | 101.531(7) | 101.575(7) |
| γ (°) | 98.577(6) | 98.564(6) | 98.535(6) | 98.508(6) | 98.486(6) | 98.467(6) | 98.437(6) |
| V_c (Å³) | 1987.1 | 1984.4 | 1983.2 | 1982.5 | 1981.8 | 1981.3 | 1980.4 |

Table S3a (cont). Selected bond lengths, angles and unit-cell parameters during the HS₁^{2ir} → LS₁ relaxation.

| | | | | | | | |
|----------------------------------|---------------|---------------|---------------|---------------|---------------|---------------|---------------|
| Time(s) | 2451 | 2777 | 3104.5 | 3340 | 3503.5 | 3667 | 3830.5 |
| Fe(1)-N(2) | 2.139 | 2.137 | 2.131 | 2.116 | 2.09 | 2.059 | 2.02 |
| Fe(1)-N(3) | 2.144 | 2.144 | 2.111 | 2.114 | 2.09 | 2.06 | 2.02 |
| Fe(1)-N(5) | 2.154 | 2.152 | 2.145 | 2.151 | 2.14 | 2.09 | 2.08 |
| Fe(1)-N(6) | 2.11 | 2.106 | 2.094 | 2.1 | 2.068 | 2.05 | 2.017 |
| Fe(1)-N(8) | 2.125 | 2.117 | 2.116 | 2.118 | 2.11 | 2.09 | 2.07 |
| Fe(1)-N(9) | 2.148 | 2.143 | 2.134 | 2.119 | 2.107 | 2.068 | 2.03 |
| Fe – N | 2.137 | 2.133 | 2.122 | 2.12 | 2.101 | 2.07 | 2.04 |
| a (Å) | 9.1702(7) | 9.1650(7) | 9.1532(9) | 9.1083(1) | 9.0968(1) | 9.0644(1) | 9.0529(2) |
| b (Å) | 10.2411(7) | 10.2526(8) | 10.2755(1) | 10.3493(2) | 10.3793(1) | 10.4367(2) | 10.4700(2) |
| c (Å) | 21.790(2) | 21.785(2) | 21.783(3) | 21.757(4) | 21.714(4) | 21.644(5) | 21.573(4) |
| α (°) | 91.387(7) | 91.434(7) | 91.574(9) | 91.896(1) | 91.900(1) | 91.603(1) | 91.280(1) |
| β (°) | 101.666(7) | 101.753(8) | 102.013(10) | 102.747(1) | 103.003(1) | 103.486(2) | 103.733(2) |
| γ (°) | 98.388(6) | 98.355(6) | 98.252(8) | 97.960(1) | 97.753(1) | 97.474(1) | 97.202(1) |
| V _c (Å ³) | 1979.6 | 1979.7 | 1979.6 | 1976.7 | 1975.1 | 1970.6 | 1967.8 |

| | | | | | | |
|----------------------------------|---------------|---------------|--------------|---------------|---------------|---------------|
| Time(s) | 4085 | 4411.5 | 4738.5 | 5065.5 | 5392 | 5451 |
| Fe(1)-N(2) | 2.022 | 1.991 | 1.987 | 1.986 | 1.987 | 1.981 |
| Fe(1)-N(3) | 2.026 | 2.012 | 2.008 | 2.002 | 2.002 | 2 |
| Fe(1)-N(5) | 2.023 | 2.022 | 2.014 | 2.016 | 2.013 | 2.007 |
| Fe(1)-N(6) | 1.963 | 1.961 | 1.96 | 1.965 | 1.964 | 1.962 |
| Fe(1)-N(8) | 1.989 | 1.978 | 1.968 | 1.968 | 1.974 | 1.971 |
| Fe(1)-N(9) | 2.019 | 1.995 | 1.99 | 1.987 | 1.986 | 1.986 |
| Fe – N | 2.007 | 1.993 | 1.988 | 1.987 | 1.988 | 1.985 |
| a (Å) | 9.0258(1) | 9.0113(7) | 9.0078(7) | 9.0052(7) | 9.0053(7) | 9.0051(7) |
| b (Å) | 10.5229(1) | 10.5472(9) | 10.5511(8) | 10.5560(8) | 10.5576(8) | 10.5576(8) |
| c (Å) | 21.465(3) | 21.405(2) | 21.385(2) | 21.381(2) | 21.378(2) | 21.3771(2) |
| α (°) | 90.750(1) | 90.403(8) | 90.316(7) | 90.294(7) | 90.284(7) | 90.281(7) |
| β (°) | 104.243(1) | 104.476(8) | 104.532(8) | 104.558(8) | 104.577(8) | 104.560(7) |
| γ (°) | 96.838(9) | 96.691(7) | 96.643(7) | 96.642(7) | 96.630(7) | 96.644(6) |
| V _c (Å ³) | 1960.1 | 1955.1 | 1953 | 1952.8 | 1952.7 | 1952.7 |

Table S3b: Selected bond lengths at nominally* 80 K in the dark before and after LS₁ → HS irradiation and corresponding [Fe(*n*Bu-im)₃(tren)](PF₆)₂ structure.

| | HS. RT | 80K dark | HS80K under irradiation |
|-----------------------------------|--------------|--------------|-------------------------|
| Fe(1)-N(2) | 2.179 | 1.981 | 2.193 |
| Fe(1)-N(3) | 2.185 | 1.989 | 2.192 |
| Fe(1)-N(5) | 2.186 | 1.997 | 2.189 |
| Fe(1)-N(6) | 2.164 | 1.963 | 2.158 |
| Fe(1)-N(8) | 2.170 | 1.963 | 2.158 |
| Fe(1)-N(9) | 2.204 | 1.979 | 2.2 |
| $\overline{\text{Fe} - \text{N}}$ | 2.181 | 1.979 | 2.182 |

Figure S12. Numbering for Table S3a and S3b.

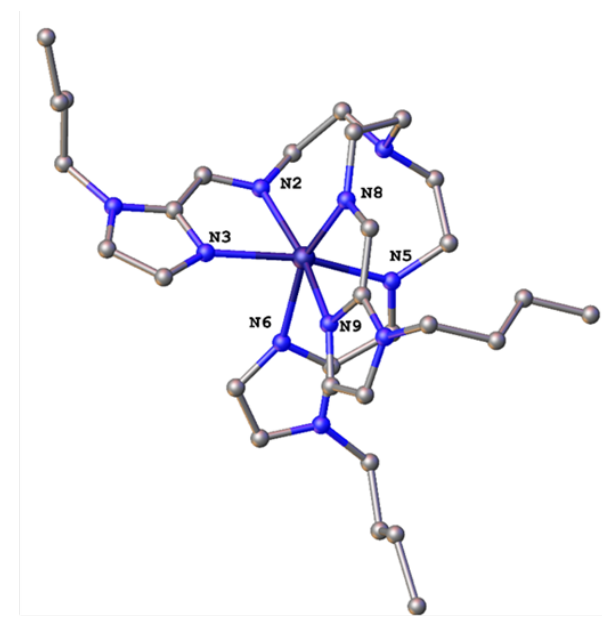


Figure S13. $[\text{Fe}(n\text{Bu-im})_3(\text{tren})](\text{PF}_6)_2$ structure (left) and view of the metastable $\text{HS}_{2^{2r}}$ structure along the b axis (right). The HS unit cell is represented by the black lines. The LS_1 unit cell, obtained via the axis transformation $\begin{pmatrix} -1 & 0 & -1 \\ 0 & 1 & 0 \\ 0 & 0 & -1 \end{pmatrix}$, is represented by the blue line.

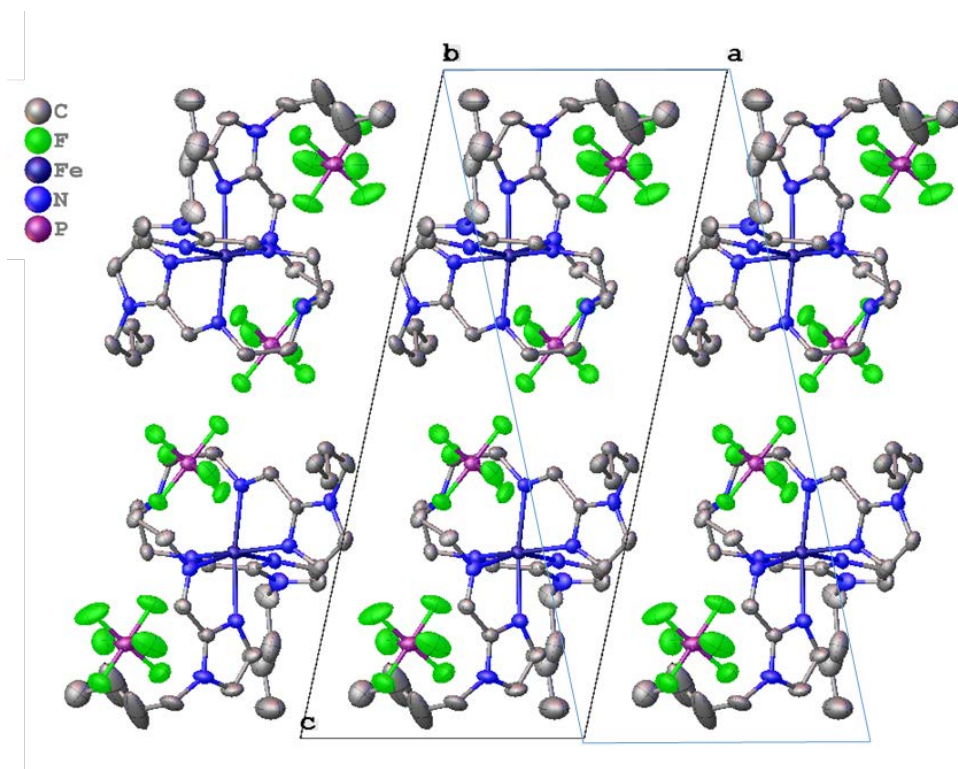


Table S4. Tables of short intermolecular contacts between the hydrogen atoms of the butyl chains and neighbouring molecules for the structure number 1 (HS, beginning of the relaxation). All contacts less than 3 Å are indicated.

| <i>H atom</i> | <i>Neighbouring atom, distance, symmetry code*</i> |
|---------------|---|
| H27A | F1 2.49 2_665 F4 2.49 2_665 H20B 2.64 1_545 H20E 2.89 1_545 |
| H27B | F1 2.50 1_645 H19D 2.86 1_545 F2 2.94 1_645 § |
| H28A | H20A 2.34 2_765 H20D 2.60 2_765 F1 2.68 2_665 H19B 2.74 2_765 H20E 2.95 2_765 |
| H28B | - |
| H29A | - |
| H29B | - |
| H30A | H25 2.69 1_655 H19A 2.69 1_655 H18A 2.71 1_655 H16 2.80 1_655 |
| H30B | H26 2.45 2_765 F4 2.85 1_655 |
| H30C | H20D 2.46 2_765 |

| <i>H atom</i> | <i>Neighbouring atom, distance, symmetry code*</i> |
|---------------|--|
| H17C | F3 2.55 1_655 |
| H17D | H9A 2.56 1_565 |
| H18C | H5 2.58 1_565 |
| H18D | H5 2.78 1_565 |
| H19C | H5 2.55 1_565 |
| H19D | F1 2.74 1_655 C24 2.83 1_565 H27B 2.86 1_565 N10 2.89 1_565 H23 2.91 1_565 C23 2.94 1_565 |
| H20D | H30C 2.46 2_765 H28A 2.60 2_765 |
| H20E | H27A 2.89 1_565 H28A 2.95 2_765 |
| H20F | H20B 2.45 2_675 H26 2.99 2_665 |

| <i>H atom</i> | <i>Neighbouring atom, distance, symmetry code*</i> |
|---------------|--|
| H17A | F3 2.89 1_655 |
| H17B | H5 2.75 1_565 C5 2.79 1_565 H9A 2.89 1_565 |
| H18A | H30A 2.71 1_455 |
| H18B | - |
| H19D | F1 2.74 1_655 C24 2.83 1_565 H27B 2.86 1_565 N10 2.89 1_565 H23 2.91 1_565 C23 2.94 1_565 |
| H19C | H5 2.55 1_565 |
| H20A | H28A 2.34 2_765 |
| H30B | H26 2.45 2_765 F4 2.85 1_655 |
| H30C | H20D 2.46 2_765 |

*The symmetry code after the distance gives the symmetry operation to generate the neighbouring molecule. The symmetry generators are given as S_XYZ where S=1 indicates the identity operation and 2 the inversion and the XYZ part indicates the translation (X-5 gives the translation in integer number of a, Y-5 in integer number of b and Z-5 in integer number of c).

Table S5. Tables of short intermolecular contacts between the hydrogen atoms of the butyl chains and neighbouring molecules for the structure number 20 (LS, end of the relaxation). All contacts of less than 3 Å are indicated.

| H atom | Neighbouring atom, distance, symmetry code* |
|--------|--|
| H27A | F1 2.40 2_665 F4 2.79 2_665 H20C 2.91 1_545 |
| H27B | F1 2.44 1_645 F2 2.74 1_645 H20B 2.85 1_545 H19B 2.91 1_545 |
| H28A | H20B 2.29 2_765 F1 2.95 2_665 |
| H28B | - |
| H29A | F6 2.98 1_655 |
| H29B | F1 2.79 2_665 |
| H30A | H25 2.94 1_655 H20B 3.00 2_765 |
| H30B | H25 2.70 1_655 H16 2.80 1_655 C16 2.94 1_655 |
| H30C | H26 2.45 2_765 F4 2.92 1_655 |

| H atom | Neighbouring atom, distance, symmetry code* |
|--------|--|
| H17A | H9A 2.89 1_565 F3 2.97 1_655 |
| H17B | H9A 2.56 1_565 H6 2.84 1_565 C6 2.97 1_565 |
| H18A | F3 2.92 1_655 |
| H18B | - |
| H19A | H5 2.53 1_565 |
| H19B | H27B 2.91 1_565 F3 2.94 1_655 |
| H20A | H26 2.70 2_665 H20C 2.72 2_675 |
| H20B | H28A 2.29 2_765 F1 2.48 1_655 H27B 2.85 1_565 H30A 3.00 2_765 |
| H20C | H20C 2.55 2_675 H20A 2.72 2_675 H27A 2.91 1_565 |

*The symmetry code after the distance gives the symmetry operation to generate the neighbouring molecule. The symmetry generators are given as S_XYZ where S=1 indicates the identity operation and 2 the inversion and the XYZ part indicates the translation (X-5 gives the translation in integer number of a, Y-5 in integer number of b and Z-5 in integer number of c).

Figure S14. LIESST experiment followed by magnetism in order to extract the corresponding values of T_{LIESST} for the HS state photogenerated from a) LS_1 and b) LS_2 .

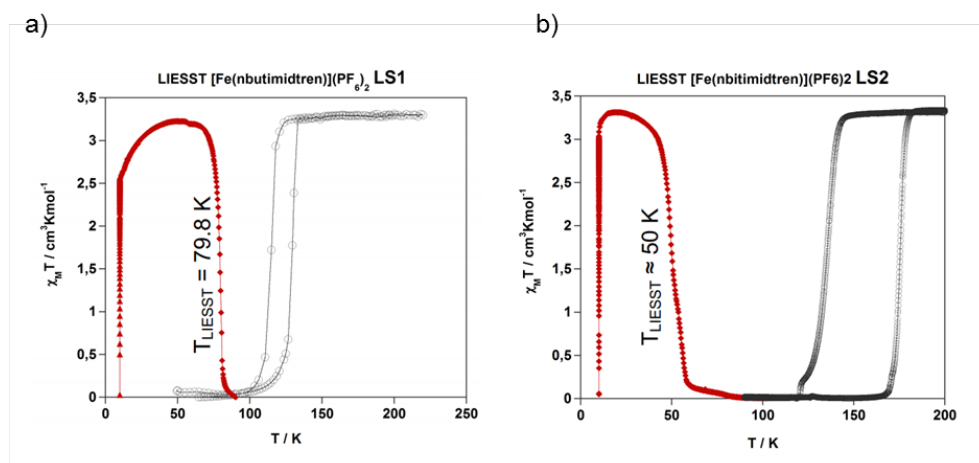


Figure S15. a) Photo-generation of HS after irradiation of LS_1 at 80 K on a polycrystalline in the SQUID magnetometer. The HS is fully populated as observed by absorption spectroscopy and X-ray diffraction. b) $\text{HS}_1^{2\text{irr}} \rightarrow \text{LS}_1$ relaxation followed by magnetism.

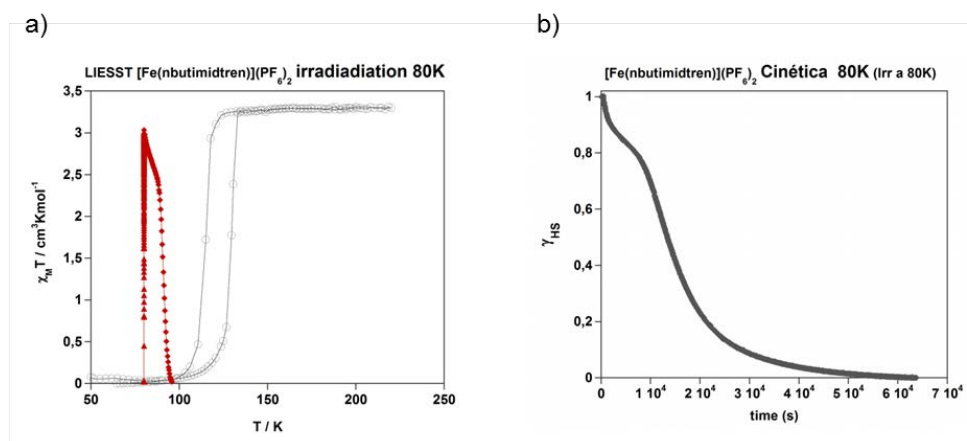


Figure S16. a) Evolution of the diffraction pattern of the sample during the $\text{HS}_1^{2\text{irr}} \rightarrow \text{LS}_1$ relaxation at 90 K after photo-excitation at 690 nm with 10 mW/mm^2 during 10 min and b) corresponding time evolution of the $\text{HS}_1^{2\text{irr}}$ fraction.

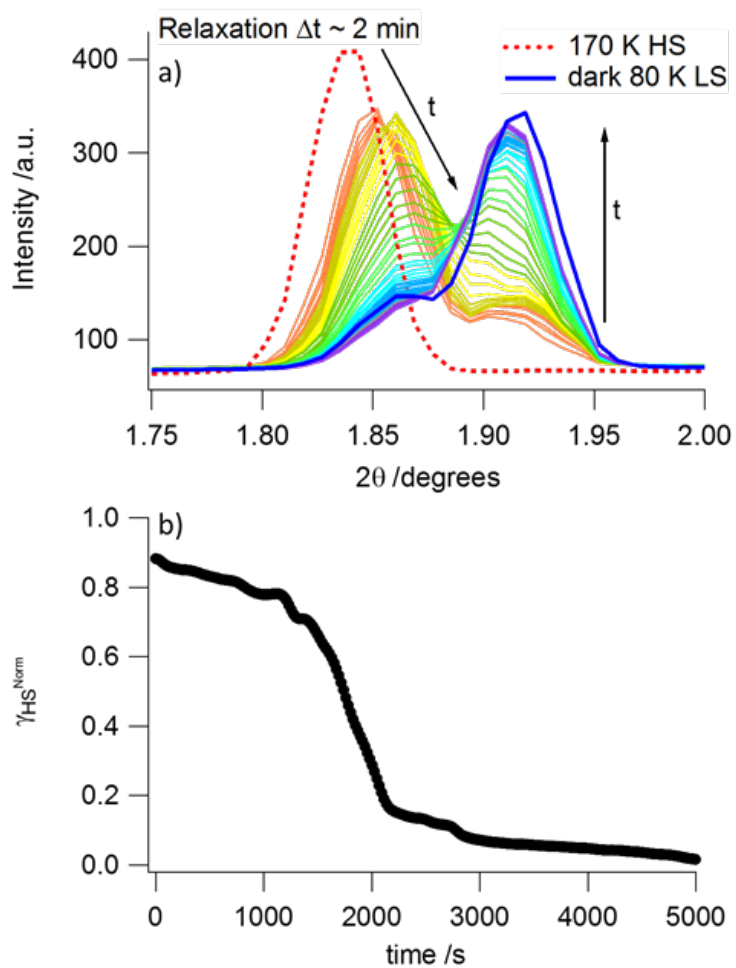
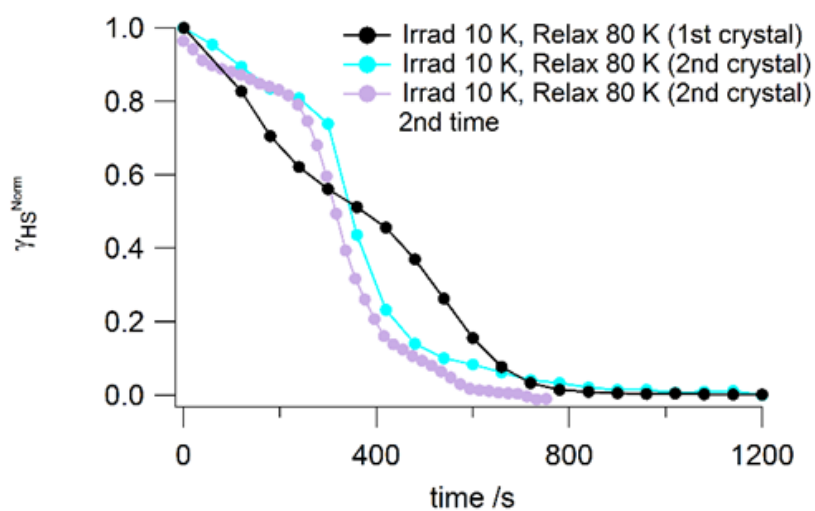
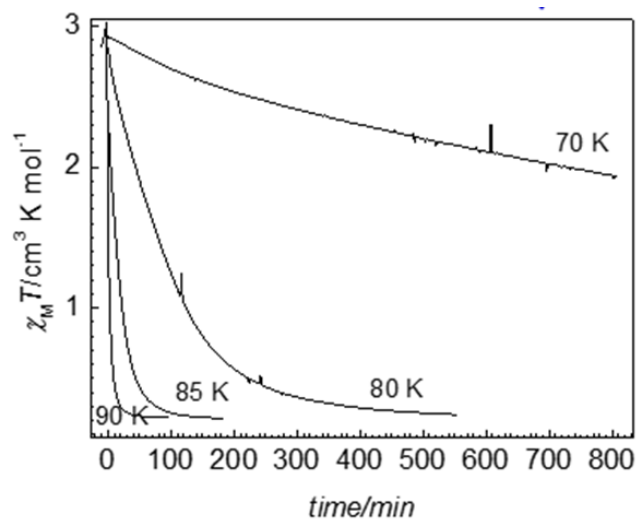


Figure S17. $HS_1^{irr} \rightarrow LS_1$ relaxation curves obtained at 80 K after irradiation at 10 K.



A first crystal was irradiated at 10 K, heated up at 80 K (at 20 K/min) and its relaxation curve is shown in black.

A second crystal was irradiated at 10 K, heated up at 80 K (at 20 K/min) and the relaxation curve is shown in blue. It was then cooled back to 10 K at 4 K/min, irradiated again at 10 K, heated up at 80 K (at 20 K/min) and the relaxation curve is shown in purple.

Figure S18. Relaxation curves after thermal quenching at the indicated temperatures.**Table S6.** Different measured relaxation time at 80 K and 90 K.

| phase | Measurement method | Sample | T (K) | Relaxation time (s) |
|---------------------------------|----------------------------|------------------------|-------|---------------------|
| HS ₁ ^{1irr} | Absorption spectroscopy | Single crystal | 80 | 800 |
| HS ₁ ^{2irr} | Absorption spectroscopy | Single crystal | 80 | 70000 |
| HS ₁ ^{2irr} | Absorption spectroscopy | Single crystal | 90 | 6000 |
| HS ₁ ^{2irr} | Absorption spectroscopy | Cracked single crystal | 90 | 4000 |
| HS ₁ ^{2irr} | Single crystal diffraction | Single crystal | 90 | 5000 |
| HS ₁ ^{2irr} | Powder diffraction | Powder | 90 | 5000 |
| HS ₁ ^{2irr} | Magnetic measurements | Powder | 80 | 60000 |
| HS _q ^{2irr} | Magnetic measurements | Powder | 80 | 40000 |

Table S7a. Structure of the different quenched states obtained at different temperatures.

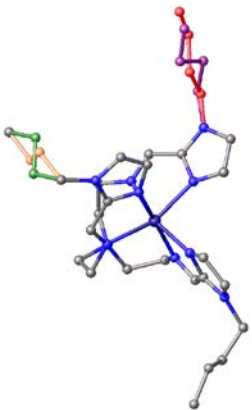
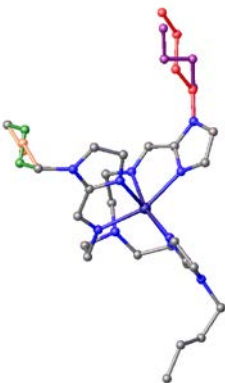
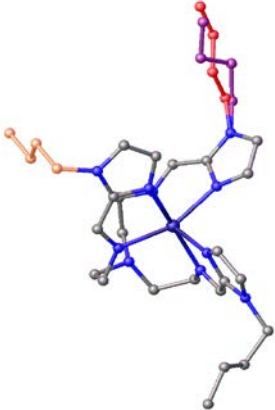
| Quenched HS at 10 K | Quenched HS at 125 K | Quenched at 125 K, then slowly cooled to 100 K |
|---|--|---|
|  |  |  |
| <p>Chain A is disordered (red, violet)</p> <p>Chain B is slightly disordered (orange, green).</p> | <p>Chain A is disordered (red, violet)</p> <p>Chain B is disordered (orange, green).</p> | <p>Chain A is disordered (red, violet)</p> <p>Chain B is ordered (orange).</p> |

Table S7b. Crystal data and structure refinement for the quenched HS state at 10 K.

| | | | |
|-----------------------------------|---|------------------|------------------|
| Empirical formula | C ₃₀ H ₄₈ F ₁₂ Fe N ₁₀ P ₂ | | |
| Formula weight | 894.57 | | |
| Temperature | 10(2) K | | |
| Wavelength | 0.71073 Å | | |
| Crystal system | Triclinic | | |
| Space group | P-1 | | |
| Unit cell dimensions | a = 9.2011(7) Å | b = 10.1991(9) Å | c = 21.9496(8) Å |
| | α = 91.624(5)° | β = 101.414(5)° | γ = 98.816(7)° |
| Volume | 1991.6(2) Å ³ | | |
| Z | 2 | | |
| Density (calculated) | 1.492 Mg/m ³ | | |
| Absorption coefficient | 0.552 mm ⁻¹ | | |
| F(000) | 924 | | |
| Theta range for data collection | 2.842 to 30.508° | | |
| Index ranges | -12 ≤ h ≤ 13, -14 ≤ k ≤ 13, -31 ≤ l ≤ 31 | | |
| Reflections collected | 30700 | | |
| Independent reflections | 12061 [R(int) = 0.0349] | | |
| Completeness to theta = 25.242° | 99.8% | | |
| Absorption correction | Analytical | | |
| Max. and min. transmission | 0.964 and 0.909 | | |
| Refinement method | Full-matrix least-squares on F ² | | |
| Data / restraints / parameters | 12061 / 7 / 511 | | |
| Goodness-of-fit on F ² | 0.985 | | |
| Final R indices [I > 2σ(I)] | R1 = 0.0540, wR2 = 0.1171 | | |
| R indices (all data) | R1 = 0.0697, wR2 = 0.1304 | | |
| Extinction coefficient | n/a | | |
| Largest diff. peak and hole | 1.981 and -1.646 e.Å ⁻³ | | |

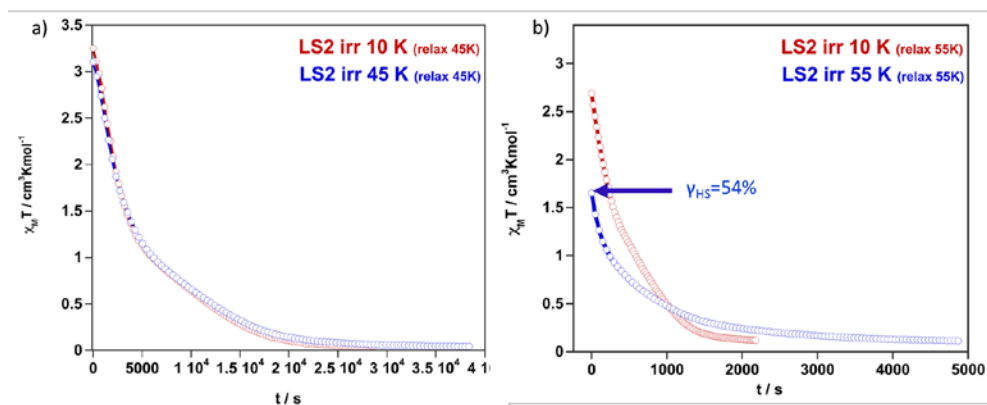
Table S7c. Crystal data and structure refinement for the quenched HS state at 125 K.

| | | | |
|-----------------------------------|---|------------------|-------------------|
| Empirical formula | C ₃₀ H ₄₈ F ₁₂ Fe N ₁₀ P ₂ | | |
| Formula weight | 894.57 | | |
| Temperature | 125(2) K | | |
| Wavelength | 0.71069 Å | | |
| Crystal system | Triclinic | | |
| Space group | P-1 | | |
| Unit cell dimensions | a = 9.2642(4) Å | b = 10.2705(5) Å | c = 22.0624(11) Å |
| | α = 91.906(4)° | β = 101.684(4)° | γ = 98.679(4)° |
| Volume | 2027.73(17) Å ³ | | |
| Z | 2 | | |
| Density (calculated) | 1.465 Mg/m ³ | | |
| Absorption coefficient | 0.542 mm ⁻¹ | | |
| F(000) | 924 | | |
| Theta range for data collection | 2.848 to 30.505° | | |
| Index ranges | -13 ≤ h ≤ 13, -14 ≤ k ≤ 13, -31 ≤ l ≤ 31 | | |
| Reflections collected | 25896 | | |
| Independent reflections | 12375 [R(int) = 0.0447] | | |
| Completeness to theta = 25.240° | 99.8% | | |
| Absorption correction | Analytical | | |
| Max. and min. transmission | 0.946 and 0.874 | | |
| Refinement method | Full-matrix least-squares on F ² | | |
| Data / restraints / parameters | 12375 / 7 / 516 | | |
| Goodness-of-fit on F ² | 1.037 | | |
| Final R indices [I > 2σ(I)] | R1 = 0.0546, wR2 = 0.1329 | | |
| R indices (all data) | R1 = 0.0785, wR2 = 0.1516 | | |
| Extinction coefficient | n/a | | |
| Largest diff. peak and hole | 0.543 and -0.417 e.Å ⁻³ | | |

Table S7d. Crystal data and structure refinement for the quenched HS state at 125 K slowly cooled at 100K.

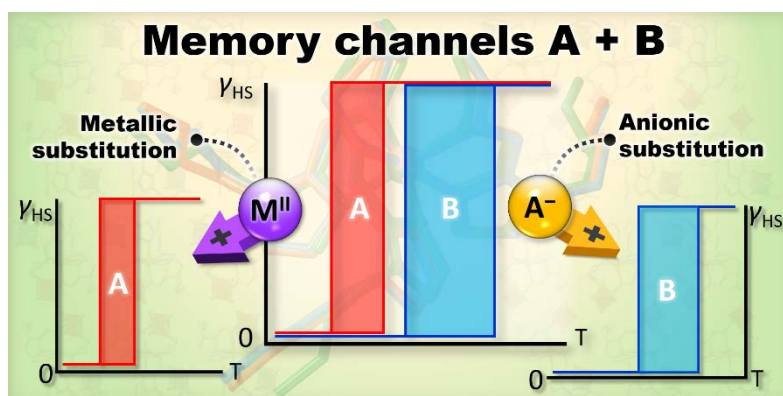
| | | | |
|-----------------------------------|---|------------------|-------------------|
| Empirical formula | C ₃₀ H ₄₈ F ₁₂ Fe N ₁₀ P ₂ | | |
| Formula weight | 894.57 | | |
| Temperature | 100(2) K | | |
| Wavelength | 0.71073 Å | | |
| Crystal system | Triclinic | | |
| Space group | P-1 | | |
| Unit cell dimensions | a = 9.2763(6) Å | b = 10.2063(5) Å | c = 22.0345(13) Å |
| | α = 91.425(5)° | β = 101.334(5)° | γ = 98.996(5)° |
| Volume | 2017.0(2) Å ³ | | |
| Z | 2 | | |
| Density (calculated) | 1.473 Mg/m ³ | | |
| Absorption coefficient | 0.545 mm ⁻¹ | | |
| F(000) | 924 | | |
| Theta range for data collection | 2.833 to 30.508° | | |
| Index ranges | -13 ≤ h ≤ 13, -14 ≤ k ≤ 12, -30 ≤ l ≤ 31 | | |
| Reflections collected | 24051 | | |
| Independent reflections | 12303 [R(int) = 0.0873] | | |
| Completeness to theta = 25.242° | 99.8% | | |
| Absorption correction | Semi-empirical from equivalents | | |
| Max. and min. transmission | 1.00000 and 0.94950 | | |
| Refinement method | Full-matrix least-squares on F ² | | |
| Data / restraints / parameters | 12303 / 4 / 509 | | |
| Goodness-of-fit on F ² | 1.040 | | |
| Final R indices [I > 2σ(I)] | R1 = 0.0949, wR2 = 0.2099 | | |
| R indices (all data) | R1 = 0.2072, wR2 = 0.2651 | | |
| Extinction coefficient | n/a | | |
| Largest diff. peak and hole | 1.045 and -0.640 e.Å ⁻³ | | |

Figure S19: Magnetic measurements of the relaxation at 45 K (a) and 55 K (b). For both measurements, a first relaxation curve was collected after irradiation at 10 K, and then a second one was collected after irradiation at the relaxation temperature (45 K for a and 55 K for b). For measurement b, only 54% conversion to the HS state could be reached at 55 K. This dropped to about 15% when irradiating at 65 K (The relaxation was not measured) and almost no conversion could be achieved with irradiation at 80 K).



CAPÍTULO 6

Discrimination between two memory channels by molecular alloying in a doubly bistable spin crossover material



REVISTA: Chemical Science

ÍNDICE DE IMPACTO: 9.556

CAPÍTULO 6

Discrimination between two memory channels by molecular alloying in a doubly bistable spin crossover material

6.1.- Abstract

A multistable spin crossover (SCO) molecular alloy system $[\text{Fe}_{1-x}\text{M}_x(\text{nBu-im})_3(\text{tren})](\text{P}_{1-y}\text{As}_y\text{F}_6)_2$ ($\text{M} = \text{Zn}^{\text{II}}, \text{Ni}^{\text{II}}; \text{nBu-im})_3(\text{tren}) = \text{tris}(n\text{-butyl-imidazol}(2\text{-ethylamino}))\text{amine}$) has been synthesized and characterized. By controlling the composition of this isomorphous series, two cooperative thermally-induced SCO events featuring distinct critical temperatures (T_c) and hysteresis widths (ΔT_c , memory) can be selected at will. The pristine derivative **100As** ($x = 0, y = 1$) displays a strong cooperative two-step SCO and two reversible structural phase transitions (PTs). The low temperature PT^{LT} and the SCO occur synchronously involving conformational changes of the ligand's *n*-butyl arms and two different arrangements of the AsF_6^- anions [$T_c^1 = 174 \text{ K}$ ($\Delta T_c^1 = 17 \text{ K}$), $T_c^2 = 191 \text{ K}$ ($\Delta T_c^2 = 23 \text{ K}$) (scan rate 2 K min^{-1})]. The high-temperature PT^{HT} takes place in the high-spin state domain and essentially involves rearrangement of the AsF_6^- anions [$T_c^{\text{PT}} = 275 \text{ K}$ ($\Delta T_c^{\text{PT}} = 16 \text{ K}$)]. This behavior strongly contrasts with that of the homologous **100P** [$x = 0, y = 0$] derivative where two separate cooperative one-step SCO can be selected by controlling the kinetics of the coupled PT^{LT} at ambient pressure: (i) one at low temperatures, $T_c = 122 \text{ K}$ ($\Delta T_c = 9 \text{ K}$), for temperature scan rates ($> 1 \text{ K min}^{-1}$) (memory channel A) where the structural modifications associated with PT^{LS} are inhibited; (ii) the other centered at $T_c = 155 \text{ K}$ ($\Delta T_c = 41 \text{ K}$) for slower temperature scan rates $\leq 0.1 \text{ K min}^{-1}$ (memory channel B). These two SCO regimes of the **100P** derivative transform reversibly into the two-step SCO of **100As** upon application of hydrostatic pressure (ca. 0.1 GPa) denoting the subtle effect of internal chemical pressure on the SCO behavior. Precise control of $\text{AsF}_6^- \leftrightarrow \text{PF}_6^-$ substitution, and hence of the PT^{LT} kinetics, selectively selects the memory channel B of **100P** when $x = 0$ and $y \approx 0.7$]. Meanwhile, substitution of Fe^{II} with Zn^{II} or Ni^{II} [$x \approx 0.2, y = 0$] favors the low temperature memory channel A at any scan rate. This intriguing interplay between PT, SCO and isomorphous substitution was monitored by single crystal and powder X-ray diffractometries, and magnetic and calorimetric measurements.

6.2.- Introduction

Responsive switchable materials attract great attention due to affording excellent study examples for understanding the mechanisms of phase transitions (PTs) and provide application prospects for future and emerging technologies.^[1] Some of the most investigated switchable molecular materials are pseudo-octahedral Fe^{II} spin-crossover (SCO) complexes, reversibly altering the high-spin (HS, $t_{2g}^4 e_g^2$) and low-spin (LS, $t_{2g}^6 e_g^0$) electronic states by the action of physicochemical stimuli (temperature, pressure, light, and chemical substrates). The LS-HS conversion involves an electron transfer between the e_g and t_{2g} orbitals strongly coupled with structural changes in the coordination core of the Fe^{II} centres, which essentially affect Fe-ligand bond lengths and angles, and in turn the molecular conformation. In favourable cases these changes propagate cooperatively in the crystal, conferring bistability (memory) to the magnetic, optical, dielectric, structural and mechanical properties.^[2]

New developments in this area are crucial not only for elucidating background mechanisms behind observed properties and understanding the fundamental aspects of the SCO behavior, but also for opening new perspectives in the field, such as the use of SCO compounds for creation of fully controllable “smart” materials responding to external stimuli in a desired way.^[3] For example, SCO can be combined with other relevant functions such as fluorescence,^[3c,4] electroluminescence,^[3e] electronic transport,^[5] and non-linear optic response^[6] thereby transferring their intrinsic bistable nature to the second property resulting in multifunctional materials that can be processed at different levels, from bulk to nanoscale.^[7]

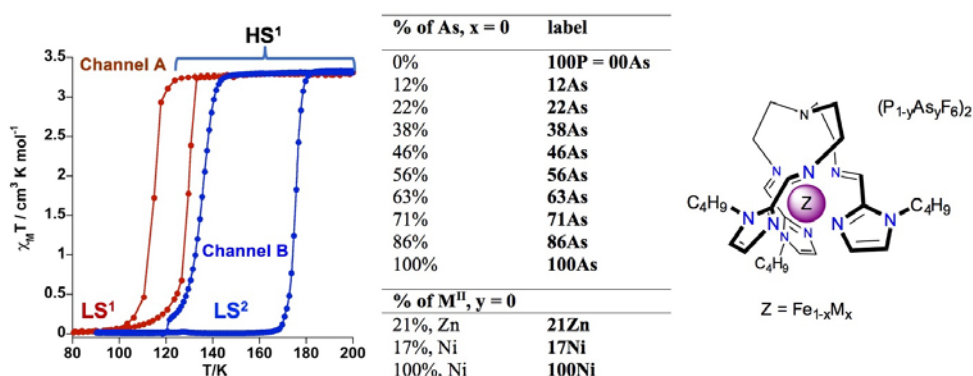
The control of the SCO characteristics, *i.e.* critical temperature and hysteresis width, remains one of the key focuses in the field. Tackling this problem by chemical methods requires engineering both the coordination site of the SCO centers and the cohesive elastic interactions between them through supramolecular and/or polymeric approaches. Furthermore, the strong sensitivity of the SCO behavior to subtle changes in the elastic interactions makes it possible to control the SCO through crystal lattice rearrangements. In this respect, isomorphous substitution of SCO metal centres/complexes with non-SCO metal ions^[8]/non-SCO complexes^[9] is an effective means to modulate the SCO behavior. For example, substantial dilution with passive Ni^{II} or Zn^{II}-based complexes breaks cooperativity between SCO centres and brings on a considerable downward shift of the SCO

equilibrium/critical temperature $T_{1/2}/T_c$, while low concentrations of the dopant can fine tune the SCO behavior.^[2d] Metal dilution is a particular case of a more general concept of solid solution of molecules, also known as molecular alloys, consisting in precise control of the stoichiometry of mixed ionic or molecular components during the synthetic step. This offers an unrivalled tool for optimization of desired magnetic, optical or electrical properties, as demonstrated by examples from adjacent fields,^[10] and for a few SCO systems.^[3a] Another relevant strategy, yet little explored, is based on the possibility of controlling the SCO properties by a PT.^[11] It has been demonstrated for several systems that changes in the interaction binding between the components of the crystal due to a solid-solid or solid-liquid/liquid crystal PT may be sufficient for altering the spin state.^[11b, 12]

In this context, the complex $[\text{Fe}(\text{nBu-im})_3(\text{tren})](\text{PF}_6)_2$ ($(\text{nBu-im})_3(\text{tren}) = \text{tris}(n\text{-butyl-imidazol}(2\text{-ethylamino}))\text{amine}$) affords an uncommon example of thermal hysteretic SCO behavior deeply influenced by a synchronous symmetric crystallographic PT, leading to a reorganization of the crystal lattice due to significant conformational changes of the alkyl groups and displacement and rotation of the PF_6^- anions, taking place during the $\text{LS} \leftrightarrow \text{HS}$ conversion.^[11b] Playing with the slow kinetics featuring this PT, two well separate hysteretic thermally induced SCO behaviors (two memory channels) were found.^[11b] Thus, high-temperature sweep rates ($\geq 2 \text{ K min}^{-1}$) quench the crystallographic PT thereby stabilizing channel A, which is characterized by a cooperative SCO, between the phases HS^1 and LS^1 , centred at 122 K with a hysteresis 14 K wide. In contrast, low temperature-sweep rates ($\leq 0.1 \text{ K min}^{-1}$) stabilize channel B, characterized by a much more cooperative SCO, between the HS^1 and LS^2 phases, centred at ca. 155.5 K featuring a hysteresis loop 41 K wide (see Scheme 1). The phases display different arrangement 1 and arrangement 2 of the flexible butyl groups and of the anions. Furthermore, the LS^1 phase affords an uncommon very long-lived photogenerated HS^{1*} phase after light irradiation at 80 K. The very slow relaxation kinetics is controlled by conformational rearrangements of the butyl groups during the $\text{HS}^{1*} \rightarrow \text{LS}^1$ transformation.^[11f]

In order to understand more in depth the correlation between SCO and structural PT in **100P** and find reliable chemical means to discriminate between the two thermal memory channels, we have investigated the isostructural compound $[\text{Fe}(\text{nBu-im})_3(\text{tren})](\text{AsF}_6)_2$ (**100As**) and the solid solutions $[\text{Fe}_{1-x}\text{M}_x(\text{nBu-im})_3(\text{tren})](\text{P}_{1-y}\text{As}_y\text{F}_6)_2$ (see Scheme 1). Herein, we show that the SCO behavior of **100P** ($x = 0$; $y = 0$) is highly sensitive to application of

external hydrostatic low pressure and, consequently, the resulting SCO behavior is similar to that of **100As** ($x = 0$; $y = 1$) which also displays double bistability due to SCO and PTs but at higher temperatures. Furthermore, modulating the internal “chemical pressure” built up by partial substitution of Fe(II) with M(II) (xM , $x < 100$ and $y = 0$, $M = \text{Zn, Ni}$) or P with As ($y\text{As}$, $x = 0$ and $y < 100$) leads to effective discrimination of the two memory channels resulting from interplay of the SCO and a PT in the pure **100P**.



Scheme 1. Description of the SCO behavior of **100P**. $[\text{Fe}_{1-x}\text{M}_x(\text{nBu-im})_3(\text{tren})](\text{P}_{1-y}\text{As}_y\text{F}_6)_2$ system ($M = \text{Ni, Zn}$).

6.3.- Results

6.3.1.- SCO properties of 100As

The magnetic behavior of **100As**, recorded at 1 K min^{-1} between 10 and 300 K, is shown in Figure 1a in the form of $\chi_M T$ vs T (χ_M is the molar magnetic susceptibility and T is the temperature). At 300 K, the $\chi_M T$ value is close to $3.68 \text{ cm}^3 \text{ K mol}^{-1}$ as expected for Fe^{II} compound in the HS state ($S = 2$). On cooling a gradual decrease of $\chi_M T$ value down to $3.56 \text{ cm}^3 \text{ K mol}^{-1}$ is followed by a limited but abrupt jump up to $3.80 \text{ cm}^3 \text{ K mol}^{-1}$. This bistable behavior is associated with a reversible crystallographic PT within the HS phase [$\text{HS}^1 \leftrightarrow \text{HS}^2$] (*vide infra*).

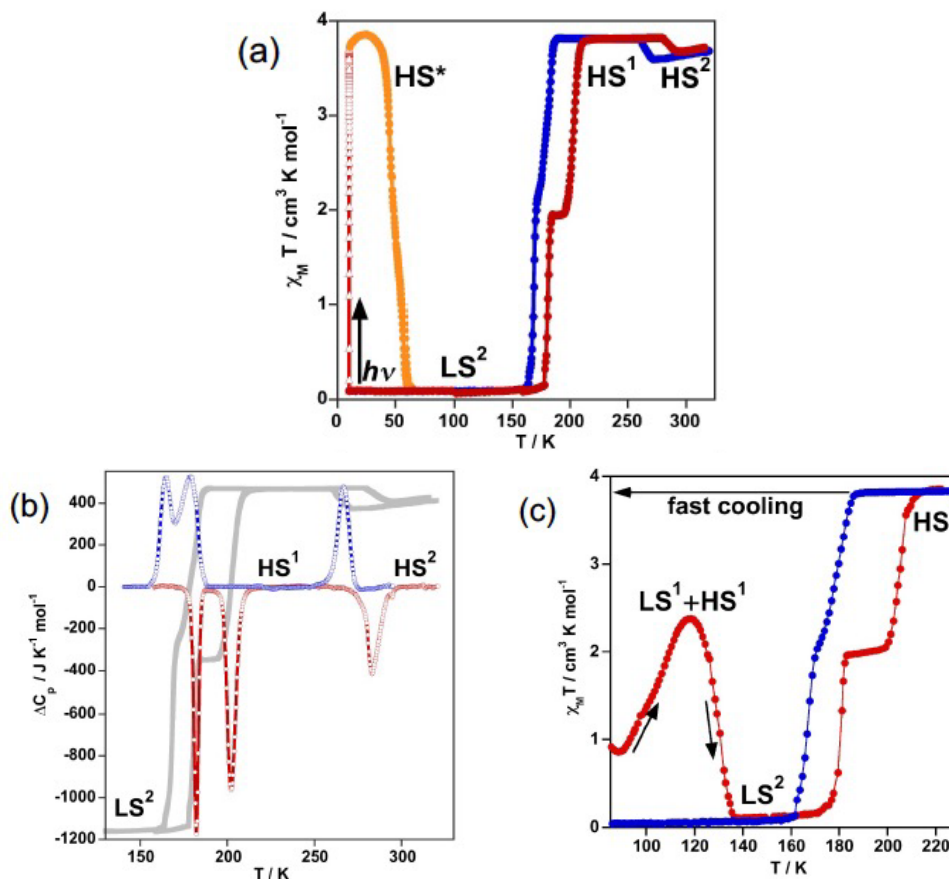


Figure 1. Spin crossover behavior of **100As**: (a) magnetic and photomagnetic properties; (b) differential scanning calorimetry (DSC); and (c) quenching of the HS state. Blue and red filled circles correspond to the cooling and heating modes, respectively. Gray lines correspond to the heat flow measured by DSC.

The shaped hysteresis is centered at $T_c^{\text{PT}} = 276 \text{ K}$ with the loop width $\Delta T_c^{\text{PT}} = 17 \text{ K}$. Further cooling does not reveal any marked evolution of $\chi_M T$ down to 188 K , where an abrupt two-step decrease down to zero value is detected ($S = 0$) with a well-defined plateau of the ascending curve at 50% conversion upon subsequent heating. The two-steps centred at $T_c^1 = 175 \text{ K}$ and $T_c^2 = 193 \text{ K}$ are characterised by a hysteresis loops $\Delta T_c^1 = 14 \text{ K}$ and $\Delta T_c^2 = 23 \text{ K}$, respectively. In opposite to **100P**, no remarkable kinetic effects were observed for

the range of temperature-sweeping rates 4-0.5 K min⁻¹ in the magnetic response of **100As** (Figure S1). However, when cooling from 300 K to 80 K in ca. 15 s (\approx 900 K min⁻¹) partial thermal trapping of the sample was observed (Figure 1c). At 80 K the $\chi_{\text{M}}T$ value of the trapped sample is ca. 1 cm³ K mol⁻¹ and upon heating at 0.3 K min⁻¹ it increases to reach a maximum value of 2.37 cm³ K mol⁻¹ at 120 K, which corresponds to ca. 62% of the Fe^{II} centres in the HS state. Then, at higher temperatures, the compound relaxes back to the LS state and upon further heating reaches the HS state. As a hypothesis and by similarity with **100P** the trapped state could be a mixture of the states LS¹ and HS¹ and the LS state attained after relaxation should correspond to the LS² phase (*vide infra*).

Quantitative photo-generation of the metastable HS* state at low temperature, the so-called light induced excited spin state trapping (LIESST) experiment,^[13] was carried out at 10 K by irradiating a microcrystalline sample (0.75 mg) of **100As** with red light (λ = 633 nm) over 3 h. Further heating of the sample in the photo-stationary HS* state in the dark at 0.3 K min⁻¹ uncovers a two-step LIESST relaxation process with T_{LIESST1} = 45 K and T_{LIESST2} = 57 K (Figure 1a) relevant to the two-step thermal SCO.

Differential scanning calorimetry (DSC) measurements were carried out for **100As** in the cooling and heating modes to support the magnetic bistability data and quantify the thermodynamic parameters associated with the SCO and PT. The corresponding anomalous variation of the heat capacity ΔC_p vs T plots is depicted in Figure 1b overlaid with the magnetic data. Upon cooling/heating three processes are detected at critical temperatures T_c^1 = 174 K (ΔT_c^1 = 17 K), T_c^2 = 191 K (ΔT_c^2 = 23 K) and T_c^{PT} = 275 K (ΔT_c^{PT} = 16 K) confirming reversibility of the two-step SCO process and of the PT. The enthalpy and entropy changes of the PT averaged over both runs, ΔH^{PT} = 3.94 kJ mol⁻¹ and ΔS^{PT} = 14.29 J K⁻¹ mol⁻¹, account for the substantial rearrangements associated with order/disorder events of the butyl groups and the anions (*vide infra*). The averaged enthalpy and entropy for the two low temperature peaks, ΔH_{SCO} = 10.3 kJ mol⁻¹ and ΔS_{SCO} = 59.5 J K⁻¹ mol⁻¹, respectively, exceed values reported for each of the two transitions LS \leftrightarrow HS in **100P** [$\Delta H_{\text{SCO}}(\text{LS}^1 \leftrightarrow \text{HS}^1)$ = 5.2 kJ mol⁻¹ and $\Delta S_{\text{SCO}}(\text{LS}^1 \leftrightarrow \text{HS}^1)$ = 41.6 J K⁻¹ mol⁻¹; $\Delta H_{\text{SCO}}(\text{LS}^2 \leftrightarrow \text{HS}^1)$ = 6.8 kJ mol⁻¹ and $\Delta S_{\text{SCO}}(\text{LS}^2 \leftrightarrow \text{HS}^1)$ = 39.5 J K⁻¹ mol⁻¹].^[11b]

6.3.2.- SCO properties of 100P under pressure

The SCO properties of **100P** (channel A and channel B) and **100As** differ in critical temperatures, hysteresis width and more notably in nature (one or two step). The observed 30 K upward shift of the average critical temperature when replacing PF_6^- with AsF_6^- suggests the introduction of additional chemical pressure in **100As** as a result of the slightly larger ionic radius of As. To support this hypothesis, we have investigated the effect of small applied hydrostatic pressure on the SCO behaviour of **100P**. At ambient pressure, in the cooling mode (1 K min^{-1}), **100P** displays essentially the behaviour of channel A. At a pressure of 0.11 GPa the SCO shifts upwards by 100 K, and, surprisingly, it becomes two-step with critical temperatures centred at $T_c^1 = 221 \text{ K}$ and $T_c^2 = 251 \text{ K}$, characterised by a hysteresis loop $\Delta T_c^1 = 13 \text{ K}$ and $\Delta T_c^2 = 39 \text{ K}$, respectively, and a well-defined intermediate plateau on heating as shown in Figure 2. This SCO is practically that of **100As** at ambient pressure. Increasing pressure up to 0.14 GPa shifts the transition to higher temperatures ($T_c^1 = 245 \text{ K}$, $\Delta T_c^1 = 13 \text{ K}$ and $T_c^2 = 285 \text{ K}$, $\Delta T_c^2 = 36 \text{ K}$). Interestingly, these results demonstrate very similar effects on the SCO of the complex cation whatever the nature of the applied pressure, *i.e.* external or “internal” generated by $\text{PF}_6^- \leftrightarrow \text{AsF}_6^-$ anion substitution. A second relevant finding is hypersensitivity of **100P** towards imposed external pressure with dependence $d\langle T_c \rangle / dp \approx 1000 \text{ K/GPa}$, where $\langle T_c \rangle = (T_{c1} + T_{c2})/2$, although regularly observed value lies in the range of 150–200 K/GPa^[14] (Figure S2).

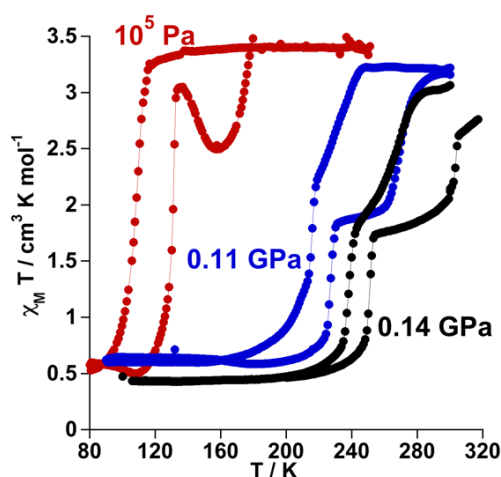


Figure 2. Temperature dependence of $\chi_M T$ vs. T for **100P** at different pressure values.

6.3.3.- Study of $[\text{Fe}_{1-x}\text{M}_x(\text{nBu-im})_3(\text{tren})](\text{P}_{1-y}\text{As}_y\text{F}_6)_2$ molecular alloys

The high sensitivity of the SCO properties of **100P** to external hydrostatic pressure, also apparent when internal “chemical pressure” increases when replacing PF_6^- with AsF_6^- , prompted us to study solid solutions based on anion ($\text{PF}_6^- \rightarrow \text{AsF}_6^-$) and metal ($\text{Fe}^{\text{II}} \rightarrow \text{M}^{\text{II}}$) substitution. A series of solid solutions were prepared in the same way as **100P** and **100As** but containing mixtures of PF_6^- and AsF_6^- anions in calculated ratio. It was found that the PXRD profiles of **22As–56As**, as well as of **21Zn** and **17Ni**, are indistinguishable from that of **100P** (Figure 3). On the other hand, for **71As**, a shift/coalescence of diffraction peaks is observed in the high angle range, in addition to the change of peaks intensity, although in the low angle range the diffraction patterns perfectly match that of **100P**. These findings are consistent with the evolution of the magnetic properties on isostructural substitution in the aforementioned series.

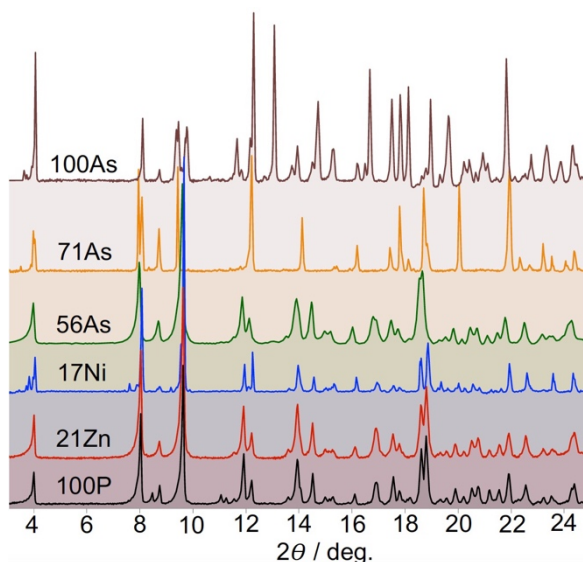


Figure 3. X-ray powder diffraction patterns of indicated diluted compounds at RT.

Gradual substitution of PF_6^- with AsF_6^- anions continuously reshapes the original SCO behaviour of **100P** stabilizing a phase which compares well with channel B. This is illustrated in Figures 4b-g where the SCO of pristine **100P**, recorded at scan rate 2 K min^{-1} , is also included for comparison (grey line). For **22As**, channel A is prevailing and a low temperature hysteresis is still observed but an increase of the relaxation rate favouring

channel B is obvious (Figure 4b). Increasing the concentration of AsF_6^- in **29As**, **38As**, **46As** and **56As** progressively accelerates relaxation and suppresses channel A in favour of channel B, which finally in **71As** produces a single-step hysteresis loop centred at $T_c = 171$ K with $\Delta T_c = 34$ K. Further increase of AsF_6^- affords compound **86As** that gives rise to a narrow two-step SCO similarly to that of the pristine **100As** (Figure S3). It is worth mentioning that the PT within the HS phase $\text{HS}^1 \leftrightarrow \text{HS}^2$ increases in amplitude and decreases in temperature as the amount of AsF_6^- increases in the molecular alloy (see Figure S4).

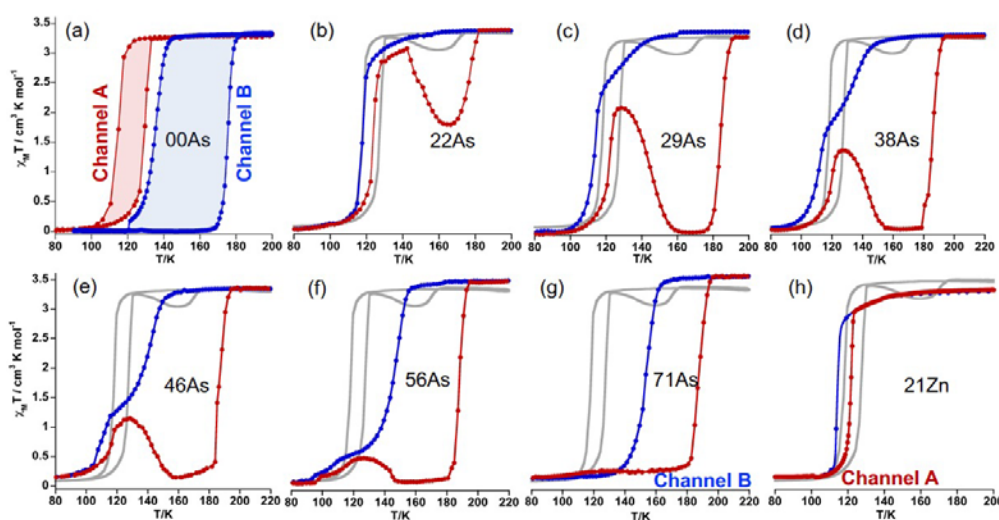


Figure 4. (a) SCO behavior of **100P**, (red and blue curves measured at 4 K min^{-1} and 0.25 K min^{-1} , respectively) (b-f) Influence of successive replacement of PF_6^- and AsF_6^- on the SCO properties. The red curve corresponds to heating, blue curve to cooling, and grey curve to the SCO of **100P** measured at 2 K min^{-1} . (g and h) Effective separation of the two channels.

Interestingly, stabilization of channel A is achieved by partial substitution above certain threshold value of Fe^{II} with Zn^{II} or Ni^{II} , *i.e.* $y \geq 0.21$ for Zn^{II} or $y \geq 0.17$ for Ni^{II} . The resulting isostructural solid solutions **21Zn** or **17Ni** display one step cooperative SCO with critical temperatures centred at $T_c = 117$ and 121 K, characterized by $\Delta T_c = 7$ and 3 K wide hysteresis loops, respectively, at any rate down to 0.5 K min^{-1} (Figure 4h for **17Ni**, see also Figure S5). The pure compound **100Ni** shows a constant susceptibility value of $\chi_{\text{MT}} \approx 1.2 \text{ cm}^3 \text{ K mol}^{-1}$ in the temperature range $50\text{--}300$ K without any irregularities (Figure S6).

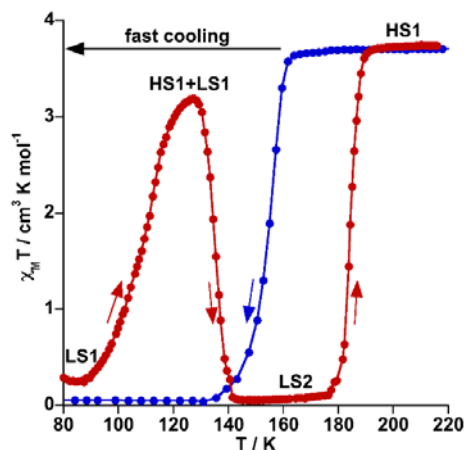


Figure 5. Thermal quenching of the HS state for **71As**. Blue and red filled circles correspond to the cooling and heating modes, respectively.

It is worth noting that despite the clear kinetic stabilization of channel B for **71As**, thermal quenching allows trapping the sample into the hidden channel A. For example, after cooling **71As** from 300 K to 80 at ca. 800 K min⁻¹ the $\chi_M T$ value is essentially that of the Fe^{II} in the LS state (0.22 cm³ K mol⁻¹) (see Figure 5). Then, when heating at 0.3 K/min, $\chi_M T$ increases to attain a value of 3.20 cm³ K mol⁻¹ at 127 K, indicating that the compound is essentially HS. Upon further heating the system first relaxes back to a LS phase and later attains the thermodynamically stable HS state.

6.3.4.- Structural analysis

6.3.4.1.- Structure of **100As**

Compound **100As** is essentially a structural analogue of **100P**. Based on the magnetic behaviour (see Figure 1a and b), the crystal structure of **100As** was investigated at 120 K, 230 K and 300 K where, respectively, the LS², HS¹ and HS² phases are stable. The transformation between these three phases involves two consecutive crystallographic PTs associated with important structural reorganisation, which involves remarkable volume change without symmetry changes (space group $P\bar{1}$, Table S1). However, after many attempts, it was impossible to achieve a full structural analysis of the LS² phase because single crystals shatter during the HS¹ → LS² transformation. The same reason prevented us from structurally characterising the plateau centred at 190 K in the heating branch of the LS²

→ HS¹ transition. The unit cell consists of two crystallographically identical complex cations of opposite chirality and four AsF₆⁻ counterions (two crystallographically distinct sites, denoted As1 and As2) balancing the charge. The Fe^{II} ion is wrapped by three *n*-butyl-1*H*-imidazol-2-ylimino moieties, defining a pseudo-octahedral [FeN₆] coordination environment (Figure 6a), with Fe–N average bond lengths typical for the HS state and does not change substantially due to the PT: 2.199(4) Å and 2.190(7) Å at 230 K (HS¹) and 300 K (HS²), respectively (Figure 6b, Table S2).

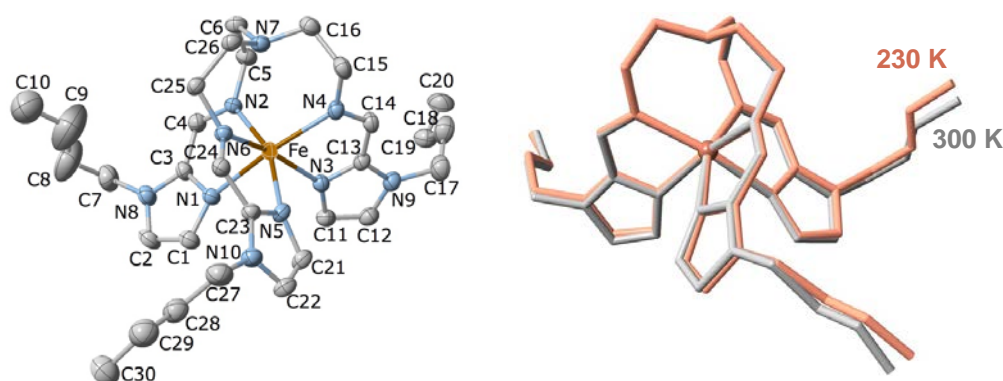


Figure 6. (a) Projection of the cation **100As** with atom numbering scheme at 230 K. Displacement ellipsoids are shown at the 30% probability level. Hydrogen atoms are omitted for clarity. (b) Minimized overlay of the complex cation in the HS¹ (red) and HS² (grey) phases.

Upside-down arranged complex molecules are self-organized in bilayer assemblies extending in the *ab* plane whereas the AsF₆⁻ anions occupy both surfaces and the inner space of the bilayer (Figure 7). At 230 K (HS¹ phase), the inner space anions (As1F₆⁻) are substantially shifted from the centre whereas the axes of anions are inclined with respect to the layer plane; the anions are ordered as well as butyl substituents of the complex cations, arrangement 1 in Figure 7. On passing the temperature of the PT, the anisotropic change of the lattice decreases the lattice parameter *c* by 0.44 Å that is reflected on shrinking the interlayer distance from 22.01 Å at 230 K down to 21.85 Å at 300 K. Furthermore, the PT promotes arrangement 2 (HS² phase), for which inner space anions As1F₆⁻ are located

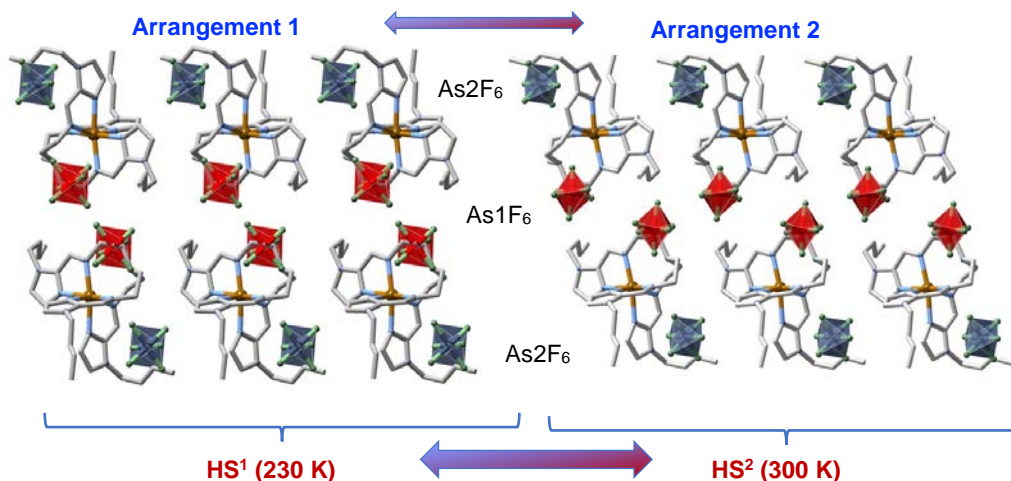


Figure 7. Supramolecular bilayer organization of the complex molecules showing the location of the two crystallographically distinct $\text{AsF}_6^-/\text{PF}_6^-$ anions [blue $\text{As}_2\text{F}_6^-/\text{P}_2\text{F}_6^-$ and red $\text{As}_1\text{F}_6^-/\text{P}_1\text{F}_6^-$ octahedrons], illustrating arrangement 1 and arrangement 2.

closer to the centre of the interspace between layers with their axes almost perpendicular to the layer plane (Figure 7). Substantial disorder of the anions and butyl groups suggests that increasing entropy of the system is the driving force of the PT. Clearly, the transition is not related to the SCO as the coordination sphere of the Fe^{II} remains practically intact, although the rearranged anions and butyl groups change the pattern of intermolecular contacts $\text{CH}\cdots\text{F}$ in the lattice. For example, in the HS^1 phase one discrete interaction $\text{C}_{24}\cdots\text{F}_2(\text{As}1) = 3.087(4) \text{ \AA}$ is below the van der Waals radii (3.17 \AA),^[15] in contrast to the HS^2 phase where no viable $\text{C}\cdots\text{F}$ contacts are operative. Furthermore, percentage of weak intermolecular contacts $\text{C}\cdots\text{F}$, $\text{N}\cdots\text{H}$ and $\text{C}\cdots\text{H}$ substantially changes due to the PT too, see Table S4. This lattice dynamics in close proximity to the metal centre seems to noticeably affect the ligand field strength/ g -factor and produce detectable magnetic bistability.^[16]

It is worth recalling that similar structural rearrangement was observed for **100P**. For cooling rates higher than 0.5 K min^{-1} , **100P** displays arrangement 1 in the LS state (LS¹ phase) through channel A, while above $T_c^{\text{PT}} \approx 127 \text{ K}$ it adopts arrangement 2 (LS² phase) from channel B. Finally, on further heating it recovers arrangement 1 once the system reaches the HS state (HS¹ phase) just above $T_c^\uparrow = 176 \text{ K}$ (Figure 3). It deserves to be noted the increase of disorder in the alkyl chains when both compounds adopt the arrangement 2,

see comparison of the colour mapped complex cation in pairs LS¹–LS² and HS¹–HS² in Figure S7, which is supposed to be driving force of the observed PTs.

On cooling **100As**, a second transition occurs as deduced from the magnetic data (Figure 1a), however, the crystal rapidly and irreversibly deteriorates due to the SCO and therefore it was impossible to collect crystallographic data of the LS² phase at 120 K or of the intermediate plateau at 190 K.

6.3.4.2.- Structure of **71As** and **100Ni**

The impossibility of obtaining sufficient structural information about the nature of the LS state of **100As**, prompted us to try more robust single crystals from the xAsF₆⁺:(100-x)PF₆⁻ solid solutions. It was expected to obtain direct information not only about the type of arrangement adopted by the LS state in this solid solution, which could be extrapolated to **100As**, but also to obtain structural information about the HS state, in particular that of the metastable quenched HS^{1q} at 120 K (see Figure 5). Indeed, robust single crystals of 71AsF₆⁺:29PF₆⁻ (**71As**) appropriate for single crystal X-ray analysis were prepared. A single crystal of **71As** was firstly measured at 230 K (see Tables S1 and S2) where the structure presents, as expected, the arrangement 1 and the Fe^{II} centres are in the HS state (average Fe–N distance = 2.196 Å). The whole cation complex is virtually identical to that of **100As** including the conformation of the butyl groups. Afterwards, the same crystal was slowly cooled from 230 K to 120 K to avoid any thermal quenching, and then the temperature was increased up to 157 K to place the system in the middle of the LS branch of the hysteresis and measured at this temperature (see Figure 5). The corresponding structure exhibits the arrangement 2 for the counterions with the butyl groups showing strong configurational differences with respect to the structure at 230 K (Figure 8a). According to the magnetic properties, the Fe–N average distance, 1.964 Å, shows the occurrence of a complete HS¹ → LS² phase transformation (Table S2).

Another single crystal of **71As** was cooled directly from 300 K to 120 K and the structure of the HS^{1q} phase analysed (see Tables S1 and S2). Despite the crystals being rather robust, we observed their deterioration of them during the measurement process due to relaxation from the quenched HS^{1q} to the LS² phase at 120 K. Consequently, in order to get reasonably good crystal data, initial partial data collection for the resolution of the

structure was recorded. Indeed, this relaxation was slow enough to allow the acquisition of the required data (stable for ca. 45 min) to determine the structure before the collapse of the crystal. The analysis of the structure is consistent with the magnetic data and, based on the Fe–N average bond length, only ca. 5% of the Fe^{II} centres have relaxed to the LS² state. The metastable quenched HS^{1q} retains the arrangement 1 of the parent HS¹ phase and the [Fe(*n*Bu-im)₃(tren)]²⁺ cation is essentially the same except for the butyl [Im–C7–C8–C9–C10] which adopts a divergent configuration (see Figure 8b).

The crystal structure of **100Ni**, solved at 110 K, closely resembles that of **100P** in LS¹ phase,^[11b] *i.e.* shows arrangement 1 (Figure S8 and Table S1 and S3).

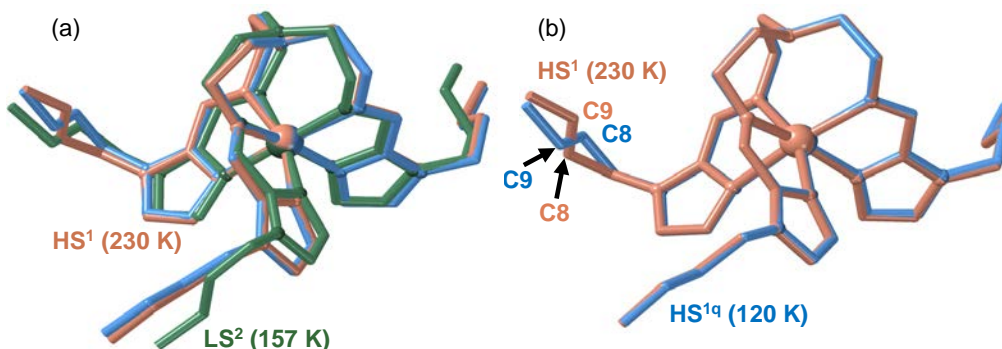


Figure 8. Overlay of the complex cation in **71As**: (a) combination of the HS¹ (red, 230 K) and LS² (green, 157 K) and HS^{1q} (blue, 120 K) phases; (b) combination of the HS¹ (red, 230 K) and HS^{1q} (blue, 120 K) phases showing the different configuration of the [Im-C7-C8-C9-C10] moiety.

6.4.- Discussion

The underlying reason for the observed rich magnetic behaviour of the systems **100P** and **100As** lies in their ability to exhibit ordered arrangement 1 and less ordered arrangement 2 in addition to the SCO transition between the HS and LS spin states. Both systems exhibit SCO behaviour synchronized with a structural PT featuring very slow kinetics compared with that of the SCO. Playing with this kinetics, the bistability domains of both transitions can overlap in temperature or can occur separately so that **100P** and **100As** can potentially form phases LS¹, HS¹ and LS², HS² and display transitions between them.

Indeed, for **100P** the phase bistability is operative in a temperature region overlapping with the SCO bistability giving transition $HS^1 \rightarrow LS^2$. Additionally, a narrow temperature window exists where the transition $HS^1 \rightarrow LS^1$ occurs without change of the lattice arrangement. Moreover, the transition $LS^1 \rightarrow LS^2$ is operative without change of the spin state but with a change of the lattice arrangement. The experimental data show possibility of such transitions also for **100As** and, additionally, at higher temperature another structural rearrangement $HS^1 \rightarrow HS^2$ occurs within the HS state.

Thus, both systems can exhibit "ordered" LS^1 and HS^1 phases and "disordered" LS^2 and HS^2 phases. For **100As** we observe all four phases, for **100P** all except the HS^2 , which is shifted so much in temperature that it does not occur below the melting temperature of **100P**. The transition to the arrangement 2 phase occurs because the disordered *n*-butyl chains increase the entropy and decrease the Gibbs free energy of the system. The more prone tendency of **100As** to disorder can be associated with the small volume expansion of the lattice induced by the $PF_6^- \rightarrow AsF_6^-$ substitution and evidenced by the much faster kinetics featuring the $LS^2 \leftrightarrow HS^1$ transition. The slightly larger AsF_6^- anions separate the SCO complex cations, thereby facilitating their *n*-butyl groups to become disordered and favoring the phases LS^2 and HS^2 . This is corroborated by the transition $HS^1 \leftrightarrow HS^2$ (not coupled with the SCO) and by the fact that this transition is not observed for **100P**.

The shift of the SCO and phase bistabilities of the PT on passing from **100P** to **100As** might be rationalized considering the "chemical pressure" (CP) of the anions as a qualitative measure of average intermolecular interactions and electrostatic pressure in the lattices. Indeed, external pressure applied to **100P** progressively shifts $HS^1 \leftrightarrow LS^2$ transition toward higher temperature and, more importantly, changes the hysteresis loop, which becomes two-step similarly to **100As**. It is worth mentioning that the positive CP generated by application of "external" hydrostatic pressure increases the intermolecular contacts and stabilises the LS state by reducing the unit cell volume. In contrast, similar positive "internal" CP is generated upon $PF_6^- \rightarrow AsF_6^-$ substitution, which involves an increase of the unit cell volume in 42.44 \AA^3 . To explain this apparent paradox we compared the crystal structures of **100P** and **100As** at the same temperature (230 K) making use of the Hirshfeld surface analysis.^[17] This analysis shows that the percentage of C...F contacts doubles when replacing PF_6^- with AsF_6^- (more moderate increase of contacts is also observed for F...H

and C...H) (Figure S9, Table S4). This can be rationalised from the estimated void space, 46.54 and 43.83 Å³, available for **100P** and **100As**, respectively.^[17] Interestingly, the smaller empty space found for **100As** shows that void space does not increase in parallel with of the unit cell volume increase. This the reason why the number of F...C contacts is larger for **100As**. A fact in line with the observed increase of CP in **100As**.

The similar chemical nature of both compounds makes them well suited for the study of isomorphous series with varying ratio between the both. At fixed scan rate of 2 K min⁻¹ the kinetics of transitions HS¹ → LS¹ and HS¹ → LS² (memory channels A and B, respectively) is dramatically affected by changing the PF₆⁻ : AsF₆⁻ ratio. This is reflected in the changing contribution of the two channels to the shape of the observed hysteresis loops. Progressively increasing the amount of AsF₆⁻ favours the SCO with structural rearrangement and makes observation of the process HS¹ → LS¹ impossible on passing a threshold concentration. Thus, for **71As** the coalescence of the two hysteretic spin transitions vanishes affording a rectangular well-shaped hysteresis loop, which corresponds to the transition HS¹ → LS² where the structural rearrangement is realized.

Opposite to the [Fe(*n*Bu-im)₃(tren)](P_{1-y}As_yF₆)₂ substituted systems, where included AsF₆⁻ anions create “positive” internal pressure and shift SCO upward in temperature, metal substitution in [Fe_{1-x}M_x(*n*Bu-im)₃(tren)](PF₆)₂ (**21Zn** or **17Ni**) can be considered as creating “negative” internal pressure, stabilizing low temperature SCO. Indeed, as follows from the experimental data, dilution with Zn^{II} or Ni^{II} ions, both more voluminous than the LS Fe^{II} ion, predictably favours SCO transition to the more voluminous LS¹ phase and disfavours compact LS² (cell volume 1994.7(5) and 1950.8(15) Å³, respectively)^[11b] and makes the low temperature transition LS¹ ↔ HS¹ the only option for the system. Thus, metal dilution with the Ni^{II} or Zn^{II} stabilizes the voluminous arrangement 1 in both spin states and effectively suppresses transition to the arrangement 2.

6.5.- Conclusion

In summary, we have reported an isomorphically substituted series of unusual Fe^{II} SCO complex displaying two memory channels. We found that metal substitution with Ni^{II} or Zn^{II} selectively favours arrangement 1 in both spin states, thus promoting a low temperature

hysteretic SCO transition (channel A). On the other hand, substitution of its PF_6^- anion with AsF_6^- promotes high temperature hysteretic SCO transition (channel B) as a result of favoured transformation to disordered arrangement 2 in the LS state, and thus high temperature hysteretic transition is preferred.

For the first time, we demonstrate that decoupling of two synchronous cooperative events such as SCO and intrinsic structural phase transition can be chemically achieved by choosing the appropriate isomorphous substitution (metal ion or anion in the present case) to selectively discriminate between two separate hysteretic SCO behaviours. The design of fully controllable smart materials able to respond to external stimuli in a desired way is a challenging target in materials science. The results here reported supports the idea that bistable molecular materials exhibiting synergetic interplay between two or more phase transitions in the same crystal are particularly well-suited to this end.

6.6.- Experimental section

All chemicals were purchased from commercial sources and used without further purification. 1-Butyl-1*H*-imidazole-2-carbaldehyde and the complexes were synthesized according to the reported procedures.^[11b]

6.6.1.- Synthesis of 100As

A filtered solution of $\text{FeCl}_2 \cdot 4\text{H}_2\text{O}$ (0.043 g, 0.21 mmol) in absolute ethanol (5 mL) was added dropwise to a boiling solution of 1-butyl-1*H*-imidazole-2-carbaldehyde (0.10 g, 0.65 mmol), tris(2-ethanolamine)amin (tren) (0.031 g, 0.21 mmol) and $[\text{TBA}]\text{AsF}_6$ (0.17 g, 0.43 mmol) in 5 ml of absolute ethanol. The resulting dark red-purple solution was stirred for 5 min. After keeping the solution for several days at 25 °C in a thermostat bath, well-shaped red-brown crystals of the product were formed and isolated. Calcd for $\text{C}_{30}\text{H}_{48}\text{As}_2\text{F}_{12}\text{FeN}_{10}$: C, 36.68; H, 5.01; N, 14.10. Found: C, 36.39; H, 5.35; N, 14.25.

6.6.2.- Synthesis of substituted compounds

The series $[\text{Fe}(\text{nBu-im})_3(\text{tren})](\text{P}_{1-y}\text{As}_y\text{F}_6)_2$ was synthesized in analogy to **100P** and **100As** by adding the appropriate mixture of $[\text{TBA}]\text{AsF}_6$ and $[\text{TBA}]\text{PF}_6$ salts to the freshly prepared ethanolic solution of the complex cation $[\text{Fe}(\text{nBu-im})_3\text{tren}]^{2+}$. Energy-dispersive X-ray spectroscopy (EDXS) was used to confirm the P and As stoichiometry of the formed crystals: **100P** (100% P, 0% As); **12As** (88% P, 12% As); **22As** (78% P, 22% As); **38As** (62% P, 38% As); **46As** (54% P, 46% As); **56As** (44% P, 56% As); **63As** (37% P, 63% As); **71As** (29% P, 71% As); **86As** (14% P, 86% As); **100As** (0% P, 100% As). The successive replacement $\text{PF}_6^- \leftrightarrow \text{AsF}_6^-$ was semi-quantitatively monitored following their characteristic IR modes: $\nu_1(\text{PF}_6^-) = 839 \text{ cm}^{-1}$ (vs), $\nu_2(\text{PF}_6^-) = 557 \text{ cm}^{-1}$, $\nu_1(\text{AsF}_6^-) = 700 \text{ cm}^{-1}$ (vs) (see Figure S10).

Similarly, the solid solutions $[\text{Fe}_{1-x}\text{M}_x(\text{nBu-im})_3(\text{tren})](\text{PF}_6)_2$ ($\text{M} = \text{Zn}^{\text{II}}, \text{Ni}^{\text{II}}$) were confirmed via EDXS analysis: **17Ni** (83% Fe, 17% Ni), **21Zn** (79% Fe, 21% Zn).

6.6.3.- Magnetic measurements

Variable-temperature magnetic susceptibility data for bulk crystalline/microcrystalline samples $[\text{Fe}_{1-x}\text{M}_x(\text{nBu-im})_3(\text{tren})](\text{P}_{1-y}\text{As}_y\text{F}_6)_2$ (ca. 20 mg) were recorded with a Quantum Design MPMS2 SQUID susceptometer equipped with a 7 T magnet, operating at 1 T and at temperatures 10–400 K. Experimental susceptibilities were corrected for diamagnetism of the constituent atoms by the use of Pascal's constants. The LIESST experiments were performed at 10 K in a commercial sample holder (Quantum Design Fiber Optic Sample Holder), wherein a quartz bucket containing 0.75 mg of microcrystals of **100As**, was held against the end of a quartz fiber coupled with a red laser (633 nm). The raw data was corrected for a background arising from the sample holder. The resulting magnetic signal was calibrated by scaling to match obtained high temperature values with those of bulk sample. Magnetic measurements under pressure were performed on **100P** using a hydrostatic pressure cell made of hardened beryllium bronze with silicon oil as the pressure transmitting medium and operating over the pressure range 10^5 – 10^9 Pa.^[18] The compound, 10 mg, was packed in a cylindrically shaped sample holder (1 mm in diameter and 5-7 mm in length) made up of very thin aluminum foil. The pressure was calibrated using the transition temperature of superconducting lead of high-purity 99.999%.^[19]

6.6.4.- Calorimetric measurements

Differential scanning calorimetry measurements were performed using a Mettler Toledo DSC 821e calorimeter. Low temperatures were obtained with an aluminium block attached to the sample holder, refrigerated with a flow of liquid nitrogen and stabilized at a temperature of 110 K. The sample holder was kept in a dry box under a flow of dry nitrogen gas to avoid water condensation. The measurements were carried out using around 12 mg of microcrystalline **100As** sealed in aluminium pans with a mechanical crimp. Temperature and heat flow calibrations were made with standard samples of indium by using its melting transition (429.6 K, 28.45 J g⁻¹). An overall accuracy of ±0.2 K in temperature and ±2% in the heat capacity is estimated. The uncertainty increases for the determination of the anomalous enthalpy and entropy due to the subtraction of an unknown baseline.

6.6.5.- Powder X-ray diffraction measurements (PXRD)

PXRD measurements were performed on a PANalytical Empyrean X-ray powder diffractometer (monochromatic CuK α radiation).

6.6.6.- Single crystal X-ray diffraction

Single-crystal X-ray data were collected with an Oxford diffraction supernova single crystal diffractometer using graphite monochromated MoK α radiation ($\lambda = 0.71073 \text{ \AA}$). A multi-scan absorption correction was performed. The structures were solved by direct methods using SHELXS-2014 and refined by full-matrix least squares on F^2 using SHELXL-2014.^[20] Non-hydrogen atoms were refined anisotropically and hydrogen atoms were placed in calculated positions refined using idealized geometries (riding model) and assigned fixed isotropic displacement parameters.

6.7.- References

- [1] (a) Bennemann, K. H. *J. Phys.: Condens. Matter*, **2011**, 23, 073202. (b) Sato, O. *Nat. Chem.* **2016**, 8, 644. (c) Koshihara, S.-y. *J. Phys.: Conf. Ser.* **2005**, 21, 7.

- [2] (a) König, E. *Struct. Bonding* **1991**, 76, 51. (b) Gütlich, P.; Hauser, A.; Spiering, H. *Angew. Chem., Int. Ed. Engl.* **1994**, 33, 2024. (c) Real, J. A.; Gaspar, A. B.; Niel, V.; Muñoz, M. C. *Coord. Chem. Rev.* **2003**, 236, 121. (d) *Spin Crossover in Transition Metal Compounds*, ed. Gütlich, P.; Goordwin, H. *Top. Curr. Chem.* **2004**, 233-235. (e) Real, J. A.; Gaspar, A. B.; Muñoz, M. C. *Dalton Trans.* **2005**, 2062. (f) Halcrow, M. A. *Polyhedron.* **2007**, 26, 3523. (g) Bousseksou, A.; Molnár, G.; Salmon, L.; Nicolazzi, W. *Chem. Soc. Rev.* **2011**, 40, 3313.
- [3] (a) Kahn, O.; Martínez, J. *Science.* **1998**, 279, 44. (b) Ohba, M.; Yoneda, K.; Agustí, G.; Muñoz, M. C.; Gaspar, A. B.; Real, J. A.; Yamasaki, M.; Ando, H.; Nakao, Y., Sakaki, S.; Kitagawa, S. *Angew. Chem., Int. Ed.* **2009**, 48, 4767. (c) Salmon, L.; Molnár, G.; Zitouni, D.; Quintero, C.; Bergaud, C.; Micheau, J.-C.; Bousseksou, A. *J. Mater. Chem.* **2010**, 20, 5499. (d) Prins, F.; Monrabal-Capilla, M.; Osorio, E. A.; Coronado, E.; Van der Zant, H. S. J. *Adv. Mater.* **2011**, 23, 1545. (e) Matsuda, M.; Kiyoshima, K.; Uchida, R.; Kinoshita, N.; Tajima, H. *Thin Solid Films*, **2013**, 531, 451. (f) Shepherd, H. J.; Gural'skiy, I. A.; Quintero, C. M.; Tricard, S.; Salmon, L.; Molnár, G.; Bousseksou, A. *Nat. Commun.* **2013**, 4, 2607.
- [4] (a) Matsukizono, H.; Kuroiwa, K.; Kimizuka, N. *Chem. Lett.* **2008**, 37, 446. (b) Lochenie, C.; Schotz, K.; Pnzer, F.; Kurz, H.; Maier, B.; Puchtler, F.; Agarwal, S.; Kohler, A.; Weber, B. *J. Am. Chem. Soc.* **2018**, 140, 700. (c) Delgado, T.; Meneses-Sánchez, M.; Piñeiro-López, L.; Bartual-Murgui, C.; Muñoz, M. C.; Real, J. A. *Chem. Sci.* **2018**, 9, 8446.
- [5] (a) Chen, Y.-C.; Meng, Y.; Ni, Z.-P.; Tong, M.-L. *J. Mater. Chem. C* **2015**, 3, 945. (b) Koo, Y.-S.; Galán-Mascarós, J. R. *Adv. Mater.* **2014**, 26, 6785.
- [6] Bonhommeau, S.; Lacroix, P. G.; Talaga, D.; Bousseksou, A.; Seredyuk, M.; Fritsky, I. O.; Rodríguez, V. *J. Phys. Chem. C* **2012**, 116, 11251.
- [7] (a) Molnár, G.; Rat, S.; Salmon, L.; Nicolazzi, W.; Bousseksou, A. *Adv. Mater.* **2018**, 30, 17003862. (b) Senthil Kumar, K.; Ruben, M. *Coord. Chem. Rev.* **2017**, 346, 176.
- [8] (a) Tayagaki, T.; Galet, A.; Molnár, G.; Muñoz, M. C.; Zwick, A.; Tanaka, K.; Real, J. A.; Bousseksou, A. *J. Phys. Chem. B.* **2005**, 109, 14859. (b) Baldé, C.; Desplanches, C.; Gütlich, P.; Freysz, E.; Létard, J. F. *Inorg. Chim. Acta* **2008**, 361, 3529. (c) Yu, Z.; Kuroda-Sowa, T.; Kume, H.; Okubo, T.; Maekawa, M.; Munakata, M. *Bull. Chem. Soc.*

- Jpn.* **2009**, *82*, 333. (d) Chakraborty, P.; Enachescu, C.; Humair, A.; Egger, L.; Delgado, T.; Tissot, A.; Guenee, L.; Besnard, C.; Bronisz, R.; Hauser, A. *Dalton Trans.* **2014**, *43*, 17786. (e) Baldé, C.; Desplanches, C.; Létard, J. F.; Chastanet, G. *Polyhedron* **2017**, *123*, 138.
- [9] (a) Tovee, C. A.; Kilner, C. A.; Thomas, J. A.; Halcrow, M. A. *CrystEngCommun* **2009**, *11*, 2069. (b) Halcrow, M. A. *Chem. Commun.* **2010**, *46*, 4761.
- [10] (a) Braga, D.; Cojazzi, G.; Paolucci, D.; Grepioni, F. *Chem. Commun.* **2001**, 803. (b) Zhao, M.; Peng, H.; Hu, J.; Han, Z. *Sens. Actuators B* **2008**, *129*, 953. (c) Zhang, R.; Jifan, H.; Zhouxiang, H.; Ma, Z.; Zhanlei, W.; Zhang, Y.; Hongwei, Q. *J. Rare Earths*, **2010**, *28*, 591. (d) Pajerowski, D. M.; Yamamoto, T.; Einaga, Y. *Inorg. Chem.* **2012**, *51*, 3648. (e) Sun, Y.; Zhu, Z.; Li, J.; Gao, S.; Xia, H.; You, Z.; Wang, Y.; Tu, C. *Opt. Mater.* **2015**, *49*, 85. (f) Chorazy, S.; Stanek, J. J.; Stanek, W.; Majcher, A. M.; Rams, M.; Koziel, M.; Juszynska-Galazka, E.; Nakabayashi, K.; Ohkoshi, S.-I.; Sieklucka, B.; Podgajny, R. *J. Am. Chem. Soc.* **2016**, *138*, 1635.
- [11] (a) Seredyuk, M.; Gaspar, A. B.; Ksenofontov, V.; Galyametdinov, Y.; Kusz, J.; Gütllich, P. *J. Am. Chem. Soc.* **2008**, *130*, 1431. (b) Seredyuk, M.; Muñoz, M. C.; Romero-Morcillo, T.; Gaspar, A. B.; Real, J. A. *Chem. – Eur. J.* **2013**, *19*, 6591. (c) Seredyuk, M.; Muñoz, M. C.; Ksenofontov, V.; Gütllich, P.; Galyametdinov, Y.; Real, J. A. *Inorg. Chem.* **2014**, *53*, 8442. (d) Romero-Morcillo, T.; Seredyuk, M.; Muñoz, M. C.; Real, J. A. *Angew. Chem., Int. Ed.* **2015**, *54*, 14777. (e) Seredyuk, M.; Znovnyak, K.; Muñoz, M. C.; Galyametdinov, Y.; Fritsky, I. O.; Real, J. A. *RSC Adv.* **2016**, *6*, 39627. (f) Delgado, T.; Tissot, A.; Guénée, L.; Hauser, A.; Valverde-Muñoz, F. J.; Seredyuk, M.; Real, J. A.; Pillet, S.; Bendeif, E.-E.; Besnard, C. *J. Am. Chem. Soc.* **2018**, *140*, 12870.
- [12] (a) Jeftic, J.; Romstedt, H.; Hauser, A. *Phys. Chem. Solids* **1996**, *57*, 1743. (b) Hayami, S.; Komatsu, Y.; Shimizu, T.; Kamihata, H.; Lee, Y. H. *Coord. Chem. Rev.* **2011**, *255*, 1981. (c) Schlamp, S.; Weber, B.; Naik, A. D.; Garcia, Y. *Chem. Commun.*, **2011**, *47*, 7152. (d) Yamasaki, M.; Ishida, T. *J. Mater. Chem. C*, **2015**, *3*, 7784. (e) Gaspar, A. B.; Seredyuk, M. *Coord. Chem. Rev.* **2014**, *268*, 41. (f) Rosario-Amorin, D.; Dechambenoit, P.; Bentaleb, A.; Rouzières, M.; Mathonière, C.; Clérac, R. *J. Am. Chem. Soc.* **2018**, *140*, 98. (g) Fujinami, T.; Nishi, K.; Hamada, D.; Murakami, K.; Matsumoto, N.; Iijima, S.; Kojima, M.; Sunatsuki, Y. *Inorg. Chem.* **2015**, *54*, 7291. (h) Ueno, T.; Ii, Y.; Fujinami, T.; Matsumoto, N.; Iijima, S.; Sunatsuki, Y. *Polyhedron* **2017**, *136*, 13. (i) Weselski, M.,

- Ksiazek, M.; Rokosz, D., Dreczko, A.; Kusz, J., Bronisz, R. *Chem. Commun.* **2018**, *54*, 3895.
- [13] Létard, J. F.; Guionneau, P., Nguyen, O.; Costa, J. S.; Marcen, S.; Chastanet, G.; Marchivie, M.; Goux-Capes, L. *Chem. – Eur. J.* **2005**, *11*, 4582.
- [14] Ksenofontov, V.; Gaspar, A. B.; Gütllich, P. *Top. Curr. Chem.* **2004**, *235*, 23.
- [15] Bondi, A. *J. Phys. Chem.* **1964**, *68*, 441.
- [16] Juhász, G.; Matsuda, R.; Kanegawa, S.; Inoue, K.; Sato, O.; Yoshizawa, K. *J. Am. Chem. Soc.* **2009**, *131*, 4560.
- [17] (a) Turner, M. J.; Mckinnon, J. J.; Wolff, S. K.; Grimwood, D. J.; Spackman, P. R.; Jayatilaka, D.; Spackman, M. A. *CrystalExplorer 17.5*. The University of Western Australia **2018** (b) Turner, M. J.; Mckinnon, J. J.; Jayatilaka, D.; Spackman, P. R. *CrystEngComm*, **2011**, *13*, 1804.
- [18] Baran, M.; Dyakonov, V. P.; Gladczuk, L., Levchenko, G. G.; Piechota, S.; Szymczak, G. *Phys. C*, **1995**, *241*, 383.
- [19] Eiling, A.; Schilling, J. S. *J. Phys. F: Met. Phys.* **1981**, *11*, 623.
- [20] Sheldrick, G. M. *Acta Crystallogr., Sect. C: Struct. Chem.* **2015**, *71*, 3.

6.8.- Supporting Information

Table S1.- Crystallographic parameters for 100As, 71As, and 100Ni.

| | 100As | | 71As | | | 100Ni |
|---|---|-------------|--|---------------------|-----------|--|
| <i>T</i> (K) | 230 K | 300 K | 230 K | 120 K (quenched) | 157 K | 110 K |
| Empirical formula | C ₃₀ H ₄₈ As ₂ F ₁₂ FeN ₁₀ | | C ₃₀ H ₄₈ As _{1.42} F ₁₂ FeN ₁₀ P _{0.58} | | | C ₃₀ H ₄₈ F ₁₂ N ₁₀ NiP ₂ |
| Mr | 982.47 | | 956.98 | | | 897.43 |
| Crystal system | triclinic | | triclinic | | | triclinic |
| Space group | <i>P</i> 1 | | <i>P</i> 1 | | | <i>P</i> 1 |
| <i>a</i> (Å) | 9.4189(8) | 9.6140(7) | 9.411(3) | 9.2858(5) | 9.588(3) | 9.1245 (3) |
| <i>b</i> (Å) | 10.3506(9) | 10.2571(6) | 10.309(3) | 10.4090(6) | 10.065(2) | 10.5150 (2) |
| <i>c</i> (Å) | 22.444(2) | 21.9999(13) | 22.379(5) | 22.272(2) | 21.074(4) | 21.6376 (4) |
| α | 91.428(7) | 91.522(5) | 91.520(11) | 83.796(5) | 93.89(2) | 83.769 (2) |
| β | 100.894(7) | 96.193(6) | 100.995(12) | 78.275(5) | 93.68(2) | 78.852 (2) |
| γ | 99.001(7) | 98.456(6) | 98.955(16) | 81.416(5) | 100.47(2) | 81.928 (2) |
| <i>V</i> (Å ³) | 2118.8(3) | 2131.3(2) | 2101.8(11) | 2077.5(2) | 1989.2(8) | 2009.56 (9) |
| <i>Z</i> | 2 | | 2 | | | 2 |
| <i>F</i> (000) | 996 | 996 | 976.0 | 975 | 975 | 928 |
| <i>D</i> _c (mg cm ⁻³) | 1.540 | 1.531 | 1.514 | 1.530 | 1.598 | 1.483 |
| μ (Mo-K α)(mm ⁻¹) | 1.993 | 1.982 | 1.597 | 1.597 | 1.668 | |
| No. of total reflections [<i>I</i> >2 σ (<i>I</i>)] | 5545 | 3523 | 10380 | 4016 | 2958 | 6677 |
| <i>R</i> [<i>I</i> >2 σ (<i>I</i>)] | 0.0646 | 0.0903 | 0.0563 | 0.0516 | 0.1247 | 0.042 |
| <i>wR</i> [<i>I</i> >2 σ (<i>I</i>)] | 0.1470 | 0.2341 | 0.1406 | 0.0969 | 0.2859 | 0.131 |
| <i>S</i> | 1.013 | 0.946 | 1.050 | 1.047 | 1.008 | 0.72 |

Table S2.- Selected bond lengths (Å) and angles (°) for **100As** and **71As** at indicated temperatures.

| | 100As | | 71As | | |
|----------|----------------------------------|----------------------------------|---|----------------------------------|----------------------------------|
| | 230 K (HS ¹) | 300 K (HS ²) | 120 K (HS ¹ + LS ¹) | 157 K (LS ²) | 230 K (HS ²) |
| Fe-N1 | 2.228(4) | 2.219(7) | 2.206(5) | 1.962(11) | 2.222(3) |
| Fe-N2 | 2.184(4) | 2.185(6) | 2.164(4) | 1.969(10) | 2.181(3) |
| Fe-N3 | 2.214(4) | 2.212(6) | 2.204(4) | 1.967(10) | 2.215(3) |
| Fe-N4 | 2.194(4) | 2.173(7) | 2.194(5) | 1.948(11) | 2.196(3) |
| Fe-N5 | 2.174(4) | 2.165(6) | 2.154(3) | 1.959(10) | 2.173(3) |
| Fe-N6 | 2.198(4) | 2.169(7) | 2.190(4) | 1.980(9) | 2.192(3) |
| <Fe-N> | 2.199 | 2.187 | 2.185 | 1.964 | 2.197 |
| N1-Fe-N2 | 75.0(2) | 74.9(2) | 75.4(2) | 80.6(4) | 74.99(10) |
| N1-Fe-N3 | 92.9(2) | 91.6(2) | 93.8(2) | 93.0(4) | 92.64(11) |
| N1-Fe-N4 | 167.6(2) | 166.4(3) | 168.9(2) | 173.8(4) | 167.34(11) |
| N1-Fe-N5 | 84.4(2) | 85.2(2) | 84.5(2) | 91.4(4) | 84.38(11) |
| N1-Fe-N6 | 88.2(2) | 88.9(2) | 87.8(2) | 89.1(4) | 88.57(11) |
| N2-Fe-N3 | 98.2(2) | 97.8(2) | 97.60(14) | 92.1(4) | 98.22(11) |
| N2-Fe-N4 | 102.5(2) | 103.4(2) | 102.4(2) | 96.0(4) | 102.73(11) |
| N2-Fe-N5 | 158.4(2) | 159.7(2) | 159.0(2) | 171.8(4) | 158.30(11) |
| N2-Fe-N6 | 97.1(2) | 99.5(2) | 97.19(14) | 96.6(4) | 96.78(11) |
| N3-Fe-N4 | 75.3(2) | 75.2(2) | 75.6(2) | 81.9(4) | 75.24(10) |
| N3-Fe-N5 | 89.2(2) | 86.7(2) | 89.49(14) | 90.3(4) | 89.26(11) |
| N3-Fe-N6 | 164.4(2) | 162.1(2) | 165.05(13) | 171.3(4) | 164.74(11) |
| N4-Fe-N5 | 99.0(2) | 97.0(2) | 98.4(2) | 92.1(4) | 98.87(11) |
| N4-Fe-N6 | 104.3(2) | 104.7(3) | 103.3(2) | 96.5(4) | 104.08(10) |
| N5-Fe-N6 | 75.4(2) | 75.5(3) | 75.85(14) | 81.3(4) | 75.72(11) |

Table S3.- Selected bond lengths (Å) and angles (°) for **100Ni** at 110 K.

| 100Ni | |
|--------------|-----------|
| Ni-N1 | 2.100(2) |
| Ni-N2 | 2.119(2) |
| Ni-N3 | 2.098(2) |
| Ni-N4 | 2.131(2) |
| Ni-N5 | 2.064(2) |
| Ni-N6 | 2.147(2) |
| <Fe-N> | 2.110 |
| | |
| N1-Ni-N2 | 78.43(6) |
| N1-Ni-N4 | 172.44(6) |
| N1-Ni-N6 | 88.44(6) |
| N2-Ni-N4 | 96.71(6) |
| N2-Ni-N6 | 94.45(6) |
| N3-Ni-N1 | 95.96(6) |
| N3-Ni-N2 | 95.34(6) |
| N3-Ni-N4 | 78.62(6) |
| N3-Ni-N6 | 169.90(6) |
| N4-Ni-N6 | 97.76(6) |
| N5-Ni-N1 | 89.36(6) |
| N5-Ni-N2 | 166.24(6) |
| N5-Ni-N3 | 92.20(7) |
| N5-Ni-N4 | 96.06(6) |
| N5-Ni-N6 | 78.72(6) |

Table S4.- Percentage of intermolecular contacts and void space obtained from Hirshfeld surface^[1] for **100P** and **100As** at 230 K (HS¹) and 100As at 300 K (HS²).

| Intermolecular contact | 100P (HS¹, 150 K) | 100As (HS¹, 230 K) | 100As (HS², 300 K) |
|---------------------------------|---|--|--|
| C...F (%) | 0.7 | 1.4 | 0.9 |
| F...H (%) | 31.9 | 33.1 | 34.1 |
| N...H (%) | 3.7 | 3.1 | 1.7 |
| C...H (%) | 6.4 | 8.2 | 3.0 |
| Void space/Å ³ [a.2] | 46.54 | 43.83 | 27.10 |
| Unit cell volume/Å ³ | 2076.46 | 2118.8 | 2131.3 |
| % void space ^[b] | 2.24 | 2.07 | 1.27 |

^a Isovalue 0.0003 e AU³; ^b Referred to unit cell volume.

[1] Turner, M. J.; McKinnon, J. J.; Wolff, S. K.; Grimwood, D. J.; Spackma, P. R.; Jayatilaka, D.; Spackman, M. A. *CrystalExplorer17* (2017). University of Western Australia. <http://hirshfeldsurface.net>

[2] Turner, M. J.; McKinnon, J. J.; Jayatilaka, D.; Spackman, M. A. *CrystEngComm* 2011, 13, 1804.

Figure S1.- Dependence of $\chi_M T$ vs T on the scan rate of 100As.

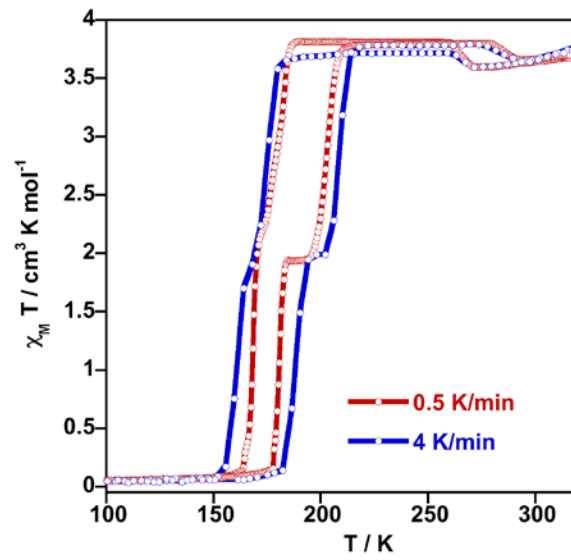


Figure S2.- Pressure dependence of the averaged values of T_c for 100P.

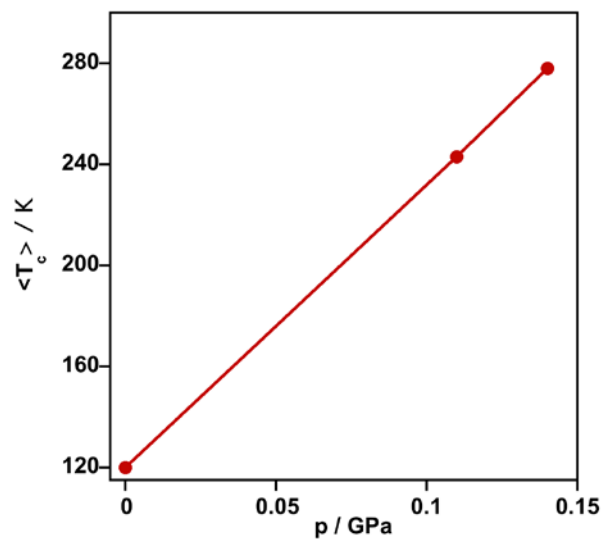


Figure S3.- Temperature dependence of $\chi_M T$ vs T for the molecular alloys **86As**, **63As**, and **12As** (scan rate 2 K min⁻¹).

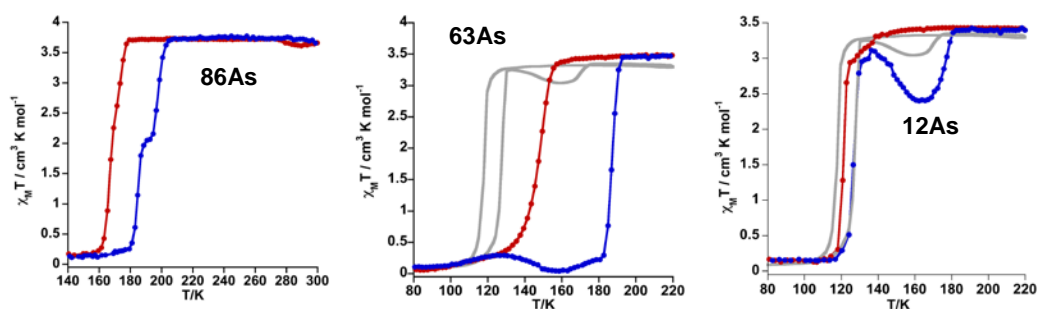


Figure S4.- Dependence of the hysteretic behavior of the HS¹ ↔ HS² structural phase transition on the concentration of three selected samples (**100As**, **71As**, and **56As**).

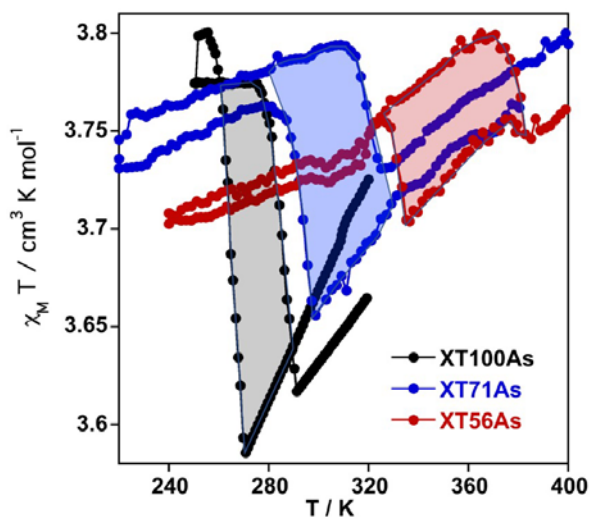


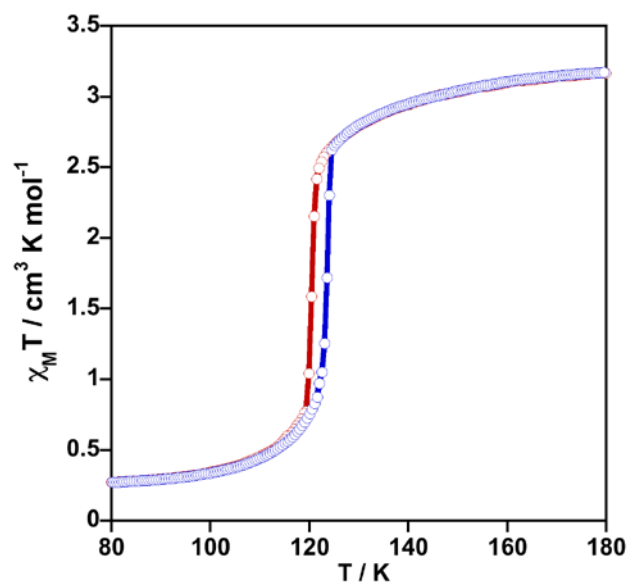
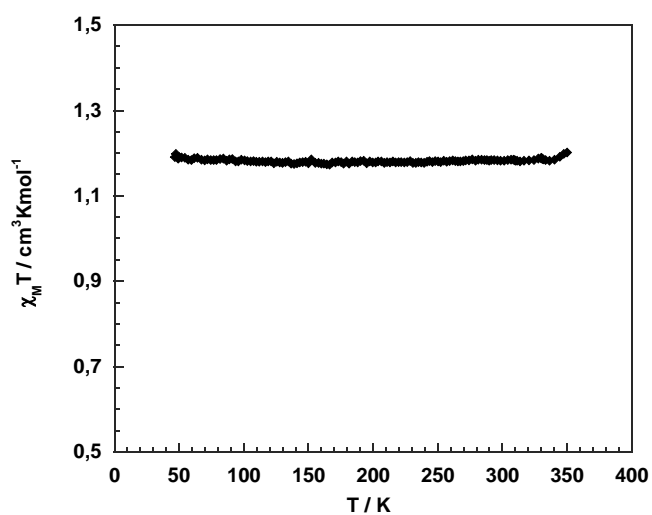
Figure S5.- Temperature dependence of $\chi_M T$ vs T for 17Ni.**Figure S6.-** Temperature dependence of $\chi_M T$ vs T for 100Ni.

Figure S7.- Comparison of cation $[\text{Fe}(n\text{Bu-im})_3(\text{tren})]^{2+}$, illustrating larger disorder of butyl groups in LS^2 and HS^2 phases in comparison with LS^1 and HS^1 , respectively. Brighter color as well as larger size of thermal ellipsoids shown at 50% probability corresponds to larger disorder.

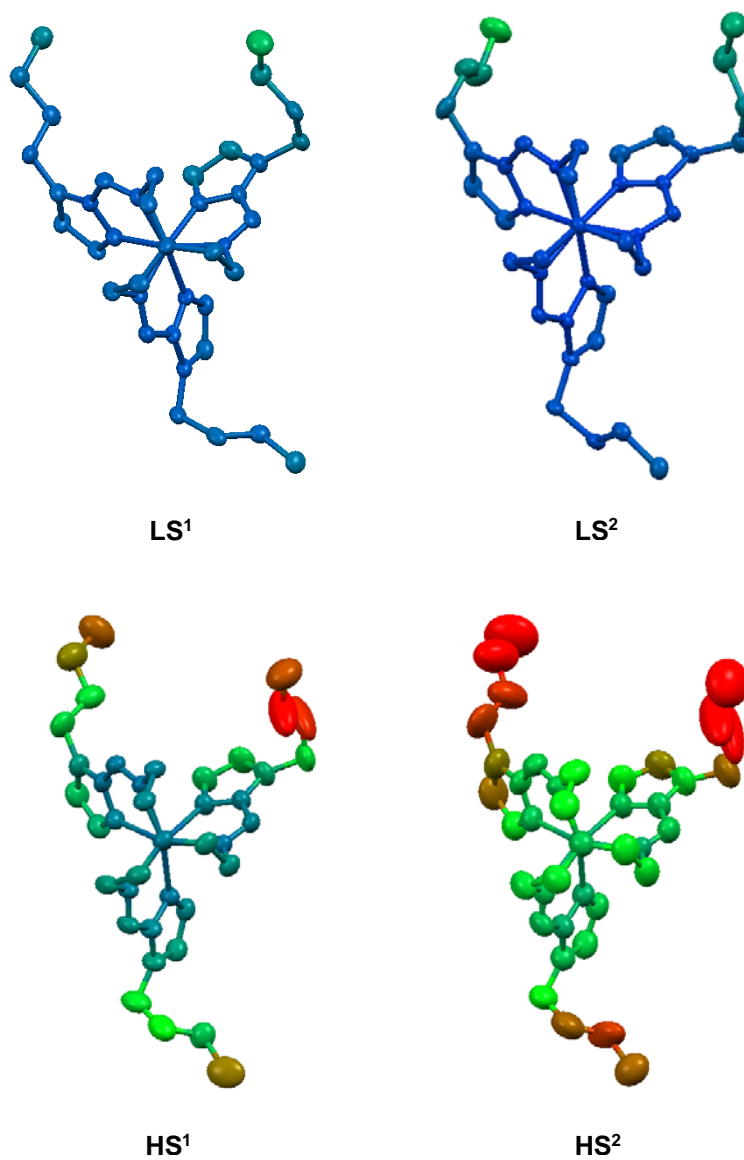


Figure S8.- (a) Projection of the cation and two anions of **100Ni** with atom numbering scheme. Displacement ellipsoids are shown at the 50% probability level. Hydrogen atoms are omitted for clarity. (b) Overlay of the unit cells for **100P** in LS¹ phase (grey bonds) and 100Ni (red bonds and atoms), both structures at 110 K.

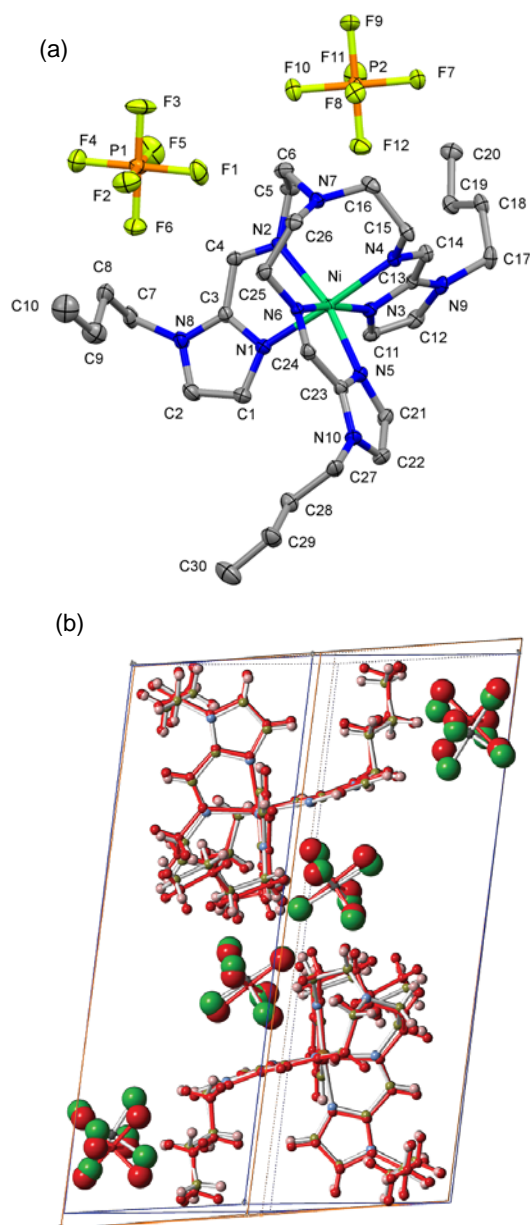


Figure S9. The Hirshfeld surface mapped with d_{norm} for the complex cation $[\text{Fe}(n\text{Bu-im})_3(\text{tren})]^{2+}$ (top) and unit cell voids (bottom) for indicated phases.

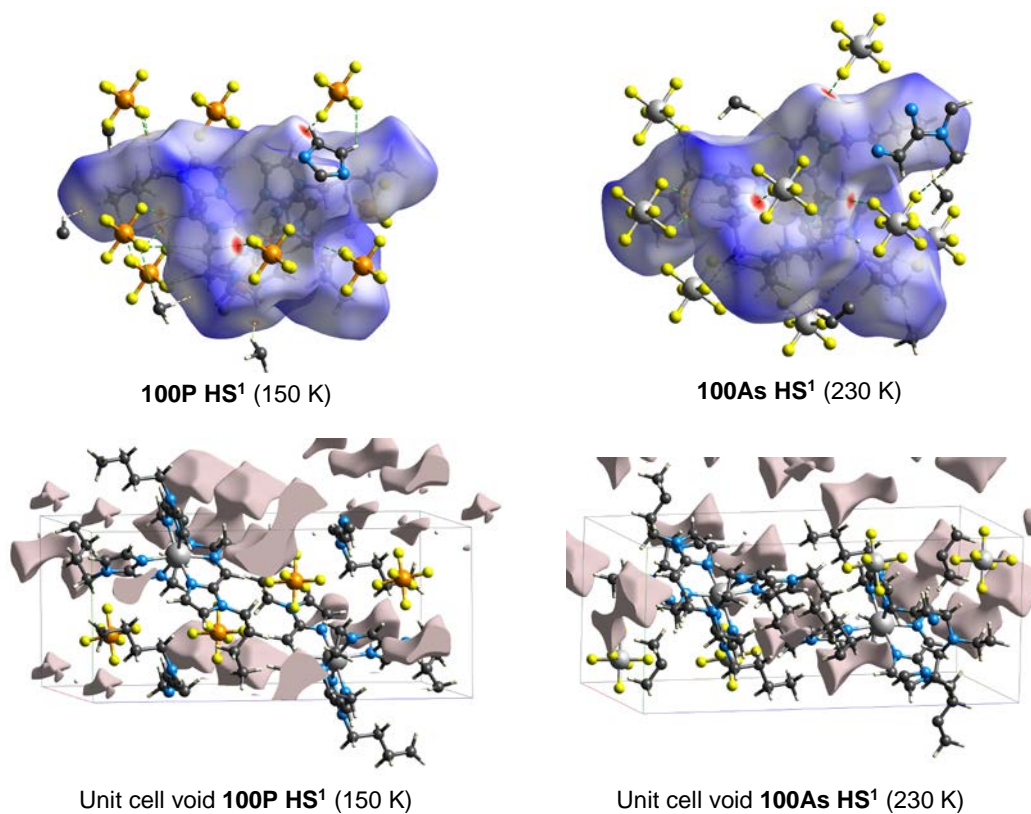
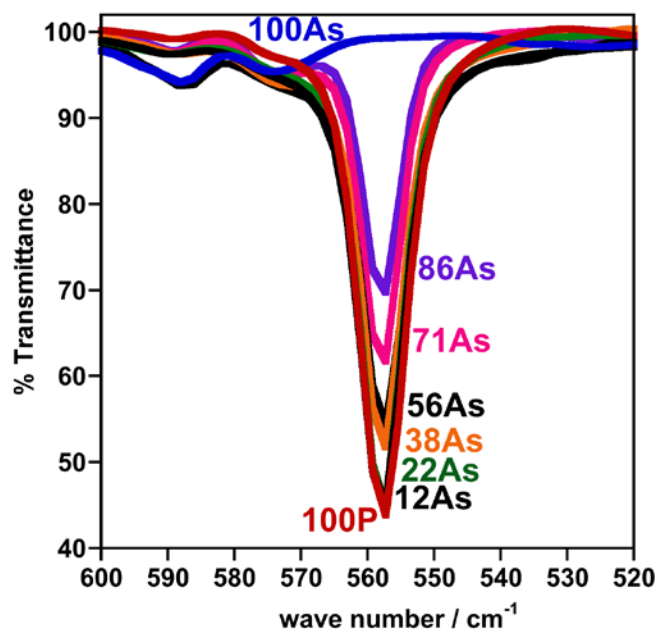
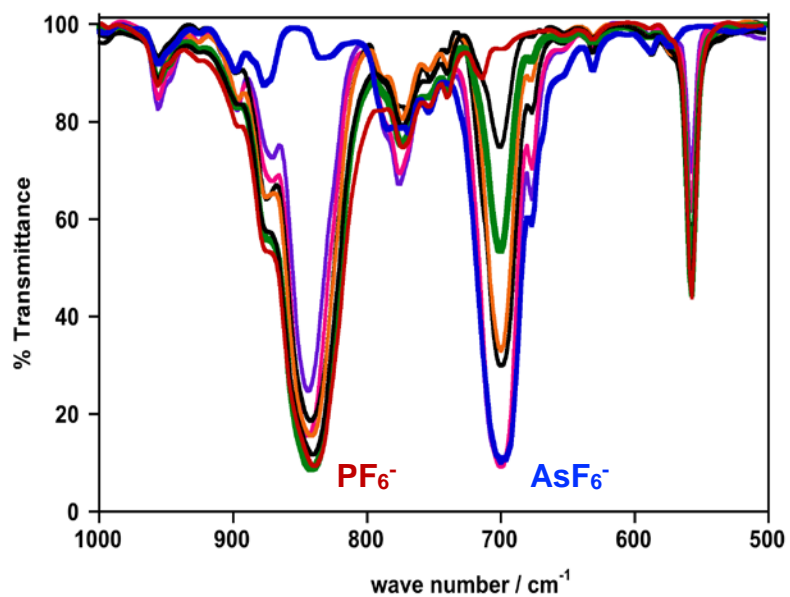
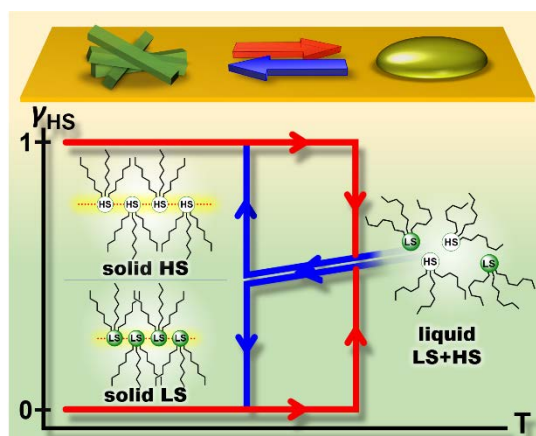


Figure S10.- Infra-red spectra of representative [Fe(nBu-im)3(tren)](P1-yAsyF6)2 molecular alloys.



CAPÍTULO 7

Breaking the rule: access to thermodynamically prohibited “reverse” spin crossover in iron(II) complexes



REVISTA: Angewandte Chemie International Edition (*submitted*)

ÍNDICE DE IMPACTO: 12.257

CAPÍTULO 7

Breaking the rule: access to thermodynamically prohibited “reverse” spin crossover in iron(II) complexes

7.1.- Abstract

Modulation of the spin-crossover (SCO) behaviour by phase transitions in amphiphilic Fe^{II} complexes with aliphatic chains is a relevant strategy to find new cooperative behaviours and potential applications. In this context, we report on a series of charge neutral [Fe^{II}(Lⁿ)₂] meltable complexes based on Schiff bases Lⁿ = **pm2-n** or **pyH-n** derived from condensation of 2-pyrimidinyl ethyl ketone or pyridine aldehyde, respectively, with aromatic hydrazide functionalized with three aliphatic chains C_nH_{2n+1}. In the solid-state [Fe^{II}(**pm2-n**)₂] show two different crystal packing motifs depending on n. However, upon heating, the compounds melt into an isotropic phase and, due to releasing the solid-state effects, reveal identical SCO behaviour for all the compounds with the SCO transition midpoint temperature $T_{1/2} \approx 354$ K. In contrast, in solid state, for short chain compounds (n = 4, 6, 8), $T_{1/2}$ is far above 400 K in solid state, therefore they show an abrupt jump of the susceptibility on passing to the liquid phase. Cooling back shapes regular LS-to-HS (“forward”) spin transition hysteresis loop with the centre shifting down on n growth. For the long chain compounds (n = 10, 12, 14), the solid state $T_{1/2}$ is at ca. 275 K, *i.e.* below the liquid value. Due to this, the long chain compounds on going to liquid phase show thermodynamically prohibited HS-to-LS (“reverse”) spin transition of up to 50% of Fe^{II} ions, while the centre of the shaped hysteresis shifts up with increasing n. This finding is unprecedented and provides a method of guiding the spin transition direction and its location in temperature.

7.2.- Introduction

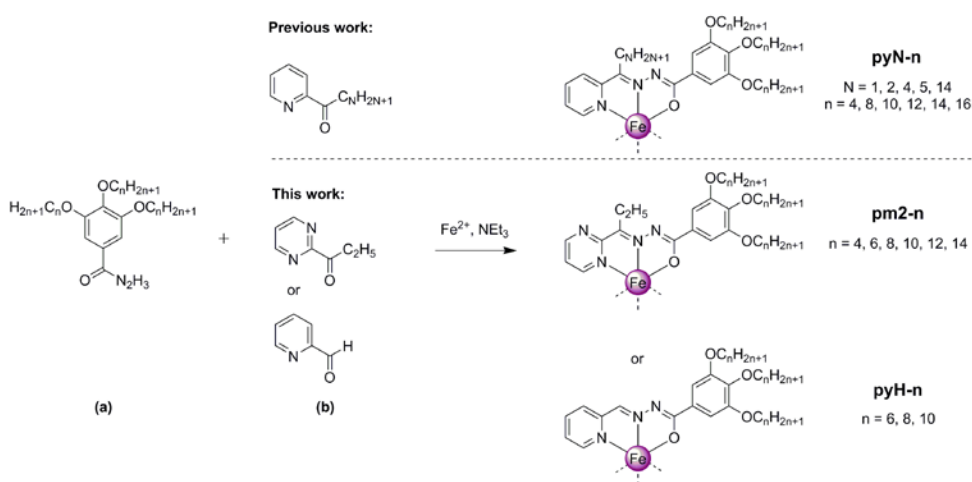
The search for responsive materials with switching properties is a very active research area having prospects for future and emerging technologies.^[1] One of the most investigated switchable molecular materials are pseudo-octahedral Fe^{II} spin-crossover (SCO) complexes, reversibly switching between the low-spin (LS, $t_{2g}^6 e_g^0$) and high-spin (HS, $t_{2g}^4 e_g^2$) electronic states by action of physicochemical stimuli (temperature, pressure, light,

chemical substrates *etc.*).^[2] The LS-to-HS conversion on temperature rise is observed for the absolute majority of the SCO compounds in solution and in solid state.^[2b, c] The reason for this regular or "forward" SCO is that the process is an entropy-driven event due to noticeable metal-to-ligand bond lengths elongation on passing to the HS state and consequent increasing freedom degree of the systems. In the fluid phase the SCO process follows the Boltzmann population of the excited HS state, whereas in solid state, the intermolecular bonding and electrostatic interactions come into play that drastically changes completeness, cooperativity, and occurrence in temperature up to the stabilization of the LS or HS states. The adopted lattice type, the chemical nature of the ligand and the ligand substituents are among the most important factors influencing the SCO behavior.^[3]

Particularly, aliphatic substituents in amphiphile SCO compounds are known to promote formation of two-dimensional lamellar packing with microphase separation to head-groups and aliphatic sublattices.^[4] The latter acts mostly as a buffer diminishing communication between SCO centers and deteriorating cooperativity with some exceptions^[5] but, on the other hand, aliphatic-based Fe^{II} compounds can form liquid crystalline phases due to the low melting character.^[6] That is, aliphatic compounds can exhibit "solid" SCO up to the melting point and, additionally, after melting to liquid crystalline phase can exhibit "liquid" SCO with partially or completely eliminated solid-state effects. If the manifestation of the two SCOs is different at the melting point, a jump-like change of the susceptibility is observed.^[7] Most of the meltable systems reported up to now, however, or suffer irreversibility on passing phase transition (PT) point,^[4, 8] or their melting to liquid crystalline does not substantially change the SCO,^[7a-f, 9] so that on melting/solidifying only a minor variation of the susceptibility is observed.

Further development of the concept of meltable SCO material lead us to understanding of essential criteria to achieve effective synchronicity between phase transition and SCO. We assumed that the compound should be: i) mononuclear Fe(II) complex with aromatic planar substituents for π - π interactions; ii) neutral to avoid buffering action of anions; iii) with optimal number of aliphatic substituents imparting controllable melting character to the compound; iv) meltable directly to isotropic phase omitting ordered liquid crystalline phases. Following this line we reported on a series of aliphatic Fe^{II} neutral complexes **pyN-n**, derivatives of deprotonable Schiff base with the donor set NNO, obtained by condensation of aromatic hydrazide with three aliphatic C_nH_{2n+1} groups (**a**) and 2-pyridinyl

ketones with aliphatic substituent C_nH_{2n+1} (**b**) (see Scheme 1). The complexes exhibit abrupt and perfectly reversible “forward” SCO upon melting to isotropic liquid, so that their magnetic curves resemble regularly observed hysteretic SCO transition of solid state compounds.^[10] We found, that the hysteresis width of the phase transition is a function of n , while the temperature of melting/solidification point is dependent on N . As a continuation of the work we report here new thermally isotropisable Fe^{II} complexes, derivatives of 2-pyrimidinyl ethyl ketone or 2-pyridine aldehyde, **pm2-n** or **pyH-n**, respectively (Scheme 1).



Scheme 1. Synthetic procedure followed for the preparation of the series **pyN-n** ($m = 1, 2, 4, 5, 14$; $n = 4, 8, 10, 12, 14, 16$), **pm2-n** ($n = 4, 6, 8, 10, 12, 14$) and **pyH-n** ($n = 6, 8$).

We found that on melting the complexes can display “forward” and additionally rare “reverse” SCO of Fe^{II} ions as a function of n . The “reverse” SCO is unexpected since it contradicts the fact that increasing temperature should favor the less ordered HS state of Fe^{II} . The thermally induced “reverse” HS-to-LS transition on temperature rise is known for aliphatic Co^{II} complexes undergoing solid-solid transitions,^[11] and also observed for a few Fe^{II} complexes on passing solid-solid^[5b,12] or solid-liquid crystal phase transition.^[7b, 7e] However, the “reverse” SCO on heating is minor for all Fe^{II} compounds reported up to now due to substantial entropy loss on passing back the LS state which disfavors such a transition. This observation even raised the question on the origin of the effect, because the magnitude of the change might be attributed as well to the changing geometry of the

coordination polyhedron and the corresponding g value associated with a crystal-to-crystal phase transition.^[5b, 12] A strong correlation of the spin state on the adopted phase in the complexes reported here, however, demonstrates that the thermodynamically prohibited "reverse" SCO can be a realistic scenario for Fe^{II} compounds too and involve substantial fraction of the Fe^{II} SCO centers.

7.3.- Results and discussion

7.3.1.- Magnetic properties

The magnetic behaviour of compounds **pm2-n**, recorded at 0.5 K min⁻¹ is shown in figure 1 in the form of $\chi_M T$ vs T ($\chi_M T$ is molar susceptibility, T is temperature). Compound **pm2-4** is LS ($\chi_M T = 0$) in the whole temperature range while **pm2-6** and **pm2-8** undergo abrupt conversion from the LS state to paramagnetic state on melting and reach $\chi_M T$ of 2.7 cm³ K mol⁻¹ at 400 K for both compounds. Cooling down the samples leads to abrupt drop of the $\chi_M T$ back to zero at the solidification point. The shaped hysteresis is centered at $T_C^F = 366$ K with the loop width $\Delta T_h^F = 28$ K for **pm2-6**, and 352 K and 29 K, respectively, for **pm2-8** (F stands for "forward" SCO). Since both samples melt into a fluid phase, the SCO after melting is gradual as it obeys simple Boltzmann distribution.^[2a]

Compounds with longer chains behave differently. The homologue **pm2-10** shows gradual increase of $\chi_M T$ alternating with two abrupt drops on heating (Figure 1). Cooling down restores the initial gradual curve with a minor "reverse" SCO hysteresis loop at $T_C^R = 287$ K, $\Delta T_h^R = 12$ K and a major loop at $T_C^R = 346$ K, $\Delta T_h^R = 26$ K (R stands for "reverse" SCO). Compound **pm2-12**, behaves similarly to **pm2-10** but in the low temperature region it shows two minor anomalies of $\chi_M T$ centered at 288 and 320 K related to unidentified solid-solid phase transitions (Figure 1). The main reverse SCO hysteresis loop is located at $T_C^R = 351$ K, $\Delta T_h^R = 21$ K. On the contrary, the compound **pm2-14** does not suffer interfering solid-solid phase transitions in the low temperature region and therefore shows complete regular SCO centered at $T_{1/2} = 275$ K with a 1 K wide hysteresis. Upon further heating a "reverse" SCO occurs with $T_C^R = 355$ K, $\Delta T_h^R = 17$ K. For the three compounds a trend towards rise "reverse" SCO midpoint temperature is observed with the highest value for **pm2-14**.

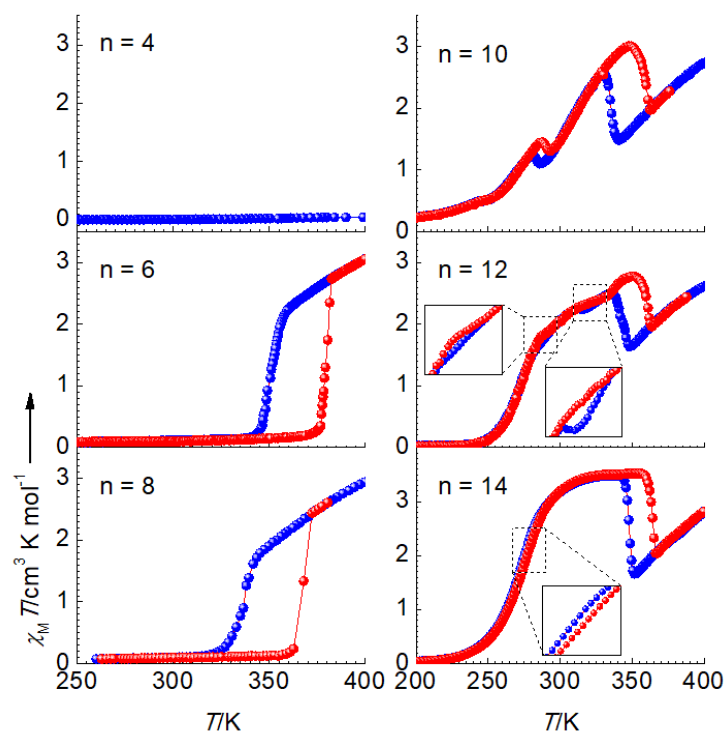


Figure 1. Temperature dependence of $\chi_M T$ vs T for annealed indicated compounds at 0.5 K min^{-1} . The insets show mismatch of cooling (blue) and heating (red) curves.

The percentage of Fe^{II} ions undergoing the phase transition driven SCO was evaluated for compounds **pm2-n** as a difference between $\chi_M T$ values of cooling and heating curves at temperature T_C^{F} or T_C^{R} , accounting that the complete SCO LS-to-HS corresponds to $\Delta\chi_M T = 3.52 \text{ cm}^3 \text{ K mol}^{-1}$ (as measured for **pm2-14** with complete SCO before melting). The calculated values are collected in Table 1.

The “forward” and “reverse” SCO in the studied compounds are sensitive to scan rate as higher rates greatly distort hysteresis loops due to the quenching of samples on cooling and subsequent relaxation on heating (Figure S6), which reflects the occurrence of a kinetically hindered crystallization process of the compounds. On the other hand, both “forward” and “reverse” SCOs are robust as follows from tests performed on samples **pm2-6**

and **pm2-10** over ten heating-cooling cycles (Figure S9). It is well-known, that due to brittleness, the molecular SCO compounds suffer the self-grinding effect resulting in deterioration of SCO characteristics (completeness, abruptness, hysteresis width), which is the major obstacle for a real physical application.^[13] In the case of **pm2-6** or **pm2-10** no sign of fatigue is observed, supposedly as a result of “self-healing” due to complete reversibility of changes on passing the melting/solidification point.

Worth to note, that the **pm2-n** series is not the only NNO-ligand based system displaying a switch from “forward” to “reverse” SCO on changing the aliphatic chain length. We found that compound **pyH-6** displays phase transition driven “forward” SCO at the melting point with $T_c^F = 340$ K and $\Delta T_h^F = 1$ K (Figure S5). For longer chains a gradual SCO in solid is observed which is interrupted on heating by a “reverse” SCO with $T_c^R = 346$ K and $\Delta T_h^R = 8$ K for **pyH-8**, and $T_c^R = 351$ K and $\Delta T_h^R = 3$ K for **pyH-10** (Figure S5). It should be said, however, that the effect of the “reverse” SCO is weaker for **pyH-n** in comparison to the **pm2-n** series, apparently because of a little difference between midpoint SCO temperatures in solid and fluid phase.

Table 1. Parameters of the hysteresis loops and thermodynamic parameters evaluated from the DSC profiles.

| Compound | T_c , K | ΔT_h , K | SCO type | % of Fe ^{II} undergoing phase-transition driven SCO | ΔH , kJ mol ⁻¹ | ΔS , J K ⁻¹ mol ⁻¹ |
|---------------|-----------|------------------|----------|--|-----------------------------------|--|
| pm2-6 | 366 | 28 | forward | 60 | 46,9 | 128,1 |
| pm2-8 | 352 | 29 | forward | 50 | 46.6 | 132.3 |
| pm2-10 | 287 | 12 | reverse | 10 | 4.8 | 16.7 |
| | 346 | 26 | reverse | 43 | 54.0 | 156.1 |
| pm2-12 | 351 | 21 | reverse | 33 | 71,4 | 203,4 |
| pm2-14 | 355 | 17 | reverse | 50 | 66,3 | 186,8 |
| pyH-6 | 340 | 1 | forward | 58 | 4,0 | 11,7 |
| pyH-8 | 346 | 8 | reverse | 7 | 5,2 | 15,1 |
| pyH-10 | 351 | 4 | reverse | 6 | 8,4 | 23,8 |

7.3.2.- Calorimetric measurements

Differential scanning calorimetry (DSC) experiments collected at 0.5 K min^{-1} reveal the presence of exothermic/endothermic processes on the cooling/warming paths, respectively, peaked at similar temperatures to those observed for the magnetic data of the compounds at 0.5 K min^{-1} (Table 1, Figure S7). The evaluated variations of enthalpy (ΔH) and entropy (ΔS) far exceed the corresponding typical values for strong cooperative SCO transitions (that is, $\Delta H \approx 20 \text{ kJ mol}^{-1}$ and $\Delta S \approx 100 \text{ kJ mol}^{-1}$).^[14] The thermodynamic values observed for the title compounds confirm occurrence of high-energetic processes of melting synchronized with the SCO.

7.3.3.- Structural characterization: single-crystal and powder X-ray diffraction

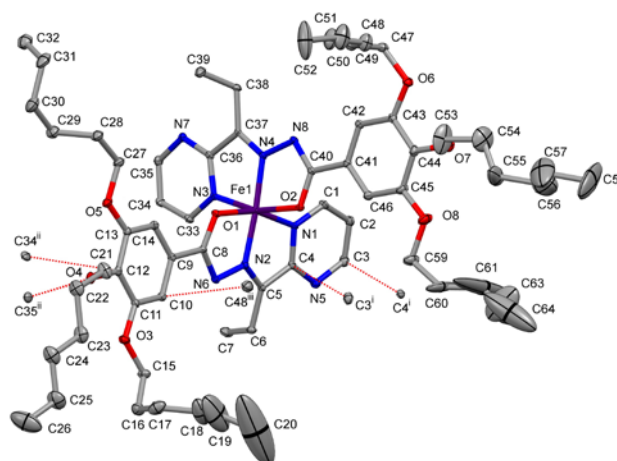


Figure 2. Molecular structure of **pm2-6** at 30% probability ellipsoids. Short inter-molecular contacts below sum of the van der Waals radii are shown as dashed lines. Symmetry codes: (i) $-x, -y, -z$, (ii) $-x, 1-y, -z$, (iii) $-1 + x, y, z$. Displacement ellipsoids are drawn at the 30% probability level. The hydrogen atoms are omitted for clarity.

To structurally characterize the solid state structure of the as-synthesized and annealed compounds, single crystal X-ray diffraction and powder X-ray diffraction studies were done. The study of **pm2-6** reveals that the Fe^{II} -center is located in a distorted octahedral N_4O_2 coordination environment generated by the two deprotonated ligand molecules (Figure 2; Tables S1 and S2). At 120 K, the average bond lengths, $\langle \text{Fe-N} \rangle =$

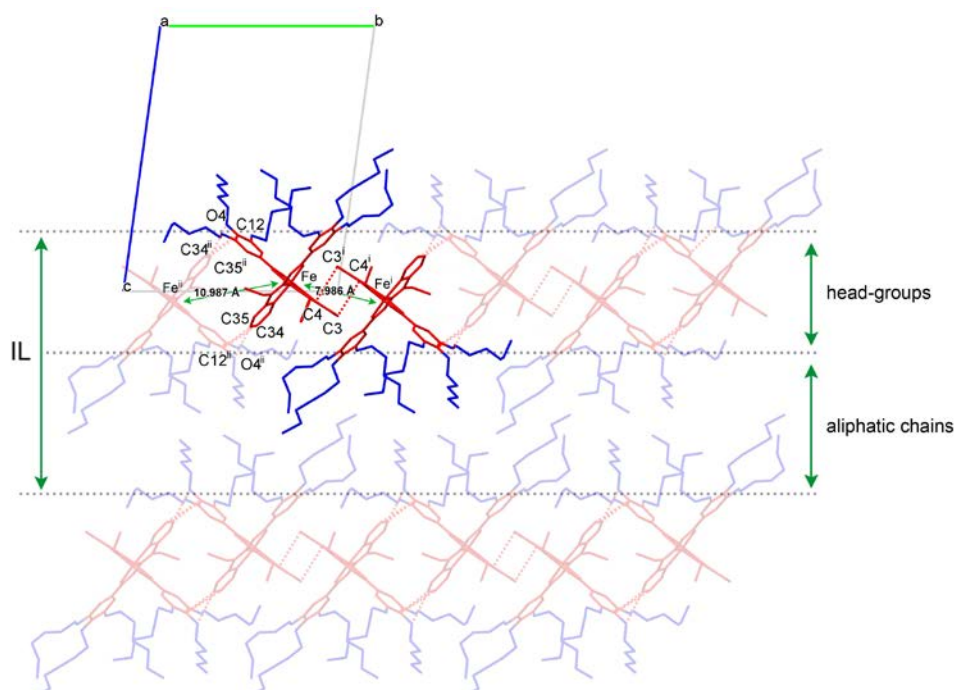


Figure 3. Projection of the crystal lattice **pm2-6** along [100]. Highlighted is the supramolecular dimer of complex molecules with the shortest Fe...Fe separation. IL stands for inter-layer distance d^L . Symmetry codes: (i) $-x, -y, -z$; (ii) $-x, 1-y, -z$.

1.901(3) Å and $\langle \text{Fe}-\text{O} \rangle = 1.962(3)$ Å, are within the region reported for LS Fe^{II} complexes of similar type.^[10, 13] Because of the asymmetric substitution of the ligand, the coordination part remains undecorated enabling effective displaced π - π stacking between coplanar pyrimidine rings of neighbour molecules in a dimer, the basic supramolecular fragment of the structure; the closest C3...C4ⁱ and C4...C3ⁱ contacts below the sum of the van der Waals radii are 3.313 Å, Fe...Feⁱ separation is 7.986 Å (i: $-x, -y, -z$) (Figure 3). The dimers are bound by inter-dimer contacts C12...C34ⁱⁱ, C12...C35ⁱⁱ and O4...C35ⁱⁱ (ii: $-x, 1-y, -z$), with separation 3.390, 3.388 and 3.143 Å, serially, into a 1D supramolecular chain along [010]; the closest Fe...Feⁱⁱ is 10.987 Å. Worth noting, that a similar pyridine-based complex with a methyl instead of ethyl substituent of ketone consists of uniform supramolecular chains with Fe...Fe separation of 7.676 Å.^[10] This points out a hampering of a closer approach of neighbour dimers due to the ethyl groups. The supramolecular chains are stacked in layers within [110] with the closest inter-chain separation coinciding with cell parameter $a = 8.8252(3)$ Å.

Finally, the layers are stacked into a lipid-like structure formed by alternating layers of head-groups and interlayer space filled by hexyl chains with methylene groups in *trans* and *gauche* conformations. Some chains are severely disordered (Figure 2 and 3).

Powder X-ray diffraction (PXRD) characterization of the as-synthesized compounds confirms the formation of highly crystalline lamellar structures (Figure 4a). For **pm2-6**, a good coincidence with the theoretical profile calculated from single crystals data is observed (Figure S2). At 400 K, all samples become fluid and display featureless XRD profiles corresponding to the isotropic phase (Figures 4b, S3).

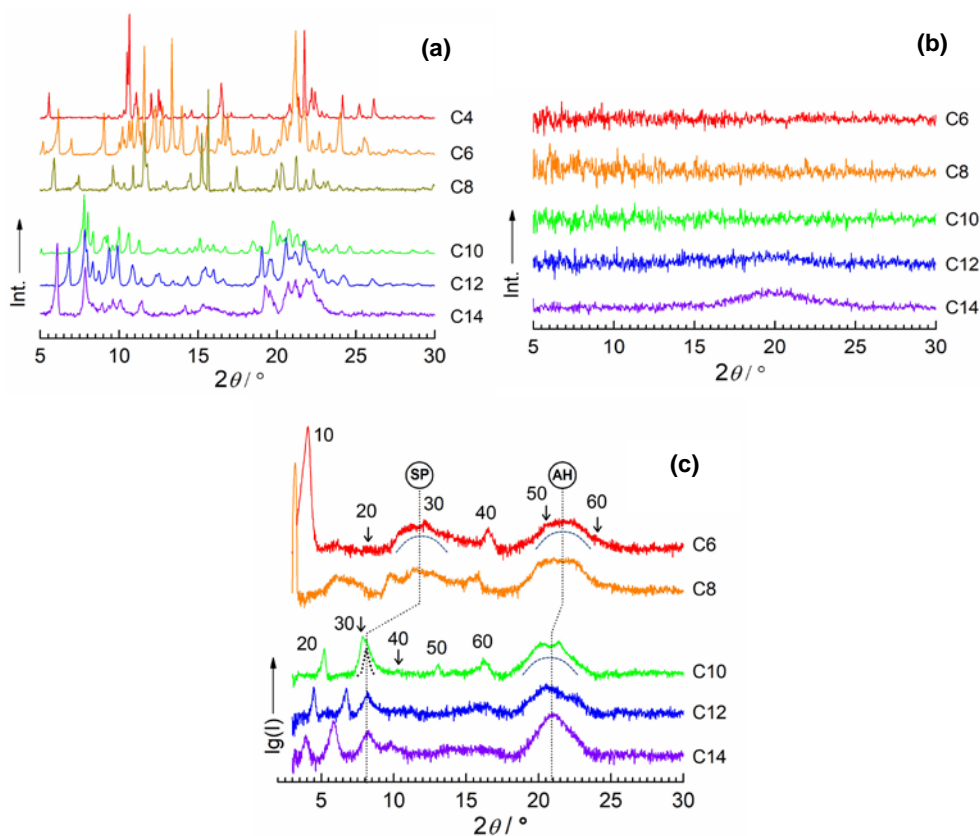


Figure 4. XRD profiles of **pm2-n** with indicated aliphatic chains: (a) as-synthesized at RT; (b) at 400 K; (c) after cooling at RT. SP stands for stacking periodicity; AH – for alkyl halo.

Upon cooling the samples solidify and partially recover the crystal-like character of the PXRD profiles (Figure 4c). The XRD profiles render well separated lamellar peaks up to the 6th order revealing retention of a long-range periodicity of annealed samples. The number of carbon atoms (*n*) plotted against the corresponding interlayer distance d^L , calculated from Miller's index peaks (10) (**pm2-6** and **pm-8**) or (20) (**pm2-10**, **pm2-12**, **pm2-14**) show a linear regression (Figure S4), thereby confirming their similar structural arrangement. However, similarly to the magnetic data, additional analysis of the profiles points out two subgroups of compounds. The diffractograms of annealed **pm2-6** and **pm2-8** manifest a broad peak with the barycentre at $2\theta \approx 11.5^\circ$, d -spacing = 7.7 Å, corresponding to the Fe...Fe stacking periodicity within sublattice formed by head-groups.^[16] This is an indication of retained uniform 1D supramolecular chains similarly to the reported crystalline and annealed pyridine-based systems (7.676 Å) also exhibiting “forward” SCO.^[10] For annealed **pm2-10**, **pm2-12** and **pm2-14**, this stacking periodicity peak appears at 8.1° , d -spacing ≈ 10.9 Å, presumably reflecting formation of supramolecular chains with a larger separation Fe...Fe, similar to the observed between dimers of the **pm2-6**. Another common feature of all profiles is the presence of a broad peak with the barycentres at $2\theta \approx 21.5^\circ$, d -spacing = 4.12 Å (**pm2-6**, **pm2-8**) or $2\theta \approx 21^\circ$, d -spacing = 4.21 Å (**pm2-10**, **pm2-12**, **pm2-14**), a signature of the aliphatic sublattice.^[17]

On the basis of the obtained experimental data we postulate distinct packing motifs for short and long chain compounds which contribute differently to the macroscopic properties of solid samples. Indeed, lower *n* promotes formation of an aliphatic sublattice that stabilize dense packing with short Fe...Fe distances stabilizing the LS state of the Fe^{II} ions, while longer aliphatic chains fortuitously antagonises the dense packing of head-groups and stabilize the HS state.

7.3.4.- Infrared spectroscopy

To elucidate the conformation of aliphatic chains, the IR absorptions spectra of the **pm2-n** compounds were evaluated.^[18] For chains with significant presence of *gauche* methylene units, the characteristic values of C–H groups lie in the regions 2924–2928 and 2854–2856 cm^{-1} for ν_{anti} and ν_{sym} absorption bands, respectively. For all-*trans* extended chains, the bands are in the regions 2915–2920 and 2846–2850 cm^{-1} , respectively. On this

basis, for **pm2-6** and **pm2-8** the ν_{anti} at ca. 2925 cm^{-1} and ν_{sym} at ca. 2856 cm^{-1} suggest significant *gauche* population of aliphatic chains that corroborates the single crystal data of **pm2-6** (Figure 5). On the other hand, peak frequencies at ca. 2922 and ca. 2850 cm^{-1} are suggesting that the majority of methylene units of aliphatic chains of **pm2-10**, **pm2-12**, **pm2-14** are in the *trans* conformation. Obviously, on passing from **pm2-8** to **pm2-10** we observe a change in conformation of aliphatic chains that impact their packing as follows from the changed position of the aliphatic halo.

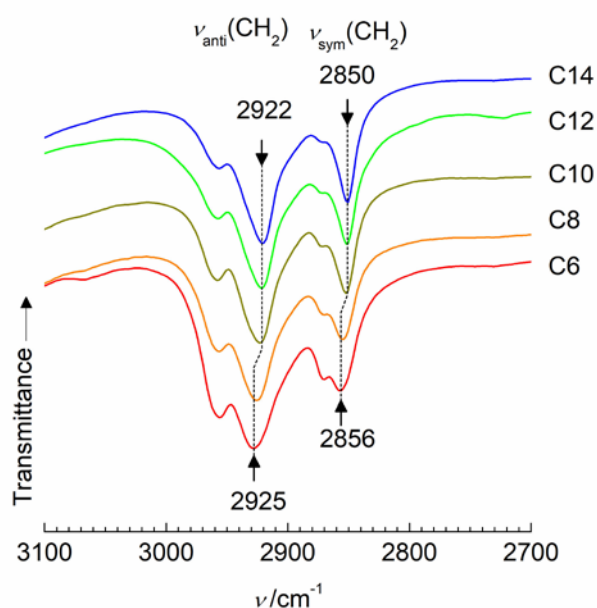


Figure 5. A fragment of the IR absorbance spectra of annealed **pm2-n** with indicated aliphatic chains showing the position of characteristic C–H absorption bands.

7.4.- Conclusion

In summary, this report gives an excellent example of how the dependence of SCO properties on the adopted structure or state of matter aggregation can be exploited to control the SCO direction (“forward” or “reverse”) and its occurrence in temperature. As discussed by Halcrow *et al.*, in solid state the lattice packing caused therefore molecular deformation which, together with chemical pressure of the surrounding, shift the intrinsic midpoint SCO value $T_{1/2}$ by $\Delta T(\text{latt})$ in temperature.^[19] We have discovered that within the

series of the herein reported compounds **pm2-n** the packing effect can vary from positive to negative with respect to the intrinsic SCO midpoint value $T_{1/2}$ observed under unconstrained conditions in fluid phase. Despite the precise study of the local structure of annealed **pm2-n** or **pyH-n** is a non-trivial task accounting their poorly ordered soft nature, the XRD and IR give the scent of the gross and local packing features in solid. As follows from the experimental data, after passing a threshold chain length n , which is 10 for **pm2-n** and 8 for **pyH-n**, aliphatic chains form a sublattice with most of the methylene groups in *trans* conformation while shorter chains form sublattice with substantial fraction of *gauche* methylene groups. Different conformation of the chains is influencing their packing and in turn also the packing of covalently tethered head-groups. It was elucidated that shorter Fe...Fe distances are observed for short chains and larger distances for longer chains. The changed head-groups packing changes also the lattice contribution to the ligand field strength by affecting the incorporated Fe^{II} ions. This shifts the solid SCO transition midpoint below or above the corresponding value in fluid phase. On melting/solidification a jump-like change of the susceptibility is observed, while the hysteresis is reflecting the structural phase transition solid↔liquid.

We have demonstrated that up to 50% of Fe^{II} ions can be converted back to the LS state on heating, but, actually, there is no fundamental reason why the "reverse" SCO cannot be observed as a quantitative process with 100% HS-to-LS transition on temperature elevation. The approach reported here demonstrates that this is the question of the sufficient difference between midpoint SCO values on both sides of the phase transition. Further experimental efforts in this regard are underway.

7.5.- Experimental section

7.5.1.- Synthesis of precursors and complexes

All chemicals were purchased from commercial suppliers and used without further purification. The long chain 3,4,5-triaikoxybenzohydrazides and 2-pyrimidinyl ethyl ketone were synthesized according to the reported procedures.^[10]

The complexes were obtained by condensation of 1 eq. of the corresponding hydrazide and 1.1 eq of ketone in abs. EtOH overnight in the presence of a two drop of glacial acetic acid and by subsequent complexation with 0.5 eq. of $\text{Fe}(\text{BF}_4)_2 \cdot 6\text{H}_2\text{O}$ to give a violet cationic complex. Then a green solution was obtained after deprotonation with 1 eq. of NEt_3 . The neutral complexes were isolated by slow cooling the solution to ambient temperature and subsequent filtering off the formed crystalline dark green precipitate.

pm2-4: From 3,4,5-tris(butyloxy)benzohydrazide (208 mg, 0.59 mmol), 2-pyrimidinyl ethyl ketone (94 mg, 0.65 mmol), $\text{Fe}(\text{BF}_4)_2 \cdot 6\text{H}_2\text{O}$ (100 mg, 0.29 mmol) and NEt_3 (60 mg, 82 μL , 0.59 mmol) in 40 mL of absolute EtOH. Crystals were obtained by slow diffusion of vapours of diethyl ether over one week. Elemental analysis calcd (%) for $\text{C}_{52}\text{H}_{74}\text{FeN}_8\text{O}_8$: C, 62.77; H, 7.50; N, 11.26. Found C, 62.87; H, 7.47; N, 11.23.

pm2-6: From 3,4,5-tris(hexyloxy)benzohydrazide (258 mg, 0.59 mmol), 2-pyrimidinyl ethyl ketone (94 mg, 0.65 mmol), $\text{Fe}(\text{BF}_4)_2 \cdot 6\text{H}_2\text{O}$ (100 mg, 0.29 mmol) and NEt_3 (60 mg, 82 μL , 0.59 mmol) in 40 mL of absolute EtOH. Crystals were obtained by slow diffusion of vapours of diethyl ether over one week. Elemental analysis calcd (%) for $\text{C}_{64}\text{H}_{98}\text{FeN}_8\text{O}_8$: C, 66.07; H, 8.49; N, 9.63. Found C, 66.10; H, 8.43; N, 9.65.

pm2-8: From 3,4,5-tris(octyloxy)benzohydrazide (307 mg, 0.59 mmol), 2-pyrimidinyl ethyl ketone (94 mg, 0.65 mmol), $\text{Fe}(\text{BF}_4)_2 \cdot 6\text{H}_2\text{O}$ (100 mg, 0.29 mmol) and NEt_3 (60 mg, 82 μL , 0.59 mmol) in 40 mL of absolute EtOH. Crystals were obtained by slow diffusion of vapours of diethyl ether over one week. Elemental analysis calcd (%) for $\text{C}_{76}\text{H}_{122}\text{FeN}_8\text{O}_8$: C, 68.55; H, 9.23; N, 8.41. Found C, 68.50; H, 9.20; N, 8.39.

pm2-10: From 3,4,5-tris(decyloxy)benzohydrazide (357 mg, 0.59 mmol), 2-pyrimidinyl ethyl ketone (94 mg, 0.65 mmol), $\text{Fe}(\text{BF}_4)_2 \cdot 6\text{H}_2\text{O}$ (100 mg, 0.29 mmol) and NEt_3 (60 mg, 82 μL , 0.59 mmol) in 40 mL of absolute EtOH. Crystals were obtained by slow diffusion of vapours of diethyl ether over one week. Elemental analysis calcd (%) for $\text{C}_{88}\text{H}_{146}\text{FeN}_8\text{O}_8$: C, 70.46; H, 9.81; N, 7.47. Found C, 70.53; H, 9.87; N, 7.53.

pm2-12: From 3,4,5-tris(dodecyloxy)benzohydrazide (407 mg, 0.59 mmol), 2-pyrimidinyl ethyl ketone (94 mg, 0.65 mmol), $\text{Fe}(\text{BF}_4)_2 \cdot 6\text{H}_2\text{O}$ (100 mg, 0.29 mmol) and NEt_3 (60 mg, 82 μL , 0.59 mmol) in 40 mL of absolute EtOH. Crystals were obtained by slow

diffusion of vapours of diethyl ether over one week. Elemental analysis calcd (%) for $C_{100}H_{170}FeN_8O_8$ C, 71.99; H, 10.27; N, 6.72. Found C, 72.05; H, 10.20; N, 6.65.

pm2-14: From 3,4,5-tris(tetradecyloxy)benzohydrazide (456 mg, 0.59 mmol), 2-pyrimidinyl ethyl ketone (94 mg, 0.65 mmol), $Fe(BF_4)_2 \cdot 6H_2O$ (100 mg, 0.29 mmol) and NEt_3 (60 mg, 82 μ L, 0.59 mmol) in 40 mL of absolute EtOH. Crystals were obtained by slow diffusion of vapours of diethyl ether over one week. Elemental analysis calcd (%) for $C_{112}H_{194}FeN_8O_8$ C, 73.24; H, 10.65; N, 6.10. Found C, 73.30; H, 10.70; N, 6.09.

pyH-6: From 3,4,5-tris(hexyloxy)benzohydrazide (258 mg, 0.59 mmol), 2-pyridine aldehyde (70 mg, 0.65 mmol), $Fe(BF_4)_2 \cdot 6H_2O$ (100 mg, 0.29 mmol) and NEt_3 (60 mg, 82 μ L, 0.59 mmol) in 40 mL of absolute EtOH. Crystals were obtained by slow diffusion of vapours of diethyl ether over one week. Elemental analysis calcd (%) for $C_{62}H_{92}FeN_6O_8$: C, 67.37; H, 8.39; N, 7.60. Found C, 67.28; H, 8.32; N, 7.67.

pyH-8: From 3,4,5-tris(octyloxy)benzohydrazide (307 mg, 0.59 mmol), 2-pyridine aldehyde (70 mg, 0.65 mmol), $Fe(BF_4)_2 \cdot 6H_2O$ (100 mg, 0.29 mmol) and NEt_3 (60 mg, 82 μ L, 0.59 mmol) in 40 mL of absolute EtOH. Crystals were obtained by slow diffusion of vapours of diethyl ether over one week. Elemental analysis calcd (%) for $C_{74}H_{116}FeN_6O_8$: C, 69.79; H, 9.18; N, 6.60. Found C, 69.83; H, 9.21; N, 6.65.

pyH-10: From 3,4,5-tris(decyloxy)benzohydrazide (357 mg, 0.59 mmol), 2-pyridine aldehyde (70 mg, 0.65 mmol), $Fe(BF_4)_2 \cdot 6H_2O$ (100 mg, 0.29 mmol) and NEt_3 (60 mg, 82 μ L, 0.59 mmol) in 40 mL of absolute EtOH. Crystals were obtained by slow diffusion of vapours of diethyl ether over one week. Elemental analysis calcd (%) for $C_{86}H_{140}FeN_6O_8$ C, 71.64; H, 9.79; N, 5.83. Found C, 71.58; H, 9.84; N, 5.79.

7.5.2.- Magnetic measurements

Variable-temperature magnetic susceptibility data (10 mg) were recorded on thermally treated samples (already heated up to 400 K) at the rate 0.5 K min^{-1} with a Quantum Design MPMS2 SQUID susceptometer equipped with a 7 T magnet, operating at 1 T and at temperatures 10–400 K.

7.5.3.- Calorimetric measurements

DSC measurements were performed on already heated samples on a Mettler Toledo TGA/SDTA 821e, in the 200–400 K temperature range under a nitrogen atmosphere with a rate of 0.5 K min⁻¹. The DSC data were analyzed with Netzsch Proteus software with an overall accuracy of 0.2 K in the temperature and 2% in the heat flow.

7.5.4.- Powder X-ray diffraction measurements (PXRD)

X-ray measurements were performed on a PANalytical Empyrean X-ray powder diffractometer (monochromatic Cu K α radiation). Each plot is superposition of three scans collected at the rate 5.6° min⁻¹. The interlayer distances were calculated according Bragg's equation.

7.5.5.- Single crystal X-ray diffraction

Single-crystal X-ray data of **pm2-6** were collected on a Nonius Kappa-CCD single crystal diffractometer using graphite mono-chromated MoK α radiation ($\lambda = 0.71073 \text{ \AA}$). A multi-scan absorption correction was performed. The structures were solved by direct methods using SHELXS-2014 and refined by full-matrix least squares on F^2 using SHELXL-2014.^[20] Non-hydrogen atoms were refined anisotropically and hydrogen atoms were placed in calculated positions refined using idealized geometries (riding model) and assigned fixed isotropic displacement parameters.

7.6.- References

- [1] (a) Koshihara, S.-y. *J. Phys.: Conf. Ser.* **2005**, 21, 7. (b) Bennemann, K. H. *J. Phys. Condens. Matter.* **2011**, 23, 073202. (c) Sato, O. *Nat. Chem.* **2016**, 8, 644. (c) Senthil Kumar, K.; Ruben, M. *Coord. Chem. Rev.* **2017**, 346, 176.
- [2] (a) Gütlich, P.; Hauser, A.; Spiering, H. *Angew. Chem., Int. Ed. Engl.* **1994**, 33, 2024. (b) *Spin Crossover in Transition Metal Compounds*, ed. Gütlich, P.; Goodwin, H. *Top. Curr. Chem.* **2004**, 233-235. (c) *Spin-Crossover Materials: Properties and Applications*, ed. Halcrow, M. A. **2013**.

- [3] (a) Halcrow, M. A. In *Spin-Crossover Materials: Properties and Applications*, **2013**, 147. (b) Gütlich, P.; Goodwin, H. A. *Top. Curr. Chem.* **2004**, 233, 1. (c) Halcrow, M. A. *Crystals* **2016**, 6, 58.
- [4] (a) Zhang, W.; Zhao, F.; Liu, T.; Yuan, M.; Wang, Z. M.; Gao, S. *Inorg. Chem.* **2007**, 46, 2541. (b) Galadzhun, I.; Kulmaczewski, R.; Cespedes, O.; Yamada, M.; Yoshinari, N.; Konno, T.; Halcrow, M. A. *Inorg. Chem.* **2018**, 57, 13761.
- [5] (a) Schlamp, S.; Weber, B.; Naik, A. D.; Garcia, Y. *Chem. Commun.* **2011**, 47, 7152. (b) Rosario-Amorin, D.; Dechambenoit, P.; Bentaleb, A.; Rouzières, M.; Mathonière, C.; Clérac, R. *J. Am. Chem. Soc.* **2018**, 140, 98.
- [6] Gaspar, A. B.; Seredyuk, M. *Coord. Chem. Rev.* **2014**, 268, 41.
- [7] (a) Seredyuk, M.; Gaspar, A. B.; Ksenofontov, V.; Galyametdinov, Y.; Kusz, J.; Gütlich, P. *Adv. Funct. Mater.* **2008**, 18, 2089. (b) Seredyuk, M.; Gaspar, A. B.; Ksenofontov, V.; Galyametdinov, Y.; Kusz, J.; Gütlich, P. *J. Am. Chem. Soc.* **2008**, 130, 1431. (c) Gaspar, A. B.; Seredyuk, M.; Gütlich, P. *Coord. Chem. Rev.* **2009**, 253, 2399. (d) Lee, Y. H.; Ohta, A.; Yamamoto, Y.; Komatsu, Y.; Kato, K.; Shimizu, T.; Shinoda, H.; Hayami, S. *Polyhedron* **2011**, 30, 3001. (e) Seredyuk, M.; Muñoz, M. C.; Ksenofontov, V.; Gütlich, P.; Galyametdinov, Y.; Real, J. A. *Inorg. Chem.* **2014**, 53, 8442. (f) Fitzpatrick, A. J.; Martinho, P. N.; Gildea, B. J.; Holbrey, J. D.; Morgan, G. G. *Eur. J. Inorg. Chem.* **2016**, 385. (g) Seredyuk, M.; Znovjyak, K.; Muñoz, M. C.; Galyametdinov, J. A.; Fritsky, I. O.; Real, J. A. *RSC Adv.* **2016**, 6, 39627.
- [8] (a) Bodenthin, Y.; Schwarz, G.; Tomkowicz, Z.; Geue, T.; Haase, W.; Pietsch, U.; Kurth, D. G. *J. Am. Chem. Soc.* **2009**, 131, 2934. (b) Seredyuk, M. *Inorg. Chim. Acta* **2012**, 380, 65. (c) Seredyuk, M.; Gaspar, A. B.; Ksenofontov, V.; Reiman, S.; Galyametdinov, Y.; Haase, W.; Rentschler, E.; Gütlich, P. *Hyperfine Interactions* **2005**, 166, 385.
- [9] Akiyoshi, R.; Hirota, Y.; Kosumi, D.; Tsutsumi, M.; Nakamura, M.; Lindoy, L. F.; Hayami, S. *Chem. Sci.* **2019**, 10, 5843.
- [10] Romero-Morcillo, T.; Seredyuk, M.; Muñoz, M. C.; Real, J. A. *Angew. Chem., Int. Ed.* **2015**, 54, 14777.
- [11] (a) Agustí, G.; Bartual, C.; Martínez, V.; Muñoz-Lara, F. J.; Gaspar, A. B.; Muñoz, M. C.; Real, J. A. *New J. Chem.* **2009**, 33, 1262-1267. (b) Hayami, S.; Komatsu, Y.; Shimizu,

- T.; Kamihata, H. Lee, Y. H. *Coord. Chem. Rev.* **2011**, *255*, 1981. (c) Hayami, S.; Nakaya, M.; Ohmagari, H.; Alao, A. S. Nakamura, M.; Ohtani, R.; Yamaguchi, R.; Kuroda-Sowa, t.; Clegg, J. K. *Dalton Trans.* **2015**, *44*, 9345.
- [12] (a) Valverde-Muñoz, F. J.; Seredyuk, M.; Meneses-Sanchez, M.; Muñoz, M. C.; Bartual-Murgui, C.; Real, J. A. *Chem. Sci.* **2019**, *10*, 3807. (b) Weselski, M.; Ksiazek, M.; Mess, P.; Kusz, J.; Bronisz, R. *Chem. Commun.* **2019**, *55*, 7033.
- [13] (a) Niel, V.; Muñoz, M. C.; Gaspar, A. B.; Galet, A.; Levchenko, G.; Real, J. A. *Chem.-Eur. J.* **2002**, *8*, 2446. (b) Miyazaki, Y.; Nakamoto, T.; Ikeuchi, S.; Saito, K.; Inaba, A.; Sorai, M.; Tojo, T.; Atake, T.; Matouzenko, G. S.; Zein, S.; Borshch, S. A. *J. Phys. Chem. B* **2007**, *111*, 12508. (c) Varret, F.; Slimani, A.; Boukheddaden, K.; Chong, C.; Mishra, H.; Collet, E.; Haasnoot, J.; Pillet, S. *New J. Chem.* **2011**, *35*, 2333. (d) Senthil Kumar, K.; Heinrich, B.; Vela, S.; Moreno-Pineda, E.; Bailly, C.; Ruben, M. *Dalton Trans.* **2019**, *48*, 3825.
- [14] Muñoz, M. C.; Real, J. A. *Coord. Chem. Rev.* **2011**, *255*, 2068.
- [15] Nakanishi, T.; Sato, O. *Crystals* **2016**, *6*, 131.
- [16] Weihermüller, J.; Schlamp, S.; Milius, W.; Puchtler, F.; Breu, J.; Ramming, P.; Hüttner, S.; Agarwal, S.; Göbel, C.; Hund, M.; Papastavrou, G.; Weber, B. *J. Mater. Chem. C* **2019**, *7*, 1151.
- [17] Dorset, D. L. *Crystallography of the polymethylene chain: an inquiry into the structure of waxes* Oxford University Press, Oxford, New York, **2005**.
- [18] (a) Fujigaya, T.; Jiang, D. L.; Aida, T. *J. Am. Chem. Soc.* **2003**, *125*, 14690. (b) Park, S.-H.; Lee, C. E. *Chem. Mater.* **2006**, *18*, 981.
- [19] Halcrow, M. A.; Capel Berdiell, I.; Pask, C. M.; Kulmaczewski, R. *Inorg. Chem.* **2019**, *58*, 9811.
- [20] Sheldrick, G. *Acta Crystallogr. Sect.: C Struct. Chem.* **2005**, *71*, 3.

7.7.- Supporting Information

Table S1.- Crystallographic data for **pm2-6** at 120 K

| | |
|---|--|
| Crystal size (mm) | 0.04×0.06×0.06 |
| Empirical formula | C ₆₄ H ₉₈ N ₈ O ₈ Fe |
| <i>Mr</i> | 1163.35 |
| Crystal system | triclinic |
| Space group | <i>P</i> -1 |
| <i>a</i> (Å) | 8.8252(3) |
| <i>b</i> (Å) | 17.5445(10) |
| <i>c</i> (Å) | 21.5988(12) |
| α (°) | 96.159(5) |
| β (°) | 97.440(4) |
| γ (°) | 101.926(4) |
| <i>V</i> (Å ³) | 3213.4(3) |
| <i>Z</i> | 2 |
| <i>D_c</i> (mg cm ⁻³) | 1.202 |
| <i>F</i> (000) | 1256 |
| μ (Mo-K α) (mm ⁻¹) | 0.293 |
| No. of total reflections | 16164 |
| No. of reflections [<i>I</i> >2 σ (<i>I</i>)] | 9301 |
| <i>R</i> [<i>I</i> >2 σ (<i>I</i>)] | 0.0993 |
| <i>wR</i> [<i>I</i> >2 σ (<i>I</i>)] | 0.2552 |
| <i>S</i> | 0.949 |

$$R_1 = \sum ||F_o| - |F_c|| / \sum |F_o|; wR = [\sum [w(F_o^2 - F_c^2)^2] / \sum [w(F_o^2)^2]]^{1/2}.$$

$$w = 1 / [\sigma^2(F_o^2) + (m P)^2 + n P] \text{ where } P = (F_o^2 + 2F_c^2) / 3; m = 0.1765; n = 7.7911.$$

Table S2. Bond lengths (Å), angles (°), distortion parameters Σ^a , Φ^b and inter-molecular contacts below sum of the van der Waals radii for **pm2-6** at 120 K.

| | |
|--------------------------|------------|
| Fe-O(1) | 1.955(3) |
| Fe-O(2) | 1.969(3) |
| Fe-N(1) | 1.933(4) |
| Fe-N(2) | 1.861(3) |
| Fe-N(3) | 1.937(4) |
| Fe-N(4) | 1.873(3) |
| O(1)-Fe-O(2) | 91.94(13) |
| O(1)-Fe-N(1) | 161.80(13) |
| O(1)-Fe-N(2) | 80.60(14) |
| O(1)-Fe-N(3) | 89.5(2) |
| O(1)-Fe-N(4) | 96.91(14) |
| O(2)-Fe-N(1) | 88.21(14) |
| O(2)-Fe-N(2) | 102.89(13) |
| O(2)-Fe-N(3) | 162.12(13) |
| O(2)-Fe-N(4) | 80.48(13) |
| N(1)-Fe-N(2) | 81.6(2) |
| N(1)-Fe-N(3) | 95.9(2) |
| N(1)-Fe-N(4) | 101.1(2) |
| N(2)-Fe-N(3) | 94.9(2) |
| N(2)-Fe-N(4) | 175.8(2) |
| N(3)-Fe-N(4) | 81.7(2) |
| C3...C4 ⁱ | 3.313 |
| O4...C35 ⁱⁱ | 3.143 |
| C12...C34 ⁱⁱ | 3.390 |
| C12...C35 ⁱⁱ | 3.388 |
| C10...C48 ⁱⁱⁱ | 3.398 |
| Σ | 10.43 |
| Φ | 81.55 |

^a $\Sigma = \sum_1^{12} (|\phi_i - 90|)$, ϕ_i is the *cis*-N-Fe-N angles in the coordination sphere;^[1]

^b $\Phi = \sum_1^{24} (60 - \theta_i)$, θ_i is the angle generated by superposition of two opposite faces of the octahedron;^[2]
Symmetry codes: (i) $-x, -y, -z$; (ii) $-x, 1 - y, -z$; (iii) $-1 + x, y, z$.

Figure S1. Calorimetric profile for **pm2-4** on heating.

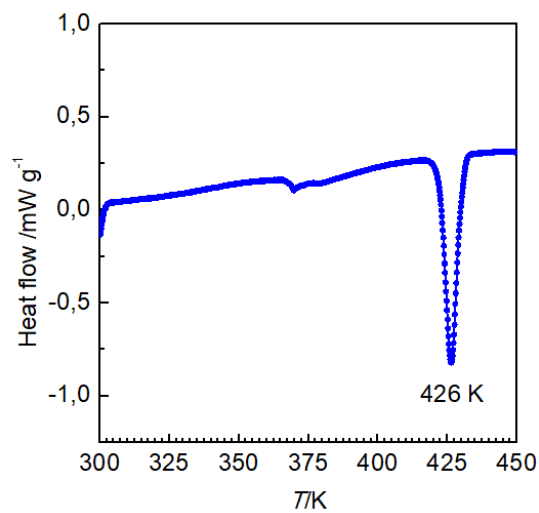


Figure S2. Comparison of experimental XRD profile of **pm2-6** with the profile calculated from the single crystal data.

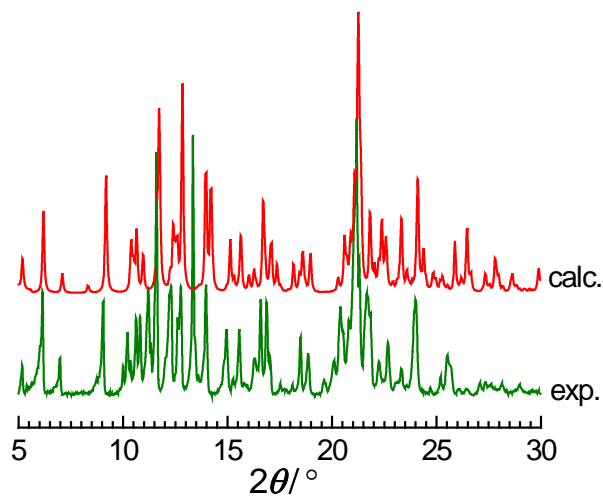


Figure S3. A series of XRD profiles of **pm2-6** on heating from 300 K up to 390 K with photographs of a crystal before and after melting.

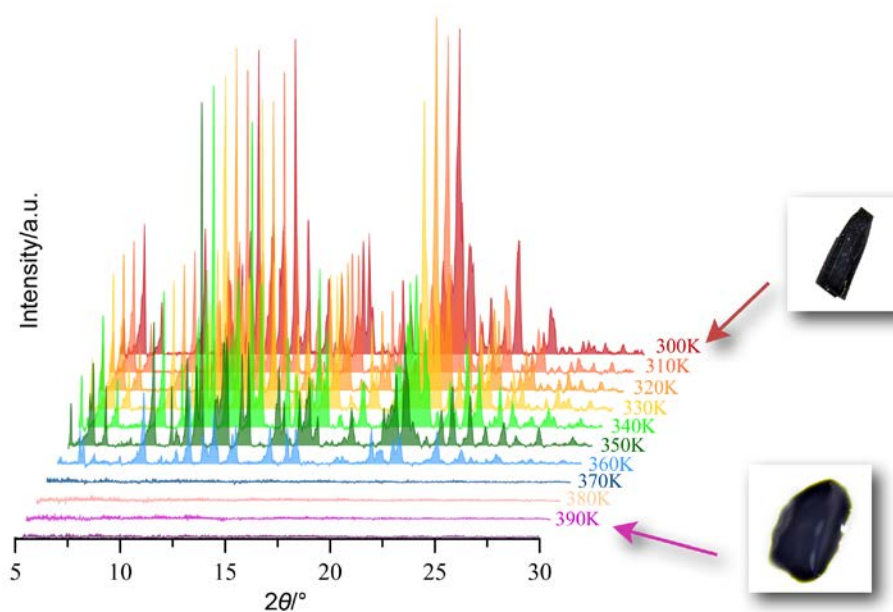
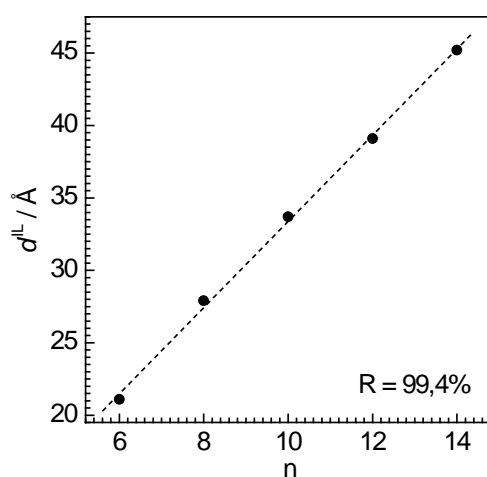


Figure S4. d^L vs n for annealed **pm2-n**.



| | 2θ of (10) or (20) | $d^L / \text{Å}$ |
|---------------|------------------------------|------------------|
| pm2-6 | 4.09 | 21.1 |
| pm2-8 | 3.18 | 27.9 |
| pm2-10 | 5.21 | 33.7 |
| pm2-12 | 4.48 | 39.1 |
| pm2-14 | 3.94 | 45.2 |

Figure S5. Magnetic plot $\chi_M T$ vs T for indicating compounds displaying "forward" and "reverse" SCOs.

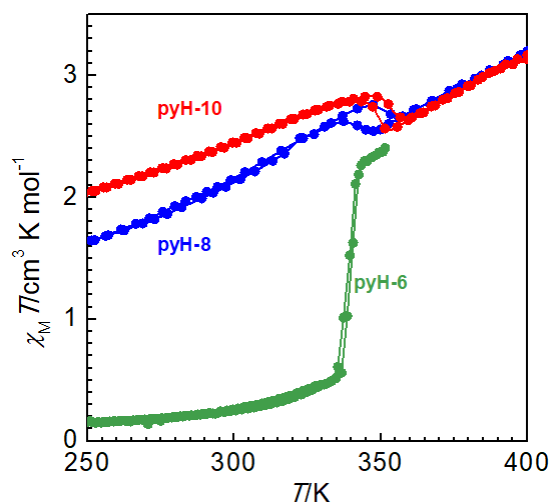


Figure S6. Magnetic plots $\chi_M T$ vs T for **pm2-6** (left) and **pm2-10** (right) illustrating dependence of the $\chi_M T$ vs T on the scan rate.

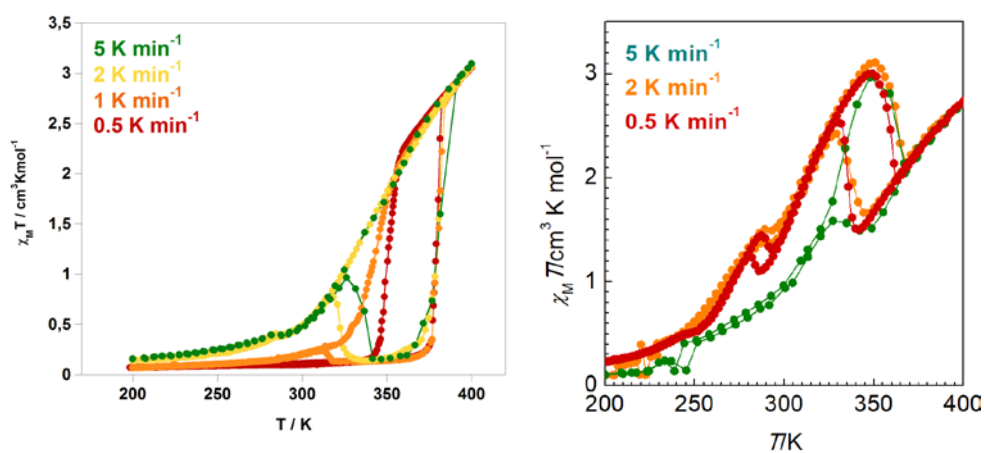


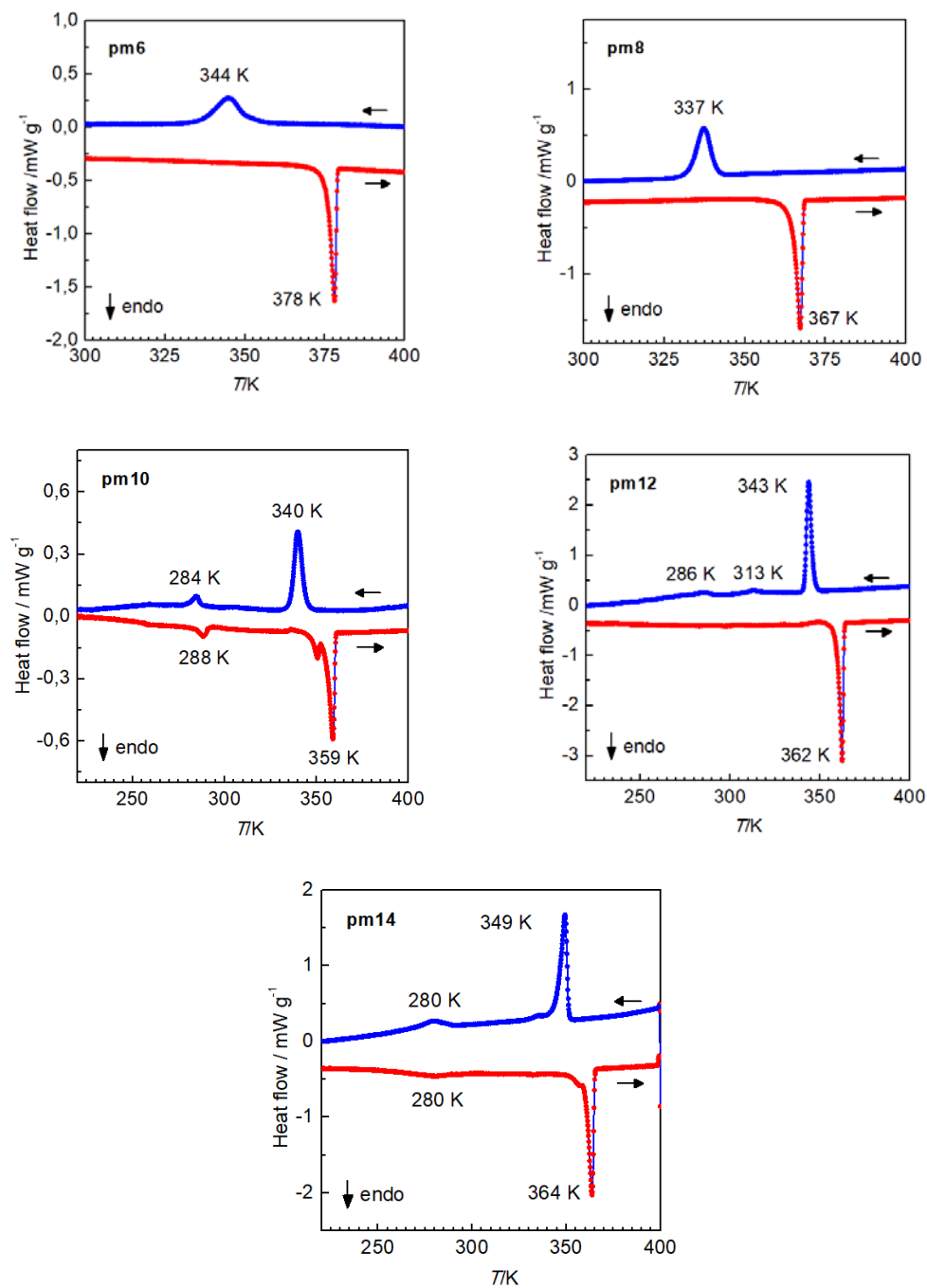
Figure S7. DSC profiles of indicated compounds at 0.5 K min⁻¹.

Figure S8. The plots $\chi_M T$ vs T in fluid phase for **pm2-n** with indicated aliphatic chains illustrating essentially the same behavior.

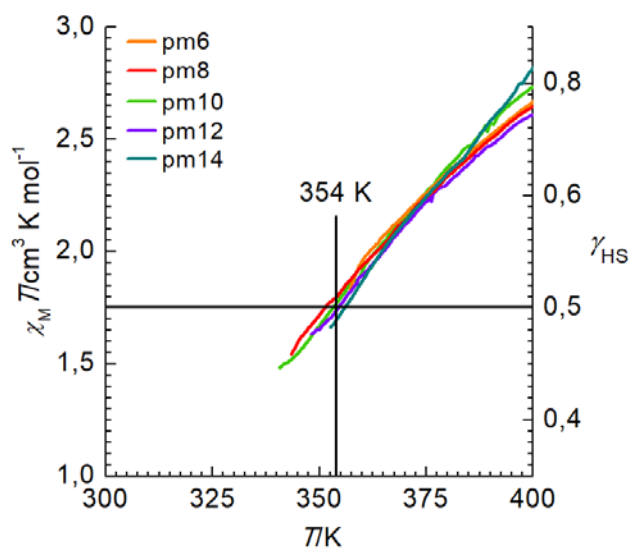
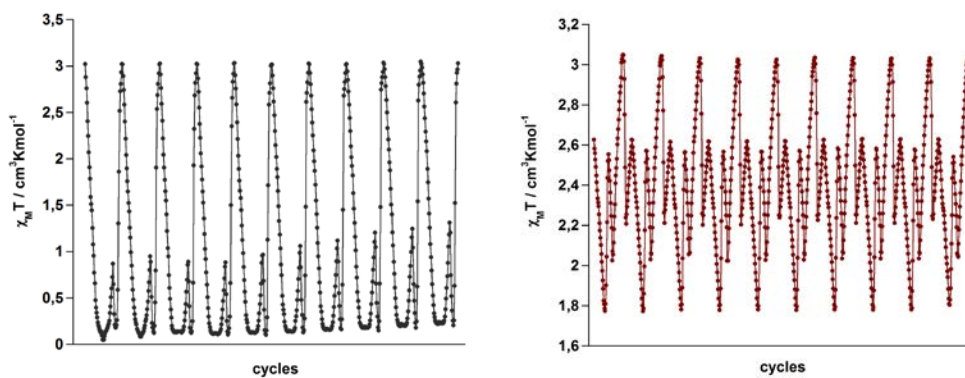


Figure S9. Cycling $\chi_M T$ vs T within 300–400 K for **pm2-6** (left) and **pm2-10** (right).



References

- [1] Drew, M. G. B.; Harding, C. J.; McKee, V.; Morgan, G. G.; Nelson, J. *J. Chem. Soc., Chem. Commun.* **1995**, 1035.
- [2] Chang, H. R.; McCusker, J. K.; Toftlund, H.; Wilson, S. R.; Trautwein, A. X.; Winkler, H.; Hendrickson, D. N. *J. Am. Chem. Soc.* **1990**, *112*, 6814

CAPÍTULO 8

Conclusiones finales

CAPÍTULO 8

CONCLUSIONES FINALES

Strong Cooperative Spin Crossover in 2D and 3D Fe^{II}-M^{I,II} Hofmann-Like Coordination Polymers Based on 2-Fluoropyrazine

En el capítulo dos se ha presentado el comportamiento SCO de una nueva serie de compuestos 2D y 3D de Fe(II) con estructuras de tipo Hofmann, obtenidos a partir del autoensamblaje de iones de Fe(II), el ligando ambidentado fluopiracina (Fpz) y las unidades de construcción $[M^{II}(\text{CN})_4]^{2-}$ ($M^{II} = \text{Ni, Pd, Pt}$) y $[\text{Au}^I(\text{CN})_2]$. Los compuestos constituidos por los aniones puente $[M^{II}(\text{CN})_4]^{2-}$ son polímeros de coordinación bidimensionales de fórmula molecular $\{\text{Fe}(\text{Fpz})_2[M^{II}(\text{CN})_4]\}$ ($M^{II} = \text{Ni, Pd, Pt}$) (**FpzM**). Los derivados **FpzPd** y **FpzPt** presentan una transición de espín termo- y fotoinducida cooperativa acompañada de un cambio de color amarillo pálido (HS) a rojo oscuro (LS), a diferencia del derivado **FpzNi** que permanece en el estado HS incluso a presiones hidrostáticas cercanas a 0.7 GPa. El análisis de las temperaturas críticas $T_{1/2}$ refleja una clara desestabilización del estado LS según la tendencia **FpzPt** > **FpzPd** > **FpzNi**. La ausencia de cambio de estado de espín en el derivado **FpzNi** se asocia al empaquetamiento singular de las capas onduladas en su estado HS. La red metal-orgánica tridimensional $\{\text{Fe}(\text{Fpz})[\text{Pt}(\text{CN})_4] \cdot 1/2\text{H}_2\text{O}$ (**FpzPt3D**), obtenida mediante una ruta sintética alternativa, es una versión distorsionada del compuesto modelo tipo Hofmann $\{\text{Fe}(\text{pz})[\text{Pt}(\text{CN})_4]\}$. Este derivado es HS en todo el rango de temperaturas estudiado y presenta una estabilidad térmica baja atribuida a tensiones estructurales. Por el contrario, el compuesto tridimensional $\{\text{Fe}(\text{Fpz})[\text{Au}(\text{CN})_2]_2\}$ (**FpzAu**) constituido por dos redes 3D idénticas interpenetradas presenta un comportamiento SCO muy cooperativo y asimétrico con una histéresis térmica por encima de los 40 K de anchura.

Switchable Spin-Crossover Hofmann-Type 3D Coordination Polymers Based on Tri- and tetratopic Ligands

En el capítulo tres se presenta la formación de nuevas redes metalorgánicas SCO de tipo Hofmann sintetizadas a partir de la combinación de Fe(II) y $[M^I(CN)_2]^-$ ($M^I = Ag, Au$) con dos nuevos ligandos puente, uno tridentado y otro tetradentado, que presentan modos de coordinación trigonal (L^{N3}) y cuadrado (L^{N4}). Utilizando métodos de difusión lenta en presencia de moléculas huésped adecuadas se han obtenido seis nuevos compuestos isoestructurales con fórmula molecular general $\{Fe(L^{N3})[M^I(CN)_2]_2\} \cdot G$ [$M^I = Ag$ (**1·G**), Au (**2·G**), $G = PhCN, PhNO_2, o-PhCl_2$] empleando el ligando L^{N3} . La estructura cristalina del derivado $PhNO_2$ pone de manifiesto que L^{N3} actúa como ligando bis-monodentado, condición impuesta muy probablemente por la métrica de las capas $\{Fe[M^I(CN)_2]_2\}_n$, actuando como un pilar conectando centros de Fe(II) de capas consecutivas, y generando una red tridimensional de elevada porosidad. Dos redes idénticas se interpenetran en el mismo espacio manteniéndose unidas a través de interacciones intermoleculares y metalofílicas $M^I \cdots M^I$ débiles. Los seis clatratos presentan transiciones de espín termo- y foto-inducidas de primer orden. A diferencia de L^{N3} , el ligando L^{N4} en condiciones similares actúa saturando sus cuatro posiciones de coordinación para dar el compuesto $\{Fe(L^{N4})[Ag^I(CN)_2][Ag_2^I(CN)_3]\} \cdot H_2O$ (**3·H₂O**) en el que además se generan especies $[Ag_2^I(CN)_3]^-$ in-situ, las cuales son necesarias para la congruencia geométrica de la red 3D triplemente interpenetrada formada. En este sistema los planos están formados por especies $\{Fe[Ag^I(CN)_2][Ag_2^I(CN)_3]\}_n$ que se apilan unidos por la coordinación de L^{N4} con los iones Fe(II) y Ag(I) (de las especies $[Ag_2^I(CN)_3]^-$) pertenecientes a planos adyacentes. La inercia química de $[Au^I(CN)_2]^-$ para dar una especie equivalente a $[Ag_2^I(CN)_3]^-$ impide la formación de un compuesto isoestructural al de Ag(I). Este hecho confirma la existencia de incompatibilidades estructurales en $[Ag^I(CN)_2]^-$, que $[Ag^I(CN)_2]^-$ “resuelve” generando $[Ag_2^I(CN)_3]^-$ y coordinando los grupos piridina de L^{N4} . De forma similar a los derivados de L^{N3} el compuesto **3·H₂O** presenta una transición de espín termo-inducida completa y efecto LIESST casi completo (74%).

Influence of Host-Guest and Host-Host Interactions on the Spin-Crossover 3D Hofmann-type Clathrates $\{Fe^II(pina)[M^I(CN)_2]_2\} \cdot xMeOH$ ($M^I = Ag, Au$)

En el capítulo cuatro se describe la síntesis, caracterización estructural y propiedades magnéticas de dos nuevas redes metal-orgánicas porosas 3D isoestructurales con fórmula general $\{Fe(pina)[M^I(CN)_2]_2\} \cdot xMeOH$ ($M^I = Ag$ (**1·xMeOH**), Au (**2·xMeOH**), $x \sim 5$), siendo *pina* N-(piridin-4-il)-isonicotinamida, un ligando lineal puente bisonodentado del tipo piridina funcionalizado con un grupo amida. La estructura de ambos compuestos está constituida por dos redes 3D equivalentes interpenetradas que interaccionan entre si mediante interacciones argentofílicas (o aurofílicas) y puentes de hidrógeno $C=O \cdots HC$ a través de interacciones interligando puente. A pesar de la doble interpenetración de las redes el compuesto presenta espacio vacío accesible capaz de adsorber un máximo de 5 moléculas de metanol, las cuales definen una subred de puentes de hidrógeno que se extienden por los canales definidos por la doble red. En la forma solvatada, los derivados **1·xMeOH** y **2·xMeOH** presentan comportamiento SCO cooperativos, térmicamente inducidos, que presentan la singularidad de transcurrir en dos y cuatro etapas, respectivamente, y caracterizados por la presencia de histéresis térmica. La pérdida de las moléculas de metanol transforma el comportamiento cooperativo en gradual e incompleto. La desorción de las moléculas de disolvente tiene lugar sin destrucción de los cristales lo que ha permitido seguir el proceso por difracción de rayos X y correlacionar las modificaciones estructurales y de SCO.

Very Long-Lived Photogenerated High-Spin Phase of a Multistable Spin-Crossover Molecular Material

En el capítulo cinco se ha demostrado que el comportamiento singular SCO termo- y fotoinducido del complejo mononuclear $[Fe(nBu-im)_3(tren)](PF_6)_2$ está directamente relacionado con la inestabilidad de las cadenas butilo unidas a los anillos imidazol. En estudios realizados anteriormente en nuestro grupo se describió la presencia de dos transiciones de espín muy cooperativas en este complejo, caracterizadas por dos fases LS diferentes (LS_1 y LS_2). Las dos fases están controladas por la cinética de una transición de fase cristalográfica en la que los grupos butilo junto con los aniones PF_6^- juegan un papel fundamental. Las fases LS_1 y LS_2 presentan organizaciones diferentes de las unidades PF_6^-

y los grupos alquílicos butilo. Este comportamiento, previamente analizado por medidas de susceptibilidad magnética en función de la temperatura, ha sido reinvestigado y confirmado en este capítulo mediante espectroscopia UV-vis sobre monocristal.

Además, la combinación de las técnicas de espectroscopia de absorción óptica sobre monocristales, difracción de rayos-X de monocristal con radiación sincrotrón y medidas de SQUID revelan que los grupos butilo también están involucrados en las relajaciones inusualmente lentas cuando los estados metaestables HS* termo- y fotoinducido se relajan al estado fundamental LS₁. Dependiendo de la temperatura de irradiación, se ha observado la formación de dos estados fotoexcitados HS ligeramente diferentes: el estado HS₁^{1irr}, cuya estructura se ha determinado al irradiar el complejo a 25 K, y el estado HS₁^{2irr}, cuya estructura se obtiene al irradiar la fase LS₁ a 90 K. Las conformaciones de las tres cadenas de butilo que definen el ligando tripodal del complejo son idénticas para los estados HS₁^{1irr} y LS₁, mientras que dos de las cadenas en el estado HS₁^{2irr} adoptan una conformación completamente diferente. Durante el proceso de relajación a 90 K de la fase HS₁^{2irr} se observa la reorientación de las cadenas butilo a través de transiciones orden/desorden. Aparentemente, esta reorientación de las cadenas butilo es el principal responsable de la observación de tiempos inusualmente largos de relajación después de fotoexcitar el sistema por encima de 70 K. Curiosamente, el estado HS^{quench}, que puede generarse vía bloqueo térmico desde temperatura ambiente, presenta una estructura cristalina idéntica al estado HS₁^{2irr}. El periodo de relajación para ambos estados isoestructurales es del mismo orden de magnitud.

Es importante subrayar que, a excepción de un pequeño número de análogos Fe-Co de “Azul de Prussia”, existen solo dos sistemas SCO puros que presentan temperaturas T_{LIESST} por encima de 100 K, además de unos pocos complejos de Fe(II) que tienen una T_{LIESST} sobre 90 – 100 K. A diferencia de los ejemplos mencionados, [Fe(*n*Bu-im)₃(tren)](PF₆)₂ representa una plataforma excelente para investigar la sinergia entre dos transiciones de fase, una consustancial al SCO y la otra asociada a la inestabilidad conformacional de las cadenas alquílicas del ligando. Dicha inestabilidad proporciona una oportunidad para poblar cuantitativamente el estado metastable HS₁^{2irr} irradiando a temperaturas tan elevadas como 80-90 K gracias al mecanismo extraordinariamente lento de reconversión estructural asociado con la discordancia de las cadenas butilo entre el estado excitado HS₁^{2irr} y el fundamental LS₁.

Discrimination between two memory channels by molecular alloying in a doubly bistable spin crossover material

En el capítulo seis se muestra la relación entre la transición de fase cristalográfica y la observación de dos comportamientos SCO cooperativos diferentes (referidos como canales de conmutación) en el compuesto $[\text{Fe}(\text{nBu-im})_3(\text{tren})](\text{PF}_6)_2$. La estrategia sintética utilizada está basada en la preparación de dos tipos de aleaciones isomorfas diferentes: i) los centros activos Fe(II) son sustituidos por iones Zn(II) y Ni(II) para obtener los compuestos con fórmula molecular $[\text{Fe}_{1-x}\text{M}_x(\text{nBu-im})_3(\text{tren})](\text{PF}_6)_2$ (M = Ni, Zn); ii) los contra-aniones PF_6^- son sustituidos parcial o totalmente por el anión ligeramente más grande AsF_6^- para generar la familia de derivados $[\text{Fe}(\text{nBu-im})_3(\text{tren})](\text{P}_{1-x}\text{As}_x\text{F}_6)_2$. En el primer caso, la sustitución del centro metálico favorece la disposición de las cadenas butilo y de los aniones PF_6^- característica de la fase LS_1 en ambos estados de espín (HS, LS), estabilizando así la transición de espín cooperativa ubicada a temperaturas bajas (canal A). En el segundo caso, la sustitución progresiva de aniones PF_6^- por AsF_6^- lleva a la estabilización de la transición de espín cooperativa desplazada hacia temperaturas más elevadas (canal B) favorecida por la organización más desordenada de las cadenas butilo y de los aniones típica de la fase LS_2 .

En este capítulo se demuestra, por primera vez, que es posible desacoplar dos eventos sincronizados que combinan SCO y transición de fase cristalográfica mediante modificación química eligiendo adecuadamente la sustitución isomórfica apropiada (ion metálico o el contra-anión) que discrimine selectivamente entre dos comportamientos SCO separados caracterizados por las fases LS_1 y LS_2 . El diseño de materiales inteligentes totalmente controlables capaces de responder a estímulos externos de manera deseada supone uno de los retos más ambiciosos en el campo de investigación de ciencia de los materiales. Los resultados presentados en este capítulo refuerzan la idea de que los materiales moleculares biestables que exhiben sinérgicamente la interacción entre dos o más transiciones de fase en un mismo dominio cristalino son particularmente adecuados para este fin.

Breaking the rule: access to thermodynamically prohibited “reverse” spin crossover in iron(II) complexes

En el capítulo siete se describe una nueva serie de complejos SCO de Fe(II) anfifílicos contituidos por ligandos tridentados ionogénicos, con núcleos de coordinación $[N_2O]$, funcionalizados con cadenas alquílicas lipofílicas, las cuales tienen la capacidad de inducir polimorfismo lipídico y/o transiciones de fase (incluyendo procesos de fusión), hechos que pueden afectar de manera drástica a las propiedades SCO. En un trabajo anterior desarrollado en nuestro grupo de investigación se demostró que se puede lograr un control razonable de los parámetros característicos SCO (temperaturas críticas, $T_{1/2}$, y anchuras de histéresis, ΔT) seleccionando adecuadamente la longitud de la cadena alquílica en una familia de complejos SCO de Fe(II) derivados de la condensación de la 2-piridina alquilcetona con una benzohidrazida trialquilada. En este capítulo se ha demostrado que la sustitución de la unidad de piridina por la 2-pirimidina etilcetona permite la generación de una nueva familia de complejos anfifílicos de Fe(II) SCO. A diferencia de los complejos definidos por alquilpiridinas, en esta nueva serie se observa cómo la longitud de las cadenas alquílicas conectadas a las unidades de benzohidrazida afectan de forma notable al empaquetamiento molecular y a las propiedades magnéticas de los nuevos compuestos de bajo punto de fusión, definiéndose dos sub-grupos bien diferenciados. Los complejos funcionalizados con cadenas alquílicas cortas (átomos de carbono entre 4 y 8) presentan un comportamiento SCO muy cooperativos acoplados íntimamente a una transformación sólido \leftrightarrow líquido. De forma sorprendente, los compuestos sustituidos por cadenas carbonadas más largas (átomos de carbono entre 10 y 14) muestran, al calentar, una transformación HS \rightarrow LS termodinámicamente prohibida durante el proceso de fusión que implica una conversión de iones Fe(II) cercana al 50%. La modificación de las propiedades magnéticas al superar un umbral mínimo de longitud de cadena alquílica se asocia al cambio de organización de los complejos en el estado sólido. Concretamente, debido a la disposición a nivel local de los centros de coordinación de Fe(II) de moléculas adyacentes pertenecientes a una misma capa. A pesar de no poder obtener una información detallada de la estructura de los complejos funcionalizados con cadenas largas, los difractogramas correspondientes obtenidos a temperatura ambiente muestran un empaquetamiento menos efectivo en comparación con los derivados funcionalizados con cadenas alquílicas más cortas.

CAPÍTULO 8

CONCLUSIONS

Strong Cooperative Spin Crossover in 2D and 3D Fe^{II}-M^{I,II} Hofmann-Like Coordination Polymers Based on 2-Fluoropyrazine

Chapter two presents the SCO behavior of a new series of 2D and 3D Hofmann-like Fe^{II} compounds obtained from the self assembly of Fe^{II} ions, fluoropyrazine (Fpz), and [M^{II}(CN)₄]²⁻ (M^{II} = Ni, Pd, Pt) and [Au^I(CN)₂]⁻ building blocks. The compounds based on [M^{II}(CN)₄]²⁻ building blocks are stable 2D coordination polymers with formula {Fe(Fpz)₂[M^{II}(CN)₄]} (M^{II} = Ni, Pd, Pt) (**FpzM**). The **FpzPd** and **FpzPt** derivatives undergo strong cooperative thermal- and light-induced SCO behavior accompanied by drastic color changes from light-yellow (HS) to deep-red (LS), in contrast to the **FpzNi** derivate that is HS at all temperatures even at a pressure of 0.7 GPa. From $T_{1/2}$ values destabilization of the LS state follows the trend **FpzPt** > **FpzPd** > **FpzNi**. The lack of SCO in the Ni derivate has tentatively been associated with dense packing of the corrugated layers. The 3D metal organic framework {Fe(Fpz)[Pt(CN)₄]}·1/2H₂O (**FpzPt3D**), obtained from different synthetic conditions, is a distorted version of the well-known Hofmann-like compound {Fe(pz)[Pt(CN)₄]}₂. It displays unusual low thermal stability tentatively ascribed to structural strain and is HS at all temperatures. By contrast, the 3D compound {Fe(Fpz)[Au(CN)₂]}₂ (**FpzAu**) constituted of two identical interpenetrated 3D frameworks displays very cooperative and asymmetric SCO with a stable hysteresis larger than 40 K.

Switchable Spin-Crossover Hofmann-Type 3D Coordination Polymers Based on Tri- and tetratopic Ligands

Chapter three introduces two new ligands with unusual coordination denticities, trigonal (L^{N3}) and square (L^{N4}), and are included in the library of SCO Hofmann-type metal-organic frameworks derived from [M^I(CN)₂]⁻ (M^I = Ag, Au). Using slow diffusion methods in presence of appropriate guest molecules, L^{N3} affords six new isostructural clathrate

compounds generically formulated as $\{\text{Fe}(\text{L}^{\text{N}3})[\text{M}^{\text{I}}(\text{CN})_2]_2\}\cdot\text{Guest}$ [$\text{M}^{\text{I}} = \text{Ag}$ (**1-Guest**), Au (**2-Guest**), $\text{Guest} = \text{PhCN}$, PhNO_2 , $o\text{-PhCl}_2$]. The structure of the PhNO_2 derivative shows that $\text{L}^{\text{N}3}$ works as a bis-monodentate ligand to satisfy, most likely, the metrics imposed by the $\{\text{Fe}[\text{M}^{\text{I}}(\text{CN})_2]_2\}_n$ layers, thereby acting as a pillar between the layers, thus affording an open 3D framework. Two identical frameworks interpenetrate in the same space and hold together through short intermolecular interactions including weak $\text{M}^{\text{I}}\cdots\text{M}^{\text{I}}$ metallophilic interactions. The six clathrates exhibit thermal- and light-induced SCO properties. Concerning the ligand $\text{L}^{\text{N}4}$, one should expect the coordination to four Fe^{II} and generation of a complicated framework mediated by the $[\text{M}^{\text{I}}(\text{CN})_2]^-$ bridges; however, the occurrence of geometric incompatibilities is apparent, which are solved for the Ag^{I} derivative by virtue of its much more labile coordination sphere. Consequently, the structure of $\{\text{Fe}(\text{L}^{\text{N}4})[\text{Ag}^{\text{I}}(\text{CN})_2][\text{Ag}_2^{\text{I}}(\text{CN})_3]\}\cdot\text{H}_2\text{O}$ (**3-H₂O**) is made up of extended $\{\text{Fe}[\text{Ag}^{\text{I}}(\text{CN})_2][\text{Ag}_2^{\text{I}}(\text{CN})_3]\}_n$ layers pillared by two opposite pyridine rings of $\text{L}^{\text{N}4}$, which act as axial ligands of Fe^{II} , while the remaining two pyridine rings coordinate the Ag^{I} centers of the in situ generated $[\text{Ag}_2^{\text{I}}(\text{CN})_3]^-$ units. The much more inert of Au^{I} prevents the formation of this uncommon triple-interpenetrated network. The higher characteristic $T_{1/2}$ value of the SCO in **3-H₂O** derivative is consistent with the incomplete photogeneration of the HS state at low temperatures.

Influence of Host-Guest and Host-Host Interactions on the Spin-Crossover 3D Hofmann-type Clathrates $\{\text{Fe}^{\text{II}}(\text{pina})[\text{M}^{\text{I}}(\text{CN})_2]_2\}\cdot x\text{MeOH}$ ($\text{M}^{\text{I}} = \text{Ag}, \text{Au}$)

Chapter four describes the synthesis, structural characterization and magnetic properties of two new isostructural porous 3D compounds with general formula $\{\text{Fe}(\text{pina})[\text{M}^{\text{I}}(\text{CN})_2]_2\}\cdot x\text{MeOH}$ ($\text{M}^{\text{I}} = \text{Ag}$ (**1-xMeOH**), Au (**2-xMeOH**), $x \sim 5$), where *pina* is N-(pyridin-4-yl)-isonicotinamide, a bis-monodentate pyridine-like pillar ligand functionalized with an amide group. The structure of both compounds is constituted of two equivalent 3D frameworks interpenetrated held together through argentophilic (or aurophilic) interactions and interligand $\text{C}=\text{O}\cdots\text{HC}$ H-bonds. Despite the two-fold interpenetration of the frameworks, they display accessible void volume capable of docking a maximum of 5 molecules of methanol defining an infinite network of hydrogen bonds which extend along the channels defined by the two interpenetrated frameworks. In the solvated form, the **1-xMeOH** and **2-xMeOH** undergo two- and four-step hysteretic thermally induced SCO, respectively. The

loss of the solvent molecules transforms the cooperative behaviors into gradual and incomplete SCO. Interestingly, the solvent desorption from **1**·*x*MeOH (**2**·*x*MeOH) takes place via single-crystal-to-single-crystal transformation to give **1** (**2**), thereby allowing to correlate the structural modifications and the SCO.

Very Long-Lived Photogenerated High-Spin Phase of a Multistable Spin-Crossover Molecular Material

Chapter five shows that the singular thermal and light induced SCO behavior of the mononuclear compound $[\text{Fe}(n\text{Bu-im})_3(\text{tren})](\text{PF}_6)_2$ is essentially linked to structural instability of the butyl tails attached to the imidazole rings. A previous study reported by our research group described the occurrence of two different strong cooperative thermal SCO transitions characterized by two LS phases (LS₁ and LS₂) for this compound. The two LS phases are controlled by the kinetics of crystallographic phase transitions, where conformational changes in the butyl tails play a key role together with the PF₆⁻ anions. Indeed, the LS₁ and LS₂ states are characterized by two distinct arrangements of the butyls chains and PF₆⁻ anions. This behavior, previously analyzed by our magnetic data, is reinvestigated and confirmed by single crystal UV-vis spectroscopy in this chapter.

Furthermore, a combination of single-crystal UV-vis spectroscopy, single-crystal X-ray synchrotron studies and SQUID measurements reveals that the butyl tails are also involved in the unusual long relaxation times when thermal- and photo-generated metastable HS* relaxes back to the fundamental LS₁ state. Depending on the irradiation temperature, it is possible to reach two different photoexcited HS states: HS₁^{1irr} state, whose structure was determined under irradiation at 25 K, and the HS₁^{2irr} state, whose structure was determined under irradiation of LS₁ at 90 K. The conformations of the butyl chains of the ligand are identical in HS₁^{1irr} and in LS₁ state, whereas two of the HS₁^{2irr} butyl chains adopt a different conformation. During the relaxation process at 90 K, reorientations of the butyl chains occur through order/disorder transitions. We believe that these reorientations of the butyl chains are responsible for the unexpected longer relaxation time for the HS₁^{2irr} than for the HS₁^{1irr} phase. Interestingly, the structure of the HS^{quench} state, generated via thermal quenching from room temperature, is identical to that of HS₁^{2irr} and, hence, the relaxation time of those structurally identical states are of the same order of magnitude.

It is worth noting that, with the exception of a few Fe-Co charge transfer Prussian blue analogues, there are only two SCO systems with T_{LIESST} above 100 K, while a few other Fe(II) SCO complexes present a T_{LIESST} around 90 - 100 K. Unlike precious examples, $[\text{Fe}(n\text{Bu-im})_3(\text{tren})](\text{PF}_6)_2$ is an excellent platform to investigate the interplay between SCO and conformational instability associated to the ligand. This instability affords the unusual opportunity to fully populate the metastable $\text{HS}_1^{2\text{irr}}$ state, irradiating at as high temperature 80 – 90 K, thanks to the long time of structural reconversion arising from the mismatch between the excited and fundamental configurations.

Discrimination between two memory channels by molecular alloying in a doubly bistable spin crossover material

Chapter six unveils the relationship between the crystallographic phase transition and the occurrence of two different cooperative thermal SCO behaviors (so called memory channels) in compound $[\text{Fe}(n\text{Bu-im})_3(\text{tren})](\text{PF}_6)_2$. The followed strategy involves the preparation of two different isomorphous molecular alloys: i) the active Fe(II) centers are substituted with the Zn(II) and Ni(II) ions to give compounds $[\text{Fe}_{1-x}\text{M}_x(n\text{Bu-im})_3(\text{tren})](\text{PF}_6)_2$ (M = Ni, Zn); ii) the PF_6^- counter-anions are partially or totally substituted with the more voluminous anion AsF_6^- to give $[\text{Fe}(n\text{Bu-im})_3(\text{tren})](\text{P}_{1-x}\text{As}_x\text{F}_6)_2$ derivatives. In the former case metal, substitution selectively favours the arrangement of the butyl tails and PF_6^- anions characteristic of the phase LS_1 in both spin states (HS, LS), thus promoting a low temperature hysteretic SCO transition (channel A). In the latter case, substitution of the PF_6^- anion with AsF_6^- promotes a high temperature hysteretic SCO transition (channel B) favoured by the more disordered arrangement of the butyl tails and anions characteristic of the LS_2 state, thereby affording a high temperature hysteretic transition.

In this chapter we demonstrate, for the first time, that decoupling of two synchronous cooperative events such as a SCO and an intrinsic structural phase transition can be chemically achieved by choosing the appropriate isomorphous substitution (metal ion or anion in the present case) to selectively discriminate between two separated hysteretic SCO behaviours. The design of fully controllable smart materials able to respond to external stimuli in a desired way is a challenging target in materials science. The herein reported

results supports the idea that bistable molecular materials exhibiting synergetic interplay between two or more phase transitions in the same crystal are particularly well-suited to this end.

Breaking the rule: access to thermodynamically prohibited “reverse” spin crossover in iron(II) complexes

Chapter seven describes a new series of amphiphilic Fe(II) SCO complexes derived from tridentate ionogenic ligands, with $[N_2O]$ coordination core, functionalized with lipophilic alkyl chains, which are prone to lipid polymorphism and phase transition (including melting), facts that can dramatically affect the SCO properties. In a previous work, reported by our group, it was demonstrated that a full control of the SCO characteristic parameters (critical temperature, $T_{1/2}$, and hysteresis width, ΔT) can be reached by selecting the length of the alkyl chains in a family of Fe(II) SCO complexes derived from the condensation of 2-pyridine alkylketone with a tri-alkylated benzohydrazide. In this chapter, we have demonstrated the replacement of the pyridine moiety with a 2-pyrimidine ethylketone affords a new family of related amphiphilic Fe(II) SCO complexes. Unlike their pyridine ketone counterparts, the molecular packing and hence the SCO properties are critically affected by the length of the alkyl chains attached to the benzohydrazide moiety in this novel low-melting-point series of compounds, defining two well-separated sub-groups. Complexes functionalized with short alkyl tails (ranging from 4 to 8 carbon atoms) undergo regular hysteretic SCO behavior intimately coupled by a solid \leftrightarrow liquid transformation. Surprisingly, compounds functionalized with larger carbon chains (ranging from 10 to 14 carbon atoms) show, upon heating, a thermodynamically prohibited HS \rightarrow LS SCO transformation during the melting process which involves up to the 50% conversion of Fe(II) ions. The occurrence of this anomalous behavior, once overcome a certain threshold chain length, is ascribed to a different arrangement of the complexes in solid state. More precisely, due to the distinct local disposition of Fe(II) coordination centers of adjacent molecules inside the same layers. Despite the absence of precise structural data of the long tail functionalized complexes, room temperature X-ray powder diffraction patterns have shown a looser packing in comparison with shorter alkyl chains derivatives.

Apéndice

Strong Cooperative Spin Crossover in 2D and 3D Fe^{II}–M^{I,II} Hofmann-Like Coordination Polymers Based on 2-Fluoropyrazine

Francisco Javier Valverde-Muñoz,[†] Maksym Serebyuk,^{*,†,‡} M. Carmen Muñoz,[§] Kateryna Znovnyak,[‡] Igor O. Fritsky,[‡] and José Antonio Real^{*,†}

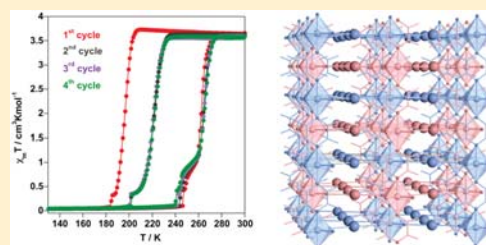
[†]Institut de Ciència Molecular (ICMol), Departament de Química Inorgànica, Universitat de València, C/Catedrático José Beltrán Martínez, 2, Paterna 46980, Valencia, Spain

[‡]Department of Chemistry, Taras Shevchenko National University, Volodymyrska Strasse 64, Kyiv 01601, Ukraine

[§]Departament de Física Aplicada, Universitat Politècnica de València, Camino de Vera s/n, Valencia 46022, Spain

Supporting Information

ABSTRACT: Self-assembling iron(II), 2-fluoropyrazine (Fpz), and [M^{II}(CN)₄]²⁻ (M^{II} = Ni, Pd, Pt) or [Au^I(CN)₂]⁻ building blocks have afforded a new series of two- (2D) and three-dimensional (3D) Hofmann-like spin crossover (SCO) coordination polymers with strong cooperative magnetic, calorimetric, and optical properties. The iron(II) ions, lying on inversion centers, define elongated octahedrons equatorially surrounded by four equivalent centrosymmetric μ_4 -[M^{II}(CN)₄]²⁻ groups. The axial positions are occupied by two terminal Fpz ligands affording significantly corrugated 2D layers {Fe(Fpz)₂[M^{II}(CN)₄]}_n. The Pt and Pd derivatives undergo thermal- and light-induced SCO characterized by $T_{1/2}$ temperatures centered at 155.5 and 116 K and hysteresis loops 22 K wide, while the Ni derivative is high spin at all temperatures, even at pressures of 0.7 GPa. The great stability of the high-spin state in the Ni derivative has tentatively been ascribed to the tight packing of the layers, which contrasts with that of Pt and Pd derivatives in the high- and low-spin states. The synthesis and structure of the 3D frameworks formulated {Fe(Fpz)[Pt(CN)₄]}·1/2H₂O and {Fe(Fpz)[Au(CN)₂]}₂, where Fpz acts as bridging ligand, which is also discussed. The former is high spin at all temperatures, while the latter displays very strong cooperative SCO centered at 243 K accompanied by a hysteresis loop 42.5 K wide. The crystal structures and SCO properties are compared with those of related complexes derived from pyrazine, 3-fluoropyridine, and pyridine.



INTRODUCTION

Iron(II) spin crossover (SCO) complexes are a well-known class of switchable molecular materials.¹ They switch between the electronic low-spin (LS) and high-spin (HS) states in a reversible, controllable, and detectable manner through the action of external stimuli, i.e., temperature, light, pressure, analytes, and electric and magnetic fields. The switch occurs with concomitant changes in the magnetic, optical, electric, and structural properties. In some cases the changes are strongly cooperative and confer to the material a bistable character, i.e., hysteresis. These features have fueled much activity in the field and created important expectancies in view of potential applications in molecular spintronics, sensors, and memories.²

Hofmann-like SCO compounds are one of the most important sources of bistable SCO materials and have stimulated much research in the last 15 years. The prototypical Hofmann-like compound, {Ni(NH₃)₂[Ni(CN)₄]}_n, was reported by Hofmann and Küspert in 1897.³ Its structure was described in the 1950s by Powell and Rainer as a pile of two-dimensional (2D) layers constituted of square-planar [Ni(CN)₄]²⁻ centers equatorially linked to octahedral Ni(II) sites,

which saturate its coordination sphere with two axial NH₃ molecules.⁴ Schwarzenbach⁵ and later Iwamoto⁶ and co-workers synthesized the first heterobimetallic 2D {M(NH₃)₂[M'(CN)₄]} derivatives and three-dimensional (3D) {M(L)[M'(CN)₄]} homologues, generically referred as Hofmann clathrates due to their ability to adsorb small aromatic molecules. In 1996 Kitazawa and co-workers reported the first Hofmann-like 2D SCO coordination polymer {Fe(pyridine)₂[Ni(CN)₄]}.⁷ This compound displays a cooperative thermal-induced SCO accompanied by drastic changes of the magnetic and optical (color) properties. Later, our group extended this idea to the homologous [Pd(CN)₄]²⁻ and [Pt(CN)₄]²⁻ SCO derivatives, the new 3D porous {Fe(pyrazine)[M^{II}(CN)₄]} (M^{II} = Ni, Pd, Pt),⁸ and the 2D and 3D {FeL_x[M^I(CN)₂]}₂ related families of SCO coordination polymers (L = monodentate or bis-monodentate ligand; M^I = Cu, Ag, Au).⁹ Systematic replacement of pyridine and pyrazine with related monodentate and bisonodentate L ligands

Received: August 5, 2016

Published: September 29, 2016

afforded an important number of coordination polymers with interesting thermo-, piezo-, photo-, and chemoswitchable cooperative SCO behaviors, which combine with a rich variety of additional relevant properties such as reversible ligand exchange in the solid state, polymorphism, metallophilic interactions, or porosity and inclusion chemistry. Furthermore, the amenability to being processed as thin films and nanocrystals has converted the porous $\{\text{Fe}(\text{L})[\text{Pt}^{\text{II}}(\text{CN})_4]\}$ derivatives in excellent platforms to systematically investigate the SCO behavior at nanoscale. The structure and properties of these thermo-, piezo-, photo-, and chemoswitchable SCO iron(II)–metallocyanate-based coordination polymers have been recently reviewed.¹⁰

Despite the short time elapsed since this review, interest in these materials has been continuously growing. For example, in the series of $\{\text{Fe}(\text{pyrazine})[\text{M}^{\text{II}}(\text{CN})_4]\}$, the quality of continuous and nanopatterned thin films of $\{\text{Fe}(\text{pyrazine})[\text{Pt}^{\text{II}}(\text{CN})_4]\}$ has been assessed by means of atomic force microscopy and surface plasmon resonance¹¹ as well as by synchrotron X-ray diffraction.¹² The cooperative SCO properties of $\{\text{Fe}(\text{pyrazine})[\text{M}^{\text{II}}(\text{CN})_4]\}$ nanocrystals were modulated through chemical pressure, induced by different polymeric coatings ($\text{M}^{\text{II}} = \text{Pt}$),¹³ and through correlative effects between size decrease and increase of stiffness in ultrasmall (ca. 2 nm) nanoparticles ($\text{M}^{\text{II}} = \text{Ni}$).¹⁴ Interest has also been focused on the modulation of the critical temperatures and cooperativity of the SCO induced by guests. In this respect, precise control of the critical SCO temperature has been achieved through the combined effects of oxidative I_2 adsorption, on the Pt^{II} sites, and chemical migration of the iodine centers.¹⁵ Modulation of cooperativeness has been described for clathrate systems constituted of thiourea ($\text{M}^{\text{II}} = \text{Pd}, \text{Pt}$),¹⁶ maleic anhydride ($\text{M}^{\text{II}} = \text{Pt}$),¹⁷ and five-membered aromatic rings (furan, thiophene, pyrrole; $\text{M}^{\text{II}} = \text{Pt}$)¹⁸ as guest molecules. In addition, the effect of the spin state on the adsorption of CO_2 ,¹⁹ the stabilization of the LS state upon SO_2 adsorption,²⁰ and the adsorption of H_2 and its catalytic ortho–para conversion in the pores²¹ have been recently investigated. The effect of host–guest interactions and its influence on the SCO behavior has also been a subject of interest from a theoretical point of view.^{16,18,20,22} Application of specific physical techniques have uncovered new important properties of $\{\text{Fe}(\text{pyrazine})[\text{M}^{\text{II}}(\text{CN})_4]\}$. For example, combination of neutron spectroscopy and NMR solid-state studies has demonstrated, for $\text{M}^{\text{II}} = \text{Pt}$, that the pyrazine pillars act as switchable molecular rotators whose frequency depends on the spin state of the iron(II) center and on the presence of guests.²³ Synchrotron powder diffraction on microcrystalline samples of $\text{M}^{\text{II}} = \text{Pt}$ showed complete photoconversion of the LS state to the metastable HS state and subsequent relaxation at 10 K.²⁴ Photoconversion between the LS and the HS states at ca. 290 K irradiating inside the hysteresis loop has been analyzed through differential scanning calorimetry (DSC)²⁵ and single-crystal X-ray diffraction.²⁶

The synthesis of new 2D and 3D Hofmann-like coordination polymers has also attracted much interest in the last years. On one hand, replacement of pyrazine with longer rod-like ditopic ligands, L, has allowed us to investigate new series of 3D $\{\text{Fe}(\text{L})[\text{M}^{\text{II}}(\text{CN})_4]\}$ SCO homologues with enhanced porous capacity.²⁷ Similarly, the use of monodentate ligands conveniently functionalized has afforded 2D $\{\text{Fe}(\text{L})_2[\text{Pt}^{\text{II}}(\text{CN})_4]\}$ SCO compounds featuring interdigitated interlayer structures with tailored host–host and host–guest interactions.²⁸ On the

other hand, interesting inclusion chemistry and cooperative SCO behaviors have been described for the series of related 2D and 3D Hofmann-like compounds based on the $[\text{M}^{\text{I}}(\text{CN})_2]^-$ ($\text{M}^{\text{I}} = \text{Ag}$ and Au) bridging ligands.²⁹

In this context Gural'skiy and co-workers recently reported a new family of 2D Hofmann-like coordination polymers $\{\text{Fe}(\text{L})_2[\text{M}^{\text{II}}(\text{CN})_4]\}$ ($\text{M}^{\text{II}} = \text{Ni}, \text{Pd}, \text{Pt}$) based on 2-substituted pyrazine ligands.^{28e} Cooperative SCO was observed for the 6 complexes derived from 2-chloropyrazine and 2-methylpyrazine complexes. Coincidentally, with the aforementioned work, we focused our attention on the synthesis of Fe^{II} SCO Hofmann-like coordination polymers based on 2-fluoropyrazine (Fpz). Here, we report on the synthesis, crystal structure, magnetic, photomagnetic, and calorimetric properties of $\{\text{Fe}(\text{Fpz})_2[\text{M}^{\text{II}}(\text{CN})_4]\}$ ($\text{M}^{\text{II}} = \text{Ni}$ (**FpzNi**), Pd (**FpzPd**), Pt (**FpzPt**)), $\{\text{Fe}(\text{Fpz})[\text{M}^{\text{II}}(\text{CN})_4]\} \cdot 1/2\text{H}_2\text{O}$ (**FpzPt3D**), and $\{\text{Fe}(\text{Fpz})_2[\text{Au}^{\text{I}}(\text{CN})_2]\}$ (**FpzAu**).

RESULTS

Magnetic Properties. The thermal dependence of the $\chi_{\text{M}}T$ product measured at 2 K/min (χ_{M} is the molar magnetic susceptibility and T temperature) for **FpzNi**, **FpzPd**, and **FpzPt** is shown in Figure 1a. The $\chi_{\text{M}}T$ value about $3.84 \text{ cm}^3 \text{ K mol}^{-1}$ indicates that the three derivatives are HS at 300 K. It remains practically constant down to 151 and 118 K for **FpzPt** and **FpzPd**. Upon further cooling, $\chi_{\text{M}}T$ drops abruptly to a value of $0.16 \text{ cm}^3 \text{ K mol}^{-1}$ at 137 K (**FpzPt**) and $0.22 \text{ cm}^3 \text{ K mol}^{-1}$ at 100 K (**FpzPd**), indicating that these derivatives undergo a complete spin transition characterized by equilibrium temperatures $T_{1/2} \approx 144.5$ (**FpzPt**) and 105 K (**FpzPd**). The $\chi_{\text{M}}T$ vs T plot in the heating mode shows the occurrence of a 22 K wide hysteresis loop with $T_{1/2} \approx 166.5$ (**FpzPt**) and 127 K (**FpzPd**). Consequently, these spin transitions are strongly cooperative. The magnetic behavior of **FpzNi** is characteristic of an Fe^{II} ion in the HS state; the slight decrease of $\chi_{\text{M}}T$ below 100 K can be ascribed to the effect of zero-field splitting and/or very weak magnetic coupling. This HS behavior persists even at pressures as high as 0.7 GPa (see Figure S1 in SI). A similar thermal dependence of $\chi_{\text{M}}T$ at ambient pressure has been observed for **FpzPt3D** (see Figure S2 in SI).

Photogeneration of the metastable HS* state at low temperature, the so-called light-induced excited spin state trapping experiment (LIESST),³⁰ was carried out on microcrystalline samples of **FpzPt** (1.7 mg) and **FpzPd** (2.1 mg) spread over a 16 mm^2 surface, fastened with permanent adhesive (Figure 1b and 1c). The samples were cooled down to 10 K, where $\chi_{\text{M}}T \approx 0.10 \text{ cm}^3 \text{ K mol}^{-1}$, and then irradiated with green (**FpzPt**, $\lambda = 532 \text{ nm}$) or red (**FpzPd**, $\lambda = 633 \text{ nm}$) light, attaining a $\chi_{\text{M}}T$ saturation value of ca. 1.80 (**FpzPt**) and $2.15 \text{ cm}^3 \text{ K mol}^{-1}$ (**FpzPd**) in ca. 3 h. The light was then switched off and temperature increased at a rate of 0.3 K min^{-1} . In the 10–39 K temperature range $\chi_{\text{M}}T$ increased up to a maximum value of ca. 2.26 (**FpzPt**) and $3.21 \text{ cm}^3 \text{ K mol}^{-1}$ (**FpzPd**) at 39 K, which reflects the thermal population of the different microstates arising from the zero-field splitting of the HS* ($S = 2$) state and/or antiferromagnetic coupling. This suggests that the light-induced population of the HS* state is ca. 57% and 85% at 10 K for **FpzPt** and **FpzPd**, respectively. For **FpzPd**, $\chi_{\text{M}}T$ drops slowly to attain a value of $3.04 \text{ cm}^3 \text{ K mol}^{-1}$ at 60 K and then rapidly decreases and reaches a value of about $0.24 \text{ cm}^3 \text{ K mol}^{-1}$ at ca. 72 K, indicating complete HS* \rightarrow LS relaxation. By contrast, $\chi_{\text{M}}T$ drops rapidly to $0.16 \text{ cm}^3 \text{ K mol}^{-1}$ at 58 K. The T_{LIESST} temperature³¹ determined from the

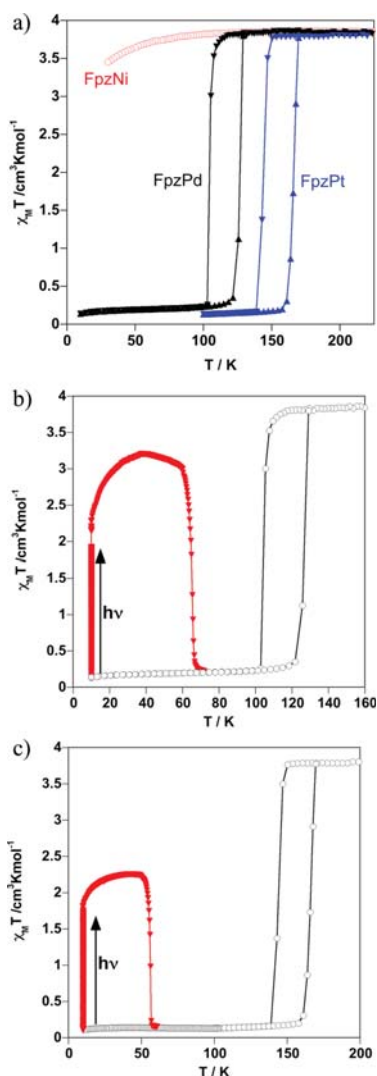


Figure 1. (a) $\chi_M T$ vs T plots for FpzNi, FpzPd, and FpzPt (temperature scan rate 2 K min^{-1}). LIESST effect for compounds FpzPd (b) and FpzPt (c) (see text for experimental details).

maximum variation of $\chi_M T$ in the HS \rightarrow LS relaxation is 56.3 and 65.5 K for FpzPt and FpzPd, respectively. These values reflect the relative stabilization of the LS state with respect to the HS state in each compound, and it is a consequence of the so-called inverse energy-gap law, i.e., the metastability of the photogenerated HS* species decreases as the stability of the LS increases.³²

The magnetic properties of compound FpzAu measured at 1 K/min are displayed in Figure 2. At 300 K $\chi_M T$ is ca. 3.6 and remains practically constant down to 208 K . Below this temperature $\chi_M T$ displays a steep and complete spin transition ($\chi_M T \approx 0$ at 180 K) characterized by a small plateau at ca. 91% of the HS \rightarrow LS transformation (centered at 187 K) and $T_{1/2}^{\downarrow} =$

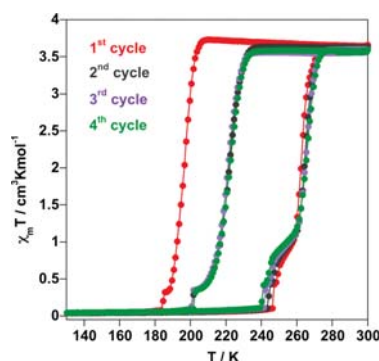


Figure 2. $\chi_M T$ vs T plots for compound FpzAu (see text; temperature scan rate 1 K min^{-1}).

196 K . Upon heating $\chi_M T$ does not match the cooling mode. Indeed, a more marked plateau occurs at 23% of LS \rightarrow HS transformation, and $T_{1/2}^{\uparrow} = 262 \text{ K}$ shows the occurrence of a hysteresis 66 K wide. In order to check the hysteresis stability, the same cooling–heating cycle was repeated three times more at the same scan temperature rate. In the second cycle, the cooling mode shows that the spin transition takes place at $T_{1/2}^{\downarrow} = 221 \text{ K}$, 25 K higher than observed for the first cycle, while small differences are observed in the heating mode ($T_{1/2}^{\uparrow} = 263 \text{ K}$). The third and fourth cycles give essentially the same transition as the second one. Consequently, the stable hysteresis loop is 42 K wide, which indeed reflects a strong cooperative behavior. It deserves to be noted that these measurements were performed on single crystals and that after the cycles the crystals are self-destroyed becoming powder. Precipitated microcrystalline samples of FpzAu behave in a similar way (see Figure S3 and Table S1 in SI). However, they show the following relevant differences with respect to the single-crystal ones: (i) they display approximately 10% of residual paramagnetism; (ii) the first and second cycles show $T_{1/2}^{\downarrow}$ values ca. 14 K smaller (larger hysteresis) while essentially coincide for the third and fourth cycles; (iii) the small step observed in the $\chi_M T$ vs T plot for the single-crystal samples is not observed for the precipitated ones. The different texture of these samples and/or the presence of residual paramagnetism are two reasonable speculative explanations for this observation.

Calorimetric Properties. Quantitative differential scanning calorimetry (DSC) measurements were carried out at a temperature scan rate of 10 K/min for FpzPt and FpzAu ($T_{1/2}$ values for FpzPd are out of the temperature range of our DSC). The anomalous variation of the molar specific heat ΔC_p versus T for the cooling and heating modes is displayed in Figure 3. The average enthalpy ΔH and entropy ΔS variations are gathered in Table 1 together with the critical temperatures obtained from the maximum/minimum values of ΔC_p . The critical temperatures obtained from these DSC data agree reasonably well with those deduced from the magnetism measurements for FpzPt and FpzAu. The large ΔS and ΔH values are consistent with those reported for related Hofmann-like coordination polymers undergoing strong cooperative spin transitions.¹⁰

Crystal Structure. Structures of the 2D Complexes FpzM. The crystal structure was measured at 200 K for FpzNi, FpzPd, and FpzPt and at 98.5 and 120 K for FpzPd and FpzPt,

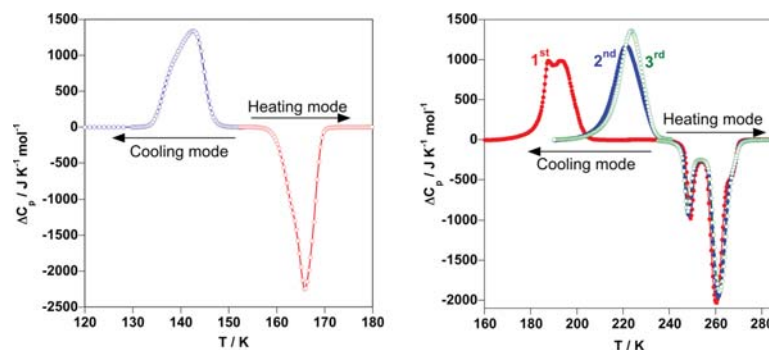


Figure 3. Anomalous heat capacity (DSC) for **FpzPt** (left) and **FpzAu** (right). Red blue and green curves in **FpzAu** refer to the first, second, and third cooling–heating cycles (temperature scan rate 10 K min⁻¹).

Table 1. Thermodynamic Data Obtained from Calorimetric DSC Measurements for the SCO of **FpzPt** and **FpzAu**

| | FpzPt | FpzAu | | |
|---|--------------|--------------|--------------|-------------|
| | | first cycle | second cycle | third cycle |
| $T_{1/2}^{\text{I}}$ (K) | 142.5 | 193.1 | 221.5 | 223.4 |
| $T_{1/2}^{\text{II}}$ (K) | 165.7 | 260.4 | 261.0 | 261.0 |
| ΔT (K) | 22 | 66 | 39.5 | 37.6 |
| ΔS^{sw} (J K ⁻¹ mol ⁻¹) | 71.2 | 73.4 | 73.7 | 75.1 |
| ΔH^{sw} (kJ mol ⁻¹) | 10.95 | 16.57 | 17.34 | 18.14 |

respectively. These compounds are isostructural (see Figure S4 in SI) and, in the temperature interval investigated, show the orthorhombic *Pmna* space group. Crystallographic data, bond distances, and angles are given in Tables 2 and 3. Figure 4a displays an ORTEP view of a fragment of the structure showing the asymmetric unit with the numbering atom scheme representative for the three compounds. The Fe^{II} atom lies at an inversion center which defines an elongated octahedral coordination site [Fe^{II}N₆]. The equatorial positions are occupied by the nitrogen atoms of four equivalent centrosymmetric square-planar [M(CN)₄]²⁻ groups. The Fe–N_{eq} bond distances [Fe–N(2)_{eq} = 2.145(3) Å (**FpzNi**), 2.138(2) Å (**FpzPd**), and 2.135(3) Å (**FpzPt**) at 200 K] are shorter than the axial positions, which are occupied by the nitrogen atoms of the Fpz ligands [Fe–N(1)_{ax} = 2.240(4) Å (**FpzNi**), 2.229(3) Å (**FpzPd**), and 2.225(4) Å (**FpzPt**)]. The M^{II}–C and C–N bond distances are in the range 1.855–1.998 and 1.137–1.157 Å, respectively. The Fe–N average bond length of about 2.170 Å is consistent with the Fe^{II} in the HS state, in agreement with the magnetic data at this temperature.

At 98.5 (**FpzPd**) or 120 K (**FpzPt**) the Fe–N(1)_{ax} are shortened by 0.242 (**FpzPd**) and 0.235 (**FpzPt**) Å while the decrease of the Fe–N(2)_{eq} bond lengths is slightly smaller, 0.195 (**FpzPd**) and 0.194 (**FpzPt**) Å. The total average variation of about 0.21 Å is consistent with complete transformation of the [Fe^{II}N₆] core from the HS state to the LS state, a fact confirmed by the magnetic data. The sum of deviations from the ideal octahedron of the 12 “cis” N–Fe–N angles ($\sum = \sum_{i=1}^{12} |\theta_i - 90|$) shows that the coordination center is weakly distorted in the HS state with \sum values in the range 15–19° and do not change significantly in the LS state.

The [M(CN)₄]²⁻ groups link four equivalent Fe^{II}, thereby generating 2D [Fe₂M^{II}₂(CN)₄]_n grids which are markedly corrugated (Figure 4b). The equatorial [FeN₄]²⁺ plane defines

an angle of 36.9° (**FpzNi**), 35.7° (**FpzPd**), and 33.1° (**FpzPt**) with respect to the [M(CN)₄]²⁻ plane at 200 K and decreases down to 26.1° and 20.3° for the Pd and Pt derivatives at 98.5 and 120 K, respectively (Figure 4c). The layers stack in such a way that the metallic atoms of a layer, which lie in the (100) plane, project on the center of the [Fe–CN–M]₄ square windows defined by adjacent layers. The separation between consecutive planes is 7.213(6) (**FpzNi**), 7.388(5) (**FpzPd**), and 7.523(7) Å (**FpzPt**) at 200 K and 7.385(6) (**FpzPd**) and 7.496(6) Å (**FpzPt**) at 98.5 and 120 K respectively. The protruding Fpz ligands of consecutive layers interdigitate, defining almost face-to-face superposition along the [100] direction with centroid-to-centroid distances indicating the occurrence of weak π stacking: 3.642 (**FpzNi**), 3.726 (**FpzPd**), and 3.727 Å (**FpzPt**) at 200 K and 3.632 (**FpzPd**) and 3.629 Å (**FpzPt**) at 98.5 and 120 K, respectively (Figure 4c). Interestingly, due to the singular disposition of consecutive layers, the uncoordinated N atom of the Fpz of one layer points directly toward the unsaturated axial coordination positions of the [M(CN)₄]²⁻ groups of the adjacent layers, with the distance being particularly short for **FpzNi** (*d*(Ni⋯N(3)) is 2.981(5) Å). Other very short contacts between layers are defined by the atoms N(3) and F with the C(5) atom of the CN group (*d*(N(3)⋯C(5)) = 3.292(6) Å) and the C(4) atom (*d*(F⋯C(4)) = 3.130(7) Å), respectively. These short contacts are remarkably larger for Pd and Pt, and interestingly, the M⋯N(3) contact increases by ca. 0.3 Å when moving from the HS to the LS state (see Table 4). Most likely, this is a consequence of the aforementioned change of dihedral angle between the equatorial FeN₄ and the [M(CN)₄]²⁻ planes.

Structure of the 3D Complex FpzPt3D. Compound **FpzPt3D** shows the monoclinic *P2/m* unit cell in the temperature range 120–200 K (Tables 2 and 3). Figure 5a displays an ORTEP view of a fragment of the structure showing the asymmetric unit together with atom numbering. The Fe^{II} and Pt^{II} atoms lie at an inversion center. The former defines a slightly elongated octahedral coordination [Fe^{II}N₆] site with axial and equatorial Fe–N bond distances Fe–N(1) = 2.175(9) Å and Fe–N(2) = 2.133(5) Å, respectively. The latter defines square-planar [Pt(CN)₄]²⁻ units with usual Pt–C and C–N bond distances [Pt–C(3) = 1.978(5) Å and C–N = 1.154(8) Å]. The average Fe–N bond length, 2.147 Å, clearly indicates that this compound is HS at 120 K, in agreement with the magnetic properties.

Table 2. Crystal Data of FpzM (M = Ni, Pd, Pt), FpzPt3D, and FpzAu

| empirical formula | FpzNi | | FpzPd | | FpzPt | | FpzPt3D | | FpzAu | |
|---|-----------------------|-----------------------|-----------------------|-----------------------|-----------------------|-----------------------|--------------------|--------------------|--------------------|--------------------|
| | $C_{12}H_{18}F_6NiFe$ | $C_{12}H_{18}F_6PdFe$ | $C_{12}H_{18}F_6PtFe$ | $C_{12}H_{18}F_6PtFe$ | $C_{12}H_{18}F_6PtFe$ | $C_{12}H_{18}F_6PtFe$ | $C_8H_6F_3O_3PtFe$ | $C_8H_6F_3O_3PtFe$ | $C_8H_6F_3Au_2Fe$ | $C_8H_6F_3Au_2Fe$ |
| M_r | 414.81 | 462.50 | 462.50 | 551.19 | 551.19 | 461.10 | 651.93 | 651.93 | 651.93 | 651.93 |
| cryst. syst. | orthorhombic | orthorhombic | orthorhombic | orthorhombic | orthorhombic | orthorhombic | monoclinic | orthorhombic | orthorhombic | orthorhombic |
| space group | <i>Pnma</i> | <i>Pnma</i> | <i>Pnma</i> | <i>Pnma</i> | <i>Pnma</i> | <i>Pnma</i> | <i>P2/m</i> | <i>Cmca</i> | <i>Cmca</i> | <i>Cmca</i> |
| <i>T</i> (K) | 200 | 98.5 | 200 | 120 | 200 | 120 | 120 | 120 | 250 | 250 |
| <i>a</i> (Å) | 7.2842(2) | 7.2646(2) | 7.4526(5) | 7.2572(3) | 7.4534(4) | 7.2782(3) | 7.1107(10) | 7.1107(10) | 7.2563(3) | 7.2563(3) |
| <i>b</i> (Å) | 6.9449(2) | 6.9726(3) | 7.1125(4) | 6.9861(3) | 7.1275(4) | 7.5613(2) | 10.1715(13) | 10.1715(13) | 10.1992(5) | 10.1992(5) |
| <i>c</i> (Å) | 14.4255(5) | 14.7703(5) | 14.7770(11) | 14.9922(6) | 15.0455(10) | 7.4820(4) | 17.657(2) | 17.657(2) | 17.8959(7) | 17.8959(7) |
| β (deg) | | | | | | 101.494(5) | | | | |
| <i>V</i> (Å ³) | 729.75(5) | 748.17(5) | 783.28(9) | 760.10(5) | 799.28(8) | 403.50(3) | 1277.1(3) | 1277.1(3) | 1324.46(10) | 1324.46(10) |
| <i>Z</i> | 2 | 2 | 2 | 2 | 2 | 1 | 4 | 4 | 4 | 4 |
| <i>D_c</i> (mg cm ⁻³) | 1.888 | 2.053 | 1.961 | 2.408 | 2.290 | 1.898 | 3.391 | 3.391 | 3.270 | 3.270 |
| <i>F</i> (000) | 412 | 448 | 448 | 512 | 512 | 210 | 1143 | 1143 | 1143 | 1143 |
| μ (Mo K α) (mm ⁻¹) | 2.319 | 2.206 | 2.107 | 10.181 | 9.682 | 9.559 | 24.040 | 24.040 | 23.180 | 23.180 |
| cryst size (mm) | 0.12 × 0.15 × 0.15 | 0.08 × 0.08 × 0.15 | 0.08 × 0.08 × 0.15 | 0.06 × 0.10 × 0.10 | 0.06 × 0.10 × 0.10 | 0.06 × 0.10 × 0.10 | 0.06 × 0.06 × 0.08 | 0.06 × 0.06 × 0.08 | 0.06 × 0.06 × 0.08 | 0.06 × 0.06 × 0.08 |
| no. of total reflns | 1006 | 1018 | 1144 | 1091 | 1167 | 1413 | 812 | 812 | 906 | 906 |
| no. of reflns [<i>I</i> > 2 σ (<i>I</i>)] | 869 | 761 | 933 | 816 | 968 | 1384 | 524 | 524 | 659 | 659 |
| <i>R</i> [<i>I</i> > 2 σ (<i>I</i>)] | 0.0482 | 0.0346 | 0.0349 | 0.0200 | 0.0242 | 0.0406 | 0.0516 | 0.0516 | 0.0301 | 0.0301 |
| <i>R</i> [all data] | 0.0482 | 0.0564 | 0.0496 | 0.0318 | 0.0319 | 0.0421 | 0.0825 | 0.0825 | 0.0439 | 0.0439 |
| <i>S</i> | 0.970 | 0.975 | 1.178 | 0.951 | 1.088 | 0.985 | 0.885 | 0.885 | 1.005 | 1.005 |

^a $R_1 = \sum ||F_o| - |F_c|| / \sum |F_o|$; $wR_2 = [\sum [w(F_o^2 - F_c^2)]^2 / \sum [w(F_o^2)]]^{1/2}$; $w = 1 / [\sigma^2(F_o^2) + (mP)^2]$, where $P = (F_o^2 + 2F_c^2) / 3$; $m = 0.0231$ (200 K), 0.0177 (98.5 K), 0.0121 (200 K), 0.0254 (120 K), 0.0172 (200 K), 0.0702 (120 K), 0.0155 (120 K), 0.0324 (250 K), $n = 6.0177$ (200 K), 0.7115 (200 K), 1.5654 (98.5 K), 0.9728 (120 K), 1.7518 (200 K), 0.000 (120 K), 160.1028 (120 K), 0.000 (250 K).

Table 3. Selected Bond Lengths [Angstroms] and Angles [degrees] of FpzM (M = Ni, Pd, Pt), FpzPt3D, and FpzAu

| T (K) | FpzNi | | FpzPd | | FpzPt | | FpzPt3D | | FpzAu | |
|-------------------|-----------|-----------|----------|-----------|-----------|----------|-----------|----------|-------|--|
| | 200 | 98.5 | 200 | 120 | 200 | 120 | 120 | 120 | 250 | |
| Fe–N(1) | 2.240(4) | 1.987(4) | 2.229(3) | 1.990(4) | 2.225(4) | 2.175(9) | 2.046(9) | 2.235(7) | | |
| Fe–N(2) | 2.145(3) | 1.943(3) | 2.138(2) | 1.941(3) | 2.135(3) | 2.133(5) | 2.04(2) | 2.131(6) | | |
| Fe–N(3) | | | | | | | 2.07(2) | 2.142(6) | | |
| Ni–C(5) | 1.855(3) | | | | | | | | | |
| Pd–C(5) | | 1.998(3) | 1.992(3) | | | | | | | |
| Pt–C(5) | | | | 1.989(4) | 1.986(3) | | | | | |
| Pt–C(3) | | | | | | 1.978(5) | | | | |
| Au–C(2) | | | | | | | 1.78(5) | 1.990(7) | | |
| Au–C(3) | | | | | | | 2.05(2) | 1.981(8) | | |
| N(1)–Fe–N(2) | 87.71(11) | 88.39(11) | 88.27(8) | 88.54(12) | 88.37(11) | 88.1(2) | 90.00 | 90.00 | | |
| N(1)–Fe–N(3) | | | | | | | 90.00 | 90.00 | | |
| N(2)–Fe–N(3) | | | | | | | 87.0(6) | 86.9(3) | | |
| C(2)–Au–C(3) | | | | | | | 176.1(11) | 179.8(3) | | |
| Fe–N _i | 2.177 | 1.958 | 2.168 | 1.957 | 2.165 | 2.147 | 2.052 | 2.169 | | |
| Σ | 19.12 | 15.28 | 16.04 | 15.28 | 14.76 | 18 | 12 | 12.4 | | |

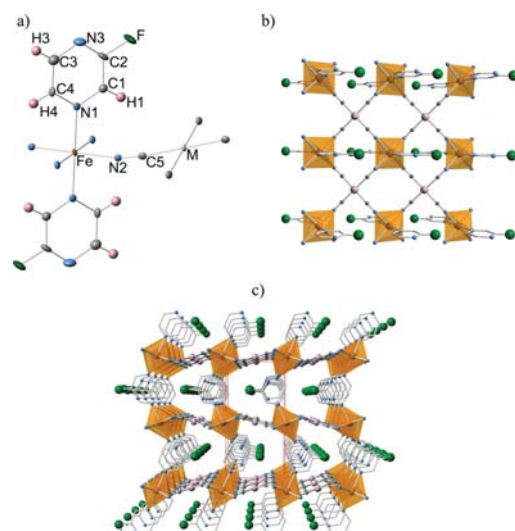


Figure 4. (a) ORTEP representation of a molecular fragment of FpzM (M = Ni, Pd, Pt) (thermal ellipsoids are given at 50% probability for M = Ni at 200 K). (b) View of a layer along the [001] direction. (c) Crystal packing view along the [100] direction. Hydrogen atoms have omitted for simplicity in b and c.

As described for the FpzM series, 2D $[\text{Fe}_2\text{M}^{\text{II}}_2(\text{CN})_4]_n$ grids are generated by coordination of the equatorial Fe^{II} sites by four equivalent $[\text{Pt}(\text{CN})_4]$ units, thus generating an infinite stack. However, at variance with FpzM the $[\text{Fe}_2\text{M}^{\text{II}}_2(\text{CN})_4]_n$ 2D layers are almost planar and the Fpz ligands act as pillars

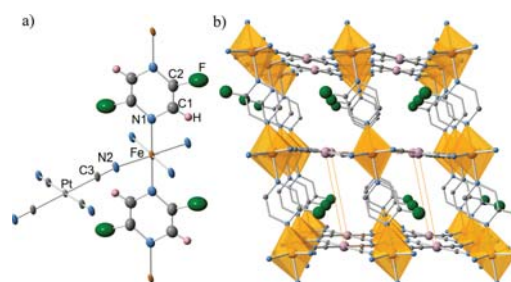


Figure 5. (a) ORTEP representation of a molecular fragment of FpzPt3D (thermal ellipsoids are given at 30% probability). (b) Crystal packing view along the [010] direction showing only one of the two equivalent positions for the F atom (hydrogen atoms have been omitted for simplicity).

linking adjacent layers through the Fe^{II} centers in a similar way as described for the 3D Hofmann clathrate system $\{\text{Fe}(\text{pz})\text{M}(\text{CN})_4\}$ (Figure 5b). Indeed, the structure of FpzPt3D is a slightly distorted version of $\{\text{Fe}(\text{pz})[\text{Pt}(\text{CN})_4]\}$ since the equatorial plane of the $[\text{Fe}^{\text{II}}\text{N}_6]$ sites is not strictly in the same plane of the $[\text{Pt}(\text{CN})_4]^{2-}$ sites. In spite of this, the angle defined between these sites, 13.7° , is ca. 59% smaller than that observed for compound FpzPt. The F atom displays static disorder with an occupation factor of 0.5. The water molecules are located at the middle of the channels, showing positional disorder (see Figure S5 in SI).

Structure of the 3D FpzAu Complex. The compound FpzAu was investigated at 250 and 120 K. At both temperatures the unit cell corresponds to the orthorhombic $Cmca$ space group (Tables 2 and 3). The Fe^{II} lies in an inversion center and defines an elongated $[\text{FeN}_6]$ octahedron

Table 4. Interlayer Short Contacts of FpzM (M = Ni, Pd, Pt)

| short contact | FpzNi | | FpzPd | | FpzPt | |
|----------------------|----------|----------|----------|----------|----------|--|
| | 200 K | 200 K | 98.5 K | 200 K | 120 K | |
| M...N3 ⁱ | 2.981(5) | 3.206(4) | 3.514(5) | 3.358(6) | 3.670(5) | |
| C5...N3 ⁱ | 3.292(6) | 3.485(4) | 3.482(5) | 3.545(7) | 3.532(5) | |
| F...C4 ⁱ | 3.130(7) | 3.281(5) | 3.270(6) | 3.327(7) | 3.352(7) | |

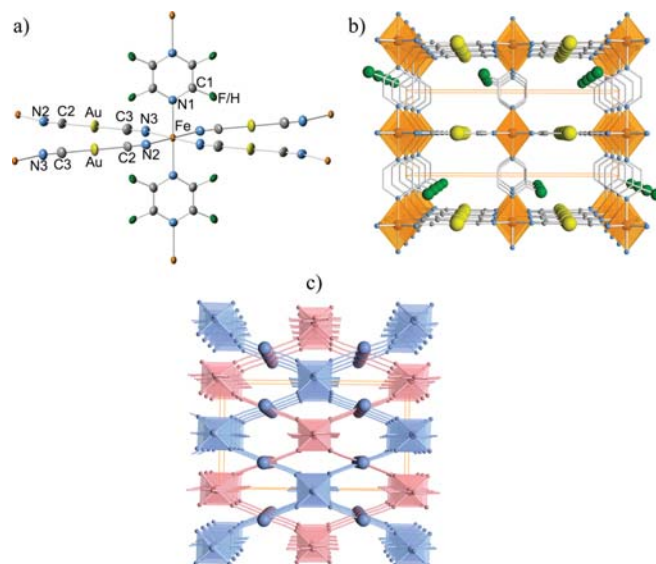


Figure 6. (a) ORTEP representation of a molecular fragment of **FpzAu** (thermal ellipsoids are given at 50% probability). (b) Crystal packing view along the [010] direction showing only one of the four equivalent positions for the F atom (hydrogen atoms have been omitted for simplicity). (c) View illustrating the two interpenetrated 3D frameworks.

whose axial positions are occupied by two equivalent Fpz ligands, while the equatorial positions are occupied by four equivalent $[\text{Au}(\text{CN})_2]^-$ groups (Figure 6a). It is worth noting that due to symmetry reasons the fluorine atom is occupationally disordered (occupation factor of 0.25). At 250 K, the axial bond lengths, $\text{Fe}-\text{N}(1) = 2.235(7)$ Å, are remarkably longer than the equatorial ones ($\text{Fe}-\text{N}(2) = 2.131(6)$ Å and $\text{Fe}-\text{N}(3) = 2.142(6)$ Å). As in the precedent examples the angular distortion of the coordination center is small ($\Sigma = 12.4^\circ$) and the $\text{Fe}-\text{NCAu}$ linkage is not linear since it forms an average angle of 156.8° and changes very little with the spin state change. The average $\text{Fe}-\text{N}$ bond length of 2.169 Å is consistent with HS state of the Fe^{II} fully populated, in agreement with the magnetic properties at the same temperature. However, at 120 K the axial ($\text{Fe}-\text{N}(1)$) and equatorial ($\text{Fe}-\text{N}(2)$, $\text{Fe}-\text{N}(3)$) bond lengths decrease down to 2.046(9) and 2.04(2) Å and 2.07(2) Å, respectively. The average decrease of the axial bond length, 0.19 Å, is ca. 20% smaller than observed for the **FpzM**, while the average decrease of the equatorial bond lengths, 0.08 Å, is ca. 58% smaller than expected. Despite the satisfactory *R* value obtained for this structure at 120 K, and as aforementioned, the single crystals deteriorate markedly during the SCO. This is particularly reflected in the strong distortion of the thermal ellipsoids of the C2 atoms in the LS.

The four $[\text{Au}(\text{CN})_2]^-$ groups equatorially coordinated to the Fe^{II} site act as bis-monodentate bridging ligands linking four equivalent Fe^{II} sites, thus generating 2D $\{[\text{FeAu}(\text{CN})_4]_n\}$ grids which lie in the plane (011). In a similar way as described for **FpzPt3D**, the grids stack along the [100] direction and are pillared through the Fpz ligands, which act as bridges linking the Fe^{II} sites (Figure 6b). However, at variance with **FpzPt3D**, the $[\text{Au}(\text{CN})_2]^-$ group defines a much more expanded 3D framework which allows the mutual interpenetration of two identical 3D coordination polymers (Figure 6c).

DISCUSSION

This work was undertaken to investigate the coordination abilities of the Fpz ligand to form new 3D Hofmann-like SCO materials based on $[\text{M}^{\text{II}}(\text{CN})_4]^{2-}$ and $[\text{M}^{\text{I}}(\text{CN})_2]^-$ ($\text{M}^{\text{II}} = \text{Ni}, \text{Pd}, \text{Pt}$; $\text{M}^{\text{I}} = \text{Ag}, \text{Au}$) building blocks. A priori, the steric hindrance and electron withdrawing induced by the F atom should debilitate the capability of Fpz to act as a bridging ligand and, consequently, favor the formation of 2D frameworks. The results obtained with $[\text{M}^{\text{II}}(\text{CN})_4]^{2-}$ confirm in part this conjecture. Three light-yellow 2D coordination polymers, **FpzM** ($\text{M}^{\text{II}} = \text{Ni}, \text{Pd}, \text{Pt}$), are obtained by direct precipitation and slow diffusion in H-shaped containers. However, the presence of the F atom in the pyrazine ring does not fully deactivate the capability of Fpz to act as a bimonodentate ligand. Indeed, slow diffusion of the components using the layering method forms exclusively the red porous 3D Hofmann-like coordination polymer **FpzPt3D** (the homologous Pd compound is also formed in the same conditions but with much lower yield). By contrast, whatever the synthetic method used the yellow 2D system is obtained when $\text{M} = \text{Ni}$.

The three **FpzM** ($\text{M}^{\text{II}} = \text{Ni}, \text{Pd}, \text{Pt}$) derivatives display significantly corrugated 2D layers, a fact that contrasts with the much less corrugated layers defined by the homologous **ClpzNi** structure reported by Gural'skiy and co-workers^{28e} or related 3X-pyridine ($X = \text{F}, \text{Cl}$) 2D derivatives formulated **XpyM** (Pd, Pt) previously reported by our group.³³ Similarly, the HS compound **FpzPt3D** displays almost flat $\{\text{Fe}[\text{Pt}(\text{CN})_4]\}_n$ layers, which in this case are pillared by the axial linkers Fpz. In the latter, the F atom shows positional disorder due to symmetry reasons, and consequently, the $\text{Fe}-\text{N}(1)$ (Fpz) axial bond length is averaged. Paradoxically, this bond length is ca. 0.05–0.04 Å shorter than that observed for **FpzPt** and the homologous 3D compound $\{\text{Fe}(\text{pz})[\text{Pt}(\text{CN})_4]\}$ in the HS state. In spite of this **FpzPt3D** remains HS at all temperatures.

A reasonable conjecture to explain this fact could be related to the low thermal stability shown by **FpzPt3D**. This compound includes ca. 0.5 disordered water molecules in the channels that desorb at 350 K, a temperature at which the Fpz ligand starts to be lost (see Figure S6 in SI). By contrast, the 2D **FpzPt** and 3D $\{\text{Fe}(\text{pz})[\text{Pt}(\text{CN})_4]\}$ homologues are clearly more stable since no loss of Fpz/pz occurs up to 395/480 K (see Figure S6 in SI). Although it is always speculative to give an explanation in these circumstances, the lack of SCO and low thermal stability of **FpzPt3D** might reflect a much more strained structure. By contrast, the lack of thermal SCO in **FpzNi** could be related to the tight crystal packing and very short interlayer contacts observed in the HS state, which presumably prevents the change to a more packed LS structure even at pressures of 0.7 GPa.

Furthermore, an important feature of the two SCO complexes **FpzPd** and **FpzPt** is the drastic change of color from light-yellow (HS) to dark-red (LS) upon SCO.

FpzAu invariably affords a 3D coordination polymer whatever the synthetic method employed. This structure resembles that of **FpzPt3D**, but obviously the latter is more reticulated due to the different connectivity of $[\text{M}^{\text{II}}(\text{CN})_4]^{2-}$ and $[\text{M}^{\text{I}}(\text{CN})_2]^-$ building blocks. Consequently, **FpzAu** affords a more open and presumably less strained framework. In this respect, the thermal stability of this framework is notably higher (ca. 480 K, see Figure S6 in SI) than that of **FpzPt3D**. In **FpzPt3D** the two metallic building blocks act as 4-connected nodes and must match their coordination angles as close to 90° as possible. By contrast, the **FpzAu** structure is more relaxed since there is only one type of 4-connected node, namely, the Fe^{II} linked to other equivalent sites through four $[\text{Au}(\text{CN})_2]^-$ linkers defining infinite $\{\text{Fe}_4[\text{Au}(\text{CN})_2]_4\}_n$ grids. Although the equatorial angles in the $[\text{FeN}_6]$ coordination center deviate only 3.1° from 90° the Fe–N–C–Au–C–N linkages deviate 23.2° from linearity, and consequently, the Fe_4 units define rhombuses. As in **FpzPt3D**, the $\{\text{Fe}_4[\text{Au}(\text{CN})_2]_4\}_n$ grids are similarly connected through Fpz bridges. The F atom is averaged in two positions defining Fe–N(Fpz) bonds similar to that found for **FpzPt**, which is ca. 0.06 Å longer than those found for **FpzPt3D**. The void space generated by the resulting less dense 3D framework enables interpenetration of an identical framework. This situation has been previously reported by our group for the homologous compound $\{\text{Fe}(\text{pz})[\text{Ag}(\text{CN})_2]_4\}$ and more recently by Ni and Tong et al. for $[\text{Fe}(2,5\text{-bpp})\{\text{Au}(\text{CN})_2\}_2] \cdot x\text{Solvent}$ (2,5-bpp = 2,5-bis(pyrid-4-yl)pyridine),^{29k} Kepert et al. for $[\text{Fe}(\text{bipytz})\{\text{Au}(\text{CN})_2\}_2]$ (bipytz = 3,6-bis(4-pyridyl)-1,2,4,5-tetrazine),^{29j} and more recently by Gural'skiy et al. for $\{\text{Fe}(\text{pz})[\text{Au}(\text{CN})_2]_4\}$ (hereafter **HpzAu**).³⁴

Following the same synthetic method described for **FpzAu**, mixtures of Fe^{II} /Fpz solutions with solutions of $[\text{Ag}^{\text{I}}(\text{CN})_2]^-$ gave in all cases dark-gray precipitates. After many attempts we concluded that the homologous compound **FpzAg** is not a stable species.

Table 5 gathers the spin transition temperatures for the series of complexes here investigated and related pyridine (**HpyM**),^{7,8,35a} 3Fpyridine (**FpyM**),^{35b,33} and pyrazine $\{\text{Fe}(\text{pz})[\text{M}(\text{CN})_x]_z\}$ ($\text{M}^{\text{II}} = \text{Ni}, \text{Pd}, \text{Pt}, x = 4, z = 1$;³⁶ and $\text{M}^{\text{I}} = \text{Au}$,³⁴ $x = 2, z = 2$) (**HpzM**) derivatives. From the critical temperatures observed for the title **FpzM** 2D compounds, it is safe to state that the LS state is destabilized when moving from Pt to Ni derivative. However, rationalizing of this trend is not obvious, as it seems to depend on the particular studied system.

Table 5. Characteristic Temperatures of the SCO for the Related Compounds HpyM, FpyM, and FpzM (see text)

| compound | $T_{1/2}^{\text{I}}$ (K) | $T_{1/2}^{\text{II}}$ (K) | ΔT (K) | nD | ref |
|----------|--------------------------|---------------------------|-------------------|------|-----------------|
| HpyNi | 186 | 195 | 9 | 2D | 7 |
| HpyPd | 208 | 213 | 5 | 2D | 8 |
| HpyPt | 208 | 216 | 8 | 2D | 8 |
| HpyAu | | | | 2D | 34 ^b |
| FpyNi | 205.8 | 234.4 | 28.6 | 2D | 35 |
| FpyPd | 213.6 | 248.4 | 34.8 | 2D | 35 |
| FpyPt | 214 | 239.5 | 25.5 | 2D | 35 |
| FpyAu | 123.9 ^c | 108.8 ^c | 15.1 ^c | 2D | 34 |
| HpzNi | 287 | 307 | 20 | 3D | 36 |
| HpzPd | 286 | 310 | 24 | 3D | 36 |
| HpzPt | 285 | 309 | 24 | 3D | 36 |
| HpzAu | 349 | 367 | 18 | 3D | 33 |
| FpzNi | HS | HS | HS | 2D | this work |
| FpzPd | 105 | 127 | 22 | 2D | this work |
| FpzPt | 144.5 | 166.5 | 22 | 2D | this work |
| FpzAu | 221.5 | 264.5 | 43 | 3D | this work |

^a $T_{1/2}^{\text{I}} = 98.2$ K, $T_{1/2}^{\text{II}} = 118.6$ K, and $T_{1/2}^{\text{I}} = 147$ K. ^bThis compound is HS at all temperatures. ^cThis compound displays two steps with $T_{1/2}^{\text{I}} = 147$ K.

For example, the opposite trend has been observed for the related series of 2D compounds **ClpzM** ($\text{M} = \text{Ni}, \text{Pd}, \text{Pt}$).^{28e} Another relevant observation is the increase of cooperativeness regarding **HpyM** ($\text{M} = \text{Ni}, \text{Pd}, \text{Pt}$). This is, presumably, due to the presence of short interlayer contacts facilitated by the presence of the fluorine atom in the pyridine and pyrazine rings in the series **FpyM** and **FpzM** ($\text{M} = \text{Ni}, \text{Pd}, \text{Pt}$). It is worth noting that when comparing **HpyM** and **FpyM** series the increase in cooperativeness is essentially reflected in the increase of the characteristic $T_{1/2}^{\text{I}}$ transition temperatures. The clear destabilization of the LS state in the 2D **FpzM** ($\text{M} = \text{Ni}, \text{Pd}, \text{Pt}$) series can be ascribed to the weaker ligand field induced by the ligand pz with respect to the ligands py and Fpy. As far as the gold derivatives are concerned, the strong cooperative behavior and much higher $T_{1/2}$ temperatures reflect the change of dimensionality from 2D to 3D.

The light-induced excited spin state trapping (LIESST) effect has been investigated for the three derivatives undergoing thermal-induced SCO. As a consequence of the characteristic high-spin transition temperature, relaxation of the photo-generated HS* state in **FpzAu** is very rapid, even at 10 K, and no LIESST effect could be recorded in our magnetometer set up. This is consistent with the rapid HS* → LS relaxation (ca. 15 min) observed at 10 K for the 3D compound $\{\text{Fe}(\text{pz})[\text{Pt}(\text{CN})_4]_2\} \cdot n\text{H}_2\text{O}$ which undergoes a cooperative SCO characterized by a hysteresis ca. 25 K wide centered at about 290 K.²⁴ Despite the average $T_{1/2}$ not being too high for **FpzPt**, only 57% of HS* population was produced at 10 K. In contrast, a practically complete transformation to the HS* was achieved. The T_{LIESST} values, 56.3 and 65.5 K, respectively, compare well with that obtained for the related 2D Hofmann-like compound **ClpyPd**, which undergoes a two-step cooperative spin transition with characteristic temperatures centered at 162 and 145 K.³⁷

CONCLUSION

The SCO behavior of a new series of 2D and 3D Hofmann-like Fe^{II} compounds obtained from self-assembly of Fe^{II} , fluoropyrazine (Fpz), and $[\text{M}^{\text{II}}(\text{CN})_4]^{2-}$ ($\text{M}^{\text{II}} = \text{Ni}, \text{Pd}, \text{Pt}$)

and $[\text{Au}^{\text{I}}(\text{CN})_2]^-$ building blocks has been investigated. The compounds based on $[\text{M}^{\text{II}}(\text{CN})_4]^{2-}$ building blocks are stable 2D coordination polymers, **FpzM**. The Pd and Pt derivatives undergo strong cooperative thermal- and light-induced SCO behavior accompanied by drastic color changes from light-yellow (HS) to deep-red (LS), in contrast to the Ni derivative that is HS at all temperatures even at a pressure of 0.7 GPa. From $T_{1/2}$ values destabilization of the LS state follows the trend $\text{Pt} > \text{Pd} > \text{Ni}$. The lack of SCO in the Ni derivative has tentatively been associated with dense packing of the corrugated layers. The 3D metal organic framework **FpzPt3D**, obtained from different synthetic conditions, is a distorted version of the well-known Hofmann-like compound $\{\text{Fe}(\text{pz})\text{-}[\text{Pt}(\text{CN})_4]\}$. It displays unusual low thermal stability tentatively ascribed to structural strain and is HS at all temperatures. By contrast, the 3D compound **FpzAu** constituted of two identical interpenetrated 3D frameworks displays very cooperative SCO with a stable hysteresis larger than 40 K.

EXPERIMENTAL SECTION

All chemicals were purchased from commercial suppliers and used without further purification. Elemental and thermogravimetric analyses were performed, respectively, on LECO CHNS-932 and Mettler Toledo TGA/SDTA 851e (working in the 290–800 K temperature range under a nitrogen atmosphere with a rate of 10 K min^{-1}) analyzers. IR spectra were recorded at 293 K by using a Nicolet 5700 FTIR spectrometer with the samples prepared as KBr discs. Powder X-ray measurements were performed on a PANalytical Empyrean X-ray powder diffractometer (monochromatic $\text{Cu K}\alpha$ radiation).

Synthesis of $\{\text{Fe}(\text{Fpz})_2[\text{M}(\text{CN})_4]\}$. Microcrystalline samples of **FpzM** ($\text{M} = \text{Ni, Pd, Pt}$) were obtained in Ar atmosphere by adding dropwise, under vigorous stirring, an aqueous solution of $\text{K}_2[\text{M}(\text{CN})_4]\cdot 3\text{H}_2\text{O}$ (0.4 mmol, 5 mL) to an aqueous solution containing $\text{Fe}(\text{BF}_4)_2\cdot 6\text{H}_2\text{O}$ (0.4 mmol, 3 mL) and fluoropyrazine (0.8 mmol, 3 mL). The resulting yellowish solid was stirred for 15 min, filtered, washed with water, and dried in air (yield ca. 80%). Suitable single crystals for X-ray studies were prepared by slow diffusion methods using a H-shaped tube. In one side of the H tube were dissolved 0.15 mmol (41.7 mg) of $\text{FeSO}_4\cdot 7\text{H}_2\text{O}$ and 0.3 mmol (29.4 mg) of fluoropyrazine in 1 mL of water, while the opposite side contained 1 mL of a solution (0.15 mol) of $\text{K}_2[\text{M}(\text{CN})_4]\cdot 3\text{H}_2\text{O}$ [36.2 mg (Ni); 51.5 mg (Pd) and 64.7 mg (Pt)]. The H vessel was carefully filled with water and sealed. Yellow single crystals of the title compounds appear in 2 weeks (yield ca. 20%). EDX analysis (energy-dispersive X-ray analysis) confirmed the stoichiometric relationship between metallic coordination centers: $[\text{Fe}:\text{Ni}] = [1:1]$, $[\text{Fe}:\text{Pd}] = [1:1]$, and $[\text{Fe}:\text{Pt}] = [1:1]$. The CN bond stretching mode features intense IR bands at $\nu(\text{CN}) = 2157 \text{ cm}^{-1}$ (shoulder) and 2145 cm^{-1} (sharp) for **FpzNi**, 2161 cm^{-1} (sharp) for **FpzPd**, and 2168 cm^{-1} (shoulder) and 2158 cm^{-1} (sharp) for **FpzPt**. Anal. Calcd for $\text{C}_{12}\text{H}_6\text{F}_2\text{FeN}_8\text{Ni}$: C, 34.75; H, 1.46; N, 27.02. Found: C, 33.98; H, 1.52; N, 27.45. Anal. Calcd for $\text{C}_{12}\text{H}_6\text{F}_2\text{FeN}_8\text{Pd}$: C, 31.16; H, 1.31; N, 24.23. Found: C, 31.01; H, 1.35; N, 23.98. Anal. Calcd for $\text{C}_{12}\text{H}_6\text{F}_2\text{FeN}_8\text{Pt}$: C, 26.15; H, 1.10; N, 20.33. Found: C, 26.38; H, 1.15; N, 20.98.

Synthesis of $\{\text{Fe}(\text{Fpz})_2[\text{Pt}(\text{CN})_4]\cdot 1/2\text{H}_2\text{O}$. Compound **FpzPt3D** was produced by slow diffusion method, more precisely by layering in standard test tubes. The layering sequence was as follows: the bottom layer contains a mixture of Mohr's salt (0.2 mmol, 76 mg), fluoropyrazine (0.4 mmol, 40 mg), and a few crystals of ascorbic acid in 3 mL of water. Then an interphase containing a mixture of water:isopropanol (5 mL, 1:1) was added. Finally, a solution of $\text{K}_2[\text{Pt}(\text{CN})_4]\cdot 3\text{H}_2\text{O}$ (0.2 mmol, 86.3 mg) in water:isopropanol (5 mL, 1:4) was gently poured on top of the interphase. The tube was sealed, and red single crystals appeared in 3–4 weeks (yield ca. 30–40%). EDX analysis confirms the stoichiometric relationship between metallic coordination centers: $[\text{Fe}:\text{Pt}] = [1:1]$. The CN bond stretching mode features an intense IR band at $\nu(\text{CN}) = 2168$

cm^{-1} . Anal. Calcd for $\text{C}_8\text{H}_3\text{FFeN}_6\text{O}_{0.5}\text{Pt}$: C, 20.84; H, 0.66; N, 18.23. Found: C, 20.68; H, 0.70; N, 18.60.

Synthesis of $\{\text{Fe}(\text{Fpz})[\text{Au}(\text{CN})_2]\}$. Microcrystalline samples of **FpzAu** were prepared in Ar atmosphere by adding dropwise, under vigorous stirring, an aqueous solution of $\text{K}[\text{Au}(\text{CN})_2]$ (0.4 mmol, 5 mL) to an aqueous solution containing $\text{Fe}(\text{BF}_4)_2\cdot 6\text{H}_2\text{O}$ (0.4 mmol, 3 mL) and fluoropyrazine (0.4 mmol, 3 mL). The resulting yellowish solid was stirred for 15 min, filtered, washed with water, and dried in air (yield ca. 85%). Suitable single crystals for X-ray studies were prepared by layering of the components as follows: the bottom layer contained a mixture of $\text{FeCl}_2\cdot 4\text{H}_2\text{O}$ (0.2 mmol, 39.8 mg), fluoropyrazine (0.2 mmol, 19.6 mg), and a few crystals of ascorbic acid in 3 mL of water. Then an interphase was generated adding 10 mL of a $\text{H}_2\text{O}:\text{MeOH}$ (3:1) mixture. Finally, a solution of $\text{K}[\text{Au}(\text{CN})_2]$ (0.4 mmol, 2 mL) in a $\text{H}_2\text{O}:\text{MeOH}$ (1:2) mixture was gently poured on top of the interphase. EDX analysis confirms the stoichiometric relationship between metallic coordination centers: $[\text{Fe}:\text{Au}] = [1:2]$. The CN bond stretching mode features an intense IR band at $\nu(\text{CN}) = 2175 \text{ cm}^{-1}$ and a shoulder at 2159 cm^{-1} . Anal. Calcd for $\text{C}_8\text{H}_3\text{Au}_2\text{FFeN}_6$: C, 14.74; H, 0.46; N, 12.89. Found: C, 14.92; H, 0.50; N, 13.05.

Single-Crystal X-ray Diffraction. Single-crystal X-ray data were collected on an Oxford Diffraction Supernova. In all cases $\text{Mo K}\alpha$ radiation ($\lambda = 0.71073 \text{ \AA}$) was used. A data scaling and empirical or multiscan absorption correction was performed. The structures were solved by direct methods using SHELXS-2014 and refined by full-matrix least-squares on F^2 using SHELXL-2014.³⁸ Non-hydrogen atoms were refined anisotropically, and hydrogen atoms were placed in calculated positions refined using idealized geometries (riding model) and assigned fixed isotropic displacement parameters.

Magnetic and Calorimetric Measurements. Variable-temperature magnetic susceptibility data (15–20 mg) were recorded with a Quantum Design MPMS2 SQUID susceptometer equipped with a 7 T magnet, operating at 1 T and at temperatures 2–400 K. Variable-temperature magnetic measurements under pressure were performed on **FpzNi** using a hydrostatic pressure cell made of hardened beryllium bronze with silicon oil as pressure transmitting medium and operating over the pressure range $10^5 \text{ Pa} < P < 1.2 \text{ GPa}$ (accuracy ca. $\pm 0.025 \text{ GPa}$). The compound was packed in a cylindrically shaped sample holder (1 mm in diameter and 5–7 mm in length) (8–10 mg) made up of very thin aluminum foil. The pressure was calibrated using the transition temperature of superconducting lead of high purity, 99.999%.³⁹ Experimental susceptibilities were corrected for diamagnetism of the constituent atoms by use of Pascal's constants.

Differential scanning calorimetry (DSC) measurements were performed on dry samples of the title compounds using a Mettler Toledo DSC 821e DSC calorimeter. Low temperatures were obtained with an aluminum block which was attached to the sample holder, refrigerated with a flow of liquid nitrogen, and stabilized at a temperature of 110 K. The sample holder was kept in a drybox under a flow of dry nitrogen gas to avoid water condensation. The measurements were carried out using about 10 mg of crystalline samples sealed in aluminum pans with a mechanical crimp. An overall accuracy of 0.2 K in the temperature and 2% in the heat capacity is estimated. The uncertainty increases for determination of the anomalous enthalpy and entropy due to subtraction of an unknown baseline.

ASSOCIATED CONTENT

Supporting Information

The Supporting Information is available free of charge on the ACS Publications website at DOI: 10.1021/acs.inorgchem.6b01901.

Magnetic data for **FpzNi** at 0.7 GPa; magnetic data, PXRD pattern of precipitated sample, and IR for **FpzPt3D**; magnetic data (several cycles) for precipitated samples, PXRD pattern, and IR of **FpzAu**; comparison of IR and PXRD patterns of the 2D systems **FpzM** ($\text{M} =$

Ni, Pd, Pt); perspective view of the porous metal-organic framework FpzPt3D showing the disordered water molecules in the middle of the channels; thermogravimetric analysis of FpzAu, FpzPt3D, and FpzPt; and equilibrium temperatures, $T_{1/2}^1$ and $T_{1/2}^2$, for single-crystal and precipitated microcrystalline samples of FpzAu (PDF)

(CIF)
(CIF)
(CIF)
(CIF)
(CIF)
(CIF)
(CIF)
(CIF)

AUTHOR INFORMATION

Corresponding Authors

*E-mail: mcs@univ.kiev.ua; mlseredyuk@gmail.com.

*E-mail: jose.a.real@uv.es.

Notes

The authors declare no competing financial interest.

ACKNOWLEDGMENTS

The research reported here was supported by the Spanish Ministerio de Economía y Competitividad (MINECO) and FEDER funds (CTQ2013-46275-P and Unidad de Excelencia María de Maeztu MDM- 2015-0538) and Generalitat Valenciana (PROMETEO/2016/147). F.J.V.M. thanks the MINECO for a predoctoral FPI fellowship.

REFERENCES

- See for example: (a) Goodwin, H. A. Spin Transitions in Six-Coordinate Iron(II) Complexes. *Coord. Chem. Rev.* **1976**, *18*, 293. (b) Gütllich, P. Spin Crossover in Iron(II)-Complexes. *Struct. Bonding (Berlin)* **1981**, *44*, 83. (c) König, E.; Ritter, G.; Kulshreshtha, S. K. The Nature of Spin-State Transitions in Solid Complexes of Iron(II) and the Interpretation of some Associated Phenomena. *Chem. Rev.* **1985**, *85*, 219. (d) Hauser. Intersystem Crossing in Iron(II) Coordination Compounds: A Model Process between Classical and Quantum Mechanical Behaviour. *A. Comments Inorg. Chem.* **1995**, *17*, 17. (e) König, E. Nature and Dynamics of the Spin-State Interconversion in Metal-Complexes. *Struct. Bonding (Berlin, Ger.)* **1991**, *76*, 51. (f) Gütllich, P.; Hauser, A.; Spiering, H. Thermal and Optical Switching of Iron(II) Complexes. *Angew. Chem., Int. Ed. Engl.* **1994**, *33*, 2024. (g) Sato, O. Optically Switchable Molecular Solids: Photoinduced Spin-Crossover, Photochromism, and Photoinduced Magnetization. *Acc. Chem. Res.* **2003**, *36*, 692. (h) Real, J. A.; Gaspar, A. B.; Niel, V.; Muñoz, M. C. Communication between Iron(II) Building Blocks in Cooperative Spin Transition Phenomena. *Coord. Chem. Rev.* **2003**, *236*, 121. (i) In Spin Crossover in Transition Metal Compounds I-III. *Topics in Current Chemistry*; Gütllich, P., Goodwin, H. A., Eds.; Springer, 2004, Vols. 233–235. (j) Real, J. A.; Gaspar, A. B.; Muñoz, M. C. Thermal, Pressure and Light Switchable Spin-Crossover Materials. *Dalton Trans.* **2005**, 2062. (k) Halcrow, M. A. The Spin-States and Spin-Transitions of Mononuclear Iron(II) Complexes of Nitrogen-Donor Ligands. *Polyhedron* **2007**, *26*, 3523. (l) Halcrow, M. A. Iron(II) Complexes of 2,6-di(pyrazol-1-yl)pyridines A Versatile System for Spin-Crossover Research. *Coord. Chem. Rev.* **2009**, *253*, 2493. (m) Olguin, J.; Brooker, S. Spin Crossover Active Iron(II) Complexes of Selected pyrazole-pyridine/pyrazine Ligands. *Coord. Chem. Rev.* **2011**, *255*, 203. (n) Bousseksou, A.; Molnár, G.; Salmon, L.; Nicolazzi, W. Molecular Spin Crossover Phenomenon: Recent Achievements and Prospects. *Chem. Soc. Rev.* **2011**, *40*, 3313. (2) (a) Meded, V.; Bagrets, A.; Fink, K.; Chandrasekar, R.; Ruben, M.; Evers, F.; Bernand-Mantel, A.; Seldenthuis, J. S.; Beukman, A.; van der Zant, H. S. J. Electrical Control over the Fe(II) Spin Crossover in a Single Molecule: Theory and Experiment. *Phys. Rev. B: Condens. Matter Mater. Phys.* **2011**, *83*, 245415. (b) Prins, F.; Monrabal-Capilla, M.; Osorio, E. A.; Coronado, E.; van der Zant, H. S. J. Room-Temperature Electrical Addressing of a Bistable Spin-Crossover Molecular System. *Adv. Mater.* **2011**, *23*, 1545. (c) Cavallini, M.; Bergenti, L.; Milita, S.; Kengne, J. C.; Gentili, D.; Ruani, G.; Salitros, I.; Meded, V.; Ruben, M. Thin Deposits and Patterning of Room-Temperature-Switchable One-Dimensional Spin-Crossover Compounds. *Langmuir* **2011**, *27*, 4076. (d) Miyamachi, T.; Gruber, M.; Davesne, V.; Bowen, M.; Boukari, S.; Joly, L.; Scheurer, F.; Rogez, G.; Yamada, T. K.; Ohresser, P.; Beaurepaire, E.; Wulfhekel, W. Robust Spin Crossover and Memristance across a Single Molecule. *Nat. Commun.* **2012**, *3*, 938. (e) Martinho, P. N.; Rajnak, C.; Ruben, M. In *Spin-Crossover Materials: Properties and Applications*; Halcrow, M. A. Ed.; Wiley: 2013, pp 376–404 and references therein. (f) Shepherd, H. J.; Molnár, G.; Nicolazzi, W.; Salmon, L.; Bousseksou, A. Spin Crossover at the Nanometre Scale. *Eur. J. Inorg. Chem.* **2013**, *2013*, 653. (g) Rotaru, A.; Dugay, J.; Tan, R. P.; Gural'skiy, I. A.; Salmon, L.; Demont, P.; Carrey, J.; Molnár, G.; Respaud, M.; Bousseksou, A. Nano-Electromanipulation of Spin Crossover Nanorods: Towards Switchable Nanoelectronic Devices. *Adv. Mater.* **2013**, *25*, 1745. (h) Gural'skiy, I. A.; Quintero, C. M.; Costa, J. S.; Demont, P.; Molnár, G.; Salmon, L.; Shepherd, H. J.; Bousseksou, A. Spin Crossover Composite Materials for Electrothermomechanical Actuators. *J. Mater. Chem. C* **2014**, *2*, 2949–2955. (i) Bartual-Murgui, C.; Akou, A.; Thibault, C.; Molnár, G.; Vieu, C.; Salmon, L.; Bousseksou, A. Spin-Crossover Metal-Organic Frameworks: Promising Materials for Designing Gas Sensors. *J. Mater. Chem. C* **2015**, *3*, 1277. (j) Aragonés, A. C.; Aravena, D.; Cerdá, J. I.; Acis-Castillo, Z.; Li, H.; Real, J. A.; Sanz, F.; Hihath, J.; Ruiz, E.; Díez-Pérez, I. Large Conductance Switching in a Single-Molecule Device through Room Temperature Spin-Dependent Transport. *Nano Lett.* **2016**, *16*, 218. (3) Hofmann, K. A.; Küspert, F. A. Verbindungen von Kohlenwasserstoffen mit Metallsalzen. *Z. Anorg. Allg. Chem.* **1897**, *15*, 204. (4) Powell, H. M.; Rayner, J. H. Clathrate Compound Formed by Benzene with an Ammonia - Nickel Cyanide Complex. *Nature (London, U. K.)* **1949**, *163*, 566. (5) Baur, R.; Schwarzenbach, G. Neue Einschlussverbindungen vom Typus des Nickelcyanid-Ammoniak-Benzols. *Helv. Chim. Acta* **1960**, *43*, 842. (6) (a) Iwamoto, T. In *Inclusion Compounds*; Atwood, J. L., Davies, J. E. D., MacNicol, D. D., Eds.; Oxford University Press: Oxford, 1991; Vol. 5, p 177. (b) Iwamoto, T. In *Chemistry of Microporous Crystals*; Inui, T., Namba, S., Tatsumi, T., Eds.; Kodansha/Elsevier: Tokyo, 1991; p 1. (c) Soma, T.; Yuge, H.; Iwamoto, T. 3-Dimensional Interpenetrating Double and Triple Framework Structures in [Cd(bpy)₂(Ag(CN)₂)₂] and [Cd(pyrz)(Ag₂(CN)₃)(Ag(CN)₂)]. *Angew. Chem., Int. Ed. Engl.* **1994**, *33*, 1665. (7) Kitazawa, T.; Gomi, Y.; Takahashi, M.; Takeda, M.; Enomoto, M.; Miyazaki, A.; Enoki, T. Spin-Crossover Behaviour of the Coordination Polymer Fe^{II}(C₅H₅N)₂Ni^{II}(CN)₄. *J. Mater. Chem.* **1996**, *6*, 119. (8) Niel, V.; Martínez-Agudo, J. M.; Muñoz, M. C.; Gaspar, A. B.; Real, J. A. Cooperative Spin Crossover Behavior in Cyanide-Bridged Fe^{II}-M^{II} Bimetallic 3D Hofmann-Like Networks (M = Ni, Pd, and Pt). *Inorg. Chem.* **2001**, *40*, 3838. (9) (a) Niel, V.; Muñoz, M. C.; Gaspar, A. B.; Galet, A.; Levchenko, G.; Real, J. A. Thermal-, Pressure-, and Light-Induced Spin Transition in Novel Cyanide-Bridged Fe^{II}-Ag^I Bimetallic Compounds with Three-Dimensional Interpenetrating Double Structures {Fe^{II}L_x[Ag(CN)₂]₂}-center dot G. *Chem. - Eur. J.* **2002**, *8*, 2446. (b) Niel, V.; Galet, A.; Gaspar, A. B.; Muñoz, M. C.; Real, J. A. Cooperative Thermal and Optical Switching of Spin States in a New Two-Dimensional Coordination Polymer. *Chem. Commun.* **2003**, 1248.

- (10) Muñoz, M. C.; Real, J. A. Thermo-, Piezo-, Photo- and Chemo-Switchable Spin Crossover Iron(II)-Metalloacyanate Based Coordination Polymers. *Coord. Chem. Rev.* **2011**, *255*, 2068.
- (11) Bartual-Murgui, C.; Salmon, L.; Akou, A.; Thibault, C.; Molnár, G.; Mahfoud, T.; Sekkat, Z.; Real, J. A.; Bousseksou, A. High Quality Nano-Patterned Thin Films of the Coordination Compound {Fe(pyrazine)[Pt(CN)₄]} Deposited Layer-by-Layer. *New J. Chem.* **2011**, *35*, 2089.
- (12) Otsubo, K.; Haraguchi, T.; Sakata, O.; Fujiwara, A.; Kitagawa, H. Step-by-Step Fabrication of a Highly Oriented Crystalline Three-Dimensional Pillared-Layer-Type Metal-Organic Framework Thin Film Confirmed by Synchrotron X-ray Diffraction. *J. Am. Chem. Soc.* **2012**, *134*, 9605.
- (13) Raza, Y.; Volatron, F.; Moldovan, S.; Ersen, O.; Huc, V.; Martini, C.; Brisset, F.; Gloter, A.; Stéphane, O.; Bousseksou, A.; Catala, L.; Mallah, T. Matrix-Dependent Cooperativity in Spin Crossover Fe(pyrazine)Pt(CN)₄ Nanoparticles. *Chem. Commun.* **2011**, *47*, 11501.
- (14) Peng, H.; Tricard, S.; Félix, G.; Molnár, G.; Nicolazzi, W.; Salmon, L.; Bousseksou, A. Re-Appearance of Cooperativity in Ultra-Small Spin-Crossover [Fe(pz){Ni(CN)₄}] Nanoparticles. *Angew. Chem., Int. Ed.* **2014**, *53*, 10894.
- (15) Ohtani, R.; Yoneda, K.; Furukawa, S.; Horike, N.; Kitagawa, S.; Gaspar, A. B.; Muñoz, M. C.; Real, J. A.; Ohba, M. Precise Control and Consecutive Modulation of Spin Transition Temperature Using Chemical Migration in Porous Coordination Polymers. *J. Am. Chem. Soc.* **2011**, *133*, 8600.
- (16) Muñoz-Lara, F. J.; Gaspar, A. B.; Aravena, D.; Ruiz, E.; Muñoz, M. C.; Ohba, M.; Ohtani, R.; Kitagawa, S.; Real, J. A. Enhanced Bistability by Guest Inclusion in Fe(II) Spin Crossover Porous Coordination Polymers. *Chem. Commun.* **2012**, *48*, 4686.
- (17) Bao, X.; Shepherd, H. J.; Salmon, L.; Molnár, G.; Tong, M. L.; Bousseksou, A. The Effect of an Active Guest on the Spin Crossover Phenomenon. *Angew. Chem., Int. Ed.* **2013**, *52*, 1198.
- (18) Aravena, D.; Arcis-Castillo, Z.; Muñoz, M. C.; Gaspar, A. B.; Yoneda, K.; Ohtani, R.; Mishima, A.; Kitagawa, S.; Ohba, M.; Real, J. A.; Ruiz, E. Guest Modulation of Spin-Crossover Transition Temperature in a Porous Iron(II) Metal-Organic Framework: Experimental and Periodic DFT Studies. *Chem. - Eur. J.* **2014**, *20*, 12864.
- (19) Culp, J. T.; Chen, D. L.; Liu, J.; Chirdon, D.; Kauffman, K.; Goodman, A.; Johnson, J. K. Effect of Spin-Crossover-Induced Pore Contraction on CO₂-Host Interactions in the Porous Coordination Polymers [Fe(pyrazine)M(CN)₄] (M = Ni, Pt). *Eur. J. Inorg. Chem.* **2013**, *2013*, 511.
- (20) Arcis-Castillo, Z.; Muñoz-Lara, F. J.; Muñoz, M. C.; Aravena, D.; Gaspar, A. B.; Sánchez-Royo, J. F.; Ruiz, E.; Ohba, M.; Matsuda, R.; Kitagawa, S.; Real, J. A. Reversible Chemisorption of Sulfur Dioxide in a Spin Crossover Porous Coordination Polymer. *Inorg. Chem.* **2013**, *52*, 12777.
- (21) Kosone, T.; Hori, A.; Nishibori, E.; Kubota, Y.; Mishima, A.; Ohba, M.; Tanaka, H.; Kato, K.; Kim, J.; Real, J. A.; Kitagawa, S.; Takata, M. Coordination Nano-Space as Stage of Hydrogen Ortho-Para Conversion. *R. Soc. Open Sci.* **2015**, *2*, 150006.
- (22) Cirera, J.; Babin, V.; Paesani, F. Theoretical Modeling of Spin Crossover in Metal-Organic Frameworks: [Fe(pz)₂Pt(CN)₄] as a Case Study. *Inorg. Chem.* **2014**, *53*, 11020.
- (23) Rodríguez-Velamazán, J. A.; González, M. A.; Real, J. A.; Castro, M.; Muñoz, M. C.; Gaspar, A. B.; Ohtani, R.; Ohba, M.; Yoneda, K.; Hijikata, Y.; Yanai, N.; Mizuno, M.; Ando, H.; Kitagawa, S. A Switchable Molecular Rotator: Neutron Spectroscopy Study on a Polymeric Spin-Crossover Compound. *J. Am. Chem. Soc.* **2012**, *134*, 5083.
- (24) Delgado, T.; Tissot, A.; Besnard, C.; Guéneé, L.; Pattison, P.; Hauser, A. Structural Investigation of the High Spin → Low Spin Relaxation Dynamics of the Porous Coordination Network [Fe(pz)₂Pt(CN)₄] center dot 2.6H₂O. *Chem. - Eur. J.* **2015**, *21*, 3664.
- (25) Castro, M.; Roubeau, O.; Piñeiro-López, L.; Real, J. A.; Rodríguez-Velamazán, J. A. Pulsed-Laser Switching in the Bistability Domain of a Cooperative Spin Crossover Compound: A Critical Study through Calorimetry. *J. Phys. Chem. C* **2015**, *119*, 17334.
- (26) Collet, E.; Henry, L.; Piñeiro-López, L.; Toupet, L.; Real, J. A. Single Laser Shot Spin State Switching of [Fe^{II}(Py)Pt(CN)₄] Inside Thermal Hysteresis studied by x-ray Diffraction. *Curr. Inorg. Chem.* **2016**, *6*, 61.
- (27) (a) Bartual-Murgui, C.; Ortega-Villar, N. A.; Shepherd, H. J.; Muñoz, M. C.; Salmon, L.; Molnár, G.; Bousseksou, A.; Real, J. A. Enhanced Porosity in a New 3D Hofmann-like Network Exhibiting Humidity Sensitive Cooperative Spin Transitions at Room Temperature. *J. Mater. Chem.* **2011**, *21*, 7217. (b) Bartual-Murgui, C.; Akou, A.; Salmon, L.; Molnár, G.; Thibault, C.; Real, J. A.; Bousseksou, A. Guest Effect on Nanopatterned Spin-Crossover Thin Films. *Small* **2011**, *7*, 3385. (c) Bartual-Murgui, C.; Salmon, L.; Akou, A.; Ortega-Villar, N. A.; Shepherd, H. J.; Muñoz, M. C.; Molnár, G.; Real, J. A.; Bousseksou, A. Synergetic Effect of Host-Guest Chemistry and Spin Crossover in 3D Hofmann-like Metal-Organic Frameworks [Fe(bpac)M(CN)₄] (M = Pt, Pd, Ni). *Chem. - Eur. J.* **2012**, *18*, 507. (d) Muñoz-Lara, F. J.; Gaspar, A. B.; Muñoz, M. C.; Arai, M.; Kitagawa, S.; Ohba, M.; Real, J. A. Sequestering Aromatic Molecules with a Spin-Crossover Fe^{II} Microporous Coordination Polymer. *Chem. - Eur. J.* **2012**, *18*, 8013. (e) Muñoz-Lara, F. J.; Gaspar, A. B.; Muñoz, M. C.; Ksenofontov, V.; Real, J. A. Novel Iron(II) Microporous Spin-Crossover Coordination Polymers with Enhanced Pore Size. *Inorg. Chem.* **2013**, *52*, 3. (f) Sciortino, N. F.; Scherl-Gruenwald, K. R.; Chastanet, G.; Halder, G. J.; Chapman, K. W.; Létard, J. F.; Kepert, C. J. Hysteretic Three-Step Spin Crossover in a Thermo- and Photochromic 3D Pillared Hofmann-type Metal-Organic Framework. *Angew. Chem., Int. Ed.* **2012**, *51*, 10154. (g) Piñeiro-López, L.; Serebyuk, M.; Muñoz, M. C.; Real, J. A. Two- and One-step Cooperative Spin Transitions in Hofmann-like Clathrates with Enhanced Loading Capacity. *Chem. Commun.* **2014**, *50*, 1833.
- (28) (a) Ohtani, R.; Arai, M.; Ohba, H.; Hori, A.; Takata, M.; Kitagawa, S.; Ohba, M. Modulation of the Interlayer Structures and Magnetic Behavior of 2D Spin-Crossover Coordination Polymers [Fe^{II}(L)₂Pt^{II}(CN)₄]. *Eur. J. Inorg. Chem.* **2013**, *2013*, 738. (b) Ragon, F.; Yaksi, K.; Sciortino, N. F.; Chastanet, G.; Létard, J. F.; D'Alessandro, D. M.; Kepert, C. J.; Neville, S. M. Thermal Spin Crossover Behaviour of Two-Dimensional Hofmann-Type Coordination Polymers Incorporating Photoactive Ligands. *Aust. J. Chem.* **2014**, *67*, 1563. (c) Klein, Y. M.; Sciortino, N. F.; Ragon, F.; Housecroft, C. E.; Kepert, C. J.; Neville, S. M. Spin Crossover Intermediate Plateau Stabilization in a Flexible 2D Hofmann-type Coordination Polymer. *Chem. Commun.* **2014**, *50*, 3838. (d) Gaspar, A. B.; Levchenko, G.; Terekhov, S.; Bukin, G.; Valverde-Muñoz, J.; Muñoz-Lara, F. J.; Serebyuk, M.; Real, J. A. The Effect of Pressure on the Cooperative Spin Transition in the 2D Coordination Polymer {Fe(phpy)₂[Ni(CN)₄]}]. *Eur. J. Inorg. Chem.* **2014**, *2014*, 429. (e) Kucheriv, O. I.; Shylin, S. I.; Ksenofontov, V.; Dechert, S.; Haukka, M.; Fritsky, I. O.; Gural'skiy, I. A. Spin Crossover in Fe^{II}-M^{II} Cyanoheterobimetallic Frameworks (M = Ni, Pd, Pt) with 2-Substituted Pyrazines. *Inorg. Chem.* **2016**, *55*, 4906.
- (29) (a) Shepherd, H. J.; Bartual-Murgui, C.; Molnár, G.; Real, J. A.; Muñoz, M. C.; Salmon, L.; Bousseksou, A. Thermal and Pressure-Induced Spin Crossover in a Novel Three-dimensional Hoffman-like Clathrate Complex. *New J. Chem.* **2011**, *35*, 1205. (b) Yoshida, K.; Kosone, T.; Kanadani, C.; Saito, T.; Kitazawa, T. Crystal Structure and magnetic property of spin crossover complex Fe^{II}(3-phenylpyridine)₂[Au^I(CN)₂]₂. *Polyhedron* **2011**, *30*, 3062. (c) Muñoz-Lara, F. J.; Gaspar, A. B.; Muñoz, M. C.; Lysenko, A. B.; Domasevitch, K. V.; Real, J. A. Fast Detection of Water and Organic Molecules by a Change of Color in an Iron(II) Microporous Spin-Crossover Coordination Polymer. *Inorg. Chem.* **2012**, *51*, 13078. (d) Arcis-Castillo, Z.; Muñoz, M. C.; Molnár, G.; Bousseksou, A.; Real, J. A. [Fe(TPT)_{2/3}{M^I(CN)₂}]₂ Center Dot nSolv (M^I = Ag, Au): New Bimetallic Porous Coordination Polymers with Spin-Crossover Properties. *Chem. - Eur. J.* **2013**, *19*, 6851. (e) Li, J. Y.; Yan, Z.; Ni, Z. P.; Zhang, Z. M.; Chen, Y. C.; Liu, W.; Tong, M. L. Guest-Effectuated Spin-Crossover in a Novel Three-Dimensional Self-Penetrating

- Coordination Polymer with Permanent Porosity. *Inorg. Chem.* **2014**, *53*, 4039. (f) Xu, H.; Xu, Z. L.; Sato, O. Water-Switching of Spin Crossover in a Gold Cluster Supramolecular System: From Metal-organic Frameworks to Catenane. *Microporous Mesoporous Mater.* **2014**, *197*, 72. (g) Piñeiro-López, L.; Arcís-Castillo, Z.; Muñoz, M. C.; Real, J. A. Clathration of Five-Membered Aromatic Rings in the Bimetallic Spin Crossover Metal-Organic Framework [Fe-(TPT)_{2/3}{M^I(CN)₂}]₂center dot G (M^I = Ag, Au). *Cryst. Growth Des.* **2014**, *14*, 6311. (h) Yan, Z.; Li, J. Y.; Liu, T.; Ni, Z. P.; Chen, Y. C.; Guo, F. S.; Tong, M. L. Enhanced Spin-Crossover Behavior Mediated by Supramolecular Cooperative Interactions. *Inorg. Chem.* **2014**, *53*, 8129. (i) Sugaya, A.; Ueno, S.; Okabayashi, J.; Kitazawa, T. Crystal Structure and Magnetic Properties of the Spin Crossover Complex Fe^{II}(ethyl nicotinate)₂[Au^I(CN)₂]₂. *New J. Chem.* **2014**, *38*, 1955. (j) Clements, J. E.; Price, J. R.; Neville, S. M.; Kepert, C. J. Perturbation of Spin Crossover Behavior by Covalent Post-Synthetic Modification of a Porous Metal-Organic Framework. *Angew. Chem., Int. Ed.* **2014**, *53*, 10164. (k) Li, J. Y.; Chen, Y. C.; Zhang, Z. M.; Liu, W.; Ni, Z. P.; Tong, M. L. Tuning the Spin-Crossover Behaviour of a Hydrogen-Accepting Porous Coordination Polymer by Hydrogen-Donating Guests. *Chem. - Eur. J.* **2015**, *21*, 1645.
- (30) (a) Decurtins, S.; Gütllich, P.; Köhler, P. C.; Spiering, H.; Hauser, A. Light-induced Excited Spin State Trapping in a Transition-Metal Complex - the hexa-1-propyltetrazole-iron(II) tetrafluoroborate Spin-Crossover System. *Chem. Phys. Lett.* **1984**, *105*, 1. (b) Hauser, A. Reversibility of Light-induced Excited Spin State Trapping in the Fe(PTZ)₆(BF₄)₂ and the Zn_{1-x}Fe_x(PTZ)₆(BF₄)₂ Spin-Crossover Systems. *Chem. Phys. Lett.* **1986**, *124*, 543. Hauser, A. Light-Induced Spin Crossover and the High-Spin -> Low-Spin Relaxation. *Top. Curr. Chem.* **2004**, *234*, 155.
- (31) Létard, J. F. Photomagnetism of Iron(II) Spin Crossover Complexes - the T(LIESST) Approach. *J. Mater. Chem.* **2006**, *16*, 2550.
- (32) (a) Hauser, A. Intersystem Crossing in Fe(II) Coordination-Compounds. *Coord. Chem. Rev.* **1991**, *111*, 275. (b) Hauser, A.; Enachescu, C.; Daku, M. L.; Vargas, A.; Amstutz, N. Low-Temperature Lifetimes of Metastable High-Spin States in Spin-Crossover and in Low-Spin Iron(II) Compounds: The Rule and Exceptions to the Rule. *Coord. Chem. Rev.* **2006**, *250*, 1642.
- (33) Martínez, V.; Gaspar, A. B.; Muñoz, M. C.; Bukin, G. V.; Levchenko, G.; Real, J. A. Synthesis and Characterisation of a New Series of Bistable Iron(II) Spin-Crossover 2D Metal-Organic Frameworks. *Chem. - Eur. J.* **2009**, *15*, 10960.
- (34) Gural'skiy, I. A.; Golub, B. O.; Shylin, S. I.; Ksenofontov, V.; Shepherd, H. J.; Raithby, P. R.; Tremel, W.; Fritsky, I. O. Cooperative High-Temperature Spin Crossover Accompanied by a Highly Anisotropic Structural Distortion. *Eur. J. Inorg. Chem.* **2016**, *2016*, 3191.
- (35) (a) Kosone, T.; Kachi-Terajima, C.; Kanadani, C.; Saito, T.; Kitazawa, T. Isotope Effect on Spin-Crossover Transition in a New Two-Dimensional Coordination Polymer [Fe^{II}(C₅H₅N)₂]-[Au^I(CN)₂]₂, [Fe^{II}(C₅D₅N)₂][Au^I(CN)₂]₂, and [Fe^{II}(C₅H₅N_{1.5})₂]-[Au^I(CN)₂]₂. *Chem. Lett.* **2008**, *37*, 754. (b) Kosone, T.; Kachi-Terajima, C.; Kanadani, C.; Saito, T.; Kitazawa, T. A Two-Step and Hysteretic Spin-Crossover Transition in New Cyano-Bridged Heterometal (FeAu^I)-Au^{II} 2-Dimensional Assemblage. *Chem. Lett.* **2008**, *37*, 422.
- (36) (a) Bonhommeau, S.; Molnár, G.; Galet, A.; Zwick, A.; Real, J. A.; McGarvey, J. J.; Bousseksou, A. One Shot Laser Pulse Induced Reversible Spin Transition in the Spin-Crossover Complex [Fe-(C₄H₄N₂){Pt(CN)₄}] at Room Temperature. *Angew. Chem., Int. Ed.* **2005**, *44*, 4069. (b) Ohba, M.; Yoneda, K.; Agustí, G.; Muñoz, M. C.; Gaspar, A. B.; Real, J. A.; Yamasaki, M.; Ando, H.; Nakao, Y.; Sakaki, S.; Kitagawa, S. Bidirectional Chemo-Switching of Spin State in a Microporous Framework. *Angew. Chem., Int. Ed.* **2009**, *48*, 4767. (c) Southon, P. D.; Liu, L.; Fellows, E. A.; Price, D. J.; Halder, G. J.; Chapman, K. W.; Moubaraki, B.; Murray, K. S.; Létard, J. F.; Kepert, C. J. Dynamic Interplay between Spin-Crossover and Host-Guest Function in a Nanoporous Metal-Organic Framework Material. *J. Am. Chem. Soc.* **2009**, *131*, 10998.
- (37) Martínez, V.; Arcís-Castillo, Z.; Muñoz, M. C.; Gaspar, A. B.; Etrillard, C.; Létard, J. F.; Terekhov, S. A.; Bukin, G. V.; Levchenko, G.; Real, J. A. Thermal-, Pressure- and Light-Induced Spin-Crossover Behaviour in the Two-Dimensional Hofmann-Like Coordination Polymer [Fe(3-Clpy)₂Pd(CN)₄]. *Eur. J. Inorg. Chem.* **2013**, *2013*, 813.
- (38) Sheldrick, G. M. A Short History of SHELX. *Acta Crystallogr., Sect. A: Found. Crystallogr.* **2008**, *64*, 112.
- (39) Eiling, A.; Schilling, J. S. Pressure and Temperature-Dependence of Electrical-Resistivity of Pb and Sn from 1–300 K and 0–10 GPa-use as Continuous Resistive Pressure Monitor Accurate Over Wide Temperature-Range - Superconductivity under Pressure in Pb, Sn, and J. *Phys. F: Met. Phys.* **1981**, *11*, 623.

Switchable Spin-Crossover Hofmann-Type 3D Coordination Polymers Based on Tri- and Tetrapotopic Ligands

Francisco Javier Valverde-Muñoz,[†] M. Carmen Muñoz,[‡] Sacramento Ferrer,[§] Carlos Bartual-Murgui,[†] and José A. Real^{*,†}

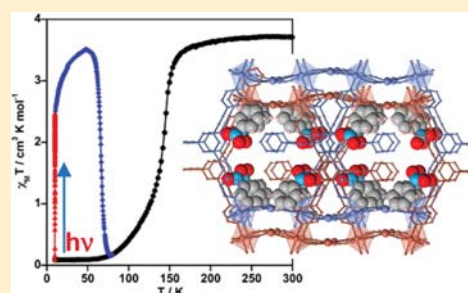
[†]Institut de Ciència Molecular (ICMol), Universitat de València, C/Catedrático José Beltrán Martínez, 2, 46980 Paterna, Valencia, Spain

[‡]Departamento de Física Aplicada, Universitat Politècnica de València, Camino de Vera s/n, 46022 Valencia, Spain

[§]Departament de Química Inorgànica, Universitat de València, Av. Vicent Andrés Estellés, s/n, 46100 Burjassot, Valencia, Spain

Supporting Information

ABSTRACT: Fe^{II} spin-crossover (SCO) coordination polymers of the Hofmann type have become an archetypal class of responsive materials. Almost invariably, the construction of their architectures has been based on the use of monotopic and linear ditopic pyridine-like ligands. In the search for new Hofmann-type architectures with SCO properties, here we analyze the possibilities of bridging ligands with higher connectivity degree. More precisely, the synthesis and structure of {Fe^{II}(L^{N3})[M^I(CN)₂]₂}·(Guest) (Guest = nitrobenzene, benzonitrile, *o*-dichlorobenzene; M^I = Ag, Au) and {Fe^{II}(L^{N4})[Ag₂(CN)₃][Ag(CN)₂]}·H₂O are described, where L^{N3} and L^{N4} are the tritopic and tetrapotopic ligands 1,3,5-tris(pyridin-4-ylethynyl)benzene and 1,2,4,5-tetrakis(pyridin-4-ylethynyl)benzene. This new series of Hofmann clathrates displays thermo- and photoinduced SCO behaviors.



INTRODUCTION

Iron(II) spin-crossover (SCO) complexes are remarkable types of responsive molecular materials that can be reversibly switched between the electronic high-spin (HS) and low-spin (LS) states in response to environmental stimuli, such as temperature, pressure, light irradiation, and analytes.¹ The LS ↔ HS switch is manifested by reversible, controllable, and detectable changes in the physicochemical properties (optical, magnetic, electrical, and structural), making these functional molecular materials excellent prototypes of sensors, switches, and memories.²

Within the so-called polymeric approach to the synthesis of Fe^{II} SCO compounds, Hofmann-type coordination polymers have been gaining considerable attention in the past decade and now they constitute an archetypal family in the SCO area.³ They are a class of two- and three-dimensional cyanide-bridged bimetallic compounds formulated as {Fe^{II}(L)_x[M^I(CN)₄]_n}_m, where M^I is Ni, Pd, or Pt and L can be an N-donor monodentate (*x* = 2) or bis-monodentate rodlike (*x* = 1) ligand. The structure is invariably constituted of parallel stacks of two-dimensional {Fe^{II}[M^I(CN)₄]_n}_m square grids in which Fe^{II} is equatorially coordinated to four [M^I(CN)₄]₂₋ planar units through the N atom while the axial positions are occupied by two L ligands, defining two-dimensional (2D)⁴ or three-dimensional (3D)⁵ coordination polymers when L is a terminal monodentate or a bis-monodentate bridging ligand,

respectively. The latter connects the M^I centers of consecutive layers, thus generating bifunctional porous fsc (RCSR database) frameworks in which SCO properties and host-guest chemistry interplay in a synergetic way.^{5f–h,6}

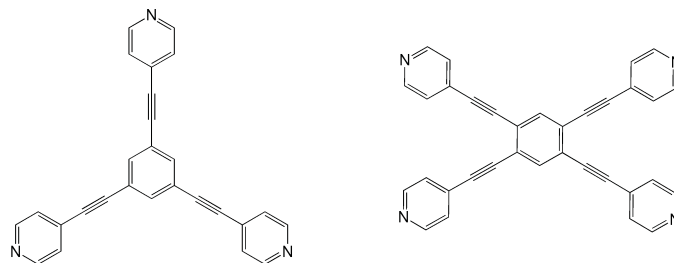
Coordination polymers with the formula {Fe^{II}(L)_x[M^I(CN)₂]₂}_m, where M^I = Cu, Ag, Au, are usually included in the family of Hofmann-type compounds. The Fe^{II} sites can be structurally described in the same terms as for {Fe^{II}(L)_x[M^I(CN)₄]_n}_m. However, the linear bis-monodentate rodlike [M^I(CN)₂]⁻ bridges produce more open frameworks with *pcu* topology, which usually favor double, triple, and even quadruple interpenetration of the frameworks.^{3a,c} At variance with {Fe^{II}(L)₂[M^I(CN)₄]_n}_m, which only form 2D frameworks, monodentate L ligands can also form 3D frameworks with more varied topologies (e.g., *nbo* and *cds* among others).⁷ Usually, the {Fe^{II}(L)_x[M^I(CN)₂]₂}_m frameworks interact with each other through short M^I–M^I metallophilic contacts. Furthermore, the susceptibility of M^I–(Cu,Ag) to expand the coordination sphere or generate oligomers (e.g., [Ag₂(CN)₃]⁻) also adds interesting features to this subfamily of compounds.

Hofmann-type Fe^{II} SCO coordination polymers have afforded excellent examples of thermo- and piezohysteretic behaviors, multistep cooperative transitions, relevant examples

Received: July 3, 2018

Published: September 12, 2018

Scheme 1. Organic Bridging Ligands Used in This Work

Table 1. Crystallographic Parameters for 1·PhNO₂, 2·PhNO₂, and 3·H₂O

| | 1·PhNO ₂ | | 2·PhNO ₂ | | 3·H ₂ O | |
|--|---|------------|---|------------|--|-------------|
| | 120 K | 250 K | 100 K | 250 K | 120 K | 250 K |
| empirical formula | C ₃₇ H ₂₀ Ag ₂ FeN ₈ O ₂ | | C ₃₇ H ₂₀ Au ₂ FeN ₈ O ₂ | | C ₃₀ H ₁₈ Ag ₃ FeN ₉ O | |
| <i>M_r</i> | 880.20 | | 1058.39 | | 008.08 | |
| cryst syst | orthorhombic | | orthorhombic | | triclinic | |
| space group | <i>Pbcn</i> | | <i>Pbcn</i> | | <i>P</i> $\bar{1}$ | |
| <i>a</i> (Å) | 36.5834(10) | 36.806(2) | 36.7927(12) | 36.931(2) | 7.9977(5) | 7.9807(5) |
| <i>b</i> (Å) | 15.2354(4) | 15.8826(5) | 15.1716(5) | 15.6980(4) | 9.5996(9) | 9.8952(6) |
| <i>c</i> (Å) | 13.2204(3) | 13.4475(5) | 13.1200(4) | 13.3384(4) | 13.5845(5) | 13.8305(8) |
| α (deg) | | | | | 89.642(5) | 89.434(4) |
| β (deg) | | | | | 80.717(5) | 80.842(5) |
| γ (deg) | | | | | 71.166(7) | 71.898(5) |
| <i>V</i> (Å ³) | 7368.6(3) | 7861.0(5) | 7323.6(4) | 7732.8(4) | 973.00(12) | 1024.00(11) |
| <i>Z</i> | 8 | 8 | 8 | 8 | 1 | 1 |
| <i>F</i> (000) | 3472 | | 3984 | | 490 | |
| <i>D_c</i> (mg cm ⁻³) | 1.587 | 1.487 | 1.920 | 1.818 | 1.720 | 1.661 |
| μ (Mo K α) (mm ⁻¹) | 1.484 | 1.391 | 8.427 | 7.982 | 1.895 | 1.804 |
| total no. of rflns (<i>I</i> > 2 σ (<i>I</i>)) | 7681 | 5381 | 7739 | 6638 | 3694 | 3496 |
| <i>R</i> (<i>I</i> > 2 σ (<i>I</i>)) | 0.0681 | 0.0672 | 0.0383 | 0.0463 | 0.0609 | 0.0670 |
| <i>R_w</i> (<i>I</i> > 2 σ (<i>I</i>)) | 0.1453 | 0.1674 | 0.0905 | 0.0859 | 0.1569 | 0.1776 |
| <i>S</i> | 1.068 | 1.014 | 1.033 | 1.066 | 1.046 | 1.050 |

of porous systems where the SCO behavior can be tuned by guest molecules favoring selective host–guest interactions, catalytic activity, and/or solid-state transformations.⁸ In addition, these compounds are excellent platforms to investigate the SCO properties at the nanoscale (nanocrystals, thin films)^{5b,9} and their potential application as prototypes of spintronic and micromechanical devices.¹⁰ Thus, the design and synthesis of new Hofmann-type Fe^{II} SCO compounds are essential steps for discovering new, interesting properties and applications. In this respect, almost all Hofmann-type Fe^{II} SCO compounds so far investigated have been prepared from mono- and ditopic L ligands. Indeed, as far as we know, the only exception corresponds to the porous coordination polymers {Fe(TPT)_{2/3}[M^I(CN)₂]₂·*n*(Guest)}, where TPT is 2,4,6-tris(4-pyridyl)-1,3,5-triazine, a tritopic ligand with *D*_{3h} symmetry.¹¹

As a further step in this study, herein we report on the synthesis and characterization of two unprecedented series of Fe^{II} SCO coordination polymers based on the tritopic and tetratopic ligands L^{N3} = 1,3,5-tris(pyridin-4-ylethynyl)benzene and L^{N4} = 1,2,4,5-tetrakis(pyridin-4-ylethynyl)benzene (Scheme 1) and ditopic [M^I(CN)₂]⁻ inorganic bridges. The L^{N3} ligand is an expanded version of the previously investigated TPT ligand, while the topology of the L^{N4} ligand is investigated for the first time in the family of Hofmann clathrates. More

precisely, we will present the crystal structures and magnetic and photomagnetic properties of {Fe^{II}(L^{N3})[M^I(CN)₂]₂·(Guest)} (M^I = Ag (**1·Guest**), M^I = Au (**2·Guest**); Guest = C₆H₅X (X = NO₂, CN), *o*-C₆H₄Cl₂) and {Fe^{II}(L^{N4})[Ag₂(CN)₃][Ag(CN)₂]₂·H₂O (**3·H₂O**)}.

RESULTS

Synthesis. The synthesis of the title compounds was conditioned by the high insolubility of the ligands L^{N3} and L^{N4} and the resulting coordination polymers. Thus, in order to get reasonably good microcrystalline samples and single crystals of **1·Guest**, **2·Guest**, and **3·H₂O**, the synthesis was carried out by slow diffusion of the components (see also the [Experimental Section](#)). The presence of guest molecules was an additional key condition for the synthesis of complexes with L^{N3}. Thus, we found that the use of an H-type diffusion system made up of four connected vessels resulted in the most appropriate strategy. In such a configuration, methanolic solutions of Fe^{II} and [M(CN)₂]⁻ were poured separately into the peripheral vessels, while L^{N3} was placed as a solid (due to its insolubility) at the bottom of the vessel next to the Fe^{II} solution, and a large excess of Guest was placed in the remainder vessel. Alternatively, to slow the diffusion, it is also possible to add the Fe^{II} and [M(CN)₂]⁻ salts as solids at the bottom of the corresponding tubes. Finally, the four vessels were filled with

Table 2. Selected Bond Lengths (Å) for 1·PhNO₂, 2·PhNO₂, and 3·H₂O

| | 1·PhNO ₂ | | 2·PhNO ₂ | | 3·H ₂ O | |
|---------|---------------------|----------|---------------------|----------|--------------------|----------|
| | 120 K | 250 K | 100 K | 250 K | 120 K | 250 K |
| Fe–N1 | 2.033(4) | 2.217(6) | 2.048(5) | 2.220(5) | 2.045(4) | 2.241(4) |
| Fe–N2 | 2.046(4) | 2.228(5) | 2.061(5) | 2.217(5) | 1.955(4) | 2.117(5) |
| Fe–N3 | 1.968(4) | 2.166(5) | 1.975(5) | 2.157(6) | 1.957(4) | 2.141(5) |
| Fe–N4 | 1.969(4) | 2.145(5) | 1.994(5) | 2.148(5) | | |
| Fe–N5 | 1.971(5) | 2.151(5) | 1.982(5) | 2.149(6) | | |
| Fe–N6 | 1.973(5) | 2.151(5) | 1.986(5) | 2.154(6) | | |
| Ag1–C28 | 2.043(5) | 2.031(6) | | | | |
| Ag1–C29 | 2.044(5) | 2.049(6) | | | | |
| Ag2–C30 | 2.053(6) | 2.052(6) | | | | |
| Ag2–C31 | 2.059(6) | 2.060(6) | | | | |
| Au1–C28 | | | 1.986(6) | 1.987(7) | | |
| Au1–C29 | | | 1.970(6) | 1.982(7) | | |
| Au2–C30 | | | 1.989(7) | 1.989(7) | | |
| Au2–C31 | | | 1.983(6) | 1.977(6) | | |
| Au1–Au2 | | | 3.268(1) | 3.270(1) | | |
| Ag1–N4 | | | | | 2.435(4) | 2.470(6) |
| Ag1–N5 | | | | | 2.119(5) | 2.095(7) |
| Ag1–C18 | | | | | 2.068(5) | 2.054(6) |
| Ag1–C19 | | | | | 2.119(5) | 2.095(7) |
| Ag2–C20 | | | | | 2.058(5) | 2.060(6) |
| Ag1–Ag2 | 3.275(1) | 3.247(1) | | | | |

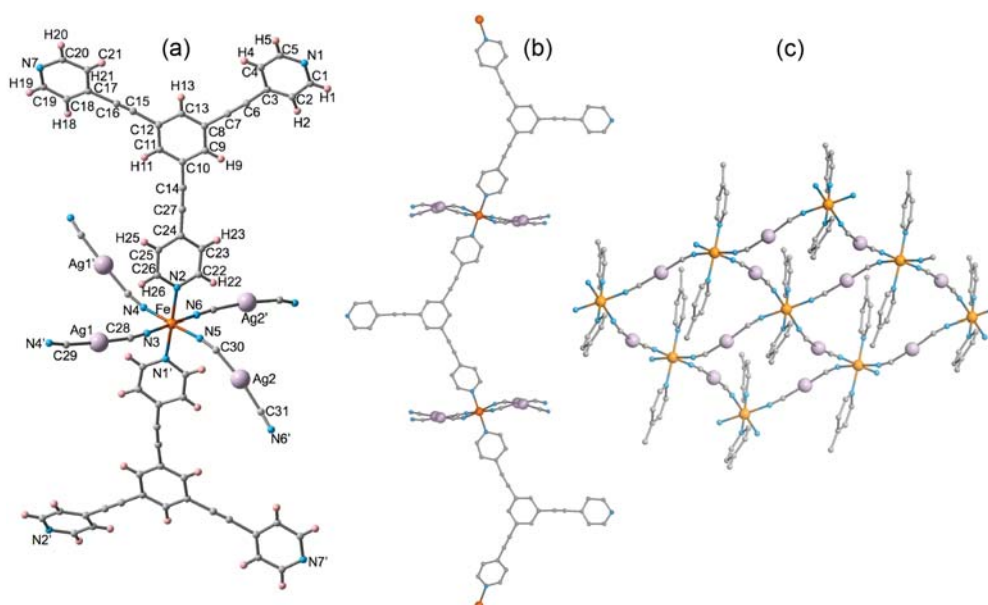


Figure 1. (a) Coordination center of 1·PhNO₂ at 120 K showing the atom labeling of the asymmetric unit (the atom labeling for the Au derivative (2·PhNO₂) is the same). (b) Fragment of the zigzag chain running along [100]. (c) {Fe₄[M(CN)₂]₄} corrugated 2D grids.

methanol and sealed (Figure S1). The most appropriate guest molecules turned out to be the following benzene derivatives: PhNO₂, *o*-PhCl₂, and PhCN. In contrast, the use of five-membered rings as guests, i.e. pyrrole, furan, and thiophene, was unsuccessful and no product was formed. PXRD patterns for the 1·Guest and 2·Guest series are practically identical, demonstrating their isostructural nature (Figure S2). Despite the high crystallinity of these compounds, adequate single

crystals to get reasonably good structural X-ray diffraction analyses were achieved only for 1·PhNO₂ and 2·PhNO₂.

Given that L^{N4} is soluble in CHCl₃ and that the structure of 3·H₂O cannot accept guest molecules (vide infra), a three-vessel modification was employed (see Figure S1). At variance with 3·H₂O, self-assembly of Fe^{II}, L^{N4}, and [Au(CN)₂][−] does not give any type of complex even in the presence of guest molecules. This may be due to metric and/or geometric

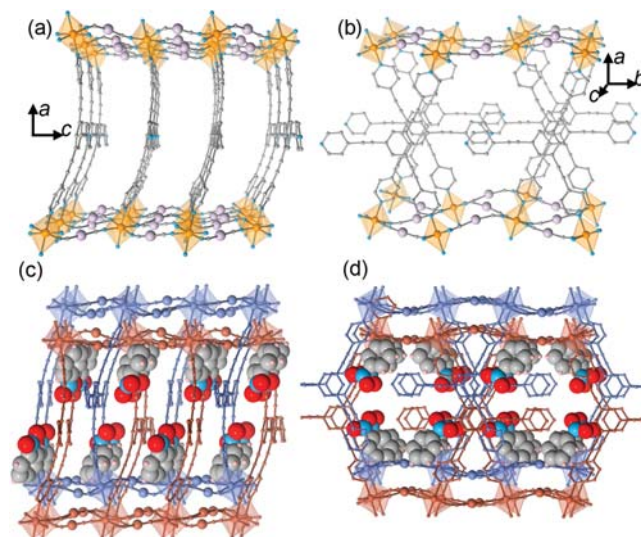


Figure 2. Perspective views of a fragment of the 3D framework of **1-PhNO₂** at 120 K: a single framework running along the [001] (a) and [010] (b) directions and the same perspectives showing the double-interpenetrated frameworks loaded with PhNO₂ (c, d).

incompatibilities between connectors and nodes and the fact that the Au atom cannot expand the coordination sphere as Ag does in the case of **3·H₂O** (vide infra).

The thermogravimetric analysis (TGA) for **1·Guest**, **2·Guest**, and **3·H₂O** confirmed the amount of guest molecules (Figure S3). The TGA for fresh samples of **1·PhNO₂** and **2·PhNO₂** shows, prior to the loss of the PhNO₂ molecule, a quite small weight loss (ca. 0.5 and 0.3%, respectively) on starting from room temperature, which could be tentatively associated with the presence of a quite small amount of methanol. Because the amount of these molecules is less than ca. 1/8 CH₃OH and these species are very labile, we have considered that, under vacuum conditions of the SQUID magnetometer or even under ambient storage conditions, these molecules spontaneously desolvate, as suggested by the structure analysis and the magnetic properties (vide infra). The average yields for **1·Guest** and **2·Guest** were ca. 15–20%, and that of **3·H₂O** was 10–15%.

Structure. The crystal structure was determined by single-crystal X-ray analysis at 120 and 250 K for **1·PhNO₂** and **3·H₂O** and at 100 and 250 K for **2·PhNO₂**. Compounds **1·PhNO₂** and **2·PhNO₂** crystallize in the orthorhombic *Pbcn* space group, while compound **3·H₂O** crystallizes in the triclinic *P1̄* space group. Relevant crystallographic parameters are shown in Table 1. Selected significant bond lengths and angles are given in Table 2 and Table S1, respectively.

Structures of 1-PhNO₂ and 2-PhNO₂. Given that **1·PhNO₂** and **2·PhNO₂** are isostructural, we will describe their structures simultaneously. There is a crystallographically unique Fe^{II} site that is situated in the center of a slightly elongated [FeN₆] octahedron. Figure 1 displays the coordination sphere of the Fe^{II} with the atom labeling of the asymmetric unit, which is the same for **1·PhNO₂** and **2·PhNO₂**. The axial positions (Fe–N1 and Fe–N2), occupied by the pyridine moieties of the ligand L^{N3}, are about 3% longer than the equatorial positions. The four equatorial positions are occupied by two crystallo-

graphically distinct [M^I(CN)₂][−] groups (Ag1/2 and Au1/2). The average ⟨[FeN₆]⟩ bond lengths are 1.993(5) [2.176(5)] Å for **1·PhNO₂** at 120 K [250 K] and 2.008(5) Å [2.174(6)] Å for **2·PhNO₂** at 100 K [250 K]. The difference values Δ*R* between high- and low-temperature forms equal to 0.183 Å (**1·PhNO₂**) and 0.166 Å (**2·PhNO₂**) are in agreement with the magnetic data and are consistent with the occurrence of a practically complete SCO transition for **1·PhNO₂** and 90% conversion at 100 K for **2·PhNO₂**. It is worth stressing at this point that, when single crystals of the latter compound are selected directly from the mother liquor and cooled to 120 K, the crystal parameters and Fe–N bond lengths are similar to those obtained at 250 K and are consistent with the results obtained from the magnetic data measured in solution: namely, that **2·PhNO₂** remains in the HS state (vide infra) (see Table S2). Consistent with the TGA, this notable difference suggests the presence of very small amounts of strongly disordered labile methanol molecules included in the structure (ca. less than 0.2 molecule) at 120 K. Indeed, there is some nonassigned electron density within the cavities of the structure. An analysis using PLATON shows the occurrence of a void volume of 2 × 67 Å³ centered at (0.0, 0.72, 0.25) close (ca. 2.7 Å) to the uncoordinated N7 atom. No such behavior was observed for the single-crystal study of **1·PhNO₂**.

The sums of deviations from the ideal octahedron of the 12 “cis” N–Fe–N angles ($\sum = \sum_{i=1}^{12} |\theta_i - 90|$) are respectively 17.3° [26.8°] and 24.1° [25.3°] for **1·PhNO₂** and **2·PhNO₂** at 120 K [250 K], confirming that the [FeN₆] site is weakly distorted, whatever the spin state of the Fe^{II} centers. The average Fe–N–C(M^I) angles separate from 180° by 15.4° (250 K) and 10.2° (120 K) for Fe–N–C(Ag) and 16.8° (250 K) and 11.7° (100 K) for Fe–N–C(Au). Similarly, the average M^I–C–N angles deviate from linearity by 6.5° (250 K) and 10.6° (120 K) for [Ag(CN)₂][−] and 4.6° (250 K) and 7.4° (100 K) for [Au(CN)₂][−].

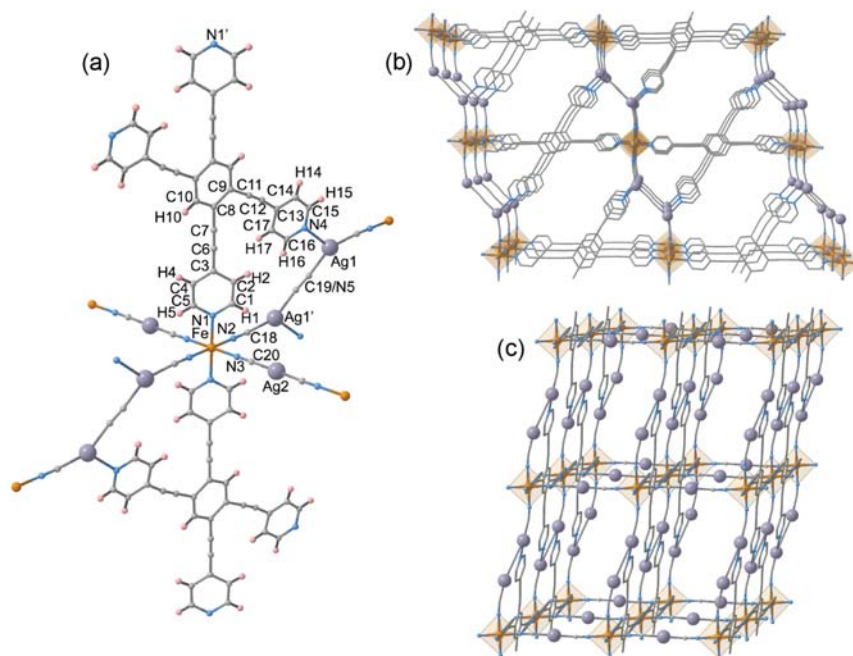


Figure 3. Coordination center of $3\cdot\text{H}_2\text{O}$ at 120 K showing the atom labeling of the asymmetric unit (a). Perspective views of a fragment of the 3D framework of $3\cdot\text{H}_2\text{O}$ at 120 K: two perspectives of the same fragment of a single framework emphasizing the coordination mode of $\text{L}^{\text{N}4}$ and $[\text{Ag}_2(\text{CN})_3]^-$ bridges (b) and the connection of the formed layers via $[\text{Ag}(\text{CN})_2]^-$ ligands (c).

The $\text{L}^{\text{N}3}$ ligand is not completely flat. Indeed, the mean planes defined by the pyridine moieties containing N1, N7, and N2 define angles with respect to the mean plane containing the benzene ring equal to 4.7° (4.2°), 18.9° (26.9°), and 5.4° (13.6°) for $1\cdot\text{PhNO}_2$ at 120 (250) K and 4.6° (4.2°), 18.9° (29.1°), and 5.1° (6.8°) for $2\cdot\text{PhNO}_2$ at 100 (250) K, respectively. It is noteworthy to stress the strong dependence of the angles defined by N2 and N7 on the spin state of the Fe^{II} . Furthermore, the pyridine–benzene connectors deviate slightly from linearity (by $5\text{--}6^\circ$). The pyridyl group containing the N7 atom does not coordinate either the Fe^{II} or M^{I} ion and is strongly disordered. Consequently, $\text{L}^{\text{N}3}$ acts as a ditopic ligand, thereby defining zigzag chains running along $[100]$. In addition, the $[\text{M}^{\text{I}}(\text{CN})_2]^-$ linkers radiate almost perpendicularly to the $[100]$ direction connecting the Fe^{II} centers of four adjacent zigzag chains. Alternatively, the structure can be seen as a parallel stack of slightly corrugated 2D grids $\{\text{Fe}_4[\text{M}^{\text{I}}(\text{CN})_2]_4\}$ connected by $\text{L}^{\text{N}3}$. The distances between two Fe^{II} centers of consecutive layers connected by $\text{L}^{\text{N}3}$ are 18.466(1) Å at 120 K for $1\cdot\text{PhNO}_2$ and 18.396(2) Å at 100 K for $2\cdot\text{PhNO}_2$. The resulting 3D network generates enough empty room so as to favor interpenetration of two identical networks (Figure 2). The frameworks interact with each other through weak metalphilic $\text{M}^{\text{I}}\cdots\text{M}^{\text{I}}$ interactions (see Table 2) but, more importantly, through the $\text{L}^{\text{N}3}$ ligands, which stack along the c direction, generating a large number of intermolecular $\text{C}\cdots\text{C}$ π short contacts smaller than the sum of the van der Waals radii (ca. 3.7 Å). These contacts increase in number and intensity when the compound moves from the HS state to the LS state

(see Figures S4 and S5 and Table S3). Despite this fact, the interpenetrating frameworks generate room for inclusion of one PhNO_2 molecule, which are located between the $\text{L}^{\text{N}3}$ ligands (Figure 2) and define strong π interactions with one of the pyridine rings coordinated to the Fe^{II} centers, while the other coordinated pyridine group also interacts via π with the central benzene ring of a $\text{L}^{\text{N}3}$ ligand belonging to the adjacent framework (see Figures S4 and S5).

Structure of $3\cdot\text{H}_2\text{O}$. Figure 3 displays a fragment of the structure of $3\cdot\text{H}_2\text{O}$ at 120 K together with the atom labeling of the asymmetric unit. There is one crystallographically unique $[\text{FeN}_6]$ site which lies in an inversion center defining a slightly elongated octahedron. The axial bond lengths are occupied by the pyridine moieties of the $\text{L}^{\text{N}4}$ ligand ($\text{Fe}\text{--}\text{N}1$), while the four equatorial positions are occupied by $[\text{Ag}(\text{CN})_2]^-$ and $[\text{Ag}_2(\text{CN})_3]^-$ units through the $\text{Fe}\text{--}\text{N}2$ and $\text{Fe}\text{--}\text{N}3$ bonds. The $\langle[\text{FeN}_6]\rangle$ values equal to 1.986(4) and 2.166(4) Å at 120 and 250 K, respectively, indicate that the Fe^{II} centers are essentially in the LS and HS spin states according to the magnetic data. In this case the angular distortions of the $[\text{FeN}_6]$ octahedron, $\sum^{120\text{K}} = 6.9(2)^\circ$ and $\sum^{250\text{K}} = 5.0(2)^\circ$, are remarkably smaller than those in the case of $1\cdot\text{PhNO}_2$ and $2\cdot\text{PhNO}_2$.

The $\text{L}^{\text{N}4}$ ligand is essentially flat, but the pyridine moiety bearing the N1 atom is rotated 27.1° with respect to the plane defined by the central benzene ring, which also lies in an inversion center. The Ag site in the $[\text{Ag}(\text{CN})_2]^-$ unit is strictly linear. In contrast, the Ag site in the in situ generated $[\text{Ag}_2(\text{CN})_3]^-$ species expands the coordination sphere to 3, affording a distorted-trigonal geometry. The trigonal geometry

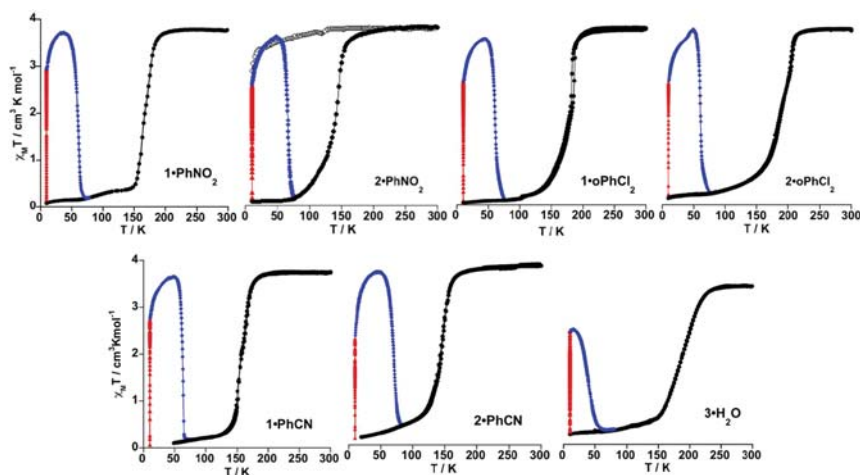


Figure 4. Magnetic and photomagnetic properties of **1-Guest**, **2-Guest**, and **3-H₂O**: irradiation at 10 K (red triangles); thermal dependence of $\chi_M T$ upon heating at 0.3 K/min (blue circles) and heating/cooling at 1 K/min (black circles); thermal variation of $\chi_M T$ for crystals of **2-PhNO₂** soaked in mother liquor (open circles).

is generated through coordination of the N4 atom belonging to L^{N4} . Consequently, L^{N4} acts as a tetratopic ligand connecting the Fe^{II} and the Ag^I of the $[Ag_2(CN)_3]^-$ units, defining an irregular 2D grid with triangular and hexagonal windows. These layers are connected through the linear $[Ag(CN)_2]^-$ bridges, thus defining a quite open 3D framework. Alternatively, the structure can be described as constituted by an infinite stack of undulated $\{Fe_4[Ag(CN)_2]_2[Ag_2(CN)_3]_2\}_n$ layers pillared by L^{N4} . The space generated by the undulated rectangular windows allows interpenetration of two additional identical frameworks, thus filling the void space and affording a triple-interpenetrated system where there is only free room for one H_2O per formula unit (see Figure S6a). A simplified version of the structure showing the topology of the resulting (2-c)(3-c)2(4-c)(6-c) 4-nodal net analyzed with ToposPro¹² is given in Figure S6b.

Magnetic and Photomagnetic Properties. The thermal dependence of the $\chi_M T$ product (χ_M is the molar magnetic susceptibility and T is the temperature) was measured at 1 K min^{-1} using a magnetic field of 1 T in the temperature region 10–300 K for compounds **1-Guest**, **2-Guest**, and **3-H₂O**. The corresponding $\chi_M T$ versus T curves are shown in Figure 4. At 300 K, the $\chi_M T$ value was found in the interval 3.70–3.76 $cm^3 K mol^{-1}$ for **1-Guest** and **2-Guest** and 3.34 $cm^3 K mol^{-1}$ for **3-H₂O**. These values are typical for an $S = 2$ ground state with noticeable orbital contribution, as usually observed for the Fe^{II} ion in the HS state. For **1-Guest** and **2-Guest**, $\chi_M T$ is nearly constant in the temperature interval 300–210 K. Upon further cooling, $\chi_M T$ decreases abruptly, attaining values in the interval 0.10–0.25 $cm^3 K mol^{-1}$ at 50 K, indicating that the LS state ($S = 0$) is practically fully populated. The equilibrium temperatures of the SCO, at which the molar fractions of the HS and the LS species are equal to $\gamma_{LS} = \gamma_{HS} = 0.5$ ($\Delta G_{HL} = 0$), have $T_{1/2}$ values equal to 156 K (**1-PhCN**), 145 K (**2-PhCN**), 166 K (**1-PhNO₂**), 143 K (**2-PhNO₂**), 180 K (**1-oPhCl₂**), and 187 K (**2-oPhCl₂**).

As mentioned in the structural analysis, an apparent inconsistency in the degree of spin-state conversion was

found when the $\chi_M T$ product and the average Fe–N bond distance of **2-PhNO₂** at 120 K were correlated. This was associated with the clathration of a variable small amount of loosely attached methanol molecules, which spontaneously desorb at higher temperatures. To clarify this, the thermal variation of $\chi_M T$ was recorded for a crystalline sample of **2-PhNO₂** soaked in mother liquor. The results included in Figure 4 (open circles) demonstrates that under these conditions **2-PhNO₂** remains in the HS state at all temperatures.

Compound **3-H₂O** experiments a similar SCO behavior starting at higher temperature (ca. 250 K), but the $\chi_M T$ product decreases more gradually. Indeed, the $\chi_M T$ value changes from 3.34 to 0.56 $cm^3 K mol^{-1}$ ($\gamma_{HS} \approx 0.17$) in the temperature interval 250–150 K. Furthermore, a subsequent smoother decrease of $\chi_M T$ is observed in the temperature range 150–50 K, attaining a value of 0.26 $cm^3 K mol^{-1}$ at 50 K ($\gamma_{HS} \approx 0.08$). The SCO can also be considered complete and characterized by a $T_{1/2}$ value of ca. 187 K.

Photogeneration of the metastable HS* state at low temperature, the so-called light-induced excited spin state trapping (LIESST) experiment,¹³ was carried out at 10 K on irradiation of microcrystalline samples (0.80 mg) of **1-Guest** and **2-Guest** with red light (λ 633 nm), in the time required to attain saturation (Figure 4 and Figure S7). Under these conditions, the samples saturate in 3 h, with values of $\chi_M T$ in the interval 2.97–2.21 $cm^3 K mol^{-1}$. Subsequently, the light irradiation was switched off and the temperature increased at a rate of 0.3 K min^{-1} . Then, $\chi_M T$ keeps on increasing to reach a maximum of 3.72–3.54 $cm^3 K mol^{-1}$ in the temperature interval 37–50 K. This increase in $\chi_M T$ corresponds to the thermal population of different microstates originating from the zero-field splitting of the $S = 2$ HS* spin state. At higher temperatures, $\chi_M T$ decreases rapidly until it joins the thermal SCO curve in the 65–84 K temperature range, indicating that the metastable HS* state has completely relaxed to the stable LS state. In contrast, after saturation $\chi_M T$ values experience just a slight increase to attain a maximum of ca. 2.47 $cm^3 K$

mol⁻¹ at 14 K for 3•H₂O. This less stable HS* state relaxes back to the LS state at significantly lower temperatures. The characteristic T_{LIESST} temperatures,¹⁴ obtained from $\partial\chi_M T/\partial T$ in the 10–77 K interval, are 63.6 K (1•PhCN), 70.5 K (2•PhCN), 61.0 K (1•PhNO₂), 66.0 K (2•PhNO₂), 60.5 K (1•oPhCl₂), 60.0 K (2•oPhCl₂), and 37 K (3•H₂O).

DISCUSSION

The objective of the present work was to investigate new cyanido-bridged bimetallic Fe^{II}-M^I SCO coordination polymers. We focused our attention on L^{N3} and L^{N4} tri- and tetraprotic ligands, respectively. As mentioned above, it is relevant to stress that the isostructural doubly interpenetrated frameworks 1•Guest and 2•Guest could only be obtained in the presence of appropriate guest molecules such as PhNO₂, o-PhCl₂, and PhCN, which apparently act as templates during the self-assembly process. In addition, this template function was critically dependent on the size of the guest molecule.

Despite being L^{N3} being topologically identical with the ligand TPT, they form in combination with Fe^{II} and [M^I(CN)₂]⁻ (M^I = Ag, Au) complexes with different stoichiometries and radically distinct {Fe[M^I(CN)₂]₂}_n frameworks.¹¹ The complexes {Fe(TPT)_{2/3}[M^I(CN)₂]₂·n(Guest)} (M^I = Ag, Au) generate two interlocking 3D networks with an NbO-type topology defined by the [N≡C–M^I–C≡N]⁻ linkers. The *c* axis of the network coincides with one of the diagonals of the NbO units, which in turn runs along the C₃ axis passing through the TPT ligands (see Figure 5). Indeed,

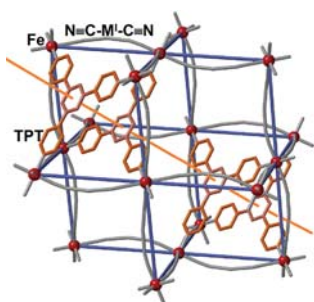


Figure 5. Fragment of the {Fe(TPT)_{2/3}[M^I(CN)₂]₂} framework displaying the NbO-type topology defined by blue bars connecting the Fe^{II} centers (red spheres). The [M^I(CN)₂]⁻ units are the undulating gray segments linking the Fe^{II} centers. The orange line denotes the diagonal and C₃ axis of the structure passing through the TPT ligands.

the TPT ligand is perfectly complementary with the voids generated by the pseudohexagonal circuits {Fe[M^I(CN)₂]₂}₆ (chair conformation) and acts as an additional tritopic bridge between the Fe^{II} centers. Obviously, extension of the linker between the pyridine and triazine moieties of the TPT ligand with alkaline spacers to afford a ligand having the same metrics as L^{N3} would provoke a severe misfit of the resulting ligand with respect to the size of the {Fe[M^I(CN)₂]₂}₆ circuits. As a consequence, the framework {Fe[M^I(CN)₂]₂}_n cannot generate the intricate 3D NbO-type structure observed for the TPT system; in contrast, it readapts to form an infinite stack of 2D corrugated layered structures pillared by L^{N3} to afford 1•Guest and 2•Guest frameworks. Apparently, there is no stable

structural arrangement compatible with L^{N3} acting as a tritopic ligand.

In contrast to L^{N3}, self-assembly of Fe^{II}, L^{N4}, and [M^I(CN)₂]⁻ only gave positive results for M^I = Ag, affording 3•H₂O in low yield. During the slow diffusion process, part of the [Ag^I(CN)₂]⁻ groups dissociate to generate in situ the relatively uncommon oligomeric species [Ag₂^I(CN)₃]⁻, which has been described for a few related SCO compounds.¹⁵ This fact together with the particular configuration of the pyridine rings in L^{N4} favors the expansion of the coordination number of the two equivalent Ag^I centers of [Ag₂^I(CN)₃]⁻ to 3 (pseudotrigonal), thereby provoking strong distortion from linearity in this species and marked corrugation in the resulting 2D {Fe[Ag(CN)₂][Ag₂(CN)₃]_n} layers. These layers stack along the [100] direction and are firmly attached to each other through L^{N4}, which act as double pillars linking two Fe^{II} and Ag^I (pseudotrigonal) pairs of adjacent layers, forming an open 3D framework. Furthermore, the wide rectangular {Fe₄[Ag(CN)₂]₂[Ag₂(CN)₃]₂} windows facilitate interpenetration of two other identical frameworks in such a way that there is no room for inclusion of guest molecules. Indeed, only a loosely attached molecule of water is retained. The much more inert nature of the Au^I coordination sphere does not enable generating similar species, and consequently, the homologous gold compound of 3•H₂O cannot form.

As far as the SCO equilibrium temperatures ($T_{1/2}$) are concerned, a moderate increase in $T_{1/2}$ is observed for 1•Guest in the sequence PhCN (156 K) < PhNO₂ (166 K) < o-PhCl₂ (180 K). A possible explanation for this trend could be related to the slightly different sizes and shapes of these molecules. Their different accommodation requirements in the available space most likely favors distinct distributions of the intermolecular interactions which enhance the stabilization of the LS. This is also valid, to a first approximation, for 2•Guest (PhCN (145 K) ≈ PhNO₂ (143 K) < o-PhCl₂ (187 K)), although it is not obvious to explain why $T_{1/2}$ for the PhNO₂ derivative is virtually the same as that for the PhCN derivative. In this respect, it is well known the high sensitivity of $T_{1/2}$ to very small changes in free energy between of the HS and LS states, ΔG_{HLD} ^{6c} is well-known, which in turn reflects the high sensitivity of the SCO centers to chemical pressure. Consequently, stabilization/destabilization of the LS (HS) state, and hence the value $T_{1/2}$, depends on a delicate balance between electronic and structural factors that often are difficult (if not impossible) to evaluate/discuss without a notable dose of speculation.

The general trend of the T_{LIESST} values is consistent with the empirical inverse-energy-gap law:¹⁶ i.e., the metastability of the photogenerated HS* species decreases as the stability of the LS increases. This is particularly true for the $T_{1/2} - T_{\text{LIESST}}$ ¹⁴ values of homologous pairs 1•Guest–2•Guest (Guest = PhCN, PhNO₂), although in the case of Guest = o-PhCl₂ the smaller difference in $T_{1/2}$ is reflected in virtually similar T_{LIESST} values (the same can be observed when 2•PhCN and 2•PhNO₂ are compared). It is important to remark that all the $T_{1/2} - T_{\text{LIESST}}$ pairs in the 1•Guest–2•Guest series are located close to the correlation line $T_{\text{LIESST}} = T_0 - 0.3T_{1/2}$, with $T_0 = 100$ K being typical for less rigid coordination centers [Fe^{II}N₆] constituted of monodentate ligands and being consistent with their isostructural nature.¹⁴ In contrast, despite the fact that [Fe^{II}N₆] centers are similar for 3•H₂O, its corresponding $T_{1/2} - T_{\text{LIESST}}$ pair is well below this line. This may reflect the distinct structural nature of the latter, which displays a densely

packed triply interpenetrated 3D rigid structure versus a less densely packed and probably less rigid doubly interpenetrated 3D structure in **1•Guest** and **2•Guest**.

It is a general fact when series of isostructural Ag^{I} and Au^{I} SCO complexes are compared that $(T_{1/2})^{\text{Ag}} > (T_{1/2})^{\text{Au}}$. This is usually rationalized in terms of lower donor ability associated with the greater electron-withdrawing ability of the cyanide group due to a more covalent NC–Au interaction. This general trend applies for the isostructural **1•Guest** and **2•Guest** compounds when Guest is PhNO_2 and PhCN , but it does not apply for *o*- PhCl_2 . In line with what is mentioned above, the presumed extra space required by *o*- PhCl_2 together with the more rigid nature of the Au^{I} framework, in comparison with the Ag^{I} framework, may favor an extra chemical pressure which results in a higher than expected $T_{1/2}$ value. This conjecture is supported by the greater number of short intermolecular contacts observed for **2•PhNO₂** in comparison with **1•PhNO₂**.

CONCLUSION

Two new ligands with unusual coordination denticities, trigonal ($\text{L}^{\text{N}3}$) and square ($\text{L}^{\text{N}4}$), have been included in the library of SCO Hofmann-type metal–organic frameworks derived from $[\text{M}^{\text{I}}(\text{CN})_2]^-$ ($\text{M}^{\text{I}} = \text{Ag}, \text{Au}$). Using slow diffusion methods in presence of appropriate guest molecules, $\text{L}^{\text{N}3}$ affords six new isostructural clathrate compounds generically formulated as **1•Guest** and **2•Guest** with Guest = PhCN , PhNO_2 , *o*- PhCl_2 . The structure of the PhNO_2 derivative shows that $\text{L}^{\text{N}3}$ works as a bis-monodentate ligand to satisfy, most likely, the metrics imposed by the $\{\text{Fe}[\text{M}^{\text{I}}(\text{CN})_2]_2\}_n$ layers, thereby acting as a pillar between the layers, thus affording an open 3D framework. Two identical frameworks interpenetrate in the same space and hold together through short intermolecular interactions including weak $\text{M}^{\text{I}}\cdots\text{M}^{\text{I}}$ metal-philic interactions. The six clathrates exhibit thermal- and light-induced SCO properties. Concerning the ligand $\text{L}^{\text{N}4}$, one should expect coordination of four Fe^{II} and generation of a complicated framework via $[\text{M}^{\text{I}}(\text{CN})_2]^-$; however, the occurrence of geometric incompatibilities is apparent, which are solved for the Ag^{I} derivative by virtue of its much more labile coordination sphere. Consequently, the structure of **3•H₂O** is made up of extended $\{\text{Fe}[\text{Ag}^{\text{I}}(\text{CN})_2][\text{Ag}_2^{\text{I}}(\text{CN})_3]\}_n$ layers pillared by two opposite pyridine rings of $\text{L}^{\text{N}4}$, which act as axial ligands of Fe^{II} , while the remaining two pyridine rings coordinate the Ag^{I} centers of the in situ generated $[\text{Ag}_2^{\text{I}}(\text{CN})_3]^-$ units. The much more inert nature of Au^{I} prevents the formation of this uncommon triple-interpenetrated network. The higher characteristic $T_{1/2}$ value of the SCO is consistent with the incomplete photogeneration of the LS state at low temperatures.

EXPERIMENTAL SECTION

Materials. $\text{Fe}(\text{BF}_4)_2 \cdot 6\text{H}_2\text{O}$, $\text{K}[\text{Ag}(\text{CN})_2]$, $\text{K}[\text{Au}(\text{CN})_2]$, and organic precursors were purchased from commercial sources and used as received.

Synthesis of Ligands. 4-Ethynylpyridine and the ligands $\text{L}^{\text{N}3}$ and $\text{L}^{\text{N}4}$ were prepared by the published methods.¹⁷

Synthesis of $\{\text{Fe}^{\text{II}}(\text{L}^{\text{N}3})[\text{M}^{\text{I}}(\text{CN})_2]\cdot\text{Guest}$ ($\text{M}^{\text{I}} = \text{Ag}$ (1•Guest**), **Au** (**2•Guest**)).** Crystals of **1•Guest** and **2•Guest** were obtained in the same manner by slow diffusion of methanolic solutions of four reagents placed in a modified H-shaped vessel with four arms. Each reagent was deposited in one of the arms, in the following order: $\text{Fe}(\text{BF}_4)_2 \cdot 6\text{H}_2\text{O}$ (0.0787 mmol, 26.6 mg), $\text{L}^{\text{N}3}$ (0.0787 mmol, 30 mg), Guest (= PhNO_2 , PhCN , *o*- PhCl_2 ; 2 mL, large excess), and $\text{K}[\text{Ag}(\text{CN})_2]$ (0.1574 mmol, 31.5 mg) (**1**)/ $\text{K}[\text{Au}(\text{CN})_2]$ (0.1574

mmol, 47.3 mg) (**2**). Finally, the vessel was filled completely with methanol and sealed. In all cases, yellow crystals appeared within 2 weeks, in low yield (ca. 20%). EDX analysis (energy dispersive X-ray analysis) confirmed the stoichiometric relationship between metallic coordination centers: for **1•Guest**, $\text{Fe}:\text{Ag} = 1:2$; for **2•Guest**, $\text{Fe}:\text{Au} = 1:2$.

Complex 1•Guest. Anal. Calcd for $\text{C}_{37}\text{H}_{20}\text{Ag}_2\text{FeN}_8\text{O}_2$ (880.20): C, 50.49; H, 2.29; N, 12.73. Found: C, 50.38; H, 2.32; N, 12.58. Calcd for $\text{C}_{37}\text{H}_{19}\text{Ag}_2\text{FeN}_7\text{Cl}_2$ (904.09): C, 49.16; H, 2.12; N, 10.85. Found: C, 50.18; H, 2.22; N, 10.98. Calcd for $\text{C}_{38}\text{H}_{20}\text{Ag}_2\text{FeN}_8$ (860.22): C, 53.06; H, 2.34; N, 13.03. Found: C, 52.58; H, 2.32; N, 12.68. IR (cm^{-1}): $\nu(\text{C}\equiv\text{C})$ 2219 (m), $\nu(\text{C}\equiv\text{N})$ 2163 (s), $\nu(\text{C}=\text{N})$ 1613 (vs), $\nu(\text{pyridine ring})$ 1418 (s), 825 (s). The symmetric and asymmetric stretching modes of the NO_2 group in PhNO_2 were unambiguously assigned to $\nu_s(\text{NO}_2)$ 1525 (vs) and $\nu_a(\text{NO}_2)$ 1344 (vs). No singular signals could be associated with PhCN and *o*- PhCl_2 .

Complex 2•Guest. Anal. Calcd for $\text{C}_{37}\text{H}_{20}\text{Au}_2\text{FeN}_8\text{O}_2$ (1058.39): C, 41.99; H, 1.90; N, 10.59. Found: C, 41.78; H, 1.98; N, 10.43. Calcd for $\text{C}_{37}\text{H}_{19}\text{Au}_2\text{FeN}_7\text{Cl}_2$ (1082.29): C, 41.06; H, 1.77; N, 9.06. Found: C, 42.03; H, 1.85; N, 10.43. Calcd for $\text{C}_{38}\text{H}_{20}\text{Au}_2\text{FeN}_8$ (1038.41): C, 43.95; H, 1.94; N, 10.79. Found: C, 43.58; H, 2.01; N, 10.68. IR (cm^{-1}): $\nu(\text{C}\equiv\text{C})$ 2220 (m), $\nu(\text{C}\equiv\text{N})$ 2170 (s), $\nu(\text{C}=\text{N})$ 1610 (vs), $\nu(\text{pyridine ring})$ 1420 (s), 820 (s). The symmetric and asymmetric stretching modes of the NO_2 group in PhNO_2 were unambiguously assigned to $\nu_s(\text{NO}_2)$ 1520 (vs) and $\nu_a(\text{NO}_2)$ 1340 (vs). No singular signals could be associated with *o*- PhCl_2 and PhCN .

Synthesis of $\{\text{Fe}^{\text{II}}(\text{L}^{\text{N}4})[\text{Ag}_2(\text{CN})_3][\text{Ag}(\text{CN})_2]\cdot\text{H}_2\text{O}$ (3•H₂O**).** Crystals of **3•H₂O** were obtained by slow diffusion of solutions of three reagents placed in a modified H-shaped vessel with three arms, the arm in the middle being broader than the peripheral arms. This feature was introduced due to the high insolubility of $\text{L}^{\text{N}4}$ (a high volume of solvent was needed to dissolve the appropriated amount of ligand). The peripheral vessel arms contained $\text{Fe}(\text{BF}_4)_2 \cdot 6\text{H}_2\text{O}$ (0.05925 mmol, 20 mg) and $\text{K}[\text{Ag}(\text{CN})_2]$ (0.1185 mmol, 23.7 mg), respectively; the central vessel arm contained a solution of $\text{L}^{\text{N}4}$ (0.05925 mmol, 28.6 mg, dissolved in 7 mL of CHCl_3). Finally, the tube was filled completely with methanol and sealed. Orange single crystals of **3•H₂O** appeared within 4 weeks, in low yield (ca. 20%).

EDX analysis (energy dispersive X-ray analysis) confirmed the stoichiometric relationship between metallic coordination centers: for **3•H₂O**, $\text{Fe}:\text{Ag} = 1:3$.

Complex 3•H₂O. Anal. Calcd for $\text{C}_{39}\text{H}_{20}\text{Ag}_3\text{FeN}_9\text{O}$ (1010.10): C, 46.37; H, 2.00; N, 12.48. Found: C, 46.59; H, 2.10; N, 12.73. IR (cm^{-1}): $\nu(\text{C}\equiv\text{C})$ 2212 (w), $\nu(\text{C}\equiv\text{N})$ 2150 (m), $\nu(\text{C}=\text{N})$ 1604 (vs), $\nu(\text{pyridine rings})$ 1419 (s), 813 (s).

Physical Characterization. Variable-temperature magnetic susceptibility measurements were performed on samples (20–30 mg) consisting of crystals, using a Quantum Design MPMS2 SQUID susceptometer equipped with a 5.5 T magnet, operating at 1 T and at temperatures in the range 300–1.8 K. Experimental susceptibilities were corrected for diamagnetism of the constituent atoms by the use of Pascal's constants. Thermogravimetric analysis was performed on a Mettler Toledo TGA/SDTA 851e instrument in the 290–800 K temperature range under a nitrogen atmosphere with a rate of 10 K min^{-1} .

Single-Crystal X-ray Diffraction. Single-crystal X-ray data were collected with an Oxford Diffraction Supernova diffractometer. In all cases, $\text{Mo K}\alpha$ radiation ($\lambda = 0.71073 \text{ \AA}$) was used. Data scaling and empirical or multiscan absorption corrections were performed. The structures were solved by direct methods with SHELXT or SIR2004 and refined by full-matrix least-squares techniques on F^2 with SHELXL.¹⁸ Non-hydrogen atoms were refined anisotropically, and hydrogen atoms were placed in calculated positions and refined in idealized geometries (riding model) with fixed isotropic displacement parameters.

■ ASSOCIATED CONTENT

● Supporting Information

The Supporting Information is available free of charge on the ACS Publications website at DOI: 10.1021/acs.inorgchem.8b01842.

Experimental setup used for the synthesis, thermal analysis, and selected bond angles of **1-Guest**, **2-Guest**, and **3-H₂O**, experimental XRPD patterns for **1-Guest** and **2-Guest**, intermolecular C...C contacts for **1-PhNO₂** and **2-PhNO₂**, and crystallographic data and bond lengths and angles for the paramagnetic form of **2-PhNO₂** at 120 K (PDF)

Accession Codes

CCDC 1852556–1852562 contain the supplementary crystallographic data for this paper. These data can be obtained free of charge via www.ccdc.cam.ac.uk/data_request/cif, or by emailing data_request@ccdc.cam.ac.uk, or by contacting The Cambridge Crystallographic Data Centre, 12 Union Road, Cambridge CB2 1EZ, UK; fax: +44 1223 336033.

■ AUTHOR INFORMATION

Corresponding Author

*E-mail for J.A.R.: jose.a.real@uv.es.

ORCID

José A. Real: 0000-0002-2302-561X

Notes

The authors declare no competing financial interest.

■ ACKNOWLEDGMENTS

We thank the Spanish Ministerio de Economía y Competitividad (MINECO) and FEDER funds (CTQ2013-46275-P and CTQ2016-78341-P and Unidad de Excelencia María de Maeztu MDM-2015-0538), and Generalitat Valenciana (PROMETEO/2016/147). F.J.V.-M. thanks MINECO for a predoctoral FPI grant. We also thank Dr. Carlos Martí for helping us with ToposPro software.

■ REFERENCES

(1) See for example: (a) Hauser, A. Intersystem Crossing in Iron(II) Coordination Compounds: A Model Process between Classical and Quantum Mechanical Behaviour. *Comments Inorg. Chem.* **1995**, *17*, 17–40. (b) König, E. Nature and Dynamics of the Spin-State Interconversion in Metal-Complexes. *Struct. Bonding (Berlin, Ger.)* **1991**, *76*, 51–152. (c) Gütlich, P.; Hauser, A.; Spiering, H. Thermal and Optical Switching of Iron(II) Complexes. *Angew. Chem., Int. Ed. Engl.* **1994**, *33*, 2024–2054. (d) Sato, O. Optically Switchable Molecular Solids: Photoinduced Spin-Crossover, Photochromism, and Photoinduced Magnetization. *Acc. Chem. Res.* **2003**, *36*, 692–700. (e) Real, J. A.; Gaspar, A. B.; Niel, V.; Muñoz, M. C. Communication between Iron(II) Building Blocks in Cooperative Spin Transition Phenomena. *Coord. Chem. Rev.* **2003**, *236*, 121–141. (f) Spin Crossover in Transition Metal Compounds I-III. *Topics in Current Chemistry*; Gütlich, P., Goodwin, H. A., Eds.; Springer: 2004, Vols. 233–235. (g) Real, J. A.; Gaspar, A. B.; Muñoz, M. C. Thermal, Pressure and Light Switchable Spin-Crossover Materials. *Dalton Trans.* **2005**, 2062–2079. (h) Halcrow, M. A. The Spin-States and Spin-Transitions of Mononuclear Iron(II) Complexes of Nitrogen-Donor Ligands. *Polyhedron* **2007**, *26*, 3523–3576. (i) Halcrow, M. A. Iron(II) Complexes of 2,6-di(pyrazol-1-yl)pyridines A Versatile System for Spin-Crossover Research. *Coord. Chem. Rev.* **2009**, *253*, 2493–2514. (j) Olguin, J.; Brooker, S. Spin Crossover Active Iron(II) Complexes of Selected pyrazole-pyridine/pyrazine Ligands. *Coord. Chem. Rev.* **2011**, *255*, 203–240. (k) Bousseksou, A.; Molnár, G.;

Salmon, L.; Nicolazzi, W. Molecular Spin Crossover Phenomenon: Recent Achievements and Prospects. *Chem. Soc. Rev.* **2011**, *40*, 3313–3335.

(2) (a) Meded, V.; Bagrets, A.; Fink, K.; Chandrasekar, R.; Ruben, M.; Evers, F.; Bernand-Mantel, A.; Seldenthuis, J. S.; Beukman, A.; van der Zant, H. S. J. Electrical Control over the Fe(II) Spin Crossover in a Single Molecule: Theory and Experiment. *Phys. Rev. B: Condens. Matter Mater. Phys.* **2011**, *83*, 245415. (b) Prins, F.; Monrabal-Capilla, M.; Osorio, E. A.; Coronado, E.; van der Zant, H. S. J. Room-Temperature Electrical Addressing of a Bistable Spin-Crossover Molecular System. *Adv. Mater.* **2011**, *23*, 1545–1549. (c) Cavallini, M.; Bergenti, I.; Milita, S.; Kengne, J. C.; Gentili, D.; Ruani, G.; Salitros, I.; Meded, V.; Ruben, M. Thin Deposits and Patterning of Room-Temperature-Switchable One-Dimensional Spin-Crossover Compounds. *Langmuir* **2011**, *27*, 4076–4081. (d) Miyamachi, T.; Gruber, M.; Davesne, V.; Bowen, M.; Boukari, S.; Joly, L.; Scheurer, F.; Rogez, G.; Yamada, T. K.; Ohresser, P.; Beaupaire, E.; Wulfhekel, W. Robust Spin Crossover and Memristance across a Single Molecule. *Nat. Commun.* **2012**, *3*, 938. (e) Martinho, P. N.; Rajnak, C.; Ruben, M. In *Spin-Crossover Materials: Properties and Applications*; Halcrow, M. A., Ed.; Wiley: 2013; pp 376–404 and references therein. (f) Shepherd, H. J.; Molnár, G.; Nicolazzi, W.; Salmon, L.; Bousseksou, A. Spin Crossover at the Nanometre Scale. *Eur. J. Inorg. Chem.* **2013**, *2013*, 653–661. (g) Rotaru, A.; Dugay, J.; Tan, R. P.; Gural'skiy, I. A.; Salmon, L.; Demont, P.; Carrey, J.; Molnár, G.; Respaud, M.; Bousseksou, A. Nano-Electromanipulation of Spin Crossover Nanorods: Towards Switchable Nanoelectronic Devices. *Adv. Mater.* **2013**, *25*, 1745–1749. (h) Gural'skiy, I. A.; Quintero, C. M.; Sánchez Costa, J.; Demont, P.; Molnár, G.; Salmon, L.; Shepherd, H. J.; Bousseksou, A. Spin Crossover Composite Materials for Electrothermomechanical Actuators. *J. Mater. Chem. C* **2014**, *2*, 2949–2955. (i) Bartual-Murgui, C.; Akou, A.; Thibault, C.; Molnár, G.; Vieu, C.; Salmon, L.; Bousseksou, A. Spin-Crossover Metal-Organic Frameworks: Promising Materials for Designing Gas Sensors. *J. Mater. Chem. C* **2015**, *3*, 1277–1285. (j) Aragonés, A. C.; Aravena, D.; Cerdá, J. I.; Acís-Castillo, Z.; Li, H.; Real, J. A.; Sanz, F.; Hihath, J.; Ruiz, E.; Díez-Pérez, I. Large Conductance Switching in a Single-Molecule Device through Room Temperature Spin-Dependent Transport. *Nano Lett.* **2016**, *16*, 218–226.

(3) (a) Muñoz, M. C.; Real, J. A. Thermo-, Piezo-, Photo- and Chemo-Switchable Spin Crossover Iron(II)-Metalloacyanate Based Coordination Polymers. *Coord. Chem. Rev.* **2011**, *255*, 2068–2093. (b) Muñoz, M. C.; Real, J. A. Polymeric Spin-Crossover Materials. In *Spin-Crossover Materials: Properties and Applications*; Halcrow, M. A., Ed.; Wiley: 2013; pp 121–146. (c) Ni, Z.-P.; Liu, J.-L.; Hoque, Md. N.; Liu, W.; Li, J.-Y.; Chen, Y.-C.; Tong, M.-L. Recent advances in guest effects on spin-crossover behavior in Hofmann-type metal-organic frameworks. *Coord. Chem. Rev.* **2017**, *335*, 28–43.

(4) (a) Martínez, V.; Gaspar, A. B.; Muñoz, M. C.; Bugin, G. V.; Levchenko, G.; Real, J. A. Synthesis and Characterisation of a New Series of Bistable Iron (II) Spin-Crossover 2D Metal-Organic Frameworks. *Chem. - Eur. J.* **2009**, *15*, 10960–10971. (b) Ohtani, R.; Arai, M.; Ohba, H.; Hori, A.; Takata, M.; Kitagawa, S.; Ohba, M. Modulation of the Interlayer Structures and Magnetic Behaviour of 2D Spin-Crossover Coordination Polymers [Fe^{II}(L)₂Pt^{II}(CN)₄]. *Eur. J. Inorg. Chem.* **2013**, *2013*, 738–744. (c) Klein, Y. M.; Sciortino, N. F.; Ragon, F.; Housecroft, C. E.; Kepert, C. J.; Neville, S. M. Spin crossover intermediate plateau stabilization in a flexible 2-D Hofmann-type coordination polymer. *Chem. Commun.* **2014**, *50*, 3838–3840. (d) Liu, W.; Wang, L.; Su, Y.-J.; Chen, Y.-C.; Tucek, J.; Zboril, R.; Ni, Z.-P.; Tong, M.-L. Hysteretic Spin Crossover in Two-Dimensional (2D) Hofmann-Type Coordination Polymers. *Inorg. Chem.* **2015**, *54*, 8711–8716. (e) Milin, E.; Patinec, V.; Triki, S.; Bendeif, E.-E.; Pillet, S.; Marchivie, M.; Chastanet, G.; Boukheddaden, K. Elastic Frustration Triggering Photoinduced Hidden Hysteresis and Multistability in a Two-Dimensional Photoswitchable Hofmann-Like Spin-Crossover Metal-Organic Framework. *Inorg. Chem.* **2016**, *55*, 11652–11661. (f) Valverde-Muñoz, F. J.; Sereydyuk, M.; Muñoz, M. C.; Znoviyak, K.; Fritsky, I. O.; Real, J. A. Strong Cooperative Spin

- Crossover in 2D and 3D $\text{Fe}^{\text{II}}\text{-M}^{\text{II}}$ Hofmann-Like Coordination Polymers Based on 2-Fluoropyrazine. *Inorg. Chem.* **2016**, *55*, 10654–10665. (g) Kucheriv, O. I.; Shylin, S. I.; Ksenofontov, V.; Dechert, S.; Haukka, M.; Fritsky, I. O.; Gural'skiy, I. A. Spin Crossover in $\text{Fe}(\text{II})\text{-M}(\text{II})$ Cyanoheterobimetallic Frameworks ($\text{M} = \text{Ni}, \text{Pd}, \text{Pt}$) with 2-Substituted Pyrazines. *Inorg. Chem.* **2016**, *55*, 4906–4914. (h) Sciortino, N. F.; Zenere, K. A.; Corrigan, M. E.; Halder, G. J.; Chastanet, G.; Létard, J.-F.; Kepert, C. J.; Neville, S. M. Four-step iron (II) spin state cascade driven by antagonistic solid state interactions. *Chem. Sci.* **2017**, *8*, 701–707. (i) Liu, F.-L.; Tao, J. Hysteretic Two-Step Spin-Crossover Behaviour in Two Two-Dimensional Hofmann-Type Coordination Polymers. *Chem. - Eur. J.* **2017**, *23*, 18252–18257.
- (5) (a) Niel, V.; Martínez-Agudo, J. M.; Muñoz, M. C.; Gaspar, A. B.; Real, J. A. Cooperative Spin Crossover Behaviour in Cyanide-Bridged $\text{Fe}(\text{II})\text{-M}(\text{II})$ Bimetallic 3D Hofmann-like Networks ($\text{M} = \text{Ni}, \text{Pd}, \text{Pt}$). *Inorg. Chem.* **2001**, *40*, 3838–3839. (b) Agustí, G.; Cobo, S.; Gaspar, A. B.; Molnár, G.; Moussa, N. O.; Szilágyi, P. A.; Pálfi, V.; Vieu, C.; Muñoz, M. C.; Real, J. A.; Bousseksou, A. Thermal and Light-Induced Spin Crossover Phenomena in New 3D Hofmann-Like Microporous Metalorganic Frameworks Produced As Bulk Materials and Nanopatterned Thin Films. *Chem. Mater.* **2008**, *20*, 6721–6732. (c) Bartual-Murgui, C.; Ortega-Villar, N. A.; Shepherd, H. J.; Muñoz, M. C.; Salmon, L.; Molnár, G.; Bousseksou, A.; Real, J. A. Enhanced porosity in a new 3D Hofmann-like network exhibiting humidity sensitive cooperative spin transitions at room temperature. *J. Mater. Chem.* **2011**, *21*, 7217–7222. (d) Sciortino, N. F.; Scherl-Gruenwald, K. R.; Chastanet, G.; Hader, G. J.; Chapman, K. W.; Létard, J.-F.; Kepert, C. J. Hysteretic Three-Step Spin Crossover in a Thermo- and Photochromic 3D Pillared Hofmann-type Metal-Organic Framework. *Angew. Chem.* **2012**, *124*, 10301–10305. (e) Muñoz-Lara, F. J.; Gaspar, A. B.; Muñoz, M. C.; Ksenofontov, V.; Real, J. A. Novel Iron(II) Microporous Spin-Crossover Coordination Polymers with Enhanced Pore Size. *Inorg. Chem.* **2013**, *52*, 3–5. (f) Muñoz-Lara, F. J.; Gaspar, A. B.; Muñoz, M. C.; Arai, M.; Kitagawa, S.; Ohba, M.; Real, J. A. Sequestering Aromatic Molecules with a Spin-Crossover Fe^{II} Microporous Coordination Polymer. *Chem. - Eur. J.* **2012**, *18*, 8013–8018. (g) Piñeiro-López, L.; Seredyuk, M.; Muñoz, M. C.; Real, J. A. Two- and one-step cooperative spin transitions in Hofmann-like clathrates with enhanced loading capacity. *Chem. Commun.* **2014**, *50*, 1833–1835. (h) Piñeiro-López, L.; Valverde-Muñoz, F. J.; Seredyuk, M.; Muñoz, M. C.; Haukka, M.; Real, J. A. Guest Induced Strong Cooperative One- and Two-Step Spin Transitions in Highly Porous Iron(II) Hofmann-Type Metal-Organic Frameworks. *Inorg. Chem.* **2017**, *56*, 7038–7047. (i) Bao, X.; Shepherd, H. J.; Salmon, L.; Molnár, G.; Tong, M. L.; Bousseksou, A. The Effect of an Active Guest on the Spin Crossover Phenomenon. *Angew. Chem., Int. Ed.* **2013**, *52*, 1198–1202. (j) Liu, W.; Peng, Y. Y.; Wu, S. G.; Chen, Y. C.; Hoque, M. N.; Ni, Z. P.; Chen, X. M.; Tong, M. L. Guest-Switchable Multi-Step Spin Transitions in an Amine-Functionalized Metal-Organic Framework. *Angew. Chem., Int. Ed.* **2017**, *56*, 14982–14986.
- (6) (a) Bartual-Murgui, C.; Salmon, L.; Akou, A.; Ortega-Villar, N. A.; Shepherd, H. J.; Muñoz, M. C.; Molnár, G.; Real, J. A.; Bousseksou, A. Synergetic Effect of Host-Guest Chemistry and Spin Crossover in 3D Hofmann-like Metal-Organic Frameworks $[\text{Fe}(\text{bpac})\text{M}(\text{CN})_4]$ ($\text{M} = \text{Pt}, \text{Pd}, \text{Ni}$). *Chem. - Eur. J.* **2012**, *18*, 507–516. (b) Muñoz-Lara, F. J.; Gaspar, A. B.; Aravena, D.; Ruiz, E.; Muñoz, M. C.; Ohba, M.; Ohtani, R.; Kitagawa, S.; Real, J. A. Enhanced bistability by guest inclusion in $\text{Fe}(\text{II})$ spin crossover porous coordination polymers. *Chem. Commun.* **2012**, *48*, 4686–4688. (c) Bartual-Murgui, C.; Amal, A.; Shepherd, H. J.; Molnár, G.; Real, J. A.; Salmon, L.; Bousseksou, A. Tunable Spin-Crossover Behavior of the Hofmann-like Network $\{\text{Fe}(\text{bpac})[\text{Pt}(\text{CN})_4]\}$ through Host-Guest Chemistry. *Chem. - Eur. J.* **2013**, *19*, 15036–15043. (d) Arcis-Castillo, Z.; Muñoz-Lara, F. J.; Muñoz, M. C.; Aravena, D.; Gaspar, A. B.; Sánchez-Royo, J. F.; Ruiz, E.; Ohba, M.; Matsuda, R.; Kitagawa, S.; Real, J. A. Reversible Chemisorption of Sulfur Dioxide in a Spin Crossover Porous Coordination Polymer. *Inorg. Chem.* **2013**, *52*, 12777–12783. (e) Aravena, D.; Arcis-Castillo, Z.; Muñoz, M. C.; Gaspar, A. B.; Yoneda, K.; Ohtani, R.; Mishima, A.; Kitagawa, S.; Ohba, M.; Real, J. A.; Ruiz, E. Guest Modulation of Spin-Crossover Transition Temperature in a Porous Iron(II) Metal-Organic Framework: Experimental and Periodic DFT Studies. *Chem. - Eur. J.* **2014**, *20*, 12864–12873.
- (7) (a) Niel, V.; Thompson, A. L.; Muñoz, M. C.; Galet, A.; Goeta, A. E.; Real, J. A. Crystalline-State Reaction with Allosteric Effect in Spin-Crossover, Interpenetrated Networks with Magnetic and Optical Bistability. *Angew. Chem., Int. Ed.* **2003**, *42*, 3760–3763. (b) Galet, A.; Niel, V.; Muñoz, M. C.; Real, J. A. Synergy between Spin Crossover and Metallophilicity in Triple Interpenetrated 3D Nets with the NbO Structure Type. *J. Am. Chem. Soc.* **2003**, *125*, 14224–14225. (c) Galet, A.; Muñoz, M. C.; Martínez, V.; Real, J. A. Supramolecular isomerism in spin crossover networks with aurophilic interactions. *Chem. Commun.* **2004**, 2268–2269.
- (8) (a) Galet, A.; Gaspar, A. B.; Muñoz, M. C.; Bukin, G. V.; Levchenko, G.; Real, J. A. Tunable Bistability in a Three-Dimensional Spin-Crossover Sensory- and Memory-Functional Material. *Adv. Mater.* **2005**, *17*, 2949–2953. (b) Ohba, M.; Yoneda, K.; Agustí, G.; Muñoz, M. C.; Gaspar, A. B.; Real, J. A.; Yamasaki, M.; Ando, H.; Nakao, Y.; Sakaki, S.; Kitagawa, S. Bidirectional Chemo-Switching of Spin State in a Microporous Framework. *Angew. Chem., Int. Ed.* **2009**, *48*, 4767–4771. (c) Murphy, M. J.; Zenere, K. A.; Ragon, F.; Southon, P. D.; Kepert, C. J.; Neville, S. M. Guest Programmable Multistep Spin Crossover in a Porous 2-D Hofmann-Type Material. *J. Am. Chem. Soc.* **2017**, *139*, 1330–1335. (d) Clements, J. E.; Price, J. R.; Neville, S. M.; Kepert, C. J. Perturbation of Spin Crossover Behavior by Covalent Post-Synthetic Modification of a Porous Metal-Organic Framework. *Angew. Chem., Int. Ed.* **2014**, *53*, 10164–10168. (e) Li, J.-Y.; Chen, Y.-C.; Zhang, Z.-M.; Liu, W.; Ni, Z.-P.; Tong, M.-L. Tuning the Spin-Crossover Behaviour of a Hydrogen-Accepting Porous Coordination Polymer by Hydrogen-Donating Guests. *Chem. - Eur. J.* **2015**, *21*, 1645–1651.
- (9) (a) Cobo, S.; Molnár, G.; Real, J. A.; Bousseksou, A. Multilayer Sequential Assembly of Thin Films That Display Room-Temperature Spin Crossover with Hysteresis. *Angew. Chem., Int. Ed.* **2006**, *45*, 5786–5789. (b) Molnár, G.; Cobo, S.; Real, J. A.; Carcenac, F.; Daran, E.; Vieu, C.; Bousseksou, A. A Combined Top-Down/Bottom-Up Approach for the Nanoscale Patterning of Spin-Crossover Coordination Polymers. *Adv. Mater.* **2007**, *19*, 2163–2167. (c) Volatron, F.; Catala, L.; Rivière, E.; Gloter, A.; Stéphane, O.; Mallah, T. Spin-Crossover Coordination Nanoparticles. *Inorg. Chem.* **2008**, *47*, 6584–6586. (d) Boldog, L.; Gaspar, A. B.; Martínez, V.; Pardo-Ibañez, P.; Ksenofontov, V.; Bhattacharjee, A.; Gütllich, P.; Real, J. A. Spin-Crossover Nanocrystals with Magnetic, Optical, and Structural Bistability Near Room Temperature. *Angew. Chem., Int. Ed.* **2008**, *47*, 6433–6437. (e) Martínez, V.; Boldog, L.; Gaspar, A. B.; Ksenofontov, V.; Bhattacharjee, A.; Gütllich, P.; Real, J. A. Spin Crossover Phenomenon in Nanocrystals and Nanoparticles of $[\text{Fe}(\text{3-Fpy})_2\text{M}(\text{CN})_4]$ ($\text{M}^{\text{II}} = \text{Ni}, \text{Pd}, \text{Pt}$) Two-Dimensional Coordination Polymers. *Chem. Mater.* **2010**, *22*, 4271–4281. (f) Bartual-Murgui, C.; Akou, A.; Salmon, L.; Molnár, G.; Thibault, C.; Real, J. A.; Bousseksou, A. Guest Effect on Nanopatterned Spin-Crossover Thin Films. *Small* **2011**, *7*, 3385–3391. (g) Bartual-Murgui, C.; Akou, A.; Thibault, C.; Molnár, G.; Vieu, C.; Salmon, L.; Bousseksou, A. Spin-crossover metal-organic frameworks: promising materials for designing gas sensors. *J. Mater. Chem. C* **2015**, *3*, 1277–1285.
- (10) Shepherd, H. J.; Gural'skiy, I. A.; Quintero, C. M.; Tricard, S.; Salmon, L.; Molnár, G.; Bousseksou, A. Molecular actuators driven by cooperative spin-state switching. *Nat. Commun.* **2013**, *4*, 2607.
- (11) (a) Arcis-Castillo, Z.; Muñoz, M. C.; Molnár, G.; Bousseksou, A.; Real, J. A. $[\text{Fe}(\text{TPT})_{2/3}\{\text{M}^{\text{I}}(\text{CN})_2\}_2] \cdot n\text{Solv}$ ($\text{M}^{\text{I}} = \text{Ag}, \text{Au}$), New Bimetallic Porous Coordination Polymers with Spin-Crossover Properties. *Chem. - Eur. J.* **2013**, *19*, 6851–6861. (b) Piñeiro-López, L.; Arcis-Castillo, Z.; Muñoz, M. C.; Real, J. A. Clathration of Five-Membered Aromatic Rings in the Bimetallic Spin Crossover Metal-Organic Framework $[\text{Fe}(\text{TPT})_{2/3}\{\text{M}^{\text{I}}(\text{CN})_2\}_2] \cdot \text{G}$ ($\text{M}^{\text{I}} = \text{Ag}, \text{Au}$). *Cryst. Growth Des.* **2014**, *14*, 6311–6319.

(12) Blatov, V. A.; Shevchenko, A. P.; Proserpio, D. M. Applied topological analysis of crystal structures with the program package ToposPro. *Cryst. Growth Des.* **2014**, *14*, 3576–3586.

(13) (a) Decurtins, S.; Gütllich, P.; Köhler, P. C.; Spiering, H.; Hauser, A. Light-induced excited spin state trapping in a transition-metal complex: The hexa-1-propyltetrazole-iron(II) tetrafluoroborate spin-crossover system. *Chem. Phys. Lett.* **1984**, *105*, 1–4. (b) Hauser, A. Reversibility of light-induced excited spin state trapping in the $\text{Fe}(\text{ptz})_6(\text{BF}_4)_2$ and the $\text{Zn}_{1-x}\text{Fe}_x(\text{ptz})_6(\text{BF}_4)_2$ spin-crossover systems. *Chem. Phys. Lett.* **1986**, *124*, 543–548.

(14) (a) Létard, J. F.; Guionneau, P.; Rabardel, L.; Howard, J. A. K.; Goeta, A. E.; Chasseau, D.; Kahn, O. Structural, magnetic, and photomagnetic studies of a mononuclear iron(II) derivative exhibiting an exceptionally abrupt spin transition. Light-induced thermal hysteresis phenomenon. *Inorg. Chem.* **1998**, *37*, 4432–4441. (b) Létard, J. F.; Chastanet, G.; Guionneau, P. Optimizing the stability of trapped metastable spin states. In *Spin-Crossover Materials: Properties and Applications*; Halcrow, M. A. Ed.; Wiley: 2013; pp 475–500.

(15) (a) Niel, V.; Thompson, A. L.; Goeta, A. E.; Enachescu, C.; Hauser, A.; Galet, A.; Muñoz, M. C.; Real, J. A. Thermal- and photoinduced spin-state switching in an unprecedented three-dimensional bimetallic coordination polymer. *Chem. - Eur. J.* **2005**, *11*, 2047–2060. (b) Kosone, T.; Suzuki, Y.; Ono, S.; Kanadani, C.; Saito, T.; Kitazawa, T. A new spin crossover heterometallic $\text{Fe}(\text{II})\text{Ag}(\text{I})$ coordination polymer with the $[\text{Ag}_2(\text{CN})_2]^-$ unit: crystallographic and magnetic study. *Dalton Trans.* **2010**, *39*, 1786–1790. (c) Li, J.-Y.; Yan, Z.; Ni, Z.-P.; Zhang, Z.-M.; Chen, Y.-C.; Liu, W.; Tong, M.-L. Guest-effected spin-crossover in a novel three-dimensional self-penetrating coordination polymer with permanent porosity. *Inorg. Chem.* **2014**, *53*, 4039–4046. (d) Piñero-López, L.; Valverde-Muñoz, F. J.; Seredyuk, M.; Bartual-Murgui, C.; Muñoz, M. C.; Real, J. A. Cyanido bridged $\text{Fe}^{\text{II}}\text{-M}^{\text{I}}$ bimetallic Hofmann-like spin-crossover coordination polymers based on 2,6-Naphthyridine. *Eur. J. Inorg. Chem.* **2018**, *2018*, 289–296.

(16) (a) Hauser, A. Intersystem crossing in $\text{Fe}(\text{II})$ coordination compounds. *Coord. Chem. Rev.* **1991**, *111*, 275–290. (b) Hauser, A.; Vef, A.; Adler, P. Intersystem crossing dynamics in $\text{Fe}(\text{II})$ coordination compounds. *J. Chem. Phys.* **1991**, *95*, 8710–8717. (c) Hauser, A.; Enachescu, C.; Daku, M. L.; Vargas, A.; Amstutz, N. Low-temperature lifetimes of metastable high-spin states in spin-crossover and in low-spin iron(II) compounds: the rule and exceptions to the rule. *Coord. Chem. Rev.* **2006**, *250*, 1642–1652.

(17) (a) Ciana, L. D.; Haim, A. J. Synthesis of 1,4-bis(4-pyridyl)butadiyne. *J. Heterocycl. Chem.* **1984**, *21*, 607–608. (b) Amoroso, A. J.; Cargill-Thompson, A. M. W.; Maher, J. P.; McCleverty, J. A.; Ward, M. D. Di-, Tri-, and Tetranucleating Pyridyl Ligands Which Facilitate Multicenter Magnetic Exchange between Paramagnetic Molybdenum Centers. *Inorg. Chem.* **1995**, *34*, 4828–4835.

(18) Sheldrick, G. M. SHELXL-2015. *Acta Crystallogr., Sect. C: Struct. Chem.* **2015**, *71*, 3–8.

Influence of Host–Guest and Host–Host Interactions on the Spin-Crossover 3D Hofmann-type Clathrates $\{\text{Fe}^{\text{II}}(\text{pina})[\text{M}^{\text{I}}(\text{CN})_2]_2\} \cdot x\text{MeOH}$ ($\text{M}^{\text{I}} = \text{Ag}, \text{Au}$)

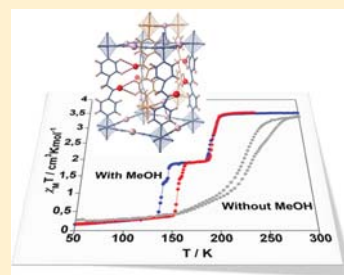
Francisco Javier Valverde-Muñoz,[†] Carlos Bartual-Murgui,^{*,†,‡} Lucía Piñeiro-López,[†] M. Carmen Muñoz,[‡] and José Antonio Real^{*,†,‡}

[†]Instituto de Ciencia Molecular (ICMol), Universitat de València, C/Catedrático José Beltrán Martínez 2, Paterna, 46980 Valencia, Spain

[‡]Departamento de Física Aplicada, Universitat Politècnica de València, Camino de Vera s/n, E-46022 Valencia, Spain

Supporting Information

ABSTRACT: The synthesis, structural characterization and magnetic properties of two new isostructural porous 3D compounds with the general formula $\{\text{Fe}^{\text{II}}(\text{pina})[\text{M}^{\text{I}}(\text{CN})_2]_2\} \cdot x\text{MeOH}$ ($x = 0-5$; *pina* = *N*-(pyridin-4-yl)-isonicotinamide; $\text{M}^{\text{I}} = \text{Ag}^{\text{I}}$ and $x \sim 5$ (**1**·*x*MeOH); $\text{M}^{\text{I}} = \text{Au}^{\text{I}}$ and $x \sim 5$ (**2**·*x*MeOH)) are presented. The single-crystal X-ray diffraction analyses have revealed that the structure of **1**·*x*MeOH (or **2**·*x*MeOH) presents two equivalent doubly interpenetrated 3D frameworks stabilized by both argentophilic (or aurophilic) interactions and interligand C=O...HC H-bonds. Despite the interpenetration of the networks, these compounds display accessible void volume capable of hosting up to five molecules of methanol which interact with the host *pina* ligand and establish an infinite lattice of hydrogen bonds along the structural channels. Interestingly, the magnetic studies have shown that solvated complexes **1**·*x*MeOH and **2**·*x*MeOH display two- and four-step hysteretic thermally driven spin transitions, respectively. However, when these compounds lose the methanol molecules, the magnetic behavior changes drastically giving place to gradual spin conversions evidencing the relevant influence of the guest molecules on the spin-crossover properties. Importantly, since the solvent desorption takes place following a single-crystal-to-single-crystal transformation, empty structures **1** and **2** ($x = 0$) could be also determined allowing us to evaluate the correlation between the structural changes and the modification of the magnetic properties triggered by the loss of methanol molecules.



INTRODUCTION

The spin crossover (SCO) is a molecular phenomenon observed for first row d^4-d^7 transition metal complexes that involves the reversible conversion between the low spin (LS) and the high spin (HS) electronic states. This spin-state switching, that has been mostly studied for Fe^{II} complexes, can be induced by the application of external perturbations (temperature or pressure changes, light, or guest molecules adsorption)¹⁻⁴ and, importantly, leads to the modification of many physical parameters, i.e., the magnetic response, dielectric constant, color, or volume of the material. Indeed, this fascinating external perturbation-physical change coupling makes of this kind of complexes promising materials for their further practical applications.

The versatility offered by the coordination chemistry when designing and synthesizing new SCO materials provides the possibility of accessing to multitude of different structural topologies and dimensionalities.^{5,6} This rational way of synthesis is crucial because the control of the degree of connectivity between SCO centers is directly related to the cooperativity of the system and therefore is the key to modulate and predict the spin transition properties. In the last

2 decades, many scientific groups have focused a special attention on two-dimensional (2D) and three-dimensional (3D) systems and, especially, on complexes presenting the Hofmann-like clathrate topology $\{\text{Fe}^{\text{II}}(\text{L})_x[\text{M}^{\text{I}}(\text{CN})_4]\}$ ($x = 1$ or 2 ; $\text{M} = \text{Pt}^{\text{II}}, \text{Pd}^{\text{II}},$ or Ni^{II}), probably due to their attracting SCO properties,⁷ host–guest chemistry,^{4,8} and the possibility of obtaining them as nanoparticles⁹⁻¹¹ or thin films.^{12,13} Hence, when L is a monotopic ligand, these compounds display 2D structures formed by planes that are pillared presenting poor, if any, porosity.¹⁴ Conversely, if L is a ditopic bridging ligand, then the resulting complexes exhibit 3D topologies and use to be porous structures.

Another well-known synthetic approach deals with introducing dicyanometalates anions ($[\text{Ag}^{\text{I}}(\text{CN})_2]^-$ or $[\text{Au}^{\text{I}}(\text{CN})_2]^-$) instead of the $[\text{M}^{\text{I}}(\text{CN})_4]^{2-}$ ones giving place to compounds of the type $\{\text{Fe}^{\text{II}}(\text{L})[\text{M}^{\text{I}}(\text{CN})_2]_2\}$.⁷ In this case, the high void space volume of the 3D generated structures is occupied by interpenetrating two (or more) networks. The first examples of this kind of compounds were published in 2002 by our group,

Received: April 24, 2019

Published: July 16, 2019

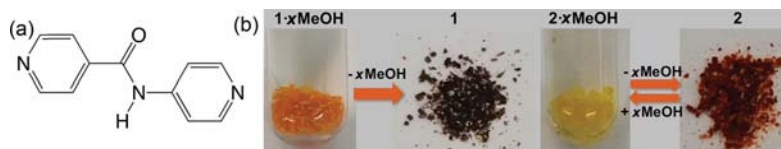


Figure 1. (a) Structure of the ligand *pina*. (b) Single crystals of compound $\{\text{Fe}^{\text{II}}(\text{pina})[\text{Ag}^{\text{I}}(\text{CN})_2]_2\} \cdot x\text{MeOH}$ (left) and $\{\text{Fe}^{\text{II}}(\text{pina})[\text{Au}^{\text{I}}(\text{CN})_2]_2\} \cdot x\text{MeOH}$ (right) in mother liquor ($1 \cdot x\text{MeOH}$ and $2 \cdot x\text{MeOH}$, $x \approx 5$) and desolvated dry product (**1** and **2**, $x = 0$).

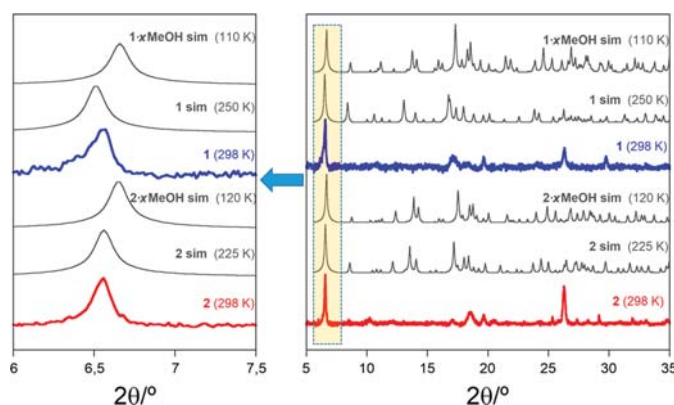


Figure 2. Ranges of $2\theta = 5\text{--}35^\circ$ (right) and $2\theta = 6\text{--}7.5^\circ$ (left) of the X-ray powder diffraction patterns for **1** (blue line) and **2** (red line), collected at room temperature. Simulated spectra of solvated ($1 \cdot x\text{MeOH}$ sim (110 K) and $2 \cdot x\text{MeOH}$ sim (120 K)) and empty (**1** sim (250 K) and **2** sim (225 K)) are also shown for comparison.

being $M^{\text{I}} = \text{Ag}^{\text{I}}$ and $L =$ pyrazine (pz), 4,4'-bipyridine (4,4'-bipy), or bis-pyridil-ethylene (bpe) which acted as ditopic bridging ligands.¹⁵ The magnetic measurements showed that the pyrazine derivative is in the LS state in the studied temperature range, whereas the 4,4'-bipy based complex is HS in all range of temperatures although an incomplete SCO can be induced by applying an external pressure of at least 4.6 kbar. Besides, the bpe derivative displays an incomplete SCO curve with a wide hysteresis (95 K) at room pressure.

This family of compounds has been enlarged in the past decade by the use of a number of bridging ligands such as bpac,^{16,17} bpmp,¹⁸ bpben,^{19,20} pz,^{21,22} 4,4'-bipy,⁸ bipytz/bipydz,^{23,24} 2,5-bpp,²⁵ 4-abpt,²⁶ Fpz,²⁷ and naphy.²⁸ Interestingly, despite their interpenetrated nature, most of these frameworks are able to host guest molecules showing an interplay between the host–guest chemistry and the SCO behavior. Moreover, in some of them,^{24,26} the adsorption of guest molecules induces the apparition of hysteretic multisteped spin transitions which are relatively rare but very interesting since they allow for the possibility to act as a multiswitching system. According to these studies, the multistep phenomenon stems from strong and directional H-bonds generated between the trapped solvents and the pillar ligand that may provoke symmetry breaking during the SCO.

Here, we report on the synthesis, crystal structures, and magnetic behavior of two new doubly interpenetrated 3D Hofmann-type clathrates formulated as $\{\text{Fe}^{\text{II}}(\text{pina})[\text{M}^{\text{I}}(\text{CN})_2]_2\} \cdot x\text{MeOH}$ [being x a value between 0 and 5; *pina* = *N*-(pyridin-4-yl)isonicotinamide (Figure 1a); $M^{\text{I}} = \text{Ag}^{\text{I}}$ and $x \approx 5$ ($1 \cdot x\text{MeOH}$) or $M^{\text{I}} = \text{Au}^{\text{I}}$ and $x \approx 5$ ($2 \cdot x\text{MeOH}$)] and its desolvated forms **1** and **2** ($x = 0$). The novelty of the *pina* bridging ligand, which was previously used to design other

SCO-active²⁹ (and -inactive)³⁰ Fe^{II} complexes, is that both carbonyl and $-\text{NH}$ moieties of the amide group are susceptible of interacting via H-bonding with the adsorbed guest molecules. Indeed, our magnetic characterizations show a strong impact of the presence of intrapore methanol guest molecules on the SCO properties and, in particular, reveal the generation of hysteretic multistep spin transitions presumably related to the presence of host–guest H-bonding interactions.

RESULTS

Synthesis. The slow diffusion of $\text{Fe}(\text{BF}_4)_2 \cdot 6\text{H}_2\text{O}$, *pina* ligand, and the corresponding $\text{K}[\text{M}^{\text{I}}(\text{CN})_2]$ salt ($M^{\text{I}} = \text{Ag}^{\text{I}}$ or Au^{I}) in methanol solutions yielded, after 2 weeks, single crystals corresponding to compounds $\{\text{Fe}^{\text{II}}(\text{pina})[\text{Ag}^{\text{I}}(\text{CN})_2]_2\} \cdot x\text{MeOH}$ ($1 \cdot x\text{MeOH}$) or $\{\text{Fe}^{\text{II}}(\text{pina})[\text{Au}^{\text{I}}(\text{CN})_2]_2\} \cdot x\text{MeOH}$ ($2 \cdot x\text{MeOH}$) with $x \approx 5$. Out of the mother liquor, the included ca. 5 molecules of methanol undergo rapid desorption provoking loss of crystallinity and apparent change of color from orange to almost black and from yellow to dark orange for samples $1 \cdot x\text{MeOH}$ and $2 \cdot x\text{MeOH}$, respectively (Figure 1b), giving rise to desolvated counterparts **1** and **2**. Figure 2 displays the X-ray powder diffraction patterns of **1** and **2** recorded at 298 K (blue and red spectra, respectively) together with the simulated ones from single-crystal X-ray diffraction data for $1 \cdot x\text{MeOH}$, $2 \cdot x\text{MeOH}$, **1**, and **2** (*vide infra*) also depicted for comparison. Although the powder samples of **1** and **2** present low crystallinity, the similarity of the spectra confirms that both compounds are essentially isostructural since the most intense peaks are clearly reproduced for both derivatives, in particular those in the intervals of $6\text{--}7^\circ$ and $15\text{--}20^\circ$. Moreover, they are also comparable to the simulated patterns of the compounds before

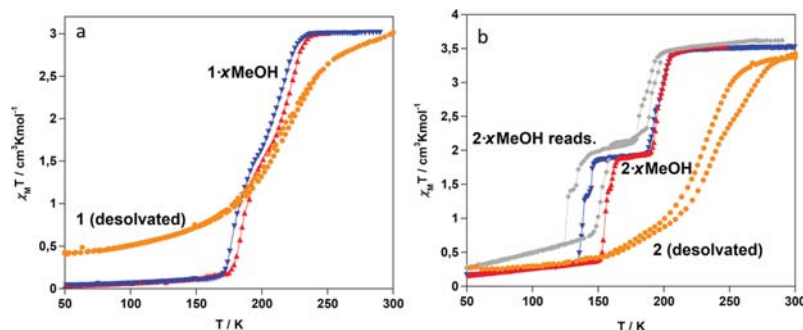


Figure 3. $\chi_M T$ versus T plots for (a) $1 \cdot x\text{MeOH}$ and **1** and (b) $2 \cdot x\text{MeOH}$, **2**, and $2 \cdot x\text{MeOH}$ reads. Red and blue triangles correspond to the cooling and heating modes for the solvated compounds, orange circles correspond the solvent free derivatives, and gray circles correspond to the readsorbed sample.

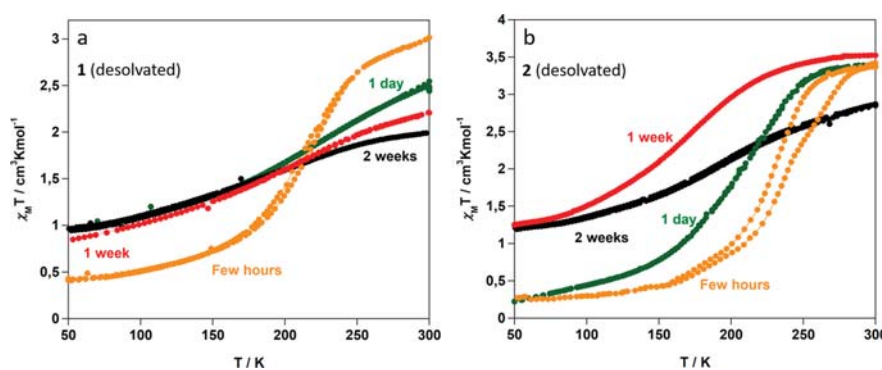


Figure 4. Aging of the desolvated compounds (a) **1** and (b) **2** monitored through time evolution of the $\chi_M T$ versus T plots.

($1 \cdot x\text{MeOH}$ sim [110 K] and $2 \cdot x\text{MeOH}$ sim [120 K]) and after (**1** sim [250 K] and **2** sim [225 K]) desorption of the methanol molecules. Indeed, in spite of the slight differences observed between the simulated patterns of the solvated and desolvated samples, it is not straightforward to assess which is more similar to the experimental spectra. Nevertheless, the slight downshift of about 0.15° observed for most of the simulated peaks in the desolvated samples (**1** sim [250 K] and **2** sim [225 K]), and especially for the peak centered around $2\theta = 6.5^\circ$ (Figure 2 left), seems to match better with the desolvated experimental ones. This shift is clearly related to an increase of the unit cell volume due to a LS \rightarrow HS transition (*vide infra*) whose structural changes facilitate the labilization and concomitant desorption of the included methanol molecules. The complete desorption of the methanol molecules in **1** and **2** was confirmed by thermogravimetric analysis of samples freshly taken (ca. 15 min) from the mother solution since no loss of mass was observed between 298 K and 500–550 K where the decomposition of the samples starts (Figure S1).

Magnetic Properties. The solvated compounds $1 \cdot x\text{MeOH}$ and $2 \cdot x\text{MeOH}$ were measured soaked with their mother liquor to prevent the desorption of the methanol molecules. Afterward, the same samples were removed from the solution to allow the desorption of MeOH to give **1** and **2**. The thermal dependence of the $\chi_M T$ product (where χ_M is the molar magnetic susceptibility and T is temperature) for $1 \cdot$

$x\text{MeOH}$ and $2 \cdot x\text{MeOH}$ and their desolvated forms (**1** and **2**), measured at 1 K min^{-1} in the cooling and heating mode, is depicted in Figure 3.

At 290 K, $1 \cdot x\text{MeOH}$ shows a $\chi_M T$ value of $3.0 \text{ cm}^3 \text{ K mol}^{-1}$, although it is consistent with an octahedral Fe^{II} ion in the HS state, this value can be considered lower than that typically observed ($3.3\text{--}3.8 \text{ cm}^3 \text{ K mol}^{-1}$). This slightly low $\chi_M T$ may be attributed to an overestimation of the considered mass which should also vary with the solvent content. This value remains practically constant down to 245 K when a relatively sharp drop of $\chi_M T$ in two steps takes place reaching a value of $0.1 \text{ cm}^3 \text{ K mol}^{-1}$ at 150 K. This behavior is consistent with a complete HS \leftrightarrow LS thermal spin transition. The $\chi_M T$ versus T curve in the heating mode does not match that of the cooling mode defining a narrow hysteresis loop $\sim 5 \text{ K}$ wide. The critical temperatures (T_c) of $1 \cdot x\text{MeOH}$ are $T_{c1}(\downarrow) = 215 \text{ K}$, $T_{c2}(\downarrow) = 179 \text{ K}$ for the cooling mode, and $T_{c1}(\uparrow) = 220 \text{ K}$, $T_{c2}(\uparrow) = 185 \text{ K}$ for the heating mode (Figure 3a).

Compound $2 \cdot x\text{MeOH}$ displays a $\chi_M T$ value of ca. $3.50 \text{ cm}^3 \text{ K mol}^{-1}$ at room temperature indicating that 100% of Fe^{II} ions are in the HS state ($S = 2$) but with slightly higher orbital contributions than $1 \cdot x\text{MeOH}$ (Figure 3b). This value remains constant until 210 K when the $\chi_M T$ product decreases abruptly, first reaching a tiny plateau at 194 K which corresponds to 25% LS/75%HS state and, later, a second wider plateau between 185 and 150 K consolidating a 50%LS/50%HS mixed spin state. Further cooling of the sample unveils two additional

Table 1. Crystallographic Parameters for the Studied Compounds at Different Temperatures

| compound | 1·xMeOH | 1 | 2·xMeOH | 2 |
|---------------------------------------|---|---|---|---|
| T (K) | 110 | 250 | 120 | 225 |
| empirical formula | C ₂₀ H ₂₉ FeAg ₂ N ₇ O ₆ | C ₁₅ H ₉ FeAg ₂ N ₇ O | C _{15.5} H _{10.5} FeAu ₂ N ₇ O _{1.5} | C ₁₅ H ₉ FeAu ₂ N ₇ O |
| M _r | 735.09 | 574.88 | 768.59 | 753.07 |
| crystal system | | | monoclinic | |
| space group | P2 ₁ /n | P2 ₁ /m | P2 ₁ /n | P2 ₁ /m |
| a (Å) | 16.4143(9) | 10.585(2) | 16.3264(4) | 10.327(2) |
| b (Å) | 10.2435(5) | 10.588(2) | 10.1192(2) | 10.3245(14) |
| c (Å) | 17.1163(8) | 13.659(2) | 17.0738(4) | 13.491(2) |
| β | 104.701(5) | 96.70(2) | 105.493(2) | 93.689(11) |
| V (Å ³) | 2783.7(2) | 1520.4(4) | 2718.27(11) | 1435.4(3) |
| Z | 4 | 2 | 4 | 2 |
| D _c (mg cm ⁻³) | 1.754 | 1.256 | 1.878 | 1.742 |
| F(000) | 1464 | 552 | 1394 | 680 |
| μ(Mo Kα) (mm ⁻¹) | 1.953 | 1.757 | 11.310 | 10.706 |

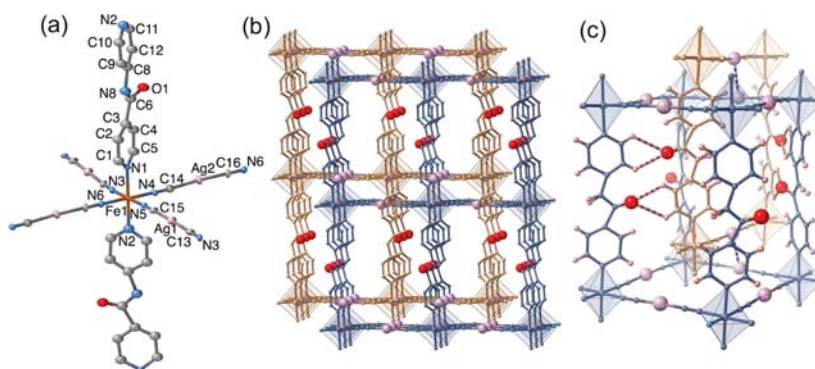


Figure 5. (a) ORTEP representation of the Fe^{II} environment displaying the numbering of the asymmetric unit for **1**·xMeOH. (b) Fragment of the two 3D interpenetrated networks denoted in beige and blue. (c) View of the C=O...HC hydrogen-bonding (red and white dashed) and metallophilic interactions (blue and white dashed).

steps giving an almost complete SCO curve. The steps are separated by a narrow plateau centered at a $\chi_M T$ value of ca. 1.40 cm³ K mol⁻¹ at 142 K which involves additional $\chi_M T$ drop of ca. 15% reaching a \approx 65LS/35HS state. In the heating mode, the steeped spin transitions for the last three steps are shifted to higher temperatures generating thermal hysteresis of 2, 16, and 17 K, for the second, third, and fourth step, respectively. The critical temperatures, extracted from the $\partial(\chi_M T)/\partial T$ versus T plot (Figure S2), are $T_{c1}(\downarrow) = 199$ K, $T_{c2}(\downarrow) = 191$ K, $T_{c3}(\downarrow) = 144$ K, $T_{c4}(\downarrow) = 137$ K for the cooling mode, and $T_{c1}(\uparrow) = 199$ K, $T_{c2}(\uparrow) = 193$ K, $T_{c3}(\uparrow) = 160$ K, $T_{c4}(\uparrow) = 154$ K for the heating mode.

As observed in Figure 3, freshly prepared **1** and **2** samples display substantial changes in the magnetic properties. At 300 K, the $\chi_M T$ values for **1** and **2**, 3.00 and 3.3 cm³ K mol⁻¹, respectively, are similar to those of the corresponding solvated forms. However, upon cooling down, an almost complete but much more gradual HS \rightarrow LS spin state conversion without marked steps takes place. The $\chi_M T$ attains values of 0.4 cm³ K mol⁻¹ (**1**, $T_{1/2\downarrow} = 204$ K) and 0.2 cm³ K mol⁻¹ (**2**, $T_{1/2\downarrow} = 225$ K) at 50 K. The $\chi_M T$ versus T plots in the heating mode do not match those observed in the cooling mode, thereby generating a hysteresis of 3 K ($T_{1/2\uparrow} = 204$ K) and 9 K ($T_{1/2\uparrow} = 234$ K) for **1** and **2**, respectively. Interestingly, evolution of these $\chi_M T$ versus T plots was observed during a period of 2 weeks. As

shown in Figure 4, the SCO behavior becomes extremely gradual and incomplete with high percentages of HS and LS centers at low and high temperatures, respectively. Comparison of the PXRD patterns of **2** freshly prepared and 2 weeks later shows that the most characteristic reflections of the structure can be identified in both patterns, namely, [0 0 1] at $2\theta = 6.5^\circ$ ($d = 13.56$ Å) associated with the first-order reflection of planes containing the {Fe₄[Au(CN)₂]₄} (vide infra) and the subsequent second- ($2\theta = 13.04^\circ$; $d = 6.78$ Å), third- ($2\theta = 19.61^\circ$; $d = 4.52$ Å), and fourth-order ($2\theta = 26.25^\circ$; $d = 3.39$ Å) planes. This indicates that the main features of the structure remain in aged sample **2** (see Figure S3).

After immersing **1** in pure methanol for 1 month, the almost black crystals (Figure 1) recover neither the orange color nor the original spin transition properties of **1**·xMeOH indicating the irreversibility of the desolvation process. In contrast, and despite being isostructural, in the same conditions, the dark orange crystals of **2** become bright yellow (Figure S4) and essentially recover the HS \leftrightarrow LS thermal spin transition likely due to the readsorption of MeOH molecules yielding **2**·xMeOH reads. Effectively, **2**·xMeOH reads shows the four-step spin transition of genuine solvated **2**·xMeOH although presenting a \sim 10 K down shift of the critical temperatures as well as an increase by 5 K of the hysteresis width ($T_{c1}(\downarrow) = 189$

K, $T_{c2}(\downarrow) = 181$ K, $T_{c3}(\downarrow) = 134$ K, and $T_{c4}(\downarrow) = 126$ K for the cooling mode, and $T_{c1}(\uparrow) = 194$ K, $T_{c2}(\uparrow) = 189$ K, $T_{c3}(\uparrow) = 156$ K, and $T_{c4}(\uparrow) = 150$ K for the heating mode (see gray line in Figure 3b).

Single Crystal X-ray Diffraction (SCXRD). Given the lability of the MeOH molecules in compounds $1 \cdot x\text{MeOH}$ and $2 \cdot x\text{MeOH}$, the crystals were picked directly from the mother liquor, immersed in oil and immediately placed on the goniometer at 110 and 120 K, respectively, and subsequently their LS crystal structures measured. Then, based on their magnetic behavior and trying to avoid any desorption of MeOH preserving the quality of the single crystals, the structures of the corresponding HS states were measured at the lowest possible temperatures, namely, 250 and 225 K, respectively. As we will see, the resulting structures corresponded to those of desolvated **1** and **2** forms. The relevant structural parameters are shown in Table 1.

Compounds $1 \cdot x\text{MeOH}$ and $2 \cdot x\text{MeOH}$ crystallize in the monoclinic $P2_1/n$ space group. Tables S1 and S2 contain a list of significant bond lengths and angles, respectively. Both solvated complexes are isostructural and will be described simultaneously. The Fe^{II} defines slightly elongated $[\text{Fe}^{\text{II}}\text{N}_6]$ octahedral sites with the axial positions occupied by the *pina* ligand and the equatorial positions by the CN moiety of two crystallographically distinct $[\text{M}^{\text{I}}(\text{CN})_2]^-$ anions (Figure 5a). The average axial $\text{Fe}-\text{N}_{\text{ax}}$ bond length, 1.996 Å ($1 \cdot x\text{MeOH}$) and 1.998 Å ($2 \cdot x\text{MeOH}$), are slightly larger than the equatorial $\text{Fe}-\text{N}_{\text{eq}}$ one, 1.929 Å ($1 \cdot x\text{MeOH}$) and 1.928 Å ($2 \cdot x\text{MeOH}$). These values are typical for the Fe^{II} ion in the LS state in agreement with the magnetic properties.

The two crystallographically distinct $[\text{M}^{\text{I}}(\text{CN})_2]^-$ groups are essentially linear and connect two adjacent Fe^{II} centers defining a stack of almost planar 2D $\{\text{Fe}^{\text{II}}[\text{M}^{\text{I}}(\text{CN})_2]_n\}$ grids. The layers are pillared by the axial *pina* ligands, thus defining a 3D framework with typical *pcu* topology. Although the two pyridine rings of the *pina* ligand are ordered, the asymmetric amide moiety that connects both rings is disordered and has been modeled in two positions with 50% occupational distribution (Figure S5). The open nature of the framework allows the interpenetration of a second equivalent network (Figure 5b) in such a way that the *pina* ligands of one framework threads the $\{\text{Fe}^{\text{II}}[\text{M}^{\text{I}}(\text{CN})_2]_n\}$ windows of the other framework. In addition to argentophyllic [$\text{Ag} \cdots \text{Ag} = 3.080$ Å, $1 \cdot x\text{MeOH}$] or aurophyllic [$\text{Au} \cdots \text{Au} = 3.131$ Å, $2 \cdot x\text{MeOH}$] short contacts, there have been observed reciprocal $\text{C}=\text{O} \cdots \text{HC}$ interactions [$\text{C}=\text{O}(1) \cdots \text{C}(11) = 3.260(14)$ Å and $\text{C}=\text{O}(1) \cdots \text{C}(12) = 3.37(2)$ Å] for $1 \cdot x\text{MeOH}$ and [$\text{C}=\text{O}(1a) \cdots \text{C}(11) = 3.33(2)$ Å and $\text{C}=\text{O}(1b) \cdots \text{C}(12) = 3.28(2)$ Å] for $2 \cdot x\text{MeOH}$ established between the $\text{C}=\text{O}$ moiety and the pyridinic hydrogen atoms of adjacent *pina* ligands belonging to different frameworks (see Figure 5c).

The free space of the structure is filled with solvent molecules but the results denote the mentioned marked lability of the MeOH molecules even at low temperatures (Figures 6 and S6). Regarding compound $1 \cdot x\text{MeOH}$, five methanol molecules per Fe^{II} are located in defined positions with occupancies ranging from 0.5 to 1 (although for practical reasons the structure has been modeled with an occupancy equal to 1 for all methanol molecules), whereas for $2 \cdot x\text{MeOH}$, due to their even larger lability, only one discrete methanol molecule with an occupancy of 0.5 could be observed. This latter methanol molecule interacts with the $-\text{NH}$ moiety of the *pina* ligand via H-bonding (2.84(4) Å). However, in the case

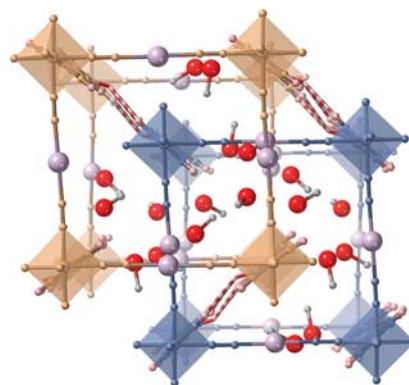


Figure 6. Top view of the two interpenetrated networks displaying the MeOH guest molecules. The red and white dashed lines represent the $\text{C}=\text{O} \cdots \text{HC}$ connections between the interpenetrated frameworks.

of complex $1 \cdot x\text{MeOH}$, an infinite virtual intricate H-bonding lattice is generated throughout the channels of the structure: three of the five guest methanol molecules interact directly with the amide group of the *pina* ligand [two of them are connected to the $-\text{NH}$ moiety ($\text{N}(7) \cdots \text{O}(2) = 2.92(3)$ Å and $\text{N}(7) \cdots \text{O}(3) = 3.22(3)$ Å) and the other is connected with the carbonyl group ($\text{O}(4) \cdots \text{O}(1) = \text{C} = 3.14(2)$ Å)]. Besides, all methanol molecules are interconnected in such a way that they establish intra- and internetwork communications between *pina* ligands through H-bond interactions (Figure S6). The distances of the strongest H-bonds found are summarized in Table 2, and the most relevant interatomic distances and angles are shown in Tables S1 and S2.

In order to characterize the HS state taking into account the lability of the MeOH molecules, we measured the crystals at temperatures as low as possible according to their magnetic curves (Figure 3), namely, at 250 K for $1 \cdot x\text{MeOH}$ and 225 K

Table 2. Selected H-Bond Lengths (Å) Found in Compounds $1 \cdot x\text{MeOH}$, $2 \cdot x\text{MeOH}$, **1**, and **2**

| | $1 \cdot x\text{MeOH}$ (110 K) | $2 \cdot x\text{MeOH}$ (120 K) | 1 (250 K) | 2 (225 K) |
|----------------------|-----------------------------------|-----------------------------------|---------------------|---------------------|
| H-bond | | | | |
| O1–O4 | 3.14(2) | | | |
| O2–O3 ^a | 3.35(2) | | | |
| O2–O6 ^a | 2.73(3) | | | |
| O3–O4 | 3.73(3) | | | |
| O3–O5 ^b | 2.82(3) | | | |
| O4–O5 | 3.50(3) | | | |
| O5–O6 | 2.69(3) | | | |
| O2–N7 | 2.92(3) | 2.84(4) | | |
| O3–N7 ^b | 3.22(3) | | | |
| O1–C11 ^c | 3.260(14) | | | |
| O1–C12 ^c | 3.37(2) | | | |
| O1a–C11 ^d | | 3.33(2) | | |
| O1b–C12 ^d | | 3.28(2) | | |
| O1–C4 ^e | | | 3.51(6) | |
| O1–C5 ^e | | | 3.60(6) | |
| O1–C4 ^f | | | | 3.47(5) |
| O1–C5 ^f | | | | 3.48(5) |

^a $-x + 3/2, y - 1/2, -z + 3/2$. ^b $-x + 3/2, y + 1/2$. ^c $-x + 1, -y + 2, -z + 1$. ^d $-x + 2, -y, -z$. ^e $-x + 2, -y + 1, -z$. ^f $-x + 1, -y + 1, -z$.

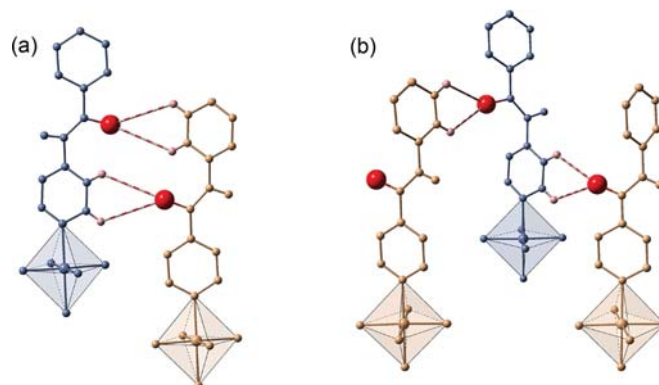


Figure 7. Two operative hydrogen bonding C=O...HC interactions established between consecutive *pina* ligands of different interpenetrated frameworks in **1** and **2**: (a) Reciprocal interactions generated between *pina* ligands with parallel pyridine groups; (b) nonreciprocal interactions arisen from the two orthogonal possible orientations of the pyridine rings.

for **2**·*x*MeOH. Upon increasing the temperature both compounds display a crystallographic transformation from the $P2_1/n$ (monoclinic) to the $P2_1/m$ (monoclinic) space group. As we will see below, this change of symmetry seems to be most likely driven by a complete loss of solvent molecules.

Although the crystal structure is essentially very similar to that described above for the LS state, it presents several important differences: (i) The Fe–N average distance increases by 0.198 Å for **1** and 0.111 Å for **2**, indicating that whereas the former presents a practically complete LS → HS spin transition, only 50–60% of the Fe^{II} ions switch to the HS state for the latter. (ii) Unlike the LS structures, the pyridine rings and the amide moiety of the *pina* ligand are disordered in two different orientations with respect to the *b* axis (Figure S7). (iii) Although the C=O...HC contacts are kept in the framework, they are significantly weaker (C=O(1)...C(4) = 3.51(6) Å and C=O(1)...C(5) = 3.60(6) Å for **1**; C=O(1)...C(4) = 3.47(5) Å and C=O(1)...C(5) = 3.48(5) Å for **2**). (iv) Due to the positional disorder of the *pina* ligand, the C=O...HC interactions are not only reciprocally established between adjacent *pina* pairs as previously shown for **1**·*x*MeOH and **2**·*x*MeOH in Figure 5c and schematized in Figure 7a but also between a given *pina* ligand and two different neighboring *pina* ligands (red dashed lines in Figure 7b). (v) The argentophyllic and aurophyllic interactions are weakened (3.110 and 3.155 Å). (vi) The lack of meaningful residual electronic density within the cavities of the structure suggests that no solvent molecules, $x \approx 0$, remain within the structural cavities.

DISCUSSION

The reaction between Fe^{II}, [Ag^I(CN)₂][−] or [Au^I(CN)₂][−], and the ditopic *pina* ligand has originated two new porous 3D Hofmann clathrates with general formula {Fe^{II}(*pina*)-[M^I(CN)₂]₂·*x*MeOH (M^I = Ag^I or Au^I). On the basis of the magnetic and structural data, the samples soaked in the mother liquor are consistent with a value of $x \approx 5$ (**1**·*x*MeOH and **2**·*x*MeOH). The $\chi_M T$ versus *T* plots reveal that both solvated complexes undergo cooperative spin transitions featuring two and four steps for **1**·*x*MeOH and **2**·*x*MeOH derivatives, respectively. However, the labile MeOH molecules spontaneously desorb affording **1** and **2** when they are out of

the mother liquor. This fact provokes subtle structural modifications accompanied by dramatic changes in the magnetic properties. Interestingly, the methanol desorption process occurs following a single-crystal-to-single-crystal transformation allowing us to determine the structures for both the solvated and desolvated counterparts and giving the possibility to relate them with their corresponding SCO properties. The higher cooperativity observed for the stepped SCO in the methanol containing derivatives is likely associated to the efficient transmission of the structural changes occurred during the SCO in the Fe^{II} environments. This cooperativity may be promoted by both the intricate H-bonding lattice generated by the MeOH molecules along the structural channels and by the reciprocal interframework C=O...HC interactions established between *pina* ligands. Contrarily, when the methanol molecules are desorbed the communication between the Fe^{II} ions is disrupted thereby affording gradual SCO curves. This decrease in cooperativity demonstrates the efficiency of the host–guest and host–host H-bonding interactions in these systems. Related results were recently reported on analogue compounds. For example, complex {Fe^{II}(bipydz)-[Au^I(CN)₂]₂·4EtOH (bipydz = 3,6-bis(4-pyridyl)-1,2-diazine), which presents a four-step hysteretic SCO similar to that of **2**·*x*MeOH, switches to a gradual one-step spin transition behavior when it desorbs the ethanol guest molecules.²⁴ In the same line, whereas compound [Fe^{II}(4-abpt)[Ag^I(CN)₂]₂·2DMF·EtOH (4-abpt = 4-amino-3,5-bis(4-pyridyl)-1,2,4-triazole) displays also a SCO in four steps, its solvent-free counterpart loses completely this property showing a constant $\chi_M T$ corresponding to a 50% HS/LS Fe^{II} ions mixture.²⁶ In addition, compound {Fe^{II}(dpni)-[Ag^I(CN)₂]₂·4CH₃CN (dpni = *N,N'*-di-(4-pyridyl)-1,4,5,8-naphthalene tetracarboxydiimide) shows an evident decrease of cooperativity and change of SCO nature (from a complete two steps to an incomplete single step spin transition) when reversibly desorbs acetonitrile molecules.³¹ All these examples highlight the close relationship between the host–guest interactions (and particularly, the H-bonding contacts) and the occurrence of a multistep SCO behavior.

The high lability of the methanol molecules observed for as-synthesized **1**·*x*MeOH and **2**·*x*MeOH compounds, even at temperatures as low as 250 K, did not allow us to characterize

the intermediate structures associated to the plateaus observed in the magnetic curves of the solvated complexes. However, despite the nominal differences in MeOH content between the single crystals used for the crystal analysis and the methanol soaked microcrystalline samples used in magnetism, the average Fe–N bond length inferred from the crystal structures at 110/120 K correlates reasonably well with the fully populated LS state expected from the magnetic curves. When heating up the crystals to 250/225 K, the absence of meaningful electronic density within the pores in both structures confirms the desorption of the MeOH molecules yielding the desolvated frameworks **1** and **2**. The variations of the average Fe–N bond length (ΔR) observed for **1** and **2** with respect to the LS structures are $\Delta R = 0.198$ and 0.111 Å, respectively. On the basis of the fact that the typical ΔR value for a complete LS \leftrightarrow HS transformation is ca. 0.2 Å, these values are consistent with ca. 99% and 55% transformation from the LS to the HS state and correlate reasonably well with the values of $\chi_M T$ at the same temperature, which correspond to ca. 86 and 53% for **1** and **2**, respectively. The slight discrepancies can be ascribed to the time dependence of the magneto-structural properties observed for both compounds (although more marked for **2**) activated upon the loss of the solvent molecules. Consequently, the HS fraction at 225/250 K markedly depends on the elapsed time (especially within the first hours after the desorption) and provokes misfits between the magnetic and the crystallographic results due to aging. Unfortunately, the rapid deterioration of the desolvated crystals quality prevented us from analyzing the aged structures. A similar time-dependent process of the SCO behavior was previously reported for the double interpenetrated coordination polymer $\{\text{Fe}^{\text{II}}(\text{TPT})_{2/3}[\text{Ag}^{\text{I}}(\text{CN})_2]_2\} \cdot n\text{Solv}$ (TPT = [(2,4,6-tris(4-pyridyl)-1,3,5-triazine)] with NbO structure type.³² In the latter case, aging was associated with subtle structural reorganization/relaxation of the structure denoted by a noticeable decrease, 25%, of the unit cell volume, which was tentatively related to the flexible nature of the $[\text{Ag}(\text{CN})_2]^-$ moiety, together with mutual displacement and/or compression of the interpenetrated frameworks. The compression mechanism was demonstrated for the double interpenetrated 3D coordination polymer $\{(\text{ZnI}_2)_3(\text{TPT})_2\} \cdot 6\text{C}_6\text{H}_5\text{NO}_2$ where desorption/sorption of the nitrobenzene molecules involves reversible distortion of the interpenetrated frameworks.³³ A similar hypothesis can be drawn for both desolvated derivatives **1** and **2**. However, it is clear that the aging process does not occur exactly in the same way in both compounds since **2** readsorbs reversibly the methanol molecules with subsequent recovering of the magnetic properties. The small difference in SCO critical temperature, $T_{1/2}$, of about 10 K between the as-synthesized ($2 \cdot x\text{MeOH}$) and readsorbed ($2 \cdot x\text{MeOH}$ reads) samples may arise from small differences in methanol content. Taking into account the isostructural character of both compounds, it is in principle surprising that, in the same conditions, **1** cannot recover the original SCO properties indicating that no methanol is readsorbed. A pure speculative explanation could be based on the higher flexibility of the $[\text{Ag}(\text{CN})_2]^-$ moiety, namely, its easy tendency to depart from linearity. This flexibility can conduct to structural differences characterized by much slower recovering kinetics, which cannot be expected for **2** due to the much more rigid nature of the $[\text{Au}(\text{CN})_2]^-$ moiety.

CONCLUSION

Herein, we have shown that functionalization of a 3D double interpenetrated porous Hofmann-type coordination polymer with a pillar ligand such *pina*, bearing an amide group, favors the interplay between host–guest and host–host interactions which have dramatic consequences on the SCO properties of the material. Similar host–guest effects were already observed for a series of iron(II) 1D coordination polymers with the general formula $[\text{Fe}^{\text{II}}\text{L1}(\textit{pina})] \cdot x\text{solvent}$ with L1 being a tetradentate $\text{N}_2\text{O}_2^{2-}$ coordinating Schiff-base-like ligand.²⁹ The spin crossover properties of these compounds turned out to be highly dependent on the solvent content which in turn was intimately interacting with the *pina* ligand via H-bonding. Similarly, the not-SCO-active 2D compound $[\text{Fe}^{\text{II}}(\text{NCS})_2(\textit{pina})_2] \cdot 2(\text{CH}_3\text{CN})$ not only presents H-bonds between the amide moieties and the acetonitrile molecules but also between the *pina* ligands through $\text{C}=\text{O} \cdots \text{HN}$ contacts.³⁰ Here, we have implemented, for the first time, the bridging *pina* ligand to build a 3D structure that exhibits accessible void volume, ca. 40%, where methanol molecules can be trapped affording an infinite lattice of H-bonds. Besides, we have proved the readsorption of the MeOH molecules, thus recovering the original SCO properties of the Au derivative. This result opens the door to investigate the adsorption of other protic and aprotic guest molecules in order to modulate the steeped SCO characteristics. Furthermore, the double interpenetrated structure is also stabilized by strong interligand $\text{C}=\text{O} \cdots \text{HC}$ interactions which are very common in biologic systems³⁴ but as far as we know are uncommon for 3D SCO porous compounds.

EXPERIMENTAL SECTION

Materials. All precursor reagents were obtained from commercial sources.

Synthesis of Ligand *N*-(Pyridin-4-yl)isonicotinamide (*pina*). First, 2 g of isonicotinic acid (16.24 mmol) and 160 mL of THF were gently stirred obtaining a white suspension. Hereafter, 1.64 g of trimethylamine (16.24 mmol, 2.26 mL) was added in one portion, and the resulting mixture was stirred over 10 min. After cooling down to 0 °C using an ice-bath, 1.95 g of ethyl chloroformate (18 mmol, 1.71 mL) was added dropwise, keeping the mixture under vigorously stirring for 30 min. Then, to the ice-cooled white suspension was gradually added 1.27 g of 4-aminopyridine (13.52 mmol) previously dissolved in 40 mL of THF, and the mixture was stirred at 0 °C for 1 h. Finally, the solution was allowed to warm up to room temperature under continuously stirring overnight, registering an apparently change of color from white to yellowish. THF solvent was removed under reduce pressure, collecting a white-yellowish powder, which was washed with K_2CO_3 aqueous solution (10% w/w) [3×10 mL], cold water [2×10 mL] and Et_2O [2×20 mL]. The resulting white powder was dried completely in a desiccator for 5 days (yield = 75%). ¹H NMR (DMSO-*d*₆) = 7.74 (2H, dd), 7.88 (2H, dd), 8.47 (2H, dd), 8.78 (2H, dd).

Synthesis of Complexes $1 \cdot x\text{MeOH}$ and $2 \cdot x\text{MeOH}$. A slow diffusion method using a modified H-shape container with 3 tubes was used for growing single-crystals of the double interpenetrated networks $\{\text{Fe}^{\text{II}}(\textit{pina})[\text{Ag}^{\text{I}}(\text{CN})_2]_2\} \cdot x\text{MeOH}$ ($1 \cdot x\text{MeOH}$) and $\{\text{Fe}^{\text{II}}(\textit{pina})[\text{Au}^{\text{I}}(\text{CN})_2]_2\} \cdot x\text{MeOH}$ ($2 \cdot x\text{MeOH}$). The peripheral tubes were filled with 0.1 mmol (33.7 mg) of $\text{Fe}(\text{BF}_4)_2 \cdot 6\text{H}_2\text{O}$ and 0.2 mmol of $\text{K}[\text{M}^{\text{I}}(\text{CN})_2]$ (39.8 mg [$\text{M}^{\text{I}} = \text{Ag}^{\text{I}}$], 58.0 mg [$\text{M}^{\text{I}} = \text{Au}^{\text{I}}$]), respectively, and finally the center arm was filled with 0.1 mmol (20 mg) of the *pina* ligand. Afterward, each individual tube was carefully filled with MeOH and sealed with parafilm. After 2 weeks, orange ($1 \cdot x\text{MeOH}$) and yellow ($2 \cdot x\text{MeOH}$) platelet crystals suitable for single-crystal X-ray analysis appeared within the H tube. Elemental Analysis: calculated for **1** [$\text{C}_{15}\text{H}_9\text{Ag}_2\text{FeN}_7\text{O}$ (574.9) (%): C 31.34; H 1.58; N

17.06. Found (%): C 31.18; H 1.65; N 16.58. Calculated for 2 [C₁₅H₉Au₂FeN₇O (753.1) (%): C 23.92; H 1.20; N 13.02. Found (%): C 24.12; H 1.22; N 12.93.

Physical Measurements. Variable-temperature magnetic susceptibility data were recorded with a Quantum Design MPMS2 SQUID magnetometer equipped with a 7 T magnet, operating at 1 T and at temperatures of 1.8–400 K. Experimental susceptibilities were corrected for diamagnetism of the constituent atoms by the use of Pascal's constants. Powder X-ray measurements were performed on a PANalytical Empyrean X-ray powder diffractometer (monochromatic Cu K α radiation). Thermogravimetric analysis was performed on a Mettler Toledo TGA/SDTA 851e, in the 290–900 K temperature range under nitrogen atmosphere with a rate of 10 K min⁻¹.

Single-Crystal X-ray Diffraction. Single-crystal X-ray data were collected on an Oxford Diffraction Supernova diffractometer using graphite monochromated Mo K α radiation ($\lambda = 0.71073$ Å). A multiscan absorption correction was performed. The structures were solved by direct methods using SHELXS-2014 and refined by full-matrix least-squares on F^2 using SHELXL-2014.³⁵ Non-hydrogen atoms were refined anisotropically and hydrogen atoms were placed in calculated positions refined using idealized geometries (riding model) and assigned fixed isotropic displacement parameters. CCDC 1910594 (1·xMeOH), 1910592 (2·xMeOH), 1910593 (1), and 1910591 (2) contain the supplementary crystallographic data for this article. These data can be obtained free of charge from The Cambridge Crystallographic Data Centre via www.ccdc.cam.ac.uk/data_request/cif.

■ ASSOCIATED CONTENT

Supporting Information

The Supporting Information is available free of charge on the ACS Publications website at DOI: [10.1021/acs.inorgchem.9b01189](https://doi.org/10.1021/acs.inorgchem.9b01189).

Selected bond lengths and angles of the studied structures, thermogravimetric analysis of compounds 1 and 2, first derivative curves ($\partial(\chi_M T)/\partial T$ versus T) of 1·xMeOH and 2·xMeOH, time-evolution of PXRD patterns for compound 2, photographs of compounds 1 and 2 after resorption of MeOH, disorder of *pina* ligand in compounds 1·xMeOH and 2·xMeOH, perspective view showing the H-bonds found in 1·xMeOH, view of the disorder of *pina* ligand in compounds 1 and 2 (PDF)

Accession Codes

CCDC 1910591–1910594 contain the supplementary crystallographic data for this paper. These data can be obtained free of charge via www.ccdc.cam.ac.uk/data_request/cif, or by emailing data_request@ccdc.cam.ac.uk, or by contacting The Cambridge Crystallographic Data Centre, 12 Union Road, Cambridge CB2 1EZ, UK; fax: +44 1223 336033.

■ AUTHOR INFORMATION

Corresponding Authors

*E-mail: jose.a.real@uv.es (J.A.R.).

*E-mail: carlos.bartual@uv.es (C.B.-M.).

ORCID

Carlos Bartual-Murgui: 0000-0003-1547-8018

José Antonio Real: 0000-0002-2302-561X

Notes

The authors declare no competing financial interest.

■ ACKNOWLEDGMENTS

We thank the Spanish Ministerio de Economía y Competitividad (MINECO), FEDER funds (CTQ2016-78341-P and Unidad de Excelencia María de Maeztu MDM-2015-0538), and Generalitat Valenciana (PROMETEO/2016/147). F.J.V.-M. thanks MINECO for a predoctoral FPI grant.

■ REFERENCES

- Gütlich, P.; Hauser, A.; Spiering, H. Thermal and Optical Switching of Iron(II) Complexes. *Angew. Chem., Int. Ed. Engl.* **1994**, *33*, 2024–2054.
- Ni, Z. P.; Liu, J. L.; Hoque, M. N.; Liu, W.; Li, J. Y.; Chen, Y. C.; Tong, M. L. Recent Advances in Guest Effects on Spin-Crossover Behavior in Hofmann-Type Metal–Organic Frameworks. *Coord. Chem. Rev.* **2017**, *335*, 28–43.
- Real, J. A.; Gaspar, A. B.; Muñoz, M. C. Thermal, Pressure and Light Switchable Spin-Crossover Materials. *Dalton Trans.* **2005**, 2062–2079.
- Ohtani, R.; Hayami, S. Guest-Dependent Spin-Transition Behavior of Porous Coordination Polymers. *Chem. - Eur. J.* **2017**, *23*, 2236–2248.
- Real, J. A.; Gaspar, A. B.; Niel, V.; Muñoz, M. C. Communication between Iron(II) Building Blocks in Cooperative Spin Transition Phenomena. *Coord. Chem. Rev.* **2003**, *236*, 121–141.
- García, Y.; Niel, V.; Muñoz, M. C.; Real, J. A. Spin Crossover in 1D, 2D and 3D Polymeric Fe(II) Networks. *Top. Curr. Chem.* **2004**, *233*, 229–257.
- Muñoz, M. C.; Real, J. A. Thermo-, Piezo-, Photo- and Chemo-Switchable Spin Crossover Iron(II)-Metalocyanate Based Coordination Polymers. *Coord. Chem. Rev.* **2011**, *255*, 2068–2093.
- Yoshida, K.; Akahoshi, D.; Kawasaki, T.; Saito, T.; Kitazawa, T. Guest-Dependent Spin Crossover in a Hofmann-Type Coordination Polymer Fe(4,4'-Bipyridyl)[Au(CN)₂]_nGuest. *Polyhedron* **2013**, *66*, 252–256.
- Martínez, V.; Boldog, I.; Gaspar, A. B.; Ksenofontov, V.; Bhattacharjee, A.; Gütlich, P.; Real, J. A. Spin Crossover Phenomenon in Nanocrystals and Nanoparticles of [Fe(3-Fpy)₂M(CN)₄] (M^{II} = Ni, Pd, Pt) Two-Dimensional Coordination Polymers. *Chem. Mater.* **2010**, *22*, 4271–4281.
- Boldog, I.; Gaspar, A. B.; Martínez, V.; Pardo-Ibañez, P.; Ksenofontov, V.; Bhattacharjee, A.; Gütlich, P.; Real, J. A. Spin-Crossover Nanocrystals with Magnetic, Optical, and Structural Bistability Near Room Temperature. *Angew. Chem., Int. Ed.* **2008**, *47*, 6433–6437.
- Volatron, F.; Catala, L.; Rivière, E.; Gloter, A.; Stéphan, O.; Mallah, T. Spin-Crossover Coordination Nanoparticles. *Inorg. Chem.* **2008**, *47*, 6584–6586.
- Haraguchi, T.; Otsubo, K.; Kitagawa, H. Emergence of Surface- and Interface-Induced Structures and Properties in Metal–Organic Framework Thin Films. *Eur. J. Inorg. Chem.* **2018**, 1697–1706.
- Otsubo, K.; Haraguchi, T.; Kitagawa, H. Nanoscale Crystalline Architectures of Hofmann-Type Metal–Organic Frameworks. *Coord. Chem. Rev.* **2017**, *346*, 123–138.
- Ueno, S.; Kawasaki, T.; Okabayashi, J.; Kitazawa, T. 2D Spin-Crossover Coordination Polymer Fe(Hexyl-Nicotinate)₂[Au(CN)₂]₂. *Bull. Chem. Soc. Jpn.* **2016**, *89*, 581–583.
- Niel, V.; Muñoz, M. C.; Gaspar, A. B.; Galet, A.; Levchenko, G.; Real, J. A. Thermal-, Pressure-, and Light-Induced Spin Transition in Novel Cyanide-Bridged Fe^{II}-Ag^I Bimetallic Compounds with Three-Dimensional Interpenetrating Double Structures [Fe^{II}L_x[Ag(CN)₂]₂]. *G. Chem. - Eur. J.* **2002**, *8*, 2446–2453.
- Shepherd, H. J.; Bartual-Murgui, C.; Molnár, G.; Real, J. A.; Muñoz, M. C.; Salmon, L.; Bousseksou, A. Thermal and Pressure-Induced Spin Crossover in a Novel Three-Dimensional Hoffman-like Clathrate Complex. *New J. Chem.* **2011**, *35*, 1205–1210.
- Mullaney, B. R.; Goux-Capes, L.; Price, D. J.; Chastanet, G.; Létard, J. F.; Kepert, C. J. Spin Crossover-Induced Colossal Positive

and Negative Thermal Expansion in a Nanoporous Coordination Framework Material. *Nat. Commun.* **2017**, *8*, 1053.

(18) Li, J.-Y.; Ni, Z.-P.; Yan, Z.; Zhang, Z.-M.; Chen, Y.-C.; Liu, W.; Tong, M.-L. Cyanide-Bridged Bimetallic 3D Hoffman-Like Coordination Polymers with Tunable Magnetic Behaviour. *CrystEngComm* **2014**, *16*, 6444–6449.

(19) Li, J.-Y.; Yan, Z.; Ni, Z.-P.; Zhang, Z.-M.; Chen, Y.-C.; Liu, W.; Tong, M.-L. Guest-Effectuated Spin-Crossover in a Novel Three-Dimensional Self-Penetrating Coordination Polymer with Permanent Porosity. *Inorg. Chem.* **2014**, *53*, 4039–4046.

(20) Li, J.-Y.; He, C.-T.; Chen, Y.-C.; Zhang, Z.-M.; Liu, W.; Ni, Z.-P.; Tong, M.-L. Tunable Cooperativity in a Spin-Crossover Hoffman-like Metal–Organic Framework Material by Aromatic Guests. *J. Mater. Chem. C* **2015**, *3*, 7830–7835.

(21) Gural'skiy, I. A.; Golub, B. O.; Shylin, S. I.; Ksenofontov, V.; Shepherd, H. J.; Raithby, P. R.; Tremel, W.; Fritsky, I. O. Cooperative High-Temperature Spin Crossover Accompanied by a Highly Anisotropic Structural Distortion. *Eur. J. Inorg. Chem.* **2016**, *2016*, 3191–3195.

(22) Gural'skiy, I. A.; Shylin, S. I.; Golub, B. O.; Ksenofontov, V.; Fritsky, I. O.; Tremel, W. High Temperature Spin Crossover in [Fe(pyrazine){Ag(CN)₂}]₂ and Its Solvate. *New J. Chem.* **2016**, *40*, 9012–9016.

(23) Clements, J. E.; Price, J. R.; Neville, S. M.; Kepert, C. J. Perturbation of Spin Crossover Behavior by Covalent Post-Synthetic Modification of a Porous Metal-Organic Framework. *Angew. Chem., Int. Ed.* **2014**, *53*, 10164–10168.

(24) Clements, J. E.; Price, J. R.; Neville, S. M.; Kepert, C. J. Hysteretic Four-Step Spin Crossover within a Three-Dimensional Porous Hofmann-like Material. *Angew. Chem.* **2016**, *128*, 15329–15333.

(25) Li, J. Y.; Chen, Y. C.; Zhang, Z. M.; Liu, W.; Ni, Z. P.; Tong, M. L. Tuning the Spin-Crossover Behaviour of a Hydrogen-Accepting Porous Coordination Polymer by Hydrogen-Donating Guests. *Chem. - Eur. J.* **2015**, *21*, 1645–1651.

(26) Liu, W.; Peng, Y.-Y.; Wu, S.-G.; Chen, Y.-C.; Hoque, M. N.; Ni, Z.-P.; Chen, X.-M.; Tong, M.-L. Guest-Switchable Multi-Step Spin Transitions in an Amine-Functionalized Metal-Organic Framework. *Angew. Chem., Int. Ed.* **2017**, *56*, 14982–14986.

(27) Valverde-Muñoz, F. J.; Seredyuk, M.; Muñoz, M. C.; Znovjyak, K.; Fritsky, I. O.; Real, J. A. Strong Cooperative Spin Crossover in 2D and 3D Fe^{II}-M^{III} Hofmann-Like Coordination Polymers Based on 2-Fluoropyrazine. *Inorg. Chem.* **2016**, *55*, 10654–10665.

(28) Piñero-López, L.; Valverde-Muñoz, F. J.; Seredyuk, M.; Bartual-Murgui, C.; Muñoz, M. C.; Real, J. A. Cyanido-Bridged Fe^{II}-M^I Dimetallic Hofmann-Like Spin-Crossover Coordination Polymers Based on 2,6-Naphthyridine. *Eur. J. Inorg. Chem.* **2018**, *2018*, 289–296.

(29) Lochenie, C.; Bauer, W.; Railliet, A. P.; Schlamp, S.; Garcia, Y.; Weber, B. Large Thermal Hysteresis for Iron(II) Spin Crossover Complexes with N-(Pyrid-4-yl)isonicotinamide. *Inorg. Chem.* **2014**, *53*, 11563–11572.

(30) Roxburgh, M. A. D.; Zaiter, S.; Hudson, X. I. B.; Mullaney, B. R.; Clements, J. E.; Moubarak, B.; Murray, K. S.; Neville, S. M.; Kepert, C. J. Structure and Magnetic Studies on a Series of Two-Dimensional Iron(II) Framework Materials with Varying Ligand Characteristics. *Aust. J. Chem.* **2017**, *70*, 623–631.

(31) Meng, Y.; Dong, Y. J.; Yan, Z.; Chen, Y. C.; Song, X. W.; Li, Q. W.; Zhang, C. L.; Ni, Z. P.; Tong, M. L. A New Porous Three-Dimensional Iron(II) Coordination Polymer with Solvent-Induced Reversible Spin-Crossover Behavior. *Cryst. Growth Des.* **2018**, *18*, 5214–5219.

(32) Arcís-Castillo, Z.; Muñoz, M. C.; Molnár, G.; Bousseksou, A.; Real, J. A. [Fe(TPT)_{2/3}{MI(CN)₂}]_nSolv (M^I = Ag, Au): New Bimetallic Porous Coordination Polymers with Spin-Crossover Properties. *Chem. - Eur. J.* **2013**, *19* (21), 6851–6861.

(33) Biradha, K.; Fujita, M. A Springlike 3D-Coordination Network That Shrinks or Swells in a Crystal-to-Crystal Manner upon Guest

Removal or Readsorption. *Angew. Chem., Int. Ed.* **2002**, *41*, 3392–3395.

(34) Wahl, M. C.; Sundaralingam, M. CH...O Hydrogen Bonding in Biology. *Trends Biochem. Sci.* **1997**, *22*, 97–102.

(35) Sheldrick, G. M. Crystal Structure Refinement with SHELXL. *Acta Crystallogr., Sect. C: Struct. Chem.* **2015**, *71*, 3–8.

Very Long-Lived Photogenerated High-Spin Phase of a Multistable Spin-Crossover Molecular Material

Teresa Delgado,[†] Antoine Tissot,[‡] Laure Guénée,[§] Andreas Hauser,[†] Francisco Javier Valverde-Muñoz,^{||} Maksym Seredyuk,^{||,⊥} José Antonio Real,^{*,||,Ⓛ} Sébastien Pillet,[∇] El-Eulmi Bendeif,[∇] and Céline Besnard^{*,§,Ⓛ}

[†]Département de Chimie Physique, Université de Genève, 1211 Genève, Switzerland

[‡]Institut des Matériaux Poreux de Paris, FRE 2000 CNRS, Ecole Normale Supérieure, Ecole Supérieure de Physique et de Chimie Industrielle de Paris, PSL Research University, 75005 Paris, France

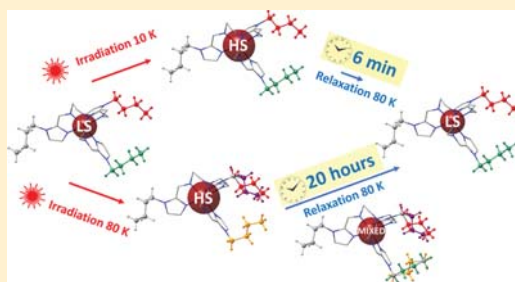
[§]Laboratoire de Cristallographie, Université de Genève, 1211 Genève, Switzerland

^{||}Departament de Química Inorgànica, Institut de Ciència Molecular (ICMol), Universitat de València, 46010 Valencia, Spain

[∇]Université de Lorraine, CNRS, CRM2 Nancy, France

Supporting Information

ABSTRACT: The spin-crossover compound $[\text{Fe}(n\text{-Bu-im})_3(\text{tren})](\text{PF}_6)_2$ shows an unusual long relaxation time of 20 h after light-induced excited spin state trapping when irradiating at 80 K. This is more than 40 times longer than when irradiating at 10 K. Optical absorption spectroscopy, magnetometry, and X-ray diffraction using synchrotron radiation were used to characterize and explain the different relaxation behaviors of this compound after irradiation below and above 70 K. Rearrangement of the butyl chains of the ligands occurring during the relaxation after irradiation above 70 K is thought to be responsible for the unusually long relaxation time at this temperature.



INTRODUCTION

Responsive switchable materials have always attracted widespread attention because they afford excellent study examples for the understanding of mechanisms involved in phase transitions and provide opportunities for future and emerging technologies.^{1–3}

Some of the most investigated switchable molecular materials are pseudo-octahedral iron(II) spin-crossover (SCO) complexes. They reversibly switch between the high-spin (HS, $t_{2g}^4e_g^2$) and low-spin (LS, $t_{2g}^6e_g^0$) electronic states by the action of external stimuli (temperature, pressure, light, and analytes). Given the antibonding nature of the e_g orbitals, the HS \leftrightarrow LS conversion is accompanied by changes in Fe–ligand bond lengths and angles, which confer bistability (memory) to the magnetic, optical, dielectric, structural, and mechanical properties, when elastic interactions between the SCO centers favor strong cooperativity in the crystal.^{4–6} This appealing feature can be combined with other relevant properties such as luminescence, electronic transport, chirality, or host–guest chemistry in a synergetic fashion, thereby transferring their intrinsic bistable nature to the second property, thus resulting in multifunctional materials that can be processed at different levels, from bulk to single molecules.^{7,8}

These important attributes have created solid expectancies for the generation of sensors, actuators, and spintronic devices

based on the on–off switching properties of the SCO materials.^{9–14} In this context, light is a desirable channel for triggering the HS \leftrightarrow LS switch since it may improve flexibility and storage density in such devices.^{1–3} In fact, it is possible to achieve a quantitative LS \rightarrow HS conversion in Fe^{II} SCO complexes by irradiating the sample in the UV–vis or near-IR regions at low temperature, typically at 10 K. This phenomenon is known as light-induced excited spin state trapping (LIESST).¹⁵ The lifetime of the photogenerated metastable HS state is inversely proportional to the thermal SCO temperature, $T_{1/2}$, at which the molar HS and LS fractions are equal to 0.5 and the Gibbs free energy difference ΔG_{HL} is equal to 0.^{16,17} The kinetic stability of the photogenerated HS state can be roughly estimated following a precise protocol that determines the characteristic temperature T_{LIESST} at which the photogenerated HS state relaxes to the LS state within a few minutes.¹⁸ The goal is to correlate $T_{\text{LIESST}} - T_{1/2}$ data with relevant structural parameters that may help chemical design aiming at increasing T_{LIESST} toward room temperature. The FeN₆ core, determined by the nature of the ligands, plays a crucial role in the magnitude of T_{LIESST} .¹⁸

Received: June 15, 2018

Published: September 14, 2018

In pure SCO compounds T_{LIESST} values are usually in the interval 20–100 K.

On the other hand crystallographic studies are crucial to provide knowledge of the structural rearrangements occurring during the spin transition.¹⁹ Different kinds of phase transitions can accompany the spin crossover, for example, order–disorder transitions originating from the counteranions,^{20–23} the solvent,^{24–27} or some part of the ligand.^{22,28–30}

$[\text{Fe}(n\text{-Bu-im})_3\text{tren}](\text{PF}_6)_2$ [$(n\text{-Bu-im})_3(\text{tren}) = n\text{-butylimidazoltris}(2\text{-ethylamino})\text{amine}$] has a complex behavior previously studied by magnetic measurements. Two different thermal spin transitions have been observed depending on the sweeping rate of the temperature.³¹ For a scan rate of 4 K/min, the SCO between the HS and the LS phase (called LS_1) is characterized by an average critical temperature of 122 K with a hysteresis loop of 14 K, while for a slower scan rate of 0.1 K/min the SCO between the HS phase and a different LS phase (called LS_2) is characterized by an average critical temperature of 156 K and a hysteresis loop of 41 K. For intermediate scan rates, coalescence of the two hysteric behaviors is observed. The phase transition occurring between the HS and LS states involves several conformational changes of the butyl chains of the substituent of the ligand. Besides the usual HS to LS FeN_6 coordination sphere rearrangements, the HS and LS_1 structures only differ by moderate structural modifications. The HS and LS_2 structures, on the other hand, strongly differ from each other in the orientation of several butyl groups and of the counteranions. In other words, the two different LS phases, LS_1 and LS_2 , present remarkable structural differences. Consequently, the crystal packing is different due to different C...F contacts between the complex and the PF_6^- groups. In the HS phase, only one discrete C...F interaction is produced, whereas in the case of the LS_1 and LS_2 phases, many interactions are present.

Herein, the scan rate dependence of the thermal spin transition of $[\text{Fe}(n\text{-Bu-im})_3\text{tren}](\text{PF}_6)_2$ is confirmed, and the LIESST behavior of the LS_1 and LS_2 phases is investigated by single-crystal optical absorption spectroscopy measurements and X-ray diffraction. Irradiating LS_1 below 70 K quantitatively photogenerates an HS state, which relaxes within half an hour at 80 K. Unexpectedly, irradiating LS_1 at the relatively high temperature of 80 K quantitatively photogenerates another HS state, which relaxes unusually slowly, in around 20 h. The structures of both HS states were characterized by single-crystal diffraction, and the structural rearrangements explaining the long relaxation after irradiation above 70 K were monitored by synchrotron single-crystal X-ray diffraction.

EXPERIMENTAL METHODS

Single-Crystal Optical Absorption Spectroscopy. Single crystals of $[\text{Fe}(n\text{-Bu-im})_3(\text{tren})](\text{PF}_6)_2$ were mounted on a copper plate with a previously drilled hole of approximately 150 μm in diameter. One crystal was deposited in the middle of the hole and fixed with silver paste to ensure a good thermal conductivity. The sample was then introduced into a closed cycle cryostat (Janis-Sumimoto SHI-4.5), which operates between 4 and 300 K and is equipped with a programmable temperature controller (Lakeshore model 331). The cryostat was introduced into a double-beam spectrometer (Varian Cary 5000).

In all experiments, an LS reference spectrum was first collected at 10 K. Then the sample was irradiated with a 690 nm laser, which corresponds to the tail of the LS band centered at 669 nm, during 10

min at 10 mW/mm², and a reference HS spectrum was recorded likewise at 10 K. The HS fraction (γ_{HS}) was obtained using eq 1.

$$\gamma_{\text{HS}} = (\text{OD}_{\text{LS}} - \text{OD}_T) / (\text{OD}_{\text{LS}} - \text{OD}_{\text{HS}}) \quad (1)$$

where OD_{LS} is the optical density of the LS state, OD_{HS} is the optical density of the HS state at 10 K, and OD_T is the optical density at a given temperature. The optical density is corrected from an eventual baseline jump or shift by taking the difference between the OD at 600 nm and the OD at 750 nm, where there is no noticeable absorption in the two states.

In the case of the LIESST experiment, after irradiation at 10 K, the temperature was quickly raised to the desired temperature for the relaxation measurement (at about 20 K/min), and spectra were then recorded in appropriate time intervals during the relaxation. In the case of the LIESST experiment at 80–100 K, the irradiation and the relaxation were performed at the same temperature. In these cases γ_{HS} is calculated using eq 1 but replacing OD_T by OD_t , which is the optical density at a given time during the relaxation.

Synchrotron-Based X-ray Diffraction. The thermal and photo-induced spin transitions were studied using X-ray diffraction at the Swiss Norwegian Beamline at the European Synchrotron Radiation Facility in Grenoble (France). The same diffractometer equipped with a 2D PILATUS2M detector was used for single-crystal and powder diffraction experiments. The temperature was controlled using an Oxford Cryostream 700. All the samples (single crystals and powders) were placed in Mitegen Kapton loops.

For single crystals, 360° phi-rotations of 6 min each were collected. Data were integrated with CryAlis Pro.³² Further X-ray data analyses were carried out using the Olex² Crystallography Software³³ and Shelx.³⁴ For the relaxation experiment, the samples were irradiated at 90 K with a DPSS 690 nm laser during around 10 min at 10 mW/mm².

For powders, the powder was obtained by carefully crushing a few single crystals of $[\text{Fe}(n\text{-Bu-im})_3(\text{tren})](\text{PF}_6)_2$. For the thermal transition, the scan rate was 4 K/min. The relaxation was followed by recording diffraction patterns every 22 s. The 2D data were integrated using the SNBL-homemade software BUBBLE.³⁵ Further X-ray data analyses were carried out using the Topas academic software.³⁶

Home-Lab X-ray Diffraction. The single-crystal diffraction data for the 10 K thermally quenched and 125 K thermally quenched states were collected with an Oxford Diffraction SuperNova diffractometer equipped with an Atlas CCD detector, using either a helium open-flow cryosystem (Oxford Diffraction Helijet), or a nitrogen cryostream cooling device, depending on the temperature. The unit-cell determination and data reduction were performed using the CryAlis Pro³² program suite on the full data set. An analytical absorption correction was carried out. The crystal structures were refined on F^2 by weighted full-matrix least-squares methods using the SHELXL97 program.³⁴

The 25 K diffraction data was collected using a Nonius Kappa CCD diffractometer equipped with a Helix He cryosystem. In a first step, the small-size (100 μm) single-crystal sample was quickly cooled to 120 K, then slowly down to 25 K in the LS_1 state. A complete data set on the LS state was recorded at 25 K. The sample was then irradiated with a laser at 532 nm (laser power of 10 mW, enlarging the beam to ensure a homogeneous irradiation) for 1 h while continuously rotating the crystal, and a complete data set on the HS state was then recorded. The diffraction data were integrated and reduced using the HKL package.³⁷ An empirical absorption correction was applied. The crystal structures were refined on F^2 by weighted full-matrix least-squares methods using the SHELXL97 program.³⁴

Magnetic Measurements. Magnetic susceptibility measurements were carried out on a Quantum Design MPMS2 SQUID susceptometer equipped with a 5.5 T magnet, operating at 1 T and from 300 to 1.8 K. Irradiations were performed at 690 nm.

RESULTS AND DISCUSSION

Thermal Spin Transition. Crystals of around $20 \pm 1 \mu\text{m}$ thickness were used for all the measurements. The dependence of the thermal spin transition behavior with the scan rate of the temperature observed by Real et al.³¹ was confirmed by absorption spectroscopy measurements (see Figure S1 in the Supporting Information for more details) and powder diffraction measurements (Figure S2). By looking more carefully at the 3D plots of the powder diffraction measurements, it is possible to observe that the transition is mainly associated with an intensity change of the HS and LS peaks without large shifts of the peaks in both heating and cooling. This can be associated with a nucleation and growth phenomenon.³⁸ Furthermore, the HS \rightarrow LS₂ thermal relaxation was followed by optical spectroscopy at different temperatures around the HS–LS₂ thermal transition. This confirmed that the relaxation rate decreases with the temperature, which is in line with a first-order phase transition.³⁹ The relaxation is strongly sigmoidal due to the kinetics of the crystallographic phase transition, reflecting the nucleation and growth mechanism (Figure S3).

Kinetics of the HS \rightarrow LS₁ Relaxation. HS \rightarrow LS₁ Relaxation after Irradiation of the LS₁ Phase at 10 K Followed by Absorption Spectroscopy. The LS₁ phase was obtained using a cooling rate of 4 K/min. The absorption spectrum collected after irradiation at 10 K corresponds to a pure HS state (Figure S4a). Considering the $T_{\text{LIESST}}(\text{HS})$ value of 79.8 K (Figure S14a), we selected six temperatures for the relaxation: 80, 77.5, 75, 72.5, 70, 65, and 60 K. For all the temperatures, a plateau is present in the relaxation curves when the HS fraction is around 0.5 (Figure 1 and Figure S7). This

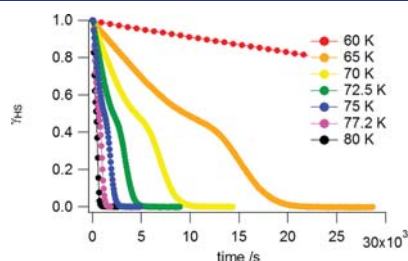


Figure 1. Evolution of the normalized photoinduced HS fraction as a function of time at various temperatures for the HS \rightarrow LS₁ relaxation after irradiation of the LS₁ phase. All the experiments start from a quantitative population of the HS state at 10 K followed by a relaxation at the indicated temperature.

can be due to a specific structural reorganization, which could be, for example, an ordering of the HS and/or LS states.⁴⁰ Evidently, the mean-field approach is not appropriate in this case. Instead, average relaxation rate constants were taken from the time necessary to relax to $\gamma_{\text{HS}} = 0.5$. The linear evolution of $\ln k_{\text{HL}}$ vs $1/T$ indicates that the relaxation from the photoinduced HS state to the ground state LS₁ is quasi thermally activated (Figure S5a). An activation energy of 10.2 kJ/mol (850 cm^{-1}) was extracted from the slope of the Arrhenius plot. This indicates that we are in a transition regime between low-temperature tunneling and classical behavior.⁴¹

HS \rightarrow LS₁ Relaxation after Irradiation of the LS₁ Phase around T_{LIESST} Followed by Magnetometry and Absorption

Spectroscopy. As shown in Figure 2a, the obtained relaxation curves at 80 K by optical spectroscopy after irradiation at 10

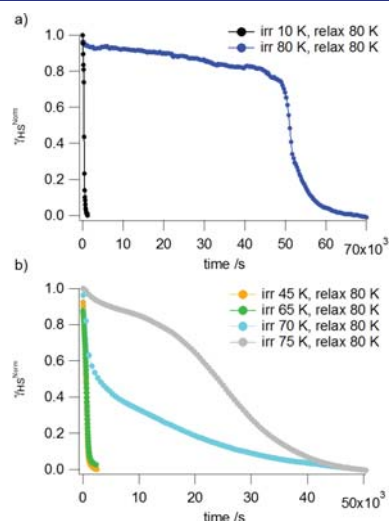


Figure 2. Evolution of the normalized photoinduced HS fraction as a function of time at 80 K for the HS \rightarrow LS₁ relaxation after irradiation of the LS₁ phase at various temperatures. (a) Optical spectroscopy data. (b) Magnetic data. All the experiments start from a quantitative population of the HS state by irradiation at the indicated temperature followed by a relaxation at 80 K.

and 80 K of the LS₁ phase differ tremendously: irradiating at 80 K leads to a relaxation time close to 20 h—more than 40 times that of the relaxation time observed when irradiating at 10 K (Figure 2a)—with a very long nucleation process of around 14 h. The relaxation curve is very sigmoidal, with a kink observed at an HS fraction of around 0.4.

Using magnetometry, we recorded the HS \rightarrow LS₁ relaxation at 80 K after irradiation at different temperatures. We observed that the relaxation gets longer after irradiation above 70 K (Figure 2b).

Experiments were also performed by absorption spectroscopy with irradiation and relaxation at 80, 87, 90, and 100 K (Figure S8b). At 87 K, the process is considerably faster (total relaxation time 11 h, nucleation time 4 h), and a second step is observed after approximately 5 h when the HS fraction is around 0.6. At 90 and 100 K the plateau can be still observed, and the relaxation becomes faster when the temperature increases.

In summary, irradiation at temperatures above 70 K of the LS₁ phase leads to unexpectedly long HS \rightarrow LS₁ relaxation times. The relaxation curves show a plateau for the HS fraction of around 0.4, and a small change in the irradiation and relaxation temperature can drastically change the relaxation time.

Structural Studies. In order to understand the different relaxation behaviors for the LIESST HS state generated below and above 70 K from the LS₁ phase, structural investigations were carried out using single-crystal X-ray diffraction. In particular the butyl chains of the ligands, which adopt different conformations in the already characterized LS₁, LS₂, and HS states, were closely examined.

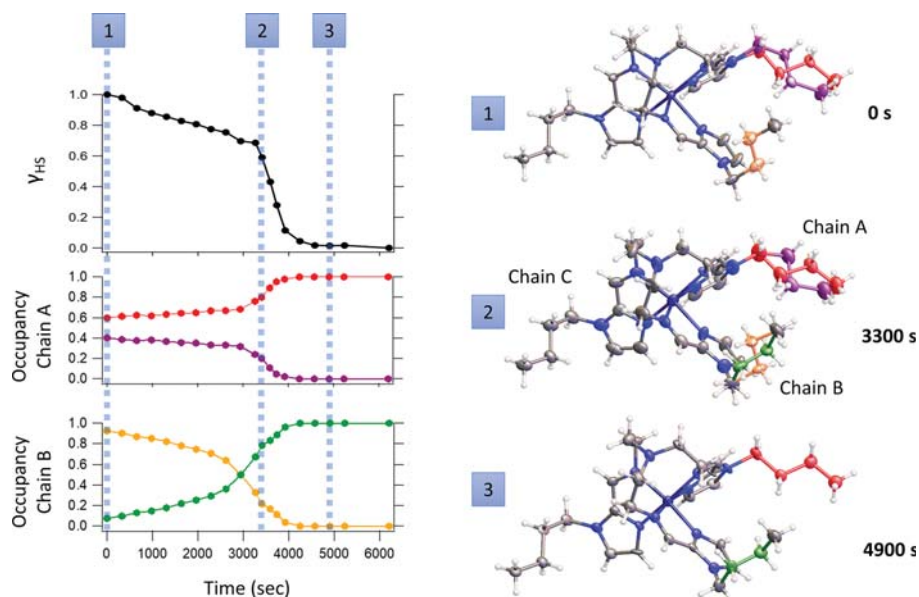


Figure 3. Relaxation curve obtained by single-crystal X-ray diffraction using synchrotron radiation at 90 K after irradiation at the same temperature of the LS_1 phase. The HS fraction curve (black) is derived from the crystallographic Fe–N distances. The structure of the complex is shown at three different relaxation times on this curve, with displacement ellipsoids depicted at the 40% probability level. An order/disorder phase transition takes place in two different butyl groups of the ligand, chains A and B, during the relaxation from HS_1^{1irr} to LS_1 . For each chain, two different positions of the butyl group are observed, represented with different colors. The occupancy factor defines the proportion of the chain being in the given position. The evolutions with time of the occupancy factors for chain A and chain B are shown below the relaxation curve.

An LS_1 structure was obtained at 25 K,⁴² which is similar to the one reported at 110 K.³¹ The sample was then irradiated with a 532 nm laser for 1 h while continuously rotating the crystal, and an HS structure was obtained (Table S1). The HS structure of the irradiated sample at 25 K, which we will call HS_1^{1irr} , presents a complete ordering of all the alkyl substituents, in the same conformation as in the LS_1 state. There is no noticeable change in the geometry of the ligands between the LS_1 and HS_1^{1irr} structures, except some structural rearrangements induced by the different Fe–N bond lengths between the two spin states (Figure S9, superposition).

Using a liquid-nitrogen cooler, an LS_1 structure was recorded around 90 K, which is very similar to the LS_1 structure determined at 25 K (Figure S10, superposition).⁴³ The sample was then irradiated at 690 nm with 10 mW/mm² during 10 min, and the structure of the metastable HS excited state that we will call HS_1^{2irr} was subsequently determined. The structures of HS_1^{1irr} and HS_1^{2irr} differ: in HS_1^{2irr} , one of the butyl chains is disordered and another butyl chain is in a different conformation compared to the structure of LS_1 or HS_1^{1irr} (Figure S11, superposition).

The $HS_1^{2irr} \rightarrow LS_1$ relaxation was also monitored by single-crystal X-ray diffraction at 90 K after photoexcitation. The time evolution of the HS fraction was calculated through Vegard's law on the Fe–N bond length (eq 2).

$$\gamma_{HS}(t) = \frac{r_{(Fe-N)}(t) - r_{(Fe-N)_{LS}}}{r_{(Fe-N)_{HS}} - r_{(Fe-N)_{LS}}} \quad (2)$$

where $r_{(Fe-N)}(t)$ is the average Fe–N distance at the time t , $r_{(Fe-N)_{HS}}$ is the average Fe–N distance of the HS state at 90 K (obtained under continuous irradiation), and $r_{(Fe-N)_{LS}}$ is the average Fe–N distance of the LS_1 state at 90 K. The corresponding used Fe–N bond length and unit-cell parameters obtained for all the structures taken during the relaxation are summarized in Table S3. The relaxation curve obtained by single-crystal diffraction is compared to the relaxation curves obtained by absorption spectroscopy in Figure S8c. The relaxation time indicates a temperature of around 90 K.

The structures during the relaxation are shown in Figure 3 alongside the obtained relaxation curve. In the photoinduced HS_1^{2irr} state, the butyl chain of one ligand is disordered (chain A) with two randomly distributed orientations (red and violet chains). The other butyl chains (B and C) are ordered. After cutting off the laser irradiation, the relaxation proceeds very slowly for approximately 1 h. During this nucleation time, disorder grows on chain B (green and orange chains). As the relaxation becomes faster, chain A orders in one of its initial orientations (red). Chain B also starts to order, flipping its initial orientation (from the initial orange chain to the final green one). Clearly, this order/disorder phase transition that takes place in two different butyl groups of the ligands is directly related with the kink observed in the middle of the relaxation and with the long relaxation time. The rearrangements of the structure create different interaction patterns between the butyl groups and the counteranions, especially through the H (butyl)–F(PF_6^-) bonds (Tables S4 and S5).

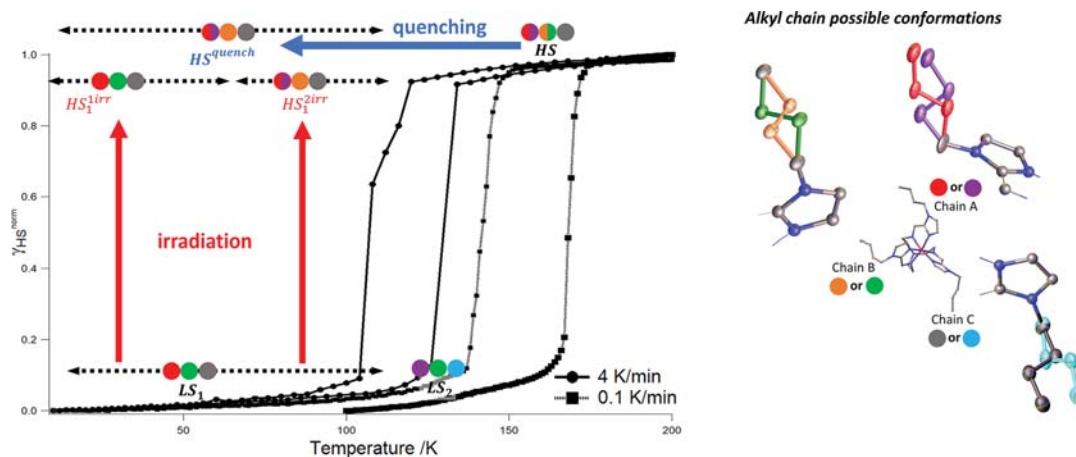


Figure 4. Simplified structural diagram of $[\text{Fe}(n\text{-Bu-im})_3\text{tren}](\text{PF}_6)_2$; $(n\text{-Bu-im})_3\text{tren} = n\text{-butyl imidazoltris}(2\text{-ethylamino})\text{amine}$. The different conformations that the alkyl chains can adopt are shown on the right. For each phase of the phase diagram, three colored disks indicate the positions adopted by chains A, B, and C. Two-colored disks indicate that the chain is disordered over both positions. For the quenched phases, a small disorder on chain B is sometimes observed, depending on the temperature, but only the main conformation of the chain has been indicated (see Table S7a).

Alternatively, the unexpectedly long time scale of the $\text{HS}_2^{\text{irr}} \rightarrow \text{LS}_1$ relaxation was also monitored by magnetic measurements (Figure S15) and synchrotron-based X-ray powder diffraction (Figure S16). The time scales of the relaxation obtained by both techniques are on the same order of magnitude as the one observed on single crystals. However, the nucleation time decreases and the relaxation speeds up compared to single-crystal XRD (Table S6 summarizes the different relaxation times obtained by the different measurements).

The differences observed between the different measurement techniques can be attributed to the sample preparation. Indeed, the crushing of the crystals to produce powdered samples affects the crystal quality. We have also observed that the exact shape of the relaxation curve differs slightly from crystal to crystal. Two relaxation cycles on the same crystal gave reproducible results (Figure S17 and Figure S8d). However, as shown in Figure S8d, we observed different relaxation curves on the same crystal after irradiation at 90 K when going back to room temperature and cooling again to 90 K between the irradiations. Cycling to room temperature induces cracks and defects in the crystals, which reduces the size of the domains and cancels the long nucleation time during which chain B is slowly disordering. As a consequence, the relaxation time is shortened and the relaxation curve depends on the size/quality of the crystals.

Finally, quenching of the HS phase by quickly lowering the temperature gave an $\text{HS}^{\text{quench}}$ phase whose structure is similar to HS_1^{irr} . The relaxation of this quenched phase was studied by magnetic measurements, and the relaxation time is on the same order of magnitude as the photoexcited HS_1^{irr} phase (Figure S18). This is expected, as the same rearrangement of the butyl chains has to occur during the relaxation.

In Figure 4, the structural diagram of the different HS and LS states, whose structures are elucidated, is presented. This system is a very nice example of how multistability can influence the spin-crossover properties. Two low-spin states

are observed for different cooling rates. Two HS states are also observed at low temperature, one that can be reached by irradiation below 70 K and one that can be reached either by irradiation above 70 K or by quenching of the room-temperature HS state. The reorganization of the butyl side chains between these states governs the LIESST relaxation kinetics.

Kinetics of the $\text{HS} \rightarrow \text{LS}_2$ Relaxation. *HS $\rightarrow \text{LS}_2$ Relaxation after Irradiation of the LS_2 Phase at 10 K Followed by Absorption Spectroscopy.* The LS_2 phase was obtained using a cooling rate of 0.1 K/min. The spectrum collected after irradiation at 10 K corresponds to a pure HS state (Figure S4b). Considering the $T_{\text{LIESST}}(\text{HS}_2)$ value of 50 K (Figure S14b), six temperatures for the relaxation were selected: 55, 50, 45, 40, 35, and 30 K. The relaxation curves show a slightly sigmoidal behavior (Figure 5). Therefore, they were fitted within the framework of the mean-field model,⁴⁴ with the relaxation rate constant k_{HL} depending not only on the temperature but also on the LS fraction (eq 3) in such a

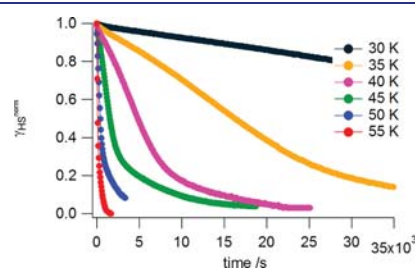


Figure 5. Evolution of the normalized photoinduced HS fraction as a function of time at various temperatures for the $\text{HS} \rightarrow \text{LS}_2$ relaxation after irradiation of the LS_2 phase. All the experiments start from a quantitative population of the HS state at 10 K followed by a relaxation at the indicated temperature.

way that in the differential equation of $d\gamma_{\text{HS}}/dt$, a new term that accounts for the cooperative effects is introduced (eq 4).

$$k_{\text{HL}}(T, \gamma_{\text{HS}}) = k_{\text{HL}}(T, \gamma_{\text{HS}} = 0)e^{\alpha\gamma_{\text{LS}}} \quad (3)$$

$$\frac{d\gamma_{\text{HS}}}{dt} = -k_{\text{HL}}^0 e^{-E_a/k_B T} e^{\alpha(1-\gamma_{\text{HS}})\gamma_{\text{HS}}} \quad (4)$$

In eq 3 k_{HL}^0 is the relaxation rate constant and E_a the activation energy at the beginning of the relaxation, and α is the acceleration factor. k_{HL}^0 was obtained from the slope of the relaxation curve considering only the first relaxation points, that is, between $t = 0$ and $t \approx 1000$ s. The apparent E_a value was then calculated from the slope of an Arrhenius plot (Figure S5b). The resulting value for E_a of 3.3 kJ/mol (276 cm⁻¹) is rather small and indicates that in the temperature interval from 30 to 55 K the system is only just above the low-temperature tunneling regime. This is also born out by the slight curvature of the Arrhenius plot. The above value of E_a has subsequently been introduced into eq 3 in order to obtain the value of α via least-squares numerical fitting. The calculated value of α is 1.5 at 35 K (Figure S6) and corresponds to a moderately cooperative relaxation curve. It should be noted that toward the end of the relaxation curve, the experimental data deviate quite strongly from the calculated mean-field curve. Such a behavior, with a long tail, is indicative of a comparatively large inhomogeneous distribution of activation energies.⁴⁴

Overall, the HS \rightarrow LS relaxation after irradiation of the LS₂ phase (irradiation at 10 K) is faster than the HS \rightarrow LS relaxation after irradiation of the LS₁ phase (irradiation at 10 K). This can be directly correlated with the thermal transition temperature, which is higher for LS₂ (see Figure S1).

HS \rightarrow LS₂ Relaxation after Irradiation of the LS₂ Phase around T_{LIESST} , Studied by Magnetometry. Contrary to what we observed with the LS₁ phase, irradiating at higher temperature does not significantly change the relaxation time for a given relaxation temperature. The relaxation curves measured at 45 K overlap wherever the irradiation is performed at 10 or 45 K (Figure S19a). As expected, the lifetime of the irradiated HS₂ is short at 55 K, and no complete conversion could be reached (Figure S19b). This suggests that for LS₂ the photogenerated state is the same, whatever the irradiation temperature.

CONCLUSIONS

The two different thermal transitions previously observed by Real et al. with the [Fe(*n*-Bu-im)₃(tren)](PF₆)₂ compound have been confirmed by single-crystal optical absorption spectroscopy. The HS \rightarrow LS relaxation after irradiation has been studied for both LS phases after excitation at 10 K. In each case, we observed a sigmoidal behavior characteristic of cooperative effects, with a plateau observed only in the HS \rightarrow LS₁ relaxation. The larger E_a values obtained for the HS \rightarrow LS₁ relaxation compared to the HS \rightarrow LS₂ relaxation (10.2 kJ/mol compared to 3.3 kJ/mol) agrees with the slower dynamics found for the HS \rightarrow LS₁ relaxation and the thermal stabilization of the LS₂ observed during the thermal spin transition.

For the LS₁ phase, we observed two relaxation behaviors depending on the irradiation temperature. Irradiation above 70 K led to an unexpected long relaxation time compared to irradiating below 70 K. This was explained by the existence of two different photogenerated HS states: the HS₁^{irr} state, whose structure was determined under irradiation of LS₁ at 25

K, and the HS₁^{2irr} state, whose structure was determined under irradiation of LS₁ at 90 K. The conformations of the butyl chains of the ligand are identical in the HS₁^{irr} and the LS₁ state, whereas two of the HS₁^{2irr} butyl chains adopt a different conformation. Alongside the relaxation, followed by single-crystal X-ray diffraction, reorientations of the butyl chains occur through order/disorder transitions. We believe that these reorientations of the butyl chains are responsible for the long relaxation time after excitation above 70 K.

Interestingly, an HS^{quench} state can also be reached via thermal quenching, with a structure identical to the HS₁^{2irr}. The relaxation time of those structurally identical states are on the same order of magnitude.

With the exception of a few Fe–Co charge transfer systems with a cyanide bridge (Prussian blue analogues) there are only two SCO pure systems that have a T_{LIESST} above 100 K,^{45,46} while other SCO complexes of Fe(II) present a T_{LIESST} of around 90–100 K. However, in the present study, a new type of spin-crossover compound is presented: a spin-crossover compound with $T_{\text{LIESST}} = 80$ K that can be completely populated back to the HS₁ by irradiating at 80 K with a surprisingly high kinetic stability of the photogenerated state.

ASSOCIATED CONTENT

Supporting Information

The Supporting Information is available free of charge on the ACS Publications website at DOI: 10.1021/jacs.8b06042.

Additional magnetic, diffraction, and spectroscopic data (PDF)

X-ray crystallographic data (CIF)

X-ray crystallographic data (CIF)

AUTHOR INFORMATION

Corresponding Authors

*Jose.A.Real@uv.es

*Celine.besnard@unige.ch

ORCID

José Antonio Real: 0000-0002-2302-561X

Céline Besnard: 0000-0001-5699-9675

Notes

The authors declare no competing financial interest.

[†]On leave from Taras Shevchenko National University, Department of Chemistry, Volodymyrska Str. 64, Kyiv 01601, Ukraine.

CCDC files 1848626–1848629, 1848631, and 1857201 contain the supplementary crystallographic data for this paper. The data can be obtained free of charge from the Cambridge Crystallographic Data Centre via www.ccdc.cam.ac.uk/structures. Table S8a indicates to which structure corresponds each deposited cif. These files and additional cif files (see Table S8b) are also available as Supporting Information.

ACKNOWLEDGMENTS

We are grateful to the Swiss-Norwegian Beamlines (ESRF, Grenoble) for the provision of synchrotron beamtime. Financial support from the Swiss National Science Foundation (Grant No 200020_152780), the French PIA project “Lorraine Université d’Excellence”, reference ANR-15-IDEX-04-LUE, and the CPER, The Spanish Ministerio de Economía y Competitividad (MINECO) (Grants CTQ2016-78341-P

and MDM-2015-0538), Generalitat Valenciana (Grant PROMETEO/2016/147), an EU Framework Program for Research and Innovation (RISE project number 734322) are gratefully acknowledged. We are also grateful to Yu Wang for the structures at 25 K of the LS_1 and HS_1^{lrr} phases.

REFERENCES

- (1) Sato, O. *Nat. Chem.* **2016**, *8* (7), 644–656.
- (2) Bennemann, K. H. *J. Phys.: Condens. Matter* **2011**, *23* (7), 073202.
- (3) Koshihara, S.-Y. *J. Phys.: Conf. Ser.* **2005**, *21* (1), 7.
- (4) König, E. *Struct. Bonding (Berlin, Ger.)* **1991**, *76*, 51–152.
- (5) Gütllich, P.; Goodwin, H. A., Eds. Spin Crossover in Transition Metal Compounds I. In *Topics in Current Chemistry*, Vol. 233; Springer-Verlag, 2004.
- (6) Halcrow, M. A., Ed. *Spin-Crossover Materials: Properties and Applications*; John Wiley & Sons Ltd, 2013.
- (7) Molnar, G.; Rat, S.; Salmon, L.; Nicolazzi, W.; Bousseksou, A. *Adv. Mater. (Weinheim, Ger.)* **2018**, Ahead of Print.301703862
- (8) Senthil Kumar, K.; Ruben, M. *Coord. Chem. Rev.* **2017**, *346*, 176–205.
- (9) Kahn, O.; Martinez, C. *J. Science (Washington, DC, U. S.)* **1998**, *279* (5347), 44–48.
- (10) Prins, F.; Monrabal-Capilla, M.; Osorio, E. A.; Coronado, E.; van der Zant, H. S. J. *Adv. Mater.* **2011**, *23* (13), 1545–1549.
- (11) Ohba, M.; Yoneda, K.; Agusti, G.; Munoz, M. C.; Gaspar, A. B.; Real, J. A.; Yamasaki, M.; Ando, H.; Nakao, Y.; Sakaki, S.; Kitagawa, S. *Angew. Chem., Int. Ed.* **2009**, *48* (26), 4767–4771.
- (12) Salmon, L.; Molnar, G.; Zitouni, D.; Quintero, C.; Bergaud, C.; Micheau, J.-C.; Bousseksou, A. *J. Mater. Chem.* **2010**, *20* (26), 5499–5503.
- (13) Matsuda, M.; Kiyoshima, K.; Uchida, R.; Kinoshita, N.; Tajima, H. *Thin Solid Films* **2013**, *531*, 451–453.
- (14) Shepherd, H. J.; Gural'skiy, I. y. A.; Quintero, C. M.; Tricard, S.; Salmon, L.; Molnar, G.; Bousseksou, A. *Nat. Commun.* **2013**, *4*, 3607/1–3607/9.
- (15) Decurtins, S.; Gütllich, P.; Köhler, C. P.; Spiering, H.; Hauser, A. *Chem. Phys. Lett.* **1984**, *105* (1), 1–4.
- (16) Hauser, A.; Vef, A.; Adler, P. *J. Chem. Phys.* **1991**, *95* (12), 8710–17.
- (17) Hauser, A. *Comments Inorg. Chem.* **1995**, *17* (1), 17–40.
- (18) Letard, J.-F. *J. Mater. Chem.* **2006**, *16* (26), 2550–2559.
- (19) Collet, E.; Guionneau, P. *C. R. Chim.* **2018**, DOI: 10.1016/j.crci.2018.02.003.
- (20) Matouzenko, G. S.; Luneau, D.; Molnár, G.; Ould-Moussa, N.; Zein, S.; Borshch, S. A.; Bousseksou, A.; Averseng, F. *Eur. J. Inorg. Chem.* **2006**, *2006* (13), 2671–2682.
- (21) König, E.; Ritter, G.; Kulshreshtha, S. K.; Nelson, S. M. *Inorg. Chem.* **1982**, *21* (8), 3022–3029.
- (22) Matouzenko, G. S.; Bousseksou, A.; Borshch, S. A.; Perrin, M.; Zein, S.; Salmon, L.; Molnar, G.; Lecocq, S. *Inorg. Chem.* **2004**, *43* (1), 227–236.
- (23) Money, V. A.; Elhaik, J.; Radosavljevic Evans, I.; Halcrow, M. A.; Howard, J. A. K. *Dalton Trans* **2004**, *1*, 65–69.
- (24) Chernyshov, D.; Hostettler, M.; Törnroos, K. W.; Bürgi, H.-B. *Angew. Chem., Int. Ed.* **2003**, *42* (32), 3825–3830.
- (25) König, E.; Ritter, G.; Kulshreshtha, S. K.; Waigel, J.; Sacconi, L. *Inorg. Chem.* **1984**, *23* (9), 1241–1246.
- (26) Wu, C.-C.; Jung, J.; Gantzel, P. K.; Gütllich, P.; Hendrickson, D. N. *Inorg. Chem.* **1997**, *36* (23), 5339–5347.
- (27) Hostettler, M.; Törnroos, K. W.; Chernyshov, D.; Vangdal, B.; Bürgi, H.-B. *Angew. Chem.* **2004**, *116* (35), 4689–4695.
- (28) Miyazaki, Y.; Nakamoto, T.; Ikeuchi, S.; Saito, K.; Inaba, A.; Sorai, M.; Tojo, T.; Atake, T.; Matouzenko, G. S.; Zein, S.; Borshch, S. A. *J. Phys. Chem. B* **2007**, *111* (43), 12508–12517.
- (29) Kusz, J.; Zubko, M.; Neder, R. B.; Gütllich, P. *Acta Crystallogr., Sect. B: Struct. Sci.* **2012**, *68* (1), 40–56.
- (30) Sheu, C.-F.; Pillet, S.; Lin, Y.-C.; Chen, S.-M.; Hsu, I. J.; Lecomte, C.; Wang, Y. *Inorg. Chem.* **2008**, *47* (23), 10866–10874.
- (31) Seredyuk, M.; Muñoz, M. C.; Castro, M.; Romero-Morcillo, T.; Gaspar, A. B.; Real, J. A. *Chem. - Eur. J.* **2013**, *19* (21), 6591–6596.
- (32) <https://www.rigaku.com/en/products/smc/crystalis>.
- (33) Dolomanov, O. V.; Blake, A. J.; Champness, N. R.; Schröder, M. *J. Appl. Crystallogr.* **2003**, *36* (5), 1283–1284.
- (34) Sheldrick, G. *Acta Crystallogr., Sect. C: Struct. Chem.* **2015**, *71* (1), 3–8.
- (35) <http://www.esrf.eu/home/UsersAndScience/Experiments/CRG/BM01/bm01/image.htm/snbl-tool-box.html>.
- (36) Coelho, A. A. *J. Appl. Crystallogr.* **2018**, *51*, 210–218.
- (37) Otwinowski, Z.; Minor, W. Processing of X-ray diffraction data collected in oscillation mode. In *Methods in Enzymology*; Academic Press, 1997; Vol. 276, pp 307–326.
- (38) Pillet, S.; Legrand, V.; Souhassou, M.; Lecomte, C. *Phys. Rev. B: Condens. Matter Mater. Phys.* **2006**, *74* (14), 140101.
- (39) Landau, L. D.; Lifshitz, E. M., Eds. *Statistical Physics Part 1*; Pergamon, 1994.
- (40) Mariette, C.; Trzop, E.; Zerdane, S.; Fertey, P.; Zhang, D.; Valverde-Munoz, F. J.; Real, J.-A.; Collet, E. *Acta Crystallogr., Sect. B: Struct. Sci., Cryst. Eng. Mater.* **2017**, *73* (4), 660–668.
- (41) Hauser, A.; Enachescu, C.; Daku, M. L.; Vargas, A.; Amstutz, N. *Coord. Chem. Rev.* **2006**, *250* (13–14), 1642–1652.
- (42) A rapid cooling of the sample freezes the HS state at low temperature, and the lack of control of the temperature of a helijet-type cooling device above 60 K hampered obtaining the LS_1 phase at 10 K. We therefore used another cooling device with the lowest possible temperature of 25 K.
- (43) The nominal temperature indicated by the cryostream was 80 K. However, the sample temperature was lower and was determined to be around 90 K by comparison with the spectroscopic measurements.
- (44) Hauser, A.; Jeftić, J.; Romstedt, H.; Hinek, R.; Spiering, H. *Coord. Chem. Rev.* **1999**, *190–192*, 471–491.
- (45) Marcén, S.; Lecren, L.; Capes, L.; Goodwin, H. A.; Létard, J. F. *Chem. Phys. Lett.* **2002**, *358* (1), 87–95.
- (46) Costa, J. S.; Balde, C.; Carbonera, C.; Denux, D.; Wattiaux, A.; Desplanches, C.; Ader, J.-P.; Gütllich, P.; Létard, J.-F. *Inorg. Chem.* **2007**, *46* (10), 4114–4119.

Cite this: *Chem. Sci.*, 2019, 10, 3807

All publication charges for this article have been paid for by the Royal Society of Chemistry

Discrimination between two memory channels by molecular alloying in a doubly bistable spin crossover material†

Francisco Javier Valverde-Muñoz,^a Maksym Seredyuk,^b Manuel Meneses-Sánchez,^a M. Carmen Muñoz,^b Carlos Bartual-Murgui^a and José A. Real^{a*}

A multistable spin crossover (SCO) molecular alloy system $[\text{Fe}_{1-x}\text{M}_x(\text{nBu-im})_3(\text{tren})](\text{P}_{1-y}\text{As}_y\text{F}_6)_2$ ($\text{M} = \text{Zn}^{\text{II}}$, Ni^{II} ; $(\text{nBu-im})_3(\text{tren}) = \text{tris}(n\text{-butyl-imidazol}(2\text{-ethylamino}))\text{amine}$) has been synthesized and characterized. By controlling the composition of this isomorphous series, two cooperative thermally induced SCO events featuring distinct critical temperatures (T_c) and hysteresis widths (ΔT_c , memory) can be selected at will. The pristine derivative 100As ($x = 0$, $y = 1$) displays a strong cooperative two-step SCO and two reversible structural phase transitions (PTs). The low temperature PT^{LT} and the SCO occur synchronously involving conformational changes of the ligand's n -butyl arms and two different arrangements of the AsF_6^- anions [$T_c^1 = 174$ K ($\Delta T_c^1 = 17$ K), $T_c^2 = 191$ K ($\Delta T_c^2 = 23$ K) (scan rate 2 K min^{-1})]. The high-temperature PT^{HT} takes place in the high-spin state domain and essentially involves rearrangement of the AsF_6^- anions [$T_c^{\text{PT}} = 275$ K ($\Delta T_c^{\text{PT}} = 16$ K)]. This behavior strongly contrasts with that of the homologous 100P [$x = 0$, $y = 0$] derivative where two separate cooperative one-step SCO can be selected by controlling the kinetics of the coupled PT^{LT} at ambient pressure: (i) one at low temperatures, $T_c = 122$ K ($\Delta T_c = 9$ K), for temperature scan rates (>1 K min^{-1}) (memory channel A) where the structural modifications associated with PT^{LS} are inhibited; (ii) the other centered at $T_c = 155$ K ($\Delta T_c = 41$ K) for slower temperature scan rates ≤ 0.1 K min^{-1} (memory channel B). These two SCO regimes of the 100P derivative transform reversibly into the two-step SCO of 100As upon application of hydrostatic pressure (ca. 0.1 GPa) denoting the subtle effect of internal chemical pressure on the SCO behavior. Precise control of $\text{AsF}_6^- \leftrightarrow \text{PF}_6^-$ substitution, and hence of the PT^{LT} kinetics, selectively selects the memory channel B of 100P when $x = 0$ and $y \approx 0.7$. Meanwhile, substitution of Fe^{II} with Zn^{II} or Ni^{II} [$x \approx 0.2$, $y = 0$] favors the low temperature memory channel A at any scan rate. This intriguing interplay between PT, SCO and isomorphous substitution was monitored by single crystal and powder X-ray diffractometries, and magnetic and calorimetric measurements.

Received 26th November 2018
Accepted 20th February 2019

DOI: 10.1039/c8sc05256e

rsc.li/chemical-science

Introduction

Responsive switchable materials attract great attention due to affording excellent study examples for understanding the mechanisms of phase transitions (PTs) and provide application prospects for future and emerging technologies.¹ Some of the most investigated switchable molecular materials are pseudo-octahedral Fe^{II} spin-crossover (SCO) complexes, reversibly

altering the high-spin (HS, $t_{2g}^4e_g^2$) and low-spin (LS, $t_{2g}^6e_g^0$) electronic states by the action of physicochemical stimuli (temperature, pressure, light and chemical substrates). The LS–HS conversion involves an electron transfer between the e_g and t_{2g} orbitals strongly coupled with structural changes in the coordination core of the Fe^{II} centres, which essentially affect Fe–ligand bond lengths and angles, and in turn the molecular conformation. In favourable cases these changes propagate cooperatively in the crystal, conferring bistability (memory) to the magnetic, optical, dielectric, structural and mechanical properties.²

New developments in this area are crucial not only for elucidating background mechanisms behind observed properties and understanding the fundamental aspects of the SCO behaviour, but also for opening new perspectives in the field, such as the use of SCO compounds for creation of fully controllable “smart” materials responding to external stimuli in a desired way.³ For example, SCO can be combined with other relevant functions

^aDepartament de Química Inorgànica, Institut de Ciència Molecular (ICMol), Universitat de València, Valencia, Spain. E-mail: jose.a.real@uv.es

^bOn leave from Department of Chemistry, Taras Shevchenko National University of Kyiv, 64/13, Volodymyrska Street, 01601, Kyiv, Ukraine. E-mail: mcs@univ.kiev.ua; mlseredyuk@gmail.com

^cDepartament de Física Aplicada, Universitat Politècnica de València, Camino de Vera s/n, E-46022, Valencia, Spain

† Electronic supplementary information (ESI) available. CCDC 1879896–1879901 and 1892385. For ESI and crystallographic data in CIF or other electronic format see DOI: 10.1039/c8sc05256e



such as fluorescence,^{3c,4} electroluminescence,^{3e} electronic transport⁵ and non-linear optical response⁶ thereby transferring its intrinsic bistable nature to the second property resulting in multifunctional materials that can be processed at different levels, from bulk to nanoscale.⁷

The control of the SCO characteristics, *i.e.* critical temperature and hysteresis width, remains one of the key focuses in the field. Tackling this problem by chemical methods requires engineering both the coordination site of the SCO centres and the cohesive elastic interactions between them through supra-molecular and/or polymeric approaches. Furthermore, the strong sensitivity of the SCO behaviour to subtle changes in the elastic interactions makes it possible to control the SCO through crystal lattice rearrangements. In this respect, isomorphous substitution of SCO metal centres/complexes with non-SCO metal ions⁸/non-SCO complexes⁹ is an effective means to modulate the SCO behaviour. For example, substantial dilution with passive Ni^{II} or Zn^{II}-based complexes breaks cooperativity between SCO centres and brings on a considerable downward shift of the SCO equilibrium/critical temperature $T_{1/2}/T_c$, while low concentrations of the dopant can fine tune the SCO behavior.^{2d} Metal dilution is a particular case of a more general concept of a solid solution of molecules, also known as molecular alloys, consisting in precise control of the stoichiometry of mixed ionic or molecular components during the synthetic step. This offers an unrivalled tool for optimization of desired magnetic, optical or electrical properties, as demonstrated by examples from adjacent fields,¹⁰ and for a few SCO systems.^{3a} Another relevant strategy, yet little explored, is based on the possibility of controlling the SCO properties by a PT.¹¹ It has been demonstrated for several systems that changes in the interaction binding between the components of the crystal due to a solid–solid or solid–liquid/liquid crystal PT may be sufficient for altering the spin state.^{11b,12}

In this context, the complex $[\text{Fe}(\text{nBu-im})_3(\text{tren})](\text{PF}_6)_2$ ($(\text{nBu-im})_3(\text{tren}) = \text{tris}(\text{n-butyl-imidazol}(2\text{-ethylamino})\text{amine})$) affords an uncommon example of thermal hysteretic SCO behaviour deeply influenced by a synchronous symmetric crystallographic PT, leading to a reorganization of the crystal lattice due to significant conformational changes of the alkyl groups and

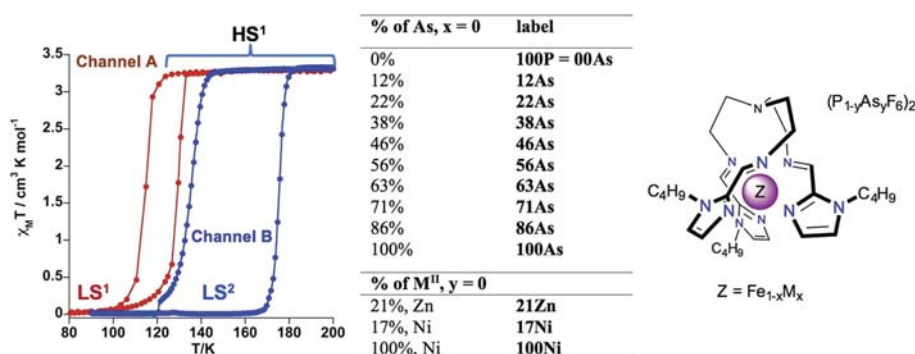
displacement and rotation of the PF_6^- anions, taking place during the $\text{LS} \leftrightarrow \text{HS}$ conversion.^{11b} Playing with the slow kinetics featuring this PT, two well separate hysteretic thermally induced SCO behaviors (two memory channels) were found.^{11b} Thus, high-temperature sweep rates ($\geq 2 \text{ K min}^{-1}$) quench the crystallographic PT thereby stabilizing channel A, which is characterized by a cooperative SCO, between the phases HS^1 and LS^1 , centred at 122 K with a hysteresis 14 K wide. In contrast, low temperature-sweep rates ($\leq 0.1 \text{ K min}^{-1}$) stabilize channel B, characterized by a much more cooperative SCO, between the HS^1 and LS^2 phases, centred at *ca.* 155.5 K featuring a hysteresis loop 41 K wide (see Scheme 1). The phases display different arrangement 1 and arrangement 2 of the flexible butyl groups and of the anions. Furthermore, the LS^1 phase affords an uncommon very long-lived photogenerated HS^{1*} phase after light irradiation at 80 K. The very slow relaxation kinetics is controlled by conformational rearrangements of the butyl groups during the $\text{HS}^{1*} \rightarrow \text{LS}^1$ transformation.^{11f}

In order to understand more in depth the correlation between SCO and structural PTs in 100P and find reliable chemical means to discriminate between the two thermal memory channels, we have investigated the isostructural compound $[\text{Fe}(\text{nBu-im})_3(\text{tren})](\text{AsF}_6)_2$ (100As) and the solid solutions $[\text{Fe}_{1-x}\text{M}_x(\text{nBu-im})_3(\text{tren})](\text{P}_{1-y}\text{As}_y\text{F}_6)_2$ (see Scheme 1). Herein, we show that the SCO behavior of 100P ($x = 0; y = 0$) is highly sensitive to application of external hydrostatic low pressure and, consequently, the resulting SCO behavior is similar to that of 100As ($x = 0; y = 1$) which also displays double bistability due to SCO and PTs but at higher temperatures. Furthermore, modulating the internal “chemical pressure” built up by partial substitution of Fe^{II} with M^{II} ($x\text{M}$, $x < 100$ and $y = 0$, $\text{M} = \text{Zn}, \text{Ni}$) or P with As ($y\text{As}$, $x = 0$ and $y < 100$) leads to effective discrimination of the two memory channels resulting from the interplay of the SCO and a PT in the pure 100P.

Results

SCO properties of 100As

The magnetic behaviour of 100As, recorded at 1 K min^{-1} between 10 and 300 K, is shown in Fig. 1a in the form of $\chi_{\text{M}}T$ vs.



Scheme 1 Description of the SCO behavior of 100P. $[\text{Fe}_{1-x}\text{M}_x(\text{nBu-im})_3(\text{tren})](\text{P}_{1-y}\text{As}_y\text{F}_6)_2$ system ($\text{M} = \text{Ni}, \text{Zn}$).



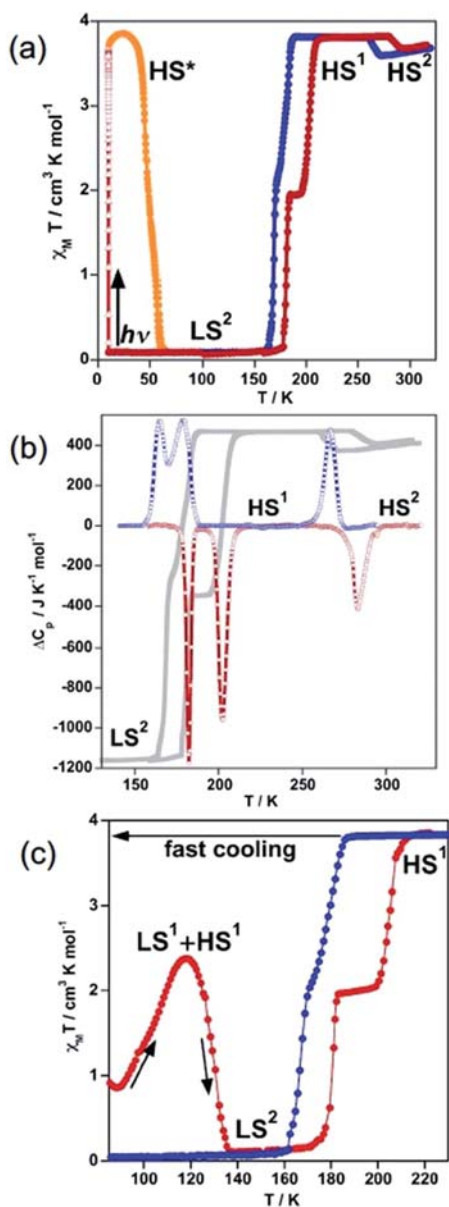


Fig. 1 Spin crossover behaviour of 100As: (a) magnetic and photo-magnetic properties; (b) differential scanning calorimetry (DSC); and (c) quenching of the HS state. Blue and red filled circles correspond to the cooling and heating modes, respectively. Gray lines correspond to the heat flow measured by DSC.

T (χ_M is the molar magnetic susceptibility and T is the temperature). At 300 K, the $\chi_M T$ value is close to $3.68 \text{ cm}^3 \text{K mol}^{-1}$ as expected for an Fe^{II} compound in the HS state ($S = 2$).

On cooling a gradual decrease of the $\chi_M T$ value down to $3.56 \text{ cm}^3 \text{K mol}^{-1}$ is followed by a limited but abrupt jump up to $3.80 \text{ cm}^3 \text{K mol}^{-1}$. This bistable behaviour is associated with a reversible crystallographic PT within the HS phase [HS¹ \leftrightarrow HS²] (*vide infra*).

The shaped hysteresis is centred at $T_c^{\text{PT}} = 276 \text{ K}$ with the loop width $\Delta T_c^{\text{PT}} = 17 \text{ K}$. Further cooling does not reveal any marked evolution of $\chi_M T$ down to 188 K, where an abrupt two-step decrease down to zero value is detected ($S = 0$) with a well-defined plateau of the ascending curve at 50% conversion upon subsequent heating. The two steps centred at $T_c^1 = 175 \text{ K}$ and $T_c^2 = 193 \text{ K}$ are characterised by a hysteresis loop $\Delta T_c^1 = 14 \text{ K}$ and $\Delta T_c^2 = 23 \text{ K}$ wide, respectively. In opposite to 100P, no remarkable kinetic effects were observed for the range of temperature-sweeping rates $4\text{--}0.5 \text{ K min}^{-1}$ in the magnetic response of 100As (Fig. S1†). However, when cooling from 300 K to 80 K in *ca.* 15 s ($\approx 900 \text{ K min}^{-1}$) partial thermal trapping of the sample was observed (Fig. 1c). At 80 K the $\chi_M T$ value of the trapped sample is *ca.* $1 \text{ cm}^3 \text{K mol}^{-1}$ and upon heating at 0.3 K min^{-1} it increases to reach a maximum value of $2.37 \text{ cm}^3 \text{K mol}^{-1}$ at 120 K, which corresponds to *ca.* 62% of the Fe^{II} centres in the HS state. Then, at higher temperatures the compound relaxes back to the LS state and upon further heating it reaches the HS state. As a hypothesis and by similarity with 100P the trapped state could be a mixture of the states LS¹ and HS¹ and the LS state attained after relaxation should correspond to the LS² phase (*vide infra*).

Quantitative photo-generation of the metastable HS* state at low temperature, the so-called light induced excited spin state trapping (LIESST) experiment,¹³ was carried out at 10 K by irradiating a microcrystalline sample (0.75 mg) of 100As with red light ($\lambda = 633 \text{ nm}$) for over 3 h. Further heating of the sample in the photo-stationary HS* state in the dark at 0.3 K min^{-1} uncovers a two-step LIESST relaxation process with $T_{\text{LIESST1}} = 45 \text{ K}$ and $T_{\text{LIESST2}} = 57 \text{ K}$ (Fig. 1a) relevant to the two-step thermal SCO.

Differential scanning calorimetry (DSC) measurements were carried out for 100As in the cooling and heating modes to support the magnetic bistability data and quantify the thermodynamic parameters associated with the SCO and PT. The corresponding anomalous variation of the heat capacity ΔC_p vs. T plots is depicted in Fig. 1b overlaid with the magnetic data. Upon cooling/heating three processes are detected at critical temperatures $T_c^1 = 174 \text{ K}$ ($\Delta T_c^1 = 17 \text{ K}$), $T_c^2 = 191 \text{ K}$ ($\Delta T_c^2 = 23 \text{ K}$) and $T_c^{\text{PT}} = 275 \text{ K}$ ($\Delta T_c^{\text{PT}} = 16 \text{ K}$) confirming the reversibility of the two-step SCO process and of the PT. The enthalpy and entropy changes of the PT averaged over both runs, $\Delta H^{\text{PT}} = 3.94 \text{ kJ mol}^{-1}$ and $\Delta S^{\text{PT}} = 14.29 \text{ J K}^{-1} \text{mol}^{-1}$, account for the substantial rearrangements associated with order/disorder events of the butyl groups and the anions (*vide infra*). The averaged enthalpy and entropy for the two low temperature peaks, $\Delta H_{\text{SCO}} = 10.3 \text{ kJ mol}^{-1}$ and $\Delta S_{\text{SCO}} = 59.5 \text{ J K}^{-1} \text{mol}^{-1}$, respectively, exceed values reported for each of the two transitions LS \leftrightarrow HS in 100P [$\Delta H_{\text{SCO}}(\text{LS}^1 \leftrightarrow \text{HS}^1) = 5.2 \text{ kJ mol}^{-1}$ and $\Delta S_{\text{SCO}}(\text{LS}^1 \leftrightarrow \text{HS}^1) = 41.6 \text{ J K}^{-1} \text{mol}^{-1}$; $\Delta H_{\text{SCO}}(\text{LS}^2 \leftrightarrow \text{HS}^1) = 6.8 \text{ kJ mol}^{-1}$ and $\Delta S_{\text{SCO}}(\text{LS}^2 \leftrightarrow \text{HS}^1) = 39.5 \text{ J K}^{-1} \text{mol}^{-1}$].^{11b}



SCO properties of 100P under pressure

The SCO properties of 100P (channel A and channel B) and 100As differ in critical temperatures, hysteresis width and more notably in nature (one or two step). The observed 30 K upward shift of the average critical temperature when replacing PF_6^- with AsF_6^- suggests the introduction of additional chemical pressure in 100As as a result of the slightly larger ionic radius of As. To support this hypothesis, we have investigated the effect of small applied hydrostatic pressure on the SCO behaviour of 100P. At ambient pressure, in the cooling mode (1 K min^{-1}), 100P displays essentially the behaviour of channel A. At a pressure of 0.11 GPa the SCO shifts upwards by 100 K, and, surprisingly, it becomes two-step with critical temperatures centred at $T_c^1 = 221 \text{ K}$ and $T_c^2 = 251 \text{ K}$, characterised by a hysteresis loop $\Delta T_c^1 = 13 \text{ K}$ and $\Delta T_c^2 = 39 \text{ K}$, respectively, and a well-defined intermediate plateau on heating as shown in Fig. 2. This SCO is practically that of 100As at ambient pressure. Increasing pressure up to 0.14 GPa shifts the transition to higher temperatures ($T_c^1 = 245 \text{ K}$, $\Delta T_c^1 = 13 \text{ K}$ and $T_c^2 = 285 \text{ K}$, $\Delta T_c^2 = 36 \text{ K}$). Interestingly, these results demonstrate very similar effects on the SCO of the complex cation whatever the nature of the applied pressure, *i.e.* external or “internal” generated by $\text{PF}_6^- \leftrightarrow \text{AsF}_6^-$ anion substitution. A second relevant finding is the hypersensitivity of 100P towards imposed external pressure with dependence $d\langle T_c \rangle / dp \approx 1000 \text{ K/GPa}$, where $\langle T_c \rangle = (T_{c1} + T_{c2})/2$, although the regularly observed value lies in the range of 150–200 K/GPa (ref. 14) (Fig. S2†).

Study of $[\text{Fe}_{1-x}\text{M}_x(\text{nBu-im})_3(\text{tren})](\text{P}_{1-y}\text{As}_y\text{F}_6)_2$ molecular alloys

The high sensitivity of the SCO properties of 100P to external hydrostatic pressure, also apparent when internal “chemical pressure” increases when replacing PF_6^- with AsF_6^- , prompted us to study solid solutions based on anion ($\text{PF}_6^- \rightarrow \text{AsF}_6^-$) and metal ($\text{Fe}^{\text{II}} \rightarrow \text{M}^{\text{II}}$) substitution. A series of solid solutions were prepared in the same way as 100P and 100As but containing mixtures of PF_6^- and AsF_6^- anions in a calculated

ratio. It was found that the PXRD profiles of 22As–56As, as well as of 21Zn and 17Ni, are indistinguishable from that of 100P (Fig. 3). On the other hand, for 71As, a shift/coalescence of diffraction peaks is observed in the high angle range, in addition to the change of peak intensity, although in the low angle range the diffraction patterns perfectly match that of 100P. These findings are consistent with the evolution of the magnetic properties on isostructural substitution in the aforementioned series.

Gradual substitution of PF_6^- with AsF_6^- anions continuously reshapes the original SCO behaviour of 100P stabilizing a phase which compares well with channel B. This is illustrated in Fig. 4b–g where the SCO of pristine 100P, recorded at scan rate 2 K min^{-1} , is also included for comparison (grey line). For 22As, channel A is prevailing and a low temperature hysteresis is still observed but an increase of the relaxation rate favouring channel B is obvious (Fig. 4b). Increasing the concentration of AsF_6^- in 29As, 38As, 46As and 56As progressively accelerates relaxation and suppresses channel A in favour of channel B, which finally in 71As produces a single-step hysteresis loop centred at $T_c = 171 \text{ K}$ with $\Delta T_c = 34 \text{ K}$. Further increase of AsF_6^- affords compound 86As that gives rise to a narrow two-step SCO similar to that of the pristine 100As (Fig. S3†). It is worth mentioning that the PT within the HS phase $\text{HS}^1 \leftrightarrow \text{HS}^2$ increases in amplitude and decreases in temperature as the amount of AsF_6^- increases in the molecular alloy (see Fig. S4†).

Interestingly, stabilization of channel A is achieved by partial substitution above a certain threshold value of Fe^{II} with Zn^{II} or Ni^{II} , *i.e.* $y \geq 0.21$ for Zn^{II} or $y \geq 0.17$ for Ni^{II} . The resulting isostructural solid solutions 21Zn or 17Ni display one step cooperative SCO with critical temperatures centred at $T_c = 117$ and 121 K , characterized by $\Delta T_c = 7$ and 3 K wide hysteresis loops, respectively, at any rate down to 0.5 K min^{-1} (Fig. 4h, for 17Ni see also Fig. S5†). The pure compound 100Ni shows a constant susceptibility value of $\chi_{\text{MT}} \approx 1.2 \text{ cm}^3 \text{ K mol}^{-1}$ in the

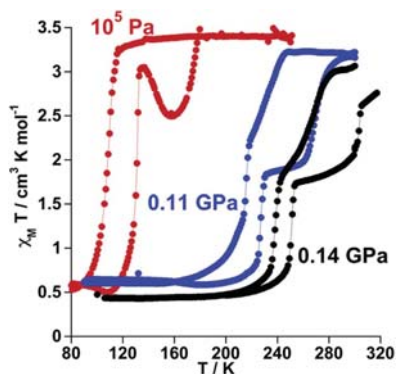


Fig. 2 Temperature dependence of χ_{MT} vs. T for 100P at different pressure values.

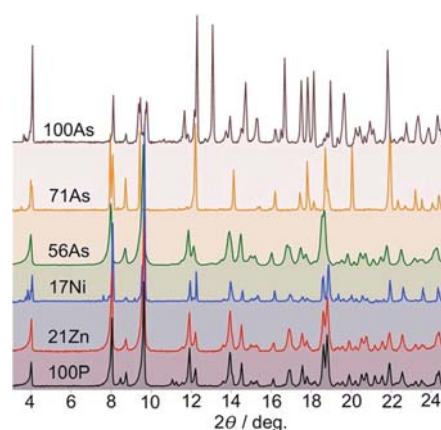


Fig. 3 X-ray powder diffraction patterns of indicated diluted compounds at RT.



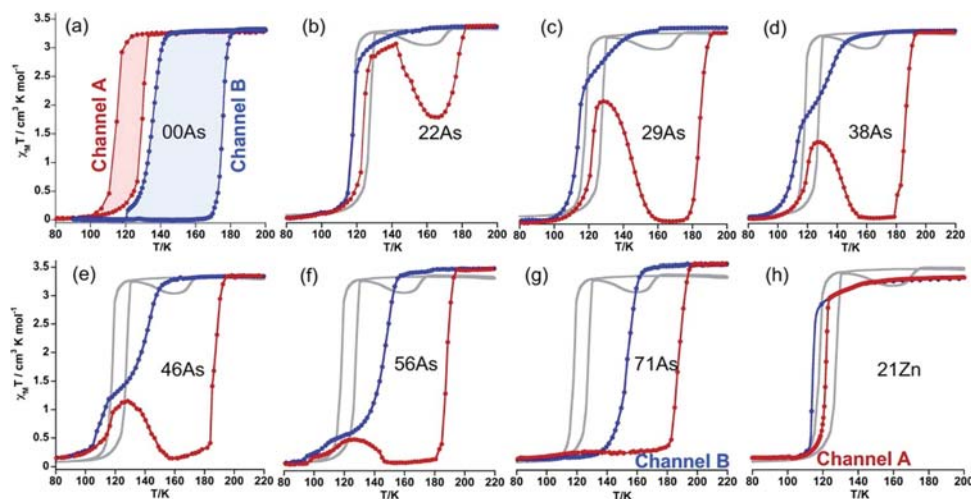


Fig. 4 (a) SCO behaviour of 100P, (red and blue curves measured at 4 K min⁻¹ and 0.25 K min⁻¹, respectively). (b–f) Influence of successive replacement of PF₆⁻ with AsF₆⁻ on the SCO properties. The red curve corresponds to heating, blue curve to cooling, and grey curve to the SCO of 100P measured at 2 K min⁻¹. (g and h) Effective separation of the two channels.

temperature range 50–300 K without any irregularities (Fig. S6†).

It is worth noting that despite the clear kinetic stabilization of channel B for 71As, thermal quenching allows trapping the sample into the hidden channel A. For example, after cooling 71As from 300 K to at ca. 800 K min⁻¹ the $\chi_{M}T$ value is essentially that of the Fe^{II} in the LS state (0.22 cm³ K mol⁻¹) (see Fig. 5). Then, when heating at 0.3 K min⁻¹, $\chi_{M}T$ increases to attain a value of 3.20 cm³ K mol⁻¹ at 127 K, indicating that the compound is essentially HS. Upon further heating the system first relaxes back to a LS phase and later attains the thermodynamically stable HS state.

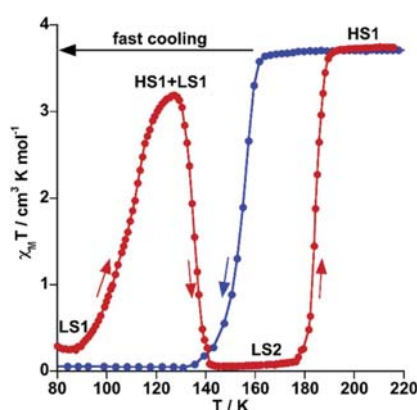


Fig. 5 Thermal quenching of the HS state for 71As. Blue and red filled circles correspond to the cooling and heating modes, respectively.

Structural analysis

Structure of 100As. Compound 100As is essentially a structural analogue of 100P. Based on the magnetic behaviour (see Fig. 1a and b), the crystal structure of 100As was investigated at 120 K, 230 K and 300 K where, respectively, the LS², HS¹ and HS² phases are stable. The transformation between these three phases involves two consecutive crystallographic PTs associated with important structural reorganisation, which involves remarkable volume change without symmetry changes (space group $P\bar{1}$, Table S1†). However, after many attempts, it was impossible to achieve a full structural analysis of the LS² phase because single crystals shatter during the HS¹ → LS² transformation. The same reason prevented us from structurally characterising the plateau centred at 190 K in the heating branch of the LS² → HS¹ transition. The unit cell consists of two crystallographically identical complex cations of opposite chirality and four AsF₆⁻ counterions (two crystallographically distinct sites, denoted as As1 and As2) balancing the charge. The Fe^{II} ion is wrapped by three *n*-butyl-1*H*-imidazol-2-ylimino moieties, defining a pseudo-octahedral [FeN₆] coordination environment (Fig. 6a), with Fe–N average bond lengths typical for the HS state and does not change substantially due to the PT: 2.199(4) Å and 2.190(7) Å at 230 K (HS¹) and 300 K (HS²), respectively (Fig. 6b, Table S2†).

Upside-down arranged complex molecules are self-organized in bilayer assemblies extending in the *ab* plane whereas the AsF₆⁻ anions occupy both surfaces and the inner space of the bilayer (Fig. 7). At 230 K (HS¹ phase), the inner space anions (As1F₆⁻) are substantially shifted from the centre whereas the axes of anions are inclined with respect to the layer plane; the anions are ordered as well as butyl substituents of the complex cations, arrangement 1 in Fig. 7. On passing the temperature of the PT, the

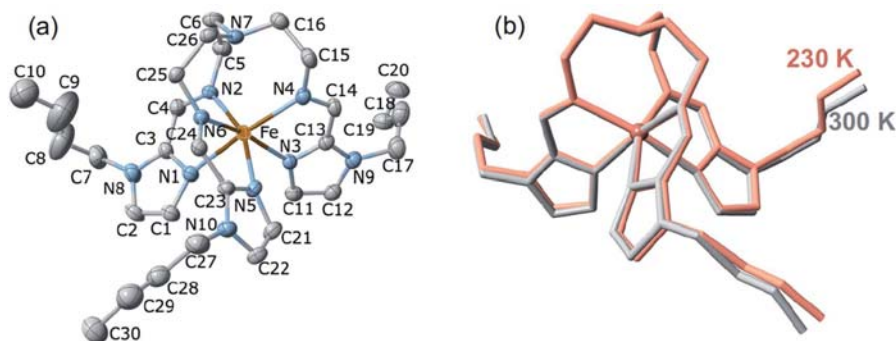


Fig. 6 (a) Projection of the cation of 100As with the atom numbering scheme at 230 K. Displacement ellipsoids are shown at the 30% probability level. Hydrogen atoms are omitted for clarity. (b) Minimized overlay of the complex cation in the HS¹ (red) and HS² (grey) phases.

anisotropic change of the lattice decreases the lattice parameter c by 0.44 Å that is reflected by the shrinking of the interlayer distance from 22.01 Å at 230 K down to 21.85 Å at 300 K. Furthermore, the PT promotes arrangement 2 (HS² phase), for which inner space anions AsF₆⁻ are located closer to the centre of the interspace between layers with their axes almost perpendicular to the layer plane (Fig. 7). Substantial disorder of the anions and butyl groups suggests that increasing entropy of the system is the driving force of the PT. Clearly, the transition is not related to the SCO as the coordination sphere of the Fe^{II} remains practically intact, although the rearranged anions and butyl groups change the pattern of intermolecular contacts CH...F in the lattice. For example, in the HS¹ phase one discrete interaction C24...F2(As1) = 3.087(4) Å is below the van der Waals radii (3.17 Å),¹⁵ in contrast to the HS² phase where no viable C...F contacts are operative. Furthermore, the percentage of weak intermolecular contacts C...F, N...H and C...H substantially changes due to

the PT too, see Table S4.† This lattice dynamics in close proximity to the metal centre seems to noticeably affect the ligand field strength/ g -factor and produce detectable magnetic bistability.¹⁶

It is worth recalling that similar structural rearrangement was observed for 100P. For cooling rates higher than 0.5 K min⁻¹, 100P displays arrangement 1 in the LS state (LS¹ phase) through channel A, while above $T_c^{PT} \approx 127$ K it adopts arrangement 2 (LS² phase) from channel B. Finally, on further heating it recovers arrangement 1 once the system reaches the HS state (HS¹ phase) just above $T_c^I = 176$ K (Fig. 3). It deserves to be noted the increase of disorder in the alkyl chains when both compounds adopt arrangement 2, see comparison of the colour mapped complex cation in pairs LS¹-LS² and HS¹-HS² in Fig. S7,† which is supposed to be the driving force of the observed PTs.

On cooling 100As, a second transition occurs as deduced from the magnetic data (Fig. 1a), however, the crystal rapidly

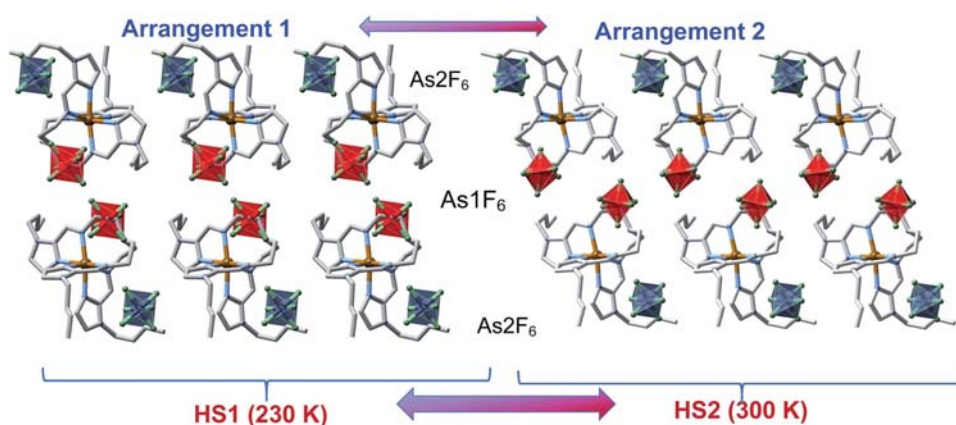


Fig. 7 Supramolecular bilayer organization of the complex molecules showing the location of the two crystallographically distinct AsF₆⁻/PF₆⁻ anions [blue As₂F₆⁻/P₂F₆⁻ and red As₁F₆⁻/P₁F₆⁻ octahedrons], illustrating arrangement 1 and arrangement 2.



and irreversibly deteriorates due to the SCO and therefore it was impossible to collect crystallographic data of the LS² phase at 120 K or of the intermediate plateau at 190 K.

Structure of 71As and 100Ni. The impossibility of obtaining sufficient structural information about the nature of the LS state of 100As prompted us to try more robust single crystals from the $x\text{AsF}_6^- : (100 - x)\text{PF}_6^-$ solid solutions. It was expected to obtain direct information not only about the type of arrangement adopted by the LS state in this solid solution, which could be extrapolated to 100As, but also to obtain structural information about the HS state, in particular that of the metastable quenched HS^{1q} at 120 K (see Fig. 5). Indeed, robust single crystals of $71\text{AsF}_6^- : 29\text{PF}_6^-$ (71As) appropriate for single crystal X-ray analysis were prepared. A single crystal of 71As was firstly measured at 230 K (see Tables S1 and S2†) where the structure presents, as expected, arrangement 1 and the Fe^{II} centres are in the HS state (average Fe–N distance = 2.196 Å). The whole cation complex is virtually identical to that of 100As including the conformation of the butyl groups. Afterwards, the same crystal was slowly cooled from 230 K to 120 K to avoid any thermal quenching, and then the temperature was increased up to 157 K to place the system in the middle of the LS branch of the hysteresis and measured at this temperature (see Fig. 5). The corresponding structure exhibits arrangement 2 for the counterions with the butyl groups showing strong configurational differences with respect to the structure at 230 K (Fig. 8a). According to the magnetic properties, the Fe–N average distance, 1.964 Å, shows the occurrence of a complete HS¹ → LS² phase transformation (Table S2†).

Another single crystal of 71As was cooled directly from 300 K to 120 K and the structure of the HS^{1q} phase was analysed (see Tables S1 and S2†). Despite the crystals being rather robust, we observed their deterioration during the measurement process due to relaxation from the quenched HS^{1q} to the LS² phase at 120 K. Consequently, in order to get reasonably good crystal data, initial partial data collection for the resolution of the structure was recorded. Indeed, this relaxation was slow enough to allow the acquisition of the required data (stable for *ca.* 45

min) to determine the structure before the collapse of the crystal. The analysis of the structure is consistent with the magnetic data and, based on the Fe–N average bond length, only *ca.* 5% of the Fe^{II} centres have relaxed to the LS² state. The metastable quenched HS^{1q} retains arrangement 1 of the parent HS¹ phase and the $[\text{Fe}(\textit{n}\text{Bu-im})_3(\text{tren})]^{2+}$ cation is essentially the same except for the butyl $[\text{Im-C7-C8-C9-C10}]$ which adopts a divergent configuration (see Fig. 8b).

The crystal structure of 100Ni, solved at 110 K, closely resembles that of 100P in LS¹ phase,^{11b} *i.e.* shows arrangement 1 (Fig. S8, Tables S1 and S3†).

Concluding remarks

The underlying reason for the observed rich magnetic behaviour of the systems 100P and 100As lies in their ability to exhibit ordered arrangement 1 and less ordered arrangement 2 in addition to the SCO transition between the HS and LS spin states. Both systems exhibit SCO behaviour synchronized with a structural PT featuring very slow kinetics compared with that of the SCO. Playing with this kinetics, the bistability domains of both transitions can overlap in temperature or can occur separately so that 100P and 100As can potentially form phases LS¹, HS¹ and LS², HS² and display transitions between them. Indeed, for 100P the phase bistability is operative in a temperature region overlapping with the SCO bistability giving the transition HS¹ → LS². Additionally, a narrow temperature window exists where the transition HS¹ → LS¹ occurs without change of the lattice arrangement. Moreover, the transition LS¹ → LS² is operative without change of the spin state but with a change of the lattice arrangement. The experimental data show the possibility of such transitions also for 100As and, additionally, at higher temperature another structural rearrangement HS¹ → HS² occurs within the HS state.

Thus, both systems can exhibit “ordered” LS¹ and HS¹ phases and “disordered” LS² and HS² phases. For 100As we observe all four phases, for 100P all except the HS², which is shifted so much in temperature that it does not occur below the melting

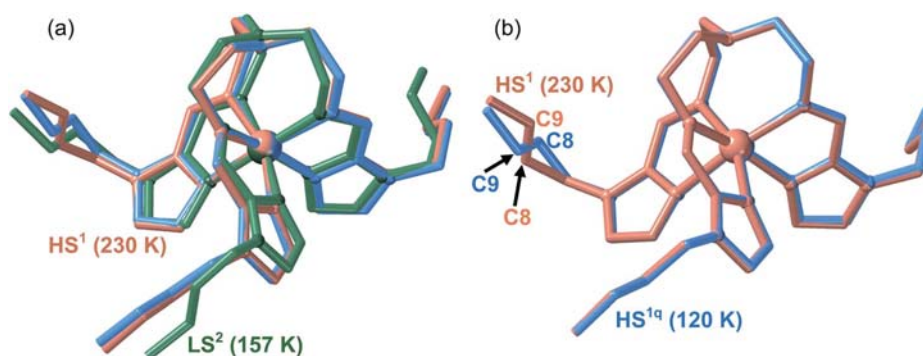


Fig. 8 Overlay of the complex cation in 71As: (a) combination of the HS¹ (red, 230 K) and LS² (green, 157 K) and HS^{1q} (blue, 120 K) phases; (b) combination of the HS¹ (red, 230 K) and HS^{1q} (blue, 120 K) phases showing the different configuration of the $[\text{Im-C7-C8-C9-C10}]$ moiety.



temperature of 100P. The transition to the arrangement 2 phase occurs because the disordered *n*-butyl chains increase the entropy and decrease the Gibbs free energy of the system. The more prone tendency of 100As to disorder can be associated with the small volume expansion of the lattice induced by the $\text{PF}_6^- \rightarrow \text{AsF}_6^-$ substitution and evidenced by the much faster kinetics featuring the $\text{LS}^2 \leftrightarrow \text{HS}^1$ transition. The slightly larger AsF_6^- anions separate the SCO complex cations, thereby facilitating their *n*-butyl groups to become disordered and favoring the phases LS^2 and HS^2 . This is corroborated by the transition $\text{HS}^1 \leftrightarrow \text{HS}^2$ (not coupled with the SCO) and by the fact that this transition is not observed for 100P.

The shift of the SCO and phase bistabilities of the PT on passing from 100P to 100As might be rationalized considering the “chemical pressure” (CP) of the anions as a qualitative measure of average intermolecular interactions and electrostatic pressure in the lattices. Indeed, external pressure applied to 100P progressively shifts the $\text{HS}^1 \leftrightarrow \text{LS}^2$ transition toward higher temperature and, more importantly, changes the hysteresis loop, which becomes two-step similarly to 100As. It is worth mentioning that the positive CP generated by application of “external” hydrostatic pressure increases the intermolecular contacts and stabilises the LS state by reducing the unit cell volume. In contrast, similar positive “internal” CP is generated upon $\text{PF}_6^- \rightarrow \text{AsF}_6^-$ substitution, which involves an increase of the unit cell volume in 42.44 \AA^3 . To explain this apparent paradox we compared the crystal structures of 100P and 100As at the same temperature (230 K) making use of the Hirshfeld surface analysis.¹⁷ This analysis shows that the percentage of C...F contacts doubles when replacing PF_6^- with AsF_6^- (more moderate increase of contacts is also observed for F...H and C...H) (Fig. S9, Table S4†). This can be rationalised from the estimated void space, 46.54 and 43.83 \AA^3 , available for 100P and 100As, respectively.¹⁷ Interestingly, the smaller empty space found for 100As shows that void space does not increase in parallel with the unit cell volume increase. This is the reason why the number of F...C contacts is larger for 100As, a fact in line with the observed increase of CP in 100As.

The similar chemical nature of both compounds makes them well suited for the study of the isomorphous series with varying ratio between the both. At a fixed scan rate of 2 K min^{-1} the kinetics of transitions $\text{HS}^1 \rightarrow \text{LS}^1$ and $\text{HS}^1 \rightarrow \text{LS}^2$ (memory channels A and B, respectively) is dramatically affected by changing the $\text{PF}_6^- : \text{AsF}_6^-$ ratio. This is reflected in the changing contribution of the two channels to the shape of the observed hysteresis loops. Progressively increasing the amount of AsF_6^- favours the SCO with structural rearrangement and makes the observation of the process $\text{HS}^1 \rightarrow \text{LS}^1$ impossible on passing a threshold concentration. Thus, for 71As the coalescence of the two hysteretic spin transitions vanishes affording a rectangular well-shaped hysteresis loop, which corresponds to the transition $\text{HS}^1 \rightarrow \text{LS}^2$ where the structural rearrangement is realized.

Opposite to the $[\text{Fe}(n\text{Bu-im})_3(\text{tren})](\text{P}_{1-y}\text{As}_y\text{F}_6)_2$ substituted systems, where included AsF_6^- anions create “positive” internal pressure and shift SCO upward in temperature, metal substitution in $[\text{Fe}_{1-x}\text{M}_x(n\text{Bu-im})_3(\text{tren})](\text{PF}_6)_2$ (21Zn or 17Ni) can be

considered as creating “negative” internal pressure, stabilizing low temperature SCO. Indeed, as follows from the experimental data, dilution with Zn^{II} or Ni^{II} ions, both more voluminous than the LS Fe^{II} ion, predictably favours the SCO transition to the more voluminous LS^1 phase and disfavours compact LS^2 (cell volume 1994.7(5) and $1950.8(15) \text{ \AA}^3$, respectively)^{11b} and makes the low temperature transition $\text{LS}^1 \leftrightarrow \text{HS}^1$ the only option for the system. Thus, metal dilution with the Ni^{II} or Zn^{II} stabilizes the voluminous arrangement 1 in both spin states and effectively suppresses the transition to arrangement 2.

In summary, we have reported an isomorphically substituted series of unusual Fe^{II} SCO complexes displaying two memory channels. We found that metal substitution with Ni^{II} or Zn^{II} selectively favours arrangement 1 in both spin states, thus promoting a low temperature hysteretic SCO transition (channel A). On the other hand, substitution of its PF_6^- anion with AsF_6^- promotes a high temperature hysteretic SCO transition (channel B) as a result of favoured transformation to disordered arrangement 2 in the LS state, and thus the high temperature hysteretic transition is preferred.

For the first time, we demonstrate that decoupling of two synchronous cooperative events such as SCO and intrinsic structural phase transitions can be chemically achieved by choosing the appropriate isomorphous substitution (metal ion or anion in the present case) to selectively discriminate between two separate hysteretic SCO behaviours. The design of fully controllable smart materials able to respond to external stimuli in a desired way is a challenging target in materials science. The results here reported support the idea that bistable molecular materials exhibiting synergetic interplay between two or more phase transitions in the same crystal are particularly well suited to this end.

Experimental

Materials

Synthesis of precursors. All chemicals were purchased from commercial sources and used without further purification. 1-Butyl-1*H*-imidazole-2-carbaldehyde and the complexes were synthesized according to the reported procedures.^{11b}

$[\text{Fe}(n\text{Bu-im})_3(\text{tren})](\text{AsF}_6)_2$ (100As). A filtered solution of $\text{FeCl}_2 \cdot 4\text{H}_2\text{O}$ (0.043 g, 0.21 mmol) in absolute ethanol (5 mL) was added dropwise to a boiling solution of 1-butyl-1*H*-imidazole-2-carbaldehyde (0.10 g, 0.65 mmol), tris(2-ethanolamine)amin (tren) (0.031 g, 0.21 mmol) and $[\text{TBA}]\text{AsF}_6$ (0.17 g, 0.43 mmol) in 5 mL of absolute ethanol. The resulting dark red-purple solution was stirred for 5 min. After keeping the solution for several days at $25 \text{ }^\circ\text{C}$ in a thermostat bath, well-shaped red-brown crystals of the product were formed and isolated. Calcd for $\text{C}_{30}\text{H}_{48}\text{As}_2\text{F}_{12}\text{FeN}_{10}$: C, 36.68; H, 5.01; N, 14.10. Found: C, 36.39; H, 5.35; N, 14.25.

Synthesis of substituted compounds. The series $[\text{Fe}(n\text{Bu-im})_3(\text{tren})](\text{P}_{1-y}\text{As}_y\text{F}_6)_2$ was synthesized in analogy to 100P and 100As by adding the appropriate mixture of $[\text{TBA}]\text{AsF}_6$ and $[\text{TBA}]\text{PF}_6$ salts to the freshly prepared ethanolic solution of the complex cation $[\text{Fe}(n\text{Bu-im})_3(\text{tren})]^{2+}$. Energy-dispersive X-ray spectroscopy (EDXS) was used to confirm the P and As





stoichiometry of the formed crystals: 100P (100% P, 0% As); 12As (88% P, 12% As); 22As (78% P, 22% As); 38As (62% P, 38% As); 46As (54% P, 46% As); 56As (44% P, 56% As); 63As (37% P, 63% As); 71As (29% P, 71% As); 86As (14% P, 86% As); 100As (0% P, 100% As). The successive replacement $\text{PF}_6^- \leftrightarrow \text{AsF}_6^-$ was semi-quantitatively monitored following their characteristic IR modes: $\nu_1(\text{PF}_6^-) = 839 \text{ cm}^{-1}$ (vs), $\nu_2(\text{PF}_6^-) = 557 \text{ cm}^{-1}$, $\nu_1(\text{AsF}_6^-) = 700 \text{ cm}^{-1}$ (vs) (see Fig. S10†).

Similarly, the solid solutions $[\text{Fe}_{1-x}\text{M}_x(\text{nBu-im})_3(\text{tren})](\text{PF}_6)_2$ ($\text{M} = \text{Zn}^{\text{II}}, \text{Ni}^{\text{II}}$) were confirmed *via* EDXS analysis: 17Ni (83% Fe, 17% Ni), 21Zn (79% Fe, 21% Zn).

Physical characterization

Magnetic measurements. Variable-temperature magnetic susceptibility data for bulk crystalline/microcrystalline samples $[\text{Fe}_{1-x}\text{M}_x(\text{nBu-im})_3(\text{tren})](\text{P}_{1-y}\text{As}_y\text{F}_6)_2$ (*ca.* 20 mg) were recorded with a Quantum Design MPMS2 SQUID susceptometer equipped with a 7 T magnet, operating at 1 T and at temperatures 10–400 K. Experimental susceptibilities were corrected for diamagnetism of the constituent atoms by the use of Pascal's constants. The LIESST experiments were performed at 10 K in a commercial sample holder (Quantum Design Fiber Optic Sample Holder), wherein a quartz bucket containing 0.75 mg of microcrystals of 100As was held against the end of a quartz fiber coupled with a red laser (633 nm). The raw data were corrected for a background arising from the sample holder. The resulting magnetic signal was calibrated by scaling to match the obtained high temperature values with those of the bulk sample. Magnetic measurements under pressure were performed on 100P using a hydrostatic pressure cell made of hardened beryllium bronze with silicon oil as the pressure transmitting medium and operating over the pressure range 10^5 to 10^9 Pa.¹⁸ The compound, 10 mg, was packed in a cylindrically shaped sample holder (1 mm in diameter and 5–7 mm in length) made up of very thin aluminum foil. The pressure was calibrated using the transition temperature of superconducting lead of high purity 99.999%.¹⁹

Calorimetric measurements. Differential scanning calorimetry measurements were performed using a Mettler Toledo DSC 821e calorimeter. Low temperatures were obtained with an aluminium block attached to the sample holder, refrigerated with a flow of liquid nitrogen and stabilized at a temperature of 110 K. The sample holder was kept in a dry box under a flow of dry nitrogen gas to avoid water condensation. The measurements were carried out using around 12 mg of microcrystalline 100As sealed in aluminium pans with a mechanical crimp. Temperature and heat flow calibrations were made with standard samples of indium by using its melting transition (429.6 K, 28.45 J g^{-1}). An overall accuracy of ± 0.2 K in temperature and $\pm 2\%$ in the heat capacity is estimated. The uncertainty increases for the determination of the anomalous enthalpy and entropy due to the subtraction of an unknown baseline.

Powder X-ray diffraction measurements (PXRD). PXRD measurements were performed on a PANalytical Empyrean X-ray powder diffractometer (monochromatic $\text{CuK}\alpha$ radiation).

Single crystal X-ray diffraction. Single-crystal X-ray data were collected with an Oxford diffraction supernova single crystal diffractometer using graphite monochromated $\text{MoK}\alpha$ radiation ($\lambda = 0.71073 \text{ \AA}$). A multi-scan absorption correction was performed. The structures were solved by direct methods using SHELXS-2014 and refined by full-matrix least squares on F^2 using SHELXL-2014.²⁰ Non-hydrogen atoms were refined anisotropically and hydrogen atoms were placed in calculated positions refined using idealized geometries (riding model) and assigned fixed isotropic displacement parameters. CCDC files CCDC 1879896–1879901 contain the supplementary crystallographic data for 100As (230 K), 100As (300 K), 71As (230 K), 71As (120 K), 71As (157 K), 100Ni (110 K), and CCDC 1892385 for 100P (230 K).†

Conflicts of interest

There are no conflicts to declare.

Acknowledgements

This work was supported by the Spanish Ministerio de Economía y Competitividad (MINECO), FEDER (CTQ2016-78341-P), Unidad de Excelencia María de Maeztu (MDM-2015-0538), and the Generalitat Valenciana through PROMETEO/2016/147 and an EU Framework Program for Research and Innovation (RISE project number 734322). F. J. V. M. and M. M. S. thank MINECO for a predoctoral (FPI) grant.

Notes and references

- (a) K. H. Bennemann, *J. Phys.: Condens. Matter*, 2011, **23**, 073202; (b) O. Sato, *Nat. Chem.*, 2016, **8**, 644–656; (c) S.-y. Koshihara, *J. Phys.: Conf. Ser.*, 2005, **21**, 7–14.
- (a) E. König, *Struct. Bonding*, 1991, **76**, 51–152; (b) P. Gütllich, A. Hauser and H. Spiering, *Angew. Chem., Int. Ed. Engl.*, 1994, **33**, 2024–2054; (c) J. A. Real, A. B. Gaspar, V. Niel and M. C. Muñoz, *Coord. Chem. Rev.*, 2003, **236**, 121–141; (d) *Spin Crossover in Transition Metal Compounds*, ed. P. Gütllich and H. Goodwin, *Top. Curr. Chem.*, 2004, vol. 233–235; (e) J. A. Real, A. B. Gaspar and M. C. Muñoz, *Dalton Trans.*, 2005, 2062–2079; (f) M. A. Halcrow, *Polyhedron*, 2007, **26**, 3523–3576; (g) A. Bousseksou, G. Molnár, L. Salmon and W. Nicolazzi, *Chem. Soc. Rev.*, 2011, **40**, 3313–3335.
- (a) O. Kahn and J. Martinez, *Science*, 1998, **279**, 44–48; (b) M. Ohba, K. Yoneda, G. Agusi, M. C. Munoz, A. B. Gaspar, J. A. Real, M. Yamasaki, H. Ando, Y. Nakao, S. Sakaki and S. Kitagawa, *Angew. Chem., Int. Ed.*, 2009, **48**, 4767–4771; (c) L. Salmon, G. Molnar, D. Zitouni, C. Quintero, C. Bergaud, J.-C. Micheau and A. Bousseksou, *J. Mater. Chem.*, 2010, **20**, 5499–5503; (d) F. Prins, M. Monrabal-Capilla, E. A. Osorio, E. Coronado and H. S. J. van der Zant, *Adv. Mater.*, 2011, **23**, 1545–1549; (e) M. Matsuda, K. Kiyoshima, R. Uchida, N. Kinoshita and H. Tajima, *Thin Solid Films*, 2013, **531**, 451–453; (f) H. J. Shepherd, I. y. A. Gural'skiy,

- C. M. Quintero, S. Tricard, L. Salmon, G. Molnár and A. Bousseksou, *Nat. Commun.*, 2013, **4**(1–9), 2607.
- 4 (a) H. Matsukizono, K. Kuroiwa and N. Kimizuka, *Chem. Lett.*, 2008, **37**, 446–447; (b) C. Lochenie, K. Schotz, F. Panzer, H. Kurz, B. Maier, F. Puchtler, S. Agarwal, A. Kohler and B. Weber, *J. Am. Chem. Soc.*, 2018, **140**, 700–709; (c) T. Delgado, M. Meneses-Sánchez, L. Piñeiro-López, C. Bartual-Murgui, M. C. Muñoz and J. A. Real, *Chem. Sci.*, 2018, **9**, 8446–8452.
- 5 (a) Y.-C. Chen, Y. Meng, Z.-P. Ni and M.-L. Tong, *J. Mater. Chem. C*, 2015, **3**, 945–949; (b) Y.-S. Koo and J. R. Galán-Mascarós, *Adv. Mater.*, 2014, **26**, 6785–6789.
- 6 S. Bonhommeau, P. G. Lacroix, D. Talaga, A. Bousseksou, M. Seredyuk, I. O. Fritsky and V. Rodriguez, *J. Phys. Chem. C*, 2012, **116**, 11251–11255.
- 7 (a) G. Molnar, S. Rat, L. Salmon, W. Nicolazzi and A. Bousseksou, *Adv. Mater.*, 2018, **30**(1–23), 17003862; (b) K. Senthil Kumar and M. Ruben, *Coord. Chem. Rev.*, 2017, **346**, 176–205.
- 8 (a) T. Tayagaki, A. Galet, G. Molnar, M. C. Muñoz, A. Zwick, K. Tanaka, J. A. Real and A. Bousseksou, *J. Phys. Chem. B*, 2005, **109**, 14859–14867; (b) C. Balde, C. Desplanches, P. Gutlich, E. Freysz and J. F. Letard, *Inorg. Chim. Acta*, 2008, **361**, 3529–3533; (c) Z. Yu, T. Kuroda-Sowa, H. Kume, T. Okubo, M. Maekawa and M. Munakata, *Bull. Chem. Soc. Jpn.*, 2009, **82**, 333–337; (d) P. Chakraborty, C. Enachescu, A. Humair, L. Egger, T. Delgado, A. Tissot, L. Guenee, C. Besnard, R. Bronisz and A. Hauser, *Dalton Trans.*, 2014, **43**, 17786–17796; (e) C. Baldé, C. Desplanches, J. F. Létard and G. Chastanet, *Polyhedron*, 2017, **123**, 138–144.
- 9 (a) C. A. Tovee, C. A. Kilner, J. A. Thomas and M. A. Halcrow, *CrystEngComm*, 2009, **11**, 2069–2077; (b) M. A. Halcrow, *Chem. Commun.*, 2010, **46**, 4761–4763.
- 10 (a) D. Braga, G. Cojazzi, D. Paolucci and F. Grepioni, *Chem. Commun.*, 2001, 803–804; (b) M. Zhao, H. Peng, J. Hu and Z. Han, *Sens. Actuators, B*, 2008, **129**, 953–957; (c) R. Zhang, H. Jifan, H. Zhouxiang, Z. Ma, W. Zhanlei, Y. Zhang and Q. Hongwei, *J. Rare Earths*, 2010, **28**, 591–595; (d) D. M. Pajeroski, T. Yamamoto and Y. Einaga, *Inorg. Chem.*, 2012, **51**, 3648–3655; (e) Y. Sun, Z. Zhu, J. Li, S. Gao, H. Xia, Z. You, Y. Wang and C. Tu, *Opt. Mater.*, 2015, **49**, 85–89; (f) S. Chorazy, J. J. Stanek, W. Nogaś, A. M. Majcher, M. Rams, M. Koziel, E. Juszyńska-Gałazka, K. Nakabayashi, S.-i. Ohkoshi, B. Sieklucka and R. Podgajny, *J. Am. Chem. Soc.*, 2016, **138**, 1635–1646.
- 11 (a) M. Seredyuk, A. B. Gaspar, V. Ksenofontov, Y. Galyametdinov, J. Kusz and P. Gütllich, *J. Am. Chem. Soc.*, 2008, **130**, 1431–1439; (b) M. Seredyuk, M. C. Muñoz, M. Castro, T. Romero-Morcillo, A. B. Gaspar and J. A. Real, *Chem.–Eur. J.*, 2013, **19**, 6591–6596; (c) M. Seredyuk, M. C. Muñoz, V. Ksenofontov, P. Gütllich, Y. Galyametdinov and J. A. Real, *Inorg. Chem.*, 2014, **53**, 8442–8454; (d) T. Romero-Morcillo, M. Seredyuk, M. C. Muñoz and J. A. Real, *Angew. Chem., Int. Ed.*, 2015, **54**, 14777–14781; (e) M. Seredyuk, K. Znovjyak, M. C. Munoz, Y. Galyametdinov, I. O. Fritsky and J. A. Real, *RSC Adv.*, 2016, **6**, 39627–39635; (f) T. Delgado, A. Tissot, L. Guénée, A. Hauser, F. J. Valverde-Muñoz, M. Seredyuk, J. A. Real, S. Pillet, E.-E. Bendeif and C. Besnard, *J. Am. Chem. Soc.*, 2018, **140**, 12870–12876.
- 12 (a) J. Jeftić, H. Romstedt and A. Hauser, *J. Phys. Chem. Solids*, 1996, **57**, 1743–1750; (b) S. Hayami, Y. Komatsu, T. Shimizu, H. Kamihata and Y. H. Lee, *Coord. Chem. Rev.*, 2011, **255**, 1981–1990; (c) S. Schlamp, B. Weber, A. D. Naik and Y. Garcia, *Chem. Commun.*, 2011, **47**, 7152–7154; (d) M. Yamasaki and T. Ishida, *J. Mater. Chem. C*, 2015, **3**, 7784–7787; (e) A. B. Gaspar and M. Seredyuk, *Coord. Chem. Rev.*, 2014, **268**, 41–58; (f) D. Rosario-Amorin, P. Dechambenoit, A. Bentaleb, M. Rouzières, C. Mathonière and R. Clérac, *J. Am. Chem. Soc.*, 2018, **140**, 98–101; (g) T. Fujinami, K. Nishi, D. Hamada, K. Murakami, N. Matsumoto, S. Iijima, M. Kojima and Y. Sunatsuki, *Inorg. Chem.*, 2015, **54**, 7291–7300; (h) T. Ueno, Y. Ii, T. Fujinami, N. Matsumoto, S. Iijima and Y. Sunatsuki, *Polyhedron*, 2017, **136**, 13–22; (i) M. Weselski, M. Książek, D. Rokosz, A. Dreczko, J. Kusz and R. Bronisz, *Chem. Commun.*, 2018, **54**, 3895–3898.
- 13 J. F. Létard, P. Guionneau, O. Nguyen, J. S. Costa, S. Marcen, G. Chastanet, M. Marchivie and L. Goux-Capes, *Chem.–Eur. J.*, 2005, **11**, 4582–4589.
- 14 V. Ksenofontov, A. B. Gaspar and P. Gütllich, *Top. Curr. Chem.*, 2004, **235**, 23–64.
- 15 A. Bondi, *J. Phys. Chem.*, 1964, **68**, 441–451.
- 16 G. Juhász, R. Matsuda, S. Kanegawa, K. Inoue, O. Sato and K. Yoshizawa, *J. Am. Chem. Soc.*, 2009, **131**, 4560–4561.
- 17 (a) M. J. Turner, J. J. Mckinnon, S. K. Wolff, D. J. Grimwood, P. R. Spackman, D. Jayatilaka and M. A. Spackman, *CrystalExplorer 17.5*, The University of Western Australia, 2018; (b) M. J. Turner, J. J. Mckinnon, D. Jayatilaka and P. R. Spackman, *CrystEngComm*, 2011, **13**, 1804–1813.
- 18 M. Baran, V. P. Dyakonov, L. Gladczuk, G. G. Levchenko, S. Piechota and G. Szymczak, *Phys. C*, 1995, **241**, 383–388.
- 19 A. Eiling and J. S. Schilling, *J. Phys. F: Met. Phys.*, 1981, **11**, 623–639.
- 20 G. M. Sheldrick, *Acta Crystallogr., Sect. C: Struct. Chem.*, 2015, **71**, 3–8.



Breaking the rule: access to thermodynamically prohibited “reverse” spin crossover in iron(II) complexes

Francisco Javier Valverde-Muñoz,^[a] Maksym Seredyuk,^{*[a,b]} M. Carmen Muñoz,^[c] and José A. Real^{*[a]}

Abstract: Modulation of the spin-crossover (SCO) behaviour by phase transitions in amphiphilic Fe^{II} complexes with aliphatic chains is a relevant strategy to find new cooperative behaviors and potential applications. In this context, we report on a series of charge neutral [Fe^{II}(Lⁿ)₂] meltable complexes based on Schiff bases Lⁿ = **pm2-n** or **pyH-n** derived from condensation of 2-pyrimidinyl ethyl ketone or pyridine aldehyde, respectively, with aromatic hydrazide functionalized with three aliphatic chains C_nH_{2n+1}. In the solid-state [Fe^{II}(**pm2-n**)₂] show two different crystal packing motifs depending on n. However, upon heating, the compounds melt into an isotropic phase and, due to releasing the solid-state effects, reveal identical SCO behaviour for all the compounds with the SCO transition midpoint temperature T_{1/2} ≈ 354 K. In contrast, in solid state, for short chain compounds (n = 4, 6, 8), T_{1/2} is far above 400 K in solid state, therefore they show an abrupt jump of the susceptibility on passing to the liquid phase. Cooling back shapes regular LS-to-HS (“forward”) spin transition hysteresis loop with the centre shifting down on n growth. For the long chain compounds (n = 10, 12, 14), the solid state T_{1/2} is at ca. 275 K, i.e. below the liquid value. Due to this, the long chain compounds on going to liquid phase show thermodynamically prohibited HS-to-LS (“reverse”) spin transition of up to 50 % of Fe^{II} ions, while the centre of the shaped hysteresis shifts up with increasing n. This finding is unprecedented and provides a method of guiding the spin transition direction and its location in temperature.

Introduction

The search for responsive materials with switching properties is a very active research area having prospects for future and emerging technologies.^[1] One of the most investigated switchable molecular materials are pseudo-octahedral Fe^{II} spin-crossover (SCO)

complexes, reversibly switching between the low-spin (LS, t_{2g}⁶e_g⁰) and high-spin (HS, t_{2g}⁴e_g²) electronic states by action of physicochemical stimuli (temperature, pressure, light, chemical substrates etc.).^[2] The LS-to-HS conversion on temperature rise is observed for the absolute majority of the SCO compounds in solution and in solid state.^[2b,c] The reason for this regular or “forward” SCO is that the process is an entropy-driven event due to noticeable metal-to-ligand bond lengths elongation on passing to the HS state and consequent increasing freedom degree of the systems. In the fluid phase the SCO process follows the Boltzmann population of the excited HS state, whereas in solid state, the intermolecular bonding and electrostatic interactions come into play that drastically changes completeness, cooperativity, and occurrence in temperature up to the stabilization of the LS or HS states. The adopted lattice type, the chemical nature of the ligand and the ligand substituents are among the most important factors influencing the SCO behavior.^[3]

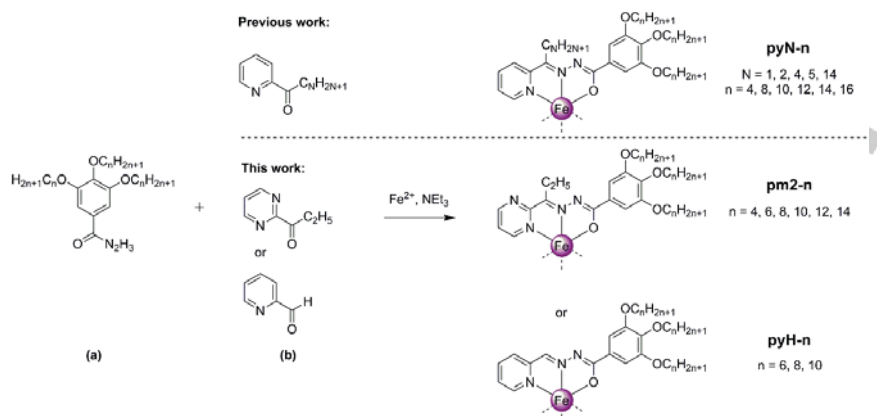
Particularly, aliphatic substituents in amphiphile SCO compounds are known to promote formation of two-dimensional lamellar packing with microphase separation to head-groups and aliphatic sublattices.^[4] The latter acts mostly as a buffer diminishing communication between SCO centers and deteriorating cooperativity with some exceptions^[5] but, on the other hand, aliphatic-based Fe^{II} compounds can form liquid crystalline phases due to the low melting character.^[6] That is, aliphatic compounds can exhibit “solid” SCO up to the melting point and, additionally, after melting to liquid crystalline phase can exhibit “liquid” SCO with partially or completely eliminated solid-state effects. If the manifestation of the two SCOs is different at the melting point, a jump-like change of the susceptibility is observed.^[7] Most of the meltable systems reported up to now, however, or suffer irreversibility on passing phase transition (PT) point,^[4, 8] or their melting to liquid crystalline does not substantially change the SCO,^[7a, 9] so that on melting/solidifying only a minor variation of the susceptibility is observed.

Further development of the concept of meltable SCO material lead us to understanding of essential criteria to achieve effective synchronicity between phase transition and SCO. We assumed that the compound should be: i) mononuclear Fe(II) complex with aromatic planar substituents for π-π interactions; ii) neutral to avoid buffering action of anions; iii) with optimal number of aliphatic substituents imparting controllable melting character to the compound; iv) meltable

[a] F.J. Valverde-Muñoz, Dr. M. Seredyuk, Prof. Dr. J. A. Real, Departament de Química Inorgànica, Institut de Ciència Molecular (ICMol), Universitat de València, Valencia, Spain.

[b] Dr. M. Seredyuk
Department of Chemistry, Taras Shevchenko National University of Kyiv, 64/13, Volodymyrska Street, Kyiv, Ukraine, 01601.

[c] Prof. Dr. M. C. Muñoz
Departament de Física Aplicada, Universitat Politècnica de València, Camino de Vera s/n, E-46022, Valencia, Spain.



Scheme 1. Synthetic procedure followed for the preparation of the series **pyN-n** ($m = 1, 2, 4, 5, 14$; $n = 4, 8, 10, 12, 14, 16$), **pm2-n** ($n = 4, 6, 8, 10, 12, 14$) and **pyH-n** ($n = 6, 8$).

directly to isotropic phase omitting ordered liquid crystalline phases. Following this line we reported on a series of aliphatic Fe^{II} neutral complexes **pyN-n**, derivatives of deprotonable Schiff base with the donor set NNO, obtained by condensation of aromatic hydrazide with three aliphatic $\text{C}_n\text{H}_{2n+1}$ groups (a) and 2-pyridinyl ketones with aliphatic substituent $\text{C}_n\text{H}_{2n+1}$ (b) (see Scheme 1). The complexes exhibit abrupt and perfectly reversible “forward” SCO upon melting to isotropic liquid, so that their magnetic curves resemble regularly observed hysteretic SCO transition of solid state compounds.^[10] We found, that the hysteresis width of the phase transition is a function of n , while the temperature of melting/solidification point is dependent on N . As a continuation of the work we report here new thermally isotropisable Fe^{II} complexes, derivatives of 2-pyrimidinyl ethyl ketone or 2-pyridine aldehyde, **pm2-n** or **pyH-n**, respectively (Scheme 1).

We found that on melting the complexes can display “forward” and additionally rare “reverse” SCO of Fe^{II} ions as a function of n . The “reverse” SCO is unexpected since it contradicts the fact that increasing temperature should favor the less ordered HS state of Fe^{II} . The thermally induced “reverse” HS-to-LS transition on temperature rise is known for aliphatic Co^{II} complexes undergoing solid-solid transitions,^[11] and also observed for a few Fe^{II} complexes on passing solid-solid^[5b, 12] or solid-liquid crystal phase transition.^[7b, 7e] However, the “reverse” SCO on heating is minor for all Fe^{II} compounds reported up to now due to substantial entropy loose on passing back the LS state which disfavors such a transition. This observation even raised the question on the origin of the effect, because the magnitude of the change might be attributed as well to the changing geometry of the coordination polyhedron and the corresponding g value associated with a crystal-to-crystal phase transition.^[5b, 12] A strong correlation of

the spin state on the adopted phase in the complexes reported here, however, demonstrates that the thermodynamically prohibited “reverse” SCO can be a realistic scenario for Fe^{II} compounds too and involve substantial fraction of the Fe^{II} SCO centers.

Results and Discussion

Magnetic properties

The magnetic behaviour of compounds **pm2-n**, recorded at 0.5 K min^{-1} is shown in figure 1 in the form of $\chi_M T$ vs T ($\chi_M T$ is molar susceptibility, T is temperature). Compound **pm2-4** is LS ($\chi_M T = 0$) in the whole temperature range while **pm2-6** and **pm2-8** undergo abrupt conversion from the LS state to paramagnetic state on melting and reach $\chi_M T$ of $2.7 \text{ cm}^3 \text{ K mol}^{-1}$ at 400 K for both compounds. Cooling down the samples leads to abrupt drop of the $\chi_M T$ back to zero at the solidification point. The shaped hysteresis is centered at $T_C^F = 366 \text{ K}$ with the loop width $\Delta T_h^F = 28 \text{ K}$ for **pm2-6**, and 352 K and 29 K, respectively, for **pm2-8** (F stands for “forward” SCO). Since both samples melt into a fluid phase, the SCO after melting is gradual as it obeys simple Boltzmann distribution.^[2a]

Compounds with longer chains behave differently. The homologue **pm2-10** shows gradual increase of $\chi_M T$ alternating with two abrupt drops on heating (Figure 1). Cooling down restores the initial gradual curve with a minor “reverse” SCO hysteresis loop at $T_C^R = 287 \text{ K}$, $\Delta T_h^R = 12 \text{ K}$ and a major loop at $T_C^R = 346 \text{ K}$, $\Delta T_h^R = 26 \text{ K}$ (R stands for “reverse” SCO). Compound **pm2-12**, behaves similarly to **pm2-10** but in the low temperature region it shows two minor anomalies of $\chi_M T$ centered at 288 and 320 K related to unidentified

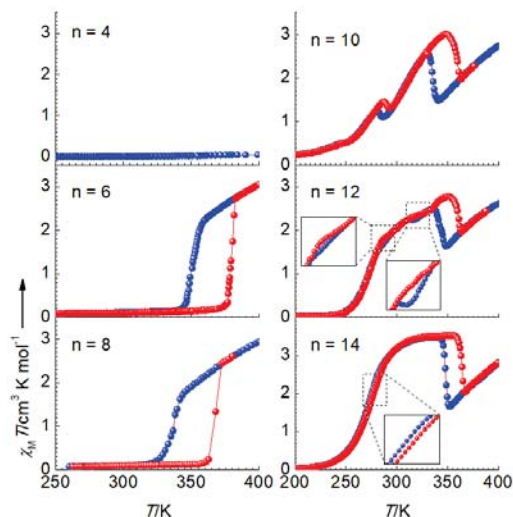


Figure 1. Temperature dependence of $\chi_M T$ vs T for annealed indicated compounds at 0.5 K min^{-1} . The insets show mismatch of cooling (blue) and heating (red) curves.

solid-solid phase transitions (Figure 1). The main reverse SCO hysteresis loop is located at $T_C^R = 351 \text{ K}$, $\Delta T_h^R = 21 \text{ K}$. On contrary, the compound **pm2-14** does not suffer interfering solid-solid phase transitions in the low temperature region and therefore shows complete regular SCO centered at $T_{1/2} = 275 \text{ K}$ with a 1 K wide hysteresis. Upon further heating a "reverse" SCO occurs with $T_C^R = 355 \text{ K}$, $\Delta T_h^R = 17 \text{ K}$. For the three compounds a trend towards rise "reverse" SCO midpoint temperature is observed with the highest value for **pm2-14**.

The percentage of Fe^{II} ions undergoing the phase transition driven SCO was evaluated for compounds **pm2-n** as a difference between $\chi_M T$ values of cooling and heating curves at temperature T_C^F or T_C^R , accounting that the complete SCO LS-to-HS corresponds to $\Delta\chi_M T = 3.52 \text{ cm}^3 \text{ K mol}^{-1}$ (as measured for **pm2-14** with complete SCO before melting). The calculated values are collected in Table 1.

The "forward" and "reverse" SCO in the studied compounds are sensitive to scan rate as higher rates greatly distort hysteresis loops due to the quenching of samples on cooling and subsequent relaxation on heating (Figure S6), which reflects the occurrence of a kinetically hindered crystallization process of the compounds. On the other hand, both "forward" and "reverse" SCOs are robust as follows from tests performed on samples **pm2-6** and **pm2-10** over ten heating-cooling cycles (Figure S9). It is well-known, that due to brittleness, the molecular SCO compounds suffer the self-grinding effect resulting in deterioration of SCO characteristics (completeness,

abruptness, hysteresis width), which is the major obstacle for a real physical application.^[13] In the case of **pm2-6** or **pm2-10** no sign of fatigue is observed, supposedly as a result of "self-healing" due to complete reversibility of changes on passing the melting/solidification point.

Worth to note, that the **pm2-n** series is not the only NNO-ligand based system displaying a switch from "forward" to "reverse" SCO on changing the aliphatic chain length. We found that compound **pyH-6** displays phase transition driven "forward" SCO at the melting point with $T_C^F = 340 \text{ K}$ and $\Delta T_h^F = 1 \text{ K}$ (Figure S5). For longer chains a gradual SCO in solid is observed which is interrupted on heating by a "reverse" SCO with $T_C^R = 346 \text{ K}$ and $\Delta T_h^R = 8 \text{ K}$ for **pyH-8**, and $T_C^R = 351 \text{ K}$ and $\Delta T_h^R = 3 \text{ K}$ for **pyH-10** (Figure S5). It should be said, however, that the effect of the "reverse" SCO is weaker for **pyH-n** in comparison to the **pm2-n** series, apparently because of a little difference between midpoint SCO temperatures in solid and fluid phase.

Table 1. Parameters of the hysteresis loops and thermodynamic parameters evaluated from the DSC profiles.

| Compound | T_C , K | ΔT_h , K | SCO type | % of Fe^{II} undergoing phase-transition driven SCO | ΔH , kJ mol^{-1} | ΔS , $\text{J K}^{-1} \text{ mol}^{-1}$ |
|---------------|-----------|------------------|----------|--|-----------------------------------|---|
| pm2-6 | 366 | 28 | forward | 60 | 46.9 | 128.1 |
| pm2-8 | 352 | 29 | forward | 50 | 46.6 | 132.3 |
| pm2-10 | 287 | 12 | reverse | 10 | 4.8 | 16.7 |
| | 346 | 26 | reverse | 43 | 54.0 | 156.1 |
| pm2-12 | 351 | 21 | reverse | 33 | 71.4 | 203.4 |
| pm2-14 | 355 | 17 | reverse | 50 | 66.3 | 186.8 |
| pyH-6 | 340 | 1 | forward | 58 | 4.0 | 11.7 |
| pyH-8 | 346 | 8 | reverse | 7 | 5.2 | 15.1 |
| pyH-10 | 351 | 4 | reverse | 6 | 8.4 | 23.8 |

Calorimetric measurements

Differential scanning calorimetry (DSC) experiments collected at 0.5 K min^{-1} reveal the presence of exothermic/endothemic processes on the cooling/warming paths, respectively, peaked at similar temperatures to those observed for the magnetic data of the compounds at 0.5 K min^{-1} (Table 1, Figure S7). The evaluated variations of enthalpy (ΔH) and entropy (ΔS) far exceed the corresponding typical values for strong cooperative SCO transitions (that is, $\Delta H \approx 20 \text{ kJ mol}^{-1}$ and $\Delta S \approx 100 \text{ kJ mol}^{-1}$).^[14] The thermodynamic values observed for the title compounds confirm occurrence of high-energetic processes of melting synchronized with the SCO.

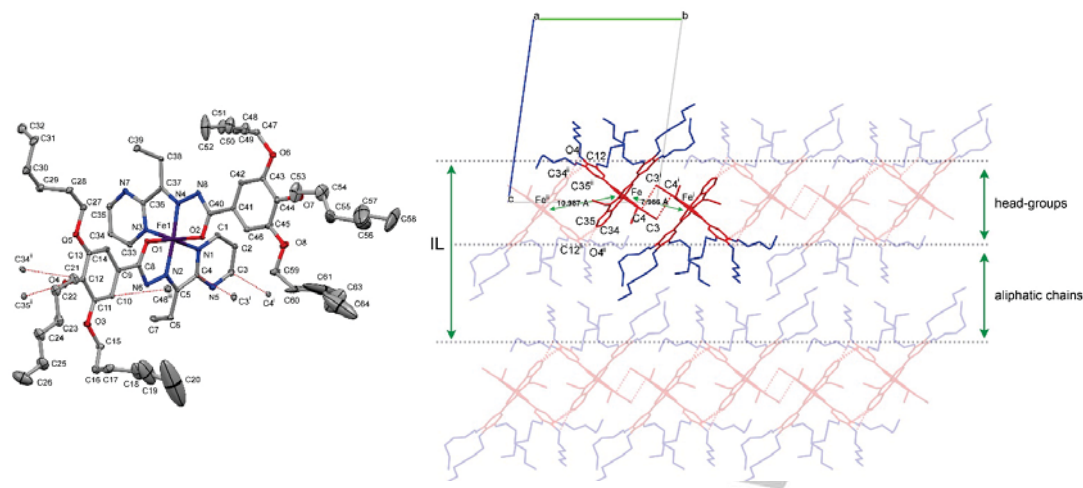


Figure 2. (Left) Molecular structure of **pm2-6** at 30% probability ellipsoids. Short inter-molecular contacts below sum of the van der Waals radii are shown as dashed lines. Symmetry codes: (i) $-x, -y, -z$; (ii) $-x, 1-y, -z$; (iii) $-1+x, y, z$. Displacement ellipsoids are drawn at the 30% probability level. The hydrogen atoms are omitted for clarity. (Right) Projection of the crystal lattice **pm2-6** along [100]. Highlighted is the supramolecular dimer of complex molecules with the shortest Fe...Fe separation. IL stands for inter-layer distance d^L . Symmetry codes: (i) $-x, -y, -z$; (ii) $-x, 1-y, -z$.

Structural characterization: single-crystal and powder X-ray diffraction

To structurally characterize the solid state structure of the as-synthesized and annealed compounds, the single crystal X-ray diffraction and powder X-ray diffraction studies were done. The study of **pm2-6** reveals that the Fe^{II}-center is located in a distorted octahedral N_4O_2 coordination environment generated by the two deprotonated ligand molecules (Figure 2; Tables S1 and S2). At 120 K, the average bond lengths, $\langle \text{Fe-N} \rangle = 1.901(3)$ Å and $\langle \text{Fe-O} \rangle = 1.962(3)$ Å, are within the region reported for LS Fe^{II} complexes of similar type.^[10, 13] Because of the asymmetric substitution of the ligand, the coordination part remains undecorated enabling effective displaced π - π stacking between coplanar pyrimidine rings of neighbour molecules in a dimer, the basic supramolecular fragment of the structure; the closest $\text{C}3 \cdots \text{C}4^i$ and $\text{C}4 \cdots \text{C}3^i$ contacts below the sum of the van der Waals radii are 3.313 Å, Fe...Feⁱ separation is 7.986 Å (i: $-x, -y, -z$) (Figure 2). The dimers are bound by inter-dimer contacts $\text{C}12 \cdots \text{C}34^i$, $\text{C}12 \cdots \text{C}35^i$ and $\text{O}4 \cdots \text{C}35^i$ (ii: $-x, 1-y, -z$), with separation 3.390, 3.388 and 3.143 Å, serially, into a 1D supramolecular chain along [010]; the closest Fe...Feⁱⁱ is 10.987 Å. Worth noting, that a similar pyridine-based complex with a methyl instead of ethyl substituent of ketone consists of uniform supramolecular chains with Fe...Fe separation of 7.676 Å.^[10] This points out a hampering of a closer approach of neighbour dimers due to the ethyl groups. The supramolecular chains are stacked in layers within [110] with the closest inter-chain separation coinciding with cell

parameter $a = 8.8252(3)$ Å. Finally, the layers are stacked into a lipid-like structure formed by alternating layers of head-groups and interlayer space filled by hexyl chains with methylene groups in *trans* and *gauche* conformations. Some chains are severely disordered (Figure 2).

Powder X-ray diffraction (PXRD) characterization of the as-synthesized compounds confirms the formation of highly crystalline lamellar structures (Figure 3a). For **pm2-6**, a good coincidence with the theoretical profile calculated from single crystals data is observed (Figure S2). At 400 K, all samples become fluid and display featureless XRD profiles corresponding to the isotropic phase (Figures 3b, S3).

Upon cooling the samples solidify and partially recover the crystalline character of the PXRD profiles (Figure 3c). The XRD profiles render well separated lamellar peaks up to the 6th order revealing retention of a long-range periodicity of annealed samples. The number of carbon atoms (n) plotted against the corresponding interlayer distance d^L , calculated from Miller's index peaks (10) (**pm2-6** and **pm-8**) or (20) (**pm2-10**, **pm2-12**, **pm2-14**) show a linear regression (Figure S4), thereby confirming their similar structural arrangement. However, similarly to the magnetic data, additional analysis of the profiles points out two subgroups of compounds. The diffractograms of annealed **pm2-6** and **pm2-8** manifest a broad peak with the barycentre at $2\theta \approx 11.5^\circ$, d -spacing = 7.7 Å, corresponding to the Fe...Fe stacking periodicity within sublattice formed by head-

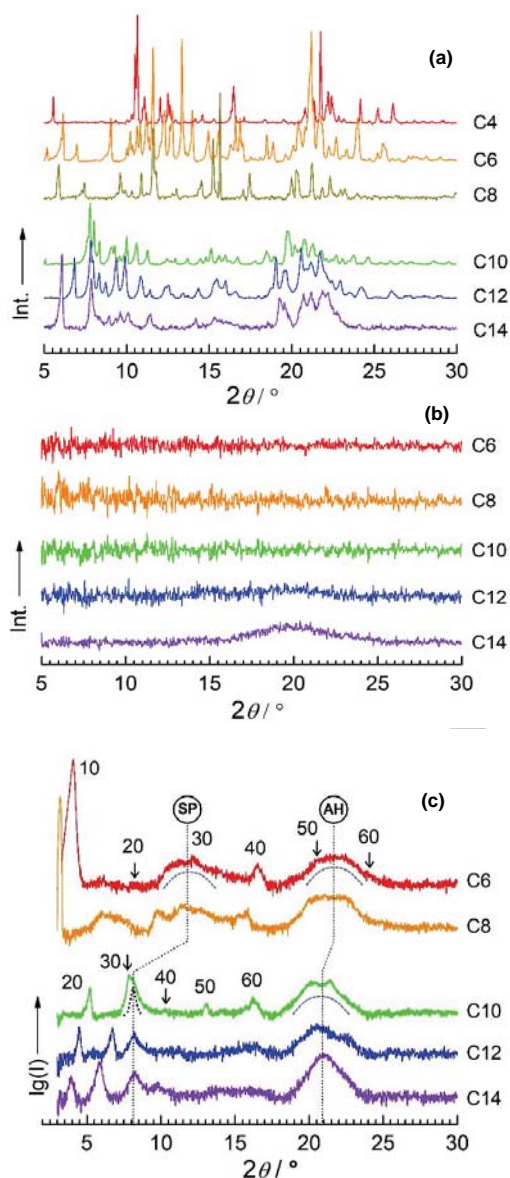


Figure 3. XRD profiles of **pm2-n** with indicated aliphatic chains: (a) as-synthesized at RT; (b) at 400 K; (c) after cooling at RT. SP stands for stacking periodicity; AH – for alkyl halo.

groups.^[16] This is an indication of retained uniform 1D supramolecular chains similarly to the reported crystalline and annealed pyridine-based systems (7.676 Å) also exhibiting “forward” SCO.^[10] For

annealed **pm2-10**, **pm2-12** and **pm2-14**, this stacking periodicity peak appears at 8.1° , d -spacing ≈ 10.9 Å, presumably reflecting formation of supramolecular chains with a larger separation Fe...Fe, similar the observed between dimers of the **pm2-6**. Another common feature of all profiles is the presence of a broad peak with the barycentres at $2\theta \approx 21.5^\circ$, d -spacing = 4.12 Å (**pm2-6**, **pm2-8**) or $2\theta \approx 21^\circ$, d -spacing = 4.21 Å (**pm2-10**, **pm2-12**, **pm2-14**), a signature of the aliphatic sublattice.^[17]

On the basis of the obtained experimental data we postulate different packing motifs for short and long chain compounds differently which contribute to on the macroscopic properties of solid samples. Indeed, lower n promotes formation of an aliphatic sublattice that stabilize dense packing with short Fe...Fe distances stabilizing the LS state of the Fe^{II} ions, while longer aliphatic chains fortuitously antagonises the dense packing of head-groups and stabilize the HS state.

Infrared spectroscopy

To elucidate the conformation of aliphatic chains, the IR absorptions spectra of the **pm2-n** compounds were evaluated.^[18] For chains with significant presence of *gauche* methylene units, the characteristic values of C–H groups lie in the regions 2924–2928 and 2854–2856 cm^{-1} for ν_{anti} and ν_{sym} absorption bands, respectively. For all-*trans* extended chains, the bands are in the regions 2915–2920 and 2846–2850 cm^{-1} , respectively. On this basis, for **pm2-6** and **pm2-8** the ν_{anti} at ca. 2925 cm^{-1} and ν_{sym} at ca. 2856 cm^{-1} suggest significant *gauche* population of aliphatic chains that corroborates the single crystal data of **pm2-6** (Figure 4). On the other hand, the peak

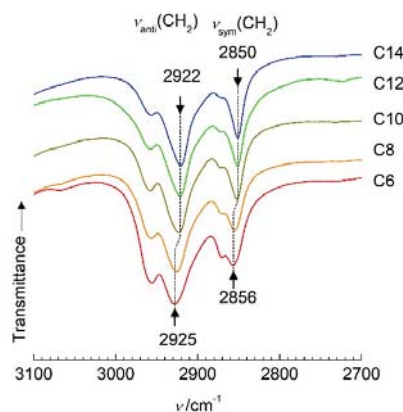


Figure 4. A fragment of the IR absorbance spectra of annealed **pm2-n** with indicated aliphatic chains showing the position of characteristic C–H absorption bands.

RESEARCH ARTICLE

frequencies at ca. 2922 and ca. 2850 cm^{-1} are suggesting that the majority of methylene units of aliphatic chains of **pm2-10**, **pm2-12**, **pm2-14** are in the *trans* conformation. Obviously, on passing from **pm2-8** to **pm2-10** we observe a change in conformation of aliphatic chains that impact their packing as follows from the changed position of aliphatic halo.

Conclusions

In summary, this report gives an excellent example of how the dependence of SCO properties on the adapted structure or state of matter aggregation can be exploited to control the SCO direction ("forward" or "reverse") and its occurrence in temperature. As discussed by Halcrow *et al.*, in solid state the lattice packing and caused therefore molecular deformation together with chemical pressure of the surrounding shift the intrinsic midpoint SCO value $T_{1/2}$ by $\Delta T(\text{latt})$ in temperature.^[19] We have discovered that within the series of the reported here compounds **pm2-n** the packing effect can vary from positive to negative with respect to the intrinsic SCO midpoint value $T_{1/2}$ observed under unconstrained conditions in fluid phase. Despite the precise study of the local structure of annealed **pm2-n** or **pyH-n** is a non-trivial task accounting their poorly ordered soft nature, the XRD and IR give the scent of the gross and local packing features in solid. As follows from the experimental data, after passing a threshold chain length n , which is 10 for **pm2-n** and 8 for **pyH-n**, aliphatic chains form a sublattice with the most of the methylene groups in *trans* conformation while shorter chains form sublattice with substantial fraction of *gauche* methylene groups. Different conformation of the chains is influencing their packing and in turn also the packing of covalently tethered head-groups. It was elucidated that shorter Fe^{II}-Fe distances are observed for short chains and larger distances for longer chains. The changed head-groups packing changes also the lattice contribution to the ligand field strength by affecting the incorporated Fe^{II} ions. This shifts the solid SCO transition midpoint below or above the corresponding value in fluid phase. On melting/solidification a jump-like change of the susceptibility is observed, while the hysteresis is reflecting the structural phase transition solid \leftrightarrow liquid.

We have demonstrated that up to 50% of Fe^{II} ions can be converted back to the LS state on heating, but, actually, there is no fundamental reason why the "reverse" SCO cannot be observed as a quantitative process with 100% HS-to-LS transition on temperature elevation. The approach reported here demonstrates that this is the question of the sufficient difference between midpoint SCO values on both sides of the phase transition. Further experimental efforts in this regard are underway.

Experimental Section

Synthesis of precursors and complexes: All chemicals were purchased from commercial suppliers and used without further purification. The long chain 3,4,5-triakoxybenzohydrazides and 2-pyrimidinyl ethyl ketone were synthesized according to the reported procedures.^[10] The complexes were obtained by condensation of 1 eq. of the corresponding hydrazide and 1.1 eq of ketone in abs. EtOH overnight in the presence of a two drop of glacial acetic acid and by subsequent complexation with 0.5 eq. of Fe(BF₄)₂·6H₂O to give a violet cationic complex. Then a green solution was obtained after deprotonation with 1 eq. of NET₃. The neutral complexes were isolated by slow cooling the solution to ambient temperature and subsequent filtering off the formed crystalline dark green precipitate.

Magnetic measurements: Variable-temperature magnetic susceptibility data (10 mg) were recorded on thermally treated samples (already heated up to 400 K) at the rate 0.5 K min⁻¹ with a Quantum Design MPMS2 SQUID susceptometer equipped with a 7 T magnet, operating at 1 T and at temperatures 10–400 K.

Calorimetric measurements: DSC measurements were performed on already heated samples on a Mettler Toledo TGA/SDTA 821e, in the 200–400 K temperature range under a nitrogen atmosphere with a rate of 0.5 K min⁻¹. The DSC data were analyzed with Netzsch Proteus software with an overall accuracy of 0.2 K in the temperature and 2% in the heat flow.

Powder X-ray diffraction measurements (PXRD): X-ray measurements were performed on a PANalytical Empyrean X-ray powder diffractometer (monochromatic Cu K α radiation). Each plot is superposition of three scans collected at the rate 5.6° min⁻¹. The interlayer distances were calculated according Bragg's equation.

Single-crystal X-ray diffraction: Single-crystal X-ray data of **pm2-6** were collected on a Nonius Kappa-CCD single crystal diffractometer using graphite mono-chromated MoK α radiation ($\lambda = 0.71073 \text{ \AA}$). A multi-scan absorption correction was performed. The structures were solved by direct methods using SHELXS-2014 and refined by full-matrix least squares on F^2 using SHELXL-2014.^[20] Non-hydrogen atoms were refined anisotropically and hydrogen atoms were placed in calculated positions refined using idealized geometries (riding model) and assigned fixed isotropic displacement parameters.

Acknowledgements

This work was supported by the Spanish Ministerio de Economía y Competitividad (MINECO), FEDER (CTQ2016-78341-P), Unidad de Excelencia María de Maeztu (MDM-2015-0538), and the Generalitat Valenciana through PROMETEO/2016/147 and an EU Framework Program for Research and Innovation (RISE project number 734322). F.J.V.M. thanks MINECO for a predoctoral (FPI) grant.

Keywords: spin-crossover • phase transition • soft matter • thermochromism • magnetism

- [1] (a) Koshihara, S.-y. *J. Phys.: Conf. Ser.* **2005**, *21*, 7. (b) Bennemann, K. *H. J. Phys. Condens. Matter.* **2011**, *23*, 073202. (c) Sato, O. *Nat. Chem.* **2016**, *8*, 644. (c) Senthil Kumar, K.; Ruben, M. *Coord. Chem. Rev.* **2017**, *346*, 176.

RESEARCH ARTICLE

- [2] (a) Gütlich, P.; Hauser, A.; Spiering, H. *Angew. Chem., Int. Ed. Engl.* **1994**, *33*, 2024. (b) *Spin Crossover in Transition Metal Compounds*, ed. Gütlich, P.; Goodwin, H. *Top. Curr. Chem.* **2004**, 233-235. (c) *Spin-Crossover Materials: Properties and Applications*, ed. Halcrow, M. A. **2013**.
- [3] (a) Halcrow, M. A. In *Spin-Crossover Materials: Properties and Applications*, **2013**, 147. (b) Gütlich, P.; Goodwin, H. A. *Top. Curr. Chem.* **2004**, 233, 1. (c) Halcrow, M. A. *Crystals* **2016**, *6*, 58.
- [4] (a) Zhang, W.; Zhao, F.; Liu, T.; Yuan, M.; Wang, Z. M.; Gao, S. *Inorg. Chem.* **2007**, *46*, 2541. (b) Galadzhun, I.; Kulmaczewski, R.; Cespedes, O.; Yamada, M.; Yoshinari, N.; Konno, T.; Halcrow, M. A. *Inorg. Chem.* **2018**, *57*, 13761.
- [5] (a) Schlamp, S.; Weber, B.; Naik, A. D.; Garcia, Y. *Chem. Commun.* **2011**, *47*, 7152. (b) Rosario-Amorin, D.; Dechambenoit, P.; Bentaleb, A.; Rouzières, M.; Mathonière, C.; Clérac, R. *J. Am. Chem. Soc.* **2018**, *140*, 98.
- [6] Gaspar, A. B.; Seredyuk, M. *Coord. Chem. Rev.* **2014**, *268*, 41.
- [7] (a) Seredyuk, M.; Gaspar, A. B.; Ksenofontov, V.; Galyametdinov, Y.; Kusz, J.; Gütlich, P. *Adv. Funct. Mater.* **2008**, *18*, 2089. (b) Seredyuk, M.; Gaspar, A. B.; Ksenofontov, V.; Galyametdinov, Y.; Kusz, J.; Gütlich, P. *J. Am. Chem. Soc.* **2008**, *130*, 1431. (c) Gaspar, A. B.; Seredyuk, M.; Gütlich, P. *Coord. Chem. Rev.* **2009**, *253*, 2399. (d) Lee, Y. H.; Ohta, A.; Yamamoto, Y.; Komatsu, Y.; Kato, K.; Shimizu, T.; Shinoda, H.; Hayami, S. *Polyhedron* **2011**, *30*, 3001. (e) Seredyuk, M.; Muñoz, M. C.; Ksenofontov, V.; Gütlich, P.; Galyametdinov, Y.; Real, J. A. *Inorg. Chem.* **2014**, *53*, 8442. (f) Fitzpatrick, A. J.; Martinho, P. N.; Gildea, B. J.; Holbrey, J. D.; Morgan, G. G. *Eur. J. Inorg. Chem.* **2016**, 385. (g) Seredyuk, M.; Znoviyak, K.; Muñoz, M. C.; Galyametdinov, J. A.; Fritsky, I. O.; Real, J. A. *RSC Adv.* **2016**, *6*, 39627.
- [8] (a) Bodenthin, Y.; Schwarz, G.; Tomkowicz, Z.; Geue, T.; Haase, W.; Pietsch, U.; Kurth, D. G. *J. Am. Chem. Soc.* **2009**, *131*, 2934. (b) Seredyuk, M. *Inorg. Chim. Acta* **2012**, *380*, 65. (c) Seredyuk, M.; Gaspar, A. B.; Ksenofontov, V.; Reiman, S.; Galyametdinov, Y.; Haase, W.; Rentschler, E.; Gütlich, P. *Hyperfine Interactions* **2005**, *166*, 385.
- [9] Akiyoshi, R.; Hirota, Y.; Kosumi, D.; Tsutsumi, M.; Nakamura, M.; Lindoy, L. F.; Hayami, S. *Chem. Sci.* **2019**, *10*, 5843.
- [10] Romero-Morcillo, T.; Seredyuk, M.; Muñoz, M. C.; Real, J. A. *Angew. Chem., Int. Ed.* **2015**, *54*, 14777.
- [11] (a) Agustí, G.; Bartual, C.; Martínez, V.; Muñoz-Lara, F. J.; Gaspar, A. B.; Muñoz, M. C.; Real, J. A. *New J. Chem.* **2009**, *33*, 1262-1267. (b) Hayami, S.; Komatsu, Y.; Shimizu, T.; Kamihata, H.; Lee, Y. H. *Coord. Chem. Rev.* **2011**, *255*, 1981. (c) Hayami, S.; Nakaya, M.; Ohmagari, H.; Alao, A. S.; Nakamura, M.; Ohtani, R.; Yamaguchi, R.; Kuroda-Sowa, t.; Clegg, J. K. *Dalton Trans.* **2015**, *44*, 9345.
- [12] (a) Valverde-Muñoz, F. J.; Seredyuk, M.; Meneses-Sanchez, M.; Muñoz, M. C.; Bartual-Murgui, C.; Real, J. A. *Chem. Sci.* **2019**, *10*, 3807. (b) Wéselski, M.; Książek, M.; Mess, P.; Kusz, J.; Bronisz, R. *Chem. Commun.* **2019**, *55*, 7033.
- [13] (a) Niel, V.; Muñoz, M. C.; Gaspar, A. B.; Galet, A.; Levchenko, G.; Real, J. A. *Chem.-Eur. J.* **2002**, *8*, 2446. (b) Miyazaki, Y.; Nakamoto, T.; Ikeuchi, S.; Saito, K.; Inaba, A.; Sorai, M.; Tojo, T.; Atake, T.; Matouzenko, G. S.; Zein, S.; Borshch, S. A. *J. Phys. Chem. B* **2007**, *111*, 12508. (c) Varret, F.; Siimani, A.; Boukheddaden, K.; Chong, C.; Mishra, H.; Collet, E.; Haasnoot, J.; Pillet, S. *New J. Chem.* **2011**, *35*, 2333. (d) Senthil Kumar, K.; Heinrich, B.; Vela, S.; Moreno-Pineda, E.; Bailly, C.; Ruben, M. *Dalton Trans.* **2019**, *48*, 3825.
- [14] Muñoz, M. C.; Real, J. A. *Coord. Chem. Rev.* **2011**, *255*, 2068.
- [15] Nakanishi, T.; Sato, O. *Crystals* **2016**, *6*, 131.
- [16] Weihermüller, J.; Schlamp, S.; Milius, W.; Puchter, F.; Breu, J.; Rammig, P.; Hüttner, S.; Agarwal, S.; Göbel, C.; Hund, M.; Papastavrou, G.; Weber, B. *J. Mater. Chem. C* **2019**, *7*, 1151.
- [17] Dorset, D. L. *Crystallography of the polymethylene chain: an inquiry into the structure of waxes* Oxford University Press, Oxford, New York, **2005**.
- [18] (a) Fujigaya, T.; Jiang, D. L.; Aida, T. *J. Am. Chem. Soc.* **2003**, *125*, 14690. (b) Park, S.-H.; Lee, C. E. *Chem. Mater.* **2006**, *18*, 981.
- [19] Halcrow, M. A.; Capel Berdiell, I.; Pask, C. M.; Kulmaczewski, R. *Inorg. Chem.* **2019**, *58*, 9811.
- [20] Sheldrick, G. *Acta Crystallogr. Sect.: C Struct. Chem.* **2005**, *71*, 3.

